

RESIDENCE AND PARTITIONING OF REE AND
SELECTED TRACE ELEMENTS IN AMPHIBOLITE-FACIES
METABASITES: AN EXAMPLE FROM THE ST. ANTHONY
COMPLEX, NORTHERN NEWFOUNDLAND

CENTRE FOR NEWFOUNDLAND STUDIES

**TOTAL OF 10 PAGES ONLY
MAY BE XEROXED**

(Without Author's Permission)

DANIEL JOSEPH MULROONEY

RESIDENCE AND PARTITIONING OF *REE* AND SELECTED TRACE ELEMENTS
IN AMPHIBOLITE-FACIES METABASITES: AN EXAMPLE FROM THE ST.
ANTHONY COMPLEX, NORTHERN NEWFOUNDLAND

by

© Daniel Joseph Mulrooney B.Sc. (Hons.)

A thesis submitted to the
School of Graduate Studies
in partial fulfilment of the degree of
Master of Science

Department of Earth Sciences
Memorial University of Newfoundland

2004

St. John's

Newfoundland



ABSTRACT

Metabasites from the metamorphic sole of the Hare Bay Allochthon, northern Newfoundland, exhibit a narrow metamorphic field gradient from greenschist- through epidote-amphibolite to amphibolite-facies. The metamorphic facies are defined from the distribution of the following mineral assemblages (all with quartz and titanite): chlorite-epidote-plagioclase-Ca amphibole (greenschist), Ca amphibole-plagioclase-epidote (epidote amphibolite), and Ca amphibole-plagioclase (plagioclase amphibolite). The assemblage Ca amphibole-plagioclase-garnet-biotite-apatite (biotite amphibolite) equilibrated in a K₂O-enriched shear-zone. Representative samples from each metamorphic facies were analyzed for rare earth elements (*REE*) and a suite of trace elements (Sc, V, Cr, Ni, Cu, Zn, Sr, Rb, Y, Zr, Nb) in bulk rocks and the major minerals Ca amphibole, plagioclase, epidote, titanite and garnet, by solution ICP-MS and laser-ablation microprobe (LAM)-ICP-MS respectively. Major-element concentrations of bulk rocks and minerals were determined by XRF and electron probe microanalysis (EPMA) respectively.

On the basis of bulk-rock, major- and trace-element data and chondrite-normalized *REE* data, two suites of metabasites were distinguished: (i) garnet-absent greenschist and amphibolite characterized by relatively low SiO₂ and Al₂O₃ and Y+*MREE*-enrichment; and (ii) garnet-bearing amphibolite with relatively low FeO_{total} + MgO, high P₂O₅ and Zr+*LREE* enrichment. The bulk P₂O₅ and *LREE* enrichment in

garnet-bearing rocks is inferred to be sequestered in unanalysed fine-grained apatite.

Ca amphibole, plagioclase, epidote, garnet and titanite exhibit systematic distributions of major- and most trace-elements, including *REE* in epidote amphibolite, plagioclase amphibolite and biotite amphibolite assemblages, indicating a close approach to equilibrium. However, variations in the distributions of a few trace elements (e.g., Rb and Nb between certain phases) suggest that equilibrium may not have been achieved for all elements at a thin-section scale.

In garnet-absent amphibolites, *LREE* are partitioned in the sequence titanite>epidote>>Ca amphibole>plagioclase, whereas *HREE* are partitioned in the sequence titanite>>Ca amphibole>epidote>>plagioclase. For biotite amphibolites, *LREE* and *HREE* are partitioned in the sequence titanite>>Ca amphibole ≈ plagioclase>garnet and titanite>garnet>>Ca amphibole>>plagioclase respectively.

Controls on trace-element incorporation in individual phases, and hence on partitioning behaviour, were qualitatively evaluated in this study. Crystal structure exerts a major control on trace-element partitioning so that the distribution of elements that occupy non-analogous sites in the two minerals (e.g., Sr in the *A* site in plagioclase and the *X* site in garnet) is characterized by a quasi-‘parabolic’ curve in Onuma-type diagrams in which distribution coefficients are plotted against ionic radius. Such diagrams are useful for the qualitative extraction of site parameters such as site radius and elasticity in the two minerals. In the case of mineral pairs that partition a trace

element on analogous sites in the two minerals (e.g., Ni in M^{VI} sites in Ca amphibole-epidote pairs), information on site size and elasticity is masked by interference between the similar competing sites and the qualitative extraction of site parameters is more problematic. In addition to crystallographic controls, several major-element compositional controls on trace-element incorporation in Ca amphibole, plagioclase, epidote and garnet were recognized and evaluated. For example, *REE* and Y partitioning into Ca amphibole, garnet and plagioclase are influenced by the major-element occupancy of the *M4*, *X* and *A* sites of these three phases respectively; and abundances of several divalent first row transition metals (Zn, Cu, Ni, Co) are positively correlated with the content of octahedral Al in *M3* sites in epidote.

Integration of mineral modes with trace-element mineral concentration data was carried out to determine mass balances for garnet-absent samples of similar bulk composition and the results were cross-checked against bulk-rock trace-element data. The results yield very good matches between the measured and reconstructed trace-element abundances in all cases, indicating that all the hosts for these elements had been analysed. They also illustrate the change in the relative importance of the four minerals, Ca amphibole, plagioclase, epidote and titanite, as carriers of the *REE* and analysed trace elements across the epidote-out isograd. In particular, they show that in most epidote-amphibolite, the trace-element enriched phases titanite and epidote, especially the former, are the dominant carriers of Y, Nb and all *REE*, accounting for approximately

Abstract

90% and 65% of the *LREE* and *HREE* budgets respectively despite their low modal abundances, and that the $\sum REE$ carried in plagioclase is negligible. However, where modal titanite and epidote are relatively less abundant (or where epidote is absent in plagioclase amphibolite), the relative capacities of these phases as trace-element or *REE* reservoirs are significantly diminished, Ca amphibole becomes the primary *REE* reservoir and $\sum REE$ in plagioclase is increased.

Major-element mineral compositions from representative epidote amphibolite and plagioclase amphibolite that straddle the epidote-out isograd were examined using the algebraic technique of singular value decomposition to quantitatively model the epidote-out reaction isograd. The following balanced reaction provides a realistic representation of the isograd, textures, and modal variations observed in natural samples throughout the study area:



where the superscripts 46 and 49 refer to compositions of minerals in samples below and above the epidote-out isograd respectively.

The results of evaluating the redistribution of selected trace elements and *REE* across the epidote-out isograd using the model reaction are compatible with the uptake of *LREE* by Ca amphibole, and to a lesser extent plagioclase, due to a reduction in *LREE* abundance in titanite and the breakdown of epidote. These linked changes indicate that there are both crystal-chemical and mineral assemblage controls on *REE* and trace-

Abstract

element partitioning in these rocks. This study illustrates the significance of the minerals epidote and titanite as the principal carriers of *REE* in epidote-amphibolite-facies metabasites and the quantitative estimation of partition coefficients shows that Ca amphibole acts as an important carrier for *REE* above the epidote-out isograd.

ACKNOWLEDGEMENTS

The production and completion of this thesis would not have been possible without the help of many people. To my supervisor Dr. Toby Rivers, I extend my sincere thanks and appreciation for suggesting and supervising this project. Toby's financial and academic support, coupled with his enthusiasm and willingness to discuss problems and offer constructive criticism related to this thesis were excellent. I thank him for providing me with an excellent learning opportunity. Many thanks are offered to the entire faculty and staff of the Department of Earth Sciences, in particular Robbie Hicks and Dr. Aphrodite Indares, whose flexibility enabled me to work as an instructional assistant during the completion of this thesis.

The technical staff of the Department of Earth Sciences are thanked for their significant contributions to this project, including Pam King (XRF), Lakamali Hewa (ICP-MS), Maggie Piranian (EPMA), and Mike Tubrett (LAM-ICP-MS). Their assistance with the preparation and completion of the analyses are what made this thesis possible. Rick Soper is thanked for preparation of thin sections and Darren Smith is acknowledged for his computer support. Maureen Moore, Ray Patzold, and Gerry Ford are thanked for their administrative support during this project. I also wish to thank Dr. Panseok Yang for freely sharing his extensive knowledge of trace-element distributions in metamorphic systems.

I am very grateful to my friends, many of whom are or were fellow graduate

Acknowledgements

students, for their support during completion of this thesis. To my good friends, John Hinchey, Darrell Hyde, Dixon Byrne, Allan Cuff, Ron Voorduow, Rod Smith, and Dr. Steve Piercey, thanks for the good times. I extend my special thanks to Mom, Dad, brother Vince, and sisters Cis and Trish, for their unwavering emotional, financial, and academic support during my university experience. Thanks M.A.P, for everything.

TABLE OF CONTENTS

ABSTRACT	ii
ACKNOWLEDGEMENTS	vii
TABLE OF CONTENTS	ix
LIST OF TABLES	xiv
LIST OF FIGURES	xvii
CHAPTER 1: INTRODUCTION	1
1.1 Introduction	1
1.2 Literature Review	3
1.2.1 <i>Trace-Element Partitioning Between Co-existing Metamorphic Minerals</i>	3
1.2.2 <i>Trace-Element Zoning in Metamorphic Minerals</i>	7
1.3 Geological Setting	10
1.3.1 <i>The Hare Bay Allochthon</i>	10
1.3.2 <i>The St. Anthony Complex</i>	13
1.3.3 <i>Lithological Units</i>	13
1.3.4 <i>Structure and Metamorphism</i>	15
1.3.5 <i>Summary</i>	20
1.4 Scope of Work	21
CHAPTER 2: PRINCIPLES OF TRACE-ELEMENT PARTITIONING AND ANALYTICAL METHODS	27
2.1 Introduction	27
2.2 Principles of Trace-Element Partitioning	28
2.2.1 <i>Trace Elements</i>	28

Table of Contents

2.2.2 <i>The Thermodynamics of Trace-Element Distribution</i>	30
2.2.3 <i>Mineral Structure and Trace-Element Substitution Schemes in Analysed Phases</i>	32
2.2.4 <i>Trace-Element Partition Coefficients</i>	36
2.2.5 <i>Mass Balances</i>	37
2.3 <i>Analytical Methods</i>	39
2.3.1 <i>Whole-rock analysis</i>	39
2.3.2 <i>Micro-Analysis</i>	40
2.3.3 <i>Modal Analysis</i>	43
CHAPTER 3: PETROGRAPHY, BULK-ROCK CHEMISTRY AND MAJOR- ELEMENT MINERAL CHEMISTRY	50
3.1 <i>Introduction</i>	50
3.2 <i>Petrography</i>	50
3.2.1 <i>The Goose Cove Schist</i>	51
3.2.2 <i>The Green Ridge Amphibolite</i>	54
3.2.3 <i>Summary</i>	55
3.3 <i>Bulk-Rock Chemistry</i>	56
3.3.1 <i>Bulk-Rock Major-Element Chemistry</i>	57
3.3.2 <i>Bulk-Rock Trace-Element Chemistry</i>	58
3.3.3 <i>Bulk-Rock Geochemical Classification</i>	59
3.4 <i>Major-Element Mineral Chemistry</i>	62
3.4.1 <i>Calcic Amphibole</i>	63
3.4.2 <i>Plagioclase</i>	65
3.4.3 <i>Epidote</i>	66
3.4.4 <i>Garnet</i>	67
3.4.5 <i>Titanite</i>	68
3.5 <i>Inferred Reactions across the Metamorphic Gradient</i>	68
CHAPTER 4: RARE EARTH MINERAL CHEMISTRY	97
4.1 <i>Introduction</i>	97

Table of Contents

4.2 Rare Earth Element Mineral Chemistry	98
4.2.1 <i>Calcic Amphibole</i>	98
4.2.2 <i>Plagioclase</i>	99
4.2.3 <i>Epidote</i>	100
4.2.4 <i>Garnet</i>	101
4.2.5 <i>Titanite</i>	101
4.2.6 <i>Eu Anomalies</i>	102
4.3 Rare Earth Element Distribution Coefficients	103
4.4 Controls on Rare Earth Element Partitioning	107
4.4.1 <i>Major-Element Compositional Effects on REE Partitioning</i>	107
4.4.2 <i>Structural Controls on REE Incorporation</i>	111
4.4.3 <i>REE Onuma-type Curves</i>	118
4.4.4 <i>Qualitative interpretations of site distributions of REE</i>	120
CHAPTER 5: TRACE-ELEMENT MINERAL CHEMISTRY	153
5.1 Introduction	153
5.2 Trace-Element Mineral Chemistry	154
5.3 Trace-Element Distribution Coefficients	157
5.4 Controls on Trace Element Partitioning	162
5.4.1 <i>Major-Element Compositional Effects on Trace-Element Partitioning</i>	162
5.4.2 <i>Crystal-structural Effects on Trace Element Partitioning</i>	166
5.4.3 <i>Trace-Element Onuma-type Curves</i>	171
CHAPTER 6: MASS-BALANCE AND REACTION-BALANCE CALCULATIONS	202
6.1 Introduction	202
6.2 Modal Abundance Data	203
6.3 Bulk Composition	204

Table of Contents

6.4 REE Mass Balance Calculations	208
6.4.1 Epidote Amphibolites: (10-3 modal % epidote)	208
6.4.2 Sample 49 - Plagioclase Amphibolite, 0 modal % epidote, bulk composition B	211
6.4.3 REE Mass Balance – Summary	212
6.5 Trace-Element Mass Balance for selected transition metals, LILEs and HFSEs	215
6.5.1 Epidote Amphibolites (10-3 modal % epidote)	216
6.5.2 Sample 49 - Plagioclase Amphibolite, 0 modal % epidote, bulk composition B	217
6.5.3 Trace-Element Mass Balance – Summary	218
6.6 Reaction Balancing: Algebraic Analysis of the Epidote-out reaction “Isograd”	221
6.6.1 Initial Subjective Assumptions	222
6.6.2 Phase Rule Variance of Assemblages	225
6.6.3 Mass Balance Analysis of Epidote-out Reaction Isograd using SVD	226
6.7 Redistribution of REEs and Selected Trace Elements Across the Epidote-out Isograd	229
6.7.1 Redistribution of REEs Across the Model Epidote-out Reaction Isograd	229
6.7.2 Redistribution of selected transition metals, LILEs and HFSEs Across the Model Epidote-out Reaction Isograd	232
CHAPTER 7: CONCLUSIONS	257
7.1 Introduction	257
7.2 Discussion of Results	258
7.2.1 Approach to Equilibrium	258
7.2.2 Trace-Element Partition Coefficients	260
7.2.3 Crystal-chemical Controls on Trace-Element Partitioning	262
7.2.4 Mass Balance Considerations	266
7.2.5 Epidote-out Reaction-Balance Considerations	268
7.3 Conclusions	271

Table of Contents

7.4 Directions for Further Study	276
REFERENCES	R1
APPENDIX A: EPMA and LAM-ICP-MS Data	A1
APPENDIX B: Assessment of Precision and Accuracy of Data	A34
APPENDIX C: Singular Value Decomposition Analysis	A46

LIST OF TABLES

Table 2.1	(a) General mineral formulae and cation site distribution of the five major phases in this study. Cation distributions based on mineral structure (Deer <i>et al.</i> , 1992) and the charge and size of the substituting cation (Smyth and Bish, 1988). See Figure 2.1 for explanation of element colours. C.N. # is the site coordination number.	47
	(b) Common end-member mineral formulae (Deer <i>et al.</i> , 1992) and the average site size of the major phases analyzed in this study. Average site sizes were obtained by subtracting the ionic radius of the O^{2-} ion (1.38Å) from the measured average-cation-oxygen-bond lengths (Smyth and Bish, 1988). C.N. # is the site coordination number.	48
	(c) Effective ionic radii of <i>REE</i> and analysed trace elements shown for appropriate ionic charge and coordination number (C.N. #) (taken from Shannon, 1976).	49
	(d) Chondrite normalization factors used in this study (after Taylor and McLennan, 1985).	49
Table 3.1	Petrography of the Goose Cove Schist metabasites	70
Table 3.2	Petrography of the Green Ridge Amphibolite metabasites	75
Table 3.3	Bulk-rock compositions of metabasites from the St. Anthony Complex determined by XRF and solution mode ICP-MS. EA is epidote amphibolite, PA is plagioclase amphibolite and GS is greenschist.	80
Table 3.4	(a-d) Average major element compositions and structural formulae of the five major minerals analysed in this study. <i>Italics</i> indicate Zr group.	87
Table 4.1	Average <i>REE</i> concentration (ppm) of the five major minerals by LAM-ICP-MS. <i>Italics</i> indicate Zr group. Blank indicates below detection limit.	122
Table 4.2	(a) Average values ($n = 3$) of $D^{Min1/Min2}$ for analysed mineral pairs. SD is the standard deviation at one sigma. No standard deviation represents single determination. Maximum values underlined. Blank indicates	

List of Tables

	below detection limits for one phase. <i>Italics</i> indicate Zr group.	131
	(b) Average values ($n = 3$) of $D^{Min1/Min2}$ for analysed mineral pairs. SD is the standard deviation at one sigma. No standard deviation represents single determination. Maximum values underlined. Blank indicates below detection limits for one phase. <i>Italics</i> indicate Zr group.	134
Table 5.1	Average absolute abundances of selected trace elements of the five major minerals analysed by LAM-ICP-MS. <i>Italics</i> indicate Zr group. Blank indicates element not determined.	177
Table 5.2	(a) Average values ($n = 3$) of $D^{Min1/Min2}$ for analysed mineral pairs. SD is the standard deviation at one sigma. No standard deviation represents single determination. Maximum values underlined. Blank indicates below detection limits for one phase. <i>Italics</i> indicate Zr group.	184
	(b) Average values ($n = 3$) of $D^{Min1/Min2}$ for analysed mineral pairs. SD is the standard deviation at one sigma. No standard deviation represents single determination. Maximum values underlined. Blank indicates below detection limits for one phase. <i>Italics</i> indicate Zr group.	187
Table 6.1	REE mass balance for selected samples. Reconstructed lanthanide concentrations are compared to the measured whole rock total as an independent quality control. See text for full explanation. Results presented here are illustrated in Figure 6.1(a-d).	238
Table 6.2	Trace element mass balance for selected samples. Reconstructed lanthanide concentrations are compared to the measured whole rock total as an independent quality control. See text for full explanation. Results presented here are illustrated in Figure 6.2(a-d).	245
Table 6.3	Model balanced epidote-out 'reaction' isograd based on SVD analysis of composite compositional matrix (M). Percent deviation from perfect mass balance given for percent difference of cations between product and reactant side. See text for explanation. One sigma error estimates based on average mineral cation abundances per formula unit (Appendix A). Reconstructed totals accepted if within three times 1 sigma analytical uncertainty.	252

List of Tables

- Table 6.4 Redistribution of *REE* among analysed phases using the balanced model epidote-out reaction isograd. Reconstructed concentrations based on measured abundances (Table 4.1) and reaction coefficients (Table 6.3). Percent deviation from perfect mass balance and relative enrichment factors for Ca amphibole, plagioclase and titanite based on the relative differences of reconstructed *REEs* between product and reactant side of *R* 6.1. See text for explanation. 253
- Table 6.5 Redistribution of selected trace elements among analysed phases using the balanced model epidote-out reaction isograd. Reconstructed concentrations based on measured abundances (Table 5.1) and reaction coefficients (Table 6.3). Percent deviation from perfect mass balance and relative enrichment factors for Ca amphibole, plagioclase and titanite based on the relative differences of reconstructed abundances between product and reactant side of *R* 6.1. See text for explanation. 255

LIST OF FIGURES

- Figure 1.1 General geology of the Hare Bay Allochthon, Great Northern Peninsula, Newfoundland (modified from Williams, 1995). Black box on inset map of Newfoundland shows location of Figure 1.1. Red box shows location of Figure 1.2. 23
- Figure 1.2 Simplified geological map of the southeastern part of the St. Anthony Complex showing metamorphic isograds (after Jamieson, 1979) and sample locations. Legend on facing page. 24
- Figure 1.3 Schematic diagram showing the assembly of the St. Anthony Complex within a high-temperature ductile shear zone and the preservation of residual mineral assemblages in zones of low strain (after Jamieson, 1986). The tectonic setting is inferred to have been in the upper part of a subduction zone, illustrated schematically at the top of the diagram. 26
- Figure 2.1 The periodic table of the elements, showing main groups of trace elements of interest in this study; the *REE* (yellow), first series transition elements (grey), *LILE* (green) and *HFSE* (blue). *Y* is not a *REE*, nor is it treated as a *REE* in this study. 44
- Figure 2.2 Activity-composition (a - X) relations for component y in phase A ; (i) ideal solutions (Raoult's Law), and (ii) non-ideal solutions, and (iii) for trace element components obeying Henry's Law (modified from Wood and Fraser, 1976). 45
- Figure 2.3 The structures of (a) amphibole (after Thompson, 1981), (b) plagioclase (after Nesse, 2000), (c) epidote (after Povarennykh, 1972), (d) garnet (after Novak and Gibbs, 1971), and (e) titanite (after Taylor and Brown). Open circles represent oxygens, tetrahedra are in yellow, octahedra are in grey. Red circles in (a) denote hydroxyl ions. Amphibole (a) is a cross sectional view parallel to double chains, crystallographic orientations shown in red (b), (c) and (e). Garnet (d) is cubic ($a = b = c$). 46
- Figure 3.1 (a-b) Deformed spotted' Goose Cove greenschist. Mineral aggregates (dashed white outlines) consist of fine-grained epidote, calcite, plagioclase and muscovite. Matrix consists of amphibole and chlorite. Both photomicrographs PPL, 2.5 cm horizontal field of view. 71

List of Figures

- Figure 3.2 (a) S_1 defined by amphibole and chlorite layering folded by F_2 in Goose Cove Schist. 72
(b) Folded S_1 fabric (defined by amphibole and chlorite) that is overprinted by S_2 . Horizontal field of view is 2cm in (a), 1 cm in (b). 72
- Figure 3.3 (a) Epidote amphibolite facies assemblage of the Goose Cove Schist. Horizontal field of view in 1.5 cm. (b) BSE image of epidote amphibolite. Notice 'patchy' zoning in epidote. 73
- Figure 3.4 Epidote-rich domain in epidote-amphibolite facies member of the Goose Cove Schist in (a) plane polarized light and (b) cross polarized light. Horizontal field of view is 2.5 cm. 74
- Figure 3.5 Biotite amphibolite from the Green Ridge Amphibolite showing porphyroclasts of garnet, hornblende and plagioclase in a matrix of biotite and quartz (a) PPL (b) XPL. Horizontal field of view is 2.5 cm. 76
- Figure 3.6 Illustration of textural variations within garnet porphyroclasts of the Green Ridge Amphibolite. Inclusions in (a) (XPL) exhibit concentric arrangement around the garnet core (horizontal field of view is 2.5 cm) whereas inclusions in (b) (PPL) are restricted to the garnet core (horizontal field of view is 2 cm). 77
- Figure 3.7 The general appearance of the plagioclase amphibolite member of the Green Ridge Amphibolite in (a) PPL and (b) XPL. Horizontal field of view is 2.5 cm. 78
- Figure 3.8 (a) Plagioclase amphibolite with green-brown hornblende and saussuritized plagioclase (PPL). 79
(b) Plagioclase amphibolite exhibiting typical corroded (sericitized) core (XPL). Horizontal field of view in both (a) and (b) is 2 cm. 79
- Figure 3.9 Bivariate plots for ten bulk rock major oxides analysed by XRF utilizing MgO as the abscissa. Group 1 (blue) with solid outline, group 2 (green) samples with dashed outline. The symbol r' is the Spearman rank correlation coefficient. MgO was selected as the independent variable since it is appropriate for rocks containing minerals with mafic end members. 82

List of Figures

- Figure 3.10 Chondrite-normalized *REE* chemistry of whole rocks in a) group 1, and b) group 2. Chondrite values from Taylor and McLennan (1985, see table 2.1d) 83
- Figure 3.11 Absolute abundances of trace elements other than *REE* in whole rocks a) group 1 and b) group 2 analysed by XRF and solution ICP-MS. 84
- Figure 3.12 (a) Jensen (1976) cation plot for the classification of volcanic rocks. All samples plot in the high-Fe tholeiite basalt field. 85
(b) ACF diagram showing the positions of common end-members in metabasites at greenschist to amphibolite-facies grade. 85
(c) Ti-Zr-Y diagram for basalts (after Pearce and Cann, 1973). Suite 1 samples are relatively Y-enriched whereas suite 2 rocks are relatively Zr-enriched. A, B, C, and D are possible tectono-magmatic affinities. 85
- Figure 3.13 Estimate of the relative bulk rock mass enrichment/depletion of (i) major oxides, (ii) *REE* and (iii) selected trace elements in Zr group samples from an amphibolite-facies shear zone. Normalization elements *italicized*. See text for explanation. 86
- Figure 3.14 (a) The clin amphibole rectangle showing the exchange vectors relating the compositions of FeMg clin amphiboles to calcic clin amphiboles and the limit of solid solution in both groups (after Leake *et al.*, 1997, 2003). Red dashed outline in (i) is enlarged in (ii). Two Y group samples (46, 48) are relatively Fe-Mg enriched relative to all other analysed samples 91
(b) The nomenclature of calcic amphiboles expressed as numbers of (Na + K)⁴ atoms in A sites and Si and tetrahedral Al^{IV} atoms per formula unit (after Leake *et al.*, 1997, 2003). □⁴ represents vacancy in the A site. Filled circles denote position of specific end-members. Y group shown with normal font, Zr group in *italics*. 92
(c) Diagram illustrating the relative role roles of the edenite and tschermak exchange vectors in analysed calcic amphibole. Analysed samples cluster into two group: (i) 'edenitic' amphibole with the edenite exchange the predominant substitution, and (ii) 'tschermakitic' amphibole with the tschermak exchange the predominant substitution. There is no clear trend for a dominant substitution vector. See text for full explanation. 93

List of Figures

- Figure 3.15 (a) Plagioclase compositions plotted in Ab-An-Or ternary composition space 94
(b) histogram showing plagioclase compositions expressed as X_{An}^{Pl} . Y group shown with normal font, Zr group in *italics*. 94
- Figure 3.16 (a) Epidote compositions on the basis of Al, Fe and Mn cation distribution in the $M3$ site of the ideal epidote formula $X_2M_3T_3(O,OH,F)_{13}$. 95
(b) Garnet compositions on the basis of dodecahedrally coordinated Fe, Mg, Mn and Ca. Compositions approach almandine. 95
- Figure 3.17 (i) Titanite compositions on the basis of octahedrally coordinated Fe^{3+} , Ti and Al. Fe^{3+} and Al are minor constituents in the octahedral site. Box represents area of enlargement for the Y and Zr groups, (ii) and (iii) respectively. 96
- Figure 4.1 Ca amphibole (a) and plagioclase (b) compositions on the basis of light, middle, and heavy *REE* distribution. In (a) 'edenitic' amphibole in dashed outline, 'tschermakitic' amphibole in solid outline. Note *LREE* enrichment in plagioclase in (b). 124
Epidote (c) and garnet (d) compositions on the basis of light, middle and heavy *REE* distribution. Epidote is *LREE* enriched whereas garnet incorporates middle and heavy *REE*. 125
Titanite (e) compositions on the basis of seven-fold coordinated light, middle and heavy *REE*. 126
- Figure 4.2 Chondrite-normalized *REE* diagrams for Y group amphibole (a) and Zr group amphibole (b) compositions. 127
Chondrite-normalized *REE* diagrams for Y group plagioclase (c) and Zr group plagioclase (d) compositions. 128
Chondrite-normalized *REE* diagrams for Y group epidote (e) and Zr group garnet (f) compositions. 129
Chondrite-normalized *REE* diagrams for Y group titanite (g) and Zr group titanite (h) compositions. 130
- Figure 4.3 (a) *REE* distribution coefficients (D_{REE}^* , left column and D_{REE} , right column) for six Y group mineral pairs. Error bars represent one standard deviation. Superscripts denote rock type (E = epidote amphibolite, P = plagioclase amphibolite). 137
(b) *REE* distribution coefficients (D_{REE}^* , left column and D_{REE} , right

List of Figures

- column) for six Zr group mineral pairs. Error bars represent one standard deviation. Superscript 'G' denotes biotite amphibolite. 139
- Figure 4.4 Bivariate plots showing correlations between major-element composition and *REE* concentration in a-b) Ca amphibole; c-d) plagioclase, e) epidote and f-g) garnet. r' denotes the Spearman rank correlation coefficient. 141
- Figure 4.5 Schematic illustration of the effect of lattice control on the shape of an ionic radius *versus* partition coefficient plot. In (a), melt exhibits no preference for selected elements and the partition plot approaches a parabola where the ideal ionic radius of a cation for a selected mineral site defines the vertex (i.e., Onuma Curve). In (b), the second mineral exhibits little preference for selected elements such that the partition plot is similar to (a). In (c), two minerals exhibit sites of different ideal radius, but similar elasticity such that concentrations of selected elements are similar. The resulting partition plot does not approach a parabolic shape. Red dashed lines show equal partitioning (modified from Yang, personal communication, 2003). 143
- Figure 4.6 Chondrite-normalized abundance curves for *REE* in : a-b) Ca amphibole; c-d) plagioclase; e) epidote; f) garnet and g-h) titanite. Major-element compositions of analysed indicated as mole fractions. Dashed lines are optimal site radius (r_o) obtained by subtracting the ionic radius of the O^{2-} anion (1.38\AA) from the observed average cation-oxygen bond length (Smyth and Bish, 1988). 144
- Figure 4.7 (a-l) Onuma-type $D_i^{*mineral1/mineral2}$ plots for *REE* in mineral pairs analysed by LAM-ICP-MS. Major-element compositions of analysed phases indicated as mole fractions. 146
- Figure 4.8 (a-g) Pairs of plots comprising mineral/chondrite and $D_{REE}^{*mineral1/mineral2}$ Onuma-type diagrams for Y group mineral pairs examined in this study. In mineral/chondrite plots, solid lines represent measured values, dashed lines are schematic representations of site properties (IR and elasticities) in the two minerals inferred from *REE* distributions. The shapes of the corresponding Onuma-type plots can be qualitatively derived by subtracting the site distribution curves for the two phases. Two pairs of diagrams are illustrated for Ca amphibole (low X_{Cum} and high X_{Cum}). 148

List of Figures

- Chondrite-normalization factors from Taylor and McLennan (1985). 148
- Figure 4.9 (a-e) Pairs of plots comprising mineral/chondrite and $D_{REE}^{*mineral1/mineral2}$ Onuma-type diagrams for Zr group mineral pairs examined in this study. In mineral/chondrite plots, solid lines represent measured values, dashed lines are schematic representations of site properties (IR and elasticities) in the two minerals inferred from REE distributions. The shapes of the corresponding Onuma-type plots can be qualitatively derived by subtracting the site distribution curves for the two phases. Chondrite-normalization factors from Taylor and McLennan (1985). 151
- Figure 5.1 Absolute abundances (ppm) of selected trace elements in Ca amphibole from the (a) Y group, and (b) Zr group. Blank indicates element not determined. 179
- Absolute abundances (ppm) of selected trace elements in plagioclase from the (c) Y group, and (d) Zr group. Blank indicates element not determined. 180
- Absolute abundances (ppm) of selected trace elements in (e) epidote (Y group) and, (f) garnet (Zr group). Blank indicates element not determined. 181
- Absolute abundances (ppm) of selected trace elements in titanite from the (g) Y group, and (h) Zr group. Blank indicates element not determined. 182
- Figure 5.2 (a-l) Trace-element concentrations Ca amphibole, plagioclase, epidote, garnet, titanite and whole rock. Y group samples arranged in order decreasing modal epidote. Zr group samples (*italicized*) comprise the garnet-amphibolite assemblage. 183
- Figure 5.3 Distribution coefficients (D and D*) for mineral pairs for selected trace elements. Y group samples arranged in order of decreasing modal epidote. Zr group samples (*italicized*) comprise the garnet-amphibolite assemblage. Error bars represent 1 standard deviation. 190
- Figure 5.4 (a-l) Bivariate plots showing correlations between major element composition and selected trace element concentration in analysed phases. r' denotes Spearman correlation coefficient. 196
- Figure 5.5 Chondrite-normalized trace element abundance *versus* ionic radius curves

List of Figures

- for Y and Zr groups in: a-b) Ca amphibole, c-d) plagioclase, e) epidote, f) garnet, and g-h) titanite. Major element compositions of analysed phases indicated as mole fractions. Dashed lines are optimal site radius (r_o) obtained by subtracting the ionic radius of the O^{2-} anion (1.38 Å) from the observed average cation-oxygen bond length (Smyth & Bish, 1988). Chondrite values from Taylor and McLennan (1985). 198
- Figure 5.6 (a-l) X_i mineral 1/ X_i mineral 2 (D_i^*) versus ionic radius plots (Onuma-type) for mineral pairs analysed by LAM-ICP-MS. Appropriate mole fractions shown for each phase. Superscripts denote rock type: E is epidote amphibolite, P is plagioclase amphibolite and G is garnet amphibolite. 200
- Figure 6.1 Bulk compositions of samples for which mass balances were calculated in terms of: a) ACF compositional space; b) chondrite-normalized *REE* chemistry, and; c) chondrite-normalized trace element chemistry. Chondrite normalization factors from Taylor and McLennan (1985). d) Illustration of the changes in modal epidote with changes in bulk-rock compositions in terms of, d) weight % CaO, Na₂O, Al₂O₃ and Fe₂O₃, and e), the ratios of the molecular proportions of Ca/Ca + Na and Fe³⁺/Al³⁺ + Fe³⁺. 236
- Figure 6.2 (a-d) Mass balance diagram for Y group samples (46, 48, 06, 49) showing the relative roles of amphibole, plagioclase, epidote, and titanite as *REE* carriers. Diagram(i) is a comparison of the reconstructed whole rock concentration (modal abundance x mineral concentration) compared to bulk rock *REE* concentration (measured by solution ICP MS). Diagram(ii) is the % difference between the reconstructed *REE* concentration and the measured whole rock concentration. Diagram(iii) is a bar graph illustrating the relative proportions of *REE* in each phase. 240
- Figure 6.3 Average *REE* concentrations (LAM-ICP-MS) and average reconstructed *REE* concentrations (measured x modal abundance) for samples 46+ 48 (relatively high modal titanite and epidote) relative to samples 06+49 (less modal titanite and epidote). 244
- Figure 6.4 (a-d) Mass balance diagram for Y group samples (46, 48, 06, 49) showing the relative roles of amphibole, plagioclase, epidote, and titanite as trace

List of Figures

element carriers. See Figure 6.1 for explanation of each diagram(i-iii). Selected transition metals include Sc-Zn, LILE include Sr and Rb, Y, Zr and Nb are HFSEs. 247

- Figure 6.5 Average trace-element concentrations (LAM-ICP-MS) and average reconstructed trace element concentrations (measured x modal abundance) for samples 46+ 48 (relatively high modal titanite and epidote) relative to samples 06+49 (less modal titanite and epidote).251
- Figure 6.6 (a) Bar graphs illustrating the relative proportions of *REEs* in each phase in samples 46 (below epidote-out isograd) and 49 (above isograd) on the basis of the model epidote-out reaction *R 6.1*. See text for explanation. (b) Bar graphs illustrating the relative differences in reconstructed mineral *REE* abundances above and below the isograd calculated as $[(49-46)/46]$. The percent difference of the reconstructed totals of all phases (including epidote) summed over the reactant and product side of the model reaction is calculated in the same manner (x 100) as the relative changes in *REE* mineral abundances. 254
- Figure 6.7 (a) Bar graphs illustrating the relative proportions of trace elements in each phase in samples 46 (below epidote-out isograd) and 49 (above isograd) on the basis of the model epidote-out reaction *R 6.1*. See text for explanation. (b) Bar graphs illustrating the relative differences in reconstructed trace-element mineral abundances above and below the isograd calculated as $[(49-46)/46]$. The percent difference of the reconstructed totals of all phases (including epidote) summed over the reactant and product side of the model reaction is calculated in the same manner (x 100) as the relative changes in trace-element mineral abundances. 256

Chapter 1: Introduction

1.1 Introduction

Significant portions of the Earth's lithosphere have undergone solid state recrystallization, or metamorphism, and a fundamental goal of metamorphic petrologists is to elucidate the conditions and dynamics of these changes. To accomplish this goal, numerous variables must be considered. These include, estimation of the intensive (P , T) and extensive (X) variables of metamorphism, the nature and kinetics of mineral reactions, the distance over which chemical equilibrium occurred, and the influence of deformation and the degree of re-equilibration on uplift following peak metamorphism.

Recrystallization can be viewed as the rearrangement of atoms between minerals in a metamorphic rock. In a pioneering study, Kretz (1959) showed that equilibrium element partitioning among co-existing metamorphic minerals has the potential to reflect metamorphic grade, and subsequently, in 1961 he developed the thermodynamic theory for the equilibrium distribution of elements between coexisting metamorphic minerals, thereby establishing the basis for geothermobarometry. Since then, metamorphic petrologists have focussed almost exclusively on major elements in partitioning studies, with the volume of information on trace-element partitioning remaining relatively small.

The limited investigation of trace-element distributions has mainly been due to the inherent difficulties in acquiring accurate trace-element analyses at the mineral scale. In the past, inaccuracies arose for several reasons. For instance, in some cases, high detection limits of a particular analytical technique, an instrumental cause, prevented accurate trace-element mineral analyses. More generally however, they were a result of the sampling method employed. The early studies generally used mineral separates, which are now known to potentially introduce problems associated with purity, the presence of inclusions, zoning or other forms of contamination that cannot readily be estimated or controlled. Thus, quantitative understanding of trace-element partitioning and the influence of temperature and pressure (i.e., metamorphic grade) and major-element composition in determining trace-element distribution coefficients is at an elementary level in metamorphic systems.

Trace elements have several advantages over major elements in petrogenetic studies because of their broad range in chemical properties such as ion size and charge. As a result, much potential exists in utilizing trace elements to examine the metamorphic process because they are usually more sensitive to metamorphic reactions and local chemical environments than major elements. Recent technological advances in several microbeam techniques with spatial resolution between one to tens of microns and limits of detection in the ppm to ppb range have enabled the goal of spatially resolved trace-element mineral analyses to be accomplished with considerable success. In this study,

trace-element distributions between coexisting metamorphic minerals in amphibolite-facies metabasites are investigated using a laser ablation system coupled to an ICP-MS. When integrated with major-element data, studies of trace-element distributions between coexisting metamorphic minerals enable a more complete insight into metamorphic processes.

1.2 Literature Review

1.2.1 Trace-Element Partitioning Between Co-existing Metamorphic Minerals

Analysis of trace-element distributions between co-existing metamorphic minerals in metapelitic and metabasic rocks began in earnest in the 1950's and continued through to the early 1970's (e.g., Devore, 1955a, 1955b, 1957; Kretz, 1959, 1961; Engel and Engel, 1960; Turekian and Phinney, 1962; Schwartz, 1967; Virgo, 1968; Curtis and Brown, 1971; Scotford, 1973). Devore (1955a, 1955b, 1957) compiled trace-element data from the available literature at the time and examined trace-element distributions in terms of several processes, including adsorption, crystal growth, ionic properties and bonding types. Kretz (1959) presented data for coexisting garnet, biotite, and hornblende from amphibolite-facies Grenville gneisses in terms of phase chemistry. Virgo (1968) considered the partitioning of strontium between K-feldspar and plagioclase. These early studies were based on the analyses of mineral separates by spectrographic techniques.

Although some useful results were obtained, problems with several of the data sets were evident. The high detection limits for certain elements afforded by emission spectroscopy and possible contamination during mineral separation may have contributed to inaccurate results.

Later studies involving mineral separates used more modern analytical techniques. For example, Sorensen and Grossman (1989, 1993) utilized X-ray fluorescence (XRF) and instrumental neutron activation (INA) to study trace-element enrichment in amphibolites from mélanges in Washington and California. They showed that amphibolites from both localities were enriched in rare earth elements (*REE*), high field strength elements (HFSE) and Th and that these elements were predominantly held in the minor and trace phases titanite, rutile, apatite, zircon and *REE*-rich epidote.

The XRF and INA techniques reached a mature state of development in the 1980's. More recently, the advent of solution ICP-MS (inductively coupled plasma mass spectrometry) has provided another analytical method for researchers to perform studies on the distribution of elements present in very low concentrations (i.e., sub-ppb level), but the technique also involves mineral separates and so is prone to potential problems resulting from zoning and contamination from micro-inclusions in host minerals of interest. For instance, Dahl *et al.* (1993) reported analyses of trace-element partitioning between biotite and muscovite mineral separates from metapelites using a solution ICP-MS method. They explored the effects of crystal chemistry, crystal field stabilization,

and temperature on the distribution of nearly 20 elements between biotite and muscovite occurring between the staurolite and the sillimanite zones. More recently, microprobe techniques have become available and been utilized to study trace-element distributions. For instance, Mazzucchelli *et al.* (1992) utilized an ion microprobe to study trace-element distributions between clinopyroxene and garnet in deep crustal metagabbro and Witt-Eickschen and Harte (1994) used the same technique to study trace-element partitioning between amphibole and clinopyroxene in peridotites from West Germany. Kretz *et al.* (1999) employed both bulk analysis techniques (XRF, INA) and probe techniques (particle-induced X-ray emission: PIXE) to elucidate the distribution of trace elements amongst mineral separates including garnet, pyroxene, hornblende, biotite, plagioclase and K-feldspar in granulites. They reported large variations in distribution coefficients for 23 elements, which they attributed to the degree to which equilibrium was attained in different samples, a function of the intensity, and rates of lattice and crystal boundary diffusion that they inferred are unique for the various elements analysed.

Several recent trace-element distribution studies have employed a laser ablation microprobe system coupled to a mass spectrometer (LAM-ICP-MS) which allows *in situ* trace element spot analyses and limits of detection as low as ppm or ppb. For instance, Bottazzi *et al.* (1999) utilized LAM ICP-MS to investigate site preferences for light and heavy *REE* in a variety of igneous amphibole species (pargasite, kaersutite and K-richterite) and showed that distinct ordering patterns for *REE* can be recognized from the

shape of Onuma curves constructed from accurately determined mineral—liquid *REE* distribution coefficients (D_{REE}). Yang *et al.* (1999) carried out an integrated LAM-ICP-MS, electron probe microanalyser (EPMA) study and reported on the crystal-chemical and thermal controls that govern trace-element partitioning between garnet and biotite in rocks that equilibrated in lower greenschist to upper amphibolite facies. They reported systematic distributions for some trace elements (i.e., V, Cr, Co, Zn) between garnet and biotite that are consistent with equilibrium partitioning during metamorphism. The data showed how the proportions of trace elements in garnet and biotite are controlled by bulk composition and the assemblage of co-existing minerals, as in the case of Zn depletion in garnet and biotite in the staurolite zone, inferred to be a result of the sequestration of this element in staurolite. They concluded that temperature, major-element composition, and ionic radius and charge all influence trace-element distributions between garnet and biotite. In a similar fashion, Yang and Rivers (2000) considered the structural, compositional, and thermal controls on the trace-element partitioning between coexisting biotite and muscovite from 10 metapelitic and quartzofeldspathic rocks.

In light of these results that indicate widespread equilibrium partitioning of trace elements, the non-systematic trace-element distributions that were reported in many of the earlier studies were likely produced by: (i) poor data quality because of the spectroscopic technique used, (ii) impurities and micro-inclusions in the analysed mineral separates, (iii) trace-element zoning in the analysed phases, and (iv) selection of

non-equilibrium mineral pairs. With respect to the latter point, disequilibrium partitioning of trace elements in studies involving mineral separates may also have been important because spatial relationships among grains are lost during crushing and mineral separation. The *in situ* analytical capability of probe instruments such as the LAM-ICP-MS, coupled with BSE imaging and/or X-ray mapping for selection of equilibrium mineral pairs enables many of these problems to be avoided (Yang *et al.*, 1999, Yang and Rivers, 2000).

1.2.2 Trace-Element Zoning in Metamorphic Minerals

Studies of trace-element zoning in conjunction with major-element zoning in metamorphic minerals (e.g., Hickmott *et al.*, 1987; Hickmott and Shimzu 1990; Hickmott and Spear, 1992; Griffin *et al.*, 1995; Fedorowich *et al.*, 1995; Lanzirotti, 1995; Schwandt *et al.*, 1996; Bea *et al.*, 1997; Chernoff and Carlson, 1999; Yang *et al.*, 1999; Yang and Rivers, 2001) have shed significant light on several metamorphic processes. Hickmott and co-workers (1987, 1990, 1992) focussed on trace-element zoning in garnet from pelitic rocks utilizing an ion microprobe. They measured trace-element zoning in amphibolite-facies garnet and reported peaks in zoning profiles for Na, Sc, V, Y, and the *HREE* that they correlated to portions of the major-element zoning profiles corresponding to a *P-T* reversal (determined from major-element distribution) and concluded that the peaks indicated short periods of open system (metasomatic)

behaviour. Hickmott and Shimizu (1990) reported irregular garnet zoning profiles for Ti, Cr, and V which they attributed to trapping of these elements on the garnet surface during rapid growth. Hickmott and Spear (1992) studied major- and trace-element zoning in garnet from calc-pelites. They identified key indicator trace elements for deciphering garnet-producing metamorphic reactions, and suggested that elevated concentrations of Sc, Y, Zr and *HREE* in garnet may implicate clinozoisite in the garnet-producing reaction, whereas they interpreted decreases in concentrations of Y, Zr, and *HREE* in garnet to indicate that clinozoisite grew in equilibrium with garnet.

Griffin *et al.* (1995) studied trace-element zoning in garnet from peridotite xenoliths using a proton microprobe and they also concluded from the zoning patterns that short periods of open system behaviour occurred during garnet growth. They reported that the relative lengths of zoning profiles for trace elements in garnet indicated that diffusion coefficients over the temperature range 1200-1400°C decreased in the order of $Ni \geq Fe$, $Mn > Ti$, $Zr \geq Y$ (and *HREE*) $\approx Ca > Cr, Ga, V$. Fedorowich *et al.* (1995) analysed trace-element abundances in pyrope-rich garnet using a LAM-ICP-MS and compared the results from analyses on the same garnets by electron microprobe, PIXE and nebulizer-mode ICP-MS. They concluded that the *in situ* LAM-ICP-MS method is unparalleled in terms of rapidity, ease of sample preparation and flexibility in the selection of external calibration standards and provides excellent data.

Other studies focussed on the pattern of zoning of specific trace elements in

garnet. For instance, Lanzirotti (1995) and Chernoff and Carlson (1999) examined Y zoning, and interpreted the oscillatory patterns in terms of kinetic factors, i.e., the slow diffusion of Y in garnet. In contrast, Yang and Rivers (2002) interpreted Y zoning in garnet to be related to local reaction history such as the breakdown of nearby Y-bearing phases such as apatite or epidote. Yang and Rivers (2001) used various techniques including X-ray mapping, and LAM-ICP-MS and EPMA analyses to assess controls on Cr and Mn zoning in amphibolite-facies garnet and kyanite. They emphasised that the growth rate may be a key factor in determining both the presence or absence of inclusions and the type of zoning exhibited by major and trace elements. They concluded that during fast growth, inclusions are preferentially incorporated into a porphyroblast and slow diffusing elements such as Cr are essentially immobile (overprint Cr zoning), whereas during slow growth, inclusions are not generally incorporated into a porphyroblast and Cr zoning is concentric.

Some trace-element geothermobarometers have recently been proposed. For instance, Pyle and Spear (2000) proposed a thermometer based on the negative correlation between Y concentration in garnet and temperature in xenotime-bearing metapelites. They reported a large decrease in Y concentration in garnet coexisting with xenotime from 5500 ppm to less than 100 ppm over a temperature range of 150°C. Bea *et al.* (1997) proposed a barometer based on the increase in concentration of REE in garnet with increasing pressure. This barometer is reported to be reliable within a range

of 4-9 kbar, but is strongly influenced by bulk-rock composition and appears most effective in rocks which have coexisting garnet and monazite.

This thesis involves an integrated EPMA/LAM-ICP-MS approach to study major- and trace-element behaviour of coexisting minerals in amphibolite-facies metabasites from northwestern Newfoundland. The regional geological framework of the region, previously described by Williams (1975, 1995) and Jamieson (1979) is outlined in the next section.

1.3 Geological Setting

1.3.1 The Hare Bay Allochthon

The Taconic Hare Bay Allochthon encompasses the area from Canada Bay to Cape Bauld on the Great Northern Peninsula of insular Newfoundland (Figure 1.1). It contains six separate rock units that make up distinct structural slices, with no single vertical section that contains all six rock units. The lowest structural slices comprise sedimentary rocks separated by *mélange* (*Northwest Arm, Maiden Point, and Irish formations*), overlain by a structurally higher *mélange* (*Milan Arm Mélange*) and volcanic rocks (*Cape Onion Formation*), which are capped by an ophiolite complex (*St. Anthony Complex*). The geology of the St. Anthony complex is best understood when viewed in its context as the highest structural slice of the Hare Bay Allochthon, the

Chapter 1: Introduction

tectonostratigraphy of which is briefly described below (Williams, 1975, 1995; Jamieson, 1979).

The structural base of the allochthon, the Northwest Arm slice, comprises sedimentary rocks of the *Northwest Arm Formation*, which are of limited areal extent and primarily occur at the western flank of the allochthon. The formation has a chaotic internal structure due to tectonic transport during formation of the allochthon, and comprises black and green shale, argillite, white to grey limestone and chert (Williams, 1995). Shale of the formation contains the graptolite *Staurograptus dichotomus* indicating a Tremadocian age (Tuke, 1968).

The *Maiden Point Formation* extends the entire length of the Hare Bay Allochthon and exhibits pre-emplacement west-facing recumbent folds as well as post-emplacement east-dipping upright folds. It comprises mainly quartzo-feldspathic conglomerate, greywacke, and slate with abundant blue quartz suggesting a provenance from the nearby Grenville basement. The formation also contains mafic agglomerate, tuff, and tholeiitic basalt (Williams, 1995).

The *Irish Formation* (Williams and Smyth, 1983) comprises quartzite breccia overlain by siliceous limestone and slate, and a thick unit of sandy limestone. The age of the formation is unknown, but the mixture of carbonate and sandstone has been inferred to indicate derivation from Lower and Middle Cambrian impure limestone and quartz sandstone near the base of the autochthonous sequence (Williams, 1995).

Williams (1975) described the *Milan Arm Mélange* as the best example of ophiolitic *mélange* in western Newfoundland. It comprises assorted igneous, metamorphic, and sedimentary blocks in a chaotically deformed black shale matrix. The commonest blocks include: serpentized peridotite, mafic volcanic rocks, amphibolite, foliated gabbro, greywacke, diorite, and coarse-grained pyroxenite and hornblendite associated with tonalite and hornblende-biotite schist.

The *Cape Onion Formation* comprises black to green variolitic pillow lava with isolated agglomerate and tuff units with subordinate black shale. These rocks are relatively undeformed compared to the underlying Maiden Point Formation and the overlying St. Anthony Complex. Many pillows retain their original shapes and fossiliferous shale interlayered with the volcanic rock is unclesaved. *Dictyonema flabelliforme* and other graptolites from the shale indicate the formation is Tremadocian in age (Williams, 1995).

The *St. Anthony Complex* is the highest structural slice of the Hare Bay Allochthon. The White Hills Peridotite at the top of the complex is typical of ultramafic rocks that occur at the stratigraphic base of ophiolite suites. The underlying Green Ridge Amphibolite, Goose Cove Schist and Ireland Point Volcanics constitute a metamorphic sole beneath the peridotite (Williams, 1995). The St. Anthony Complex is discussed in more detail in the next section.

1.3.2 The St. Anthony Complex

The study area (Figure 1.2) constitutes the metamorphic sole of the Hare Bay Allochthon and comprises a polygenetic assemblage of ultramafic and metavolcanic rocks. Metamorphic grade increases structurally upward towards the base of the peridotite, with the progression from relatively undeformed and unmetamorphosed mafic volcanics to greenschist and amphibolite being distinct enough to enable separation of the Ireland Point, Goose Cove, and Green Ridge formations. A summary of the geological history of the St. Anthony Complex, based principally on the work of Jamieson (1979, 1986) and Williams (1995) follows.

1.3.3 Lithological Units

Cooper (1937) named the mafic volcanic rocks exposed on the north side of Hare Bay the *Ireland Point Volcanics*. Agglomerate is the dominant lithology in the formation, occurring as an undeformed green unit with angular volcanic fragments from 2 to 15 cm in diameter and as green, red, and purple varieties consisting of amygdaloidal red and green lava fragments in a green to grey matrix. Pillow lava occurs locally in the agglomerate. Towards the top, volcanic fragments are flattened and contained in a schistose matrix which grades into the Goose Cove Schist (Williams, 1995).

The *Goose Cove Schist* surrounds the White Hills Peridotite in map view and also occurs on the Fishot Islands (Figure 1.1). This unit is a polydeformed and

metamorphosed sequence of green tuff, agglomerate and mafic pillow lava with thin units of greywacke, black pyritic slate and minor marble. Finely laminated dark schist is the most voluminous lithology. The laminations represent relict bedding in the tuffaceous rocks and in areas of greater strain indicate heterogeneity within the pyroclastic rocks. Other varieties of greenschist include tuff and agglomerate containing stretched volcanic fragments in a grey/green matrix and fine-grained massive altered rocks with deformed phenocrysts of plagioclase, which give the rocks a distinct “spotted” appearance. Greenschist at Goose Cove is infolded with black pyrite-bearing pelitic units and thin psammitic units. At Fishot Islands, tuff is interbedded with thin limestone beds. Heterogeneous strain has resulted in variation from semi-schist to intensely foliated varieties. Primary protolith features are only preserved in areas of low strain. The thickness of the unit is estimated to be 180 m (Williams, 1995).

Green Ridge Amphibolite refers to amphibolite and related higher grade metamorphic rocks which occur structurally above the Goose Cove Schist and beneath the White Hills Peridotite. The dominant lithology is green to black hornblende-plagioclase schist. The protolith of the schist is inferred to be mafic volcanic rocks and gabbro, although few primary features are preserved. Heterogeneity within the unit suggests a pyroclastic derivation whereas banded rocks likely represent tuffaceous protoliths. The hornblende-plagioclase schist coarsens from the base to the top of the formation where garnetiferous amphibolite becomes the predominant lithology

Chapter 1: Introduction

(Jamieson, 1979). Subordinate lithologies include garnet-biotite schist and marble which are interlayered with hornblende schist. Metagabbro occurs locally near the top of the formation beneath the White Hills. The estimated structural thickness of the formation is 120 m (Williams, 1995).

The *White Hills Peridotite* comprises ultramafic rocks which form a tabular peridotite sheet that outcrops in the eastern and western White Hills. Typical of ultramafics, these rocks are brown weathering and largely barren of vegetation. Harzburgite, dunite and minor pyroxenite comprise the unit. The harzburgite is medium to coarse grained and exhibits a strong foliation defined by flattened orthopyroxene. Fine-grained equigranular dunite exhibits a weaker foliation. Pyroxenite occurs as both primary layers within the main foliation and as a less conspicuous cross-cutting variety. Finely banded recrystallized rocks at the base of the White Hills Peridotite contain leucocratic bands of brown amphibole, colourless clinopyroxene, brown biotite, and garnet and alternate with melanocratic bands of serpentinite. The White Hills Peridotite is less than 300 m in structural thickness (Williams, 1995).

1.3.4 Structure and Metamorphism

Each unit of the St. Anthony Complex is characterized by a different structural style and metamorphic grade. In terms of their tectonic context, the metamorphic rocks of the St. Anthony Complex are best interpreted as a high-temperature shear zone formed

between cold lower-plate continental margin rocks and hot overriding oceanic lithosphere (Jamieson, 1979, 1986; Figure 1.3). High-grade rocks directly below the oceanic lithosphere exhibit retrograde assemblages in high-strain zones whereas lower-grade rocks display prograde metamorphism in high-strain zones. Mylonite zones in metabasites throughout the complex exhibit epidote-amphibolite-facies conditions. These relationships imply that the 'inverted metamorphic gradient' within the St. Anthony Complex results from the preservation of metamorphic assemblages at different levels in an epidote-amphibolite-facies shear zone (Jamieson, 1986). The metamorphic and structural history of the St. Anthony Complex, involving prograde metamorphism, retrograde metamorphism, and mylonite development, is discussed below.

The *White Hills Peridotite* preserves a four-stage structural and metamorphic history (Jamieson, 1986). (i) Initially, a high temperature deformation affected the peridotite prior to its emplacement. This pre-emplacement deformation resulted in fabrics typical of mantle tectonites that formed within the stability field of spinel lherzolite. Mineral assemblages in the high-temperature mantle tectonite indicate temperatures between 1100-1300°C based on numerous geothermometers (Lindsley, 1983; Gasparik, 1984, in Jamieson 1986). A pressure range between 10-20 kbar is inferred, within the stability field of spinel lherzolite (Jamieson, 1986). The earliest stage (ii) of emplacement-related metamorphism resulted in the formation of high-temperature mylonites in the basal 200 m of the peridotite (Calon, 1980) with the sub-

assemblage plagioclase-Ca amphibole associated with minerals of the original spinel lherzolite assemblage (Jamieson, 1981). A temperature of 850-1050°C and pressure between 8.5-12 kbar is inferred for this deformation (Jamieson, 1986). The third stage (iii) involved formation of narrow, discontinuous zones of fine-grained, low-temperature mylonite locally close to the base of the peridotite. Tremolite and chlorite (650-850°C) overprint the high-temperature mylonites and are deformed by later structures. Talc and secondary diopside (500-600°C) occur in fractures associated with the low-temperature mylonite (Jamieson, 1986). Stage (iv) involved formation of serpentine in the White Hills Peridotite, which post-dates all displacement-related deformation and metamorphism. Post-tectonic Al-poor diopside replaces amphibole in the basal zone suggesting temperatures less than 500°C for the post-emplacement cooling of the peridotite (Jamieson, 1986).

The *Green Ridge Amphibolite* preserves a polyphase metamorphic and structural history in which increasing strain is accompanied by retrograde metamorphism. Peak metamorphic conditions (i) are preserved in spinel-bearing metagabbro adjacent to the peridotite contact. Coronas containing spinel-orthopyroxene-clinopyroxene and spinel-hornblende assemblages are developed between primary plagioclase and olivine. Jamieson (1981) estimated temperatures between 900-950°C based on two pyroxene geothermometry and pressures of 7-10 kbar based on the spinel-plagioclase assemblage. Migmatic amphibolites (ii) containing K-feldspar-biotite-bearing syntectonic leucosomes

yielded P - T estimates between 3-5 kbar and 700-800°C. Marble associated with these migmatitic amphibolites indicates temperatures of approximately 680°C based on calcite-dolomite thermometry (Jamieson, 1981). These early granulite-facies assemblages in both the metagabbro and amphibolite are overprinted by an assemblage comprising hornblende-plagioclase-quartz-titanite (iii). This retrogression is most intense where rocks are strongly foliated. The most strained rocks exhibit residual clinopyroxene partially replaced by hornblende and mantling of ilmenite by titanite. The hornblende-plagioclase assemblage is stable over a wide P - T range, and temperatures were inferred to be greater than 775°C based on the local preservation of clinopyroxene (Jamieson, 1979). The formation of titanite at the expense of ilmenite suggests temperatures between 600-650°C and pressures in the range of 3-5 kbar (Jamieson, 1986). An epidote amphibolite (iv) unit occurs between the amphibolite and greenschist. These fine-grained well foliated rocks exhibit mylonitic banding and isoclinal folding. They contain the assemblage hornblende-epidote-plagioclase-quartz-titanite (Jamieson, 1986). The presence of epidote limits the maximum temperature to approximately 650°C (Maruyama *et al.*, 1983). A zone of (v) mylonitic biotite-garnet amphibolite cuts across on the amphibolite and epidote-amphibolite. Jamieson and Strong (1981) interpreted this as a shear zone affected by K-metasomatism and estimated temperatures between 475-625°C utilizing garnet-biotite pairs.

The transition between the *Goose Cove Schist* and the relatively undeformed

Chapter 1: Introduction

Ireland Point Volcanics is a complex shear zone with no change in metamorphic grade across it. The undeformed to weakly deformed pillow lavas of the Ireland Point Volcanics crop out directly above the post-metamorphic Hare Bay Thrust. These rocks (i) contain a variably developed epidote-albite-chlorite mineral assemblage indicative of lower greenschist-facies metamorphism. The absence of prehnite and pumpellyite and metamorphic hornblende constrain temperatures to between ca. 300–450°C (Jamieson, 1986). These pillow lavas pass into (ii) a narrow shear zone where they are strongly sheared and interleaved. The metamorphic grade is also lower greenschist facies but the assemblages are more penetratively developed. Metavolcanic greenschists (iii) are the most voluminous rocks in the Goose Cove Schist. Strain in these rocks is heterogeneous. Low strain zones contain the assemblage actinolite-chlorite and exhibit relict pillow structures and porphyritic textures. High strain zones contain the assemblage plagioclase-epidote-hornblende-hematite. The formation of hornblende after chlorite suggests a temperature range between 450–550°C based on the phase relations established by Apter and Liou (1983 in Jamieson, 1986). Metasedimentary rocks (iv) of the Goose Cove Schist are mainly psammite and semi-pelite which contain the assemblage muscovite-garnet-biotite-chlorite-albite-quartz-epidote. Competent metagabbro sills within the metasediments form boudins with sheared margins. The cores of the sills are relatively undeformed and contain the metamorphic assemblage actinolite-chlorite-albite-epidote-titanite, whereas the deformed sill margins comprise

hornblende-plagioclase assemblages. Well layered (v) epidote amphibolite ultramylonite occurs near contacts between metavolcanic and metasedimentary lithologies. These rocks contain the same mineral assemblage as the epidote amphibolites of the Green Ridge Amphibolite and are presumed to have equilibrated under similar *P-T* conditions (Jamieson, 1986).

1.3.5 Summary

Jamieson (1986) viewed the St. Anthony Complex as a large shear zone in which different lithologies are juxtaposed along mylonite zones. The mylonite zones contain mineral assemblages that indicate the *P-T* conditions which prevailed during the assembly of the complex. The basal peridotite mylonites comprise mineral assemblages ranging from granulite- to lower amphibolite-facies conditions. Mylonites within the Green Ridge Amphibolite comprise amphibolite and epidote-amphibolite assemblages, whereas mylonites in the Goose Cove Schist exhibit greenschist- and epidote-amphibolite facies assemblages. Thus, mylonites in the peridotite and amphibolite are retrograde and those in the greenschist are prograde. Considering the St. Anthony complex as a whole, mylonites display a convergence of metamorphic grade under epidote amphibolite-facies conditions.

1.4 Scope of Work

The objective of this study is to examine the behaviour of trace elements in metabasites across a range of metamorphic grade from upper greenschist facies to upper amphibolite facies using samples from the metamorphic sole of the Hare Bay Allochthon. Using the geological map of Jamieson (1979) as a guide, sampling of mafic metamorphic rocks of the St. Anthony Complex was carried out during the summer of 2000. Several factors were considered in the choice of samples for analysis: (i) an attempt was made to sample as wide a range of bulk composition as possible; (ii) several samples were collected from single sites to assess the consistency of trace-element partitioning; (iii) rocks with coarse grain size were sought in order to facilitate *in situ* mineral analysis.

On return to the lab, samples were chosen for whole-rock analysis (major and trace element) and for mineral analysis by EPMA and LAM-ICP-MS. An attempt was made to analyze identical points by both EPMA and LAM-ICP-MS methods thereby enabling cross-calibration of the major- and trace-element determinations. Before analysis, backscattered electron (BSE) images were used to identify any major-element zoning and the possible presence of micro-inclusions in individual grains, thereby aiding the selection of sample locations for analyses by EPMA and LAM-ICP-MS. However, BSE is insufficiently sensitive to record trace-element zoning, which could therefore be present in analysed grains. EPMA provides major-element data (limits of detection \approx

150 ppm under ideal conditions) and spatial resolution of less than 10 μm for spot analyses on individual grains. *In situ* sampling of individual grains by LAM-ICP-MS allows direct trace-element analysis within the context of the spatial distribution and major-element zoning of the analysed minerals and adjacent grains. Detection limits of 1 ppm (or lower) enable compositional zoning of trace elements to be investigated in large grains although the laser spot size of approximately 30 μm may result in the homogenization of some zoning if present at a smaller scale. Thus the combined BSE, EPMA and LAM-ICP-MS approach allows determination of both major- and trace-element concentrations for selected portions of mineral grains. This integrated approach permits the chemical analysis to be made in the context of textural features, thereby permitting an assessment of equilibrium. Consequently, in detail, the analytical goals of this study involve determination of an integrated suite of major- and trace-element data (selected trace and rare-earth elements [REE]) for metabasic rocks in order to: (i) determine the approach to equilibrium for a range of trace elements; (ii) provide quantitative partition coefficient data; (iii) investigate the compositional influences (e.g., major-element mineral composition, bulk composition, *etc.*) on partitioning between selected trace elements; (iv) perform mass balance calculations to determine the major carriers for specific trace elements in metamorphic rocks at this range of metamorphic grade; and (v) determine trace element loss/gains across the metamorphic gradient.

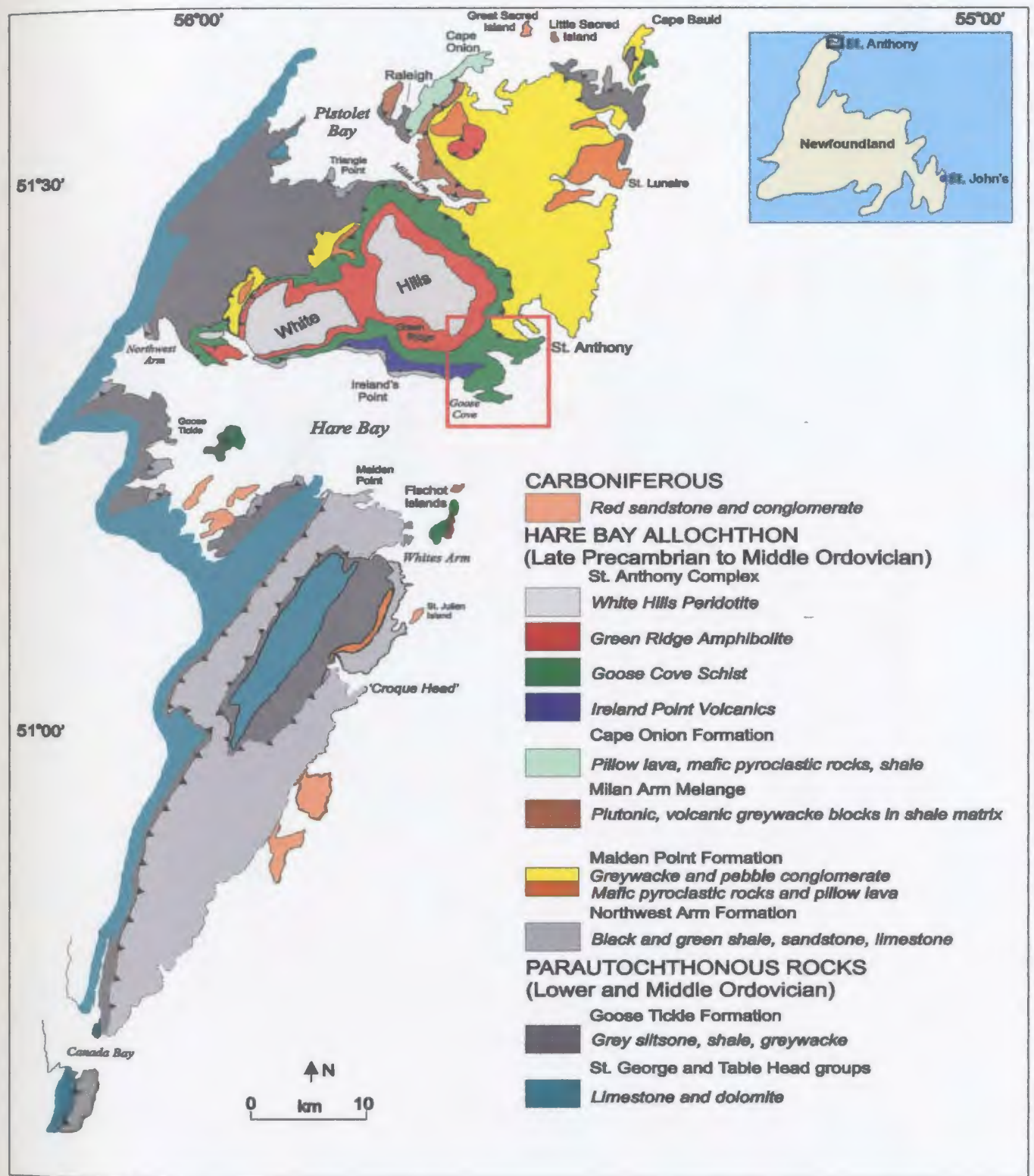


Figure 1.1 General geology of the Hare Bay Allochthon, Great Northern Peninsula, Newfoundland (modified from Williams, 1995). Black box on inset map of Newfoundland shows location of Figure 1.1. Red box shows location of Figure 1.2.

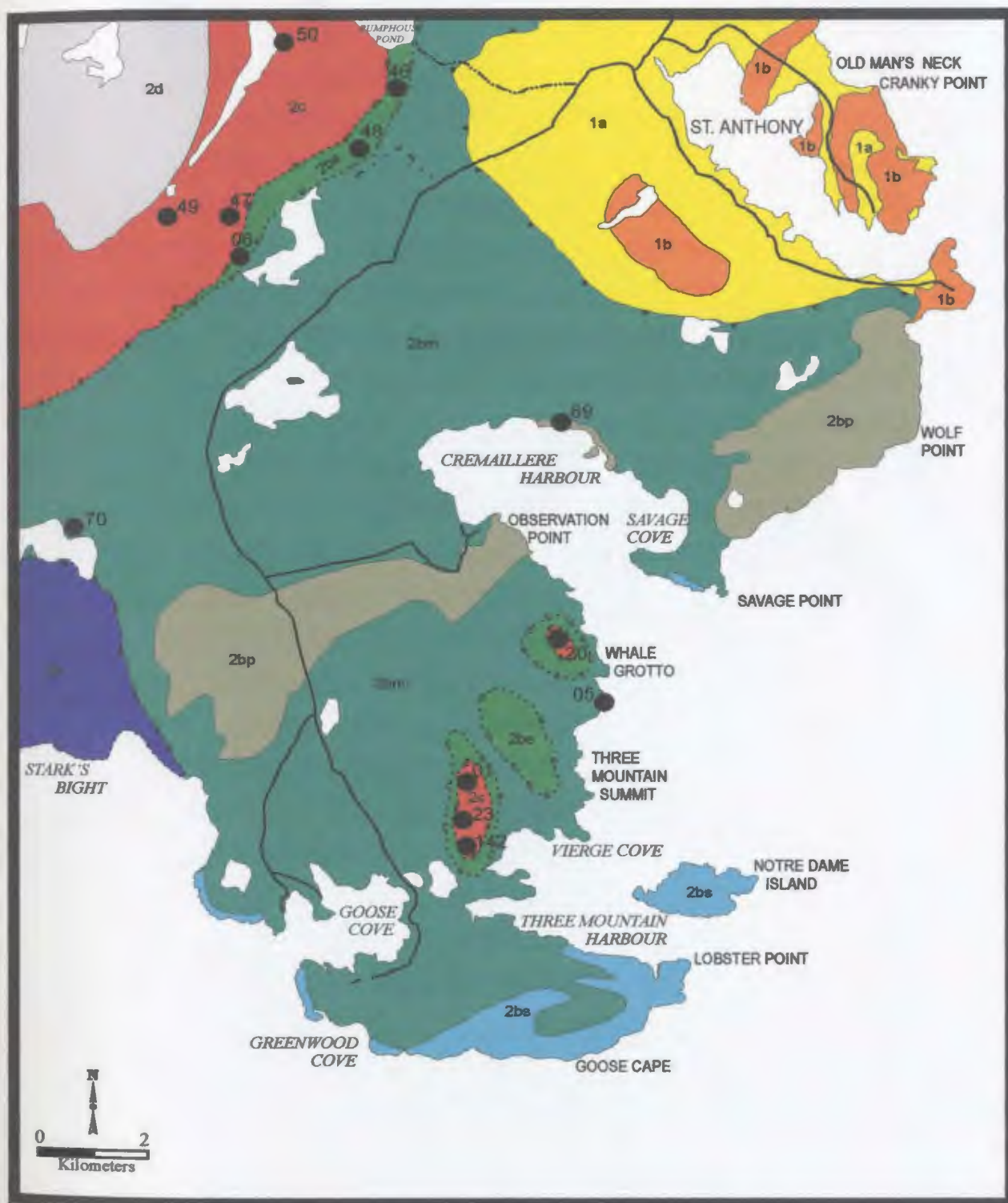
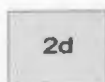


Figure 1.2 Simplified geological map of the southeastern part of the St. Anthony Complex showing metamorphic isograds (after Jamieson, 1979) and sample locations. Legend on facing page.

LEGEND

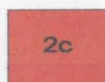
2 ST. ANTHONY COMPLEX

2d WHITE HILLS PERIDOTITE



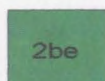
harzburgite, minor dunite, lherzolite,
gabbro, pyroxenite

2c GREEN RIDGE AMPHIBOLITE

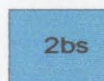


undivided biotite/plagioclase amphibolite

2b GOOSE COVE SCHIST



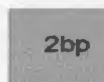
epidote amphibolite



metasediments

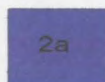


massive/banded
greenschist



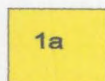
spotted greenschist

2a IRELAND POINT VOLCANICS

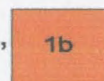


vesicular pillow lava

1 MAIDEN POINT FORMATION



undivided greywacke,
shale, conglomerate



gabbro

SYMBOLS

Thrust fault



Isograds



Road



Track



Sample Location



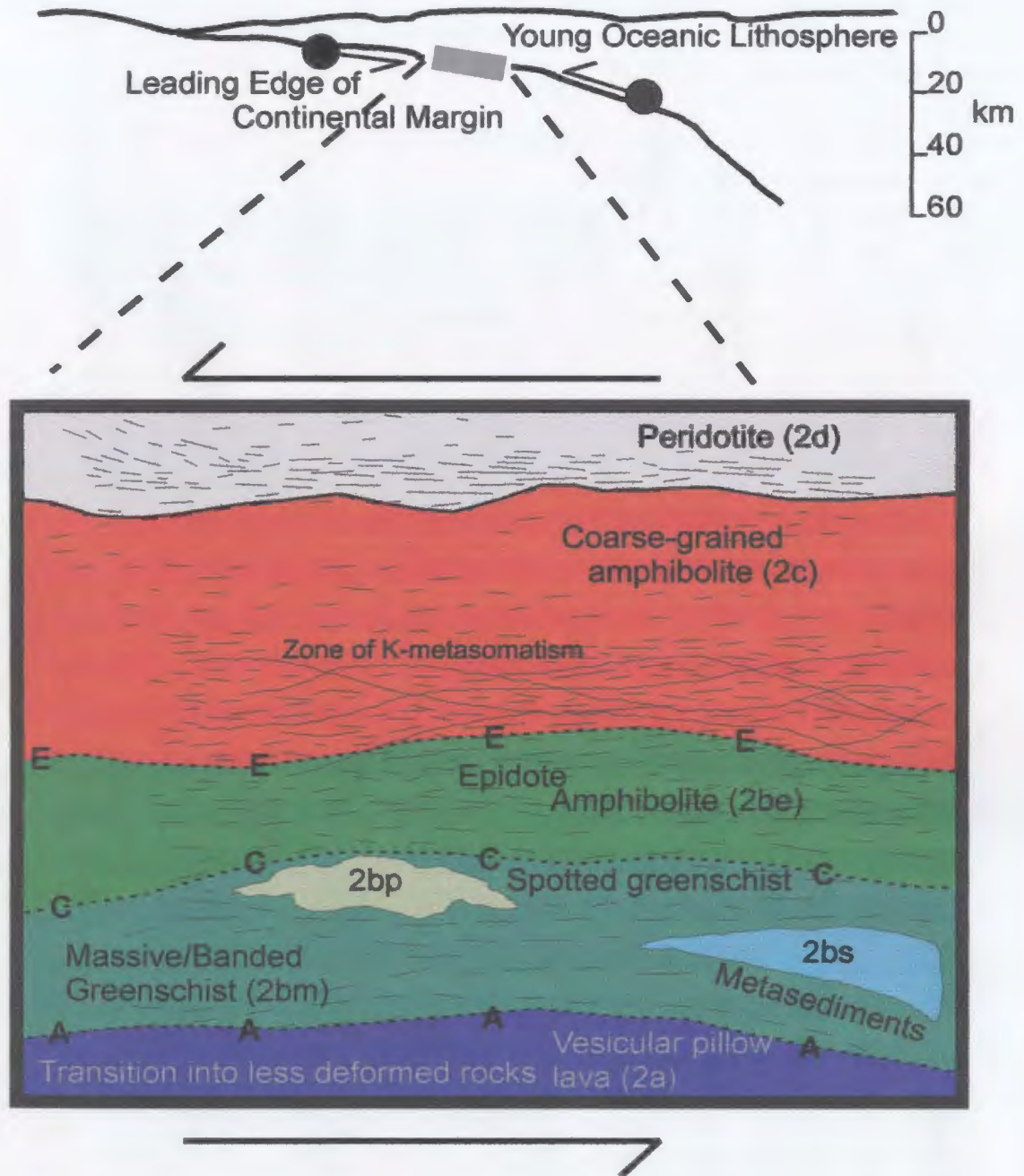


Figure 1.3. Schematic diagram showing the assembly of the St. Anthony Complex within a high-temperature ductile shear zone and the preservation of residual mineral assemblages in zones of low strain (after Jamieson, 1986). The tectonic setting is inferred to have been in the upper part of a subduction zone, illustrated schematically at the top of the diagram.

Chapter 2: Principles of Trace-Element Partitioning and Analytical Methods

2.1 Introduction

Kretz (1959, 1961) showed that knowledge of the distribution of major elements among coexisting phases in a mineral assemblage is a crucial facet in the quantification of equilibrium phase relationships as a function of the pressure (P), temperature (T), and bulk rock chemical composition (X) of the system. Theoretically, the principles established by Kretz should extend to trace-element distributions, thereby enabling their utility in investigations of the P - T - X conditions of metamorphism (e.g., Bea *et al.*, 1997; Yang *et al.*, 1999; Pyle and Spear, 2000). However, although trace elements may be more sensitive to metamorphic reactions and changes in local chemical environment than major elements, trace-element partitioning studies in metamorphic petrology were for many years of subordinate importance, largely due to apparent non-systematic trace-element behaviour with changes in metamorphic grade. It is now apparent that these misleading results were, to a great extent, a result of the analytical technique used, i.e., bulk mineral analyses of mineral separates which may have been contaminated by micro-inclusions and did not consider the possible effects of zoning. The relatively recent

advent of *in situ* microbeam techniques, including laser ablation microprobe-inductively coupled plasma-mass spectrometry (LAM-ICP-MS) has provided an opportunity to reinvestigate trace-element partitioning between coexisting metamorphic phases (e.g., Fedorowich *et al.*, 1995; Yang and Rivers, 2000).

2.2 Principles of Trace-Element Partitioning

2.2.1 Trace Elements

By convention, elements are categorized as major, minor or trace depending on their relative abundances in the system of interest. The divisions between the three categories have not been fixed, but a trace element is broadly defined as an element which is present in a rock in concentrations of less than 0.1 wt %. Trace elements are usually studied as groups with deviations from group behaviour or regular changes in behaviour within a group being used as indicators of petrological processes. Typically, trace elements are classified on the basis of their position in the periodic table or according to their behaviour in magmatic systems (Rollinson, 1993). Figure 2.1 is a reproduction of the periodic table of the elements showing the main groups of trace elements that are the focus of this study, the lanthanides or rare earth elements (*REE*, atomic numbers 57 to 71), the first series transition metals (atomic numbers 21 to 30), the large ion lithophile elements (LILEs) Sr and Rb, and the high field strength elements

(HFSEs) Y, Zr and Nb. Low-atomic number members of the *REE* (La to Nd) are termed the light *REE*, or *LREE*, the middle members of the group (Sm to Ho) are known as the middle *REE* or *MREE* and those with higher atomic number (Er to Lu) are the heavy *REE* (*HREE*). Most *REE* have similar chemical properties (i.e., 3^+ charge) and generally exhibit similar geochemical behaviour. However, Eu (2^+ or 3^+) and Ce (3^+ or 4^+) often occur in multiple valence states. Certain geological processes can fractionate elements within the group due to the subtle differences in their geochemical properties, thereby making the *REEs* of particular interest to a geochemist. In contrast to the *REEs*, each of which is dissolved in trace proportions in most minerals, the first series transition metals include two elements, Fe and Mn that are major constituents of many minerals. The behaviour of transition metals is more complex than the *REE* because most of them can assume several oxidation states. Some electrons in their second shells have approximately the same energy as the outer valence electrons, enabling them to act as additional valence electrons (Krauskopf and Bird, 1995). As a result, these elements exhibit less regularity in their properties (i.e., valence state, ionic radius) than elements in other 'groups'. Trace elements are also classified on the basis of their ionic potential (charge/size ratio). HFSEs (ionic potential >2) and LILEs (ionic potential <2) were also analyzed in this study. In essence, the *REE* are a group of HFSEs which exhibit coherent behaviour. In addition, trace elements exhibit a range of mobility in common chemical systems. First series transition elements Sc, Co, Ni, V, and Cr and the HFSEs are

commonly 'immobile' in comparison to the transition metals Fe, Mn, Zn and Cu and the LILEs, which are considered relatively 'mobile' during hydrothermal alteration and low grade metamorphism (Seewald and Seyfried, 1990).

2.2.2 The Thermodynamics of Trace-Element Distribution

The thermodynamic basis for the distribution of a trace element between a coexisting mineral pair can be viewed in terms of an exchange reaction with a major element (Kretz 1959, 1961). For instance, the distribution of major element x and trace element y between phases A and B can be represented by the equation:

$$y^A + x^B = x^A + y^B \quad (2.1)$$

At equilibrium,

$$\mu y^A + \mu x^B = \mu x^A + \mu y^B \quad (2.2)$$

where μy^A is the chemical potential of y in A etc. The chemical potential of element y in phase A is related to its concentration, the mixing behaviour in the solid solution, and the chemical potential of the end-member y^A by the expression:

$$\mu y^A = G y^A + nRT \ln X y^A \gamma y^A \quad (2.3)$$

where $G y^A$ is the Gibbs Free Energy of pure end-member y^A , R is the gas constant, $X y^A$ is the concentration of y in A measured as a molar fraction ($y/y+x$) on a particular site, γy^A is an expression that describes the mixing of components x and y in A , and n is the number of sites on which mixing takes place. If three additional equations for each of x^B ,

x^A , y^B , akin to equation 2.3 for y^A , are substituted into equation 2.2 and rearranged, the result is:

$$K_{Dy,n}^{A,B} = \left[\frac{[X_y/X_x]^A}{[X_y/X_x]^B} + \frac{[\gamma_x/\gamma_y]^A}{[\gamma_x/\gamma_y]^B} \right] \exp(-\Delta G^\circ/RT)^n \quad (2.4)$$

where $K_{Dy,n}^{A,B}$ is the distribution coefficient for trace element y between phases A and B on n mixing sites and ΔG° is the Gibbs free energy difference between the pure end-members under some specified standard state conditions.

Despite the possibility of strong interactions of trace elements with adjacent ions in the lattices in which they substitute, the mathematical formulation of activity-composition (a - X) relationships remains relatively simple due to the intrinsic small concentrations of trace elements. Figure 2.2 schematically illustrates a - X relationships for major and trace elements. In an ideal major-element mixing situation (Raoult's Law), there is no enthalpy of mixing, activity coefficients (γ) are equal to unity, and the activities of components mixing on one site are given by the Raoult's Law expression:

$$a_Y^A = X_Y \quad (2.5)$$

In the non-ideal case, the substituting element interacts with the lattice of the host mineral and the thermodynamic activity of the solid solution deviates from the ideal mixing curve to some degree, either positively or negatively. With regard to trace-element solutions, which are by definition dilute solutions, trace ions are dispersed such

that they may be considered to be surrounded by a uniform environment. Although trace components may interact strongly with other lattice components present, these interactions do not affect the average environment because of the low concentrations involved, leading to linear activity-composition relationships. Thus, the activity coefficient remains constant and the activities of trace components become proportional to their concentrations, a relationship known as Henry's Law:

$$a_y^A = k_y^A X_y^A \quad (2.6)$$

Here, the proportionality constant k_y^A for trace component y in phase A is the Henry's Law constant. It follows from Henry's Law that ΔG° is mainly dependent on temperature variations. The effect of pressure is generally small due to the small changes in volume resulting from exchange reactions involving trace elements.

2.2.3 Mineral Structure and Trace-Element Substitution Schemes in Analysed Phases

Before evaluating major-element compositional and mineral structural effects on trace-element partitioning in Ca amphibole, plagioclase, epidote, garnet and titanite, it is instructive to review the mineral structures (Figure 2.3), mean atomic site sizes, the dominant cation distributions of common end-members, and ionic radii of trace elements analysed in this study (Tables 2.1a-c).

The essential feature of the structure of *amphibole* (Figure 2.3a) is the presence of double chains of (Si,Al)O₄ tetrahedra with the composition (Si,Al)₄O₁₁ (e.g., Deer *et al.*

1992). These chains repeat along their length at intervals of approximately 5.3 Å and are separated and bonded together laterally by strips MO_6 octahedra, the oxygens being shared with the apices of the chain-forming tetrahedra. The structure contains five such MO_6 octahedra (2M1, 2M2, 1M3) for every eight tetrahedra as well as a two larger M4 sites with seven- or eight-fold coordination, a large 12-fold coordinated A site and two hydroxyl sites per formula unit. A general amphibole formula may be written as $A_{0-1}M4_2M1-3T_8O_{22}(OH,F)_2$. In calcic amphiboles, the M4 site is predominantly occupied by Ca with minor Fe, Mg, Mn and Sr substitution (Table 2.1a). REE are known to substitute for Ca in the large M4 site but it has been recently suggested that HREE can enter the smaller M2 site (e.g., Bottazzi *et al.*, 1999). The A site contains variable amounts of Na, K and minor Rb and may be partially vacant. The M1-3 sites predominantly contain Mg + Fe, Al and Fe^{3+} and can host transition metals and HFSEs. T sites are occupied by Si and Al.

Plagioclase has the general formula AT_4O_8 where A is an irregular 5- to 9-fold coordinated site and T is a tetrahedral site. The structure (Figure 2.3b) is described as a framework of corner-sharing Si and Al tetrahedra (e.g., Nesse, 2000). The tetrahedra are arranged to form four-member rings with the apices of two tetrahedra pointing “up” and two pointing “down,” parallel to the *a* axis. The rings are joined to each other by shared oxygen anions to form “crankshaft-like” chains, which are themselves joined to other chains by sharing the remaining oxygens, resulting in the formation of 5- to 9- fold

coordinated *A* sites between chains that can accept large cations (e.g., Ca, Na in the plagioclase series). It is convenient to consider trace-element substitutions in terms of the two structural sites, i.e., those elements substituting for Al or Si (*T* sites) or for Ca and Na (*A* sites). Common minor substitutions in plagioclase include Ti and Fe³⁺ (*T* sites) and Ba and Sr (*A* sites). Sc, V and HFSE are typically minor constituents in plagioclase (*T* sites) whereas *REE* (especially *LREE*) can occur in more significant amounts in *A* sites (Table 2.1a; Deer *et al.*, 1992).

Epidote has the general formula $X_2M1-3_3T_3O_{12}(OH,F)$ where *X* is an 8- or 9-fold coordinated site, *M* is an octahedral site, and *T* is a tetrahedral site. The structure (Figure 2.3c) contains chains, parallel to *y*, of octahedra of three types: (i) edge sharing octahedra (*M2*), and (ii) chains of *M1* octahedra and (iii) *M3* octahedra that attach on alternate sides of isolated SiO₄ tetrahedra along their length (Povarennykh 1972). *M1* and *M2* sites are centrosymmetric whereas *M3* is a non-centrosymmetric site. Single tetrahedra (SiO₄) and double tetrahedral (Si₂O₇) groups aligned in the direction of the *c* axis share oxygens with the octahedra and the resulting framework contains large cavities (*X* sites) occupied by calcium. The location of hydroxyl group has not been determined unequivocally (Deer *et al.*, 1992). Ercit (2002) compiled data on known end-members of the epidote group and showed that the *M1* and *M2* sites predominantly contain Al. The *M3* site contains the most non-Al atoms (Fe³⁺ in epidote [pistacite molecule] and Mn³⁺ in piemontite). HFSEs and transition metals can occupy this site as well. Appreciable *REE*

and Y (especially *LREE*) and lesser amounts of LILEs substitute for Ca in *X* sites (Table 2.1a).

The unit cell of *garnet*, shown in Figure 2.3d, contains eight $X_3Y_2T_3O_{12}$ formula units (Deer *et al.* 1992). The structure consists of alternating ZO_4 tetrahedra and YO_6 octahedra that share corners forming a three-dimensional network. Within this network are distorted cubic cavities that contain the *X* cations in 8-fold coordination. In common garnet, the *T* sites are filled by Si, the *Y* sites by Al and the cubic sites by Fe, Mg, Ca, and Mn corresponding to the end-members almandine, pyrope, grossular and spessartine. Appreciable Sc, V and Cr substitution for Al in *Y* sites has been reported (e.g., Yang, 2001). Minor amounts of HFSEs can also occupy this site. Some transition metals (Co, Ni, Cu, Zn) and *REE* (especially *HREE*) are compatible in garnet *X* sites (Table 2.1a).

Titanite has the general formula $AMTO_4(O,OH,F)$. The structure, shown in Figure 2.3e, consists of corner-sharing TiO_6 octahedra parallel to *a* which are linked to SiO_4 tetrahedra by sharing the remaining four oxygens. This linkage produces a $[TiOSiO_4]^-$ framework with large cavities (*A* sites) that enclose Ca atoms in irregular seven-coordination polyhedra (Deer *et al.*, 1992). The principal substitutions in titanite include the coupled substitution ${}^MTi^{4+} + O_2^- = {}^M(Al,Fe^{3+}) + (F,OH)^-$, and Al, Fe^{3+} , Fe^{2+} , Mg, Sc, V, Cr and HFSEs can substitute for Ti in octahedral *M* sites. Specific LILEs (e.g., Sr, Na) and *REE* are known to substitute for Ca in *A* sites (Table 2.1a).

2.2.4 Trace-Element Partition Coefficients

Numerous geological investigations (e.g., Kretz, 1959, 1961; Hickmott and Spear, 1992; Dahl *et al.*, 1993; Yang *et al.*, 1999, Yang and Rivers, 2000) have attempted to model trace-element variations in natural metamorphic systems. Many of these studies have employed the Nernst distribution coefficient:

$$D_i = C_i^A / C_i^B \quad (2.7)$$

where the distribution (D) of trace element i is the ratio of the concentrations (C) of component i in ppm in phases A and B . At trace concentrations, the graphical manifestation of a Nernst distribution coefficient is a straight line intersecting the origin. D_i is a whole-phase partition coefficient and does not consider the sites trace element i occupies in phases A and B . From a thermodynamic and mineralogical perspective, it is more useful to calculate the proportion of specific atomic sites in the lattice filled by the trace element i , out of the number of sites available to that element. To account for site occupancies of a trace cation i , Nielsen (1985) introduced the term D_i^* :

$$D_i^* = X_i^A / X_i^B \quad (2.8)$$

where X_i^A is the mole fraction of component i in a particular site in phase A . In many cases, mole fraction distribution coefficients (D_i^*) yield more realistic estimates of partitioning between phases because they eliminate the partial compositional dependence created by D_i . Nonetheless, due to the inherent difficulty in defining atomic site occupancies and proper solution components for many trace elements in metamorphic

2.2.4 Trace-Element Partition Coefficients

Numerous geological investigations (e.g., Kretz, 1959, 1961; Hickmott and Spear, 1992; Dahl *et al.*, 1993; Yang *et al.*, 1999, Yang and Rivers, 2000) have attempted to model trace-element variations in natural metamorphic systems. Many of these studies have employed the Nernst distribution coefficient:

$$D_i = C_i^A / C_i^B \quad (2.7)$$

where the distribution (D) of trace element i is the ratio of the concentrations (C) of component i in ppm in phases A and B . At trace concentrations, the graphical manifestation of a Nernst distribution coefficient is a straight line intersecting the origin. D_i is a whole-phase partition coefficient and does not consider the sites trace element i occupies in phases A and B . From a thermodynamic and mineralogical perspective, it is more useful to calculate the proportion of specific atomic sites in the lattice filled by the trace element i , out of the number of sites available to that element. To account for site occupancies of a trace cation i , Nielsen (1985) introduced the term D_i^* :

$$D_i^* = X_i^A / X_i^B \quad (2.8)$$

where X_i^A is the mole fraction of component i in a particular site in phase A . In many cases, mole fraction distribution coefficients (D_i^*) yield more realistic estimates of partitioning between phases because they eliminate the partial compositional dependence created by D_i . Nonetheless, due to the inherent difficulty in defining atomic site occupancies and proper solution components for many trace elements in metamorphic

phases, it is routine to report trace element distributions as Nernst distribution coefficients. Both D_i and D_i^* are used in this study. Cation mineral site occupancies (Table 2.1a) are based on the number and size of specific sites in the phase of interest (Table 2.1b; Smyth and Bish, 1988) and the ionic radii and charges of the substituting cation (Table 2.1c; Shannon, 1976), and in general follow the suggestions of previous authors.

2.2.5 Mass Balances

Mass balance calculations have been used in magmatic and metamorphic rocks to evaluate the relative roles of specific phases as hosts for certain trace elements (e.g., Sorensen and Grossman, 1989; Zack *et al.*, 2001 for examples in metamorphic systems). To calculate mineral-bulk rock mass balances, the following factors must be considered: bulk rock major- and trace-element chemistry, mineral major- and trace-element chemistry, and the modal abundance of each phase. Consider the simple case of a rock composed of two phases, A and B . Ideally, the sum of the concentrations (C) of an element (i) in each phase multiplied by the modal abundance (M) of each phase should equal the whole rock concentration of i (C_i^{WR}), i.e.,

$$(C_i^A)(M^A) + (C_i^B)(M^B) = C_i^{WR}$$

The left side of this equation is referred to as the *reconstructed whole-rock concentration* of element *i* and the right side is the *measured whole-rock concentration*. Given the many possible sources of error, Sorensen and Grossman (1989) considered that if the reconstructed whole-rock concentration is within approximately $\pm 30\%$ difference of the measured whole-rock total, the mass balance was reasonable. Possible sources of error include: a heterogeneous mineral distribution that biases the mode; analytical inaccuracies in the determination of mineral and whole-rock concentrations; inaccurate estimations of the modal abundances of any phase, especially trace phases that contain a significant part of the trace-element budget for particular elements; the presence of trace-element zoning in one or several phases; or overlooked accessory minerals which may sequester trace elements. For an accurate mass balance, it is imperative that *all* phases in a rock be included in the reconstructed whole-rock concentration. This is especially the case for trace phases which sequester major proportions of some elements.

In addition, mass balance analysis using the algebraic technique of singular value decomposition (SVD, described by Fisher, 1989, see Appendix C) was used to quantify and balance a model epidote-out reaction isograd, enabling an assessment of the redistribution of *REE* and selected trace elements formerly sequestered in epidote to other phases above the reaction isograd. Commercial software Mathematica[®] was used to perform the analysis. Required inputs are the major-element mineral compositions of phases involved in the epidote-out reaction (measured by EPMA).

2.3 Analytical Methods

2.3.1 Whole-rock analysis

For thirteen samples, whole-rock concentrations of major elements and first series transition elements were measured using a Fisons/ARL® model 8420+ sequential wavelength-dispersive X-ray fluorescence (XRF) spectrometer at the Department of Earth Sciences, Memorial University of Newfoundland, utilizing the method described by Longerich (1995). Samples were prepared as pressed pellets using a mixture of 5 grams of rock powder and 0.7 grams of BRP-5933 Bakelite® phenolic resin in a 100 ml glass jar. Two 1.25 cm diameter stainless steel ball bearings were added and a plastic lid attached. The jar was placed on a roller mixer and rolled for 10 minutes to mix the rock powder with the resin, and the resultant mixture was placed in a pellet press (29 mm diameter mold) and pressed for 5 seconds at a pressure of 20 tonnes. The pellets were placed in a 200°C oven for 15 min. Reference pellets were prepared by mixing Chemplex single-element X-ray powdered Spectro Standard Preparation Kit materials with 1 μm polishing alumina (Al_2O_3). FeO/ Fe_2O_3 was estimated by the wet-chemical method of Maxwell (1968), which is described in Appendix B.

Whole-rock concentrations of fourteen rare-earth elements (*REE*) and six other trace elements (Y, Zr, Nb, Ba, Hf, and Ta) were determined from solutions using a Hewlett Packard 4500⁺ inductively coupled plasma-mass spectrometer (ICP-MS) at

Memorial University of Newfoundland using a sodium peroxide (Na_2O_2) sinter digestion procedure outlined by Longerich *et al.* (1990). Synthetic solutions were used to calibrate the instrument and standard reference materials, MRG-1 and BR-688, and reagent blanks were analyzed for quality-control. Details of sample preparation and information detailing precision and accuracy of the method are provided in Longerich *et al.* (1990) and summarized in Appendix B.

2.3.2 Micro-Analysis

Back-scattered electron (BSE) imaging was employed to determine the choice of locations of the analysis spots since it enables assessment of major-element mineral zoning and the presence of inclusions or alteration. Standard microprobe operating conditions with a 10 nA beam current and 35 mm working distance were used. Selected images of potential microanalysis sites were printed on a thermal wax printer to enable close spatial correlation between major-element (EPMA) and trace-element (LAM-ICP-MS) analyses in subsequent analytical work.

Quantitative major-element analyses of selected 100 μm thick polished thin sections were carried out using a Cameca® SX-50 electron probe microanalyzer (EPMA) with a Link® ED detector in energy-dispersion (ED) mode at the Department of Earth Sciences, Memorial University of Newfoundland. An accelerating voltage of 10 to 20 kV, a beam current of 10 nA and a beam diameter of 1 to 5 μm were used. The Link® ED

system was calibrated using a cobalt standard along with U.S. National Museum standard reference material 143965. Data reduction of raw counts was performed with Link® ZAF matrix correction software.

Trace-element concentrations were determined by laser ablation microprobe (LAM) ICP-MS at Memorial University of Newfoundland using the same 100 μm thick polished thin sections that had been previously analysed by EPMA. Instrumentation and analytical procedures are described by Taylor *et al.* (1997) and Sylvester (2001). The instrument comprises a laser sampler utilizing a frequency quadrupled Nd:YAG laser source with a 266 nm wavelength coupled to a Fisons® VG PQII+ “S” ICP-MS. The laser was operated in Q-switched mode with a pulse energy optically reduced to 0.5 mJ at a frequency of 10 Hz. Calibrations were made using the U.S. National Institute of Science and Technology (NIST) standard reference material (SRM) 612, a synthetic silicate glass which has a ‘spiked’ abundance of 50 ppm for 61 different elements (Pearce *et al.* 1997). Major-element concentrations, obtained by EPMA, were used as internal standards (Ca for Ca amphibole, epidote, titanite, garnet and Si for plagioclase) to adjust for differences in ablation yield between samples and the calibration standard. Data acquisition was performed in peak jumping mode (one point per peak, time resolved analyses: TRA) which resulted in singular intensity data per mass peak. Typical acquisition parameters were 60 to 80 seconds measurement of the argon carrier gas blank with 20 to 50 seconds of measurement with the laser switched on and material being

ablated. Pit sizes varied from 30-60 μm depending on the target material, pulse energy, and duration of ablation. The raw counts were processed off-line with CONVERT software and data reduction was performed using LAMTRACE software (Jackson, 2001). Examination of LAMTRACE graphical output allows the selection of appropriate background and signal time intervals for integration (Appendix B).

Since LAM-ICP-MS is a destructive *in situ* technique, it is impossible to perform repeated measurements on the same spot, thereby rendering it difficult to measure precision. To alleviate this problem, repeated analyses of a U.S. Geological Survey glass reference BCR-2G were performed under operating parameters similar to those of the unknown routine analyses, and in turn, were used to estimate precision. The analytical precision for most elements in BCR-2G was within approximately 10 % relative standard deviation (RSD) except for Cr, Ni, Zn and Cu (Longerich 1996). A more detailed discussion of analytical error for LAM ICP-MS analyses is given in Appendix B.

Potential sources of error are similar to those reported by Yang *et al.* (1999) and Yang and Rivers (2000). These include: (i) spatial mismatch between, and the different sizes of the electron beam spot and laser ablation spot for the combined EPMA and LAM-ICP-MS approach; (ii) contamination from already ablated grains or micro-inclusions within ablation spots; and (iii) fractionation of chalcophile elements (Cu, Zn) relative to the internal element standard (Ca or Si) during sample ablation and transportation to the mass spectrometer. Despite carefully matching EPMA and LAM-

ICP-MS beam spots, the inherent difference in sampling resolutions (beam diameter in μms for EPMA compared to tens of μms for LAM-ICP-MS) between the two techniques can reduce accuracy if the normalizing elements (determined by EPMA) exhibit significant zoning at this scale. The detection and elimination of inclusions of different composition from the host mineral (e.g., zircon in amphibole) was done during interval selection with LAMTRACE. Inclusions of similar composition to the host grains are more difficult to detect with the only check being the internal consistency of the results. To reduce fractionation within each run, the laser was defocused approximately 100-200 μms above the sample (Sylvester, 2001).

2.3.3 Modal Analysis

The extreme size range of minerals in the samples (i.e., tens of μm for titanite *versus* tens of mm for amphibole) rendered point counting impractical, so modal analyses were carried out using the program MODAN (Paktunc, 1998), and verified by visual estimates. Input data for MODAN are the bulk-rock composition and the major-element compositions of all the phases. Uncertainties on the modes have not been calculated, but are likely small, although they may be significant for trace element enriched phases such as titanite and epidote, as discussed later. Due to its low modal abundance and importance as a trace element carrier, estimates of titanite modal abundance were refined using bulk-rock TiO_2 concentrations.

Transition Metals

1 H		21 Sc	22 Ti	23 V	24 Cr	25 Mn	26 Fe	27 Co	28 Ni	29 Cu	30 Zn		2 He				
3 Li	4 Be											5 B	6 C	7 N	8 O	9 F	10 Ne
11 Na	12 Mg											13 Al	14 Si	15 P	16 S	17 Cl	18 Ar
19 K	20 Ca											31 Ga	32 Ge	33 As	34 Se	35 Br	36 Kr
37 Rb	38 Sr	39 Y	40 Zr	41 Nb	42 Mo	43 Tc	44 Ru	45 Rh	46 Pd	47 Ag	48 Cd	49 In	50 Sn	51 Sb	52 Te	53 I	54 Xe
55 Cs	56 Ba	57 La	72 Hf	73 Ta	74 W	75 Re	76 Os	77 Ir	78 Pt	79 Au	80 Hg	81 Tl	82 Pb	83 Bi	84 Po	85 At	86 Rn
87 Fr	88 Ra	89 Ac	104 Rf	105 Db	106 Sg	107 Bh	108 Hs	109 Mt	110 Uun	111 Uuu	112 Uub						

High Field Strength Elements

Large Ion Lithophile Elements

Rare Earth Elements

58 Ce	59 Pr	60 Nd	61 Pm	62 Sm	63 Eu	64 Gd	65 Tb	66 Dy	67 Ho	68 Er	69 Tm	70 Yb	71 Lu
----------	----------	----------	----------	----------	----------	----------	----------	----------	----------	----------	----------	----------	----------

90 Th	91 Pa	92 U	93 Np	94 Pu	95 Am	96 Cm	97 Bk	98 Cf	99 Es	100 Fm	101 Md	102 No	103 Lr
----------	----------	---------	----------	----------	----------	----------	----------	----------	----------	-----------	-----------	-----------	-----------

Figure 2.1 The periodic table of the elements, showing main groups of trace elements of interest in this study; the *REE* (yellow), first series transition elements (grey), LILE (green) and HFSE (blue). Y is not a *REE*, nor is it treated as a *REE* in this study.

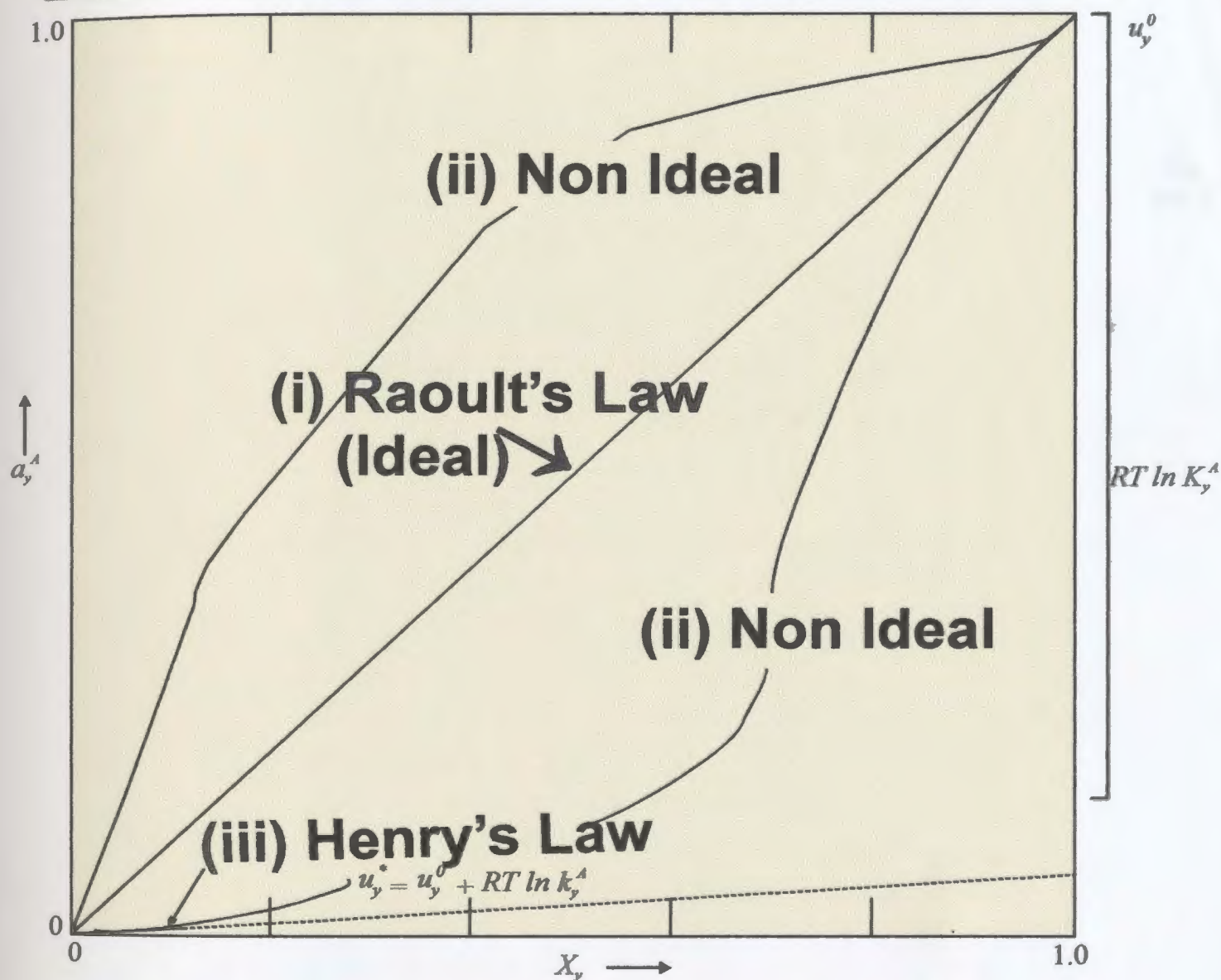


Figure 2.2 Activity-composition (a - X) relations for component y in phase A ; (i) ideal solutions (Raoult's Law), and (ii) non-ideal solutions, and (iii) for trace element components obeying Henry's Law (modified from Wood and Fraser, 1976).

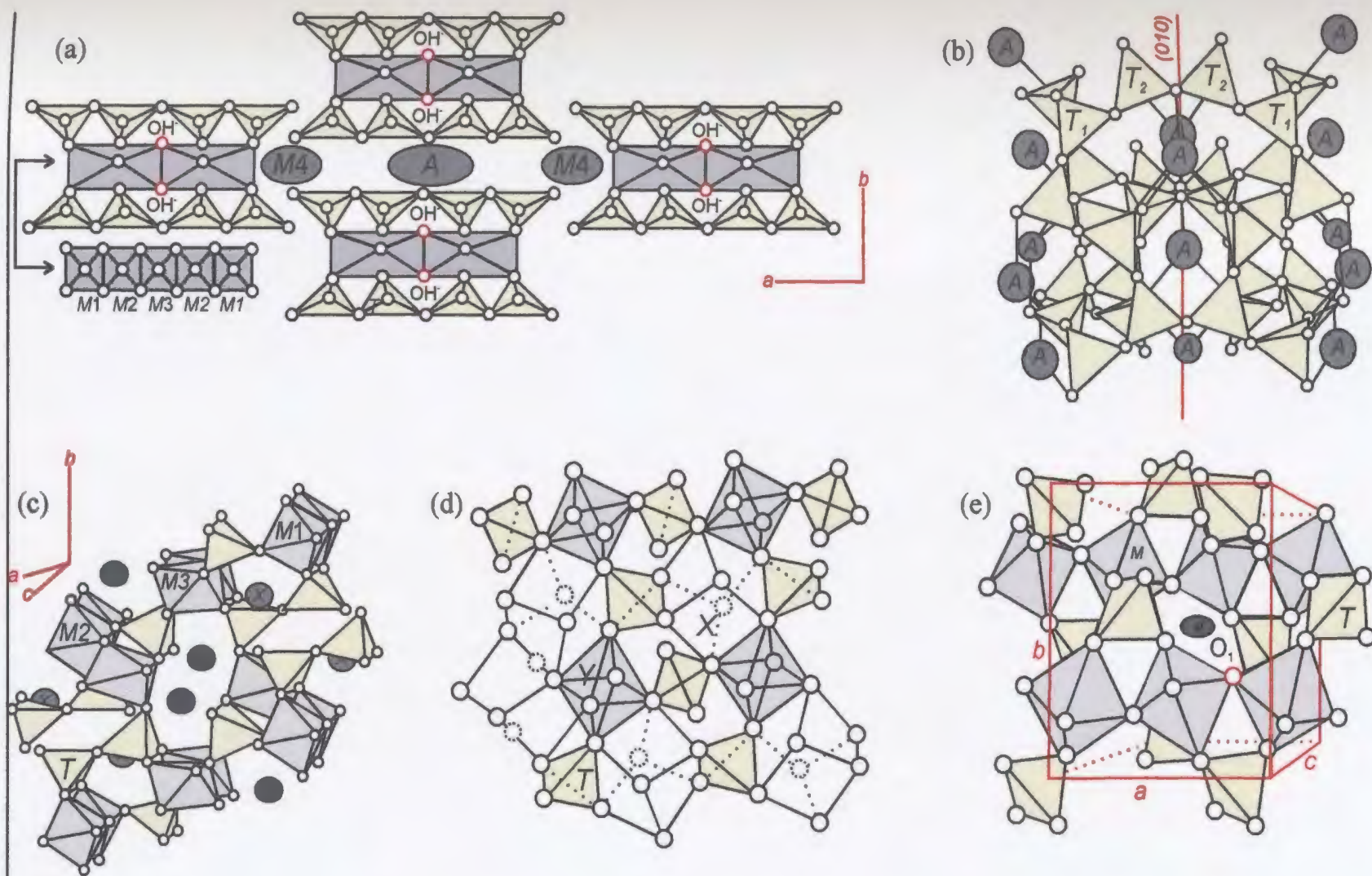


Figure 2.3 The structures of (a) amphibole (after Thompson, 1981), (b) plagioclase (after Nesse, 2000), (c) epidote (after Povarennykh, 1972), (d) garnet (after Novak and Gibbs, 1971), and (e) titanite (after Taylor and Brown, 1976). Open circles represent oxygens, tetrahedra are in yellow, octahedra are in grey. Red circles denote hydroxyl ions. Amphibole (a) is a cross sectional view parallel to double chains, crystallographic orientations shown in red (b), (c) and (e). Garnet (d) is cubic ($a = b = c$).

Table 2.1(a) General mineral formulae and cation site distributions of the five major phases analyzed in this study. Cation distributions based on mineral structure (Deer *et al.*, 1992) and the charge and size of the substituting cation (Smyth and Bish, 1988). See Figure 2.1 for explanation of element colours. C.N.# is the site coordination number.

MINERAL	SITE and OCCUPANT			
CALCIC AMPHIBOLE $A_{0.1}M_4M_{1-3}T_8O_{22}(OH, O, F, Cl)$	A C.N.# = 12	M4 C.N.# = 8	M1-3 C.N.# = 6	T C.N.# = 4
	Na, K, Rb	Ca, Mg + Fe, Mn Na, Sr, Y, REE	Al, Ti, Fe ³⁺ , Mg, Mn Sc, V, Cr, Co, Ni, Zn Cu, Nb, Zr	Si, Al
PLAGIOCLASE $A[T_4]O_8$	A C.N.# = 5 - 9	T C.N.# = 4		
	Ca, Na, K, Sr, Rb, Mn Fe ²⁺ , Co, Ni, Cu, Zn REE, Y	Si, Al, Ti, Cr, Sc, V, Nb, Zr		
EPIDOTE $X_2M_{1-3}T_3O_{12}(OH, F)$	X C.N.# = 8 or 9	M1-2 C.N.# = 6	M3 C.N.# = 6	T C.N.# = 4
	Ca, Na, K, Sr, Rb, Y REE	Al	Al, Fe ³⁺ , Fe ²⁺ , Mn, Mg Ti, Sc, V, Cr, Co, Ni Cu, Zn, Nb, Zr	Si
GARNET $X_3Y_2T_3O_{12}$	X C.N.# = 8	Y C.N.# = 6	T C.N.# = 4	
	Ca, Fe ²⁺ , Mg, Mn, Co Ni, Cu, Zn, Rb, Sr REE, Y	Al, Ti, Sc, V, Cr, Nb Zr	Si	
TITANITE $AM[TO_4](O, OH, F)$	A C.N.# = 7	M C.N.# = 6	T C.N.# = 4	
	Ca, Na, K, Rb, Sr REE, Y, Fe ³⁺ , Mg, Mn Co, Ni, Cu, Zn	Ti, Al, Fe ³⁺ , Sc, V, Cr Nb Zr	Si	

Table 2.1(b) Common end-member mineral formulae (Deer *et al.*, 1992) and average site size of the five major phases analyzed in this study. Average site sizes obtained by subtracting the ionic radius of the O^{2-} ion (1.38 Å) from the measured average cation-oxygen-bond lengths (Smyth and Bish, 1988). C.N.# is the site coordination number.

MINERAL		AVERAGE SITE SIZE (Å)				
CLINO AMPHIBOLE (A ₀₋₁)M ₄ 2M1-3 ₅ T ₈ O ₂₂ (OH, O, F, Cl)	A C.N.# = 12	M4 C.N.# = 8	M1	M2 C.N.# = 6	M3	T C.N.# = 4
<u>Pargasite:</u> (KNa)Ca ₂ (MgFe) ₄ Al[Si ₆ Al ₂ O ₂₂](OH) ₂	1.67	1.11	0.71	0.66	0.70	0.30
<u>Cummingtonite (A site vacant):</u> □(Mg,Fe,Mn) ₇ [Si ₆ O ₂₂](OH) ₂	N/A	0.92	0.72	0.71	0.72	0.25
PLAGIOCLASE A[T ₄]O ₈	A C.N.# = '(5-6) '(7-9)	T C.N.# = 4				
<u>Anorthite:</u> Ca[Al ₂ Si ₂ O ₈]	1.19	0.30				
<u>Albite:</u> Na[AlSi ₃ O ₈]	1.21	0.36				
EPIDOTE X ₂ M1-3 ₃ T ₃ O ₁₂ (OH, F)	X C.N.# = 8 or 9	M1 C.N.# = 6	M2	M3 C.N.# = 6	T C.N.# = 4	
<u>Pistacite:</u> Ca ₂ Al ₂ O(AlFe ³⁺)OH[Si ₂ O ₇][SiO ₄]	1.20	0.53	0.50	0.62	0.26	
<u>Zoisite:</u> Ca ₂ Al ₂ AlOH[Si ₂ O ₇][SiO ₄]	1.18	0.53	0.50	0.59	0.26	
GARNET X ₃ Y ₂ T ₃ O ₁₂	X C.N.# = 8	Y C.N.# = 6		T C.N.# = 4		
<u>Almandine:</u> Fe ₃ Al ₂ Si ₃ O ₁₂	0.84	0.52		0.25		
<u>Grossular:</u> Ca ₃ Al ₂ Si ₃ O ₁₂	0.94	0.54		0.27		
<u>Pyrope:</u> Mg ₃ Al ₂ Si ₃ O ₁₂	0.80	0.51		0.26		
TITANITE AM[TO ₄](O, OH, F)	A C.N.# = 7	M C.N.# = 6		T C.N.# = 4		
<u>Titanite:</u> CaTi[SiO ₄](O,OH,F)	1.08	0.58		0.27		

Table 2.1(c) Effective ionic radii of *REE* and analysed trace elements shown for appropriate ionic charge and coordination numbers (C.N.#) (taken from Shannon, 1976).

Ionic Radius (Å)					Ionic Radius (Å)		Ionic Radius (Å)			
C.N.#	4	6	8	12	6	8	4	6	8	12
Major Elements					<i>REE</i>		Trace Elements			
Si ⁴⁺	0.26				La ³⁺	1.032	1.16	Sc ³⁺	0.745	0.87
Ti ⁴⁺	0.42	0.605	0.74		Ce ³⁺	1.01	1.143	V ⁵⁺	0.355	0.54
Al ³⁺	0.39	0.535			Pr ³⁺	0.99	1.126	Cr ³⁺		0.615
Fe ³⁺	0.49	0.645	0.78		Nd ³⁺	0.983	1.109	Co ²⁺	0.58	0.65
Fe ²⁺	0.63	0.78	0.92		Sm ³⁺	0.958	1.079	Ni ²⁺	0.55	0.69
Mn ²⁺	0.66	0.67	0.96		Eu ³⁺	0.947	1.066	Cu ²⁺	0.57	0.73
Mg ²⁺	0.57	0.72	0.89		Gd ³⁺	0.938	1.053	Zn ²⁺	0.6	0.74
Ca ²⁺		1.00	1.12	1.34	Tb ³⁺	0.923	1.04	Sr ²⁺	1.18	1.21
Na ¹⁺	0.99	1.02	1.18	1.39	Dy ³⁺	0.912	1.027	Rb ¹⁺		1.52
K ¹⁺	1.37	1.38	1.51	1.62	Ho ³⁺	0.901	1.015	Y ³⁺		0.96
					Er ³⁺	0.89	1.004	Zr ⁴⁺	0.59	0.72
					Tm ³⁺	0.88	0.994	Nb ⁵⁺	0.48	0.69
					Yb ³⁺	0.868	0.985			0.74
					Lu ³⁺	0.861	0.977			
					Eu ²⁺	1.17	1.25			
					Ce ⁴⁺	0.87	0.97			

2.1(d) Chondrite Normalization Values used in this study (after Taylor and McLennan, 1985).

wt %		ppm		ppm	
SiO ₂	57.3	La	16	Sc	30
TiO ₂	0.9	Ce	33	V	230
Al ₂ O ₃	15.9	Pr	3.9	Cr	185
FeO	9.1	Nd	16	Co	29
MnO	0.18	Sm	3.5	Ni	105
MgO	5.3	Eu	1.1	Cu	75
CaO	7.4	Gd	3.3	Zn	80
Na ₂ O	3.1	Tb	0.6	Sr	260
K ₂ O	1.1	Dy	3.7	Rb	32
P ₂ O ₅	0.2	Ho	0.78	Y	20
		Er	2.2	Zr	100
		Tm	0.32	Nb	11
		Yb	2.2		
		Lu	0.3		

Chapter 3: Petrography, Bulk-Rock Chemistry and Major-Element Mineral Chemistry

3.1 Introduction

This chapter describes the petrography, bulk-rock chemistry, and major-element mineral chemistry of the investigated samples in order to establish a framework for the discussion of trace-element distributions amongst the co-existing metamorphic minerals. Petrographic analysis of the samples subdivided according to field-based groups is used as the basis to determine detailed information on equilibrium mineral assemblages, modes, textures, and mineral reactions. Bulk rock and mineral chemistry are used to compare the samples for fundamental chemical similarities and differences. These approaches are then combined to provide insight into the metamorphic petrogenesis of the samples.

3.2 Petrography

The *Goose Cove Schist* and the *Green Ridge Amphibolite* are the focus of this study and a summary of their petrographic characteristics follows. The grain size of the minerals is of particular importance in this study since they must be sufficiently coarse-

grained (at least approximately 35 μm) to be analysed by LAM-ICP-MS.

3.2.1 The Goose Cove Schist

The *Goose Cove Schist*, the lower part of the St. Anthony Complex, grades structurally downward into the *Ireland Point Volcanics* and upward into the *Green Ridge Amphibolite*. It principally comprises metabasic rocks, the metamorphic equivalents of the *Ireland Point Volcanics*, as well as subordinate metasedimentary rocks (Jamieson, 1979). The metasedimentary rocks are not significant for this study and the following discussion centres on the three petrographic types of metabasic rocks that were defined within the unit, i.e., spotted and massive/banded greenschists and epidote amphibolites (Table 3.1).

Abundant white 'spots' in a green matrix characterize the appearance of the *spotted greenschists* (Figure 3.1a). The 'spots' are aggregates of fine-grained epidote, calcite, plagioclase and muscovite, which Jamieson (1979) interpreted as the sites of former plagioclase phenocrysts, with the greenschist being the deformed equivalent of porphyritic pillow lava of the *Ireland Point Volcanics*. The aggregates occur in a fine-grained matrix of Ca amphibole (actinolite on the basis of its light green to colourless pleochroism) and chlorite which typically defines a moderately developed S_1 foliation. Where deformation is more pervasive, the aggregates are lens-shaped (Figure 3.1b) and in some cases they are stretched into bands of epidote, calcite, and plagioclase which

appear similar to the banded greenschists.

Massive greenschists include fine to medium-grained sills and dykes within the Goose Cove Schist. These rocks are characterized by a relict diabasic texture with medium-grained Ca amphibole (actinolite on the basis of its light green to colourless pleochroism) intergrown with laths of plagioclase feldspar in a fine-grained matrix of plagioclase, epidote and chlorite. *Banded greenschists* exhibit narrow light green bands of epidote, plagioclase, and carbonate within a fine-grained, dark green matrix of Ca amphibole, epidote, and lesser amounts of chlorite. In contrast to the massive schists, the banded rocks exhibit a penetrative S_1 foliation defined by the alignment of Ca amphibole and chlorite (Figures 3.2a and b). In some places S_1 is folded into asymmetric F_2 folds and overprinted by a spaced S_2 schistosity. The fine-grained nature of the greenschist-facies assemblages precluded their use for LAM-ICP-MS analysis in this study.

A gradual increase in grain size (into the range adequate for LAM-ICP-MS analyses) and the loss of chlorite mark the transition from banded greenschists to *epidote amphibolite* facies rocks (Figures 3.3a and b) which are characterized by the assemblage epidote-“hornblende”-plagioclase-titanite-quartz. Hornblende (i.e., Ca amphibole with olive green-brown pleochroism) is the most abundant phase and commonly contains inclusions of quartz and titanite. Plagioclase is partially saussuritised and matrix quartz occurs as granular aggregates. BSE imaging (Figure 3.3b) reveals matrix epidote to be pervasively patchily zoned on the 5-10 μm scale. However, in some samples, epidote is also concentrated in fine-grained aggregates with minor carbonate and hornblende

forming a separate compositional domain (Figures 3.4a-b). Outside these epidote-rich domains the stable matrix assemblage is hornblende-plagioclase-quartz-titanite. The epidote-amphibolite-facies rocks exhibit similar deformation styles to the banded greenschists, i.e., an S_1 foliation defined by aligned hornblende which is asymmetrically folded by F_2 folds.

Based on these observations, certain first order conclusions related to the petrogenesis of the Goose Cove Schist can be drawn. The greenschist-facies assemblage is plagioclase-epidote-chlorite-actinolite, and the epidote-amphibolite-facies assemblage is plagioclase-epidote-Ca amphibole-titanite-quartz. The transition from the greenschist to the epidote-amphibolite-facies is marked by the disappearance of chlorite, the replacement of actinolite by "hornblende" and the appearance of quartz and titanite, with the chlorite-out isograd separating the greenschist-facies assemblages from those of the epidote-amphibolite facies. The epidote-out isograd defines the maximum stability of the assemblage epidote-plagioclase-hornblende-quartz-titanite and, above this isograd, the stable assemblage is Ca amphibole-plagioclase-titanite-quartz. Thus the Goose Cove Schist contains three metamorphic mineral assemblages indicative of the greenschist-, epidote-amphibolite, and amphibolite-facies. In the absence of any appropriate calibrated mineral geobarometers or geothermometers at that time, Jamieson (1979) estimated a P - T range of 1.75 to 4.5 kbar and 450° to 650°C based on the petrography of the Goose Cove Schist.

3.2.2 The Green Ridge Amphibolite

The Green Ridge Amphibolite comprises the upper part of the St. Anthony Complex and is composed entirely of amphibolite-facies rocks in the study area. The critical distinction between the greenschist and epidote-amphibolite facies rocks of the Goose Cove Schist and the amphibolite-facies rocks of the Green Ridge Amphibolite is the absence of prograde epidote in the latter. The unit can be subdivided into ‘garnet’ and ‘plagioclase’ amphibolites based on their mineralogical characteristics which are summarized in Table 3.2.

A *biotite amphibolite* unit separates the epidote amphibolite (Goose Cove Schist) from overlying plagioclase amphibolite. These rocks are characterized by the assemblage garnet-hornblende-plagioclase-quartz-biotite and the unit has been interpreted as a late-tectonic mylonite zone formed from the surrounding rocks by metasomatism (Jamieson & Strong, 1978; Jamieson, 1979). The proportion of biotite and quartz to hornblende increases with the intensity of deformation. A compositional layering is defined by alternating bands of hornblende and fine- to medium-grained biotite. The typical biotite amphibolite has hornblende-rich layers and porphyroblasts of hornblende, garnet, and plagioclase in a fine-grained biotite- and quartz-rich matrix (Figure 3.5a-b). Accessory phases include apatite, ilmenite, and zircon. Garnet porphyroblasts are rounded and contain concentric or planar inclusion trails of quartz and Fe-Ti oxides (Figure 3.6a) or inclusion-rich cores with inclusion free-rims (Figure 3.6 b).

Chapter 3: Petrography, Bulk-Rock Chemistry and Major-Element Mineral Chemistry

The inclusion trails are better developed in the layered rocks, where they are parallel to the compositional banding.

Plagioclase amphibolite comprises medium- to coarse-grained rocks consisting of brown-green hornblende containing inclusions of quartz and titanite interlayered with plagioclase, quartz and minor titanite (Figures 3.7 and 3.8). Plagioclase occurs as either large anhedral, saussuritised grains or as fresh, fine-grained matrix grains, some of which exhibit deformation twins. Matrix quartz is fine-grained with interlocking grain boundaries, whereas less abundant coarser quartz crystals exhibit extensive sub-grain development and undulose extinction. Fine-grained rhombic titanite is a minor modal phase. Accessory phases include pyrite, chalcopyrite, and Fe-Ti oxides. The main fabric is a foliation defined by the alignment of hornblende and elongate plagioclase crystals. It was not possible to identify isograds within the Green Ridge Amphibolite in the field since the hornblende-plagioclase assemblage is stable in metabasites over a broad range of temperatures and pressures (Spear, 1993).

3.2.3 Summary

The 'chlorite out' and 'epidote out' isograds in the Goose Cove Schist mark the transitions from greenschist to epidote-amphibolite facies and epidote-amphibolite to amphibolite facies respectively, but there is no obvious change in the mineralogy of the Green Ridge Amphibolite in the study area. It is clear the Goose Cove Schist and Green

Ridge Amphibolite were derived from mafic igneous rocks (Jamieson, 1981; this study). Jamieson (1979) concluded that the biotite amphibolite was formed by metasomatism in a syntectonic mylonite zone between epidote amphibolite and plagioclase amphibolite.

The sample suite comprises a continuous sequence of metabasic rocks that equilibrated from upper greenschist to amphibolite facies, as shown by several diagnostic mineral assemblages (all with quartz), including; (i) actinolite-epidote-chlorite-plagioclase-carbonate \pm muscovite; (ii) hornblende-epidote-plagioclase-titanite; (iii) hornblende-garnet-plagioclase-biotite; and (iv) hornblende-plagioclase-titanite. With the exception of the greenschist facies rocks, all samples are sufficiently coarse-grained for LAM ICP-MS analyses.

3.3 Bulk-Rock Chemistry

Thirteen samples encompassing all the mineral assemblages from the narrow metamorphic field gradient described in the preceding section were selected for whole-rock major- and trace-element analysis by XRF and solution mode ICP-MS. Sample locations are shown in Figure 1.2. The bulk geochemistry of the samples was used to characterize them into suites and also for the calculation of whole rock-mineral mass balances. On the basis of bulk-rock major and in particular, trace-element data, two groups of metabasites were distinguished. The first group includes greenschists (samples 69, 70), epidote amphibolites (samples 6, 46, 48) and plagioclase amphibolites (samples

47, 49, 50) and the second group comprises biotite amphibolite (samples 1, 5, 20, 23, 142).

3.3.1 Bulk-Rock Major-Element Chemistry

Whole-rock analyses are shown in Table 3.3. In terms of their major-element contents, the rocks are predominantly mafic, SiO_2 contents ranging from 44.16 to 53.02 wt%. Bivariate plots of major elements against MgO (Figure 3.9) show that samples form two coherent groups. MgO varies from approximately 6-12 wt % and shows strong correlations with several other oxides (e.g., SiO_2 , FeO, Fe_2O_3 , Na_2O). The two groups exhibit discernible differences in their major-element chemistry. For example, MgO in group 1 samples show positive correlation with FeO and negative correlation with Fe_2O_3 ($r = 0.83$ and -0.92 respectively) whereas group 2 samples exhibit the reverse relationship. On average, group 2 has higher SiO_2 , Al_2O_3 , TiO_2 and K_2O and lower $\text{FeO}_{\text{Total}}$, MgO, CaO and Na_2O . These differences in bulk major-element chemistry between suites may explain the mineralogical differences between them. For instance, the presence of biotite in group 2 is attributed to higher K_2O relative to group 1, whereas the relative CaO enrichment of group 1 is consistent with higher modal plagioclase, amphibole and the presence of epidote. In group 1, epidote amphibolites are restricted to Ca-rich bulk compositions ($\approx 9\text{-}13$ wt% CaO: samples 6, 46, 48) and the highest amphibolite grade samples (47, 49, 50) are the most Mg-rich ($\approx 9\text{-}11$ wt% MgO). In

group 2, all major oxides among the samples, excluding sample 5 which is enriched in CaO and depleted in K₂O, show similar concentrations. Sample 5 contains little garnet and has less biotite than other samples in this suite.

3.3.2 Bulk-Rock Trace-Element Chemistry

The REE concentrations (Table 3.3) provide the best data for subdividing the samples into two suites. Relative to the group 1, group 2 is enriched in *LREE* and depleted in the *HREE*. The average ratio of *LREE/HREE* in group 1, $\text{La}_{\text{Avg1}}/\text{Lu}_{\text{Avg1}}$ is 5, whereas in group 2 the $\text{La}_{\text{Avg2}}/\text{Lu}_{\text{Avg2}}$ ratio is 113. Chondrite-normalized REE patterns for whole rocks were constructed to further examine the differences between the two groups (Figure 3.10). The contrast in REE patterns between the two groups is readily apparent with individual samples within each group exhibiting similar trends, implying coherent behaviour and presumably a common origin. The general REE pattern of group 1 is flat with a slight *MREE* enrichment and a small negative europium anomaly. In contrast, group 2 exhibits greater abundances of *L-MREE*, strong *LREE* enrichment (≈ 100 times chondrite), and a *small* negative europium anomaly (Table 3.3).

Concentrations of 15 trace elements other than REE (Sc, V, Cr, Ni, Cu, Zn, Sr, Rb, Y, Zr, Nb, Ba, Hf, Ta, and Th) are shown in Table 3.3 and plotted on Figure 3.11. Overall, the concentrations of these elements are quite variable, but the concentrations of individual elements among the samples are similar within each group. For example,

there is an approximately tenfold increase in the concentration of V compared to Sc for samples in both groups but there is little variation in the concentrations of either V or Sc among individual samples in each group. In group 1, variations in Cu concentration are attributed to variations in modal sulfides. In group 2, Rb and Ba concentrations in sample 5 are approximately an order of magnitude lower than in other samples in the suite. These elements are generally accepted to be 'mobile' during alteration or metamorphism and their variable concentrations are likely attributable to local metasomatic effects.

3.3.3 Bulk-Rock Geochemical Classification

It is not a goal of this thesis to attempt tectonomagmatic discrimination of the metabasites, but these diagrams may be used in a non-genetic way to distinguish groups on the basis of their chemistry. All samples analysed in this study, and in addition analyses of similar rocks from the St. Anthony Complex published by Jamieson (1979), were plotted on Figure 3.12a-c. The Jensen cation plot for classification of volcanic rocks (Figure 3.12a; Jensen, 1976) is based on the proportions of the cations ($\text{Fe}^{2+} + \text{Fe}^{3+} + \text{Ti}$), Al and Mg recalculated to 100%. These elements are considered relatively immobile, thus the diagram is suitable for meta-volcanic rocks that may have suffered mild metasomatic loss of alkalis (Rollinson, 1993). All samples from both groups cluster in the high-Fe tholeiite basalt field. Figure 3.12b shows the plotting position of the bulk

compositions in terms of the system components A ($\text{Al}_2\text{O}_3 + \text{Fe}_2\text{O}_3$), C (CaO) and F ($\text{FeO} + \text{MgO}$). This ternary diagram illustrates that analyzed samples form a single cluster, but exhibit some spread, i.e., (i) a relatively Al_2O_3 rich + CaO depleted population composed of biotite amphibolites, and (ii) a relatively CaO rich + Al_2O_3 depleted population consisting of greenschists, epidote-amphibolites, and plagioclase amphibolites. Greenschists, epidote-amphibolites and plagioclase amphibolites from group (ii) occupy essentially the same ACF composition space. The samples were also plotted on the Ti-Zr-Y diagram (Figure 3.12c) of Pearce and Cann (1973), which can be applied to tholeiitic basalts that fall in the compositional range between $20\% > \text{CaO} + \text{MgO} > 12\%$. Three samples slightly exceed this compositional range (samples 5, 48, 50), but given the homogeneity of the sample population as a whole and the fact that the averages of both groups are well within the prescribed compositional range they were plotted on a trial basis. This diagram clearly discriminates between the two groups. Both suites have similar Ti concentrations but relative to each other, group 1 is Y enriched and group 2 is Zr enriched. Thus, on the basis of both *REE* and HFSE bulk-rock chemistry, two separate groups were clearly distinguished: (1) a “Y-enriched + *LREE* depleted” group comprising greenschists (samples 69, 70), epidote amphibolites (samples 6, 46, 48) and plagioclase amphibolites (samples 47, 49, 50), and (2) a “Zr-enriched + *LREE* enriched” group comprising biotite amphibolites (samples 1, 5, 20, 23, 142). These two groups are referred to as the ‘Y group’ and the ‘Zr group’ in the text

that follows.

From the distribution of the Zr group samples, it is apparent that they come from the shear zone that experienced K-metasomatism and so it is likely that they do not represent original compositions (Figure 1.3, Jamieson, 1979; Dostal *et al.*, 1980; Jamieson and Strong, 1981). On the assumption that the Zr group originally had a similar chemistry to the Y group, a comparison between the two groups should indicate the relative losses and gains during metasomatism in the shear zone. To facilitate this, it is necessary to normalize the analyses to selected 'immobile' elements in the two data sets. The choice of elements is arbitrary, and the following relatively immobile oxide and elements were used in this study: major elements - Al_2O_3 ; *REE* - Dy; other trace elements - Ni. Figure 3.13 illustrates the strong relative enrichment of Zr group samples in K_2O , P_2O_5 , LILEs, HFSEs and *LREE* relative to Y group rocks. It is important to note that these results are dependent on the normalization scheme employed and cannot be considered to constitute absolute losses/gains in the Zr relative to the Y group. Nevertheless it is likely that the relatively increased amounts of K and P stabilized phases such as biotite and apatite that are restricted to the Zr group assemblage. Consequently, the presence of these phases may be linked to the relative increases in the concentrations of LILEs which are known to be compatible in interlayer sites in biotite, and *LREE* which are accommodated by the Ca site in apatite (Sorensen and Grossman, 1989, 1993; Yang, 2002).

On the other hand, it is possible that differences between the Y and Zr groups are related to their original igneous compositions. The Y group appear to be derived from MORB-like magmas, whereas the Zr group are akin to smaller degree melts (akin to OIB-like magmas). For the purpose of the interpretations presented in this thesis, it is adequate to understand that there are two distinct bulk compositions from which the metamorphic assemblages are derived.

3.4 Major-Element Mineral Chemistry

Current understanding of the abundances and distributions of the major elements in minerals in metabasites is at a less quantitative stage than that of other metamorphic rock groups such as metapelites. There are several reasons for this, including the chemical complexity of basalts and the fact that there are relatively few minerals in most metabasites (Spear, 1993). The chemical complexity of basalts implies that numerous system components are required to describe the chemical system accurately. In terms of the minerals present, the most abundant mineral encountered in many metabasites is Ca amphibole, which can display a very wide range of compositions as a function of bulk composition and metamorphic grade. Consequently, the metamorphism of mafic rocks is characterized by a limited number of mineral assemblages with the constituent minerals (e.g., Ca amphibole, plagioclase, epidote, garnet, etc.) exhibiting a wide range of composition. In this study, the major- and trace-element compositions of five major

metamorphic minerals (Ca amphibole, plagioclase, epidote, garnet and titanite) from a narrow metamorphic field gradient (epidote-amphibolite to amphibolite facies) were investigated by electron microprobe and LAM-ICP-MS. Average major-element mineral analyses, and cation site occupancies, based on ionic radii and charges (Smyth & Bish, 1988) of the 5 minerals from the 8 investigated samples are presented in Table 3.4. The 1 sigma errors listed in Table 3.4 are based on the measured concentrations of *separate grains* in each sample are not indicative of within-grain zoning. The complete major-element mineral data set is presented in Appendix A. A discussion of these results follows. *REE* and trace-element mineral chemistry of the samples are presented in chapters 4 and 5 respectively.

3.4.1 Calcic Amphibole

Ca amphibole, informally referred to as 'hornblende' earlier in this chapter, is the most abundant phase investigated and is stable in both the Y and Zr groups, generally occurring as medium to coarse grains that are unzoned with respect to major elements. Oxide weight % analyses were normalized to 23 oxygen atoms per formula unit yielding cation totals in the narrow range of 15.50 to 15.80 (Table 3.4a). In general, with increasing metamorphic grade in metabasites, the proportion of alkalis (Na + K) and aluminum in Ca amphibole increase such that compositions change from tremolite (greenschist facies) to tschermakite or pargasite (amphibolite facies) (Spear, 1993). To

classify and investigate major-element compositional changes in the samples in this study, individual amphibole analyses from epidote amphibolites (Y group: 06, 46, 48), biotite amphibolites (Zr group: 01, 20, 142) and plagioclase amphibolite (Y group: 49) were plotted on the clinoamphibole rectangle (Figure 3.14a), which shows the main exchange vectors relating the compositions of (FeMg) amphibole to calcic amphibole, i.e., $^{M4}\text{Ca} \leftrightarrow ^{M4}\text{FeMg}$. As inferred from their optical properties, all analysed amphibole is calcic, and with the exception of two Y group samples, compositions from both groups exhibit a minor (FeMg) component in $M4$ ($^{M4}X_{\text{FeMg}} = X_{\text{Cum}} \approx 0.05$). The two exceptions from the Y group (46, 48) have $^{M4}X_{\text{FeMg}} \approx 0.15$ and are relatively cummingtonite rich plotting near the stability limit of substitution of (MgFe) for Ca (Spear, 1993).

Amphibole analyses were then plotted on a Ca amphibole nomenclature diagram (Figure 3.14b; Leake *et al.* 1997, 2003). The nomenclature is based on the chemical variation of amphibole expressed as numbers of $(\text{Na} + \text{K})^{\text{A}}$ atoms in A -sites versus Si atoms in tetrahedral sites per formula unit. The samples exhibit a trend towards pargasite and cluster into two groups: (i) an $^{\text{XII}}(\text{Na} + \text{K})^{\text{A}} - \text{Si}^{\text{IV}}$ depleted group, and (ii) an $^{\text{XII}}(\text{Na} + \text{K})^{\text{A}} - \text{Si}^{\text{IV}}$ enriched group. These two groups do not correspond to the sample distribution from Figure 3.13a and are independent of the extent of cummingtonite substitution.

Since all analysed amphibole is calcic, it is logical to evaluate the two dominant exchange vectors in this species by which pargasite forms from an initial composition of

tremolite. These exchange vectors are the edenite ($\square\text{Si} \leftrightarrow \text{NaAl}^{\text{IV}}$) and tschermak ($\text{MgFe}^{2+}\text{Si} \leftrightarrow \text{Al}^{\text{VI}}\text{Al}^{\text{IV}}$) exchanges and can be combined to form an additional, but not independent exchange vector, the so-called pargasite exchange ($\text{NaAl}^{\text{VI}}\text{Al}^{\text{IV}}_2 \leftrightarrow \square\text{MgSi}_2$; Spear, 1993). To determine the relative roles of the *independent* exchange vectors, samples were plotted on an edenite exchange *versus* tschermak exchange diagram (Figure 3.14c). In this diagram, the samples cluster into the same two groups as in Figure 3.14b, and it is apparent that the grouping is a result of different degrees of edenite and tschermak substitution and is independent of the cummingtonite component. For simplicity in the text that follows, the groups are referred to as ‘edenitic’ and ‘tschermakitic’. This nomenclature is based on the relative role of each exchange vector and does not imply a specific amphibole composition. To summarize, three independent exchange vectors influence the major-element chemistry of analysed calcic amphibole, i.e., the edenite, tschermak, and cummingtonite exchanges.

3.4.2 Plagioclase

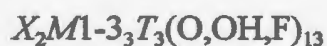
Plagioclase is stable across the entire sample suite occurring as a fine to medium-grained unzoned phase with ubiquitous sericitization, consequently making it difficult to analyse. BSE imaging was utilized to locate appropriate analysis points. Oxide weight % analyses were normalized to 8 oxygen atoms per formula unit yielding cation totals near 5.00. In general, the orthoclase component ($X_{\text{Or}}^{\text{Pl}} = \text{K}/\text{K} + \text{Na} + \text{Ca}$) is subordinate

(< 1 %), the highest measured value occurring in sample 20 from the Zr group which has 3% orthoclase. The general tendency for the anorthite component in plagioclase to increase with metamorphic grade in metabasites is well known. Above the peristerite gap, the calcification of plagioclase involves the breakdown of epidote and formation of an anorthite component in plagioclase (Spear, 1993). Therefore, plagioclase from epidote amphibolites should be more albite-rich than plagioclase from garnet and plagioclase amphibolites. Analyses plotted in the ternary feldspar diagram shown in Figure 3.15a confirm this relationship. There is a broad range of molar anorthite, ranging from approximately An 30 to 55 %. Plagioclase from epidote amphibolite is less rich in X_{An}^{Pl} than plagioclase from amphibolite above the epidote-out isograd, as illustrated in Figure 3.15b, which is a histogram of plagioclase compositions expressed as molar % anorthite. The most calcic plagioclase from an epidote amphibolite occurs in the sample (Y group: 06) with the lowest modal abundance of epidote. X_{An}^{Pl} from biotite amphibolites ranges from 35 to 45 %, transitional between plagioclase from epidote amphibolites and plagioclase from 'true' amphibolites.

3.4.3 Epidote

Epidote is restricted to calcium-rich bulk compositions in Y group samples (06, 46, 48). It occurs as a fine- to medium-grained apparently unzoned matrix phase and in separate epidote-rich domains. Only matrix grains were analysed. Epidote is not present

as an equilibrium phase in the Zr group. Oxide weight % analyses were normalized to 12.5 oxygen atoms per formula unit giving cation totals near 8.00. Compositions of epidote are plotted in the zoisite-pistacite-piemontite ternary diagram shown in Figure 3.16a. Ercit (2002) defined the nomenclature utilized in the diagram and it is based on the Al, Fe³⁺ and Mn cation distribution in one of the three *Y* sites of the ideal epidote formula:



In end-member zoisite or clinozoisite, calcium fills the *X* site, aluminum occupies all three of the *M* sites and silica fills the *T* site. In ideal end-member epidote, the *M3* site is occupied by Fe³⁺ (pistacite) and in piemontite the *M3* site is occupied by Mn³⁺. The piemontite component is minor in all analysed samples. Two samples (46, 48) cluster with X_{Zo} ranging from 25 to 34 %. Epidote from sample 06, just below the epidote-out isograd, shows more variation and is more aluminum-rich, containing between 60 to 75 % molar zoisite.

3.4.4 Garnet

Garnet is restricted to Zr group metabasites and occurs primarily as rounded porphyroclasts (Figure 3.6) that are unzoned in major elements. Oxide weight % analyses were normalized to 12 oxygen atoms per formula unit yielding approximately 8.00 cations. Garnet analyses are plotted on a ternary diagram in terms of their almandine-pyrope, spessartine and grossular proportions in Figure 3.16b. Analysed

Chapter 3: Petrography, Bulk-Rock Chemistry and Major-Element Mineral Chemistry

garnet is predominantly an almandine-grossular solid solution with X_{Alm} from 0.56 to 0.64 and X_{Grs} from 0.23 to 0.30. Both pyrope and spessartine are minor constituents in the solid solution with X_{Prp} from 0.09 to 0.11 and X_{Sps} from 0.02 to 0.05. The minor variation in end-member proportions of the garnet is attributed to the limited compositional range and the narrow P - T field gradient from which the samples were collected.

3.4.5 Titanite

Titanite is present in both the Y and Zr groups primarily as a fine-grained subhedral to euhedral matrix phase. Oxide weight % analyses were normalized to 20 oxygen atoms per formula unit giving cation totals of approximately 12. Titanite analyses are plotted in a ternary composition space defined by octahedral substitution of Fe^{3+} and Al for Ti and exhibit little variation (Figure 3.17). Minor Al (up to $\approx 8\%$) and Fe^{3+} (up to $\approx 3\%$) substitute in the octahedral site with minor Mg and Na substitution occurring in the 7-fold coordinated Ca site.

3.5 Inferred Reactions across the Metamorphic Gradient

On the basis of the observed and measured major-element mineralogical variations across the metamorphic gradient, it is possible to qualitatively determine the metamorphic reactions that occurred. The reaction across the chlorite-out isograd can be

summarized as:




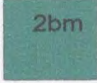
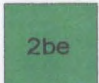
where Pl_2 is a more An-rich than Pl_1 and Ca-amp_2 is an Al-bearing amphibole with significant Na in A sites (i.e., pargasite) compared to Ca-amp_1 (actinolite). Reaction 3.1 appears to have resulted in the consumption of chlorite in the analysed samples leaving $\text{Ca-amp}_2 + \text{Pl}_2 + \text{Ttn} + \text{Ep}$ as the stable epidote-amphibolite assemblage.

The generalized reaction at the epidote-out isograd was:



in which major elements in epidote were largely taken up by slight adjustments in the chemistry and modal abundances of Ca amphibole and plagioclase, with plagioclase becoming more anorthitic rich and Ca-amp_3 more edenitic. Small variations in titanite chemistry may also have accompanied this reaction. As noted, the biotite amphibolites have a different bulk chemistry compared to the other metabasites, and so no attempt is made here to relate their mineralogy to that in the other samples.

Table 3.1 Petrography of the Goose Cove Schist Metabasites

LITHOLOGY	MINERALOGY	COMMENTS
2b Metabasites		
SPOTTED GREENSCHIST 	<p><u>Aggregates</u> (20-60%): epidote, plagioclase carbonate, muscovite</p> <p><u>Matrix</u>: actinolite (50%); plagioclase (10-20%); epidote (20-30%); titanite+quartz+opaques (<5%)</p>	<p>S₁ moderately developed → alignment of chl+amp</p> <p>Original plagioclase phenocrysts replaced by aggregates that are flattened in the plane of S₁</p>
MASSIVE/BANDED GREENSCHIST 	<p><u>Massive</u>: actinolite (40-60%); plagioclase (10-25%); epidote (15-30%); chlorite (5-20%); titanite+quartz+muscovite+opquaes (<5%: pyrite + Fe-Ti oxides).</p> <p><u>Banded</u>: amphibole (50-60%); plagioclase (10-25%); epidote (15-30%); chlorite (5-15%)</p>	<p><u>Massive</u>: relict diabasic texture with amph+plag intergrowths</p> <p><u>Banded</u>: S₁ foliation → alignment of amp+chl</p> <p>S₁ asymmetrically folded by F₂</p>
EPIDOTE AMPHIBOLITE 	<p><u>Matrix</u>: hornblende (55-75%); plagioclase (5-15%) epidote (5-20%); titanite (<5%); quartz+opaques (<5%: pyrite + Fe-Ti oxides)</p> <p><u>Aggregate</u>: epidote+amphibole₁+carbonate</p> <p>epidote + amphibole₁ → hornblende + plagioclase</p>	<p>S₁ foliation → alignment of hornblende locally folded by F₂</p> <p>No chlorite</p> <p>Rocks with epidote only as an aggregate are in the amphibolite facies</p>

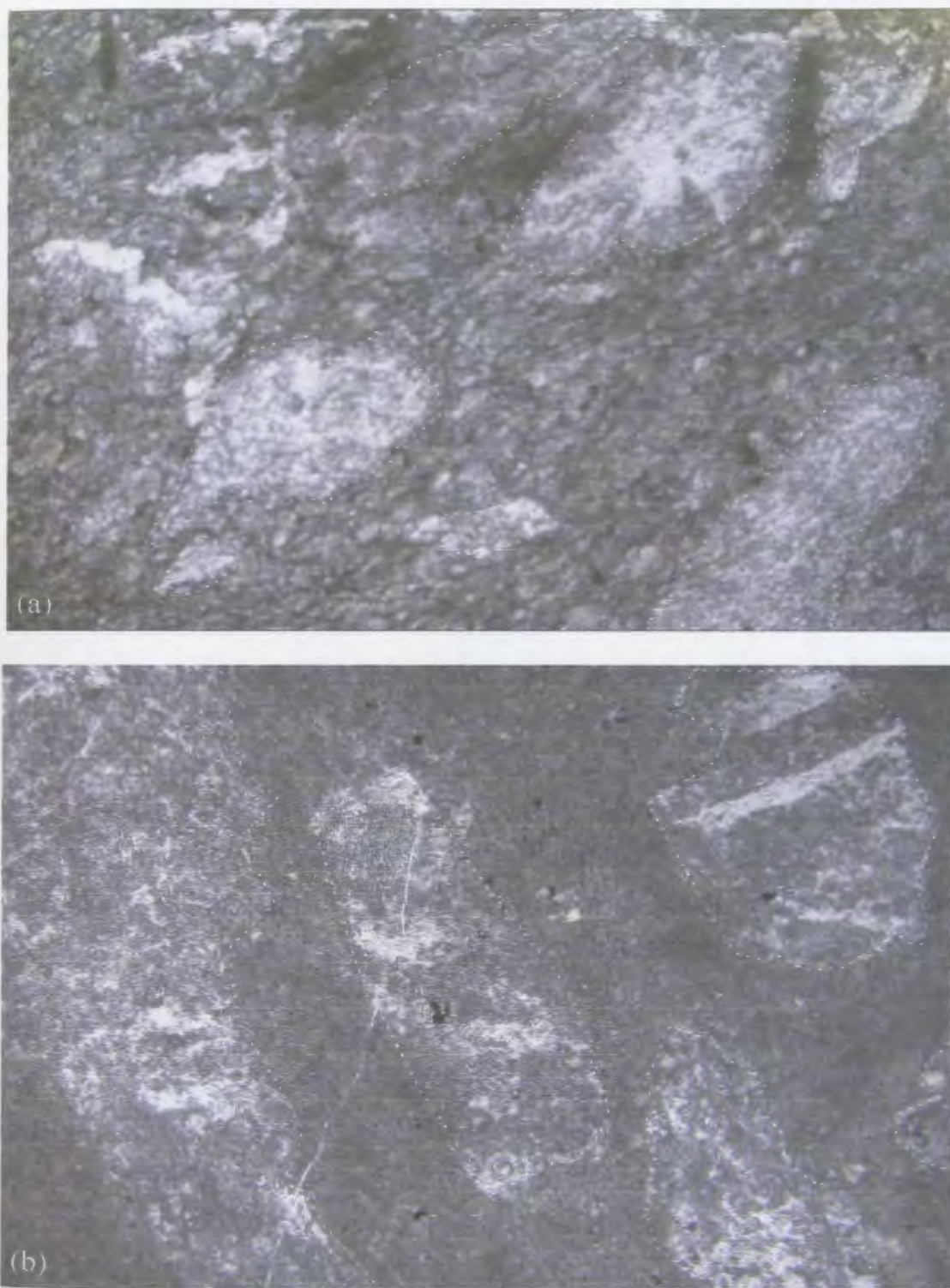


Figure 3.1 (a) and (b) Deformed 'spotted' Goose Cove greenschist showing elongation of mineral aggregates. Mineral aggregates (dashed white outlines) consist of fine-grained epidote, calcite, plagioclase and muscovite. Matrix consists of chlorite, epidote and amphibole. Both photomicrographs PPL, 2.5 cm horizontal field of view.

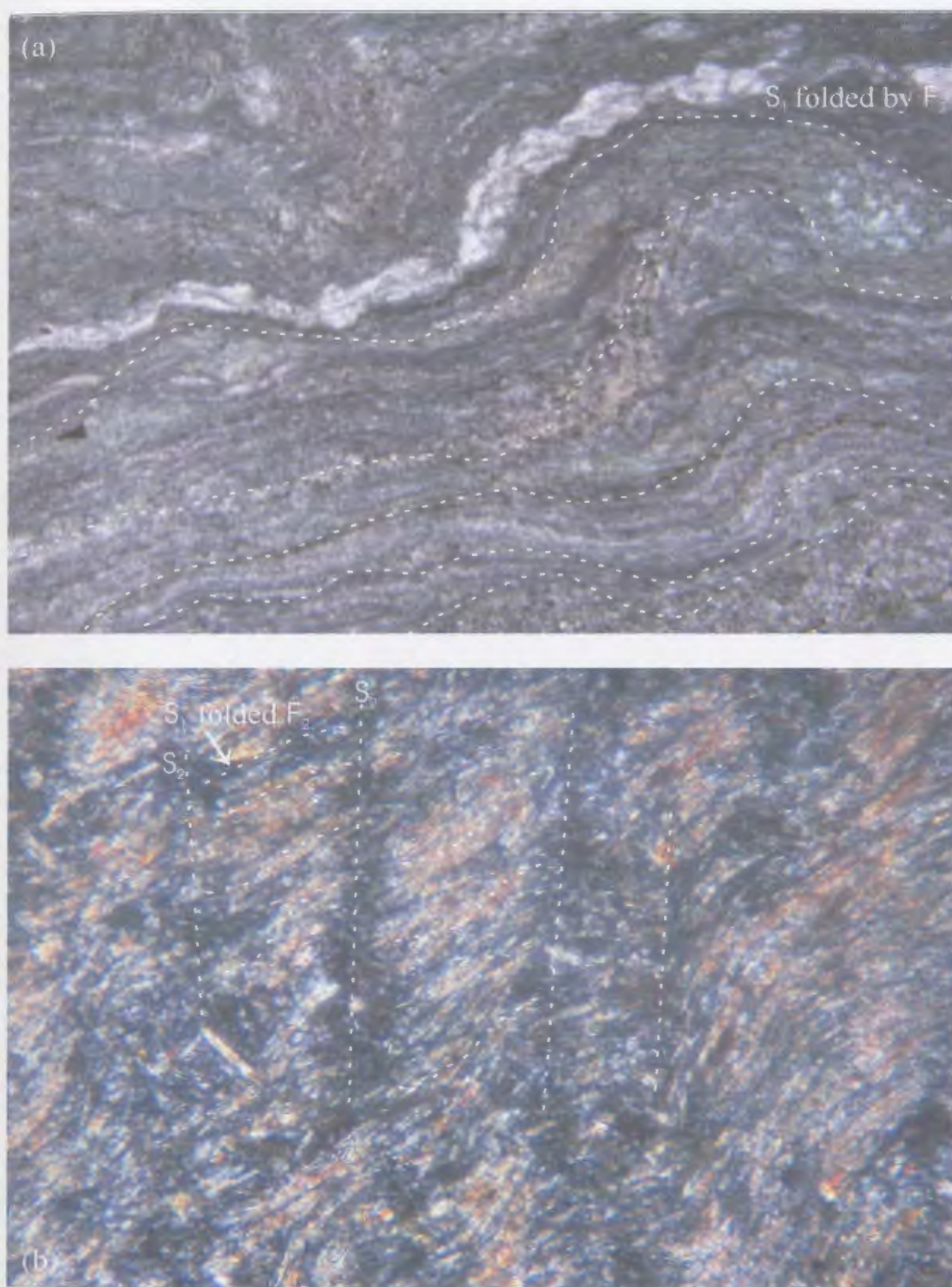


Figure 3.2 (a) S₁ defined by amphibole and chlorite layering folded by F₂ in Goose Cove Schist. (b) Folded S₁ fabric (defined by amphibole and chlorite) that is overprinted by S₂. Horizontal field of view is 2 cm in (a), 1 cm in (b).

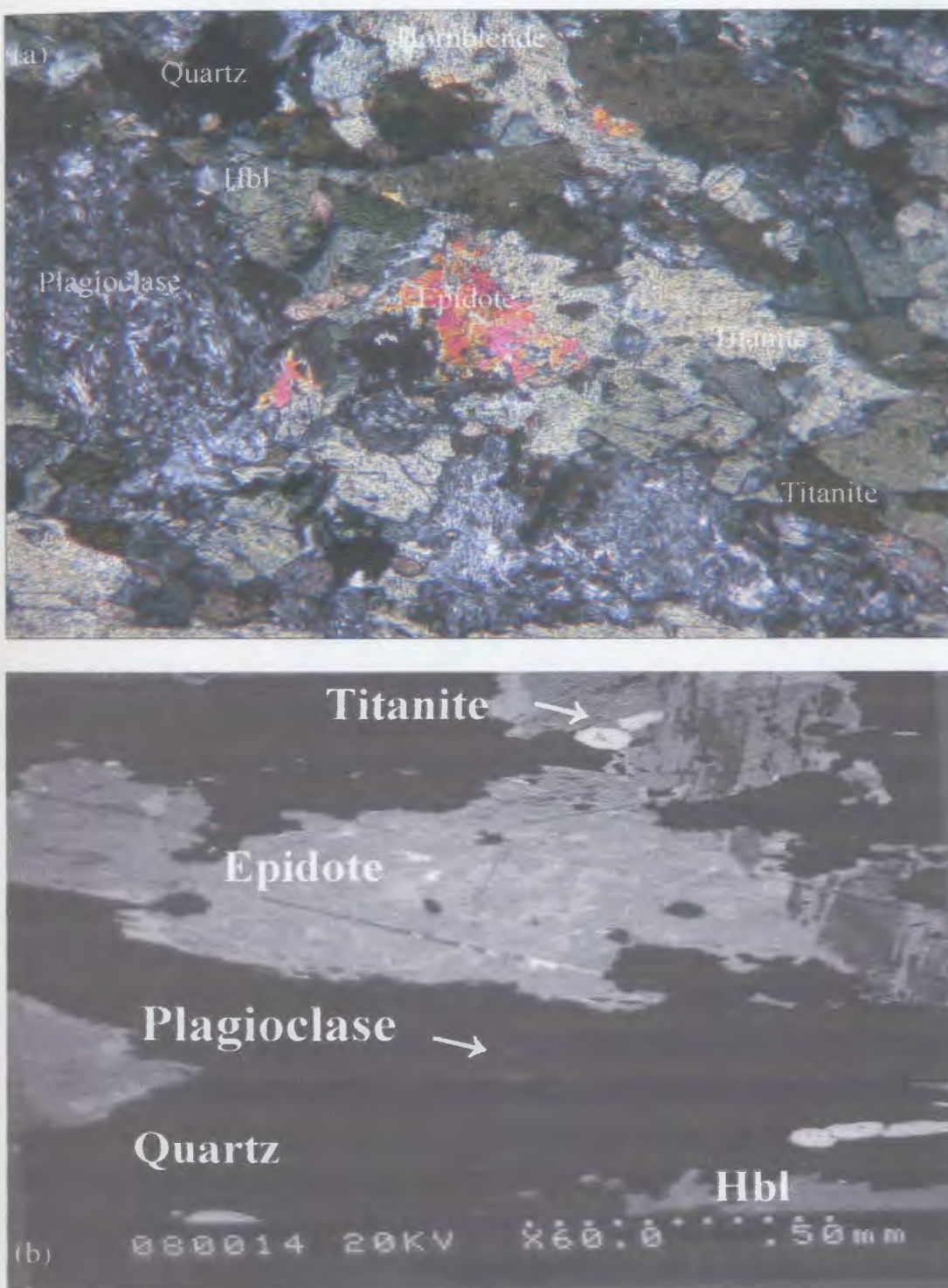


Figure 3.3 (a) Epidote amphibolite facies assemblages of the Goose Cove Schist comprising hornblende, altered plagioclase, epidote, quartz and titanite. Horizontal field of view in (a) is 2 cm. XPL (b) BSE image of epidote amphibolite. Notice 'patchy' zoning in epidote, which is characteristic of all analysed epidote in this study.

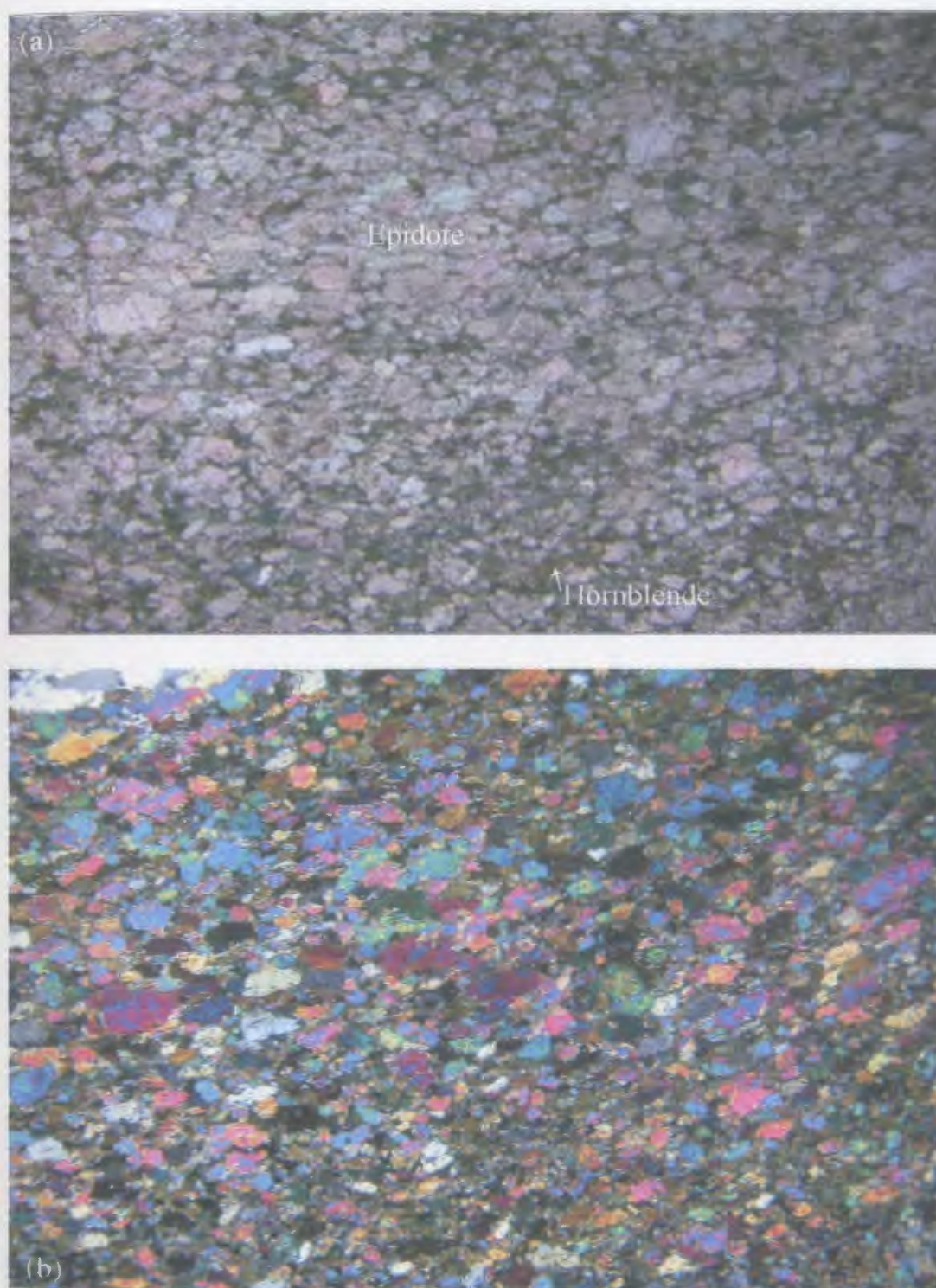


Figure 3.4 Epidote-rich domain in epidote-amphibolite facies member of the Goose Cove Schist in (a) plane polarized light and (b) cross polarized light. Horizontal field of view is 2.5 cm.

Table 3.2 Petrography of the Green Ridge Amphibolite Metabasites

LITHOLOGY	MINERALOGY	COMMENTS
2c Metabasites		
BIOTITE AMPHIBOLITE	<p><u>Primary:</u> hornblende (40-60%); garnet (5-15%); plagioclase (15-30%); quartz (5-10%); titanite (5%); minor modal ilmenite, apatite and zircon</p> <p><u>Secondary:</u> epidote, sericite</p>	<p>Compositional layering → hbl/bt</p> <p>Porphyroclastic Hbl, Grt, and Pl in a fine-grained Qtz-Bt matrix</p> <p>Rounded Grt porphyroclasts with circular or planar Qtz-Fe-Ti oxide inclusion trails</p> <p>Pl sericitized</p>
PLAGIOCLASE AMPHIBOLITE	<p><u>Primary:</u> hornblende (50-80%); plagioclase (15-35%); quartz (10-15%); titanite (5%); minor modal pyrite, chalcopyrite, Fe-Ti oxides</p> <p><u>Secondary:</u> sauss, epidote, chlorite, sericite</p>	<p>Heterogeneous development of compositional layering → Hbl/Pl</p> <p>Brown/green hornblende with inclusions of quartz and titanite</p> <p>Plagioclase either saussuritised or fine-grained with deformation twins</p> <p>Quartz aggregates show extensive sub-grain development</p>

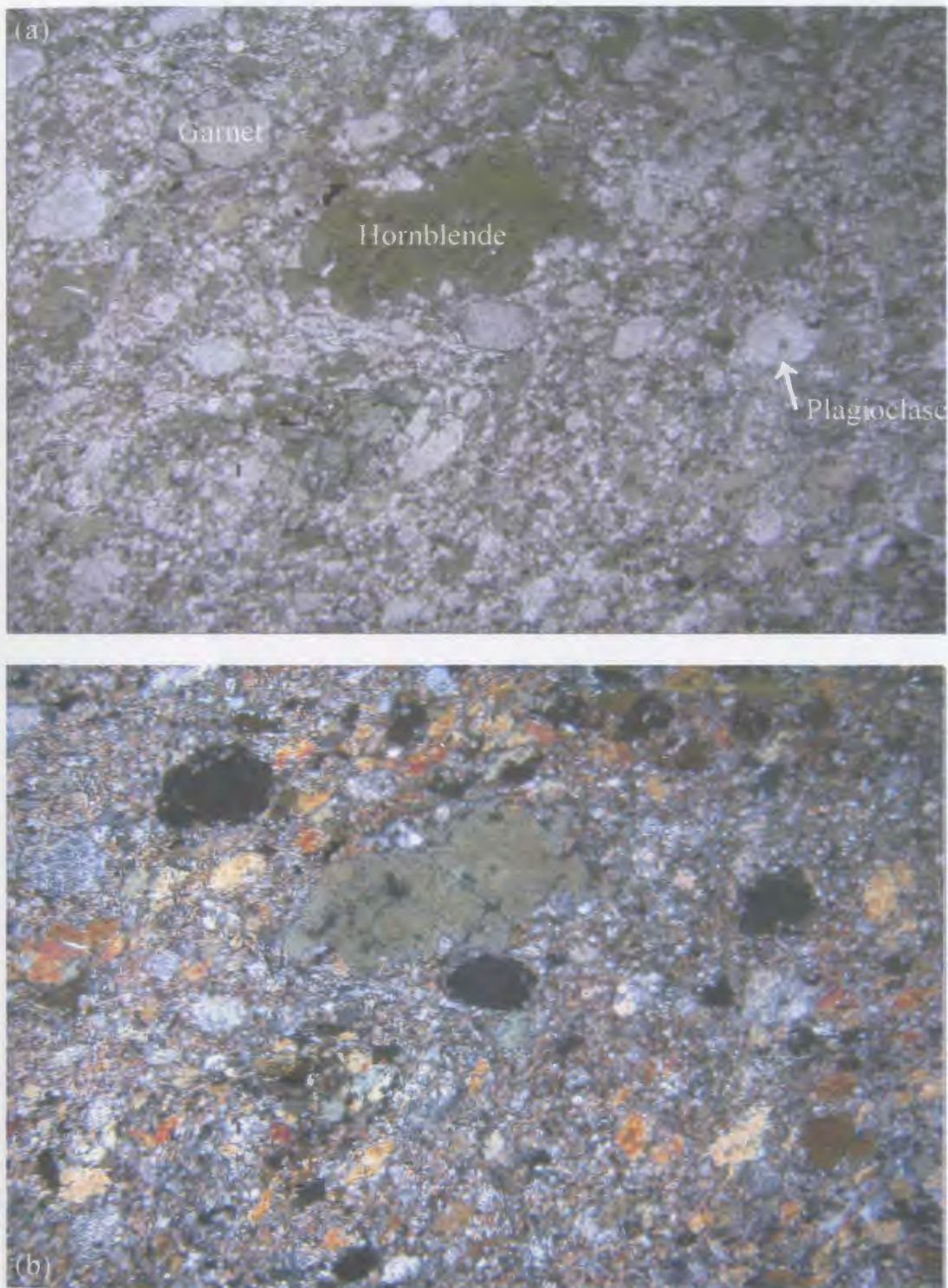


Figure 3.5 Biotite amphibolite from the Green Ridge Amphibolite showing porphyroclasts of garnet, hornblende and plagioclase in a matrix of biotite and quartz (a) PPL (b) XPL. Horizontal field of view is 2.5 cm.

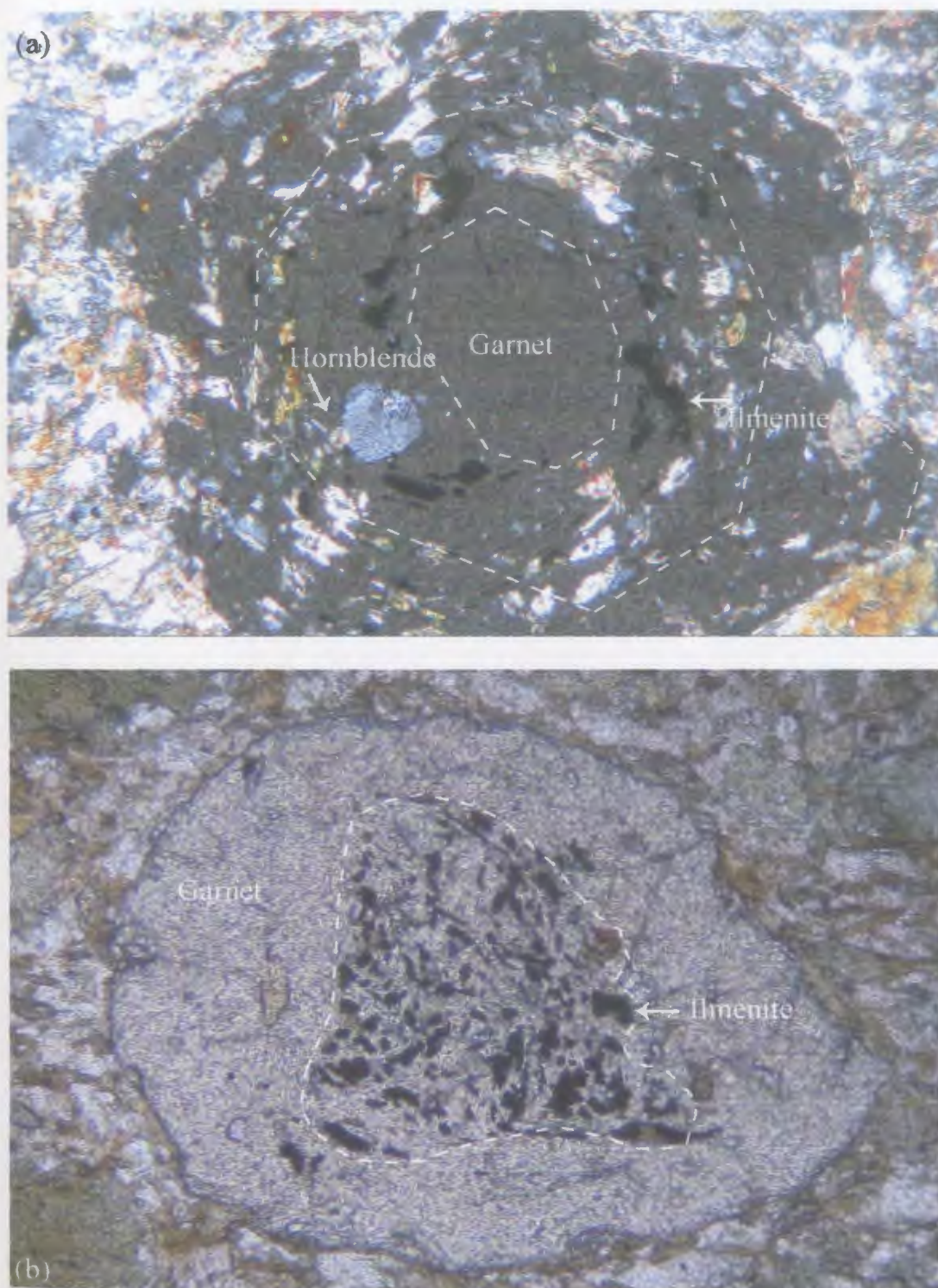


Figure 3.6 Illustration of textural variations within garnet porphyroclasts of the Green Ridge Amphibolite. Inclusions in (a) (XPL) exhibit concentric arrangement around the garnet core (horizontal field of view is 2.5 cm) whereas inclusions in (b) (PPL) are restricted to the garnet core (horizontal field of view is 2 cm).

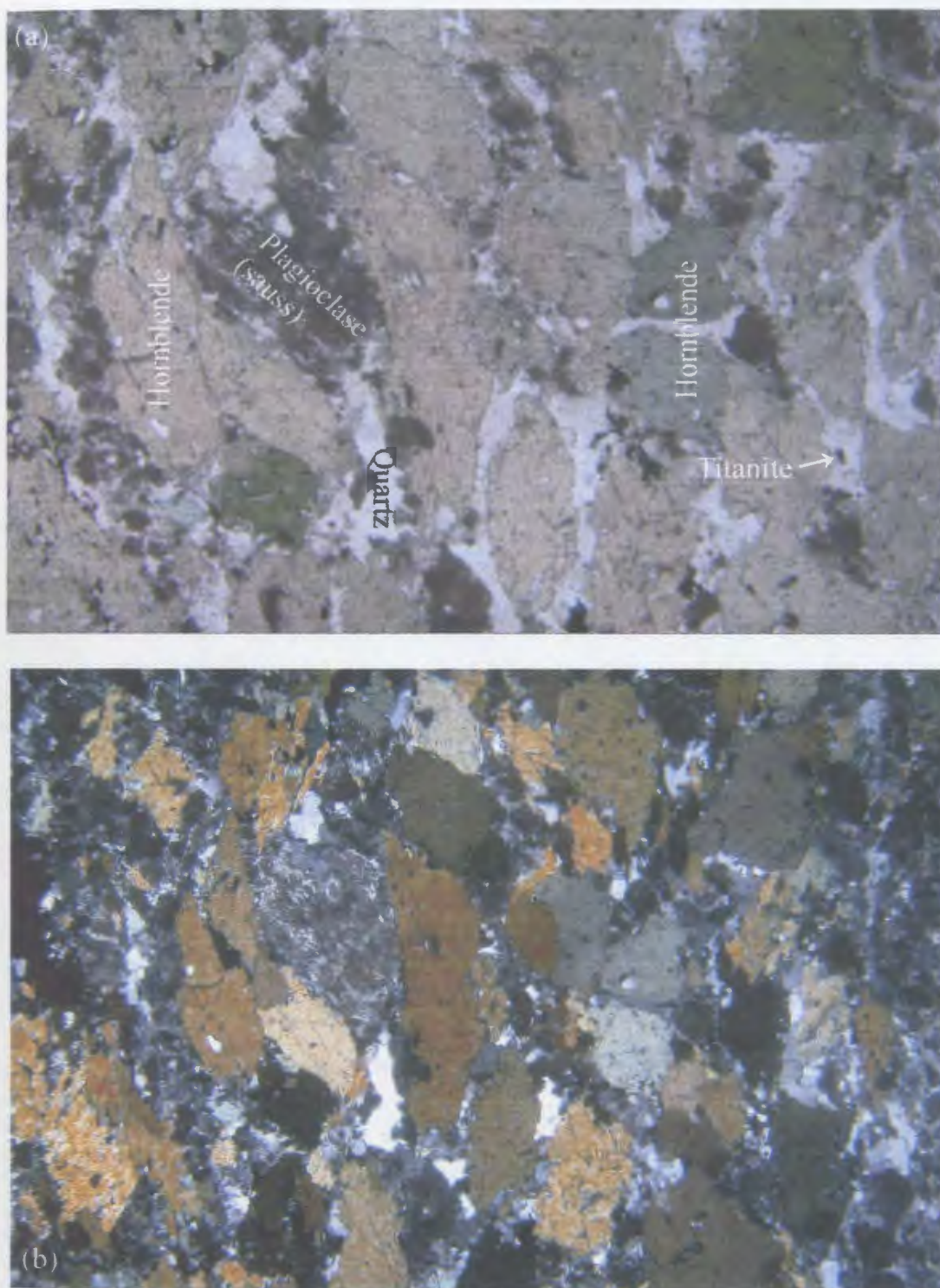


Figure 3.7 The general appearance of the plagioclase amphibolite member of the Green Ridge Amphibolite in (a) PPL and (b) XPL. Horizontal field of view is 2.5 cm.

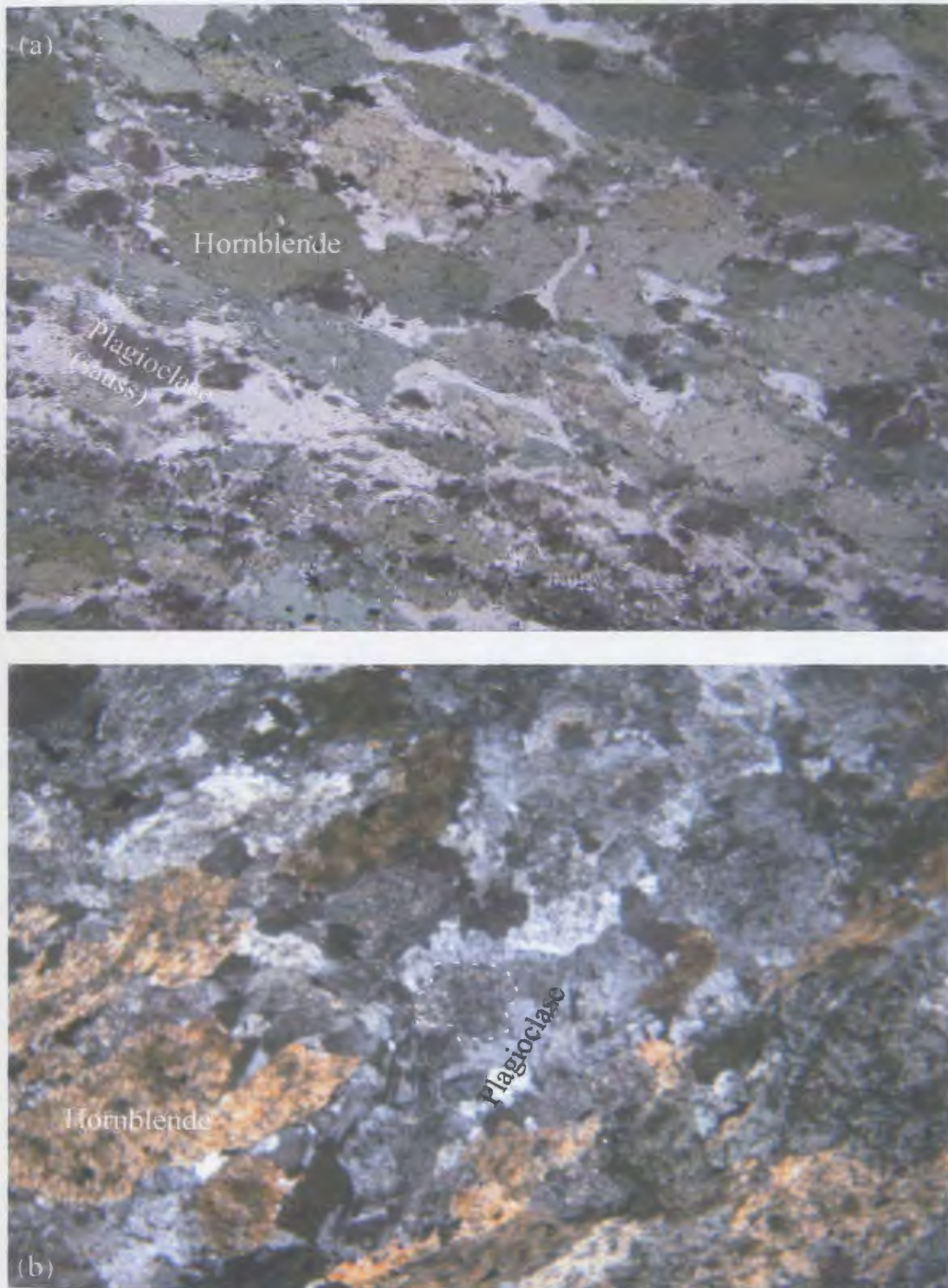


Figure 3.8 (a) Plagioclase amphibolite with green-brown hornblende and saussuritized plagioclase (PPL). (b) Plagioclase amphibolite exhibiting typical corroded (sericitized) core (XPL). Horizontal field of view in both (a) and (b) is 2 cm.

Chapter 3: Petrography, Bulk-Rock, and Major-Element Mineral Chemistry

Table 3.3 Bulk-rock compositions of metabasites from the St. Anthony Complex determined by XRF (major elements, transition metals and LILEs) and solution mode ICP-MS (*REE* and HFSEs). EA is epidote amphibolite, PA is plagioclase amphibolite BA is biotite amphibolite and GS is greenschist.

Y GROUP (group 1)								
Sample #	06	46	47	48	49	50	69	70
Lithology	EA	EA	PA	EA	PA	PA	GS	GS
(wt %)								
SiO ₂	47.79	44.45	45.05	45.85	44.16	45.71	48.42	47.93
Al ₂ O ₃	11.63	12.32	11.74	13.01	10.84	11.71	11.41	10.31
TiO ₂	1.74	1.92	1.7	1.77	1.66	1.63	2.06	1.88
FeO	8.73	8.95	10.18	6.72	10.24	12.81	7.51	8.28
Fe ₂ O ₃	4.61	5.32	4.22	6.11	3.61		7.02	5.36
MgO	9.22	7.47	11.51	6.99	9.84	11.1	6.64	6.94
MnO	0.23	0.28	0.22	0.26	0.22	0.2	0.23	0.21
CaO	9.67	12.49	7.06	13.34	8.57	10.18	11.13	12.39
Na ₂ O	2.33	2.39	2.1	2.65	2.74	2.2	3.07	2.71
K ₂ O	0.21	0.87	0.29	0.66	0.28	0.23	0.55	0.56
P ₂ O ₅	0.18	0.20	0.16	0.18	0.12	0.20	0.18	0.14
(ppm)								
Sc	46.0	53.0	46.0	48.0	46.0	42.0	53.0	47.0
V	428	403	396	376	399	311	430	343
Cr	107	181	162	260	159	440	95	107
Ni	34.0	80.0	38.0	86.0	51.0	161.0	33.0	37.0
Cu	33.0	59.0	249	31.0	8.00	44.0	82.0	65.0
Zn	75.0	66.0	131	57.0	89.0	50.0	68.0	58.0
Sr	99.0	219	152	321	99.0	147	156	203
Rb	3.00	12.0	5.00	10.0	5.00	3.00	7.00	4.00
Y	33.0	32.0	33.0	30.0	31.0	31.0	41.0	35.0
Zr	141	132	134	132	131	164	142	124
Nb	9.00	8.00	8.00	9.00	10.00	7.00	5.00	4.00
Ba	45.0	166	201	162	61.0	36.0	61.0	87.0
La	5.00	5.00	5.00	6.00	5.00	5.00	4.00	4.00
Ce	14.0	16.0	14.0	16.0	14.0	15.0	13.0	12.0
Pr	2.00	2.00	2.00	2.00	2.00	2.00	2.00	2.00
Nd	12.0	12.0	12.0	12.0	12.0	12.0	13.0	12.0
Sm	4.00	4.00	4.00	4.00	4.00	4.00	5.00	4.00
Eu	1.00	2.00	1.00	1.00	1.00	1.00	2.00	2.00
Gd	6.00	6.00	6.00	5.00	5.00	6.00	7.00	6.00
Tb	1.00	1.00	1.00	1.00	1.00	1.00	1.00	1.00
Dy	7.00	7.00	7.00	6.00	6.00	6.00	8.00	7.00
Ho	1.00	1.00	1.00	1.00	1.00	1.00	2.00	1.00
Er	4.00	4.00	4.00	4.00	4.00	4.00	5.00	4.00
Tm	1.00	1.00	1.00	1.00	1.00	1.00	1.00	1.00
Yb	4.00	4.00	4.00	3.00	4.00	4.00	5.00	4.00
Lu	1.00	1.00	1.00	1.00	1.00	1.00	1.00	1.00
Hf	4.00	4.00	4.00	3.00	4.00	4.00	4.00	4.00
Ta	1.00	1.00	0.47	1.00	1.00	0.46	0.32	0.23
Th	1.00	0.45	0.17	1.00	1.00	0.47	0.26	0.22
La/Lu	5.00	5.00	5.00	6.00	5.00	5.00	4.00	4.00
Eu/Eu*	0.63	1.26	0.63	0.69	0.69	0.63	1.04	1.26

Chapter 3: Petrography, Bulk-Rock, and Major-Element Mineral Chemistry

Table 3.3 Bulk-rock compositions of metabasites from the St. Anthony Complex determined by XRF (major elements, transition metals and LILEs) and solution mode ICP-MS (*REE* and HFSEs). EA is epidote amphibolite, PA is plagioclase amphibolite BA is biotite amphibolite and GS is greenschist.

Sample #	Zr Group (group 2)					Y Group	Zr Group
	01	05	20	23	142	AVG	AVG
Lithology	BA	BA	BA	BA	BA	AVG	AVG
(wt %)							
SiO ₂	51.19	48.28	52.87	53.02	49.04	46.17	50.88
Al ₂ O ₃	14.3	11.8	13.93	13.98	13.79	11.62	13.56
TiO ₂	2.53	2.29	2.5	2.5	2.60	1.80	2.48
FeO	8.87	5.64	9.23	9.64	10.13	9.18	8.70
Fe ₂ O ₃	2.46	5.52	2.23	1.84	2.06	5.18	2.82
MgO	5.49	6.18	5.63	5.62	5.56	8.71	5.70
MnO	0.14	0.2	0.17	0.18	0.20	0.23	0.18
CaO	6.03	15.25	5.87	6.16	8.29	10.60	8.32
Na ₂ O	1.87	1.59	1.73	1.71	2.20	2.52	1.82
K ₂ O	2.71	0.82	2.98	2.84	1.79	0.46	2.23
P ₂ O ₅	0.47	0.57	0.53	0.51	0.52	0.17	0.52
(ppm)							
Sc	22.0	25.0	23.0	22.0	31.0	47.6	24.6
V	241	166	229	236	257	385.75	226
Cr	226	208	218	223	142	189	203
Ni	76.0	76.0	75.0	87.0	60.0	65.0	74.8
Cu	80.0	47.0	47.0	66.0	41.0	71.4	56.2
Zn	62.0	44.0	62.0	63.0	66.0	74.3	59.4
Sr	324	476	335	322	376	175	367
Rb	61.0	13.0	65.0	64.0	41.0	6.13	48.8
Y	28.0	20.0	27.0	28.0	29.0	33.3	26.4
Zr	302	264	340	334	305	138	309
Nb	55.0	62.0	69.0	71.0	64.0	7.50	64.2
Ba	551	149	614	604	590	102	502
La	37.0	34.0	41.0	64.0	39.0	4.88	43.0
Ce	78.0	68.0	88.0	126	81.0	14.3	88.2
Pr	9.00	8.00	11.0	14.0	10.0	2.00	10.4
Nd	38.0	33.0	42.0	55.0	41.0	12.1	41.8
Sm	8.00	7.00	9.00	11.0	8.00	4.13	8.60
Eu	2.00	2.00	3.00	3.00	3.00	1.38	2.60
Gd	8.00	6.00	8.00	9.00	8.00	5.88	7.80
Tb	1.00	1.00	1.00	1.00	1.00	1.00	1.00
Dy	6.00	5.00	6.00	7.00	7.00	6.75	6.20
Ho	1.00	1.00	1.00	1.00	1.00	1.13	1.00
Er	3.00	2.00	3.00	3.00	3.00	4.13	2.80
Tm	0.42	0.28			0.46	1.00	0.39
Yb	3.00	2.00	2.00	3.00	3.00	4.00	2.60
Lu	0.41	0.27	0.39	0.40	0.45	1.00	0.38
Hf	7.00	6.00	7.00	7.00	7.00	3.88	6.80
Ta	3.00	3.00	4.00	4.00	3.00	0.69	3.40
Th	5.00	3.00	7.00	7.00	3.00	0.57	5.50
La/Lu	90.24	125.93	105.13	160.00	86.67	4.88	111.98
Eu/Eu*	0.77	0.95	1.09	0.93	1.16	0.86	0.98

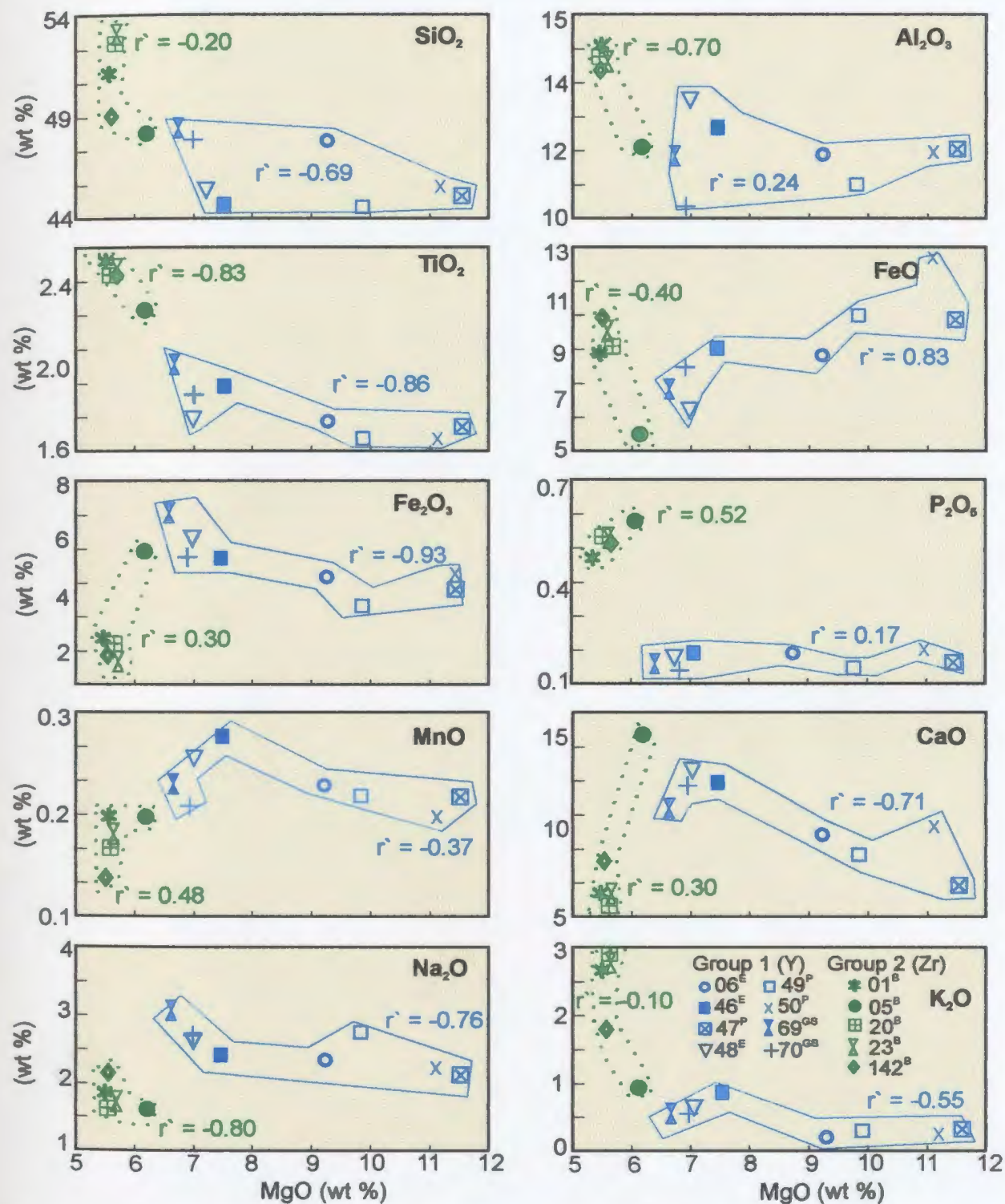


Figure 3.9 Bivariate plots for ten bulk rock major oxides analysed by XRF utilizing MgO as the abscissa. Group 1 (blue) samples with solid outline, group 2 (green) samples with dashed outline. The symbol r' is the Spearman rank correlation coefficient. MgO was selected as the independent variable since it is appropriate for rocks containing minerals with mafic end members.

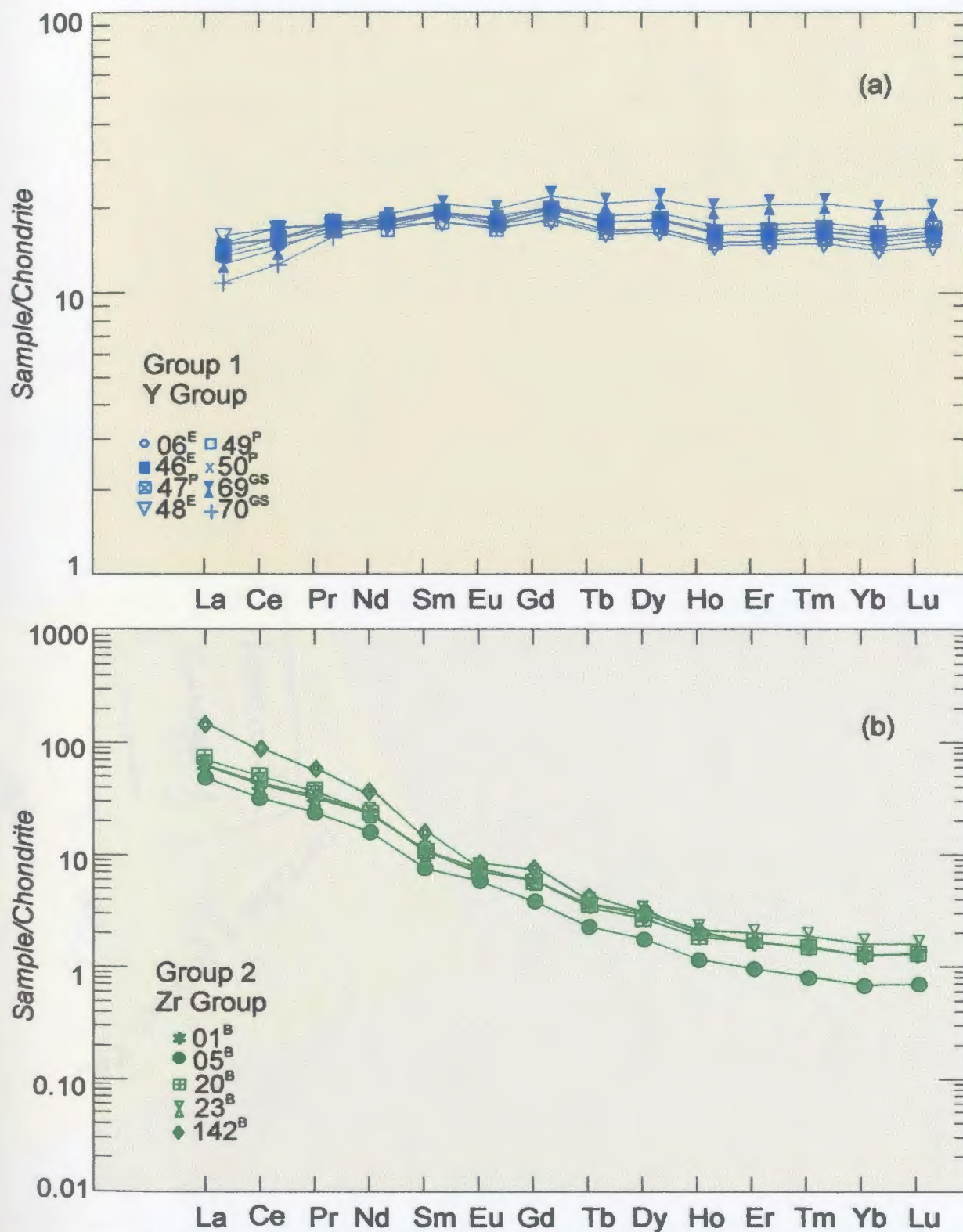


Figure 3.10 Chondrite-normalized REE chemistry of whole rocks in a) group 1, and b) group 2. Chondrite values from Taylor and McLennan (1985, see Table 2.1d). Super-scripts denote rock type. See caption Table 3.3 for explanation.

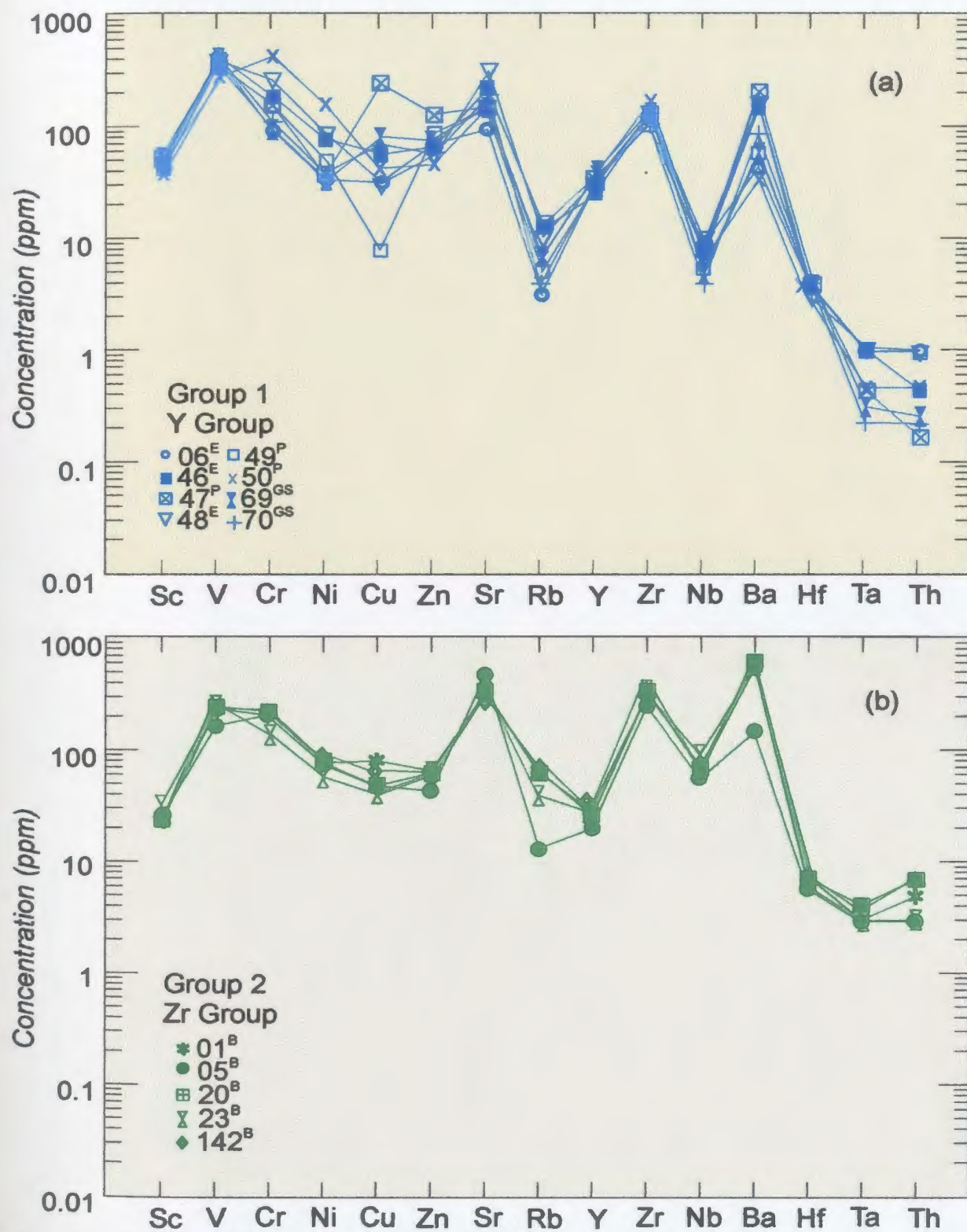


Figure 3.11 Absolute abundances of trace elements other than *REE* in whole rocks a) group 1 and b) group 2) analysed by XRF and solution ICP-MS. Superscripts denote rock type. See caption Table 3.3 for explanation.

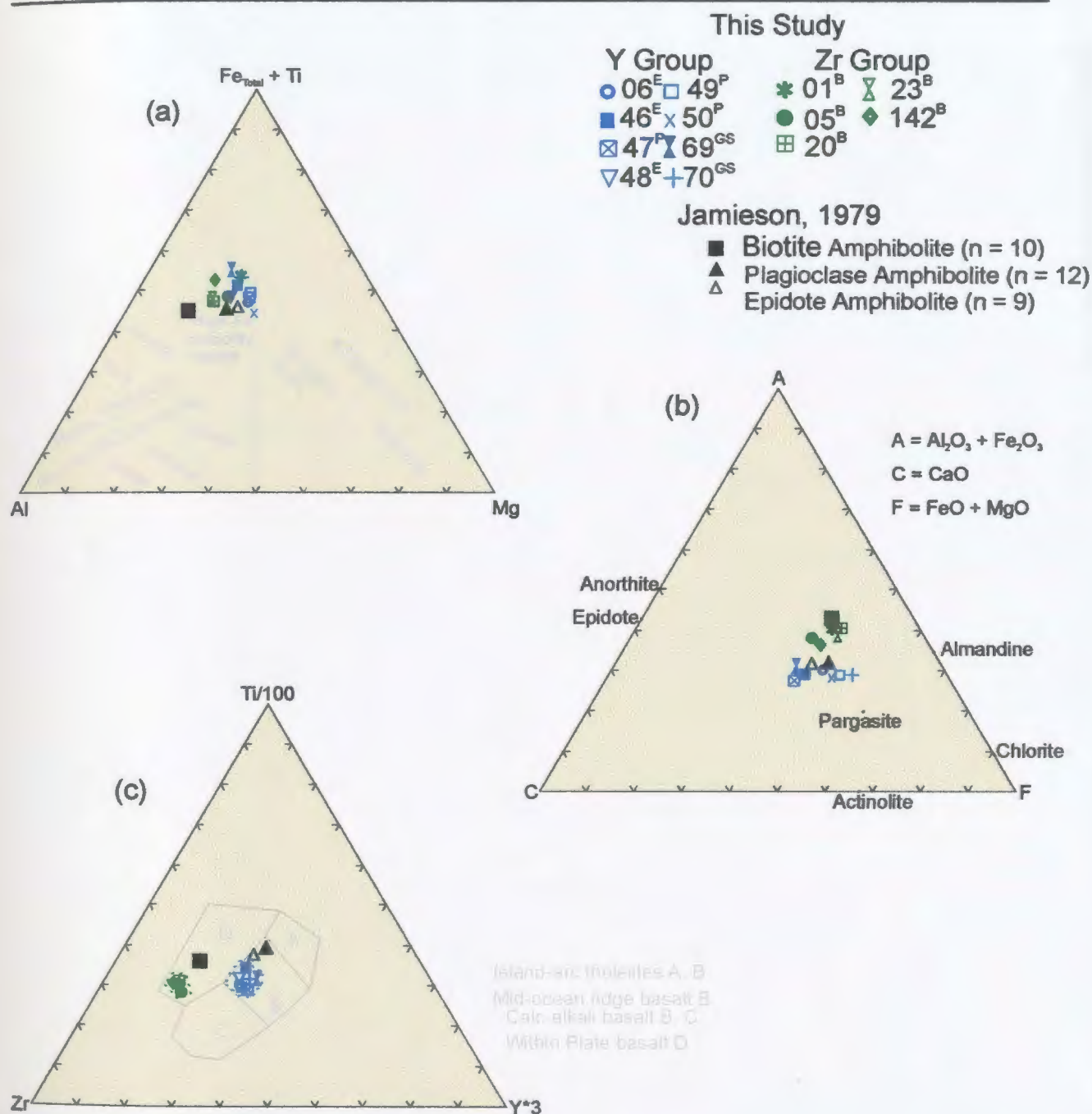
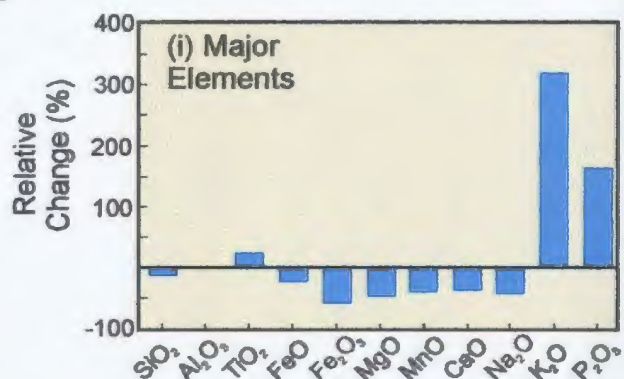


Figure 3.12 (a) Jensen (1976) cation plot for the classification of volcanic rocks. All samples plot in the high-Fe tholeiite basalt field; (b) ACF diagram showing the positions of common end-member minerals in metabasites at greenschist to amphibolite-facies grade; and (c) Ti-Zr-Y diagram for basalts (after Pearce and Cann, 1973). Suite 1 samples are relatively Y-enriched whereas suite 2 rocks are relatively Zr-enriched. A, B, C, and D are possible tectono-magmatic affinities. Superscripts denote rock type: GS = greenschist; E = epidote amphibolite; B = biotite amphibolite; P = Plagioclase amphibolite. Average values for St. Anthony Complex biotite amphibolite, plagioclase amphibolite and epidote amphibolite shown for comparison (Jamieson, 1979).

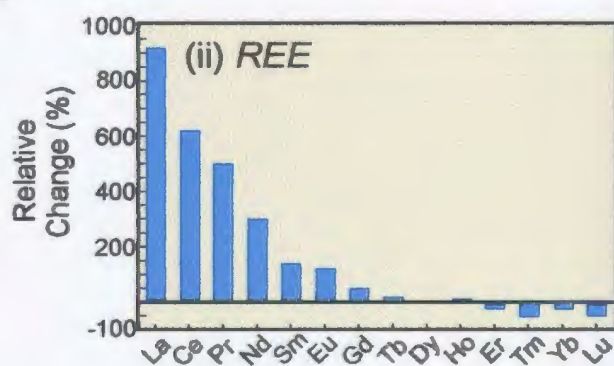
	Y group	Zr group	Zr group norm*	% Change
(i) Major Elements				
SiO ₂	46.17	50.88	43.60	-6
<i>Al₂O₃</i>	<i>11.62</i>	<i>13.56</i>	<i>11.62</i>	0
TiO ₂	1.80	2.48	2.13	19
FeO	9.18	8.70	7.46	-19
Fe ₂ O ₃	5.18	2.82	2.42	-53
MgO	8.71	5.70	4.88	-44
MnO	0.23	0.18	0.15	-34
CaO	10.60	8.32	7.13	-33
Na ₂ O	2.52	1.82	1.56	-38
K ₂ O	0.46	2.23	1.91	318
P ₂ O ₅	0.17	0.52	0.45	162

*Y Group *Al₂O₃* normalization



	Y group	Zr group	Zr group norm*	% Change
(ii) REE				
La	5	43	50	923
Ce	14	88	102	618
Pr	2	10	12	503
Nd	12	42	48	300
Sm	4	9	10	142
Eu	1	3	3	119
Gd	6	8	9	54
Tb	1	1	1	16
<i>Dy</i>	<i>7</i>	<i>6</i>	<i>7</i>	0
Ho	1	1	1	3
Er	4	3	3	-21
Tm	1	0.39	0.45	-55
Yb	4	3	3	-25
Lu	1	0.38	0.45	-55

*Y group *Dy* normalization



	Y group	Zr group	Zr group norm*	% Change
(iii) Trace elements				
Sc	48	25	21	-55
V	386	226	196	-49
Cr	189	203	176	-7
<i>Ni</i>	<i>65</i>	<i>75</i>	<i>65</i>	0
Cu	71	56	49	-32
Zn	74	59	51	-31
Sr	175	367	318	82
Rb	6	49	42	591
Y	33	26	23	-31
Zr	138	309	268	95
Nb	8	64	56	642
Ba	102	502	435	325
Hf	4	7	6	53
Ta	1	3	3	332
Th	1	6	5	738

*Y Group *Ni* normalization

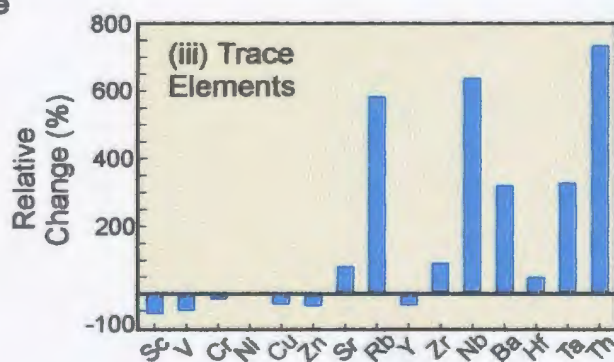


Figure 3.13 Estimate of relative bulk rock mass enrichment/depletion of (i) major oxides, (ii) REE and (iii) selected trace elements in Zr group samples from an amphibolite-facies shear zone. Normalization elements *italicized*. See text for explanation.

Chapter 3: Petrography, Bulk-Rock, and Major-Element Mineral Chemistry

Table 3.4(a) Average major-element composition (± 1 standard deviation) and structural formula of Ca amphibole analysed in this study. *Italics* indicate Zr group.

Ca amphibole	46	48	49	06	20	01	142
n	4	4	4	4	4	4	4
SiO ₂	43.37 \pm 0.43	44.48 \pm 0.52	41.40 \pm 0.16	41.77 \pm 0.65	40.40 \pm 0.65	42.07 \pm 0.70	41.89 \pm 0.51
TiO ₂	1.01 \pm 0.07	0.86 \pm 0.14	1.10 \pm 0.04	1.05 \pm 0.10	1.12 \pm 0.13	1.04 \pm 0.14	1.20 \pm 0.12
Al ₂ O ₃	11.88 \pm 0.40	12.89 \pm 0.39	12.78 \pm 0.20	12.33 \pm 0.25	12.53 \pm 0.16	13.52 \pm 0.71	14.15 \pm 0.70
FeO	15.62 \pm 0.27	15.57 \pm 0.26	19.63 \pm 0.28	19.75 \pm 0.39	20.92 \pm 0.35	18.93 \pm 0.22	19.96 \pm 0.39
MnO	0.29 \pm 0.03	0.44 \pm 0.06	0.41 \pm 0.07	0.41 \pm 0.06	0.43 \pm 0.09	0.25 \pm 0.03	0.26 \pm 0.03
MgO	11.17 \pm 0.24	11.07 \pm 0.16	8.75 \pm 0.15	8.86 \pm 0.22	7.44 \pm 0.18	7.64 \pm 0.41	7.29 \pm 0.21
CaO	10.89 \pm 0.09	11.25 \pm 0.09	12.07 \pm 0.10	11.93 \pm 0.16	11.54 \pm 0.06	11.73 \pm 0.05	11.59 \pm 0.02
Na ₂ O	1.99 \pm 0.12	1.95 \pm 0.09	1.79 \pm 0.07	1.86 \pm 0.02	1.58 \pm 0.04	1.36 \pm 0.09	1.49 \pm 0.13
K ₂ O	0.12 \pm 0.06	0.15 \pm 0.03	1.40 \pm 0.05	1.28 \pm 0.06	1.58 \pm 0.03	1.06 \pm 0.13	1.10 \pm 0.06
Total	96.32	98.66	99.32	99.24	97.54	97.60	98.94
Si	6.52	6.52	6.21	6.27	6.23	6.38	6.30
Ti	0.11	0.10	0.12	0.12	0.13	0.12	0.14
Al	2.11	2.23	2.26	2.18	2.28	2.42	2.51
Fe ³⁺	0.02	0.00	0.29	0.26	0.23	0.00	0.003
Fe ²⁺	1.94	1.91	2.17	2.22	2.47	2.40	2.51
Mn	0.04	0.06	0.05	0.05	0.06	0.04	0.03
Mg	2.50	2.42	1.96	1.98	1.71	1.73	1.63
Ca	1.76	1.77	1.94	1.92	1.91	1.91	1.87
Na	0.58	0.55	0.52	0.54	0.47	0.39	0.43
K	0.03	0.03	0.27	0.25	0.31	0.21	0.21
Cation Total	15.60	15.56	15.78	15.79	15.79	15.58	15.63
<i>T-site</i>							
Si	6.52	6.52	6.21	6.27	6.23	6.38	6.30
Al ^{iv}	1.48	1.48	1.79	1.58	1.77	1.62	1.70
Fe ³⁺							
Ti							
Total	8.00	8.00	8.00	8.00	8.00	8.00	8.00
<i>M1-3 sites</i>							
Al ^{vi}	0.63	0.74	0.47	0.45	0.50	0.80	0.81
Fe ³⁺	0.02		0.29	0.26	0.23	0.004	0.00
Ti	0.12	0.10	0.12	0.12	0.13	0.12	0.14
FeMg	4.24	4.16	4.12	4.17	4.14	4.08	4.06
Total	5.00	5.00	5.00	5.00	5.00	5.00	5.00
<i>M4-site</i>							
FeMg	0.24	0.22	0.06	0.08	0.10	0.08	0.12
Ca	1.76	1.77	1.94	1.92	1.90	1.91	1.87
Na		0.01		0.00	0.00	0.01	0.01
Total	2.00	2.00	2.00	2.00	2.00	2.00	2.00
<i>A-site</i>							
Na	0.58	0.54	0.52	0.54	0.47	0.38	0.42
K	0.03	0.03	0.27	0.25	0.31	0.22	0.21
Total	0.61	0.56	0.79	0.79	0.78	0.59	0.63
X Mg	0.56	0.56	0.47	0.47	0.41	0.42	0.39
X Fe	0.44	0.44	0.53	0.53	0.59	0.58	0.61
X _{Cum}	0.12	0.11	0.03	0.04	0.05	0.04	0.06

Chapter 3: Petrography, Bulk-Rock, and Major-Element Mineral Chemistry

Table 3.4(b) Average major-element composition (± 1 standard deviation) and structural formula of plagioclase analysed in this study. *Italics* indicate Zr group.

Plagioclase	46	48	49	06	20	01	142
n	4	4	4	4	4	3	3
SiO ₂	59.93 \pm 1.54	59.59 \pm 1.12	56.00 \pm 1.16	57.90 \pm 0.30	57.17 \pm 1.63	55.33 \pm 0.41	58.98 \pm 0.20
TiO ₂	< DL	0.08 \pm 0.05	< DL	0.07 \pm 0.04	0.07 \pm 0.08	0.09 \pm 0.04	< DL
Al ₂ O ₃	25.10 \pm 1.30	26.28 \pm 0.22	25.93 \pm 0.97	26.49 \pm 0.24	26.13 \pm 0.14	26.95 \pm 0.10	26.57 \pm 0.25
FeO	0.58 \pm 0.55	0.27 \pm 0.07	0.62 \pm 0.27	0.19 \pm 0.10	0.27 \pm 0.04	0.31 \pm 0.03	0.29 \pm 0.07
MnO	< DL	< DL	< DL	< DL	0.07 \pm 0.04	< DL	< DL
MgO	0.06 \pm 0.04	< DL	0.09 \pm 0.08	< DL	< DL	0.09 \pm 0.02	0.09 \pm 0.04
CaO	7.10 \pm 0.64	7.49 \pm 0.44	9.87 \pm 0.32	8.71 \pm 0.44	8.29 \pm 0.59	9.44 \pm 0.13	8.15 \pm 0.25
Na ₂ O	7.84 \pm 0.60	7.17 \pm 0.21	5.29 \pm 0.39	6.60 \pm 0.12	5.81 \pm 0.19	5.83 \pm 0.21	7.19 \pm 0.21
K ₂ O	0.22 \pm 0.20	0.31 \pm 0.22	0.07 \pm 0.04	0.06 \pm 0.02	0.50 \pm 0.54	< DL	0.06 \pm 0.02
Total	100.65	100.96	97.76	99.91	98.15	97.83	101.08
<i>T-site</i>							
Si	2.66	2.63	2.57	2.59	2.60	2.53	2.61
Ti					0.002		
Al	1.31	1.37	1.40	1.40	1.40	1.45	1.38
Fe	0.02	0.01	0.02	0.003	0.01	0.01	0.01
Mn			0.001			0.002	
Mg	0.002		0.005			0.005	0.01
Total	4.00	4.01	4.00	4.00	4.01	4.01	4.00
<i>A-site</i>							
Ca	0.34	0.35	0.48	0.42	0.40	0.46	0.39
Na	0.68	0.61	0.47	0.57	0.51	0.52	0.62
K	0.01	0.02	0.002	0.001	0.03		
Total	1.02	0.98	0.96	0.99	0.94	0.98	1.00
Cation Total	5.02	4.99	4.96	4.99	4.96	4.99	5.01
X Ca (An)	0.33	0.37	0.51	0.42	0.43	0.47	0.38
X Na (Ab)	0.66	0.62	0.49	0.58	0.54	0.53	0.61
X K (Or)	0.01	0.01			0.03		

Chapter 3: Petrography, Bulk-Rock, and Major-Element Mineral Chemistry

Table 3.4(c) Average major-element compositions (± 1 standard deviation) and structural formulae of epidote and garnet analysed in this study. *Italics indicate Zr group.*

Epidote	06	46	48	Garnet	01	20	142
n	4	4	3		4	4	4
SiO ₂	40.08 \pm 0.34	38.02 \pm 0.45	40.27 \pm 0.23	SiO ₂	38.13 \pm 0.16	38.74 \pm 0.41	38.37 \pm 0.05
TiO ₂	< DL	0.16 \pm 0.08	0.10 \pm 0.02	TiO ₂	0.15 \pm 0.12	0.33 \pm 0.09	0.29 \pm 0.04
Al ₂ O ₃	29.80 \pm 0.93	24.09 \pm 0.28	25.64 \pm 0.38	Al ₂ O ₃	21.31 \pm 0.05	21.35 \pm 0.06	21.21 \pm 0.10
Fe ₂ O ₃	5.68 \pm 1.07	11.93 \pm 0.47	10.40 \pm 0.63	FeO	28.26 \pm 1.21	29.70 \pm 0.25	28.26 \pm 0.58
Mn ₂ O ₃	0.12 \pm 0.09	0.09 \pm 0.04	0.16 \pm 0.04	MnO	2.00 \pm 0.57	0.88 \pm 0.07	1.90 \pm 0.37
MgO	0.09 \pm 0.06	0.17 \pm 0.04	< DL	MgO	2.52 \pm 0.19	2.75 \pm 0.14	2.44 \pm 0.16
CaO	24.53 \pm 0.06	23.44 \pm 0.27	23.47 \pm 0.25	CaO	9.90 \pm 0.82	9.03 \pm 0.05	9.75 \pm 0.23
Na ₂ O	0.09 \pm 0.09	0.10 \pm 0.07	0.32 \pm 0.10	Na ₂ O	< DL	0.23	0.12
K ₂ O	< DL	< DL	< DL	K ₂ O	< DL	0.30 \pm 0.14	0.08 \pm 0.04
Total	100.24	97.82	99.97	Total	102.21	103.08	102.28
<i>T-site</i>				<i>T-site</i>			
Si	3.05	3.08	3.14	Si	2.97	2.99	2.99
Total	3.05	3.08	3.14	Total	2.97	2.99	2.99
<i>M1-3 site</i>				<i>Y-site</i>			
Ti	0.01	0.01	0.02	Ti	0.01	0.02	0.02
Al	2.67	2.30	2.36	Al	1.96	1.94	1.95
Fe	0.36	0.81	0.68	Total	1.97	1.96	1.96
Mn	0.01	0.01	0.01				
Mg	0.01	0.02		<i>X-site</i>			
Total	3.05	3.15	3.07	Fe	1.84	1.92	1.84
				Mn	0.13	0.06	0.13
<i>X-site</i>				Mg	0.29	0.32	0.28
Ca	2.00	2.03	1.96	Ca	0.83	0.75	0.81
Na	0.01	0.02	0.05	Na		0.03	0.01
K			0.00	K		0.03	0.01
Total	2.01	2.05	2.01	Total	3.10	3.10	3.08
Cation Total	8.11	8.28	8.22	Cation Total	8.04	8.05	8.03
X Al (Zo)	0.64	0.25	0.34	X Fe (Alm)	0.60	0.63	0.60
X Fe (Ep)	0.35	0.72	0.64	X Mg (Prp)	0.09	0.10	0.09
X Mn (Pm)	0.01	0.03	0.02	X Ca (Grs)	0.27	0.25	0.27
				X Mn (Sps)	0.04	0.02	0.04

Chapter 3: Petrography, Bulk-Rock, and Major-Element Mineral Chemistry

Table 3.4(d) Average major-element composition (± 1 standard deviation) and structural formula of titanite analysed in this study. *Italics indicate Zr group.*

Titanite	46	48	49	06	01	20	142
n	3	3	2	2	3	3	2
SiO ₂	30.13 \pm 0.05	31.02 \pm 0.07	30.31 \pm 0.11	30.44 \pm 0.28	29.69 \pm 0.42	29.94 \pm 0.18	30.22 \pm 0.04
TiO ₂	37.79 \pm 0.08	38.46 \pm 0.38	37.40 \pm 0.47	36.09 \pm 0.45	36.08 \pm 0.85	36.82 \pm 0.10	37.01 \pm 0.56
Al ₂ O ₃	1.37 \pm 0.08	1.25 \pm 0.19	1.89 \pm 0.11	1.67 \pm 0.25	1.97 \pm 0.17	1.48 \pm 0.05	1.72 \pm 0.20
Fe ₂ O ₃	0.99 \pm 0.05	0.95 \pm 0.08	0.75 \pm 0.17	1.58 \pm 0.28	0.74 \pm 0.07	1.02 \pm 0.08	1.02 \pm 0.14
Mn ₂ O ₃	0.13 \pm 0.05	< DL	0.07 \pm 0.03	0.15 \pm 0.03	0.08 \pm 0.08	0.12 \pm 0.03	0.19 \pm 0.02
MgO	< DL	< DL	< DL	< DL	< DL	< DL	0.12 \pm 0.03
CaO	28.54 \pm 0.15	29.00 \pm 0.08	28.16 \pm 0.28	28.08 \pm 0.29	27.23 \pm 0.29	27.96 \pm 0.11	27.83 \pm 0.20
Na ₂ O	0.06 \pm 0.04	< DL	< DL	0.14 \pm 0.11	< DL	0.06 \pm 0.02	0.07 \pm 0.03
K ₂ O	< DL	< DL	< DL	< DL	< DL	< DL	< DL
Total	98.77	100.56	98.50	97.92	95.65	97.16	98.00
<i>T-site</i>							
Si	3.99	4.03	4.01	4.06	4.04	4.02	4.02
Total	3.99	4.03	4.01	4.06	4.04	4.02	4.02
<i>M-site</i>							
Ti	3.76	3.75	3.72	3.62	3.69	3.72	3.71
Al	0.21	0.20	0.28	0.26	0.31	0.25	0.27
Fe ³⁺	0.03	0.05		0.12		0.03	0.02
Total	4.00	4.00	4.00	4.00	4.00	4.00	4.00
<i>A-site</i>							
Mn							
Fe ²⁺		0.03	0.05	0.01	0.06	0.04	0.06
Mg	0.05	0.01					
Ca		4.03	3.99	4.02	3.97	4.02	3.97
Na	4.05			0.03		0.01	0.01
K	0.01					0.01	
Total	4.10	4.07	4.05	4.04	4.02	4.08	4.05
Cation Total	12.09	12.10	12.06	12.10	12.06	12.10	12.07
X Ti	0.76	0.75	0.72	0.62	0.69	0.72	0.71
X Al	0.21	0.20	0.28	0.26	0.31	0.25	0.27
X Fe ³⁺	0.03	0.05		0.12		0.03	0.02

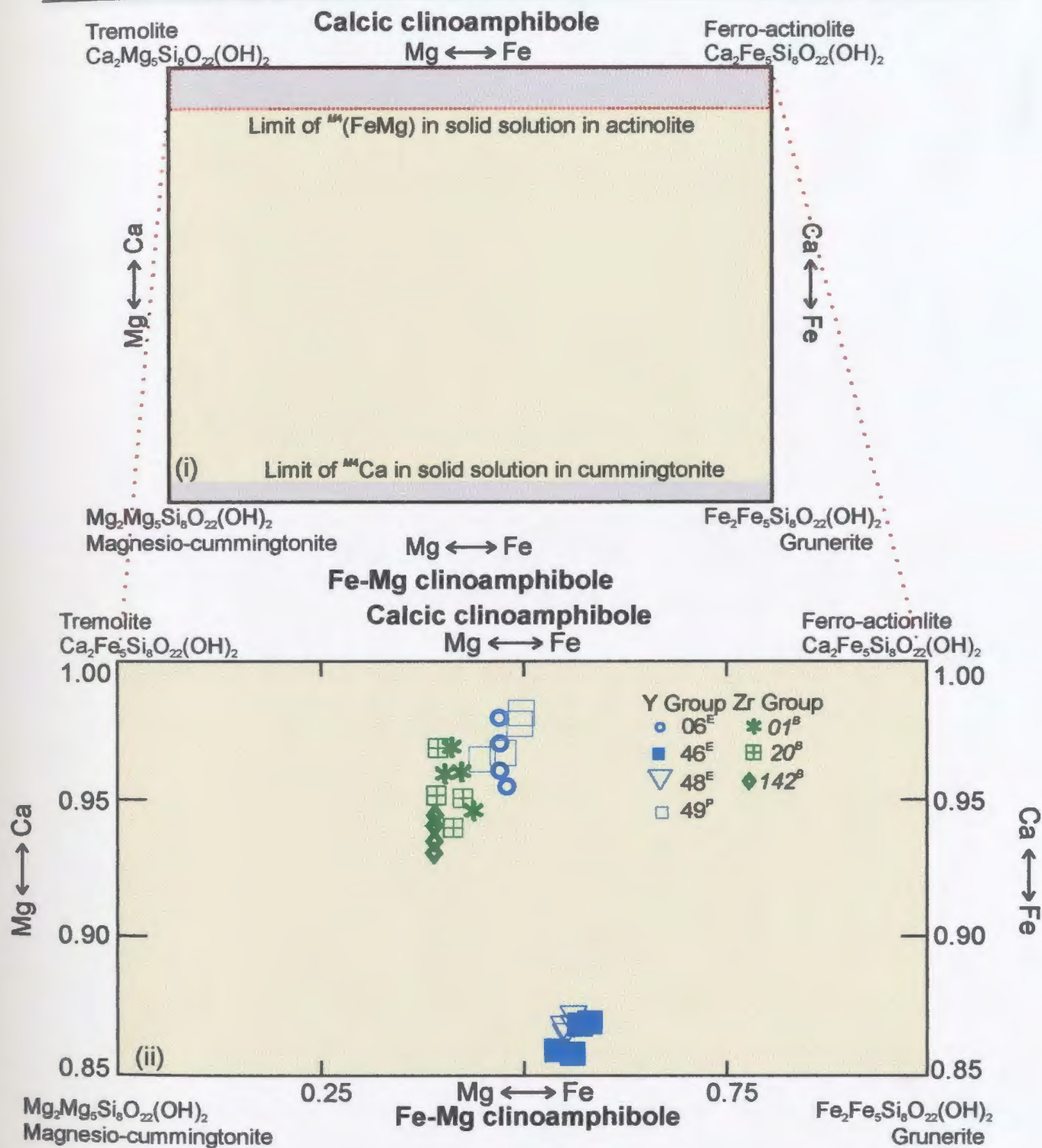


Figure 3.14 (a) The clinoamphibole rectangle showing the exchange vectors relating the compositions of FeMg clinoamphiboles to calcic clinoamphiboles and the limit of solid solution in both groups (after Leake, 1997, 2003). Red dashed outline in (i) is enlarged in (ii). Two Y group samples (46, 48) are relatively Fe-Mg enriched relative to all other analysed samples. Superscripts denote rock type. See caption Table 3.3 for explanation.

Nomenclature of Calcic Amphibole

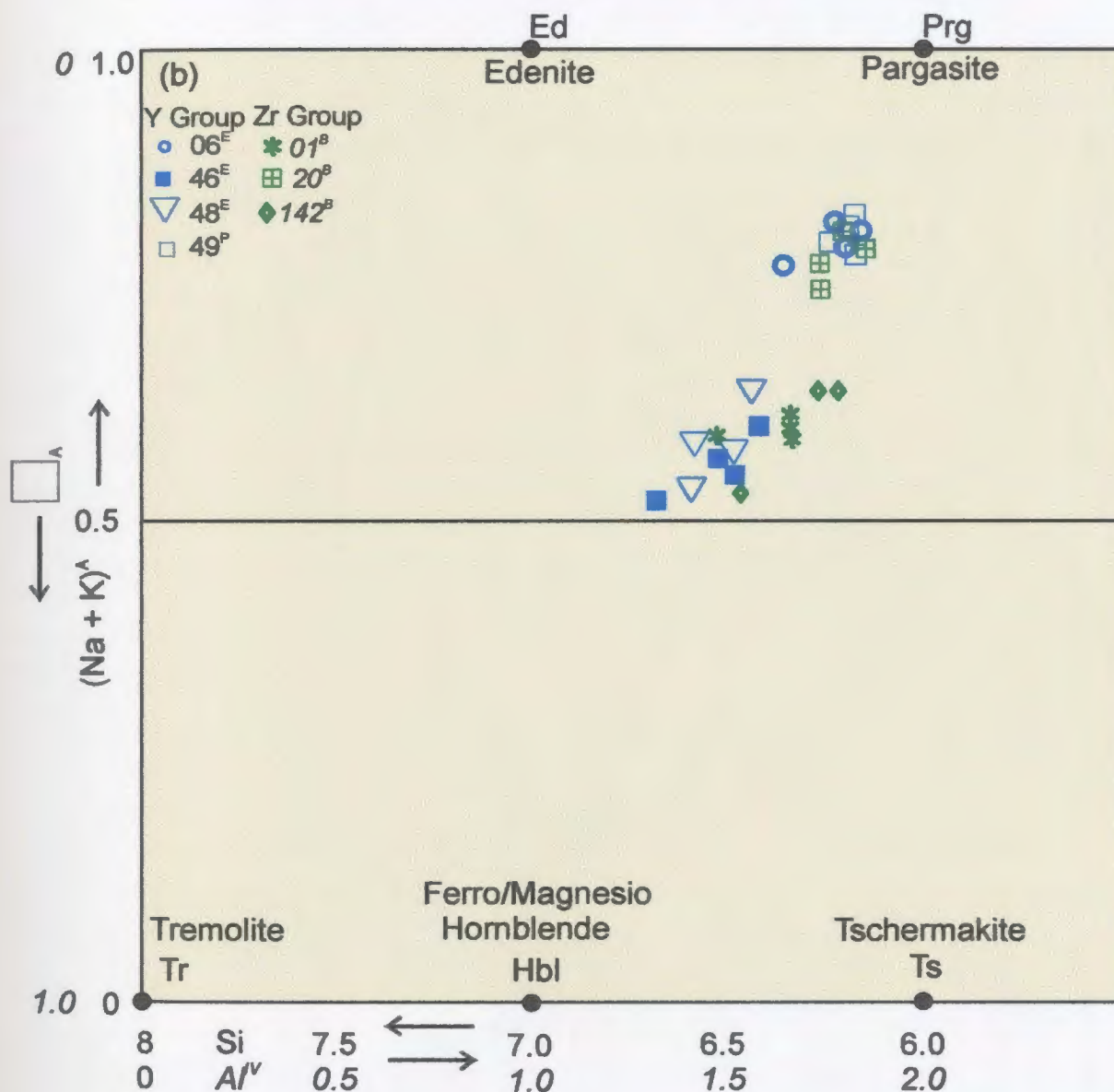


Figure 3.14 (b) The nomenclature of calcic amphiboles expressed as numbers of (Na + K)^A atoms in A sites and Si and tetrahedral Al^{IV} atoms per formula unit (after Leake *et al.*, 1997, 2003). □^A represents vacancy in the A site. Filled circles denote position of specific end-members. Y group shown with normal font, Zr group in *italics*. Superscripts correspond to rock type (E = epidote amphibolite, B = biotite amphibolite, P = plagioclase amphibolite). Mineral symbols are from Kretz (1983).

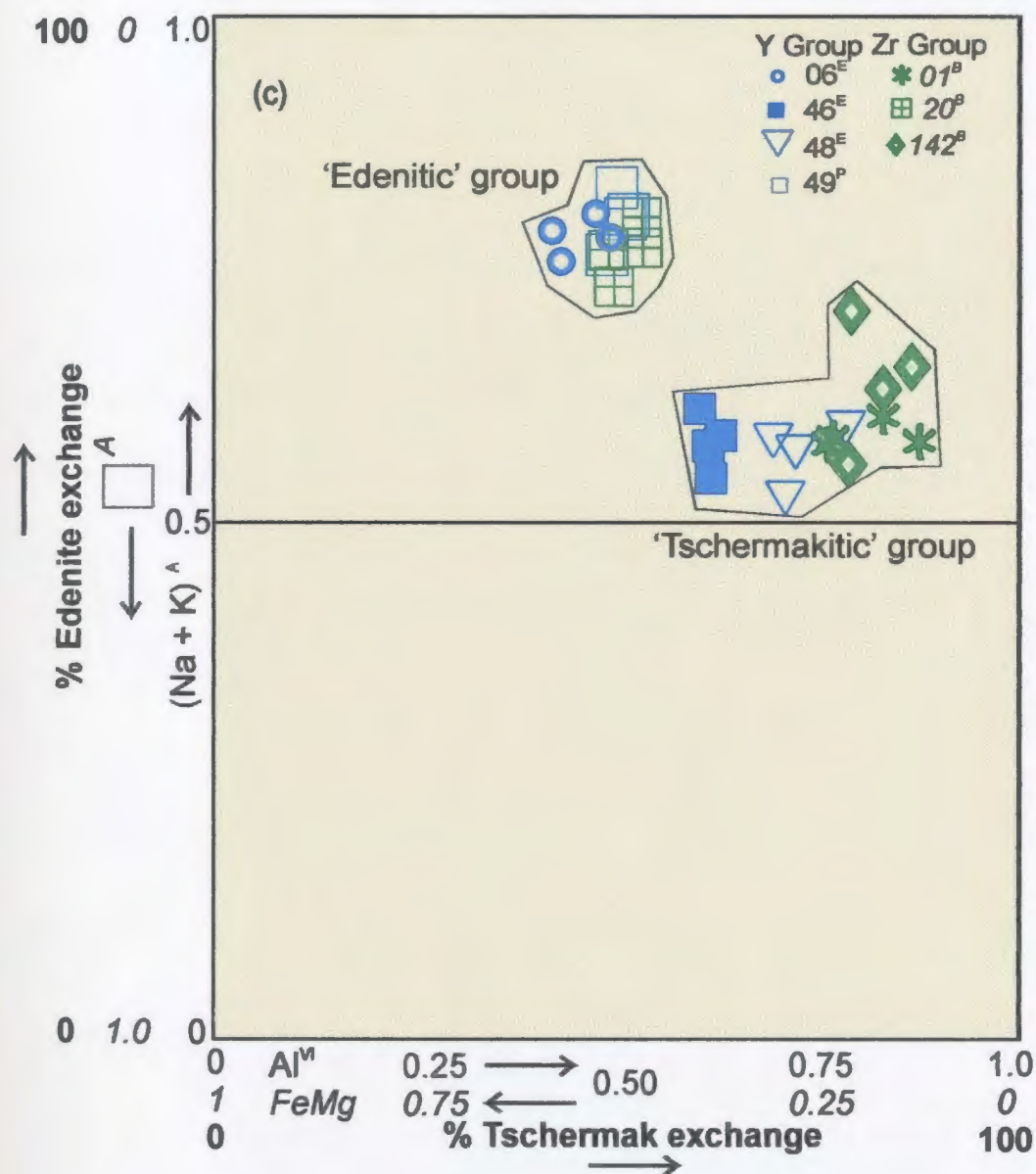


Figure 3.14(c) Diagram illustrating the relative roles of the edenite and tschermak exchange vectors in analysed calcic amphiboles. Analysed samples cluster into two groups: (i) 'edenitic' amphibole with the edenite exchange the predominant substitution, and (ii) 'tschermakitic' amphibole with the tschermak exchange the predominant substitution. There is no clear trend for a dominant substitution vector. See text for explanation. Superscripts correspond to rock type (E = epidote amphibolite, B = biotite amphibolite, P = plagioclase amphibolite).

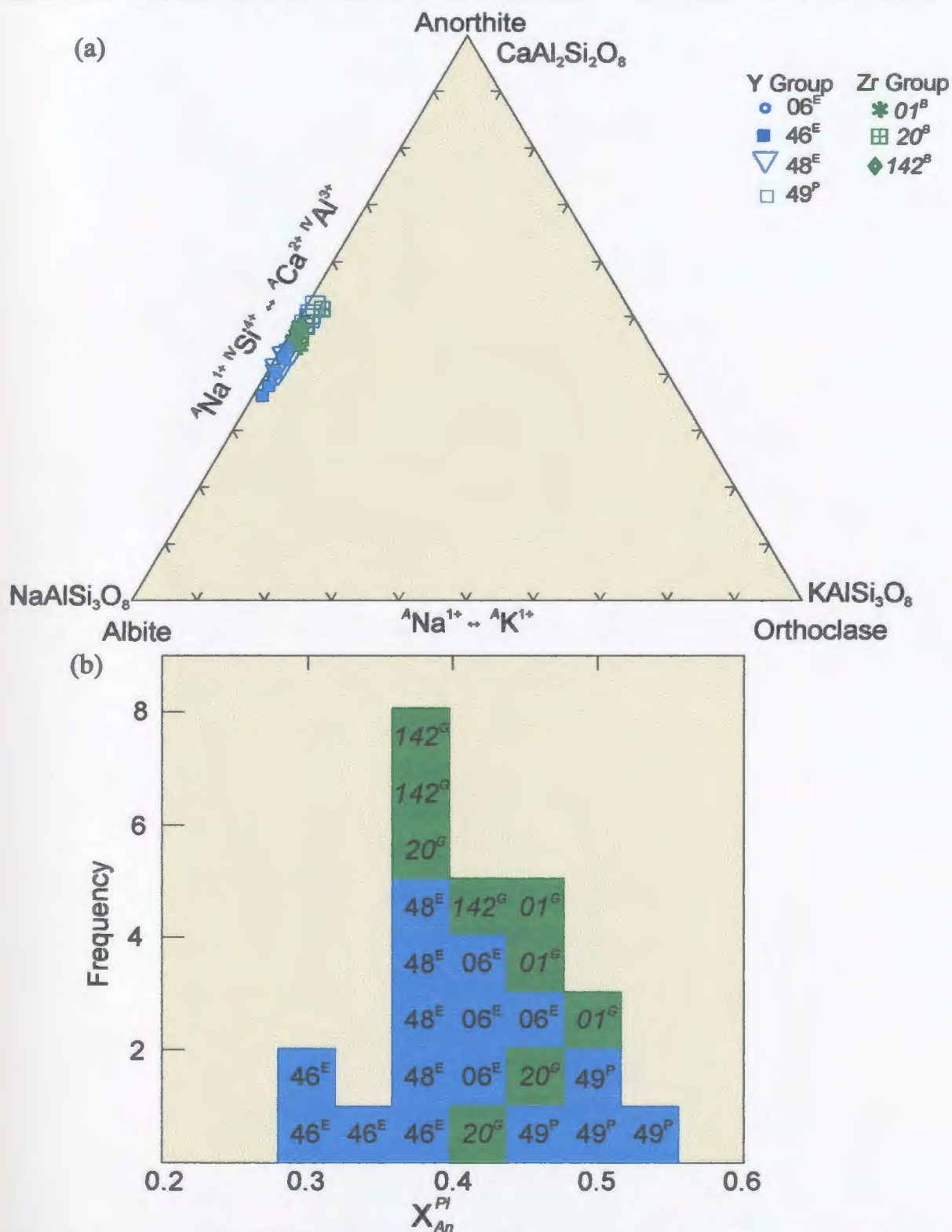


Figure 3.15 (a) Plagioclase compositions plotted in Ab-An-Or ternary composition space; (b) histogram showing plagioclase compositions expressed as X_{An}^{Pl} . Y group shown with normal font, Zr group in *italics*. The superscripts correspond to rock type (E = epidote amphibolite, B = biotite amphibolite, P = plagioclase amphibolite).

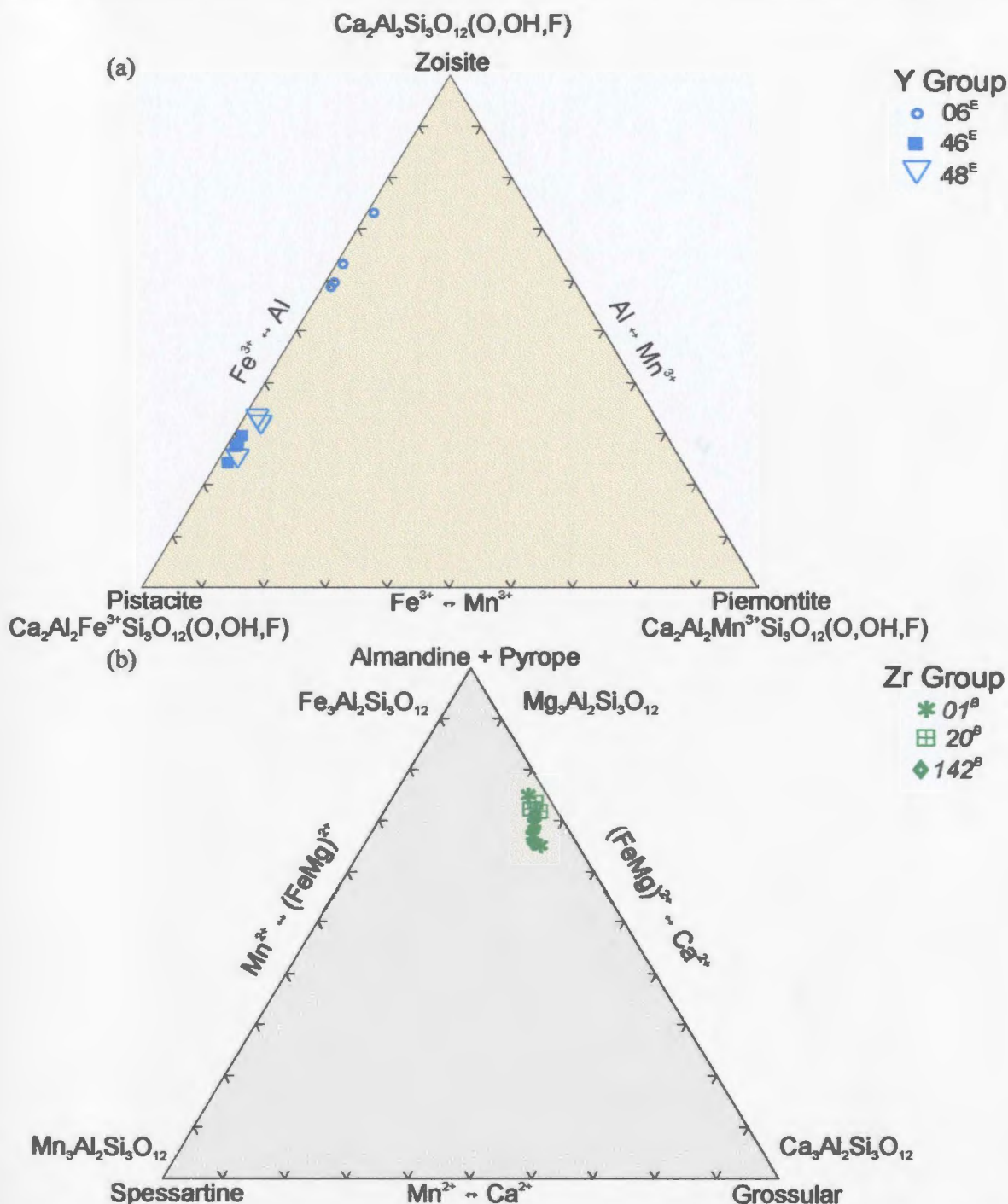


Figure 3.16 (a) Epidote compositions on the basis of Al, Fe and Mn cation distribution in the $M3$ site of the ideal epidote formula $X_2M_3T_3(\text{O},\text{OH},\text{F})_{13}$. Ca is assumed to fill the X site, Si is assumed to fill the T site, and Al occupies 2 of the 3 M sites. Zoisite is the Al end-member, pistacite the Fe end-member, and piemontite the Mn end-member. Y group in normal font. (b) Garnet compositions on the basis of dodecahedrally coordinated Fe, Mg, Mn and Ca. Compositions approach almandine. Zr group in *italics*. Superscripts correspond to rock type (E = epidote amphibolite, B = biotite amphibolite, P = plagioclase amphibolite).

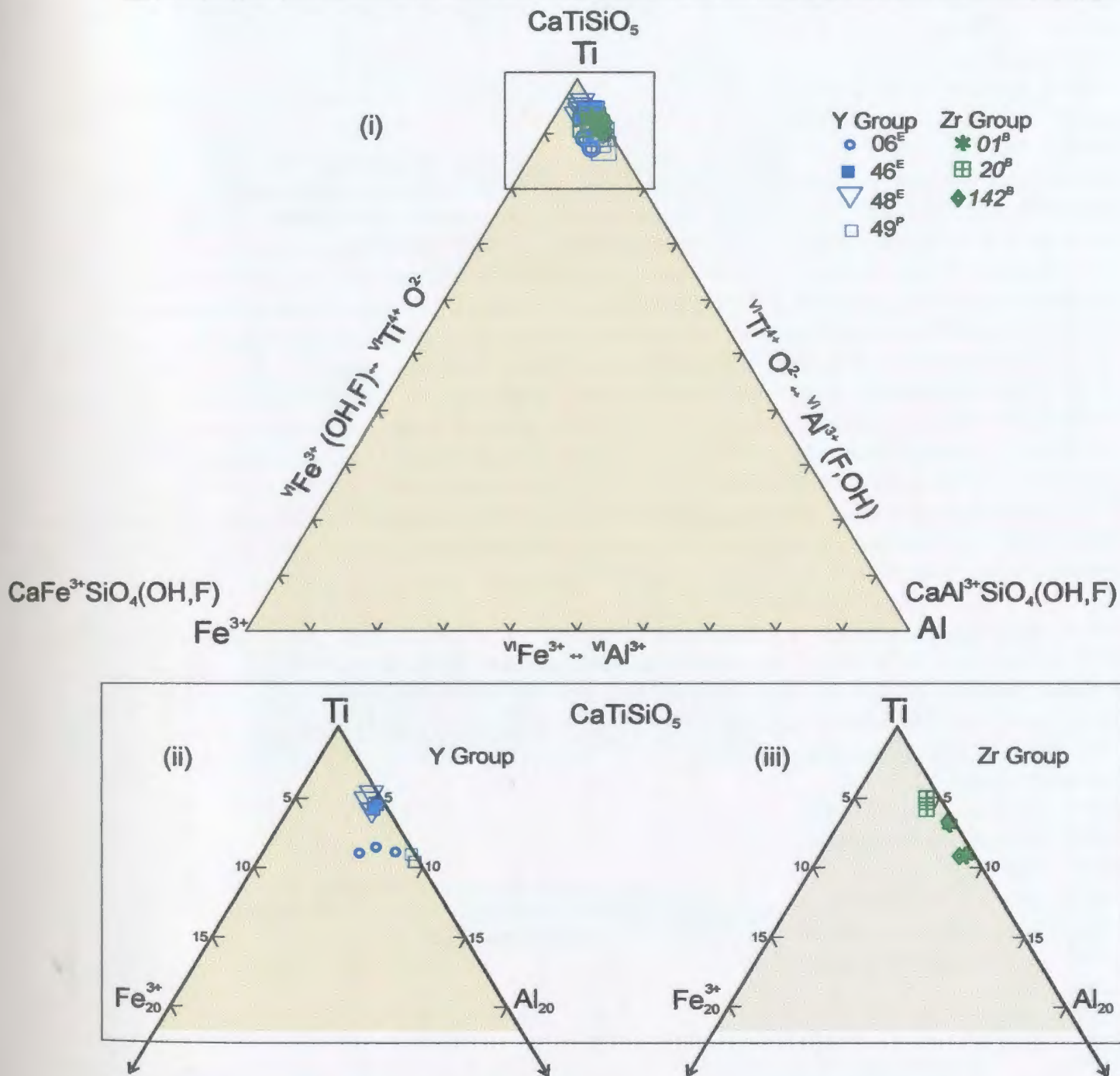


Figure 3.17 (i) Titanite compositions on the basis of octahedrally coordinated Fe³⁺, Ti and Al. Fe³⁺ and Al are minor constituents in the octahedral site. Box represents area of enlargement for the Y and Zr groups, (ii) and (iii) respectively. Superscripts denote rock type (E = epidote amphibolite, B = biotite amphibolite, P = plagioclase amphibolite).

Chapter 4: Rare Earth Element Mineral Chemistry

4.1 Introduction

Rare earth elements (*REE*) are important trace elements with numerous applications in igneous, sedimentary and, more recently, metamorphic petrology. As a group, *REEs* are generally trivalent (except E^{2+} and Ce^{4+}) and display coherent behaviour due to the small decreases in ionic radius with atomic number. Because of these characteristics, the *REEs* are sensitive indicators of many petrological processes exhibiting subtle fractionation relative to each other depending on the minerals involved. Initially, *REEs* were primarily utilized in igneous bulk-rock geochemical studies (e.g., Pearce and Cann, 1973; Pearce and Norry, 1979; Wood, 1980; Pearce, 1982; Meschede, 1986; Cabanis and Lecolle, 1989). However, with the advent of *in situ* microbeam techniques with sub-ppm detection limits, such as LAM ICP-MS, a new opportunity to study *REE* behaviour among coexisting minerals arose. This chapter involves an evaluation of the distribution of *REEs* amongst the five coexisting minerals (Ca amphibole, epidote, plagioclase, garnet, and titanite) in metabasic rocks from the metamorphic sole of the Hare Bay Allochthon.

4.2 Rare Earth Element Mineral Chemistry

Average *REE* concentrations of the analysed coexisting phases are presented in Table 4.1; the entire trace element data set is available in Appendix A. The 1 sigma variations listed in Table 4.1 are based on the measured *REE* concentrations of *separate grains* in each sample and are not indicative of within-grain zoning. Mineral compositions, normalized on the basis of their concentrations of light, middle, and heavy *REE*, and chondrite-normalized *REE* diagrams are shown in Figures 4.1(a-e) and 4.2(a-h) respectively. An overview of the *REE* chemistry of each phase follows.

4.2.1 Calcic Amphibole

Ca amphibole in both the Y and Zr groups exhibits moderate to low concentrations of *REE* ($\approx 80 \geq \sum REE \geq \approx 7$ ppm; Table 4.1), with higher abundances of light and middle *REE* relative to *HREE* (Figure 4.1a). Chondrite-normalized *REE* patterns for both groups, shown in Figure 4.2(a-b), are similar, exhibiting moderate *LREE* depletion with small negative Eu anomalies. Although $\sum REE$ appears to be linked to the degree of edenite and tschermak substitution in the Y group (Figure 4.2a), with edenitic grains exhibiting an approximate order-of-magnitude greater $\sum REE$ than tschermakitic varieties (Figure 4.2a), this pattern does not hold for the Zr group, where the reverse relationship is exhibited (Figure 4.2b). Similarly, although $\sum REE$ appears to be linked to the degree of cummingtonite substitution in the Y group, in which

cummingtonite-rich samples exhibit an approximate order-of-magnitude decrease in $\sum REE$ relative to cummingtonite-poor samples (Table 4.1; Figure 4.2a), in the Zr group the reverse relationship is shown although the range of cummingtonite substitution is limited ($X_{Cum} \approx 0.04-0.06$; Table 4.1). Thus, the data suggest that $\sum REE$ and the degree of edenite, tschermak, and cummingtonite substitution are independent variables. It thus appears likely that a combination of factors, including bulk composition, mineral assemblage and the P - T conditions of metamorphism influence $\sum REE$ in analysed Ca amphibole. La/Lu ratios range from approximately 3 to 5 for all analyses, except the cummingtonite-rich samples (46, 48), which have La/Lu ratios near unity (Table 4.1). This relationship is consistent with *HREE* favouring 'cummingtonite-like' $M4$ sites in Ca amphibole and is discussed further in sections 4.4.1 and 4.4.2.

4.2.2 Plagioclase

Plagioclase is stable across the entire sample suite. Overall, plagioclase has the lowest $\sum REE$ of all analysed phases (≤ 24 ppm in all samples and ≤ 6 ppm in 5 of 7 samples, Table 4.1) strongly favouring *LREE* over — and *HREE* (Figure 4.1b).

Chondrite-normalized *REE* patterns for plagioclase (Figure 4.2c-d) from both the Y and Zr groups are similar with *LREE*-enriched profiles and positive Eu anomalies of variable magnitudes (Table 4.1). Light to middle *REE* patterns (La-Gd) are consistent and regular but measured *HREE* abundance is irregular in some samples because concentrations

approach detection limits. However, samples with *HREE* abundances above detection limits have approximately flat *HREE* profiles. The *LREE/HREE* ratio (Table 4.1), expressed as Ce/Yb due to Lu concentrations below detection limits in some samples, ranges from approximately 10 up to 70.

4.2.3 Epidote

Epidote is restricted to the Y group, and occurs in samples 46, 48 and 06. All analyses are of matrix grains. Numerous workers (e.g., Sorensen and Grossman, 1989; Grauch, 1989; Pan and Fleet, 1996) have shown that epidote is commonly enriched in *LREEs*, which are inferred to enter the large *X* site normally occupied by calcium. Analysed epidote contains moderate to high concentrations of *REEs* ($\Sigma REE \approx 80\text{--}380$ ppm) and exhibits small variable positive to negative Eu anomalies. La/Lu ratios for epidote range from approximately 60 to 210, being highest in Al-rich (zoisite-rich) epidote. Figure 4.1c is a light, middle and heavy *REE* ternary plot which illustrates the strong *LREE* enrichment in analysed epidote. Chondrite-normalized patterns for epidote, shown in Figure 4.2e, exhibit variable levels of *LREE* enrichment from approximately 10 to 300 times chondrite, the degree of enrichment being inversely proportional to the amount of modal epidote.

4.2.4 Garnet

Garnet is restricted to Zr group metabasites. *HREEs* are known to be partitioned into garnet because of their compatibility in the *X*-site (Hickmott & Shimizu, 1990). La/Lu ratios in analysed garnets are less than 1, consistent with expected behaviour. The light, middle, and heavy *REE* concentrations and 1σ standard deviations in garnet (Figure 4.1d) indicate compositional differences among the samples. Chondrite-normalized patterns (Figure 4.2f) show variable *LREE* contents (0.1-20 times chondrite) and *HREE* contents of approximately 50-100 times chondrite. Two samples (01, 142) exhibit small positive Eu anomalies whereas sample 20 has a small negative Eu anomaly. Within each sample, chondrite-normalized *HREE* patterns are more consistent than chondrite-normalized *LREE* patterns, which is attributed to the greater *HREE* compatibility in the *X*-sites of garnet and/or presumably, the local breakdown of an *LREE* enriched phase (e.g., apatite) during garnet growth.

4.2.5 Titanite

Titanite, which is present in both groups primarily as a fine-grained subhedral to euhedral matrix phase, is extremely *REE* enriched ($\approx 1300 \text{ ppm} \leq \sum \text{REE} \leq 2800 \text{ ppm}$). The light, middle and heavy *REE* distributions in titanite are shown in Figure 4.1e. Overall, titanite exhibits *L-MREE* enrichment. Sample 06 plots away from the cluster of remaining analyses compared to the others, it is impoverished in *HREE* and clearly

exhibits variable *L-* to *MREE* contents. Chondrite-normalized *REE* patterns for titanite for both the Y and Zr groups, shown in Figure 4.2g-h, exhibit similar patterns. For most grains, the patterns are almost flat for *M-HREE*, exhibiting a slight curvature for the *LREE* and are enriched 100 to 1000 times chondrite with small negative Eu anomalies. The depletion of *HREE* in sample 06 (epidote amphibolite) is again apparent. La/Lu ratios are between 5 and 10 for all samples with the exception of sample 06, which has a La/Lu ratio of approximately 100. The reason why sample 06 differs from the others is not well understood. The discrepancy *may* be attributed to the presence of a trace phase such as zircon or xenotime, both of which are known carriers of *HREE* (Yang and Rivers, 2002) although neither was observed in this sample (or other samples collected nearby).

4.2.6 Eu Anomalies

Average europium anomalies for analysed phases are listed in Table 4.1. The large positive Eu anomalies in chondrite-normalized plagioclase, the small negative Eu anomalies in chondrite-normalized Ca amphibole and titanite, and the small variable positive to negative anomalies in epidote and garnet imply that Eu is present as both Eu^{2+} and Eu^{3+} . Preferential substitution of Eu^{2+} into the *A* site in plagioclase, giving rise to a positive Eu anomaly in that phase, is well known and the concomitant negative anomalies in Ca amphibole and titanite indicate equilibrium partitioning of this ion among these phases during metamorphism. Assuming that the small negative Eu

anomalies in some epidote and garnet grains also indicate equilibrium partitioning with plagioclase, the small positive Eu anomalies in other grains are probably a reflection of growth at the expense of plagioclase (i.e., they inherited the positive anomalies from the reactant plagioclase).

4.3 Rare Earth Element Distribution Coefficients

The distribution (D) of REE between two phases (A) and (B) is defined as the ratio of concentrations (C), in ppm: $D_{REE} = \frac{C_{REE}^A}{C_{REE}^B}$

which is the Nernst distribution coefficient. Because it considers only the total REE abundances in each phase, the Nernst distribution coefficient may incorporate a partial compositional dependence. To neutralize this compositional dependence, Nielsen (1985) introduced the term D_{REE}^* defined as

$$D_i^* = \frac{X_{REE}^A}{X_{REE}^B}$$

where X is the mole fraction of a REE (or any other cation, i) in a specific crystallographic site in minerals A and B . Theoretically, if all cations of interest enter a single site in each mineral, the values of D_{REE} and D_{REE}^* are equal. However, if a specific

cation is distributed between two different sites in a mineral or if the two minerals have different numbers of sites on which substitution can occur, the values for each type of partition coefficient will be different. Values of D_{REE} and D^*_{REE} for mineral pairs in selected Y and Zr group samples are given in Table 4.2. D^*_{REE} values are based on the assumptions that *REE* enter the 8-fold-coordinated *M4* site in Ca amphibole, the 5- to 9-fold irregularly coordinated *A* site in plagioclase, the 8-fold coordinated *X* site in epidote and garnet and the 7-fold coordinated *A* site in titanite, based on ionic radii (Shannon, 1976) and mineral site size (Smyth and Bish, 1988) considerations (see Table 2.1a-c).

REE distribution coefficients (D_{REE} and D^*_{REE}) are presented in Table 4.2a-b and illustrated in Figure 4.3a-b respectively. *REE* distributions among mineral pairs are generally consistent, i.e., maxima generally occur at a particular *REE*, although there are some exceptions, which imply several factors including, but not limited to, major-element chemistry, valence state of Eu and the influence of bulk composition on the measured distributions. In Figure 4.3, Y group samples comprise epidote amphibolite (samples 46, 48, 06) and plagioclase amphibolite (sample 49) whereas all Zr group samples comprise the garnet-amphibolite assemblage. The analytical uncertainties are given as 1σ standard deviations measured from LAM-ICP-MS counting statistics. *HREE* (i.e., Ho-Lu) in plagioclase from certain samples approaches detection limits so plagioclase-mineral partitioning for these elements is not considered in all samples. In nearly all cases, the formulation of the distribution coefficient (D_{REE} or D^*_{REE}) does not

affect the relative *REE* enrichment between each mineral pair. Where D_{REE} and D^*_{REE} diverge, this may imply that *REE* are distributed on more than one site in one or both minerals, and/or that there are analytical problems with the data. Individual cases are discussed below.

Ignoring sample 06 in which titanite is anomalous, Figure 4.3 illustrates that values of D_{REE} and D^*_{REE} for *Ca amphibole-titanite* pairs exhibit similar patterns. In both the Y and Zr groups (Figure 4.3a-b), light, middle and heavy *REE*s preferentially partition into titanite, and in the Y group, there is an approximate order-of-magnitude increase in both D_{REE} and D^*_{REE} in the epidote-free sample (#49). In the Zr group (Figure 4.3b), D_{REE} and D^*_{REE} values are similar to those for epidote-poor samples from the Y group. D_{REE} and D^*_{REE} patterns for *Ca amphibole-epidote* pairs (Y group) show that all *LREE* and *MREE* preferentially partition into epidote, whereas *HREE* are approximately equally partitioned between the two phases. In addition, there is a change linked with modal abundance of epidote, with progressively more *REE* entering amphibole with decreasing modal epidote. D_{REE} and D^*_{REE} patterns for *Ca amphibole-plagioclase* pairs are similar in the Y and Zr groups with *LREE* approximately evenly distributed between amphibole and plagioclase and middle and heavy *REE* strongly partitioned into Ca amphibole. Excluding Eu, all *REE* preferentially partition into epidote *X* sites between *plagioclase-epidote* pairs with *HREE* exhibiting erratic distribution patterns due to low abundances (i.e., near detection limits) in plagioclase. D_{REE} and D^*_{REE} patterns for this

pair do not always converge, suggesting that *REE*, especially *LREE*, may be hosted in multiple coordinated configurations in one site in one or both phases (e.g., *LREE* in 5-9-fold coordination plagioclase *A* site and 8- or 9-fold coordinated *X* site in epidote). Alternatively, the divergence may suggest that there are matrix effects, or that the measured concentrations (near detection limits for middle and *HREE* in plagioclase) and hence calculated mole fractions are inaccurate. The partitioning of *LREE* between *titanite-epidote* pairs is approximately equal, with *MREE* and *HREE* preferentially partitioned into titanite by a factor of approximately 10. D_{REE} and D^*_{REE} patterns for this pair are similar. In *plagioclase-titanite* pairs, light, middle and heavy *REE* all strongly preferentially partition into titanite in both the Y and Zr groups and D_{REE} and D^*_{REE} patterns for this pair generally parallel each other. *LREE* appear to show greater preference for plagioclase with decreasing modal epidote in the Y group, but the Zr group, which lacks epidote, exhibits a similar variation over an approximately constant grade so the correlation may be coincidence. Values for the *MREE* and *HREE* do not show consistent trends, possibly because of their low abundances near detection limits in plagioclase.

Garnet is restricted to the Zr group and D_{REE} and D^*_{REE} patterns for each mineral pair are approximately parallel. Between *Ca amphibole-garnet* pairs, *LREE* slightly preferentially partition into Ca amphibole, *HREE* slightly preferentially partition into garnet and *MREE* are approximately equally partitioned between the two phases. In

titanite-garnet pairs, light, middle and heavy *REE* all preferentially partition into titanite, but there is an approximately two order-of-magnitude decrease between D_{LREE}^* and D_{HREE}^* attributed to the greater compatibility of *HREE* in garnet *X* sites. In *plagioclase-garnet* pairs, *LREE* are preferentially partitioned into plagioclase with middle and heavy *REE* partitioned into garnet although the data for the latter are poor due to abundances near detection limits in plagioclase.

The regularity of these results for all the mineral pairs suggests that measured *REE* distributions approach equilibrium and the similarity of D_{REE} and D_{REE}^* patterns imply that *REE* mineral-site assignments are generally valid.

4.4 Controls on Rare Earth Element Partitioning

The thermodynamic framework established by the pioneering work of Kretz (1959, 1961), discussed in section 2.2.2, forms the theoretical basis for examining the distribution of trace elements between coexisting mineral pairs. In this section, the effects of mineral structure and major-element composition on *REE* partitioning are considered.

4.4.1 Major-Element Compositional Effects on REE Partitioning

A useful way to examine major-element compositional dependency of *REE* partitioning is to compare the *REE* concentration with the concentration of a major

element in one or both of the minerals. Goldschmidt (1937) established the principles of the distribution of elements in minerals and rocks and, since then, numerous authors have used these principles in experimental liquid crystal-liquid partitioning studies (e.g., Blundy and Wood, 1994; Blundy *et al.* 1998; Johnson, 1998; Botazzi *et al.*, 1999; Tiepolo *et al.* 2000, 2001, 2002 and many others). Yang and Rivers (1999, 2000) successfully extended these methods for certain elements to mineral-mineral systems in a study involving amphibolite-facies metapelites. They investigated major-element compositional effects of garnet, biotite, and muscovite on trace-element partitioning between garnet-biotite and biotite-muscovite pairs. In this study, the $\sum REE$ and selected ratios of light, middle and heavy *REEs* are compared to appropriate major-element molar fractions and exchange vectors for Ca amphibole, plagioclase, epidote (Y group) and garnet (Zr group). No significant correlations between $\sum REE$ or ratios of selected *L-M* or *HREE* and major components in titanite were discovered for Y or Zr group samples.

A comparison between the $\sum REE$ abundance in *Ca amphibole* versus the degree of edenite, tschermak, or cummingtonite exchange yielded no significant correlations, suggesting that the measured *REE* abundance is not controlled by these exchange vectors. Similarly, no significant correlations between any ratio of *L,-M-* or *HREE* and the edenite or tschermak exchanges was recognized. This is not unexpected given that these exchanges only operate on the *T* and octahedral *M1-3* sites, none of which are primary hosts for *REE* in Ca amphibole. However, the cummingtonite exchange (see

3.4.1) involves direct substitution of divalent cations (i.e., FeMg) for Ca in the $^{VI}M4$ site, which is also the primary host for *REE*. Figure 4.4a illustrates the positive correlation ($r' = 0.67$) between X_{Cum} and the ratio of $\sum(HREE + MREE)/LREE$ in analysed Ca amphibole. Consistent with this relationship there is a negative correlation ($r' = -0.70$) between X_{Cum} and the La/Lu ratio (Figure 4.4b). This relationship, also shown by Bottazzi *et al.* (1999) for kaersutitic amphibole with a significant cummingtonite component, implies that *REE* may substitute in more than one cavity in the *M4* amphibole site, possibly by the coupled substitution $^{M4}REE^{3+} IVAl^{3+} \leftrightarrow ^{M4}Ca^{2+} IVSi^{4+}$, as discussed further in section 4.4.2.

There is a broad positive correlation ($r' = 0.67$) between anorthite content (X_{An}^{Pl}) and the ratio $\sum(LREE + MREE)/(HREE)$ in analysed *plagioclase* (Figure 4.4c), which is attributed to the structural constriction of the irregular 5- to 9-fold coordinated *A* site in *plagioclase* with increasing calcium content, such that the cavity becomes closer to the ionic radii of the *LREE*. It is well established that *plagioclase* incorporates more *LREE* relative to *HREE*, a feature also exemplified by the data in this study (Table 4.1, Figure 4.1d). However, when only *plagioclase* coexisting with epidote is considered (i.e., Y group samples omitting #49), the correlation is stronger ($r^E = 0.73$) and clearly related to modal % epidote (Figure 4.4d). The positive correlation of $\sum LREE / \sum HREE$ with X_{An}^{Pl} may be attributed to net transfer of Ca and *REE* from epidote to *plagioclase* during epidote breakdown. *REE* incorporation in *plagioclase* may be charged-balanced by a

coupled substitution involving *REE*, Al, Na and P, such as: ${}^A\text{Na}^{1+}{}^T\text{P}^{5+} \leftrightarrow {}^A\text{REE}^{3+}{}^T\text{Al}^{3+}$.

There is a weak positive correlation ($r' = 0.55$) between Al content (zoisite) and the $\sum \text{REE}$ in analysed *epidote* (Figure 4.4e). However, within-sample variations in total *REE* abundance in epidote are significant, likely related to zoning at the thin section scale, making the importance of the correlation unclear. On the basis of ionic radii (Smyth and Bish, 1988), all *REE* are considered to substitute in the *X* site in epidote, normally occupied by calcium. *REE* incorporation in epidote *X* sites requires a coupled substitution, potentially: ${}^X\text{Ca}^{2+}{}^{M3}\text{Al}^{3+} \leftrightarrow {}^X\text{REE}^{3+}{}^{M3}(\text{FeMg})^{2+}$.

In the Zr group, the almandine component in *garnet* exhibits weak negative correlations with $\sum M\text{-HREE}$ ($r' = -0.65$; Figure 4.4f) and the ratio of *HREE/LREE* ($r' = -0.63$; Figure 4.4g) suggesting that *M-HREE* substitute for Fe^{2+} . Note that sample 01 (*: Figure 4.4f-g) clearly exhibits *REE* and major-element zoning on a within sample scale, indicated by the large variations in $X_{\text{Alm}}^{\text{Grt}}$, $\sum \text{REE}$ and *HREE/LREE* ratio. Numerous mechanisms for *REE* substitution into the *X* site of garnet have been proposed and involve either coupled substitutions or site vacancies to maintain charge balance. For instance, Jaffe (1951) proposed a mechanism for incorporation of yttrium (a *REE* analogue), involving substitution for divalent *X* site cations with charge-balance achieved by Al substitution for Si in the *T* sites, the so-called YAG exchange, i.e., ${}^X(\text{FeMg})^{2+}{}^T\text{Si}^{4+} \leftrightarrow {}^X\text{REE}^{3+}{}^T\text{Al}^{3+}$.

Although *REE* abundances are high in *titanite* (up to 2000 ppm), measured major-

element contents (Ti, Al, Fe³⁺, Ca, Na) in titanite exhibit little variation and are not correlated with either $\sum REE$ or any ratio of *L-M* or *HREE*. Deer *et al.* (1966) and Tiepolo *et al.* (2002) suggested the coupled substitution ${}^A\text{Ca}^{2+} {}^M\text{Ti}^{4+} \leftrightarrow {}^A\text{REE}^{3+} {}^M(\text{AlFe}^{3+})$ for *REE* incorporation in titanite. There are thus major-element controls on $\sum REE$ and the ratio between *L*, *M* and *HREE* incorporation in four of the five examined phases, implying that compositional controls on *REE* incorporation are significant factors in their measured distributions.

4.4.2 Structural Controls on REE Incorporation

The first order structural constraints on trace-element partitioning are the charge and ionic radius of the trace elements in relation to the nominal charge and volume of the host polyhedron (e.g., Onuma *et al.*, 1968, Brice, 1975, Blundy and Wood, 1994). Second order constraints are the elasticity of the lattice, i.e., crystal structures which are more elastic or 'flexible' will more readily admit misfitting cations than a more rigid crystal structure, and the ability of the lattice to accommodate an uneven distribution of charge, usually through coupled substitution or site vacancies. The current understanding of the uptake of *REEs* holds that *LREEs* are preferentially incorporated in the Ca sites in minerals such as Ca amphibole, epidote and apatite on account of the similarity between the ionic radii of calcium (1.12 Å; C.N. = 8) and *LREE* (e.g., Ce ≈ 1.14 Å; C.N. = 8). Similarly, *HREE* may be preferentially incorporated in minerals such as

zircon, almandine-pyrope garnet and orthopyroxene on account of the similarity in the ionic radii of Fe^{2+} (0.92 Å; C.N. = 8) and *HREE* (e.g., Lu 0.97 Å; C.N. = 8).

Onuma *et al.* (1968) were the first to relate crystal-liquid partition coefficients and ionic radii in order to compare the efficiency with which different ions are incorporated into different crystal structures. These diagrams were widely adopted and became known as Onuma diagrams. Jensen (1973) compiled Onuma diagrams from published data for various minerals in crystal-liquid systems and arrived at the following general conclusions:

(i) Isovalent elements fall on smooth parabolic curves, with one or more peaks which represent the ideal ionic radii of the polyhedra of interest.

(ii) Curves for ions of different valency substituting in the same polyhedra peak at approximately the same ionic radius. This is the ideal ionic radius for the host polyhedron.

(iii) A particular mineral always shows the same peaks which correspond to the ionic radii of the ideal host cation, regardless of the composition of the host rock.

Onuma's case (i.e., crystal-liquid partitioning) is a simplified example of a more general problem, the simplification resulting from the very different elastic properties of the crystal and liquid studied. However the concept can in principle be extended to mineral-mineral partitioning (see Yang *et al.*, 1999) and the resultant ionic radius versus mineral-mineral partition coefficient diagrams are referred to as *Onuma-type* diagrams.

Considering only the effects of lattice elasticity and optimal site radius, and ignoring local charge balance effects due to potential coupled substitutions, Figure 4.5 schematically illustrates three possible shapes of Onuma-type diagrams based on partitioning pairs with various elasticities. There is a nearly infinite range of possibilities for the shapes of these curves depending on the partitioning behaviour of each phase (influenced by site characteristics, major-element composition, valence state of substituting cation, etc.) for a given mineral pair and Figure 4.5 is only a simplified illustration. In the case of a crystal/liquid pair (Figure 4.5a: Onuma's case), liquid will have little influence on the shape of the Onuma curve since its structure is much more elastic than that of the coexisting mineral. The vertex of the parabola therefore represents the ideal radius of the site in the mineral on which substitution occurs, with the convexity of the parabola reflecting the elasticity of the site. Now consider cation partitioning between two minerals. If trace element i is partitioned between two minerals with distinct polyhedra on which the substitution of i occurs (i.e., exhibit differences in size and/or elasticity), possible Onuma-type curves are shown in Figure 4.5b-c. In the case of Figure 4.5b, the Onuma-type diagram will appear similar to a crystal-liquid Onuma diagram since the control on partitioning is dominated by one of the two phases (e.g., *HREE* partitioning controlled by garnet X sites in garnet-biotite pairs: Yang *et al.* 1999; LILE and HFSE partitioning dominated by Ca amphibole ^{XII}A and ^{VI}M sites respectively between Ca-amphibole-clinopyroxene pairs: Tiepolo *et al.*, 2000). In

principle, the ideal ionic radius of the site in the 'dominant' mineral may be determined from such a diagram, but the ideal ionic radius of the site in the 'subordinate' mineral is cryptic. However, if cation partitioning is considered between two minerals which contain analogous polyhedra that exhibit only slight differences in both size and elasticity (e.g., Figure 4.5c), the shape of the Onuma-type curve becomes skewed due to the combined effects of the two, or possibly more, sites in each mineral and the ideal ionic radii of sites in both phases are cryptic.

In summary, because the curves in Onuma-type diagrams commonly reflect the combined effects of the ideal site parameters (i.e., radius and elasticity) of *both* minerals, they can take on an almost infinite range of shapes, rendering quantitative extraction of the ideal site sizes and elasticities using the strain-compensated *crystal-liquid* partition coefficient equation of Blundy & Wood (1994) impractical. Because of these problems, this study utilizes a qualitative approach to the extraction of site parameters in the two minerals, which nonetheless provides significant insight into partitioning behaviour.

As a first-order observation, general information regarding the sizes and elasticities of the host sites on which *REE* partitioning took place can be inferred from chondrite-normalized concentration *versus* ionic radii plots for each phase (Figure 4.6a-h; Eu is omitted from these plots because of its 2^{+} state). This approach assumes that normalization to chondrite does not introduce significant distortion of the patterns inherent in each mineral, an assumption that is tested *a posteriori* through an evaluation

of the internal consistency of the results and their compatibility with independent data. As noted below, chondrite-normalization does introduce an artifact in the *REE* pattern for plagioclase because *HREE* in plagioclase are poorly measured due to low concentration.

Chondrite-normalized *REE* patterns for *Ca amphibole* are illustrated in Figure 4.6a-b, which also shows the optimal size of the *M4* cavity into which the *REE* are expected to substitute (Table 2.1a-b). Although all curves slope from *H-* to *LREE*, in detail, two types can be identified: (i) those that slope monotonically from *H-* to *LREE*; and (ii) those with slight convexity in the *MREE*. These patterns suggest there is more than one mechanism of *REE* incorporation in this phase. Furthermore, in the type (ii) curve, the 'ideal' site radius ($\approx 1.11\text{\AA}$) does not coincide with the peak of convexity, which occurs between Dy-Sm ($1.06\text{-}1.08\text{\AA}$). As noted in section 4.4.1, the degree of cummingtonite substitution in *M4* sites affects the site distribution of *REE* in *Ca amphibole* and this is borne out by the analysis in this study: type (i) curves correspond to relatively 'cummingtonite-rich' *Ca amphibole* ($X_{Cum}^{Amp} \approx 12\%$), whereas type (ii) curves correlate with relatively 'cummingtonite-poor' *Ca amphibole* ($X_{Cum}^{Amp} \approx <6\%$). In case (i), *Ca amphibole* has La/Lu ratios near unity (Table 4.1) reflecting the lack of preference of the *M4* site for one element relative to the other. In addition, the chondrite-normalized *REE* pattern has no peak corresponding to the ideal radius of a cation for the *M4* site in amphibole. Bottazzi *et al.* (1999) encountered a similar scenario for kaersutite and

pargasite with significant cummingtonite components. On the basis of this observation coupled with structure refinement information for both minerals, they attributed the pattern to the occurrence of two cavities within the $M4$ site ($M4$ and $M4'$) and they showed that when the curves for these cavities are 'added', the sum approximates the measured chondrite-normalized REE pattern. They explained this correlation as follows: when the $M4$ site is occupied by divalent cations smaller than Ca (e.g., FeMg: cummingtonite component), its geometry becomes distorted such that the $M4'$ site has an ideal radius of approximately Ho (1.01 Å) and the larger $M4$ site has a radius closer to $LREE$ (≈ 1.13 Å). It is inferred that the two-site model of Bottazzi *et al.* (1999) applies to amphibole with significant X_{Cum}^{Amp} in this study. However, for type (ii) curves, the geometric distortion imparted by the cummingtonite component in the $M4$ site is so small that most REE enter the $M4$ site with an optimal radius of approximately 1.07 Å ($\approx Sm$) and the effect of the $M4'$ site is subordinate. Chondrite-normalized REE patterns for these amphiboles are approximately flat exhibiting weak $LREE$ depletion (i.e., La/Lu ratios ≈ 3 -5; Table 4.1). In addition, the slight misfit of the type (i) curve with the expected peak of the average $M4$ site may reflect the presence of the subordinate $M4'$ cavity. Thus, despite the fact that Ca amphibole with negligible X_{Cum}^{Amp} is more REE enriched than Ca amphibole with significant X_{Cum}^{Amp} , $HREE$ enter 'cummingtonite-like' distorted $M4'$ cavities more easily than 'pargasite-like' $M4$ sites.

Plagioclase from both groups (Y group: $\approx An_{33}$; Zr group: $\approx An_{47}$) exhibit similar

behaviour. Not surprisingly, chondrite-normalized plagioclase *REE* patterns (Figure 4.6c-d) trend towards a peak at approximately 1.20 Å corresponding to the 5- to 9-fold coordinated *A* site that also hosts *LREE*. However, a second much smaller peak near Yb (≈ 0.97 Å) is also observed. The ionic radius of this peak is too large to correspond to the *T* site normally occupied by Al and Si in the plagioclase series and is interpreted to be an artifact of chondrite-normalization scheme. The artifact occurs because, in contrast to *LREE*, certain *HREE* (mainly odd-numbered *HREE*) abundances are less than chondrite, the cross-over at approximately Er giving rise to an apparent increase in concentration of the *HREE*.

Chondrite-normalized patterns for both *epidote* and *garnet* imply that all *REEs* enter a single site in each phase. Chondrite-normalized *REE* patterns for epidote (Figure 4.6e) slope monotonically down from a peak in the *LREE* indicating that all *REE* enter the large (≈ 1.20 Å) *A* site normally occupied by calcium. In contrast to epidote, garnet (Figure 4.6f) is *HREE*-enriched and the patterns slope monotonically down from a peak in the *HREE* with a maximum near the ionic radius of \approx Tm-Yb (0.99 Å). This approaches the ideal radius of the 8-fold coordinated *X* site in almandine-pyrope garnet.

Chondrite-normalized *REE* concentrations for *titanite* are illustrated in Figure 4.6(g-h). For all samples except 06, which as noted previously is anomalous, *HREE* patterns are essentially flat, and there is a slight peak in the *MREE* near Sm, corresponding to a first approximation to the ideal *A* site radius (≈ 1.08 Å) and a weak

LREE depletion. Thus, as suggested by previous authors, it is reasonable to assume that all *REE* enter the 7-fold Ca site ($\approx 1.08 \text{ \AA}$).

4.4.3 *REE Onuma-type Curves*

Onuma-type plots for the nine possible mineral pairs in this study are shown in Figure 4.7(a-l). Plots for *Ca amphibole-titanite* pairs do not exhibit parabolic shapes implying that the *REE* enter similar sites in both minerals and thus both minerals exert control on *REE* incorporation. However, comparison of Figures 4.6a-b and 4.7a-b indicates that Ca amphibole provides the stronger discrimination, as the shapes of the curves are closely related to the shapes for chondrite-normalized Ca amphibole patterns (Figure 4.6). The patterns for Ca amphibole-titanite pairs in which X_{Cum}^{Amp} is significant exhibit a monotonic slope from *HREE* to *LREE*, imputing a role for the $M4'$ site in sequestering *HREE*, as noted previously (Bottazzi *et al.*, 1999). In contrast, patterns for Ca amphibole-titanite pairs in which X_{Cum}^{Amp} is subordinate are flat, implying that the $M4'$ site is only a minor *REE* host. Onuma-type plots for *titanite-plagioclase* (Figure 4.7c-d) for the Y and Zr groups both exhibit asymmetric quasi-parabolic shapes. The vertices of these curves occur at an ionic radius of approximately 1.05 \AA , which is closer to the seven-fold coordinated *A* of titanite (1.07 \AA) than the larger *A* site in plagioclase (1.20 \AA), implicating the dominant control of the former phase. The small secondary peak in the *HREE* in the same samples is an artifact of low *HREE* abundances (near

detection limits) in plagioclase. Onuma-type plots for *Ca amphibole-plagioclase* pairs (Figure 4.7g-h) are broadly similar to titanite-plagioclase plots, implying that the *M4* site in *Ca* amphibole dominates over the *A* site in plagioclase for all *REE* except *La*, which is approximately equally distributed between the two phases.

Onuma-type plots for *epidote-mineral* (i.e., *titanite-epidote*, *amphibole-epidote*, *plagioclase-epidote*; Figures 4.7e, i and k respectively) also exhibit asymmetric patterns. Titanite-epidote and *Ca* amphibole-epidote pairs both exhibit quasi-monotonic trends that appear to be controlled by the strong preference of *LREE* for the epidote *X* site. Plagioclase-epidote pairs show a weakly concave-up shape, reflecting the comparable nature of the plagioclase *A* site and epidote *X* site. Unlike epidote, *garnet-mineral* Onuma-type plots exhibit quasi-parabolic shapes, likely a result of the preference of *LREE* for other phases which is consistent with the widely reported preference of the eight-fold almandine-rich garnet *X* site for cations smaller than Ca^{2+} (e.g., *M-HREE*). The *LREE* portions of the pattern for *titanite-garnet* and *Ca amphibole-garnet* pairs (Figure 4.7f and j respectively) exhibit quasi-parabolic shapes with vertices at approximately 1.12 Å. The shape of the *plagioclase-garnet* curve (Figure 4.7l) is more complex exhibiting two peaks at approximately 1.02 Å and 1.15 Å. The peak at 1.15 Å is likely due to the irregular 5-9-fold coordinated *A* site in plagioclase and the peak at 1.02 Å is attributed to the eight fold coordinated garnet *X* site.

4.4.4 Qualitative interpretations of site distributions of REE

Qualitative interpretations of the site distributions of *REE* in each phase in terms of ionic radii and elasticities are illustrated in Figures 4.8a-g (Y group) and 4.9a-f (Zr group). For each mineral pair, a representative example was chosen to demonstrate the nature of the site partitioning. Inferred ideal site radii and elasticities (dashed lines) are schematic, but their consistency in all samples suggests that they are approximately correct. In all minerals except Ca amphibole, the observed partitioning patterns are consistent with a single site elastic model. For several of the phases, the site elasticities exhibit a second-order dependence on major-element mineral composition. Details are summarised below.

For *Ca amphibole*, the $^{VIII}M4$ site is the primary host for *REE* with an optimal site radius similar to the *LREE* is the primary host for *REE*. However, as established by Bottazzi *et al.* (1999) and noted previously, with increasing X_{Cum} , a smaller cavity dubbed $M4'$ develops in the $M4$ site, which preferentially partitions *M-HREE*. Thus, *REE* distribution in Ca amphibole is linked to the occupancy of the 8-fold coordinated $M4$ site, with the presence of Ca in cummingtonite-poor amphibole preferentially partitioning *LREE* and the presence of FeMg in cummingtonite-rich amphibole favouring *M-HREE* due to the $M4'$ geometric distortion. Thus in Fig. 4.8a, two site models for Ca amphibole pairs are shown representing the cummingtonite-rich and -poor samples observed in this study.

For *plagioclase*, the *A* site preferentially incorporates *LREE*, and partitioning of *REE* is enhanced with the constriction of this site with increasing calcium. Similar to *plagioclase*, the *epidote X* site serves as the host for *REE*. However, unlike *plagioclase* which exhibits *A* site expansion with increasing sodium, *epidote* group minerals exhibit no significant solid solution at *X* sites (Ercit, 2002) and therefore any potential size distortion of this site is likely a result of substitution at adjacent sites (e.g., $M^3Al^{3+} \leftrightarrow M^3Fe^{3+}$). The eight-fold coordinated *garnet X* site exhibits such strong preference for *HREE* that this effect is typically readily extracted from garnet-mineral partitioning patterns (e.g., Figure 4.9e-f). *Titanite* is the least *REE* selective of all analysed phases, but exhibits a small preference for *MREE* which is more pronounced in *epidote-free* rocks (Figures 4.8b and 4.9a-c).

In conclusion, measured *REE* abundances in Ca amphibole, *plagioclase*, *epidote*, *garnet* and *titanite* generally exhibit consistent patterns suggesting that the measured distributions of these elements approach equilibrium, and furthermore, that these consistent patterns can be explained by the known and/or inferred site preferences of the *REE* in the various structures of these minerals. *REE* patterns of a single phase in one sample (*titanite* in sample 06) are egregiously inconsistent with the patterns for all the other samples and imply that, for reasons unknown, this mineral did not achieve equilibrium at the thin-section scale. Chapter 5 uses a similar approach to elucidate the distribution of transition element, LILE and HFSE chemistry of these samples.

Chapter 4: Rare Earth Element Mineral Chemistry

Table 4.1 Average *REE* concentrations (± 1 standard deviation) of Ca amphibole and plagioclase analysed by LAM ICP-MS. *Italics* indicate Zr group. Blank indicates below detection limit. Eu/Eu* denotes average chondrite-normalized Eu anomaly.

Ca amphibole	46	48	49	06	20	01	142
(n = 4)							
<i>REE (ppm)</i>							
La	0.22 \pm 0.02	0.10 \pm 0.02	3.81 \pm 0.17	2.79 \pm 0.98	0.52 \pm 0.21	0.69 \pm 0.08	1.90 \pm 0.25
Ce	1.18 \pm 0.18	0.57 \pm 0.07	13.0 \pm 0.84	11.8 \pm 3.07	2.18 \pm 0.87	3.79 \pm 0.35	10.0 \pm 0.92
Pr	0.22 \pm 0.03	0.14 \pm 0.02	2.27 \pm 0.11	2.25 \pm 0.40	0.42 \pm 0.17	0.91 \pm 0.12	2.54 \pm 0.21
Nd	1.44 \pm 0.02	0.96 \pm 0.16	13.1 \pm 0.30	13.7 \pm 2.17	2.40 \pm 0.89	6.36 \pm 0.84	16.8 \pm 2.25
Sm	0.66 \pm 0.02	0.56 \pm 0.10	4.63 \pm 0.11	5.07 \pm 0.58	0.76 \pm 0.31	3.04 \pm 0.49	7.71 \pm 1.09
Eu	0.23 \pm 0.03	0.15 \pm 0.02	1.54 \pm 0.08	1.79 \pm 0.25	0.34 \pm 0.14	0.89 \pm 0.20	2.87 \pm 0.51
Gd	1.12 \pm 0.10	0.98 \pm 0.14	6.55 \pm 0.20	6.76 \pm 0.57	1.00 \pm 0.37	4.00 \pm 0.78	10.2 \pm 2.25
Tb	0.19 \pm 0.02	0.18 \pm 0.02	1.10 \pm 0.05	1.21 \pm 0.12	0.16 \pm 0.07	0.66 \pm 0.15	1.67 \pm 0.40
Dy	1.66 \pm 0.20	1.31 \pm 0.22	7.75 \pm 0.42	8.21 \pm 1.04	1.06 \pm 0.48	4.28 \pm 0.90	10.8 \pm 2.44
Ho	0.37 \pm 0.06	0.31 \pm 0.03	1.65 \pm 0.14	1.69 \pm 0.16	0.23 \pm 0.10	0.77 \pm 0.16	2.09 \pm 0.45
Er	1.15 \pm 0.17	0.90 \pm 0.10	4.82 \pm 0.42	5.06 \pm 0.49	0.63 \pm 0.29	1.98 \pm 0.46	5.47 \pm 1.32
Tm	0.17 \pm 0.04	0.14 \pm 0.02	0.71 \pm 0.07	0.74 \pm 0.11	0.10 \pm 0.05	0.26 \pm 0.05	0.78 \pm 0.18
Yb	1.24 \pm 0.24	0.95 \pm 0.10	4.96 \pm 0.48	5.26 \pm 0.98	0.69 \pm 0.34	1.59 \pm 0.40	4.84 \pm 0.89
Lu	0.21 \pm 0.06	0.17 \pm 0.02	0.78 \pm 0.08	0.78 \pm 0.08	0.11 \pm 0.05	0.20 \pm 0.06	0.66 \pm 0.13
Σ REE	10.1	7.42	66.7	67.0	10.6	29.4	78.4
LREE (La-Nd)	3.06	1.78	32.2	30.5	5.51	11.8	31.3
MREE (Sm-Ho)	4.23	3.48	23.2	24.7	3.56	13.6	35.3
HREE (Er-Lu)	2.77	2.16	11.3	11.8	1.53	4.03	11.8
La/Lu	1.04	0.60	4.88	3.57	4.72	3.45	2.88
Eu/Eu*	0.83	0.53	0.83	0.93	1.21	0.78	0.99
Plagioclase	46	48	49	06	20	01	142
(n = 4)							
<i>REE (ppm)</i>							
La	0.28 \pm 0.20	0.59 \pm 0.16	1.82 \pm 0.93	3.74 \pm 1.28	0.40 \pm 0.19	2.35 \pm 1.08	6.25 \pm 0.85
Ce	0.38 \pm 0.21	0.90 \pm 0.41	1.85 \pm 0.99	7.08 \pm 1.97	0.54 \pm 0.20	2.40 \pm 0.20	11.6 \pm 1.55
Pr	0.04 \pm 0.01	0.21 \pm 0.09	0.16 \pm 0.08	0.50 \pm 0.10	0.05 \pm 0.01	0.21 \pm 0.12	0.80 \pm 0.12
Nd	0.12 \pm 0.04	0.82 \pm 0.49	0.50 \pm 0.34	1.31 \pm 0.32	0.15 \pm 0.02	0.62 \pm 0.43	2.13 \pm 0.30
Sm	0.04 \pm 0.01	0.23 \pm 0.04	0.07 \pm 0.05	0.23 \pm 0.04	0.06 \pm 0.01	0.08 \pm 0.06	0.36 \pm 0.04
Eu	0.09 \pm 0.03	1.64 \pm 0.43	0.11 \pm 0.05	0.22 \pm 0.04	0.13 \pm 0.02	0.15 \pm 0.04	0.34 \pm 0.04
Gd	0.04 \pm 0.01	0.24 \pm 0.06	0.03 \pm 0.02	0.15 \pm 0.03	0.06 \pm 0.01	0.04 \pm 0.02	0.22 \pm 0.02
Tb		0.04 \pm 0.01	0.01 \pm 0.01	0.02 \pm 0.01		0.01 \pm 0.01	0.03 \pm 0.01
Dy	0.02 \pm 0.01	0.17 \pm 0.04	0.03 \pm 0.02	0.22 \pm 0.07	0.02 \pm 0.01	0.03 \pm 0.01	0.33 \pm 0.09
Ho		0.04 \pm 0.01	0.01 \pm 0.01	0.03 \pm 0.01		0.01 \pm 0.01	0.04 \pm 0.01
Er	0.02 \pm 0.01	0.10 \pm 0.06	0.03 \pm 0.01	0.06 \pm 0.02	0.03 \pm 0.01	0.03 \pm 0.02	0.09 \pm 0.02
Tm		0.02 \pm 0.01	0.01 \pm 0.01	0.02 \pm 0.01	0.01 \pm 0.01	0.01 \pm 0.01	0.03 \pm 0.01
Yb	0.03 \pm 0.01	0.10 \pm 0.02	0.03 \pm 0.02	0.13 \pm 0.07	0.05 \pm 0.02	0.03 \pm 0.03	0.23 \pm 0.06
Lu		0.03 \pm 0.01		0.01 \pm 0.01			0.02 \pm 0.01
Σ REE	1.07	5.14	4.65	13.7	1.52	5.97	22.5
LREE (La-Nd)	0.82	2.52	4.33	12.6	1.15	5.58	20.8
MREE (Sm-Ho)	0.19	2.37	0.25	0.87	0.28	0.31	1.32
HREE (Er-Lu)	0.06	0.25	0.07	0.23	0.09	0.08	0.36
*Ce/Yb	12.7	5.9	60.7	54.5	10.8	80.0	50.4
Eu/Eu*	6.86	21.2	7.53	3.55	6.53	7.90	3.65

Chapter 4: Rare Earth Element Mineral Chemistry

Table 4.1(continued). Average REE concentrations (± 1 standard deviation) of epidote, garnet, and titanite analysed by LAM ICP-MS. *Italics* indicate Zr group. Blank indicates below detection limit. Eu/Eu* denotes average chondrite-normalized Eu anomaly.

Epidote	06	46	*48	Garnet	01	*20	142
(n = 4 *n = 3)				(n = 4 *n = 2)			
REE (ppm)				REE (ppm)			
La	76.3 \pm 27.0	35.8 \pm 21.1	10.7 \pm 8.8		0.50 \pm 0.67	0.48 \pm 0.08	1.17 \pm 0.88
Ce	166 \pm 59.4	69.4 \pm 37.2	31.7 \pm 29.4		0.91 \pm 1.09	3.45 \pm 1.83	4.35 \pm 0.88
Pr	19.1 \pm 6.93	9.00 \pm 5.10	4.15 \pm 3.90		0.14 \pm 0.12	0.46 \pm 0.17	0.88 \pm 0.80
Nd	72.7 \pm 28.9	36.4 \pm 20.1	17.8 \pm 15.9		1.20 \pm 0.47	2.92 \pm 0.13	5.30 \pm 3.87
Sm	13.9 \pm 4.39	6.78 \pm 3.51	4.20 \pm 3.62		1.72 \pm 0.18	1.44 \pm 0.16	3.04 \pm 1.52
Eu	4.87 \pm 0.98	2.38 \pm 1.48	1.43 \pm 1.23		1.82 \pm 0.11	0.56 \pm 0.01	2.32 \pm 0.77
Gd	10.4 \pm 2.73	5.06 \pm 2.46	3.09 \pm 2.41		5.71 \pm 1.51	2.95 \pm 0.89	7.64 \pm 1.98
Tb	1.43 \pm 0.23	0.68 \pm 0.25	0.45 \pm 0.25		1.24 \pm 0.37	0.63 \pm 0.01	1.63 \pm 0.44
Dy	8.12 \pm 1.32	4.15 \pm 1.25	2.60 \pm 1.88		10.7 \pm 3.88	6.43 \pm 0.39	3.90 \pm 2.77
Ho	1.40 \pm 0.16	0.75 \pm 0.14	0.49 \pm 0.35		2.47 \pm 0.94	1.73 \pm 0.17	3.20 \pm 0.81
Er	3.33 \pm 0.55	2.02 \pm 0.35	1.32 \pm 0.93		7.85 \pm 2.88	6.23 \pm 0.24	9.46 \pm 2.35
Tm	0.42 \pm 0.09	0.26 \pm 0.05	0.17 \pm 0.12		1.18 \pm 0.45	1.16 \pm 0.16	1.46 \pm 0.33
Yb	2.72 \pm 0.84	1.75 \pm 0.31	1.25 \pm 0.94		8.82 \pm 3.26	9.37 \pm 1.74	10.3 \pm 2.08
Lu	0.36 \pm 0.09	0.26 \pm 0.05	0.18 \pm 0.12		1.28 \pm 0.53	1.22 \pm 0.10	1.51 \pm 0.27
Σ REE	381	174	79.5	Σ REE	45.5	39.0	66.1
LREE (La-Nd)	334	150	64.3	LREE (La-Nd)	2.75	7.31	11.7
MREE (Sm-Ho)	40.1	19.8	12.3	MREE (Sm-Ho)	23.6	13.7	31.7
HREE (Er-Lu)	6.82	4.28	2.92	HREE (Er-Lu)	19.1	17.9	22.7
La/Lu	212	137	59.3	La/Lu	0.39	0.39	0.77
Eu/Eu*	1.24	1.24	1.21	Eu/Eu*	1.78	0.84	1.47
Titanite	46	48	*49	06	01	20	*142
(n = 3 *n = 2)							
REE (ppm)							
La	133 \pm 55.4	177 \pm 47.3	68.9 \pm 44.1	206 \pm 70.5	175 \pm 25.0	127 \pm 31.7	55.4 \pm 11.0
Ce	423 \pm 129	588 \pm 78.3	268 \pm 154	784 \pm 194	585 \pm 41.3	401 \pm 78.8	221 \pm 38.5
Pr	63.9 \pm 21.3	100 \pm 8.96	48.1 \pm 23.9	137 \pm 45.8	99.8 \pm 4.00	60.0 \pm 12.9	40.8 \pm 5.99
Nd	342 \pm 100	547 \pm 18.8	299 \pm 142	760 \pm 341	544 \pm 11.3	322 \pm 60.8	255 \pm 35.7
Sm	112 \pm 27.9	172 \pm 3.89	115 \pm 52.6	250 \pm 183	171 \pm 1.20	107 \pm 16.9	99.4 \pm 13.2
Eu	39.7 \pm 10.4	61.5 \pm 0.71	34.8 \pm 17.6	73.8 \pm 39.6	61.3 \pm 0.41	37.8 \pm 6.30	29.4 \pm 4.40
Gd	152 \pm 27.6	213 \pm 8.15	160 \pm 76.6	247 \pm 222	211 \pm 2.32	146 \pm 16.6	136 \pm 19.1
Tb	26.1 \pm 4.38	34.0 \pm 1.40	26.3 \pm 12.5	34.3 \pm 30.1	33.8 \pm 0.40	25.1 \pm 2.62	22.4 \pm 3.13
Dy	183 \pm 25.2	242 \pm 9.27	196 \pm 98.0	182 \pm 170	240 \pm 2.55	177 \pm 14.9	166 \pm 24.5
Ho	37.4 \pm 4.49	47.1 \pm 1.19	39.0 \pm 19.3	23.4 \pm 19.6	46.8 \pm 0.40	36.4 \pm 2.60	33.0 \pm 4.85
Er	110 \pm 12.9	136 \pm 1.14	113 \pm 55.1	45.3 \pm 30.7	135 \pm 0.82	107 \pm 7.16	96.6 \pm 13.8
Tm	15.5 \pm 1.99	19.0 \pm 0.57	16.5 \pm 9.23	4.57 \pm 3.43	19.1 \pm 0.28	15.0 \pm 1.11	14.1 \pm 1.98
Yb	106 \pm 13.4	129 \pm 9.23	111 \pm 48.9	21.7 \pm 12.7	129 \pm 4.37	102 \pm 7.17	96.1 \pm 12.2
Lu	14.5 \pm 2.20	16.7 \pm 1.85	14.8 \pm 6.30	1.94 \pm 1.28	16.8 \pm 0.85	13.9 \pm 1.25	12.9 \pm 1.58
Σ REE	1777	2483	1510	2772	2471	1681	1278
LREE	962	1413	684	1887	1405	911	572
MREE	551	769	571	811	765	531	487
HREE	246	301	255	73.6	301	239	219
La/Lu	8.42	10.6	4.67	106	10.5	9.12	4.31
Eu/Eu*	0.93	0.99	0.78	0.91	0.98	0.92	0.77

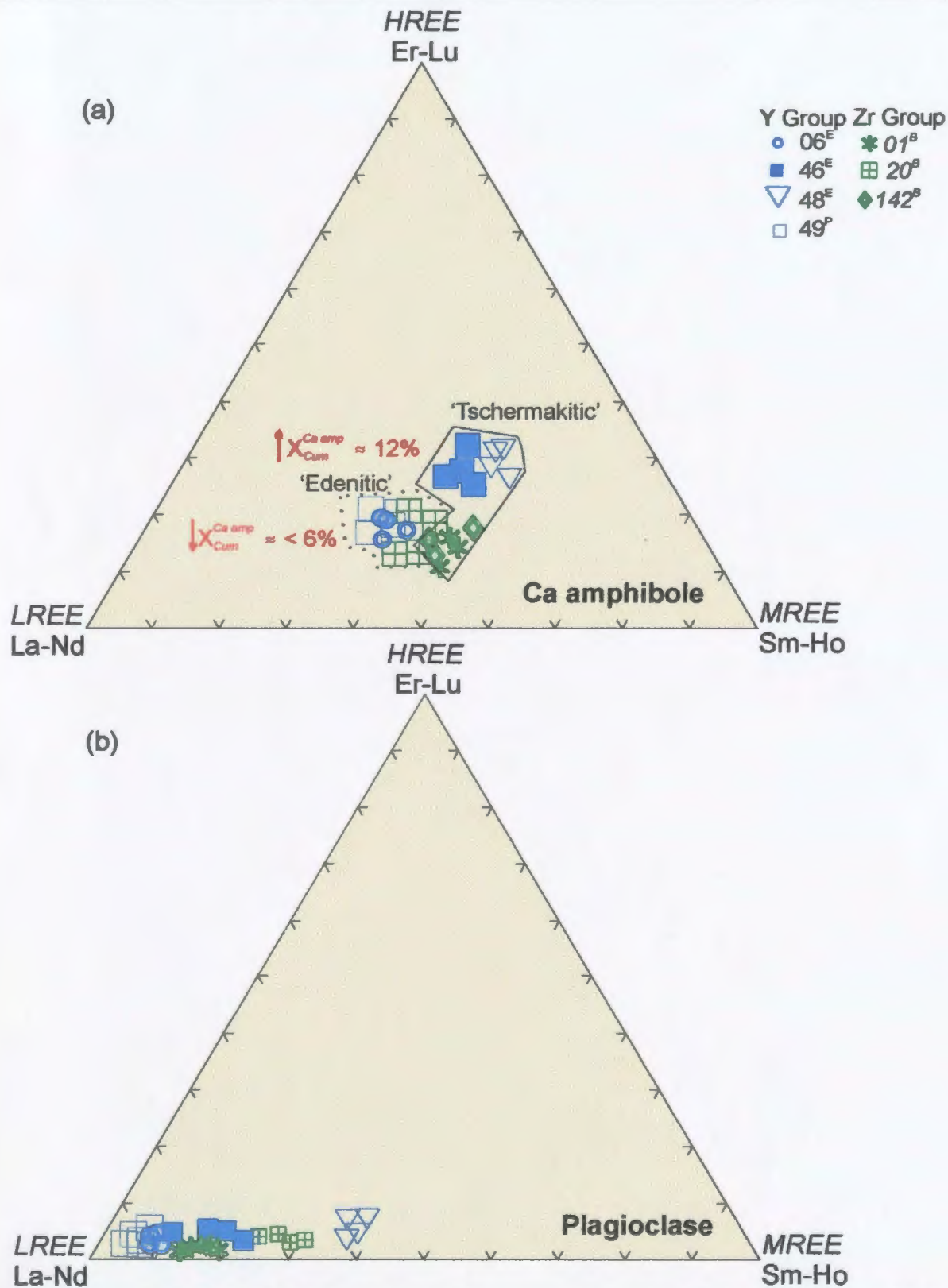


Figure 4.1 Ca amphibole (a) and plagioclase (b) compositions on the basis of light, middle and heavy *REE* distribution. Superscripts denote rock type (E = epidote amphibolite, P = plagioclase amphibolite, B = biotite amphibolite).

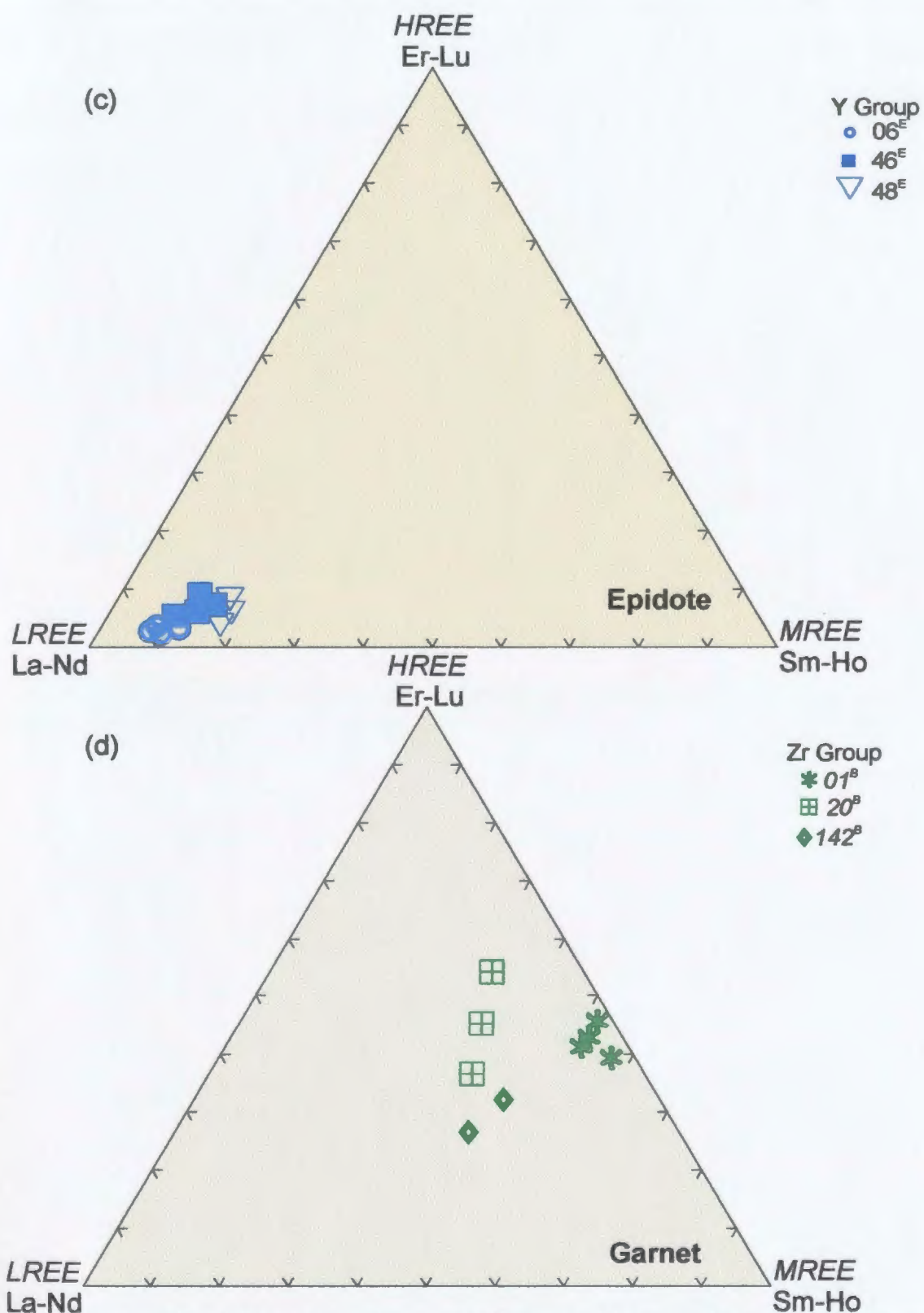


Figure 4.1 (continued) Epidote (c) and garnet (d) compositions on the basis of light, middle and heavy REE distribution. Epidote is LREE enriched whereas garnet incorporates middle and heavy REE.

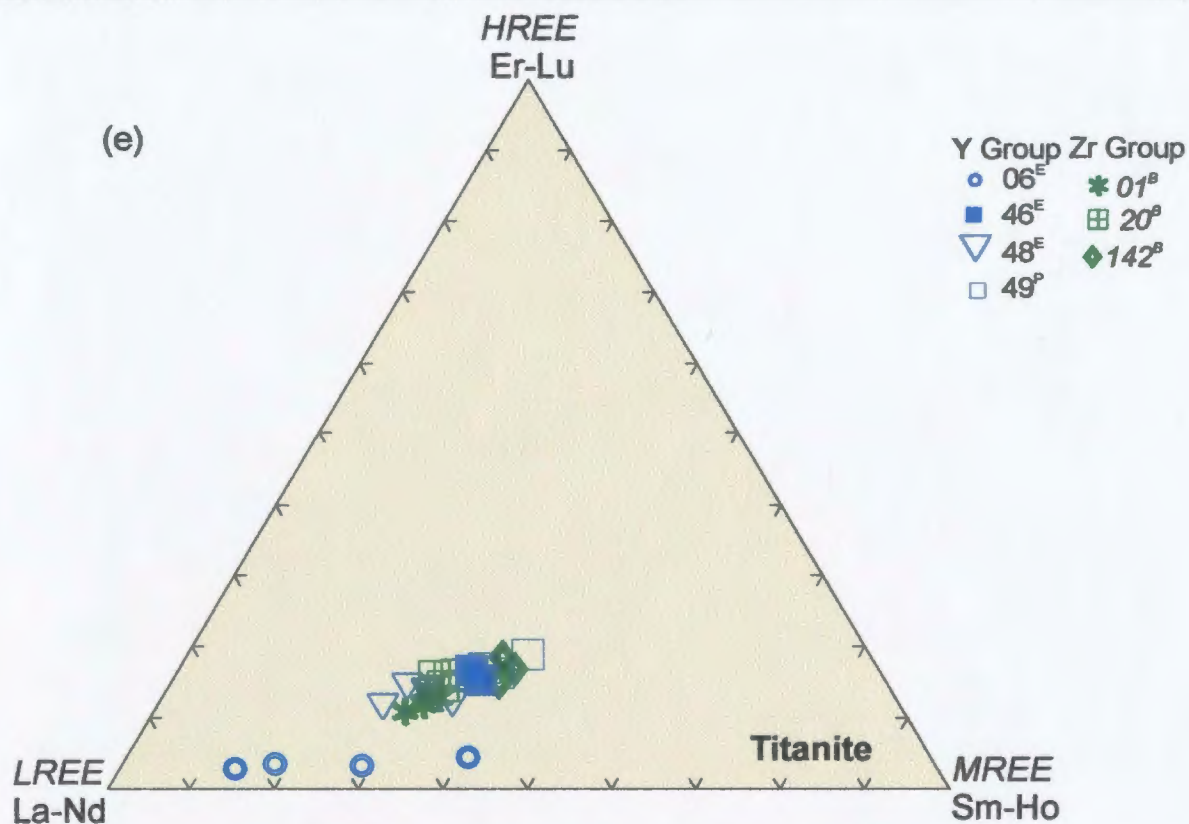


Figure 4.1 (continued) Titanite (e) compositions on the basis of the distribution of seven-fold coordinated light, middle and heavy *REE*.

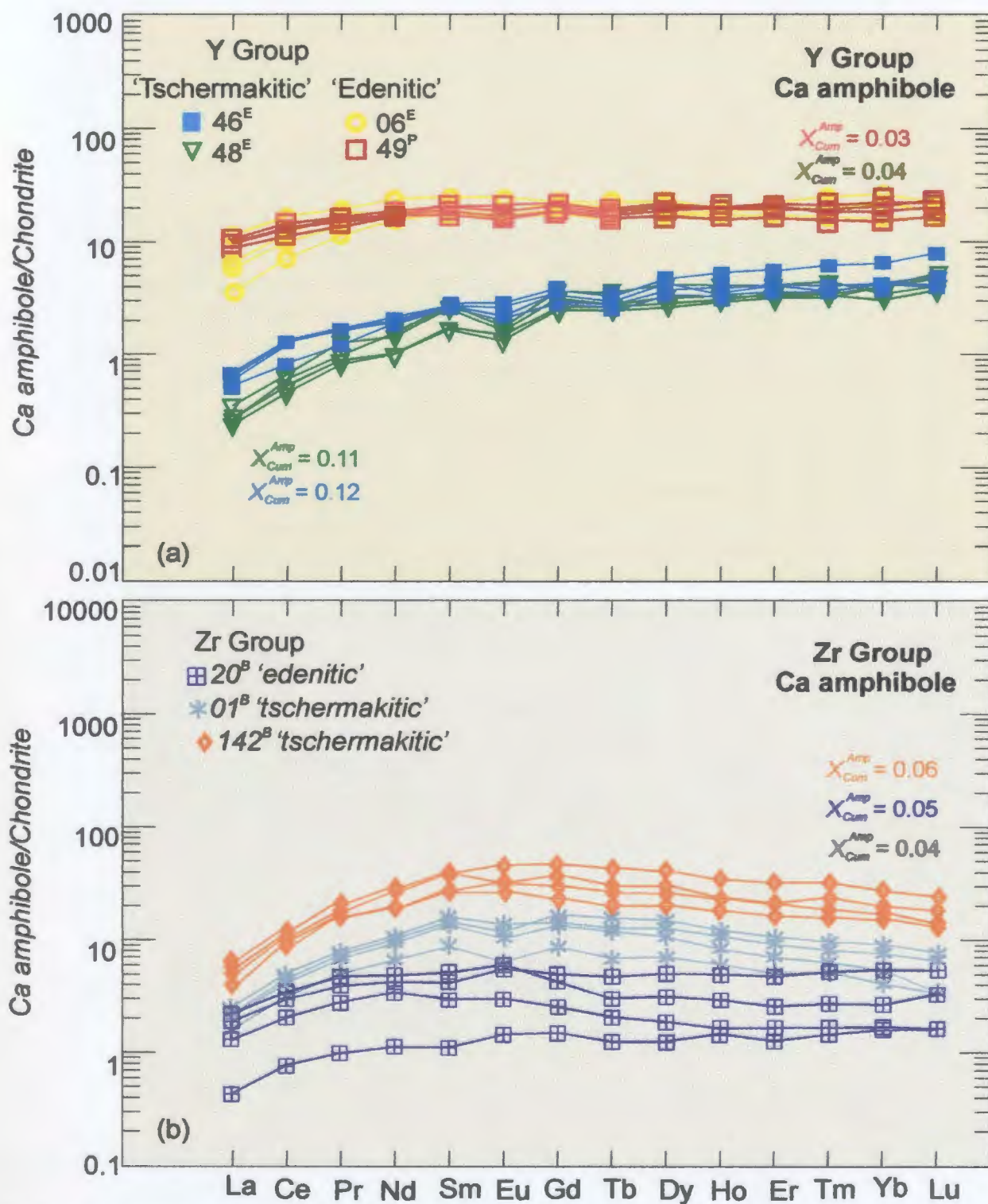


Figure 4.2 Chondrite-normalized REE diagrams for Y group amphibole (a) and Zr group amphibole (b) compositions. Chondrite normalization factors are taken from Taylor and McLennan (1985). Superscripts denote rock type (E = epidote amphibolite, P = plagioclase amphibolite, B = biotite amphibolite).

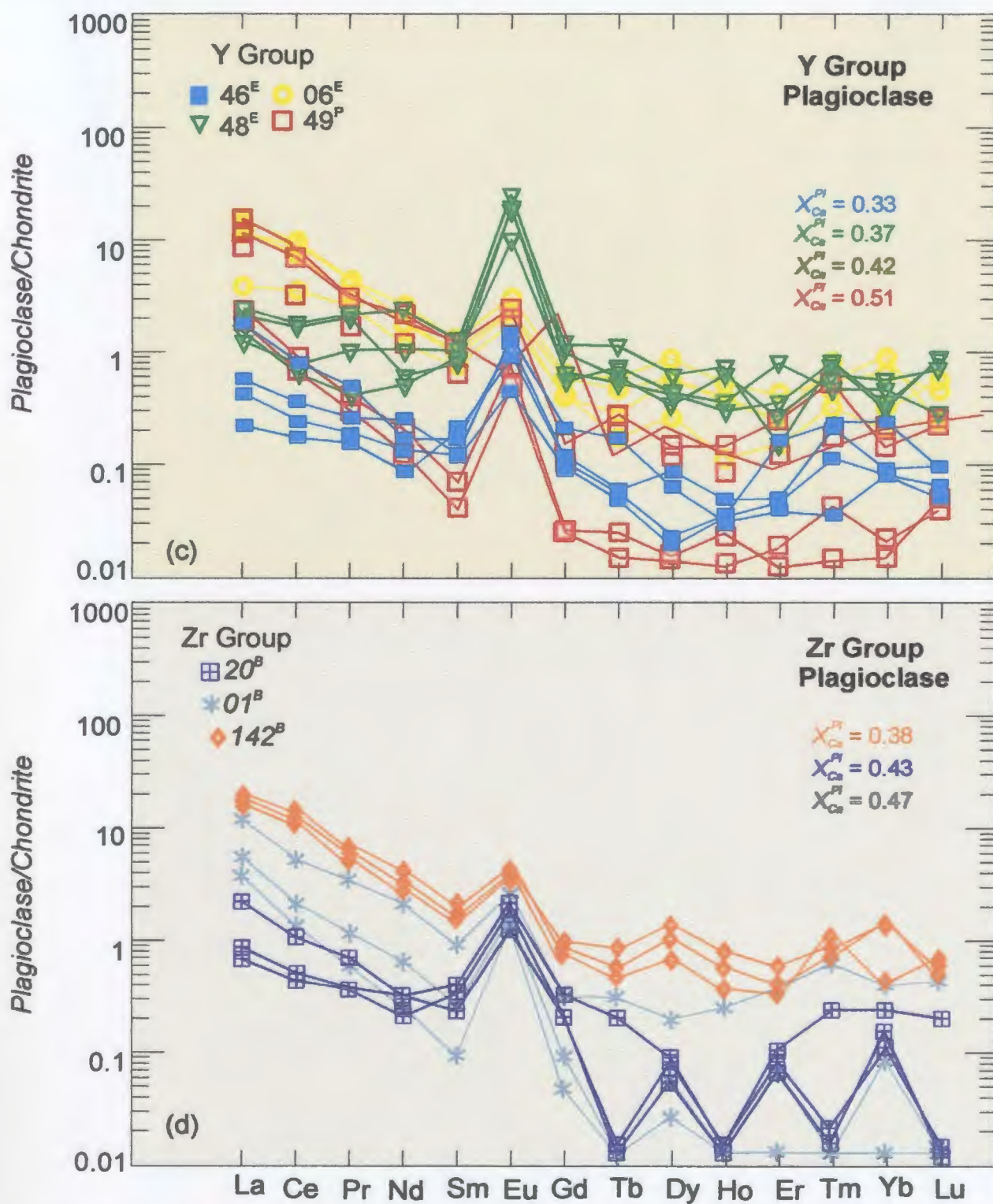


Figure 4.2 (continued) Chondrite-normalized *REE* diagrams for Y group plagioclase (c) and Zr group plagioclase (d) compositions. Chondrite normalization factors are taken from Taylor and McLennan (1985).

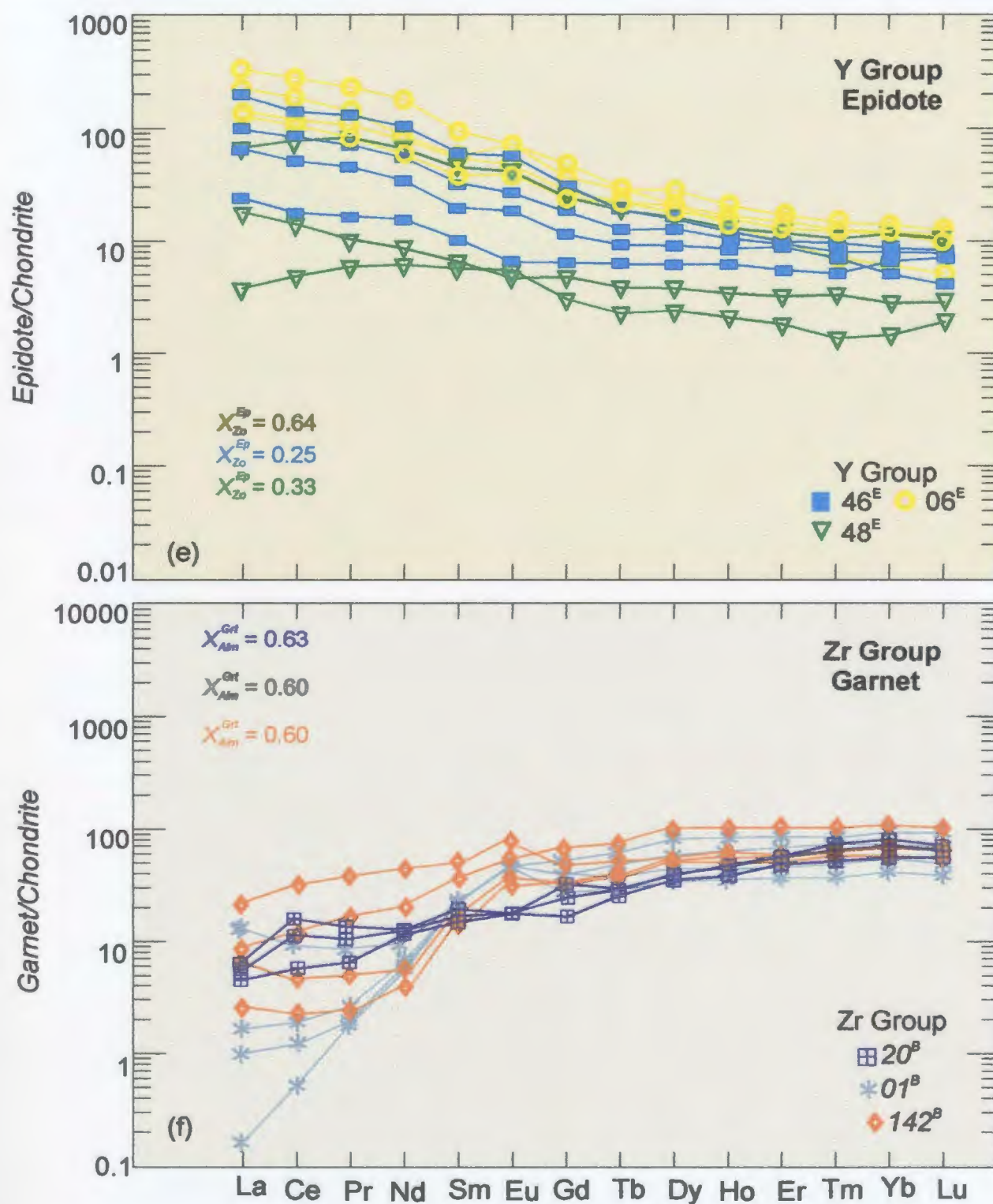


Figure 4.2 (continued) Chondrite-normalized *REE* diagrams for Y group epidote (e) and Zr group garnet (f) compositions. Chondrite normalization factors are taken from Taylor and McLennan (1985).

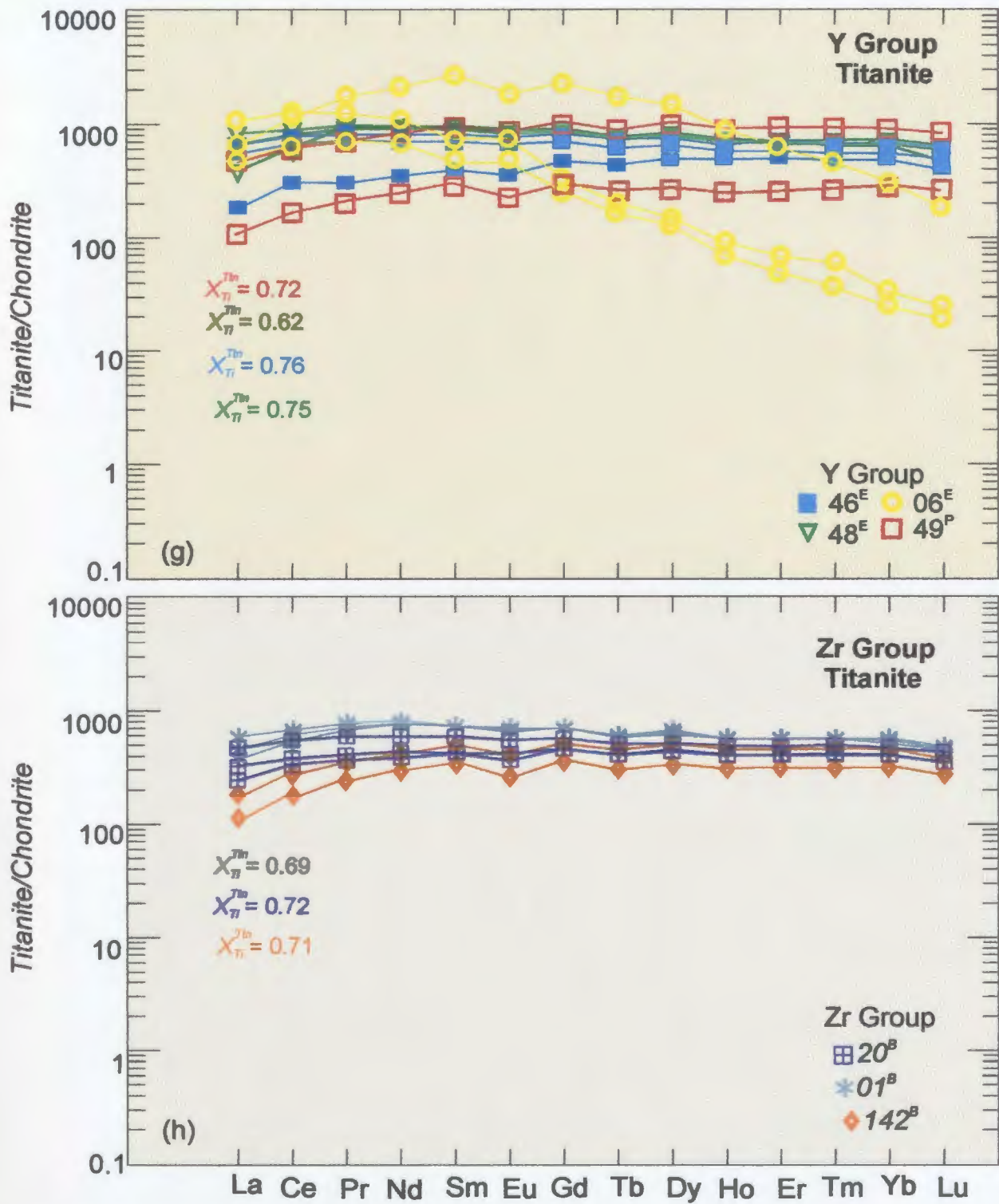


Figure 4.2 (continued) Chondrite-normalized REE diagrams for Y group titanite (g) and Zr group titanite (h) compositions. Chondrite normalization factors are taken from Taylor and McLennan (1985).

Table 4.2(a) Average values ($n = 3$) of $D^{Min 1/Min 2}$ for analysed mineral pairs. SD is the standard deviation at one sigma. No standard deviation represents single determinations. Maximum values underlined. Blank indicates below detection limits for one phase. *Italics indicate Zr group.*

$D^{Ampr/Tm}$	49	SD	06	SD	48	SD	46	SD	01	SD	20	SD	142	SD
La	<u>0.118</u>	9.16E-02	0.015	6.03E-03	0.001	3.15E-04	0.002	1.58E-03	0.004	2.46E-04	0.004	2.12E-03	0.039	6.62E-03
Ce	0.084	5.53E-02	0.016	6.59E-03	0.001	2.49E-04	0.003	1.54E-03	0.006	4.10E-04	0.006	2.36E-03	0.049	6.00E-03
Pr	0.068	3.59E-02	0.019	1.01E-02	0.001	3.51E-04	0.004	2.05E-03	0.009	1.03E-03	0.007	2.90E-03	0.066	5.91E-03
Nd	0.059	2.75E-02	0.022	8.85E-03	0.002	3.23E-04	0.005	1.62E-03	0.012	1.45E-03	0.008	2.89E-03	0.071	1.20E-02
Sm	0.052	2.41E-02	0.037	1.18E-02	0.003	5.69E-04	0.006	1.73E-03	0.018	2.91E-03	0.007	2.71E-03	0.084	1.50E-02
Eu	0.065	3.75E-02	0.033	1.07E-02	0.002	2.39E-04	0.006	2.27E-03	0.015	3.17E-03	<u>0.009</u>	3.87E-03	<u>0.109</u>	3.12E-02
Gd	0.056	2.94E-02	0.076	1.64E-02	0.005	5.96E-04	0.008	1.36E-03	0.019	3.76E-03	0.007	2.73E-03	0.085	2.25E-02
Tb	0.058	3.09E-02	0.120	2.46E-02	0.005	6.07E-04	0.007	7.39E-04	<u>0.020</u>	4.59E-03	0.006	2.97E-03	0.086	2.53E-02
Dy	0.058	3.27E-02	0.173	3.27E-02	0.005	8.63E-04	0.009	9.04E-04	0.018	3.82E-03	0.006	2.97E-03	0.075	2.14E-02
Ho	0.063	3.55E-02	0.308	5.76E-02	0.007	8.05E-04	0.010	1.38E-03	0.017	3.40E-03	0.006	3.08E-03	0.073	2.09E-02
Er	0.062	3.55E-02	0.474	9.30E-02	0.007	7.81E-04	0.010	1.03E-03	0.015	3.33E-03	0.006	2.87E-03	0.065	2.12E-02
Tm	0.062	3.28E-02	0.597	1.57E-01	0.007	1.08E-03	0.011	1.53E-03	0.014	2.52E-03	0.007	3.45E-03	0.063	1.94E-02
Yb	0.061	2.91E-02	0.953	2.35E-01	0.007	9.62E-04	0.012	1.21E-03	0.012	2.76E-03	0.007	3.50E-03	0.056	1.56E-02
Lu	0.069	2.77E-02	<u>1.308</u>	1.88E-01	<u>0.011</u>	1.37E-03	<u>0.014</u>	3.25E-03	0.012	3.00E-03	0.008	4.01E-03	0.058	1.56E-02

$D^{Tm/P}$	49	SD	06	SD	48	SD	46	SD	01	SD	20	SD	142	SD
La	72.95	32.6	62.43	20.70	349.2	149.6	895.3	490.3	87.62	31.03	387.0	160.6	9.38	2.97
Ce	296.3	141.8	115.8	17.15	799.1	296.1	1654	799.9	306.2	126.6	836.2	285.5	20.11	5.96
Pr	729.2	405.9	278.9	98.38	818.9	617.7	2251	1050	708.5	380.5	1197	402.3	54.32	16.11
Nd	2097	1335	586.9	227.9	970.2	436.3	3466	1533	1517	1019	2085	136.0	125.3	32.61
Sm	7179	4758	1097	744.4	766.0	129.4	3293	1185	4103	3097	1932	604.4	283.0	58.51
Eu	580.3	215.7	346.3	176.0	42.00	13.87	581.1	388.6	443.2	92.21	300.6	90.63	90.61	21.78
Gd	13340	7724	1884	1588	1052	377.7	3871.0	1199	8780	5184	2346	528.9	634.2	112.3
Tb	3355	2197	<u>2801</u>	3096	835.5	193.0	497.4	746.2	2238	2113	5071	2185	783.9	231.4
Dy	<u>22045</u>	12353	1404	1639	1506	316.4	<u>15116</u>	8513	<u>13260</u>	8074	<u>7637</u>	1158	576.3	230.4
Ho	3348	1756	1883	2349	1237	376.0			2641	2476			928.4	361.7
Er	2150	1153	1096	1105	<u>2096</u>	1147	8330	3539	3861	2893	4466	1724	<u>1191</u>	358.3
Tm	1664	1099	281.7	232.7	857.4	175.0	855.3	464.9	986.7	920.9	1499	317.1	534.4	74.30
Yb	2004	488	319.8	410.1	1390	399.7	4141	1402	3010	1831	2142	792.9	603.8	373.1
Lu	1544	617	191.5	174.9	774.0	287.1			1195	1085			671.1	108.7

Table 4.2(a, continued) Average values ($n = 3$) of $D^{Mn 1/Mn 2}$ for analysed mineral pairs. SD is the standard deviation at one sigma. No standard deviation represents single determinations. Maximum values underlined. Blank indicates below detection limits for one phase. *Italics indicate Zr group.*

$D^{Th/Ep}$							$D^{Th/Crt}$						
	06	SD	48	SD	46	SD		01	SD	20	SD	142	SD
La	3.94	0.52	16.57	45.12	7.04	6.53		<u>7478</u>	9189	<u>277.4</u>	98.68	118.2	93.14
Ce	6.94	0.98	18.57	52.77	11.53	10.79		<u>3272</u>	2767	174.1	116.8	<u>224.0</u>	224.5
Pr	9.38	1.31	24.23	50.98	13.76	13.13		1387	617.9	164.4	91.60	211.8	215.2
Nd	13.57	2.33	30.85	50.55	15.99	13.43		525.8	145.7	111.5	25.14	143.0	132.2
Sm	19.91	4.88	41.06	52.38	25.65	18.81		101.0	10.44	77.02	19.56	35.51	16.48
Eu	11.86	1.81	43.01	60.98	33.24	30.27		33.80	1.94	66.71	10.00	12.23	3.54
Gd	<u>22.06</u>	6.43	69.01	52.24	42.97	27.29		40.16	9.70	57.07	22.49	15.84	0.99
Tb	20.54	6.78	76.19	57.87	46.33	22.19		30.70	9.33	39.98	4.84	12.41	0.90
Dy	17.35	5.85	93.18	59.09	51.29	22.16		26.27	8.74	27.88	3.75	11.21	1.57
Ho	13.95	5.14	96.38	56.97	52.97	15.76		22.52	7.89	21.13	0.96	10.01	1.62
Er	11.26	4.21	103.2	55.42	58.91	19.53		20.39	7.09	17.22	0.67	9.91	1.62
Tm	10.26	3.91	<u>110.1</u>	43.17	<u>65.87</u>	20.88		19.51	7.24	13.12	0.97	9.39	1.40
Yb	7.24	2.83	103.4	52.45	64.10	15.88		17.25	5.84	11.23	1.26	9.03	1.23
Lu	5.10	1.92	91.11	32.77	60.90	18.27		15.91	5.77	11.49	0.49	8.08	0.90

$D^{Am/Pl}$														
	49	SD	06	SD	48	SD	46	SD	01	SD	20	SD	142	SD
La	2.09	0.55	0.74	0.62	0.18	0.04	0.77	0.67	0.25	0.06	1.75	1.11	0.31	0.06
Ce	7.01	2.87	1.66	1.04	0.63	0.20	3.09	1.40	1.33	0.37	4.86	2.80	0.89	0.16
Pr	14.28	8.12	4.47	2.01	0.69	0.67	5.88	2.07	3.68	1.20	8.68	4.74	3.30	0.77
Nd	26.40	35.39	10.47	3.00	1.17	0.51	12.32	5.09	8.59	3.11	15.88	6.26	8.17	1.98
Sm	67.29	96.39	22.40	2.78	2.40	0.23	17.83	3.39	30.71	10.58	13.81	7.26	21.88	4.70
Eu	13.68	0.88	8.28	2.06	0.09	0.02	2.54	1.15	5.35	1.27	2.73	1.37	8.50	1.00
Gd	215.2	4.87	44.17	9.03	4.08	2.32	25.89	6.28	85.74	23.03	16.48	7.47	46.06	7.67
Tb	177.9	44.69	54.90	44.82	4.04	0.93	17.44		48.81	40.39	8.56	5.69	54.20	10.90
Dy	<u>304.0</u>	40.17	37.26	30.26	7.72	2.02	<u>87.34</u>	71.90	<u>115.9</u>	26.24	<u>49.82</u>	31.92	34.23	10.45
Ho	273.9	5.15	59.92	72.10	7.13	3.27			44.32	35.11			53.20	13.34
Er	170.3	4.67	<u>81.83</u>	42.24	<u>9.10</u>	6.95	59.12	39.99	43.59	21.28	28.03	17.11	<u>61.71</u>	9.45
Tm	94.12	25.42	36.94	12.60	5.85	2.42	39.22	10.35	12.77	9.46	7.48	5.57	30.03	8.92
Yb	184.8	35.79	39.29	43.52	9.34	2.22	39.14	20.08	29.55	11.19	13.20	5.46	25.17	10.40
Lu	167.5	0.49	54.30	24.11	6.91	3.17			12.10	6.84			34.27	6.42

Table 4.2(a) Average values ($n = 3$) of $D_{\text{Min 1/Min 2}}^{\text{Amp/Ep}}$ for analysed mineral pairs. SD is the standard deviation at one sigma. No standard deviation represents single determinations. Maximum values underlined. Blank indicates below detection limits for one phase. *Italics* indicate Zr group.

$D_{\text{Amp/Ep}}^{\text{Min 1/Min 2}}$							$D_{\text{Amp/Grt}}^{\text{Min 1/Min 2}}$					
	06	SD	48	SD	46	SD	01	SD	20	SD	142	SD
La	0.04	0.02	0.04	0.05	0.01	0.01	1.40	39.36	1.38	0.37	1.63	3.56
Ce	0.07	0.03	0.06	0.07	0.03	0.02	4.15	17.46	1.13	0.67	2.31	10.64
Pr	0.12	0.05	0.10	0.10	0.04	0.03	<u>6.55</u>	6.24	<u>1.38</u>	0.68	2.88	12.53
Nd	0.19	0.05	0.12	0.09	0.06	0.04	5.31	1.58	1.01	0.16	<u>3.17</u>	7.55
Sm	0.36	0.10	0.28	0.19	0.14	0.07	1.76	0.22	0.67	0.19	2.54	1.25
Eu	0.37	0.09	0.21	0.12	0.16	0.10	0.49	0.13	0.74	0.16	1.23	0.27
Gd	0.65	0.16	0.58	0.27	0.31	0.17	0.70	0.23	0.46	0.18	1.34	0.30
Tb	0.84	0.19	0.77	0.36	0.34	0.16	0.53	0.22	0.30	0.09	1.02	0.37
Dy	1.01	0.18	0.85	0.41	0.47	0.21	0.40	0.20	0.20	0.07	0.77	0.34
Ho	1.21	0.18	1.01	0.43	0.53	0.21	0.31	0.17	0.15	0.06	0.65	0.31
Er	1.52	0.23	1.13	0.46	0.62	0.24	0.25	0.14	0.12	0.04	0.58	0.28
Tm	1.78	0.22	1.38	0.47	0.71	0.31	0.22	0.12	0.10	0.04	0.53	0.23
Yb	1.94	0.28	<u>1.45</u>	0.47	0.73	0.19	0.18	0.10	0.08	0.03	0.47	0.16
Lu	<u>2.16</u>	0.17	1.38	0.40	<u>0.83</u>	0.21	0.16	0.10	0.10	0.04	0.44	0.13

$D_{\text{Amp/Ep}}^{\text{Min 1/Min 2}}$							$D_{\text{Amp/Grt}}^{\text{Min 1/Min 2}}$					
	06	SD	48	SD	46	SD	01	SD	20	SD	142	SD
La	<u>0.05</u>	2.50E-02	0.24	3.23E-01	0.01	9.03E-03	<u>117.8</u>	1.24E+02	<u>0.80</u>	2.92E-01	14.40	4.61E+00
Ce	<u>0.05</u>	1.90E-02	0.08	7.13E-02	0.01	5.44E-03	13.53	9.82E+00	0.18	6.34E-02	<u>15.30</u>	6.50E+00
Pr	0.03	9.34E-03	0.14	7.26E-02	0.01	4.01E-03	2.77	1.85E+00	0.13	2.75E-02	5.37	2.31E+00
Nd	0.02	7.36E-03	0.09	6.12E-02	0.00	2.40E-03	0.65	4.57E-01	0.05	9.43E-03	1.54	6.13E-01
Sm	0.02	4.55E-03	0.11	7.57E-02	0.01	3.17E-03	0.05	3.17E-02	0.04	4.34E-03	0.08	2.27E-03
Eu	<u>0.05</u>	1.06E-02	<u>2.48</u>	1.56E+00	<u>0.05</u>	1.50E-02	0.08	2.06E-02	0.23	3.72E-02	0.04	3.90E-02
Gd	0.02	6.44E-03	0.15	4.71E-02	0.01	5.63E-03	0.01	4.73E-03	0.02	3.30E-03	0.01	7.37E-03
Tb	0.02	8.04E-03	0.17	6.90E-02	0.00	7.06E-03	0.004	4.70E-03	0.01	6.14E-03	0.01	7.62E-04
Dy	0.03	1.05E-02	0.10	3.24E-02	0.00	2.25E-03	0.003	1.57E-03	0.01	6.49E-04	0.01	1.65E-03
Ho	0.02	8.36E-03	0.15	4.84E-02			0.002	2.66E-03			0.01	9.10E-04
Er	0.02	7.09E-03	0.13	1.05E-01	0.01	5.15E-03	0.004	3.48E-03	0.01	2.21E-03	0.01	2.72E-04
Tm	<u>0.05</u>	1.56E-02	0.24	5.92E-02	0.01	1.35E-02	0.005	5.78E-03	0.01	4.84E-03	0.01	7.25E-03
Yb	0.05	1.91E-02	0.18	6.81E-02	0.02	1.46E-02	0.004	3.16E-03	0.01	2.10E-03	0.01	1.37E-03
Lu	0.04	9.40E-03	0.19	5.27E-02			0.003	4.04E-03			0.001	4.47E-03

Table 4.2(b) Average values ($n = 3$) of $D^{*Min 1/Min 2}$ for analysed mineral pairs. SD is the standard deviation at one sigma. No standard deviation represents single determinations. Maximum values underlined. Blank indicates below detection limits for one phase. *Italics* indicate Zr group.

$D^{*Amp/Tin}$														
	46	SD	48	SD	06	SD	49	SD	01	SD	20	SD	142	SD
La	0.004	3.99E-03	0.001	7.78E-04	0.032	1.96E-02	<u>0.128</u>	2.15E-02	0.009	7.98E-04	0.010	5.76E-06	0.078	1.64E-02
Ce	0.007	3.65E-03	0.002	6.28E-04	0.035	1.47E-02	0.112	1.64E-02	0.015	5.19E-04	0.013	7.21E-03	0.103	1.44E-02
Pr	0.008	5.00E-03	0.003	8.86E-04	0.039	2.30E-02	0.109	1.61E-02	0.021	2.70E-04	0.016	7.79E-03	0.141	1.23E-02
Nd	0.010	4.21E-03	0.004	6.46E-04	0.043	2.22E-02	0.101	1.57E-02	0.026	9.69E-05	0.018	6.33E-03	0.150	2.20E-02
Sm	0.014	4.53E-03	0.008	1.24E-03	0.048	4.27E-02	0.093	1.11E-02	0.040	1.40E-03	0.017	6.32E-03	0.176	2.63E-02
Eu	0.013	5.76E-03	0.006	4.53E-04	0.057	3.12E-02	0.103	1.12E-02	0.033	6.41E-04	0.022	1.34E-02	<u>0.221</u>	7.51E-02
Gd	0.017	3.07E-03	0.011	1.43E-03	0.065	9.04E-02	0.094	1.22E-02	0.043	4.27E-03	0.016	1.07E-02	0.169	4.62E-02
Tb	0.017	1.51E-03	0.012	1.45E-03	0.083	1.46E-01	0.097	1.21E-02	<u>0.044</u>	5.02E-03	0.015	1.32E-02	0.169	5.58E-02
Dy	0.021	1.23E-03	0.013	2.15E-03	0.107	2.05E-01	0.091	1.15E-02	0.040	2.96E-03	0.014	1.36E-02	0.147	4.65E-02
Ho	0.023	2.89E-03	0.015	1.98E-03	0.171	3.74E-01	0.098	1.08E-02	0.037	1.20E-03	0.015	1.51E-02	0.144	4.84E-02
Er	0.024	9.88E-04	0.016	1.82E-03	0.263	5.74E-01	0.098	1.13E-02	0.033	1.04E-03	0.014	1.37E-02	0.129	4.94E-02
Tm	0.025	3.31E-03	0.017	2.62E-03	0.381	7.21E-01	0.099	1.17E-02	0.031	3.37E-04	0.015	1.73E-02	0.125	4.84E-02
Yb	0.027	1.93E-03	0.017	2.24E-03	<u>0.573</u>	1.17E+00	0.103	1.19E-02	0.028	3.61E-04	0.016	1.79E-02	0.114	3.85E-02
Lu	<u>0.033</u>	6.57E-03	<u>0.037</u>	2.11E-03	0.111	1.34E+00	0.125	1.51E-02	0.030	6.81E-04	<u>0.136</u>	6.00E-01	0.090	

$D^{*Tin/Pl}$														
	46	SD	48	SD	06	SD	49	SD	01	SD	20	SD	142	SD
La	353.2	73.97	210.4	106.9	39.05	14.59	25.71	11.96	54.14	20.82	217.8	105.1	7.10	0.53
Ce	821.3	281.4	455.2	136.4	78.34	5.96	98.41	36.95	177.0	98.09	502.9	93.04	15.26	1.28
Pr	1240	435.0	340.6	418.2	191.9	65.95	206.5	49.39	350.7	308.2	743.2	146.2	40.84	3.70
Nd	2170	831.0	467.0	205.1	410.4	147.2	410.7	107.7	638.3	831.7	1419	191.9	95.79	2.25
Sm	<u>2257</u>	303.6	516.7	96.8	782.7	539.4	1143	348.3	1520	2579	1242	210.9	220.8	4.53
Eu	327.5	274.5	26.23	8.19	241.2	127.5	209.7	134.2	303.7	76.52	194.3	33.21	69.90	8.51
Gd	2608	372.1	620.7	232.3	<u>1141</u>	1183.8	3586	738.8	3913	4492	1535	186.9	497.5	86.66
Tb	7925		537.7	81.87	1102	2309	2888	1439	4882		<u>5265</u>	1008	575.7	123.2
Dy	7128	5622	<u>994.9</u>	176.8	584.4	1209	<u>5230</u>	2055	<u>5848</u>	6982	5046	463.8	398.6	64.97
Ho			758.2	201.6	586.3	1727	4398	1146	5743				642.5	119.8
Er	4214	1411	958.0	367.9	519.2	830	2729	753.3	3076		2516	505.0	<u>863.1</u>	219.7
Tm	2733		571.3	130.4	162.0	168.8	1492	720.3	2141		1343	165.8	419.9	67.30
Yb	2506	293.0	893.5	268.2	115.2	296.4	2833	313.8	2770		1295	236.3	339.4	8.96
Lu			303.0	191.0	817.7	62.91	2106	400.9	2259				686.7	110.7

Table 4.2(b, continued) Average values ($n = 3$) of $D^{*_{\text{Min 1/Min 2}}}$ for analysed mineral pairs. SD is the standard deviation at one sigma. No standard deviation represents single determinations. Maximum values underlined. Blank indicates below detection limits for one phase. *Italics* indicate Zr group.

$D^{*_{Tm/Ep}}$							$D^{*_{Tm/Grt}}$						
	46	SD	48	SD	06	SD		01	SD	20	SD	142	SD
La	3.02	0.99	13.22	26.17	2.29	0.37		466.6	22.65	<u>341.9</u>	87.01	61.63	10.77
Ce	4.94	0.58	14.82	23.93	3.97	0.30		846.0	298.0	<u>150.2</u>	8.47	<u>66.08</u>	212.0
Pr	5.75	0.84	19.34	12.95	6.07	0.51		<u>952.8</u>	233.8	167.4	7.50	<u>60.16</u>	226.9
Nd	7.61	0.68	24.62	9.14	8.83	0.74		<u>601.7</u>	109.1	142.4	0.37	62.61	129.9
Sm	13.50	0.34	32.78	1.78	15.23	0.24		131.8	13.35	96.35	1.39	42.57	4.23
Eu	13.52	1.45	34.33	8.09	12.80	1.49		44.51	1.79	86.28	1.75	16.46	7.66
Gd	24.33	0.95	55.08	35.12	20.05	0.38		48.98	1.55	64.15	3.42	23.29	3.53
Tb	30.93	0.05	60.82	43.57	20.21	0.01		36.13	4.53	51.43	0.08	17.85	3.32
Dy	35.78	1.54	74.38	41.27	18.94	0.41		29.75	5.63	35.64	0.53	15.54	3.61
Ho	40.34	0.51	76.94	40.64	14.18	0.11		25.04	6.43	27.18	0.80	13.44	3.78
Er	44.35	1.52	82.39	54.16	11.51	0.02		22.86	5.36	22.23	0.15	13.28	4.33
Tm	<u>49.26</u>	6.04	<u>87.89</u>	94.01	9.30	0.15		21.40	6.43	16.75	0.73	12.56	3.74
Yb	49.22	3.14	82.52	70.53	6.75	0.03		19.43	4.48	14.16	0.85	12.14	3.84
Lu	46.69	2.09	47.55	34.29	<u>38.86</u>	3.32		15.24	3.72	2.06	1.24	14.42	0.67

$D^{*_{Ampl/Pl}}$														
	46	SD	48	SD	06	SD	49	SD	01	SD	20	SD	142	SD
La	1.34	0.87	0.29	0.05	1.24	0.97	3.28	0.22	0.48	0.22	2.09	0.18	0.55	0.10
Ce	5.36	1.51	1.03	0.09	2.78	1.62	11.02	0.37	2.59	1.38	6.44	0.65	1.57	0.28
Pr	10.21	2.17	1.13	1.00	7.46	2.97	22.45	1.04	7.19	5.90	12.15	1.53	5.77	1.32
Nd	21.39	9.27	1.92	0.35	17.50	6.08	41.51	0.70	16.81	20.07	24.95	7.16	14.34	3.43
Sm	30.95	6.48	3.92	0.49	37.42	8.63	105.8	7.81	60.59	92.38	20.78	4.19	38.89	8.15
Eu	4.40	2.37	0.15	0.03	13.83	2.68	21.52	5.15	9.98	2.81	4.19	0.66	15.48	1.77
Gd	44.93	7.66	6.67	3.67	73.80	7.52	338.5	24.53	167.0	161.3	24.83	1.69	84.21	13.72
Tb	136.0		6.59	0.38	91.74	12.34	279.8	57.11	214.8	52.48	<u>77.97</u>	6.26	97.09	18.93
Dy	<u>151.6</u>	121.9	12.61	2.74	62.27	3.76	<u>478.0</u>	49.97	<u>235.1</u>	271.0	71.30	3.86	58.68	18.16
Ho			11.65	4.58	100.1	7.60	430.6	7.88	214.1	44.44			92.23	23.05
Er	102.6	49.80	14.86	4.37	<u>136.7</u>	25.87	267.8	6.74	101.3	32.74	34.80	1.46	<u>110.9</u>	16.60
Tm	68.06		9.56	4.13	61.73	18.41	148.0	32.44	65.39	11.41	20.51	1.43	52.55	16.54
Yb	68.28	39.97	<u>15.34</u>	2.04	65.98	19.80	292.0	43.96	76.68	16.51	20.64	0.17	38.79	18.28
Lu			11.29		90.74		263.3		68.79				61.79	

Table 4.2(b, continued) Average values ($n = 3$) of $D^{*Min 1/Min 2}$ for analysed mineral pairs. SD is the standard deviation at one sigma. No standard deviation represents single determinations. Maximum values underlined. Blank indicates below detection limits for one phase. *Italics* indicate Zr group.

	$D^{*Amp/Ep}$						$D^{*Amp/Grt}$					
	46	SD	48	SD	06	SD	01	SD	20	SD	142	SD
La	0.01	1.78E-02	0.02	2.23E-03	0.07	2.60E-02	4.17	4.78	<u>3.28</u>	1.17	4.80	1.70
Ce	0.03	5.55E-02	0.03	6.22E-03	0.14	4.82E-02	12.37	1.36	1.92	2.14	6.81	6.91
Pr	0.05	7.63E-02	0.06	1.07E-02	0.24	9.82E-02	<u>19.54</u>	13.16	2.74	2.17	8.51	12.86
Nd	0.08	8.54E-02	0.10	2.25E-02	0.38	1.11E-01	15.84	2.85	2.50	0.49	<u>9.37</u>	13.92
Sm	0.19	1.73E-01	0.25	5.30E-02	0.73	2.02E-01	5.25	0.07	1.61	0.60	7.50	3.89
Eu	0.18	2.41E-01	0.19	3.72E-02	0.73	1.64E-01	1.46	0.28	1.86	0.51	3.65	0.86
Gd	0.42	4.12E-01	0.59	1.02E-01	1.30	3.45E-01	2.09	0.34	1.04	0.57	3.94	0.87
Tb	0.53	3.78E-01	0.75	1.05E-01	1.68	3.58E-01	1.59	0.31	0.76	0.28	3.01	1.10
Dy	0.76	4.95E-01	0.94	1.41E-01	2.02	4.09E-01	1.20	0.33	0.50	0.22	2.29	1.00
Ho	0.93	4.73E-01	1.18	1.47E-01	2.42	5.27E-01	0.93	0.28	0.41	0.18	1.93	0.92
Er	1.08	5.15E-01	1.28	1.53E-01	3.03	9.16E-01	0.75	0.24	0.31	0.14	1.71	0.83
Tm	1.23	5.72E-01	1.47	1.85E-01	3.54	1.79E+00	0.65	0.22	0.26	0.13	1.57	0.73
Yb	1.34	1.78E-01	1.42	2.56E-01	3.87	2.31E+00	0.54	0.18	0.23	0.11	1.39	0.48
Lu	<u>1.52</u>	1.79E-01	<u>1.77</u>	3.30E-01	<u>4.31</u>	2.13E+00	0.46	0.20	0.28	0.13	1.30	0.40

	$D^{*Pl/Ep}$						$D^{*Pl/Grt}$					
	46	SD	48	SD	06	SD	01	SD	20	SD	142	SD
La	0.01	2.13E-03	1.54E-04	3.01E-03	<u>0.06</u>	7.53E-03	<u>8.62</u>	1.84E+00	<u>1.57</u>	4.58E-01	<u>8.68</u>	1.98E+00
Ce	0.01	1.35E-03	<u>4.55E-04</u>	2.43E-03	0.05	6.62E-03	4.78	8.72E-01	0.30	1.06E-01	4.33	8.65E-01
Pr	0.00	1.10E-03	5.93E-05	8.87E-02	0.03	8.76E-03	2.72	4.47E-01	0.23	3.98E-02	1.47	2.66E-01
Nd	0.00	1.79E-03	2.49E-04	1.14E-02	0.02	4.40E-03	0.94	1.41E-01	0.10	1.64E-02	0.65	1.15E-01
Sm	0.01	5.65E-05	5.67E-05	3.87E-02	0.02	4.37E-03	0.09	1.06E-02	0.08	1.75E-03	0.19	1.04E-02
Eu	<u>0.04</u>	1.49E-02	1.92E-05	8.57E-01	0.05	1.10E-02	0.15	9.28E-03	0.44	5.17E-02	0.24	6.71E-03
Gd	0.01	1.19E-03	4.01E-05	1.21E-01	0.02	7.13E-03	0.01	1.80E-03	0.04	7.30E-03	0.05	8.52E-03
Tb	0.00		5.76E-06	5.89E-02	0.02	9.25E-03	0.01	1.42E-03	0.01	1.21E-02	0.03	1.38E-02
Dy	0.01	2.76E-03	3.28E-05	2.80E-02	0.03	1.25E-02	0.01	6.62E-04	0.01	3.87E-04	0.04	2.29E-02
Ho			6.09E-06	9.67E-02	0.02	1.00E-02	0.00	8.11E-04			0.02	1.29E-02
Er	0.01	6.56E-05	1.62E-05	6.46E-02	0.02	6.84E-03	0.01	1.15E-03	0.01	4.62E-03	0.02	8.04E-03
Tm	0.02	1.50E-02	2.11E-06	2.00E-01	<u>0.06</u>	1.38E-02	0.01	1.74E-03	0.01	1.09E-02	0.03	2.51E-03
Yb	0.02	1.75E-02	1.50E-05	1.64E-01	<u>0.06</u>	1.15E-02	0.01	1.05E-03	0.01	3.71E-03	0.04	1.79E-02
Lu			2.17E-06		0.05		0.01	1.23E-03			0.02	2.89E-03

Y GROUP

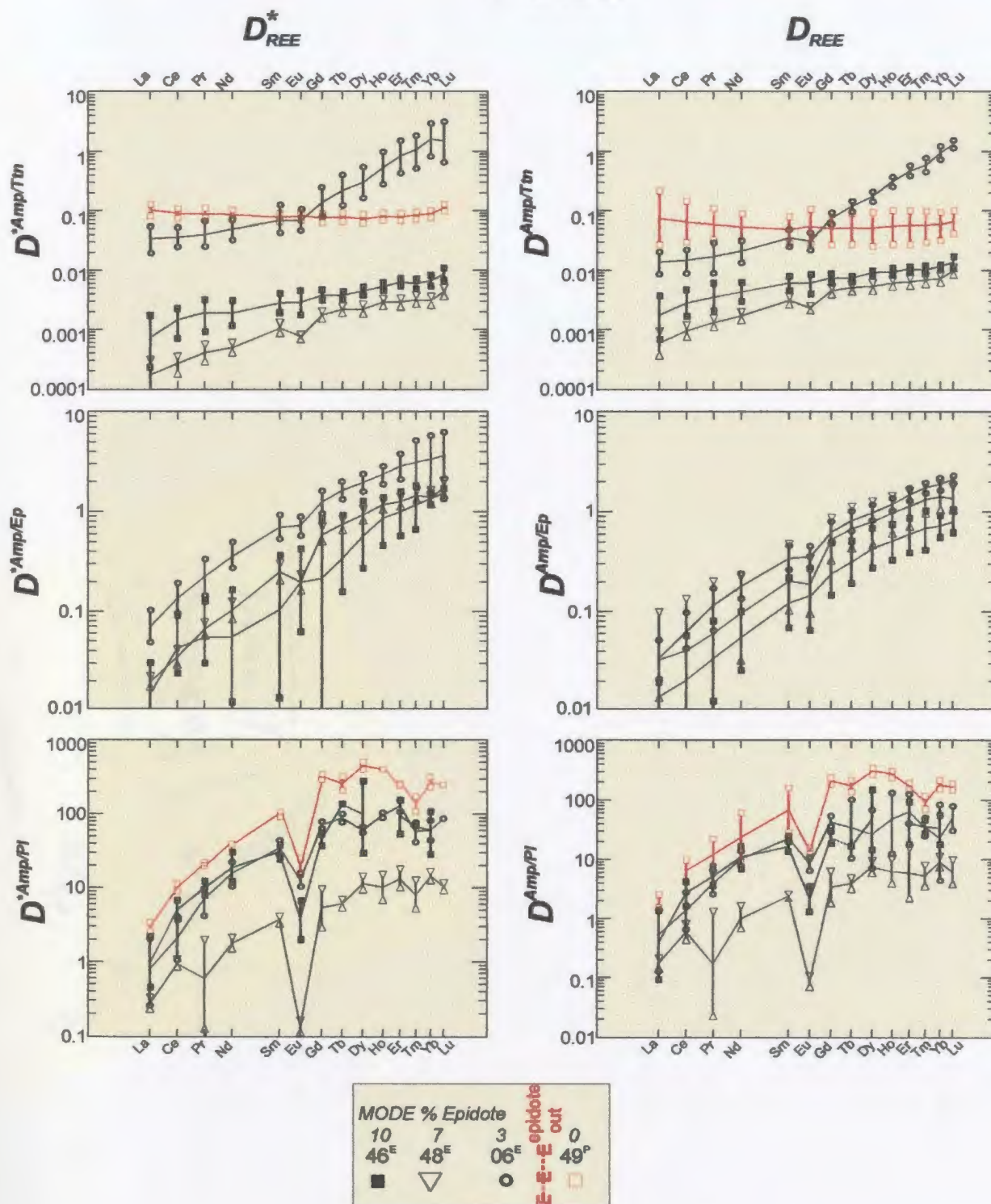


Figure 4.3(a) REE distribution coefficients (D^*_{REE} , left column and D_{REE} , right column) for six Y group mineral pairs. See text for explanation. Error bars represent 1 standard deviation. Superscripts denote rock type (E = epidote amphibolite, P = plagioclase amphibolite).

Y GROUP

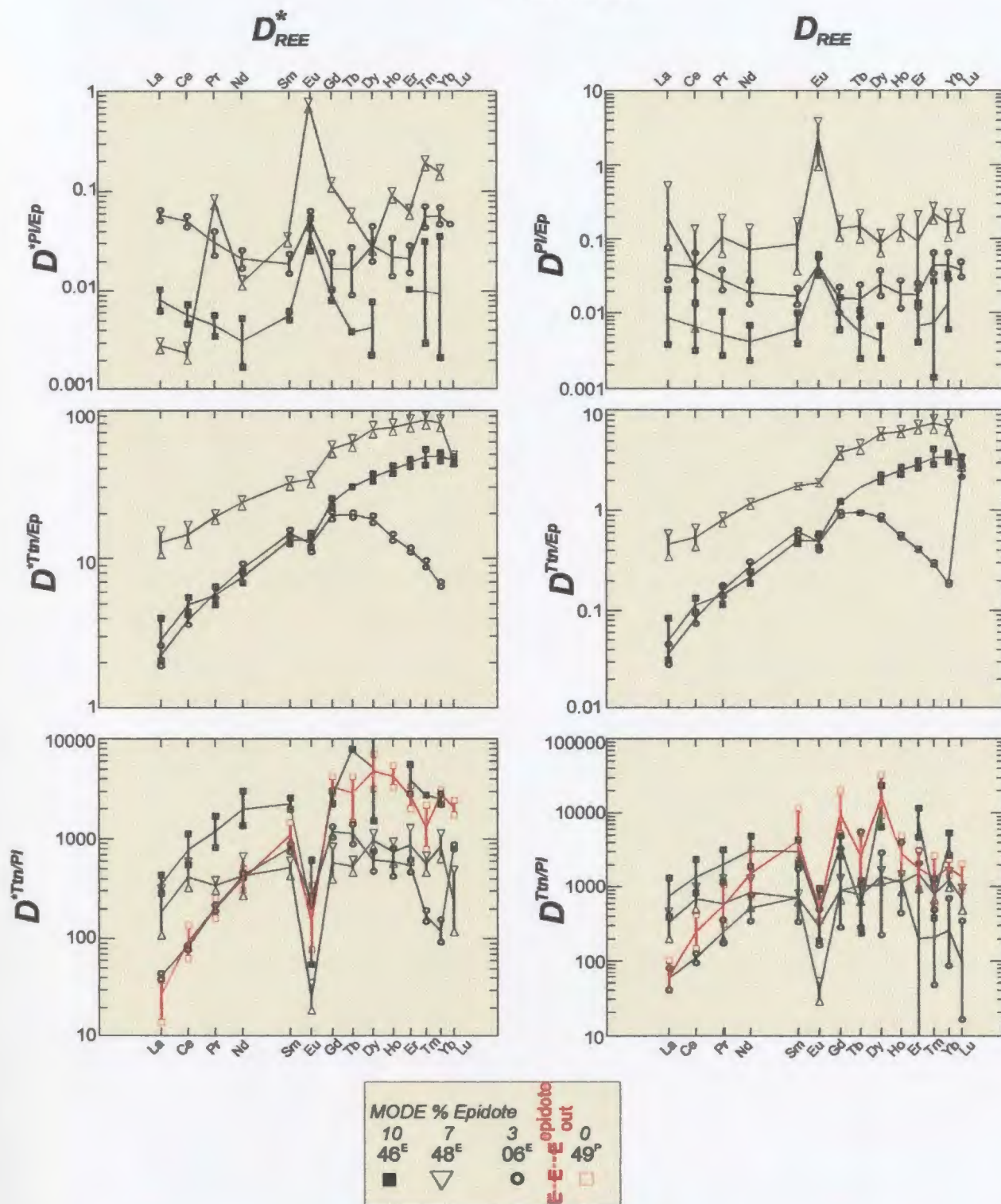


Figure 4.3(a, continued). REE distribution coefficients (D_{REE}^* , left column and D_{REE} , right column) for six Y group mineral pairs. See text for explanation. Error bars represent 1 standard deviation. Superscripts denote rock type (E = epidote amphibolite, P = plagioclase amphibolite).

Zr GROUP

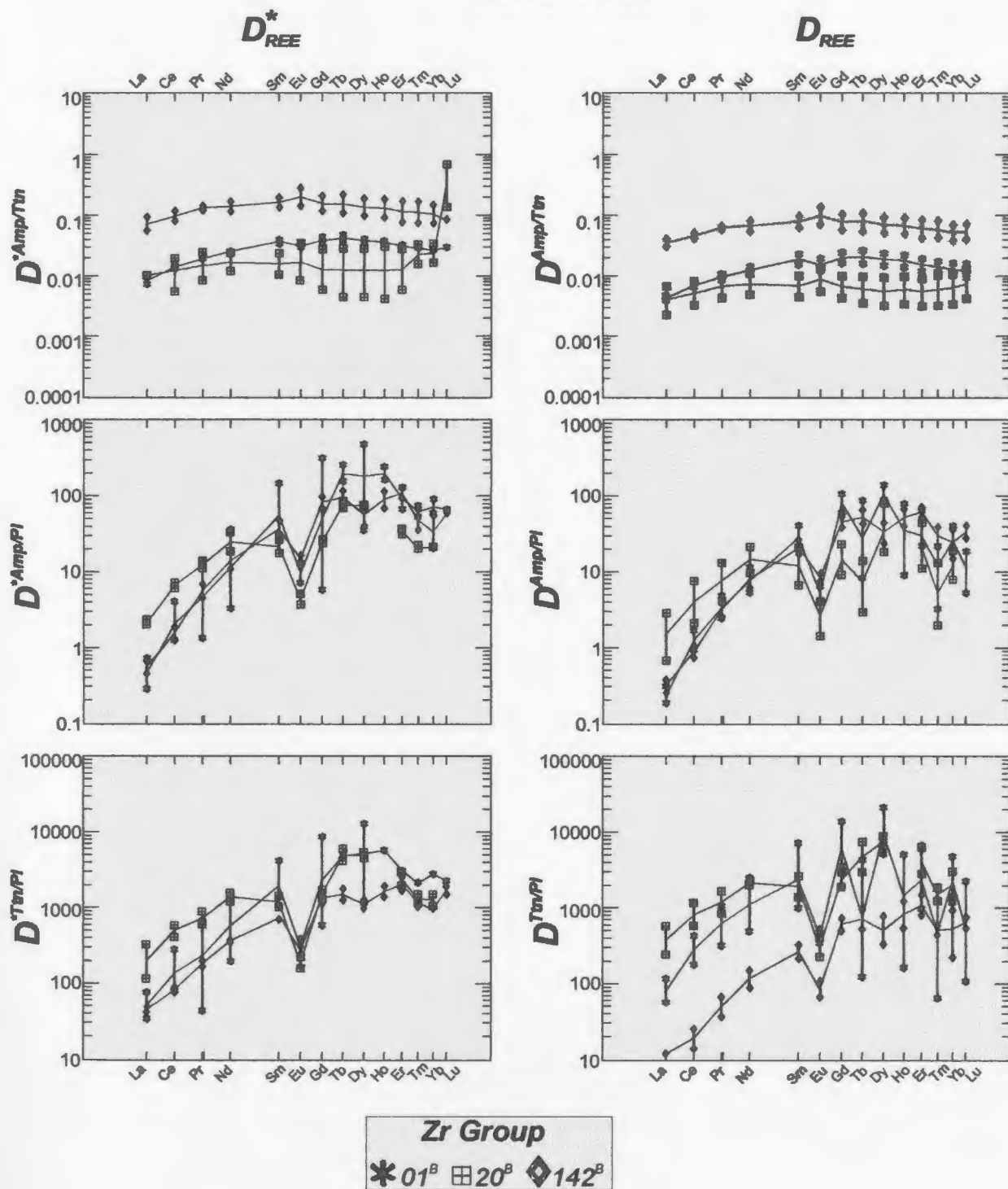


Figure 4.3(b) REE distribution coefficients (D_{REE}^* , left column and D_{REE} , right column) for six Zr group mineral pairs. See text for explanation. Error bars represent 1 standard deviation. Superscript 'B' denotes biotite amphibolite.

Zr GROUP

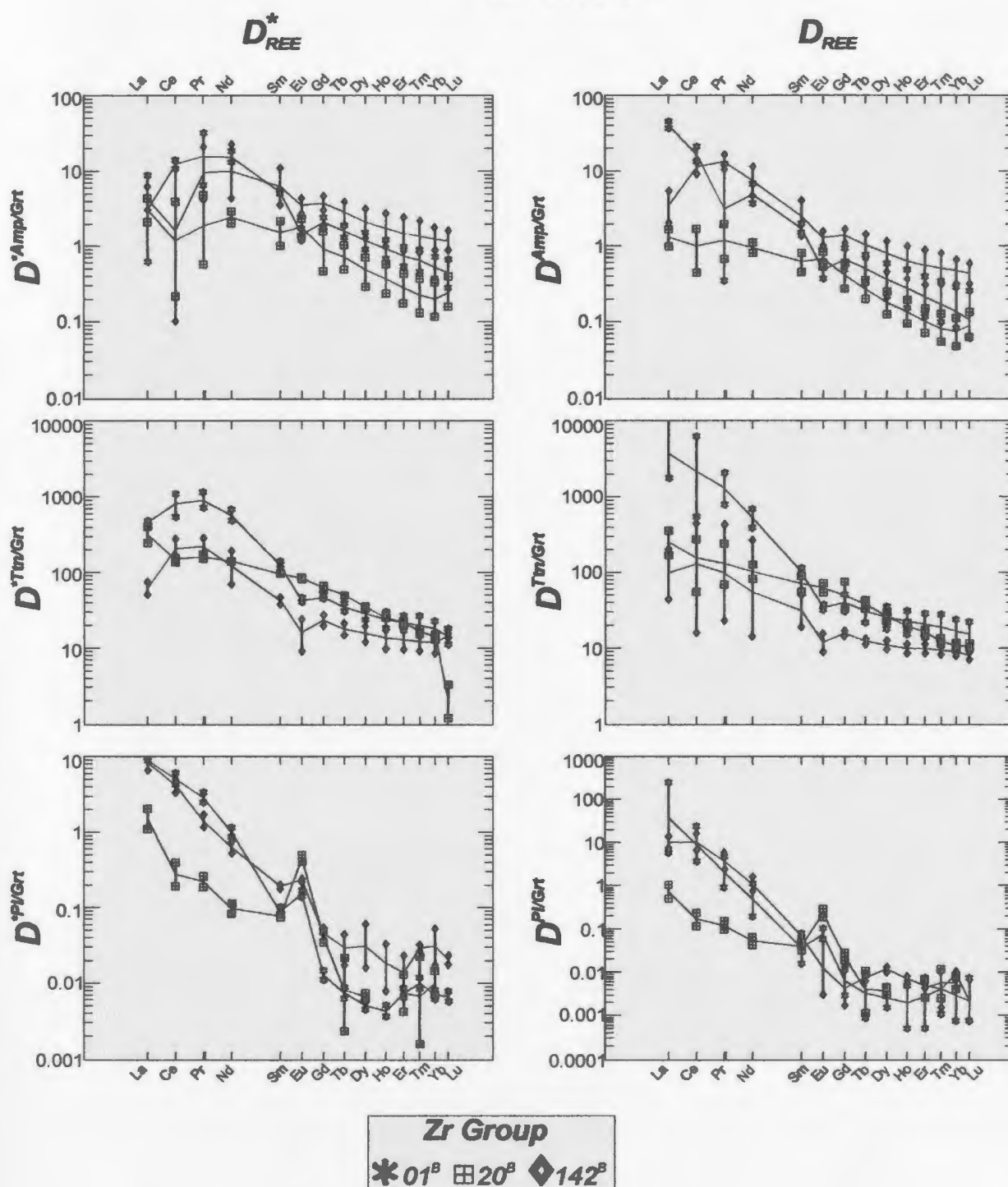


Figure 4.3(b, continued). REE distribution coefficients (D_{REE}^* , left column and D_{REE} , right column) for six Zr group mineral pairs. See text for explanation. Error bars represent 1 standard deviation. Superscript 'B' denotes biotite amphibolite.

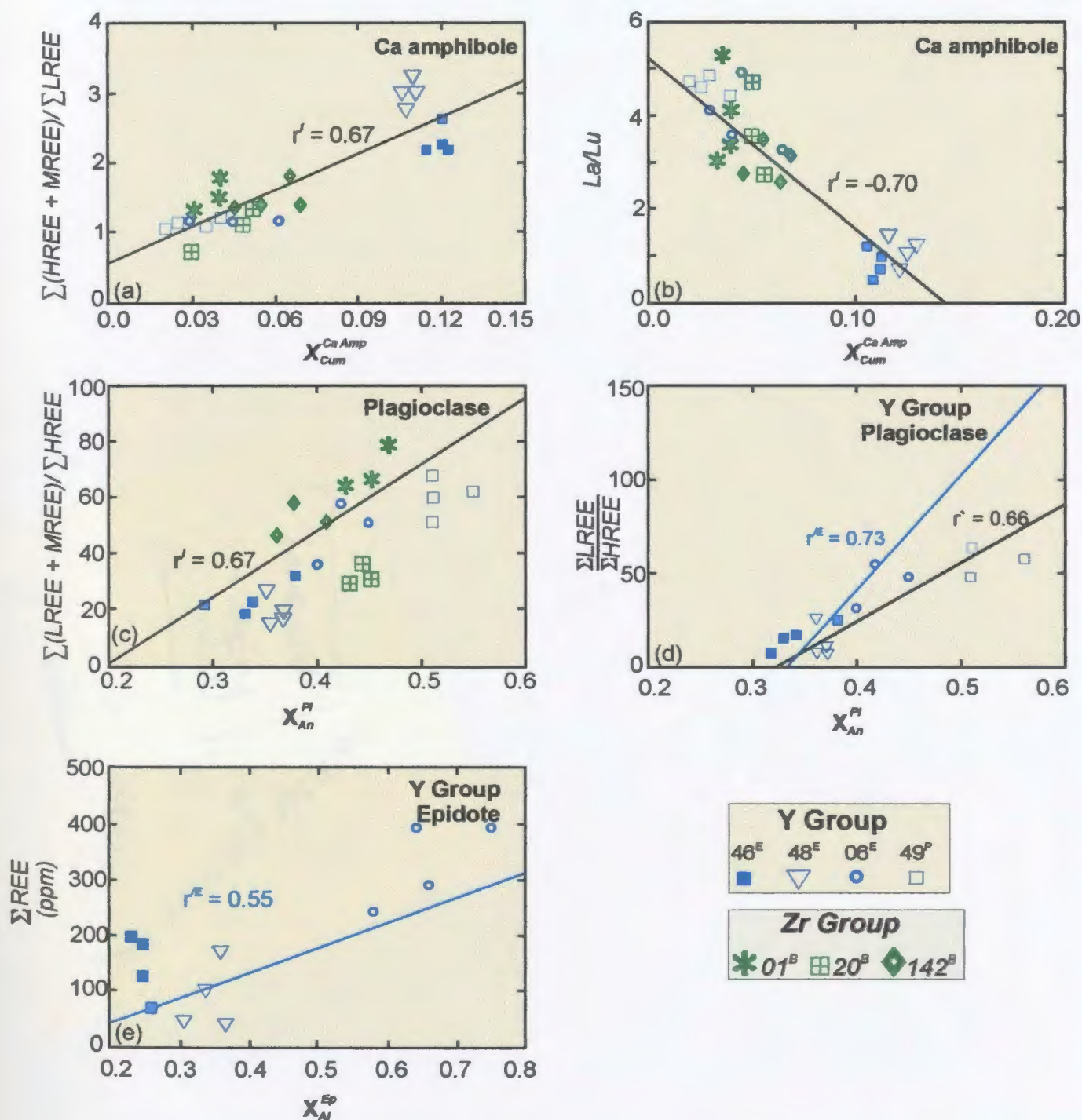


Figure 4.4 Bivariate plots showing correlations between major-element composition and REE concentration in a-b) Ca amphibole; c-d) plagioclase and e) epidote. r' denotes Spearman rank correlation coefficient, r^E Spearman correlation coefficient for epidote-amphibolites (shown as light blue regression line).

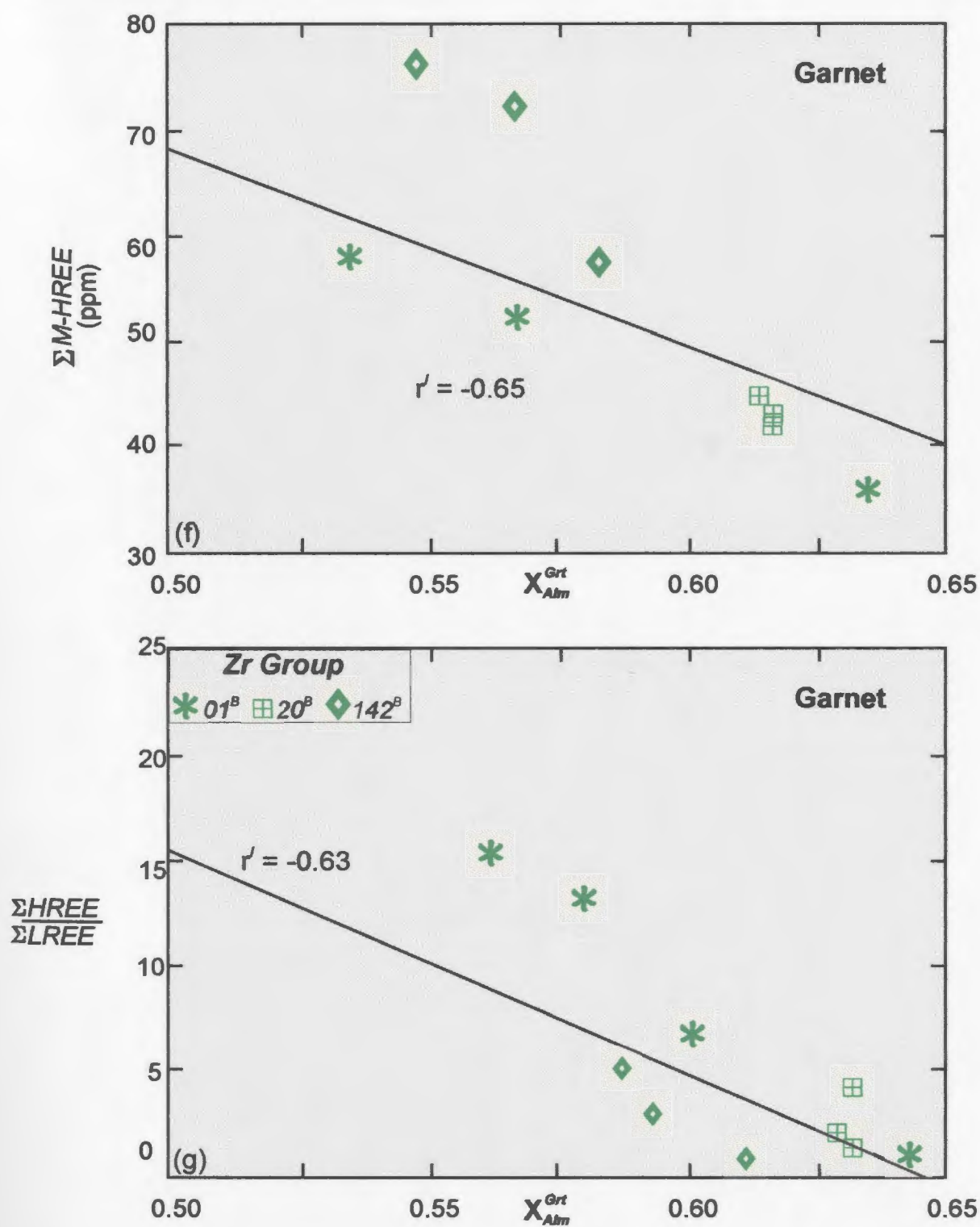


Figure 4.4 (continued) Bivariate plots for garnet illustrating f) *M*-HREE abundance versus almandine component and g) HREE/LREE versus almandine. r' denotes the Spearman rank correlation coefficient.

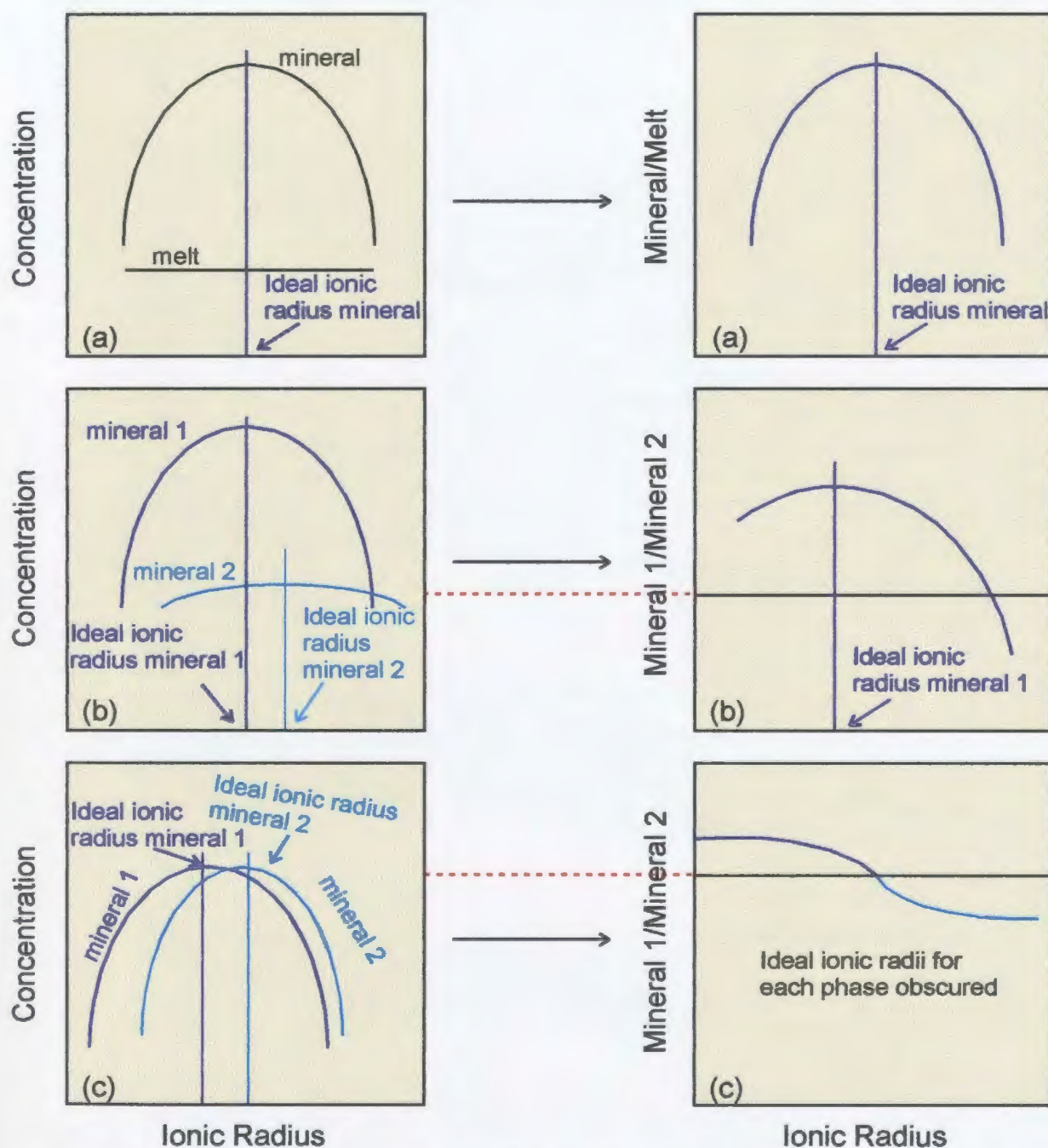


Figure 4.5 Schematic illustration of the effect of lattice control on the shape of an ionic radius *versus* partition coefficient plot. In (a), melt exhibits no preference for selected elements and the partition plot approaches a parabola where the ideal ionic radius of a cation for a selected mineral site defines the vertex (i.e., Onuma Curve). In (b), the second mineral exhibits little preference for selected elements such that the partition plot is similar to (a). In (c), two minerals exhibit sites of different ideal radius, but similar elasticity such that concentrations of selected elements are similar. The resulting partition plot does not approach a parabolic shape. Red dashed lines show equal partitioning (modified from Yang, personal communication 2003).

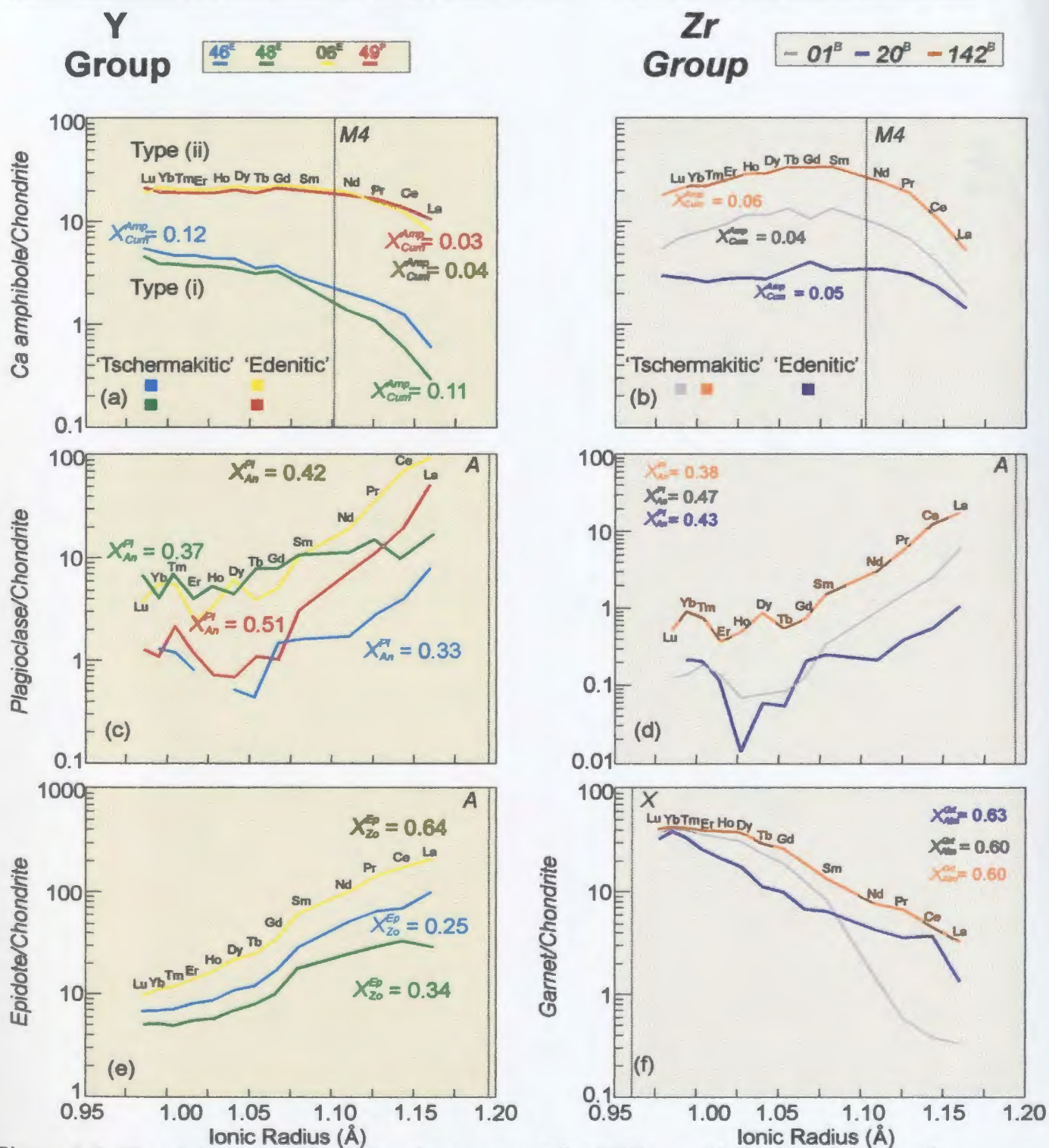


Figure 4.6 Chondrite-normalized abundance curves for REE in: a-b) Ca amphibole; c-d) plagioclase; e) epidote and f) garnet. Major-element compositions of analysed phases indicated as mole fractions. Dashed lines are optimal site radius (r_o) obtained by subtracting the ionic radius of the O^{2-} anion (1.38\AA) from the observed average cation-oxygen bond length (Smyth and Bish, 1988). Chondrite normalization factors from Taylor and McLennan (1985).

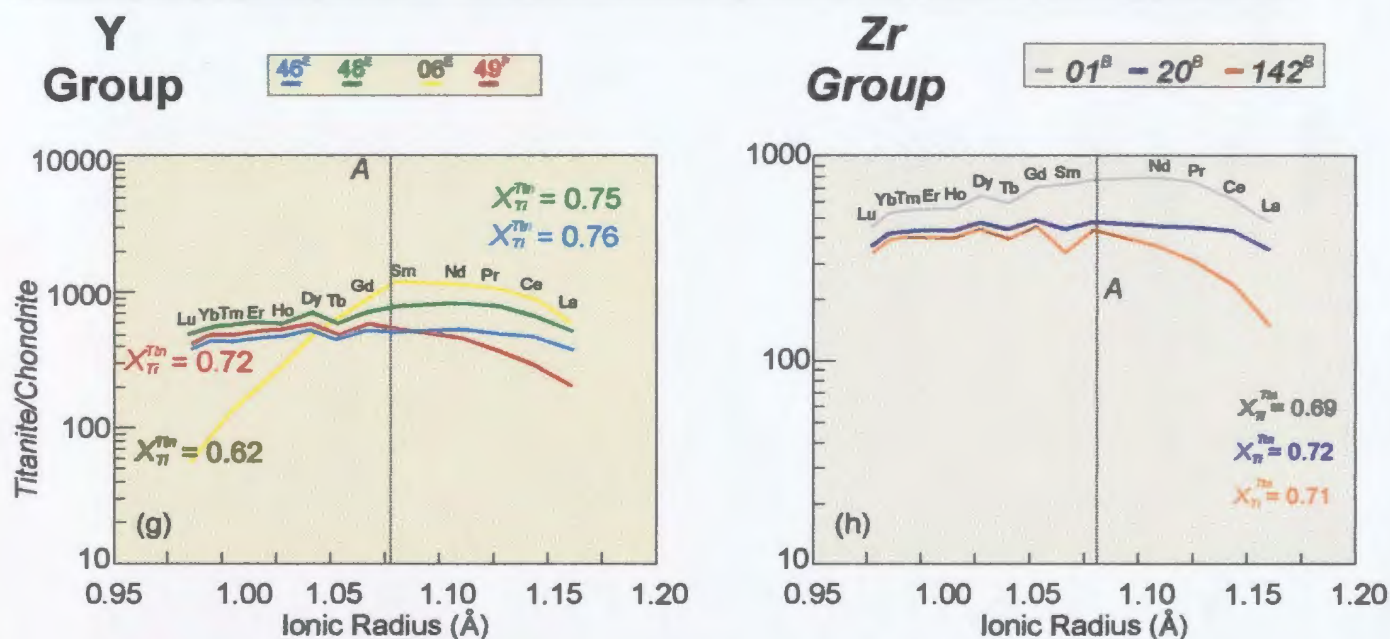


Figure 4.6 (continued) Chondrite-normalized abundance curves for REE in: g-h) titanite. Major-element compositions of analysed phases indicated as mole fractions. Dashed lines are optimal site radius (r_{o}) obtained by subtracting the ionic radius of the O^{2-} anion (1.38\AA) from the observed average cation-oxygen bond length (Smyth and Bish, 1988). Chondrite normalization factors from Taylor and McLennan (1985).

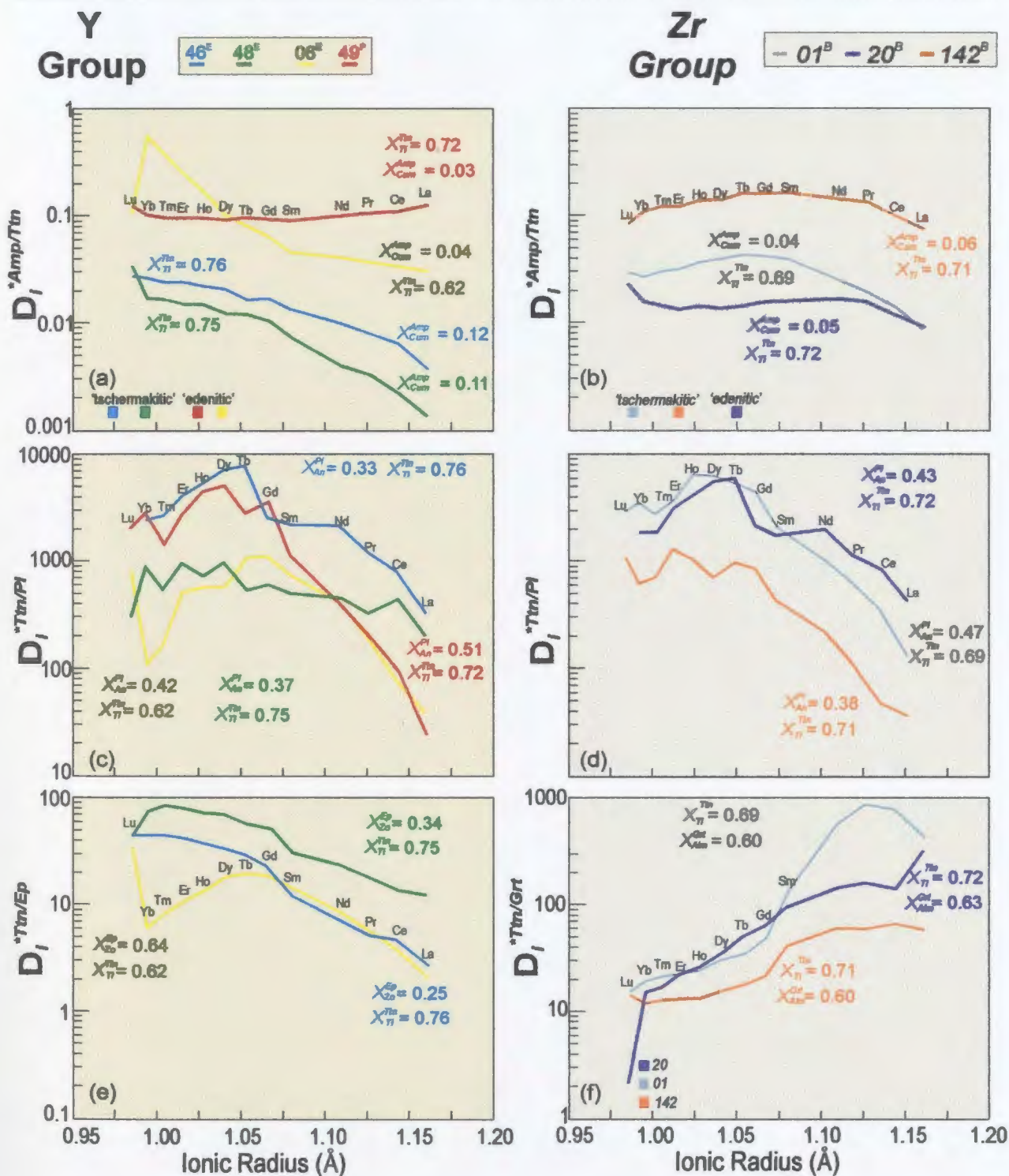


Figure 4.7(a-f) Onuma-type $D_i^{*mineral1/mineral2}$ plots for REE in mineral pairs analysed by LAM-ICP-MS. Major-element compositions of analysed phases indicated as mole fractions. Super-scripts denote rock type: E is epidote amphibolite, P is plagioclase amphibolite and B is biotite amphibolite.

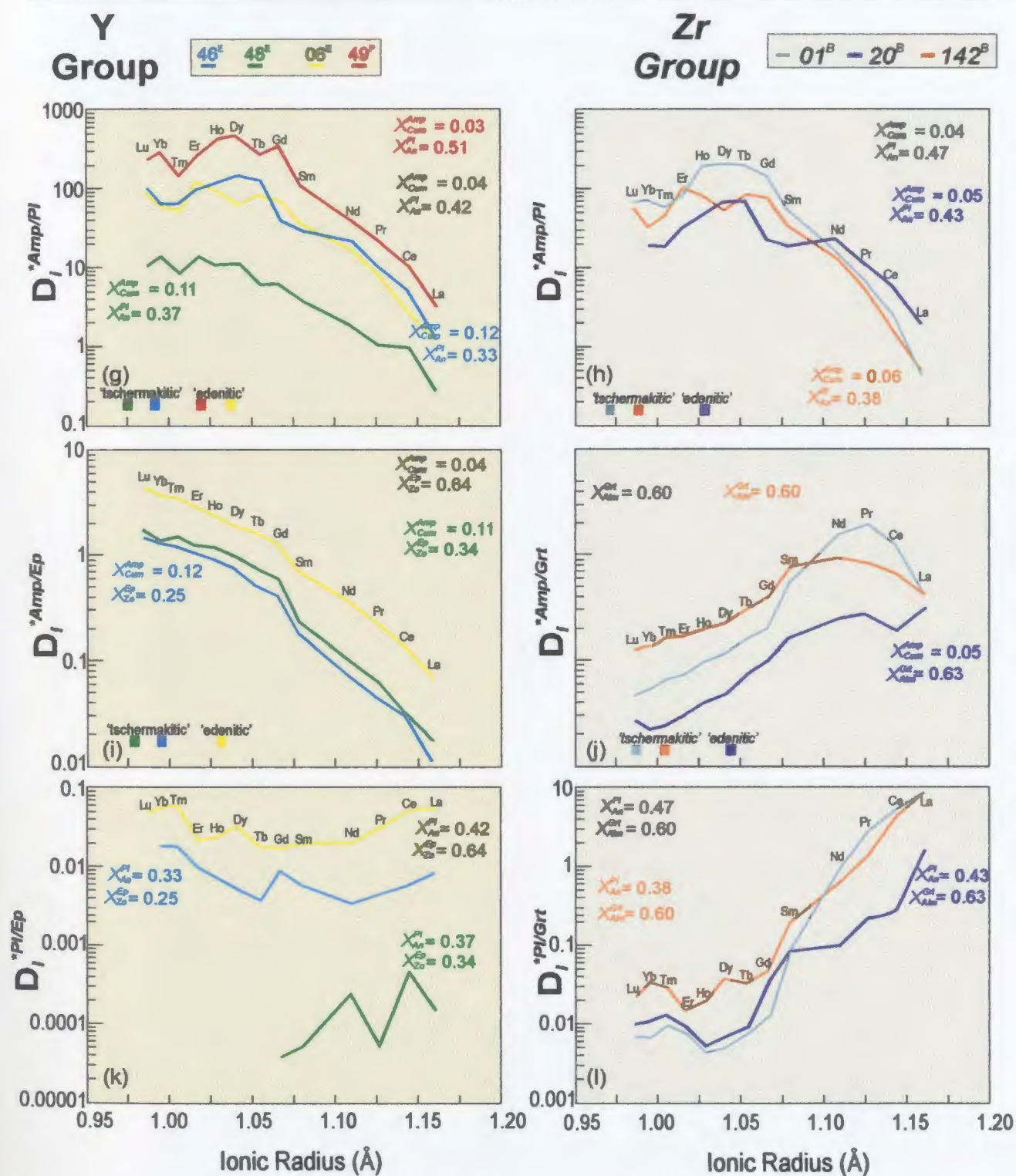


Figure 4.7(g-l) Onuma-type $D_i^{*mineral1/mineral2}$ plots for REE in mineral pairs analysed by LAM-ICP-MS. Major-element compositions of analysed phases indicated as mole fractions. Super-scripts denote rock type: E is epidote amphibolite, P is plagioclase amphibolite and B is biotite amphibolite.

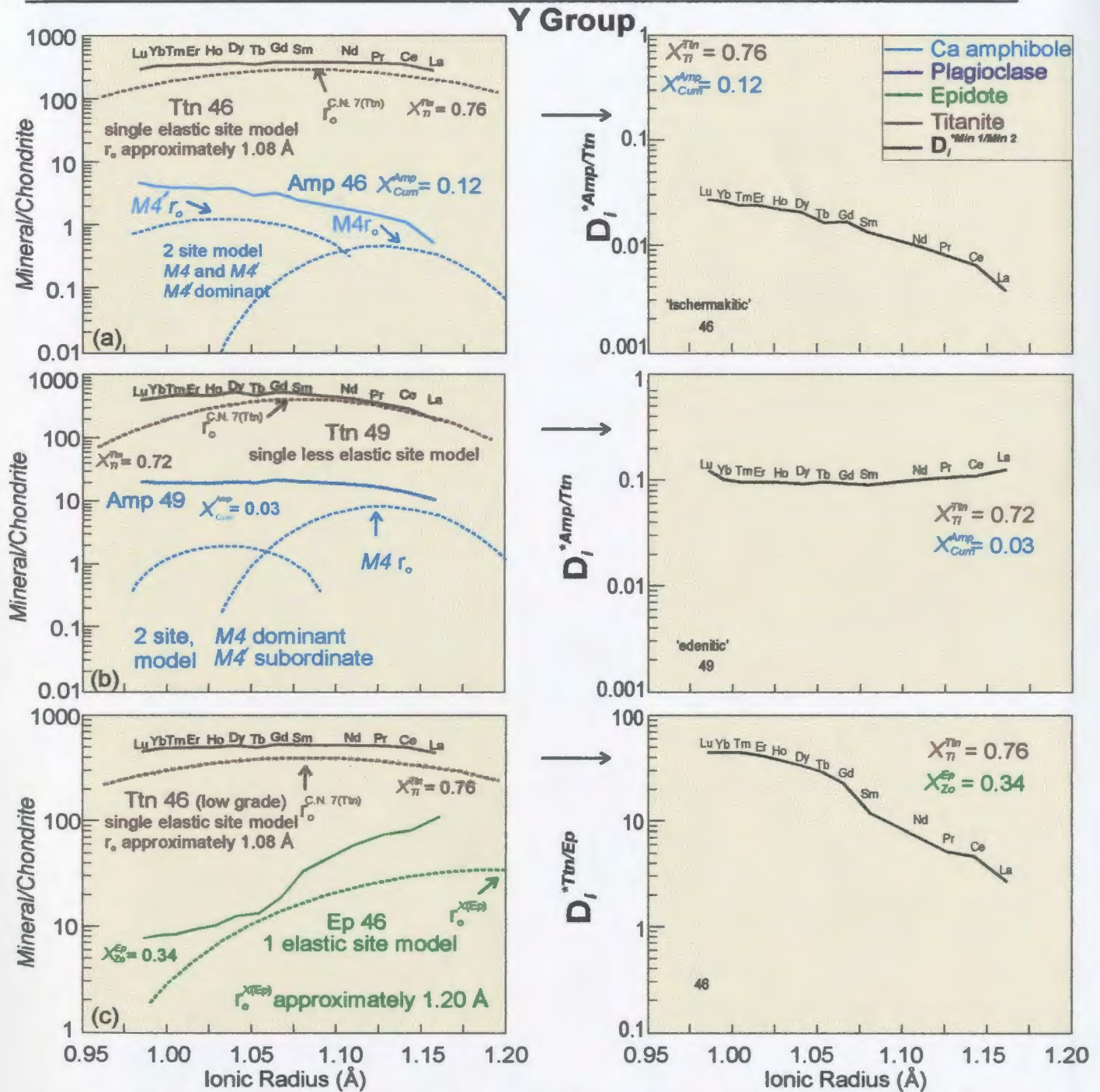


Figure 4.8 (a-c) Pairs of plots comprising mineral/chondrite and $D_{REE}^{*mineral1/mineral2}$ Onuma-type diagrams for Y group mineral pairs examined in this study. In mineral/chondrite plots, solid lines represent measured values, dashed lines are schematic representations of site properties (IR and elasticities) in the two minerals inferred from REE distributions. The shapes of corresponding Onuma-type plots can be qualitatively derived by dividing the site distribution curves for the two phases. Two pairs of diagrams are illustrated for Ca amphibole (low X_{Cum} and high X_{Cum}). Chondrite normalization factors are from Taylor and McLennan (1985).

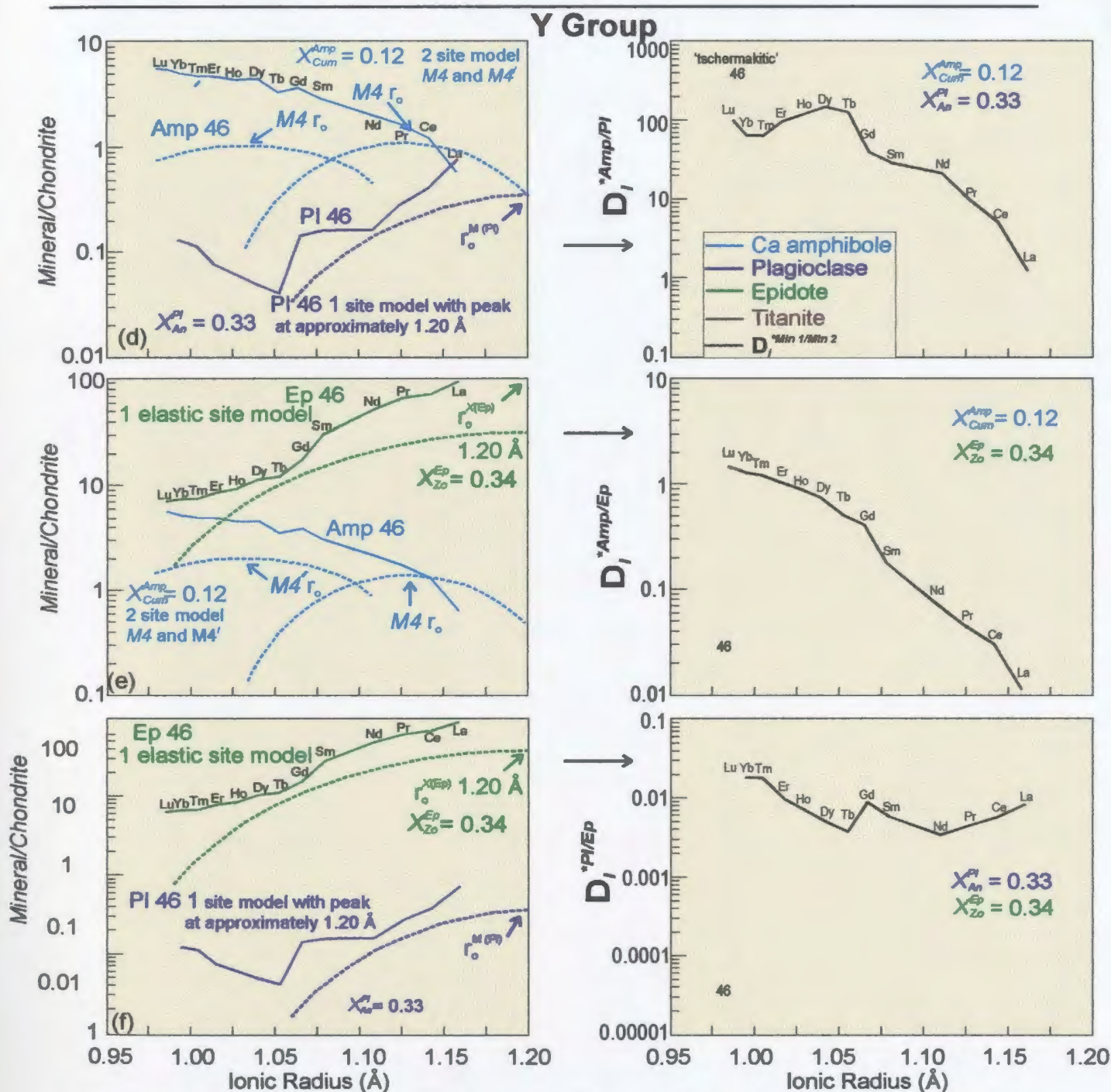


Figure 4.8 (d-f) Pairs of plots comprising mineral/chondrite and D^*_{REE} Onuma-type diagrams for Y group mineral pairs examined in this study. In mineral/chondrite plots, solid lines represent measured values, dashed lines are schematic representations of site properties (IR and elasticities) in the two minerals inferred from REE distributions. The shapes of corresponding Onuma-type plots can be qualitatively derived by dividing the site distribution curves for the two phases. Two pairs of diagrams are illustrated for Ca amphibole (low X_{Cum} and high X_{Cum}). Chondrite normalization factors are from Taylor and McLennan (1985).

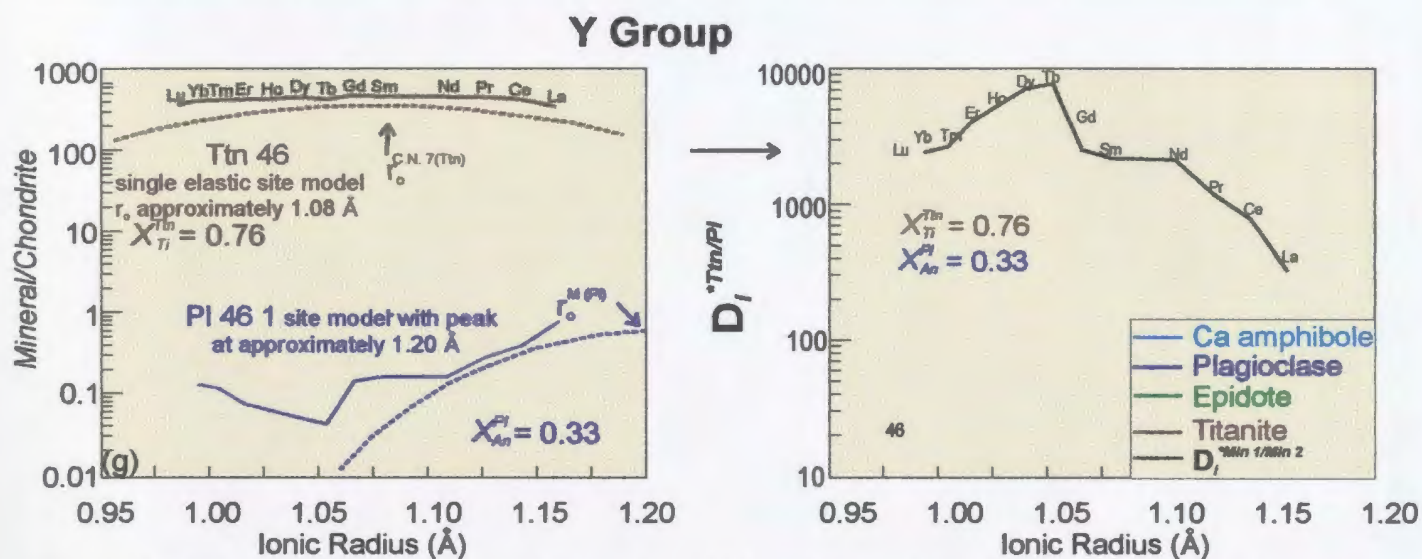


Figure 4.8 (g) Pairs of plots comprising mineral/chondrite and $D_{REE}^{*mineral1/mineral2}$ Onuma-type diagrams for Y group mineral pairs examined in this study. In mineral/chondrite plots, solid lines represent measured values, dashed lines are schematic representations of site properties (IR and elasticities) in the two minerals inferred from *REE* distributions. The shapes of corresponding Onuma-type plots can be qualitatively derived by dividing the site distribution curves for the two phases. Two pairs of diagrams are illustrated for Ca amphibole (low X_{Cum} and high X_{Cum}). Chondrite normalization factors are from Taylor and McLennan (1985).

Zr Group

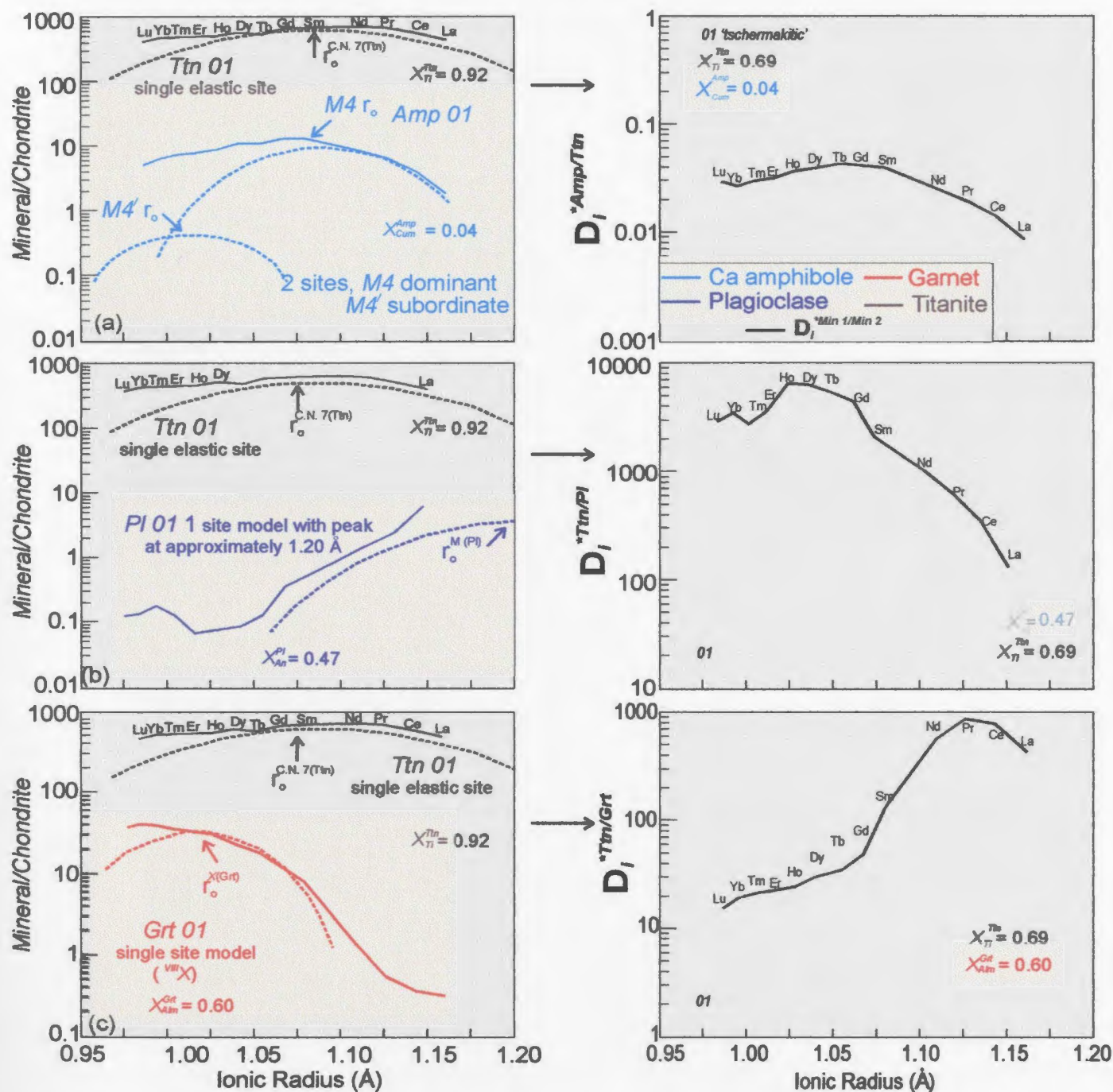


Figure 4.9 (a-c) Pairs of plots comprising mineral/chondrite and $D_{REE}^{*mineral1/mineral2}$ Onuma-type diagrams for Zr group mineral pairs examined in this study. In mineral/chondrite plots, solid lines represent measured values, dashed lines are schematic representations of site properties (IR and elasticities) in the two minerals inferred from REE distributions. The shapes of corresponding Onuma-type plots can be qualitatively derived by dividing the site distribution curves for the two phases. Chondrite normalization factors are from Taylor and McLennan (1985).

Zr Group

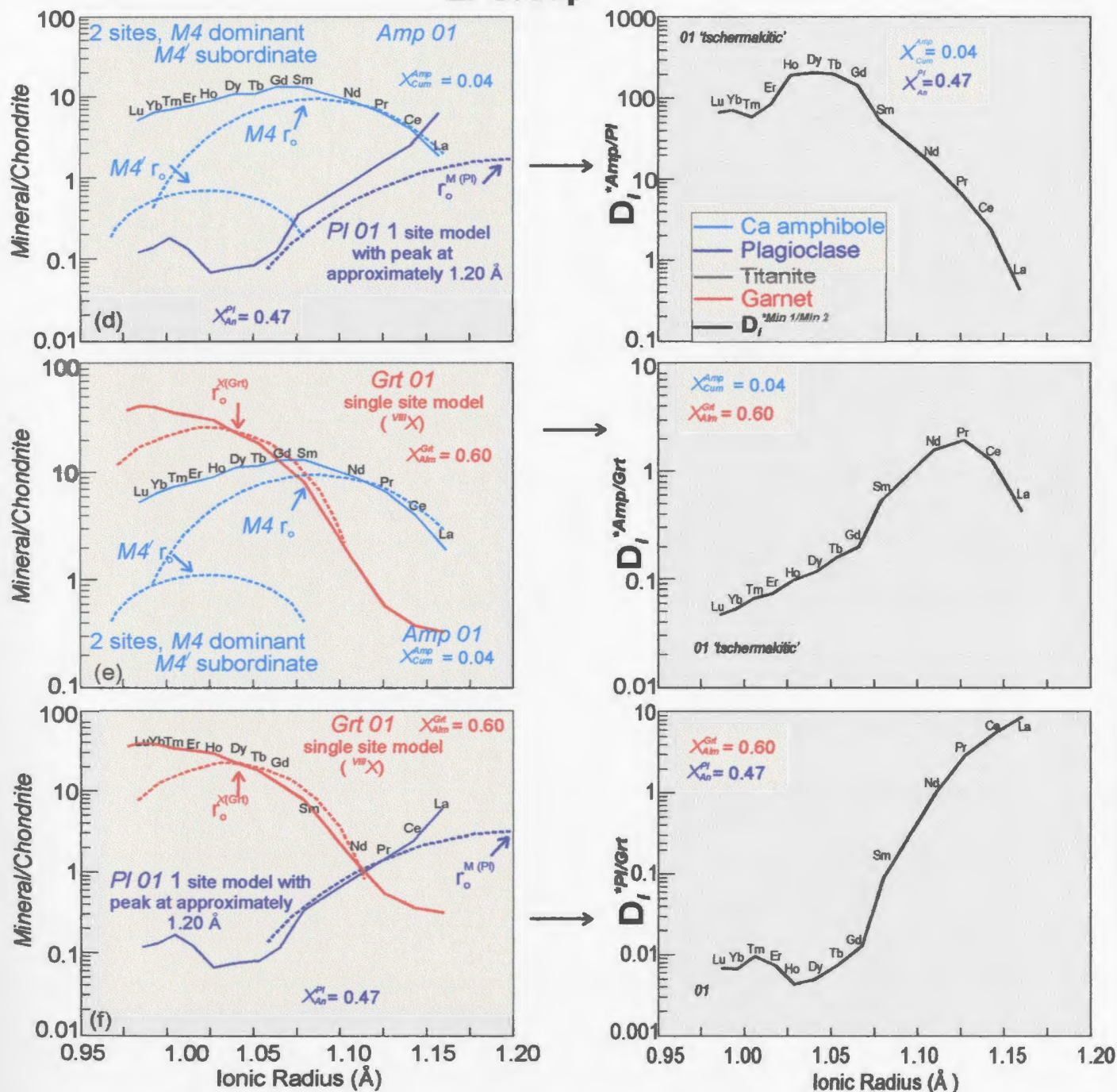


Figure 4.9 (d-f) Pairs of plots comprising mineral/chondrite and $D_{REE}^{*mineral1/mineral2}$ Onuma-type diagrams for Zr group mineral pairs examined in this study. In mineral/chondrite plots, solid lines represent measured values, dashed lines are schematic representations of site properties (IR and elasticities) in the two minerals inferred from REE distributions. The shapes of corresponding Onuma-type plots can be qualitatively derived by dividing the site distribution curves for the two phases. Chondrite normalization factors are from Taylor and McLennan (1985).

Chapter 5: Trace-Element Mineral Chemistry

5.1 Introduction

Trace elements are usually studied in groups that exhibit similar ionic properties so that deviations from group behaviour or systematic changes in behaviour within a group can be used as indicators of geological processes. In the preceding chapter, *REE* fractionation between coexisting Ca amphibole, plagioclase, epidote, garnet and titanite was utilized to investigate chemical and crystal-structural controls on *REE* incorporation in individual minerals and on *REE* partitioning between coexisting minerals. Utilizing a similar approach, this chapter is concerned with selected first row transition metals (i.e., Sc Ti, V, Cr, Fe, Co, Ni, Cu, Zn), large ion lithophile elements (LILEs: Rb, Sr) and high field strength elements (HFSEs: Y, Nb, Zr) of the same samples. In contrast to the generally homovalent *REE* (except Eu, i.e., Eu^{2+} or Eu^{3+}), which exhibit a progressive decrease in ionic radius with increasing atomic number, these trace elements exhibit broader ranges in both ionic charge and radius, and consequently do not behave as a group as do the *REE*. An attempt is made in this chapter to exploit the greater range of behaviour exhibited by these groups of trace elements in order to elucidate controls on trace-element incorporation in specific phases, and partitioning between these phases in

epidote-amphibolite, plagioclase-amphibolite and garnet-amphibolite assemblages.

5.2 Trace-element mineral chemistry

Average trace-element concentrations of analysed coexisting phases presented in Table 5.1 are illustrated as concentration *versus* element plots (Figure 5.1a-h) and are compared to bulk-rock concentrations in Figure 5.2; the entire trace-element data set is available in Appendix A. The 1σ variability in listed in Table 5.1 is based on the measured trace-element concentrations of *individual grains* in each sample and is not indicative of within-grain zoning or analytical error. Concentrations of selected LILEs, first row transition metals and HFSEs for each phase, which are broadly similar between the Y and Zr groups, are briefly summarized below.

Ca amphibole (Table 5.1) carries high concentrations (> 100 ppm) of V, Cr, and Zn, moderate concentrations (10-100 ppm) of Sc, Co, Ni, Y and LILEs and low abundances (< 10 ppm) of Nb. Figure 5.1a-b illustrates that some trace elements vary in concentration within the same sample (e.g., Cr, Co, Cu, Zr, Nb) suggesting that the compositional range is due to within-sample zoning. However, some of the variation may be linked to major-element composition (e.g., variable Ca linked to Sr variations), an effect which is evaluated in section 5.4.1. *Ca amphibole* exhibits broad variability in Rb and Y with some samples exhibiting $Rb/Y > 1$ and others $\ll 1$. Analysed *plagioclase* (Figure 5.1c-d) contains high abundances of Sr (≈ 500 -800 ppm), consistent with

observations in several other studies and low abundances (< 10 ppm) of all other analysed trace elements with the exception of Ni and Zn (≈ 10 -100 ppm). Three samples (06, 48, 142) contain ppm levels of Zr, which is attributed to the presence of micro-inclusions of a Zr-bearing phase, likely zircon. Analysed *epidote* (Figure 5.1e) exhibits significant differences in concentrations of certain trace elements (e.g., Sc, Ni, Rb, Nb) among samples, but overall the phase carries high concentrations of Sr, V, Cr, and Zn ($\approx > 100$ ppm) and, with the exceptions of Co, Cu and Rb ($\approx \leq 5$ ppm), moderate abundances (10 -100 ppm) of all other analysed elements. Analysed *garnet* (Figure 5.1f) is variably zoned in most elements and is rich (> 100 ppm) in V and Cr and exhibits moderate concentrations (10-100 ppm) of Sr, Y and Zn. The high concentrations of Zr and Nb in Sample 20 are attributed to micro-inclusions of Zr- and Ti-bearing phases, likely zircon and rutile respectively. Analysed *titanite* (Figure 5.1g-h) contains appreciable amounts (> 10 ppm) of all trace elements with the exception of Cu and Rb, and is especially enriched in V and Y (≈ 1000 ppm), and Zr and Nb (100-1000 ppm). In order to reduce the number of counts reaching the detector and thereby improve counting statistics for elements such as Nb, Y and the REE, Co was not analysed in titanite.

Variations in trace-element mineral composition cannot be separated from the effect of whole-rock (bulk) composition and Figure 5.2 provides a visual assessment of the degree of co-variation of these two factors. It enables general conclusions regarding the degree of equilibrium attained amongst analysed phases, inter-sample chemical

variations, and the relative trace-element enrichment in each phase to be drawn. For instance, the regular and consistent patterns of trace-element distributions, such as for Sc, V, Cr, Rb, Y and Nb among Ca amphibole, titanite and bulk rock over a range of concentrations and mineral assemblages (Y and Zr groups), indicate equilibration of those elements (Figures 5.2a, b, c, i, j, l). With respect to Y in yttrium group samples, the very limited bulk-rock variation among the samples, and the complementary opposing slopes of Y concentration in titanite compared to epidote and Ca amphibole, the only other significant Y-bearing phases (Figure 5.2j), indicate equilibrium redistribution of this element and point to possible changes in mineral assemblage, major-element mineral chemistry and modal abundance as possible causes, variables that are examined further in section 5.4.1. Ni and Sr abundances in analysed plagioclase (Y and Zr groups: Figures 5.2d, h) are subparallel to those for the bulk rock, indicating the first-order control exerted by bulk rock composition on the measured distributions of these elements. Epidote, which is restricted to the three Y groups samples (46, 48, 06), exhibits patterns which mimic bulk rock, Ca amphibole, and titanite for Sc, V, Cr, Ni, Rb and Y, implying equilibrium distribution of these elements (Figures 5.2a, b, c, d, i, j). Garnet, which is restricted to the Zr group, exhibits irregular patterns for most elements with the exception of V and Y (Figures 5.2b, j). The significant variations of Co concentration in analysed phases (Figure 5.2g) are likely an artifact of fractionation during sample ablation (Longerich *et al.*, 1996). The irregular distributions of Rb (Figure 5.2i) in

analysed plagioclase (Y and Zr groups) and Ca amphibole and garnet (Zr group) may indicate disequilibrium partitioning of this relatively 'mobile' element during fluid movement or retrograde metamorphism. The whole-rock abundance of Cu greatly exceeds that measured in any and all of the analysed phases (Figure 5.2e), consistent with this element being sequestered in an unanalysed Cu bearing phase (e.g., chalcopyrite).

In summary, to a first approximation the measured trace-element abundances between analysed coexisting phases can be attributed to bulk-rock composition, changes in both mineral composition and mineral assemblage during prograde metamorphism (e.g., Y redistribution between epidote-amphibolite [06] and plagioclase amphibolite [49]) and potential retrograde metamorphism (e.g., Rb distribution in plagioclase, garnet and Ca amphibole).

5.3 Trace-Element Distribution Coefficients

As in the previous chapter, two expressions for the distribution of a trace element are used, the Nernst distribution coefficient (D_i), and the ratio between mole fractions (X) of a trace element in specific crystallographic sites in the two minerals, the Nielsen distribution coefficient (D_i^*). Trace-element site occupancy assumptions for D_i^* , i.e., average site sizes and coordination numbers, and ionic radii and charge referred to in this section are listed in Table 2.1a-c respectively. In nearly all cases, the formulation of the distribution coefficient (D_i or D_i^*) does not affect the relative trace-element enrichment

between each mineral pair. Where D_i and D_i^* diverge, trace elements are either distributed on more than one site in one or both minerals, are zoned, and/or there are analytical problems with the data. Individual cases are discussed below.

Distribution coefficients (D_i and D_i^*) for selected LILE, first row transition metals and HFSE are presented in Table 5.2(a-b) respectively and illustrated as Figure 5.3. Analytical uncertainties are given as 1σ standard deviations measured from LAM-ICP-MS counting statistics. Y group samples are arranged in order of decreasing modal epidote, whereas all Zr group samples comprise the garnet-amphibolite assemblage. Differences in the partitioning behaviour of specific elements between mineral pairs from the Y and Zr groups are discussed where applicable.

D_i and D_i^* for *Ca amphibole-titanite* pairs exhibit similar patterns within each group. Sc, Zn, and Rb preferentially partition into Ca amphibole, HFSE and Y preferentially partition into titanite, and remaining analysed elements are approximately equally distributed between both phases. For Y group pairs, D_Y^* exhibits an approximate order-of-magnitude increase in the value of the partition coefficient in samples close to and above the epidote-out isograd, which is inferred to relate to the coincident decrease in cummingtonite substitution in Ca amphibole (see section 5.4.1). The approximately equal partitioning of V, Cr, Ni and Cu suggests that these elements enter similar sites in both minerals, likely the octahedral $M2$ Ca amphibole site (0.66 \AA) and the slightly smaller octahedral M site in titanite (0.58 \AA). Similarly, Sr is approximately equally

partitioned between the titanite *A* site (1.08 Å, C.N.# = 7) and the Ca amphibole *M4* site (1.11 Å, C.N.# = 8). However, Sc and Zn (≈ 0.74 Å, C.N.# = 6) preferentially partition into the relatively larger octahedral *M1* and *M3* sites in Ca amphibole (≈ 0.70 Å), as opposed to the octahedral titanite *M* site (0.58 Å).

The distribution of trace elements between *titanite-plagioclase* pairs from both groups is broadly similar and shows that Zn and LILEs (i.e., Rb, Sr) preferentially partition into the irregular 5-9-fold coordinated plagioclase *A* site (≈ 1.20 Å) as opposed to the smaller titanite *A* site (1.08 Å). As observed in several other studies, most transition metals and especially HFSEs (Y, Zr, Nb) strongly partition into titanite, with the 7-fold *A* site hosting Y and divalent transition metals and the octahedral *M* site (0.58 Å) hosting Zr and Nb. Cu is approximately equally distributed between the two phases.

Distribution patterns for *Ca amphibole-plagioclase* pairs in both Y and Zr groups are similar and show that all analyzed elements except Sr preferentially partition into Ca amphibole, reflecting both the lack of appropriate sites for most analysed elements in plagioclase, and the availability of the 5 ^{VI}*M* sites and large ^{XII}*A* site intrinsic to Ca amphibole. Surprisingly, Cu and Zn are approximately equally distributed between the two phases implying no strong preference of these elements for Ca amphibole *M* sites as opposed to the larger plagioclase *A* site (≈ 1.20 Å).

The partitioning of most analyzed transition metals is approximately equal in *titanite-epidote* pairs, with LILEs exhibiting preference for epidote *X* sites (≈ 1.19 Å)

whereas Y and HFSE preferentially partition into titanite *A* and *M* sites respectively.

$D_{Nb}^{*Tm/Ep}$ appears to be sensitive to either modal epidote or small changes in the major-element chemistry of epidote and /or titanite since it exhibits an approximate order-of-magnitude increase with decreasing modal epidote. However, no measurable correlations between $D_{Nb}^{*Tm/Ep}$ and any major constituent in either phase were discovered (5.4.1). Alternatively, the increase in may coincide with the breakdown of a Nb bearing phase (e.g., ilmenite; Zack *et al.* 2002).

First series transition metals and Y are approximately equally distributed between *Ca amphibole-epidote* pairs, whereas HFSEs and Rb preferentially partition into *Ca amphibole* octahedral *M* sites and 12-fold *A* sites respectively, and Sr exhibits preference for the epidote *X* site over the relatively smaller 8-fold *M4* site of *Ca amphibole*. With the exception of $D_Y^{*Ca\ amp/Ep}$, which appears to be linked to $^{M4}X_{Cum}^{Ca\ amp}$ (see 5.4.1), compositional variations in either phase do not exhibit strong effects on partitioning.

Sc, V, Cr, Sr, Y and HFSEs preferentially partition into epidote 6-fold *M* sites in *plagioclase-epidote* pairs reflecting the absence of suitable sites for those elements in plagioclase. Sr exhibits a slight preference for the relatively smaller epidote *X* site over the plagioclase *A* site, and several other analysed elements are also approximately equally partitioned between the two analogous sites. $D_Y^{*Pl/Ep}$ appears to be sensitive to compositional variations in epidote, exhibiting an approximate order of magnitude increase with increasing X_{Al}^{Ep} (see 5.4.1). The large variations in $D_{Zr}^{*Pl/Ep}$ may be

attributed to inclusions of zircon in one, or both, of the phases.

D_i and D_i^* patterns for *titanite-garnet* pairs closely match, with most analysed elements approximately equally distributed between each phase implying that garnet *Y* sites ($\approx 0.53 \text{ \AA}$) and titanite *M* sites (0.58 \AA) are similar and that garnet *X* sites ($\approx 0.86 \text{ \AA}$) and titanite *A* sites (1.08 \AA) exhibit relatively similar properties. However, Y and the HFSEs preferentially partition into titanite *A* and *M* sites respectively, implying these sites are more suitable hosts for those elements than garnet *Y* or *X* sites. The irregular patterns exhibited by LILEs (i.e., Sr, Rb) likely reflect disequilibrium distributions of these relatively 'mobile' elements due to metasomatism, and in the case of Rb, a lack of suitable sites in either phase for that element.

In *Ca amphibole-garnet* pairs, the transition metals and Y exhibit no strong preference for either phase implying that Ca amphibole *M* sites and garnet *X* or *Y* sites can act as suitable hosts for these elements. LILEs preferentially partition into Ca amphibole because of the presence the relatively large 8-fold *M4* (Sr) and 12-fold *A* (Rb) sites. The wide range in the magnitude of the partition coefficients for LILEs is potentially linked to disequilibrium distribution of these elements due to metasomatic effects. HFSEs exhibit irregular distribution patterns, as two samples (01, 142) exhibit preference for Ca amphibole, whereas in the other sample (20), these elements preferentially partition into garnet. This may be due to the presence of micro-inclusions of zircon or rutile in either of those phases.

D_i and D_i^* patterns for *plagioclase-garnet* pairs converge suggesting that cation site assumptions for each phase are valid. Y, Sc, V, Cr, and HFSEs preferentially partition into garnet *X* (Y) and *Y* sites, Zn and LILEs preferentially partition into plagioclase reflecting the preference of those elements for the plagioclase *A* site opposed to the smaller garnet *X* site. Other analyzed trace elements are approximately equally distributed between each phase.

5.4 Controls on Trace-Element Partitioning

The thermodynamic framework, discussed in section 2.2.2, forms the theoretical basis for the distribution of trace elements between coexisting mineral pairs. In this section, the effects of mineral structure and major-element composition on trace-element partitioning are considered.

5.4.1 Major-Element Compositional Effects on Trace-Element Partitioning

Bivariate plots, illustrated in Figure 5.4(a-l), identify correlations among selected trace- and major-elements in Ca amphibole, epidote and garnet and imply that major-element compositional controls on trace-element incorporation are likely a significant factor in their measured distributions. Similar to the *REE*, no significant correlations between major- and trace-elements were identified in analysed titanite. However, in contrast to the strong correlations reported between the anorthite component and *REE*

(particularly *LREE*) in analysed plagioclase (see 4.4.1), no correlations between any of the analysed trace elements in this section and X_{An}^{Pl} were discovered.

The positive correlation ($r' = 0.61$) between the concentration of 8-fold coordinated FeMg in the *M4* site (i.e., cummingtonite component, $^{M4}X_{Cum}^{Ca\ amp}$) and the ratio of $Y/\sum LREE$ in analysed *Ca amphibole* is shown in Figure 5.4a. Since Y is homovalent and has a similar ionic radius to the *MREE* (Y and Ho both $\approx 1.02 \text{ \AA}$, C.N.# = 8), this ratio is analogous to *MREE/LREE* ratio evaluated against the cummingtonite component in section 4.4.1. The result is similar, suggesting that the correlation is also likely explained by the structural constriction of the *M4* site with increasing concentrations of divalent cations smaller than Ca (i.e., FeMg), such that the cavity favours ions like *M-HREE* and Y. The substitution may be charge balanced by involving Y and FeMg in *M4* sites and Al and Ti in ^{VI}M sites, i.e. $^{M4}(FeMg)^{2+} ^{VI}Ti^{4+} \leftrightarrow ^{M4}Y^{3+} ^{VI}Al^{3+}$.

There is a negative correlation ($r' = -0.71$) between $\sum(ScCr)$ and ^{VI}Al in *Ca amphibole* (Figure 5.4b) that may be explained in the following manner. Since the tschermak exchange vector results in an increase in ^{VI}Al in *Ca amphibole*, and since Sc and Cr are homovalent with, and have similar ionic radii to Al^{3+} , these cations may directly substitute for ^{VI}Al in a tschermak-style exchange vector such as: $^{VI}(FeMg)^{2+} ^{IV}Si^{4+} \leftrightarrow ^{VI}(ScCr)^{3+} ^{IV}Al^{3+}$. In addition, Tiepolo *et al.* (2001) suggested another possible exchange vector for incorporation of i^{3+} cations in octahedral *M* sites involving coupled substitution with O^{2-} in the *O3* site, such as $2^{M1}(i)^{3+} 3^{O3}O^{2-} \leftrightarrow ^{M1}(FeMg)^{2+} 2^{O3}(OH^-)$.

There is a negative correlation ($r' = -0.66$) between V and ^{VI}Al in analysed Ca amphibole (Figure 5.4c). Tiepolo *et al.* (2001) suggested that t^{5+} trace elements are incorporated into Ca amphibole $^{VI}\text{M1}$ sites and contribute to the electroneutrality of the O3 (hydroxyl) site in which O^{2-} and not OH^- occurs, i.e., $^{M1}(\text{FeMg})^{2+} 2^{O3}(\text{OH}^-) \leftrightarrow 2^{M1}\text{V}^{5+} 5^{O3}\text{O}^{2-}$. However, in the absence of data on O3 site occupancy, this substitution mechanism could not be evaluated in this study.

Figure 5.4d illustrates the negative correlation ($r' = -0.60$) between Cu and $^{VI}\text{X}_{\text{Fe}}^{\text{Ca amp}}$ suggesting that these homovalent cations substitute for each other in octahedral M sites. The positive correlation ($r' = 0.60$) between $\sum(\text{CoNi})$ with $^{VI}\text{X}_{\text{Mg}}^{\text{Ca amp}}$ (Figure 5.4e) is attributed to distortion of $^{VI}\text{M1}$ site with increasing $^{VI}\text{X}_{\text{Mg}}^{\text{Ca amp}}$ so that the site can more readily admit divalent cations smaller than Mg.

There is a strong negative correlation ($r' = -0.80$) between Nb and $^{VI}\text{X}_{\text{Mg}}^{\text{Ca amp}}$ (Figure 5.3f). This is consistent with experimental crystal—liquid partitioning data for pargasite presented by Tiepolo *et al.* (2000), which show that partition coefficients for Nb and other t^{5+} HFSEs such as Ta are inversely proportional to $^{VI}\text{X}_{\text{Mg}}^{\text{Ca amp}}$. Ta was not analyzed in this study. The mechanism for Nb incorporation is the same as that for V.

Substitutions in *epidote* primarily occur at two structural sites, the irregular 8-9-fold coordinated X site normally occupied by Ca, and the octahedrally coordinated $M3$ site whose dominant constituents include Fe^{3+} , Mn^{3+} and Al^{3+} in common end-members (Table 2.1a). Analysed epidote exhibits positive correlations among the major

constituents of these sites and numerous trace elements (Figure 5.4g-i). Abundances of several divalent first row transition metals (Zn, Cu, Ni, Co), denoted i^{2+} , are positively correlated ($r' = 0.68$) with the mole fraction of zoisite ($^{M3}Al^{VI}$; Figure 5.4g). The ionic radii of each of these cations are slightly larger than the optimal radius of the $M3$ site and their divalent charge requires a coupled substitution to achieve electroneutrality, e.g., $^{X}Ca^{2+} ^{M3}Al^{3+} \leftrightarrow ^{X}i^{3+} i^{2+}$. This particular exchange vector also accounts for the positive correlation between Y^{3+} and $^{M3}X_{Al}^{Ep}$ illustrated in Figure 5.4h. In epidote, an increase in $^{M3}Al^{VI}$ results in a minor constriction of the $M3$ site, which in turn results in a slightly smaller distorted ^{VIII}X site that is closer to the ionic radius of Y (Table 2.1b). This example illustrates how a minor distortion in one site of a particular mineral due to major-element substitution can affect trace-element incorporation at an adjacent site. The positive correlation ($r' = 0.76$) between Ca and homovalent Sr, illustrated on Figure 5.4i, is surprising given that these elements typically directly substitute for each other.

Correlations between selected *garnet* X site cations and certain trace elements are shown in Figure 5.4j-l. The strong correlation ($r' = 0.95$) between X_{Grs}^{Grt} and Y shown in Figure 5.4j, despite the fact that the range of the former is quite small (0.23 - $0.27 X_{Grs}^{Grt}$), is attributed to the structural expansion of the X site with increasing calcium content such that the size of the cavity becomes closer to the ionic radius of Y (Table 2.1b). Van Westrenen *et al.* (1999, 2001) reported similar findings for experimental garnet—liquid partitioning. As noted previously, Jaffe (1951) proposed the ‘YAG’ substitution scheme

for Y (or REE^{3+}) for divalent cations (i^{2+} e.g., Fe, Mg, Mn, Ca) in the 8-fold coordinated X site, with electroneutrality achieved by Al substitution for Si in tetrahedral sites, i.e., $^{VIII}i^{2+IV}Si^{4+} \leftrightarrow ^{VIII}Y^{3+IV}Al^{3+}$. Figure 5.4k illustrates a strong negative correlation ($r' = -0.90$) between Zn and $\sum(X_{FeMg})$ suggesting that Zn directly exchanges for FeMg in X sites, i.e., $^{VIII}(FeMg)^{2+} \leftrightarrow ^{VIII}Zn^{2+}$. Figure 5.4l illustrates a negative correlation ($r' = -0.74$) between $\sum(X_{FeMg})$ and Sc concentration. Since Sc is inferred to enter the octahedral site normally occupied by Al, this is another example of how the major-element composition of one site can affect trace-element incorporation in an adjacent site. In this case, an increase in $\sum(X_{FeMg})$ (i.e., decrease in X_{Ca}) causes a structural constriction of the garnet X site, which in turn results in a decrease in the size of the adjacent Y site normally occupied by trivalent Al, making it less favourable for trivalent cations larger than Al (i.e., Sc, Table 2.1b). As a result, the direct exchange vector $^{VI}Al^{3+} \leftrightarrow ^{VI}Sc^{3+}$ likely operates more easily in grossular-rich garnet with a larger X site, and consequently larger Y sites, than in almandine-pyrope garnet.

In summary, measurable correlations exist between major- and trace-element mineral compositions in three of the five phases analyzed on both intra- and inter-mineral-site scales, demonstrating the significance of major-element composition on trace-element incorporation in these minerals.

5.4.2 Crystal-structural Effects on Trace-Element Partitioning

As discussed in section 4.4.2, the first order structural constraints imposed by a crystal lattice on trace-element partitioning are the charge and ionic radius of the trace element in relation to the nominal charge and volume of the host polyhedron (Brice, 1975). The second order constraints are the elasticity of the crystal lattice and its ability to achieve local electroneutrality, such that polyhedra which are relatively elastic and have the capacity to neutralize charge over several adjacent sites will admit misfitting cations more readily than those that are more rigid (Blundy and Wood, 1994). In the same section, problems inherent in mineral—mineral, as opposed to mineral—liquid, systems and so-called Onuma-type diagrams were introduced and discussed. Due to these problems, a qualitative approach to the extraction of site parameters of two minerals is again adopted, which notwithstanding, yields significant insight into partitioning behaviour of analysed trace elements.

General qualitative information regarding the sizes of the host sites on which trace-element partitioning took place can be inferred from chondrite-normalized concentration *versus* ionic radius plots for each phase (Figure 5.5a-h). Dashed lines on this figure depict the optimal radii (r_o) of specific sites in selected end members (i.e., pargasite, anorthite, pistacite, almandine and pure titanite) for each phase. The average r_o values (see Table 2.1b) were determined by subtracting the ionic radius of the O^{2-} anion (Shannon, 1976) from the average site size (Smyth and Bish, 1988). As expected, plots for Ca amphibole, plagioclase and titanite from the Y and Zr groups exhibit similar

patterns and they are therefore addressed together. This exemplifies the role of crystal structure as a primary control on trace-element partitioning.

Of note, the patterns for certain elements smaller than Zr (e.g., Ni, Co, Cu among others) exhibit 'spiky' patterns and are incompatible with the smooth curves on concentration *versus* IR diagrams predicted by Onuma (1968). Some of the spiky patterns may be attributed to element concentrations near detection limits. Another possibility is that they are artefacts of the normalization scheme employed, although this seems unlikely given the regular distribution of most chondrite-normalized elements and the fact that there are no systematic changes in terms of abundances greater or less than chondrite as those for *HREE* in plagioclase. It seems more probable that the reason lies in the multiple valence states, and hence also the concomitantly variable ionic radii and coordination numbers, commonly expressed by those elements. In the absence of structure refinement data, this problem, because of the multiplicity of dependent variables and the difficulty in determining the valence state(s) of elements in trace abundances *in situ* in mineral lattices, remains a major obstacle to quantitative modeling of trace-element incorporation in many phases.

Concentration *versus* ionic radius plots for *Ca amphibole* (Figure 5.5a-b) exhibit complex patterns, compatible with the several crystallographic sites intrinsic to this phase on which partitioning can occur. For instance, the 12-fold coordinated *A* site and the 8-fold coordinated *M4* site are marked by peaks near Rb and Y respectively, whereas

octahedral M sites are more difficult to distinguish due to the spiky chondrite-normalised patterns exhibited by the elements with ionic radii between 0.6 to 0.8 Å, discussed above. In detail, there are subtle differences between patterns exhibited by ‘cummingtonite-poor’ ($X_{Cum} \leq 0.06$) and ‘cummingtonite-rich’ ($X_{Cum} \approx 0.12$) types, specifically the locations of peaks for Zr, Y and Rb. ‘Cummingtonite-rich’ samples (46, 48) exhibit a higher Rb peak but have lower Y and Zr peaks than ‘cummingtonite-poor’ samples. The patterns of ‘cummingtonite-poor’ amphibole likely represent the presence of single 8-fold $M4$ and 12-fold A sites. ‘Cummingtonite-rich’ patterns are attributed to the positive correlation between the $M4'$ cavity and X_{Cum} such that the $M4$ site distorts to more readily admit cations smaller than calcium (e.g., first row transition metals, M -HREE c.f. 4.4.2). The patterns for trace elements with ionic radii less than Zr are broadly similar and exhibit three main vertices which include, in order of decreasing ionic radius: (i) Zn and Sc, (ii) Nb, and (iii) V. These vertices likely represent trace elements that best fit the octahedral $M1$ -3 sites, with the similarly sized $M1$ and $M3$ sites remaining undistinguished from each other and the Nb peak inferred to represent the smaller $M2$ site.

Excluding the ‘spiky’ patterns exhibited by Sc, Cu, Zn and Ni, shapes of concentration *versus* ionic radius plots for analysed *plagioclase* (Figure 5.5c-d) are consistent with partitioning of trace elements at two main crystallographic sites, an irregular 5-9 fold coordinated A site with a peak near the ionic radius of Sr and a

tetrahedral site with a peak near V. The presence of these peaks is not unexpected given that Sr is of similar ionic radius and homovalent with Ca and the similarity of the ionic radius of V and Si. The presence of secondary peaks centred around transition metals (Sc, Cu, Cr), previously noted for — and *HREE*, indicates that the assumptions concerning valence, ionic radius and/or coordination number of these ions are incorrect, and may imply multi-valency and/or site coordination effects. However, changes in ionic charge and coordination for those elements still result in ionic radii that are too large to be considered good ‘fits’ for plagioclase *T* sites ($\approx 0.33 \text{ \AA}$; Table 2.1b). Alternatively, although unlikely, it is possible a second cavity or ‘subsite’ in the large *A* site of plagioclase may be present that is capable of incorporating cations much smaller than Ca, although no direct evidence for this is conveyed by the data.

Concentration *versus* ionic radius plots for *epidote*, illustrated in Figure 5.5e, have maxima near the ionic radius of Sr, similar to those for plagioclase and consistent with partitioning of this element into the 8-9 fold coordinated *X* site. Two other peaks are evident, a larger site with a maximum near the ionic radii of Zn, Ni and Zr corresponding to the octahedral *M3* site and a relatively smaller site with a maximum near the ionic radius of V, inferred to represent the six-fold *M1* and *M2* sites normally occupied by Al^{3+} in most epidote-group minerals (Ercit, 2002).

Concentration *versus* ionic radius plots for *garnet* (Figure 5.5f) are more variable than those of other analyzed phases, which is attributed to trace-element zoning in this

phase. Despite this, general site information can be inferred. Patterns exhibit two main peaks, one near the ionic radius of Y corresponding to the 8-fold *X* site and a second near the ionic radius of V representing the octahedral *Y* site. One sample (20) exhibits a peak at Nb which may be due micro-inclusions of rutile (or other Nb sequestering phase). Divalent first row transition metals and Y, which have similar ionic radii to Ca, Fe and Mg, substitute for cations in the 8-fold *X* site, whereas smaller, higher charged cations substitute for Al in the octahedral *Y* site.

Unlike garnet, concentration *versus* ionic radius patterns for analysed *titanite* exhibit little variability (Figure 5.5g-h). Similar to garnet and epidote, at least two sites can be distinguished. In detail, a primary peak is centred about the ionic radius of Y corresponding to the 7-fold *A* site. The second site has an optimal radius near the ionic radius of Nb corresponding to the octahedral *M* site whose dominant constituent is Ti^{4+} . The peak near V may be a result of partitioning of this ion between the M and T sites.

5.4.3 Trace-Element Onuma-type Curves

$D_i^{*ndn/min}$ Onuma-type diagrams are illustrated for the nine possible mineral pairs in Figure 5.6(a-1). In principle, Onuma-type diagrams can be envisioned as an amalgamation of two concentration *versus* ionic radius patterns. In this context, if the two phases have non-analogous sites, a parabolic distribution of partition coefficients about a vertex (i.e., the r_0 for the site) can be observed. However, the distribution of

trace elements between two minerals that contain analogous sites can be difficult to decipher, e.g., first row transition metal partitioning between Ca amphibole *M*1-3 sites and the titanite *M* site or Sr partitioning between the epidote *X* site and plagioclase *A* site. This task becomes more tractable when general crystal site information, such as that obtained from trace-element concentration *versus* ionic radius patterns discussed above, is available.

Relative to the *REE* discussed in the preceding chapter, the group of trace elements discussed here exhibits a broader range of ionic radii and charge, and hence coordination number, and thus can potentially enter a greater variety of polyhedra resulting in complex Onuma-type curves. In general, a decrease in ionic radius for an element will result in preference for a lower coordination number, therefore polyhedra with lower coordination numbers preferentially host smaller cations. However, a problem arises when an element is partitioned into sites in a mineral pair which have different coordination numbers. For *REE* this was not problematic since their ionic radii in both six- and eight-fold coordination are proportional (Shannon, 1976). However, this is not the case for this group of elements. To alleviate this problem, the ionic radii of elements plotted on Figure 5.6a-1 were calculated as average ionic radii based on the inferred coordination of each element in each mineral pair.

Onuma-type patterns for *Ca amphibole—titanite* pairs are illustrated on Figure 5.6a-b. The Rb peak present is attributed to the large 12-fold-coordinated *A* site in Ca

amphibole coupled with the lack of suitable sites for this element in titanite. Peaks near the ionic radii of Zn and Sc are interpreted to represent the *M1* and *M3* sites of Ca amphibole, whereas the Nb trough indicates the strong preference for this element for the *M* site of titanite. Ni, Cr and V form a short segment resembling the limb of a parabola, which is surprising given the likely heterovalent character of these elements. However this pattern may be a result of overlap of patterns for the titanite *M* site and Ca amphibole octahedral *M1-3* sites.

Patterns for *titanite—plagioclase* pairs (Figure 5.6c-d) exhibit two main peaks at Y and Nb, which are attributed to the strong preference for these elements for *A* and *M* sites in titanite respectively. The trough at Sr represents the strong affinity of this element for the plagioclase *A* site. A third peak at Zr may represent the affinity of this element for the titanite *M*.

Patterns for *titanite—epidote* pairs (Figure 5.6e) are similar to those exhibited by *titanite—plagioclase* pairs with peaks at Y and Nb and a trough at Sr, in this case attributed to the preference of the latter element for the 8-9 fold coordinated epidote *X* site. Patterns for remaining elements exhibit significant overlap attributed to the similarity of the octahedral *M* sites in each phase. Little site information can be discerned from patterns for *titanite—garnet* pairs (Figure 5.6f) which is an artifact of the similarity between garnet *Y* sites and titanite *M* sites. The peak near the ionic radii of Y and Zr may represent the garnet *X* site.

The locations of peaks for Y and LILEs for *Ca amphibole—plagioclase* pairs (Figure 5.6g-h) illustrate the strong preferences for Y and Rb for the *M4* and *A* sites respectively in Ca amphibole and the trough at Sr reflects the affinity of this element for plagioclase *A* sites. Sc, V, Cr and Nb preferentially partition into Ca amphibole octahedral *M* sites with Nb and V favouring the smallest *M2* site (Tiepolo *et al.*, 2000) and Sc and Cr favouring the relatively larger *M1* and *M3* sites. The peaks near Ni and Cu are attributed to both overlap between the Ca amphibole *M4* site and plagioclase *A* site and the spiky pattern of these transition metals.

Because of similarities in the number and sizes of crystallographic sites of *Ca amphibole* and *epidote*, the Onuma-type curve for this mineral pair (Figure 5.6i) exhibits only two peaks. The presence of a Rb peak is attributed to the *A* site in Ca amphibole. The preference of Co for Ca amphibole is more difficult to rationalize given the similarity between the six-fold *M* sites of each phase.

Onuma-type curves for *Ca amphibole—garnet* pairs exhibit peaks for the LILEs, (Sr, Rb) corresponding to the *M4* and *A* sites of Ca amphibole. The pattern exhibited by transition metals cannot be rationalized to any specific site in either mineral, possibly due to the potential multivalent character of these elements. Onuma-type curves for *plagioclase—epidote* pairs (Figure 5.6k) show that Sr is approximately equally partitioned between the analogous plagioclase *A* site and epidote *X* site and Rb slightly prefers plagioclase, whereas most transition elements (except Cu and Ni) and the HFSEs

preferentially partition into the epidote *M3* site as opposed to the smaller plagioclase *T* site. The locations of a peak and trough for Sr and Y on *plagioclase—garnet* Onuma-type curves (Figure 5.6l) reflect the preference of these elements in plagioclase *A* sites and garnet *X* sites respectively. Most transition metals and HFSEs preferentially partition into garnet *Y* sites, but the uneven patterns exhibited by the remaining elements indicate possible zoning and/or multi-valent states for these elements. Surprisingly, Ni, Cu, and Zn exhibit slight preference for the plagioclase *A* over the garnet *X* site. No crystal-chemical explanation for this behaviour is forthcoming and the apparent preference for those elements in plagioclase may be due to fractionation during sample ablation (Longerich *et al.*, 1996).

To summarize, the shapes of Onuma-type curves based on measured trace element distributions (Figure 5.6a-l) generally support initial cation-site occupancy assumptions (see Table 2.1a). For instance, plots of Ca-amphibole—mineral pairs exhibit peaks at Rb indicative of the 12-fold *A* site, and plots of titanite—mineral and plagioclase —mineral pairs exhibit peaks near the ionic radii of Nb and Sr, which are attributed to the strong partitioning of these elements into titanite *M* sites and plagioclase *A* sites respectively.

However, several transition metals, especially Ni, Cu and Zn exhibit irregular spiky patterns that are attributed to a combination of factors including: (i) possible multiple-valence states, implying multiple ionic radii and hence coordination numbers;

(ii) the simplification of using average ionic radii to represent multiple coordination in different minerals; and (iii) for certain elements, possible analytical problems. It is difficult to decipher the relationship between element valency and the spiky patterns definitively since the microbeam techniques employed in this study (i.e., EPMA and LAM-ICP-MS) do not measure valence state. Analytical problems are addressed explicitly in Appendix B, but some of the elements that exhibit spiky patterns are known to be prone to fractionation during sample ablation and transportation under LAM-ICP-MS analysis (Longerich *et al.*, 1996). With respect to *Onuma-type* diagrams utilized in this chapter, plotting D^* against average ionic radius derived from the coordination numbers of 'known' host sites in each mineral resulted in the smoothest patterns. Attempts to manipulate the ionic charge, and thus radius and coordination, of elements that exhibit spiky patterns in order to smooth out their distributions did not prove successful. The next chapter use mass- and reaction-balancing techniques to link the behaviour of the *REE* and analysed trace elements in select Y group samples.

Chapter 5: Trace-Element Mineral Chemistry

Table 5.1 Average absolute abundances (± 1 standard deviation) of selected trace elements in Ca amphibole and plagioclase analysed by LAM-ICP-MS. *Italics* indicate Zr Group. Blank indicates element not determined.

Ca amphibole	46	48	49	06	20	01	142
(Ca amphibole: n =4)							
(ppm)							
Sc	63.33 \pm 13.90	49.70 \pm 6.99	70.95 \pm 4.34	63.10 \pm 4.81	52.65 \pm 23.82	30.90 \pm 10.45	60.38 \pm 7.99
V	457.5 \pm 27.44	218.5 \pm 70.88	441.5 \pm 26.96	489.2 \pm 25.48	287.3 \pm 93.01	210.5 \pm 32.01	311.75 \pm 41.28
Cr	127.9 \pm 54.34	111.2 \pm 24.94	325.6 \pm 219.20	282.3 \pm 18.29	154.3 \pm 97.84	127.0 \pm 60.14	49.88 \pm 7.89
Co	79.53 \pm 6.90	29.45 \pm 2.54	63.85 \pm 4.12	22.70 \pm 34.05	29.45	8.35 \pm 2.54	8.35 \pm 2.23
Ni	119.3 \pm 26.06	81.40 \pm 5.22	108.6 \pm 14.83	88.90 \pm 17.98	82.50 \pm 24.00	62.08 \pm 17.89	55.83 \pm 18.57
Cu	3.37 \pm 1.38	2.62 \pm 0.79	3.23 \pm 0.89	2.66 \pm 1.43	1.53 \pm 0.18	0.82 \pm 0.37	90.08 \pm 6.89
Zn	174.3 \pm 30.00	179.5 \pm 9.64	192.0 \pm 6.96	255.3 \pm 62.86	185.0 \pm 13.53	85.50 \pm 5.63	22.40 \pm 3.15
Sr	15.68 \pm 1.51	7.53 \pm 2.55	17.28 \pm 1.85	15.90 \pm 2.25	43.58 \pm 9.65	27.80 \pm 6.12	1.90 \pm 0.26
Rb	13.70 \pm 2.33	3.09 \pm 0.46	1.33 \pm 0.71	0.82 \pm 0.27	6.37 \pm 2.59	1.38 \pm 0.33	10.04 \pm 1.37
Y	9.46 \pm 0.96	7.69 \pm 1.26	41.05 \pm 2.87	44.65 \pm 3.11	5.99 \pm 2.69	20.23 \pm 4.75	2.54 \pm 0.44
Zr	15.68 \pm 2.03	17.53 \pm 3.45	90.10 \pm 60.83	27.23 \pm 13.22	17.68 \pm 3.96	70.93 \pm 64.46	16.83 \pm 6.00
Nb	0.62 \pm 0.13	0.20 \pm 0.09	2.81 \pm 0.39	1.63 \pm 0.52	4.63 \pm 2.01	8.57 \pm 1.23	7.71 \pm 2.16

Plagioclase	46	48	49	06	20	01	142
(plagioclase: n =4)							
(ppm)							
Sc	0.96 \pm 0.36	7.71 \pm 0.66	1.73 \pm 1.92	2.16 \pm 0.92	1.46 \pm 0.36	1.77 \pm 0.90	3.58 \pm 1.19
V	3.05 \pm 2.50	11.55 \pm 7.55	0.27 \pm 0.20	4.20 \pm 3.26	3.51 \pm 1.01	0.29 \pm 0.21	6.20 \pm 3.19
Cr	2.48 \pm 0.62	1.00 \pm 0.63	3.77 \pm 1.11	4.05 \pm 1.16	3.95 \pm 0.72	3.89 \pm 2.08	5.92 \pm 0.86
Co	0.06 \pm 0.05	0.04 \pm 0.01	0.88 \pm 0.70	0.04 \pm 0.03	0.09 \pm 0.10	0.84 \pm 0.51	0.06 \pm 0.05
Ni	16.52 \pm 12.11	43.35 \pm 14.37	10.97 \pm 6.88	13.66 \pm 4.84	19.06 \pm 4.38	10.24 \pm 6.92	21.21 \pm 4.22
Cu	2.95 \pm 1.55	9.87 \pm 1.40	1.27 \pm 1.01	1.54 \pm 1.25	4.90 \pm 1.74	1.30 \pm 0.67	2.36 \pm 1.20
Zn	86.48 \pm 6.82	86.70 \pm 10.01	30.83 \pm 10.01	87.83 \pm 13.96	126.63 \pm 2.33	42.57 \pm 5.56	132.8 \pm 12.34
Sr	551.8 \pm 112.4	477.5 \pm 247.9	457.0 \pm 247.9	531.3 \pm 87.61	815.8 \pm 76.38	476.2 \pm 36.26	829.5 \pm 109.1
Rb	1.06 \pm 0.90	11.57 \pm 8.82	19.35 \pm 29.92	0.37 \pm 0.08	2.15 \pm 1.25	16.15 \pm 14.23	0.58 \pm 0.04
Y	0.07 \pm 0.05	0.40 \pm 0.22	0.25 \pm 0.12	0.84 \pm 0.44	0.08 \pm 0.01	0.28 \pm 0.20	1.15 \pm 0.36
Zr	0.20 \pm 0.10	2.38 \pm 0.61	0.46 \pm 0.26	7.50 \pm 6.20	0.23 \pm 0.07	0.42 \pm 0.30	16.07 \pm 11.57
Nb	0.01 \pm 0.01	1.21 \pm 0.02	0.02 \pm 0.02	0.03 \pm 0.01	0.02 \pm 0.01	0.02 \pm 0.01	0.05 \pm 0.01

Chapter 5: Trace-Element Mineral Chemistry

Table 5.1(continued). Average absolute abundances (± 1 standard deviation) of selected trace elements in epidote, garnet and titanite analysed by LAM-ICP-MS. *Italics* indicate Zr Group. Blank indicates element not determined.

Epidote	46	48*	06	Garnet	20*	01	142
(ppm)	(epidote: n =4 *n = 3)			(ppm)	(garnet: n =4 *n = 3)		
Sc	23.78 \pm 6.86	29.25 \pm 16.84	26.48 \pm 12.63		5.76 \pm 0.90	21.03 \pm 2.01	23.23 \pm 4.11
V	260.0 \pm 85.32	228.1 \pm 93.07	218.0 \pm 95.60		532.5 \pm 100.8	247.8 \pm 53.24	235.0 \pm 52.72
Cr	202.0 \pm 48.90	114.0 \pm 110.00	58.40		201.0 \pm 20.41		208.8 \pm 99.93
Co	0.39 \pm 0.39	0.59	1.20				22.10 \pm 2.22
Ni	6.37 \pm 2.74	19.47	12.60		86.05 \pm 15.47		5.03 \pm 0.66
Cu	1.59 \pm 0.91	1.67	2.11		6.30 \pm 2.32		0.99 \pm 0.11
Zn	81.50 \pm 12.63	62.67	242.0		19.50 \pm 2.61		40.58 \pm 8.27
Sr	1185.0 \pm 227.1	306.4 \pm 154.3	675.8 \pm 85.12		37.85 \pm 3.55	3.00 \pm 2.75	43.64 \pm 37.10
Rb	0.72 \pm 0.44	1.66 \pm 1.49	0.73 \pm 0.43		0.45 \pm 0.08	0.23 \pm 0.09	6.80 \pm 5.28
Y	19.63 \pm 4.21	12.27 \pm 8.58	33.55 \pm 5.29		46.95 \pm 2.41	68.48 \pm 23.97	89.25 \pm 21.33
Zr	144.6 \pm 80.58	54.55 \pm 50.22	81.51 \pm 38.76		671.0 \pm 222.9	7.16 \pm 1.47	11.40 \pm 5.48
Nb	16.69 \pm 15.00	37.82 \pm 23.46	5.28 \pm 4.18		347.5 \pm 131.1	1.00 \pm 0.81	29.93 \pm 26.84

Titanite	46	48*	49	06	20	01	142*
(ppm)	(titanite: n =3 *n = 2)						
Sc	6.79 \pm 1.39	3.58 \pm 0.71	4.66 \pm 0.44	5.69 \pm 3.15	6.92 \pm 0.54	3.68 \pm 0.23	4.53 \pm 0.11
V	932.0 \pm 71.39	1008 \pm 263.0	1142 \pm 145.3	399.33 \pm 47.07	914.0 \pm 99.26	1008 \pm 131.8	1097 \pm 36.33
Cr	67.87 \pm 26.37	332.1 \pm 261.3	254.0 \pm 32.66	91.57 \pm 44.48	65.26 \pm 15.38	136.8 \pm 32.03	264.0 \pm 8.16
Co							
Ni	44.93 \pm 3.72	14.13 \pm 5.05	28.55 \pm 3.47	15.90 \pm 2.29	45.72 \pm 2.22	15.11 \pm 3.06	29.61 \pm 0.87
Cu	4.66 \pm 1.05	1.46 \pm 0.15	2.28 \pm 0.38	2.23 \pm 0.36	4.38 \pm 0.40	1.43 \pm 0.09	2.17 \pm 0.09
Zn	16.83 \pm 1.04	18.25 \pm 10.91	7.39 \pm 0.18	13.32 \pm 4.53	17.02 \pm 0.30	19.38 \pm 6.39	7.43 \pm 0.04
Sr	15.07 \pm 1.49	100.4 \pm 99.69	18.65 \pm 0.53	72.43 \pm 22.04	15.16 \pm 0.84	111.9 \pm 54.71	18.81 \pm 0.13
Rb	0.51 \pm 0.28	0.83 \pm 0.46	0.16 \pm 0.02	0.34 \pm 0.18	0.53 \pm 0.11	0.76 \pm 0.14	0.15 \pm 0.01
Y	1216 \pm 133.7	1243 \pm 74.94	1083 \pm 560.5	623.0 \pm 622.8	1182 \pm 72.06	1240 \pm 34.35	911.9 \pm 140.1
Zr	505.3 \pm 208.2	478.7 \pm 135.9	559.5 \pm 10.21	266.3 \pm 10.06	522.7 \pm 119.5	503.2 \pm 62.54	556.4 \pm 2.55
Nb	193.0 \pm 18.49	242.7 \pm 21.00	243.0 \pm 27.7	2000 \pm 398.2	190.0 \pm 5.61	237.1 \pm 10.78	234.5 \pm 6.94

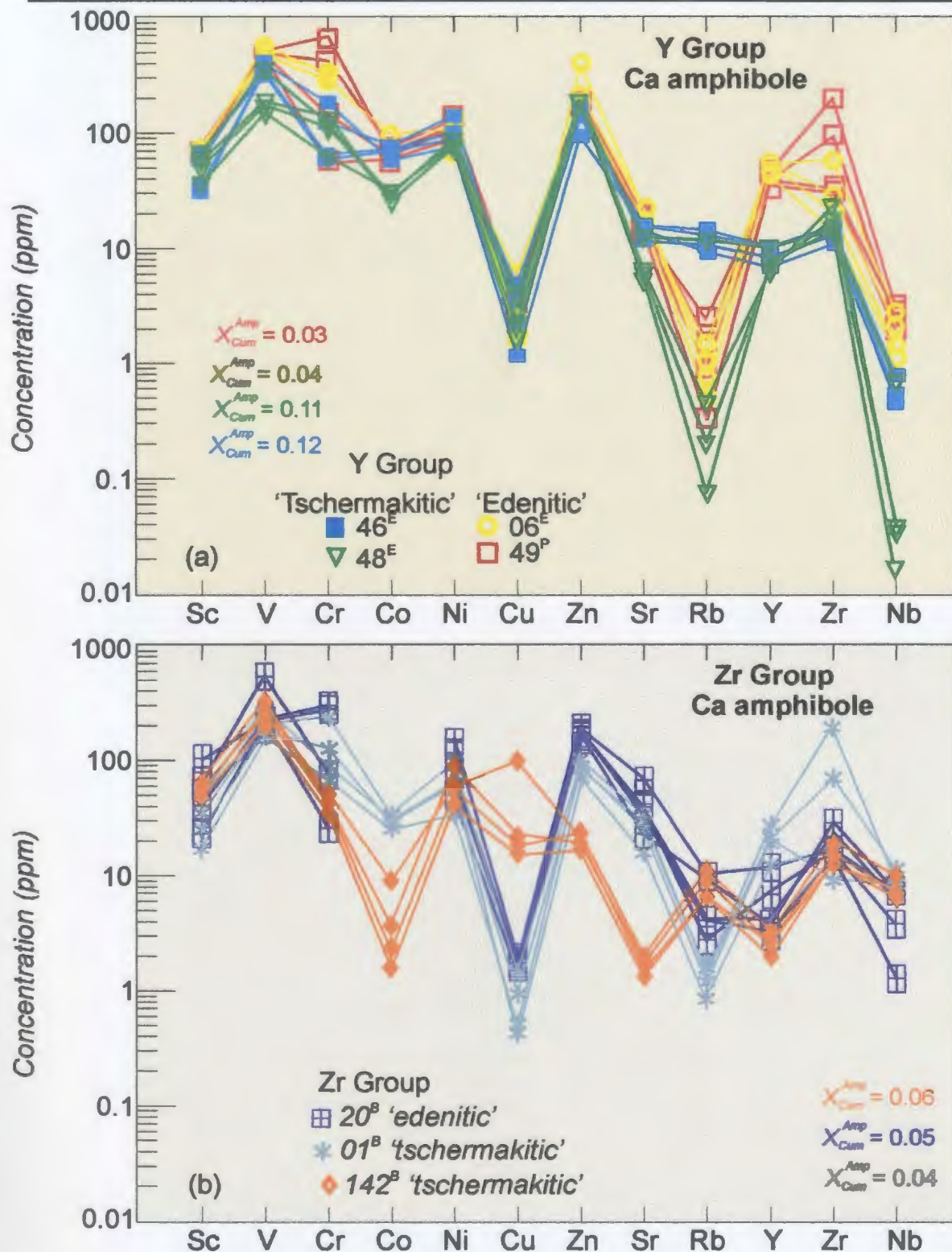


Figure 5.1 Absolute abundances (ppm) of selected trace elements in Ca amphibole from the (a) Y group, and (b) Zr group. Blank indicates element not determined. Superscripts denote rock type (E = epidote amphibolite, P = plagioclase amphibolite, B = biotite amphibolite).

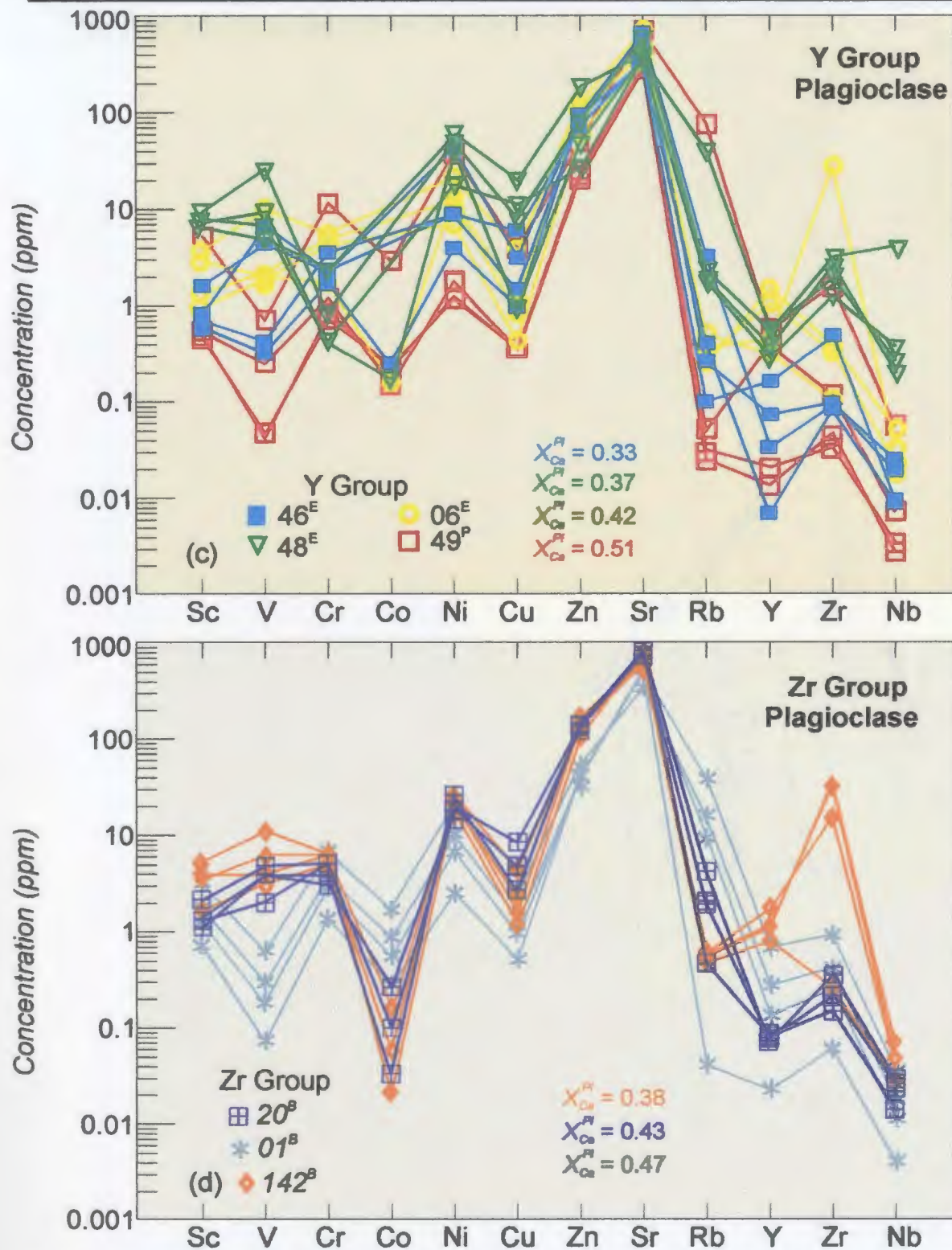


Figure 5.1 Absolute abundances (ppm) of selected trace elements in plagioclase from the (c) Y group, and (d) Zr group. Blank indicates element not determined. Superscripts denote rock type (E = epidote amphibolite, P = plagioclase amphibolite, B = biotite amphibolite).

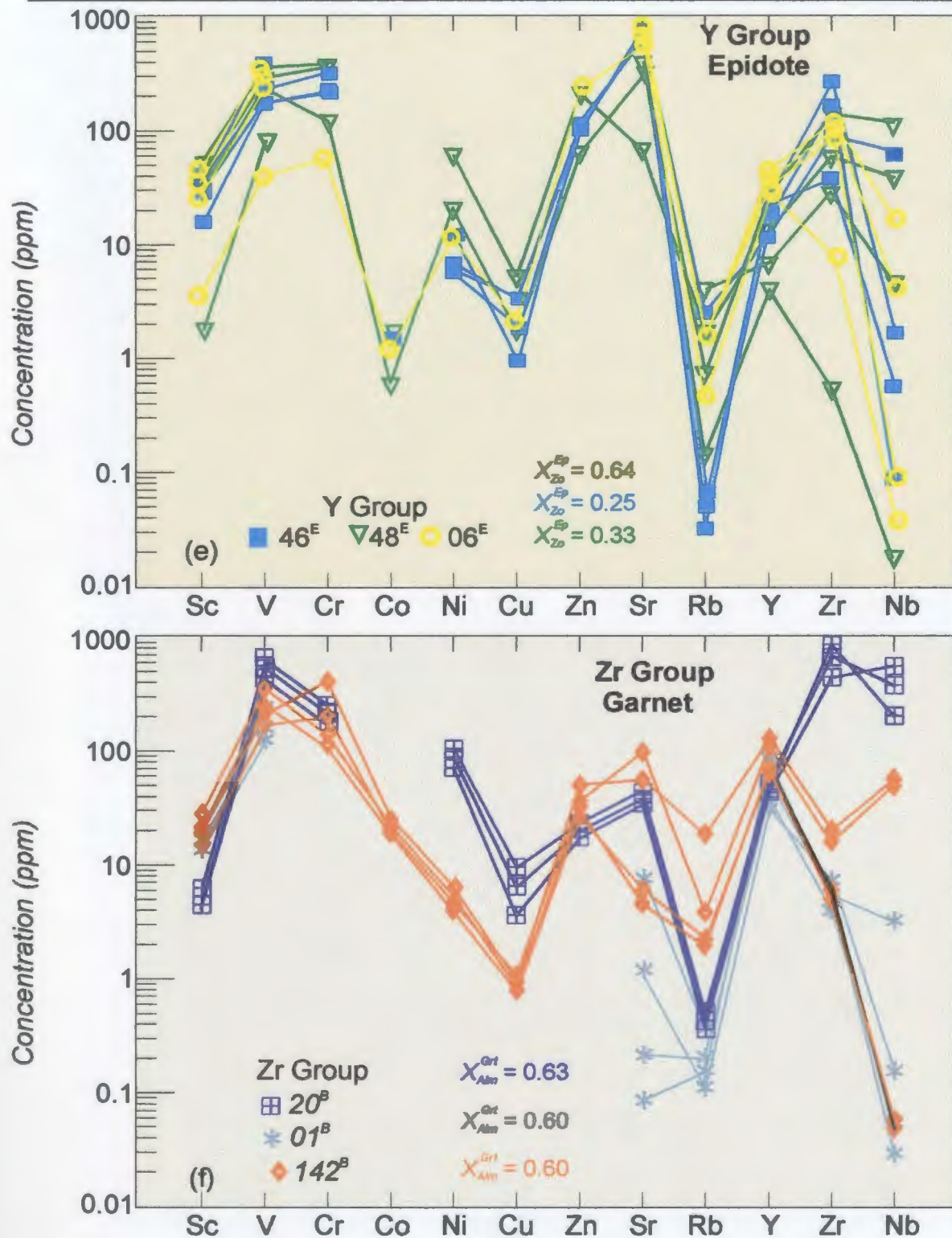


Figure 5.1 Absolute abundances (ppm) of selected trace elements in (e) epidote (Y group) and, (f) garnet (Zr group). Blank indicates element not determined. Superscripts denote rock type (E = epidote amphibolite, P = plagioclase amphibolite, B = biotite amphibolite).

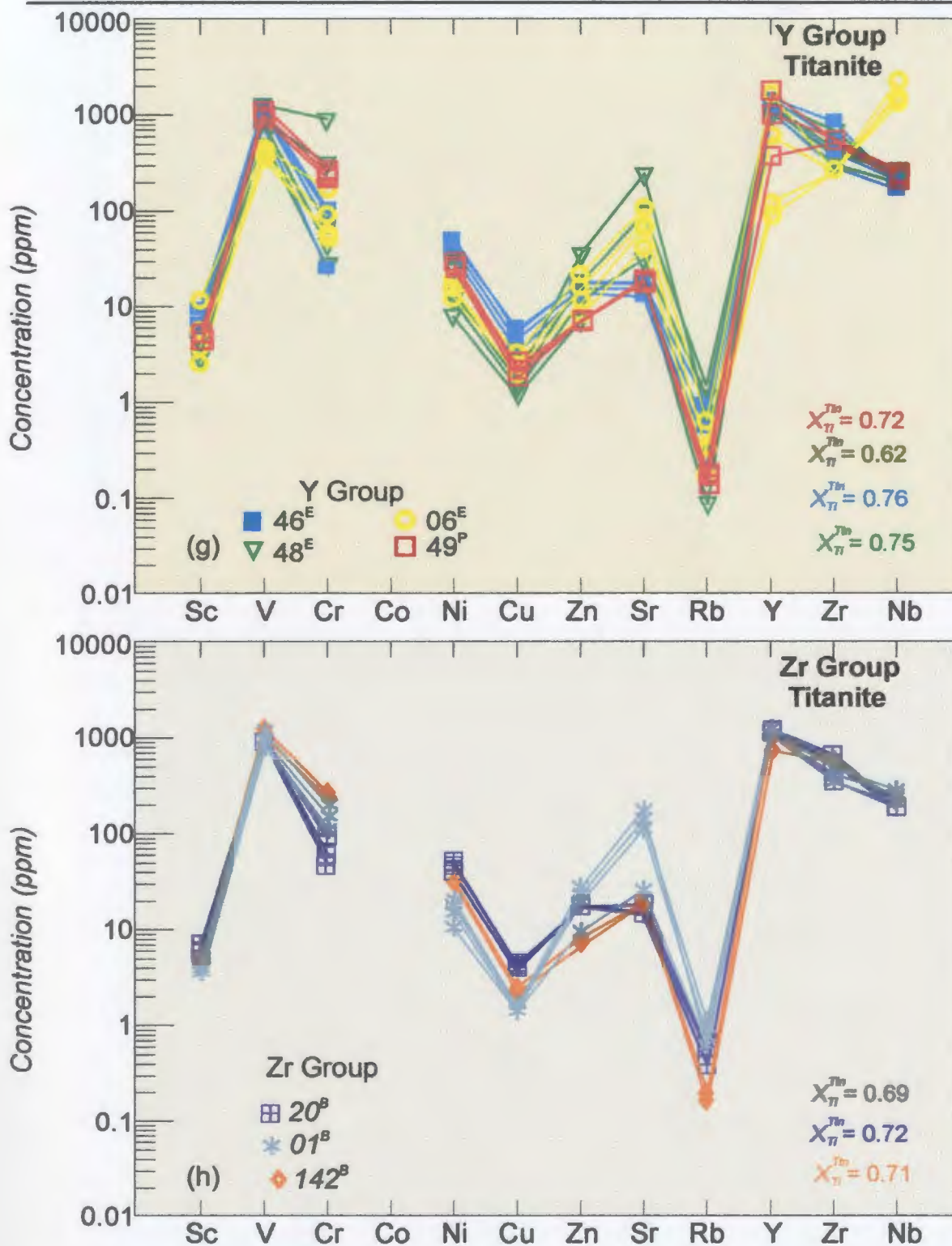


Figure 5.1 Absolute abundances (ppm) of selected trace elements in titanite from the (g) Y group and, (h) Zr group. Blank indicates element not determined. Superscripts denote rock type (E = epidote amphibolite, P = plagioclase amphibolite, B = biotite amphibolite).

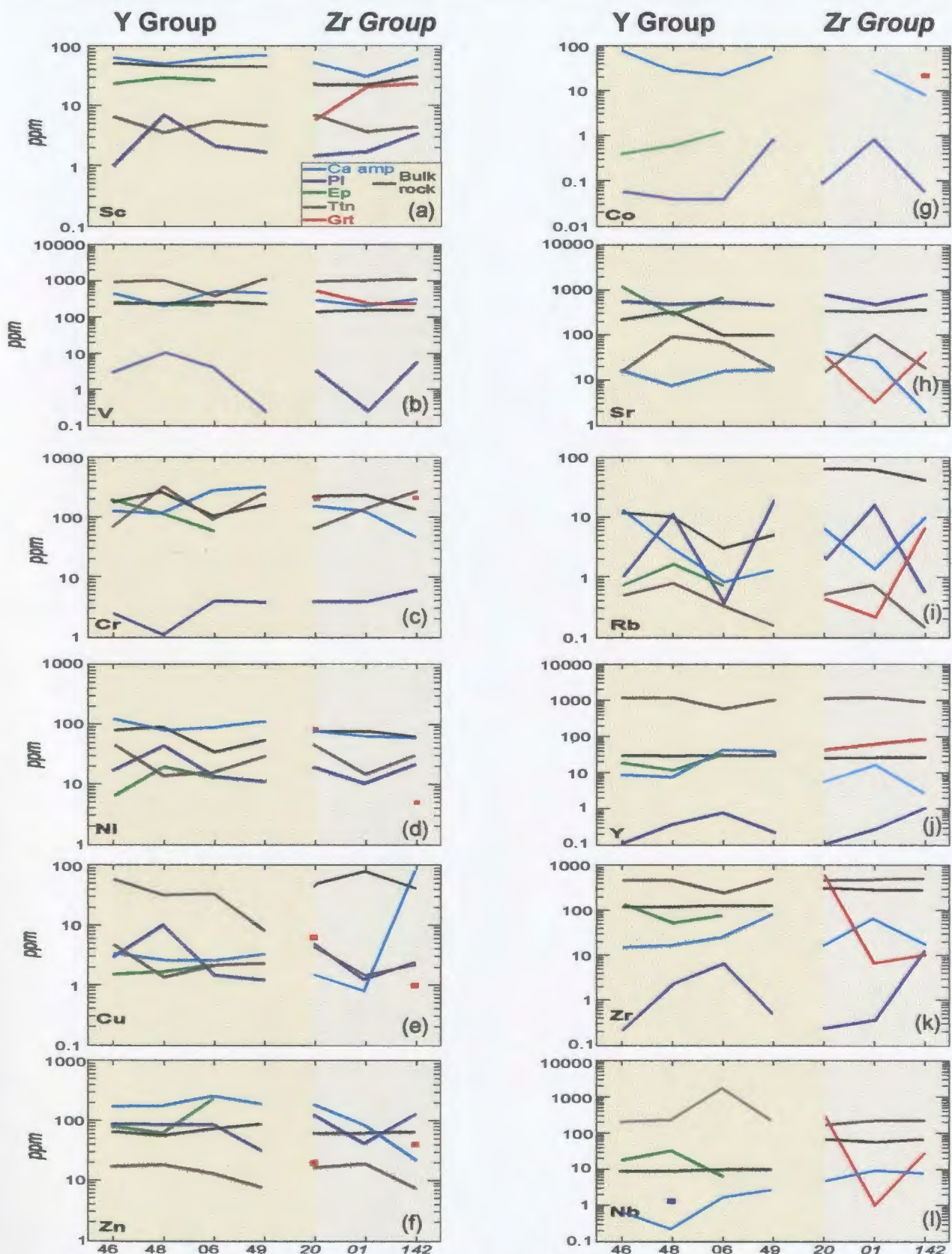


Figure 5.2(a-l) Trace-element concentrations in Ca amphibole, plagioclase, epidote, garnet, titanite and whole rock. Y group samples on abscissa arranged in order of decreasing modal epidote. Zr group samples on abscissa (*italicized*) comprise the biotite-amphibolite assemblage.

Table 5.2(a) Average values ($n = 3$) of $D^{Min 1/Min 2}$ for analysed mineral pairs. SD is the standard deviation at one sigma. No standard deviation represents single determinations. Blank indicates below detection limits or element not analyzed for one phase. *Italics indicate Zr group.*

$D^{Amp/Ten}$	49	SD	06	SD	48	SD	46	SD	01	SD	20	SD	142	SD
Sc	16.49	1.8E+00	16.71	7.8E+00	13.46	2.3E+00	9.10	2.6E+00	8.81	2.6E+00	8.98	2.7E+00	13.70	5.9E-01
V	0.42	7.4E-02	1.28	1.6E-01	0.28	1.7E-01	0.51	5.2E-02	0.21	3.3E-02	0.33	1.2E-01	0.23	3.5E-02
Cr	0.85	4.9E-01	4.19	1.7E+00	2.40	1.6E+00	3.71	3.1E+00	0.66	4.0E-02	2.92	1.0E+00	0.15	1.5E-02
Co														
Ni	4.21	5.4E-02	6.27	1.2E+00	6.68	1.8E+00	2.75	3.7E-01	3.99	6.1E-01	1.92	5.8E-01	2.01	6.2E-01
Cu	1.25	2.1E-01	1.42	8.8E-01	1.87	3.8E-01	0.55	1.1E-01	0.65	2.0E-01	0.34	3.7E-02	8.42	1.2E+00
Zn	26.74	3.2E-02	21.20	8.9E+00	15.15	7.6E+00	9.81	1.5E+00	5.35	2.0E+00	10.49	4.4E-01	2.27	1.7E-01
Sr	0.98	2.7E-03	0.26	1.2E-01	0.17	8.0E-02	1.10	1.6E-01	0.35	1.9E-01	2.64	5.4E-01	0.09	1.3E-02
Rb	7.68	6.2E-01	3.43	1.1E+00	5.31	3.6E+00	41.05	2.1E+01	1.86	7.5E-01	12.42	8.3E+00	59.78	2.1E+00
Y	0.07	3.7E-02	0.27	1.5E-01	0.01	7.9E-04	0.01	6.3E-05	0.02	4.6E-03	0.01	2.2E-03	0.00	2.9E-04
Zr	0.21	1.3E-01	0.11	5.0E-02	0.04	1.5E-02	0.04	1.5E-02	0.18	2.0E-01	0.03	1.1E-02	0.03	3.9E-03
Nb	0.01	5.3E-04	7.7E-04	1.9E-04	1.16E-03	1.3E-03	3.4E-03	5.7E-04	0.03	2.4E-03	0.02	9.9E-03	0.03	3.7E-03
D^{Tmpt}	49	SD	06	SD	48	SD	46	SD	01	SD	20	SD	142	SD
Sc	9.31	5.2E-01	4.66	4.0E-01	1.83	3.2E-01	8.59	3.3E-01	2.92	2.3E-01	5.10	6.8E-01	0.99	9.3E-03
V	24386	2.9E+03	139.7	8.1E+01	0.04	1.8E-02	1159	1.0E+03	6923	1.2E+03	298.1	1.1E+02	185.1	6.9E+01
Cr	258.99	2.2E+01	36.63	1.8E+00	6.15	4.8E+00	33.88	6.6E+00	52.69	3.6E+00	18.43	3.6E+00	40.02	2.1E+00
Co														
Ni	17.92	3.2E+00	1.41	8.9E-01	0.19	3.8E-02	5.48	2.2E+00	3.31	3.6E-01	2.60	3.7E-01	1.34	2.6E-01
Cu	6.36	9.9E-01	2.92	2.9E+00	0.92	1.2E+00	3.35	1.5E+00	1.52	7.3E-02	1.11	2.1E-01	0.93	3.3E-01
Zn	0.31	3.1E-02	0.16	4.4E-02	0.20	6.6E-02	0.19	3.5E-03	0.48	7.3E-02	0.13	4.9E-04	0.05	1.8E-03
Sr	0.06	3.5E-05	0.15	4.9E-02	0.00	2.2E-04	0.03	5.6E-03	0.23	4.9E-02	0.02	1.2E-03	0.02	3.4E-04
Rb	5.66	4.5E-01	1.09	7.0E-01	1.94	1.5E+00	3.75	1.4E+00	4.75	2.3E+00	0.60	2.1E-01	0.28	3.0E-02
Y	74891	4.2E+04	1774	2.0E+01	3120	2.5E+02	71723	6.1E+04	21910	6.4E+03	14446	1.6E+03	743.1	9.8E+01
Zr	13326	5.7E+02	1302	4.2E+01	201	6.5E+01	4503	1.4E+01	3704	7.6E+02	2696	4.3E+02	27.08	8.4E+00
Nb	84898	1.4E+04	76907	1.0E+04	20092	5.7E-01	17226	3.1E+03	26456	3.6E+03	8765	1.1E+03	4045	4.3E+02

Table 5.2(a, continued) Average values ($n = 3$) of $D^{1000/1000}$ for analysed mineral pairs. SD is the standard deviation at one sigma. No standard deviation represents single determinations. Blank indicates below detection limits or element not analyzed for one phase. *Italics indicate Zr group.*

$D^{1000/1000}$							$D^{1000/1000}$						
	06	SD	48	SD	46	SD		01	SD	20	SD	142	SD
Sc	1.10	1.9E-03	0.63	2.0E-02	0.47	8.0E-02		0.15	1.1E-02	1.23	1.9E-01	0.19	1.9E-02
V	4.35	5.6E-02	6.42	9.5E-01	4.68	9.0E-01		3.78	1.8E-01	1.77	2.4E-01	3.91	3.5E-01
Cr			0.13		0.33	6.5E-02				0.33		2.15	2.8E-01
Co													
Ni			0.38		4.84	1.4E+00				0.55	1.1E-01	6.29	2.3E-01
Cu			0.25		4.11	1.8E+00				0.78	2.1E-01	2.15	1.8E-01
Zn			0.19		0.16	6.5E-03				0.89	1.1E-01	0.18	4.1E-02
Sr	0.12	4.4E-02	1.98	1.4E+00	0.01	2.1E-03		744.3	6.2E+02	0.40	3.3E-02	1.62	1.1E+00
Rb	0.66	5.1E-01	3.16	8.4E-02	11.95	4.1E+00		4.21	1.7E+00	1.22	3.0E-01	0.04	2.3E-02
Y	22.68	5.6E-02	186.9	8.0E+01	63.63	3.8E+00		24.29	5.4E+00	25.18	6.8E-01	10.27	7.6E-01
Zr	12.53	2.6E-01	207.4	1.1E+01	2.27	6.8E-01		63.96	3.2E+00	0.81	1.5E-01	102.3	3.3E+00
Nb	28384	1.1E+03	4735	2.4E+01	119.20	3.4E+00		3086	3.0E+03	0.64	2.2E-01	4413	4.2E+02

$D^{1000/1000}$														
	49	SD	06	SD	48	SD	46	SD	01	SD	20	SD	142	SD
Sc	133.0	4.9E+00	19.55	1.6E+00	5.94	9.1E-01	45.57	2.6E+00	24.90	2.2E+00	50.09	2.6E+00	18.96	1.5E+00
V	9020	3.3E+02	150.5	8.5E+01	37.96	1.0E+00	88.10	1.6E+01	64.91	1.5E+01	113.8	6.3E+01	74.53	5.1E+01
Cr	362.9	1.7E+02	60.94	8.8E-01	320.6	1.5E+01	80.22	1.3E+01	22.67	2.1E+00	56.53	2.1E+01	9.27	3.2E+00
Co	353.1	4.2E+01			144.7								13.94	
Ni	60.60	8.1E+00	4.48	8.2E-01	3.31	1.4E+00	20.36	2.1E+00	3.67	2.4E-01	4.97	1.2E+00	2.93	2.6E-02
Cu	10.37	2.2E+00	2.02	5.2E-01	2.21	2.1E+00	1.07	6.5E-01	0.26	6.7E-03	0.38	1.1E-01	97.09	7.3E+01
Zn	7.86	9.3E-01	3.53	5.5E-01	4.82	1.5E+00	2.05	3.0E-02	0.69	7.2E-02	1.41	4.5E-02	0.18	4.9E-02
Sr	0.05	5.0E-03	0.02	4.0E-04	0.02	7.5E-03	0.03	4.1E-03	0.03	3.6E-03	0.05	1.1E-02	0.00	2.7E-05
Rb	48.29	3.5E+01	2.67	1.3E+00	2.45	2.3E+00	113.7	5.6E+01	1.04	3.2E-01	3.58	6.3E-01	18.38	7.3E-01
Y	2506	3.6E+02	60.23	2.4E+01	27.22	2.1E+00	84.27	2.7E+01	246.0	3.5E+01	89.56	3.1E+01	2.58	7.4E-01
Zr	1621	9.1E+02	17.21	1.4E+01	9.13	1.4E+00	110.5	7.6E+01	232.1	1.0E+01	72.41	4.4E-01	24.09	4.1E-01
Nb	39.33	1.3E+01	1031	5.7E+00	1.82	9.4E-03	25.67	3.5E+00	366.3	2.6E+01	214.1	8.5E+01	188.1	2.3E+00

Table 5.2(a, continued) Average values ($n = 3$) of $D^{Am 1/Am 2}$ for analysed mineral pairs. SD is the standard deviation at one sigma. No standard deviation represents single determinations. Blank indicates below detection limits or element not analyzed for one phase. *Italics* indicate Zr group.

$D^{Am/Sp}$							$D^{Am/Crt}$						
	06	SD	48	SD	46	SD		01	SD	20	SD	142	SD
Sc	1.92	2.2E-01	7.92	8.6E-03	3.72	9.3E-01	Sc	1.58	3.3E-01	8.78	2.9E+00	2.25	3.2E-01
V	1.82	1.0E-01	1.31	4.0E-01	1.82	5.4E-01	V	0.81	1.7E-02	0.73	3.5E-01	0.86	7.0E-03
Cr			0.33				Cr			0.89	4.8E-01	0.34	2.4E-02
Co			13.98				Co					0.14	2.4E-02
Ni			1.49				Ni			0.91	1.7E-01	14.20	1.4E+00
Cu			0.32				Cu			0.26	8.0E-02	20.86	2.6E+00
Zn			0.93				Zn			9.15	6.4E-01	0.48	4.8E-02
Sr	0.02	7.0E-03	0.09	7.5E-02	0.01	5.6E-04	Sr	101.4	9.4E+01	1.00	1.8E-01	0.17	6.8E-02
Rb	2.08	4.8E-01	1.65	1.1E+00	167.7	4.8E+01	Rb	6.21	5.1E-01	16.86	7.7E+00	2.45	9.4E-01
Y	1.32	1.4E-01	1.16	6.4E-01	0.54	3.9E-02	Y	0.40	8.0E-02	0.16	6.8E-02	0.03	3.3E-03
Zr	0.30	5.5E-02	11.29	1.5E-01	0.11	4.4E-02	Zr	11.42	4.8E+00	0.03	8.5E-03	3.55	6.9E-02
Nb	3.79	7.7E-02	0.67	7.9E-02	2.22	1.5E-01	Nb	96.95	2.4E+01	0.01	9.6E-05	167.5	6.3E+00

$D^{Pl/Sp}$							$D^{Pl/Crt}$						
	06	SD	48	SD	46	SD		01	SD	20	SD	142	SD
Sc	0.14	1.7E-02	0.17	6.5E-03	0.04	3.2E-03	Sc	0.06	5.9E-03	0.30	7.1E-02	0.21	1.2E-02
V	0.03	1.7E-02	0.04	6.5E-03	0.01	1.0E-02	V	9.0E-04	3.3E-04	0.01	1.5E-03	0.03	1.2E-02
Cr			0.00		0.01	1.7E-03	Cr			0.02	5.4E-04	0.05	1.3E-02
Co							Co					4.5E-04	3.7E-04
Ni			0.32		3.39	2.5E+00	Ni			0.23	1.0E-02	4.85	9.5E-01
Cu			2.16		1.34	2.7E-01	Cu			0.80	2.6E-01	3.26	1.4E+00
Zn			0.15		0.84	4.8E-02	Zn			6.77	5.5E-01	3.95	2.3E-01
Sr	0.77	1.2E-02	3.03	3.1E+00	0.46	1.5E-01	Sr	2504	1.6E+03	21.10	2.4E+00	79.46	4.7E+01
Rb	0.52	5.4E-02	25.98	2.2E+01	4.83	2.5E+00	Rb	44.79	1.3E+01	3.26	1.2E+00	0.16	5.4E-02
Y	0.03	9.6E-03	0.05	1.7E-02	4.2E-03	3.2E-03	Y	0.00	6.5E-04	0.00	7.0E-05	0.02	6.8E-03
Zr	0.01	5.3E-04	0.82	5.2E-02	3.0E-03	2.2E-03	Zr	0.04	2.2E-02	0.00	1.7E-04	2.78	9.5E-02
Nb	0.36	5.3E-02	5.54	2.1E-02	2.7E-03	2.1E-03	Nb	0.25	6.6E-02	0.00	3.2E-05	0.60	4.9E-01

Table 5.2(b) Average values ($n = 3$) of $D^{*Min 1/Min 2}$ for analysed mineral pairs. SD is the standard deviation at one sigma. No standard deviation represents single determinations. Blank indicates below detection limits or element not analyzed for one phase. *Italics* indicate Zr group.

$D^{*Amph/Trn}$	49	SD	06	SD	48	SD	46	SD	01	SD	20	SD	142	SD
Sc	16.08	5.6E-01	15.53	3.4E-01	12.21	7.7E-01	8.46	8.9E-01	6.69	6.7E-01	6.84	7.5E-01	14.13	8.0E-01
V	0.41	7.4E-03	1.19	1.0E-01	0.25	2.2E-02	0.48	5.0E-02	0.18	1.5E-02	0.33	1.0E-02	0.33	6.9E-02
Cr	0.87	5.7E-01	3.90	2.7E-01	2.17	4.0E-02	3.45	2.9E-01	1.56	4.3E-01	2.70	2.4E-01	0.20	5.9E-02
Co														
Ni	3.69	6.0E-01	5.84	7.7E-01	6.07	6.9E-01	2.56	1.9E-01	4.55	9.1E-01	1.71	2.4E-02	1.38	1.3E-01
Cu	1.25	1.1E-01	1.32	6.6E-01	1.70	1.7E-01	0.51	1.2E-01	0.41	1.3E-01	0.31	1.1E-02	71.52	5.3E+01
Zn	24.57	7.9E-01	19.82	6.2E+00	13.80	4.4E-01	9.13	6.9E-01	5.89	1.8E+00	10.13	3.0E-01	3.12	9.4E-01
Sr	2.25	9.9E-02	0.61	7.1E-02	0.38	1.1E-01	2.56	6.1E-02	1.78	1.1E+00	6.46	4.6E-01	0.22	3.4E-02
Rb	40.63	1.1E+01	15.96	3.3E+00	24.10	1.2E+01	191.0	3.0E+01	10.67	1.1E-02	62.05	1.2E+01	301.7	3.6E+01
Y	0.17	6.2E-02	0.64	1.8E-01	0.01	7.0E-05	0.02	6.4E-05	0.04	9.4E-04	0.01	3.7E-04	0.01	8.5E-04
Zr	0.19	1.1E-01	0.10	3.0E-02	0.04	8.7E-04	0.04	1.4E-02	0.15	2.2E-02	0.03	2.5E-03	0.02	7.5E-04
Nb	0.01	2.4E-03	7.2E-04	1.1E-04	1.0E-03	7.1E-06	3.1E-03	2.9E-04	0.04	1.6E-03	0.02	3.0E-03	0.03	7.3E-04
$D^{*Trn/Pl}$	49	SD	06	SD	48	SD	46	SD	01	SD	20	SD	142	SD
Sc	38.82	2.6E+00	6.29	7.6E-01	2.04	4.7E-01	29.84	4.9E-01	7.70	1.3E+00	14.69	3.1E-01	4.96	3.1E-01
V	15275	3.1E+03	605	3.7E+02	536	1.0E+01	5401	2.0E+03	15089	3.0E+03	1013	9.7E+01	1126	2.5E+02
Cr	2042	2.4E+02	340	6.2E+01	17223	5.4E+02	349	1.0E+02	1398	1.1E+02	320.0	8.1E+00	876	5.5E+01
Co														
Ni	4.69	2.8E-01	0.72	1.7E-01	0.27	1.6E-02	2.82	4.7E-01	3.13	7.0E-01	1.17	8.0E-02	1.03	2.9E-02
Cu	1.29	7.6E-02	0.58	2.1E-01	0.04	1.8E-03	0.39	7.8E-02	0.65	9.4E-02	0.45	1.0E-01	0.41	8.9E-02
Zn	0.15	4.4E-02	0.08	7.1E-04	0.18	3.6E-03	0.14	1.9E-03	0.42	8.6E-04	0.09	2.4E-04	0.04	1.8E-03
Sr	0.01	3.4E-03	0.04	2.1E-03	0.08	3.1E-02	0.01	4.8E-04	0.11	1.9E-03	0.01	6.0E-05	0.01	4.2E-04
Rb	2.38	1.2E-03	2.01	7.5E-01	0.28	1.4E-03	0.37	1.4E-01	0.72	2.5E-01	0.71	2.9E-01	0.36	5.6E-03
Y	2598	3.4E+02	764	3.5E+02	3006	2.1E+02	24574	3.2E+03	5418	1.8E+03	13169	1.7E+01	991	2.7E+02
Zr	4779	3.1E+02	711	7.2E+01	354	1.7E+01	10499	2.8E+03	2417	8.4E+02	5869	5.8E+02	50	1.4E+01
Nb	289729	8.5E+04	743671	5.4E+04	11188	2.9E+03	158461	1.4E+04	504248	1.2E+05	158686	2.4E+04	69203	2.2E+03

Table 5.2(b, continued) Average values ($n = 3$) of $D^{*Min 1/Min 2}$ for analysed mineral pairs. SD is the standard deviation at one sigma. No standard deviation represents single determinations. Blank indicates below detection limits or element not analyzed for one phase. *Italics* indicate Zr group.

D ^{*TmEp}							D ^{*TmGr}						
	06	SD	48	SD	46	SD		01	SD	20	SD	142	SD
Sc	0.03	7.6E-04	0.04	1.7E-03	0.07	5.7E-03		0.15	1.1E-02	0.89	1.6E-02	0.17	2.6E-02
V	0.20	5.6E-03	0.63	1.4E-02	0.72	5.7E-03		3.47	5.7E-01	1.31	5.7E-02	4.50	4.3E-01
Cr	0.17		0.09	6.7E-02	0.02	1.4E-04				0.21	1.1E-02	0.91	2.4E-01
Co													
Ni	0.23		0.13	3.3E-02	1.71	8.8E-03				0.62	8.1E-02	7.41	1.1E+00
Cu	0.28		0.17	7.8E-02	0.52	9.3E-02				0.80	7.9E-02	2.84	4.9E-02
Zn			0.04	6.6E-03	0.02	2.6E-04				1.04	5.0E-02	0.25	2.3E-02
Sr	0.04	2.3E-03	0.02	6.7E-03	0.00	1.5E-04		18.98	2.1E+00	0.54	4.1E-02	0.39	1.3E-01
Rb	0.65	1.5E-01	0.42	9.8E-02	7.96	6.4E+00		5.00	1.9E+00	1.31	2.2E-01	0.06	2.5E-02
Y	1.45	2.8E-02	61.00	1.7E+01	21.17	6.2E-01		25.99	8.7E+00	33.38	4.8E-01	13.40	7.5E-01
Zr	0.74	6.4E-02	3.78	2.4E+00	1.37	9.0E-01		59.88	1.2E+01	0.77	4.9E-02	30.94	5.9E+00
Nb	9852	3.7E+02	2434		338.0	4.3E+01		579.4	2.3E+02	0.39	6.9E-02	4.27	1.3E+00

D ^{*Ampl}														
	49	SD	06	SD	48	SD	46	SD	01	SD	20	SD	142	SD
Sc	515.4	1.3E+01	77.96	2.8E+00	28.31	1.3E+00	183.5	6.1E+00	56.40	2.7E+00	139.4	3.2E+01	68.80	3.6E+00
V	38838	1.0E+03	591.4	2.0E+02	165.9	5.0E+00	399.8	8.0E+01	2853	9.2E+02	266.7	4.9E+00	462.7	8.1E+01
Cr	754.2	8.2E+01	1042	2.8E+01	1244	1.7E+02	1529	2.8E+02	664.6	3.4E+02	185.2	6.3E+01	116.7	1.8E+00
Co	241.4	3.1E-01			89.75								12.85	3.8E+00
Ni	33.78	1.1E+00	6.10	5.2E-01	1.13	4.4E-02	12.97	1.0E+00	4.50	2.7E+00	3.60	3.1E-01	1.80	2.1E-02
Cu	2.36	1.0E-01	2.49	1.1E+00	0.05	1.3E-04	0.21	8.0E-02	0.28	3.3E-03	0.11	9.1E-03	1.81	1.3E-01
Zn	4.48	2.0E-01	2.27	2.4E-02	3.01	9.2E-01	1.32	3.9E-02	1.27	1.4E-01	1.00	2.0E-02	0.10	1.6E-02
Sr	0.04	2.9E-03	0.02	1.8E-04	0.02	5.7E-03	0.02	3.7E-03	0.05	9.0E-03	0.05	2.0E-04	1.8E-03	1.8E-05
Rb	133.2	4.4E+01	9.11	6.4E-01	0.42	3.4E-01	270.0	1.0E+02	0.69	9.1E-02	13.43	1.0E+00	120.9	5.0E+00
Y	216.6	2.8E+01	283.7	3.3E+01	63.56	5.2E+00	204.8	6.8E+01	181.4	2.8E+01	146.8	3.1E+01	4.11	6.2E-01
Zr	334.7	1.0E+02	78.53	9.5E+00	22.72	2.1E+00	251.2	4.3E+00	264.5	2.1E+01	119.9	5.5E+00	1.94	3.8E-01
Nb	13326	1.2E+02	654.3	6.0E+00	1.61	1.5E-01	351.2	5.1E+01	7915	2.0E+03	2633	4.4E+02	1788	2.7E+01

Table 5.2(b, continued) Average values ($n = 3$) of $D^{*Min 1/Min 2}$ for analysed mineral pairs. SD is the standard deviation at one sigma. No standard deviation represents single determinations. Blank indicates below detection limits or element not analyzed for one phase. *Italics indicate Zr group.*

	$D^{*Amphib}$						$D^{*Amph/Grt}$					
	06	SD	48	SD	46	SD	01	SD	20	SD	142	SD
Sc	0.53	4.0E-02	0.36	1.8E-03	1.34	1.4E-03	1.46	6.6E-02	5.98	1.6E+00	2.53	1.7E-01
V	0.26	1.0E-02	0.09	1.7E-02	0.30	4.5E-02	0.63	1.4E-01	0.60	8.7E-02	1.01	7.9E-02
Cr			0.02	5.2E-03					0.18	7.6E-02	0.23	4.8E-02
Co			12.32	5.8E+00							0.16	3.7E-02
Ni			0.59	2.2E-01					1.21	5.0E-02	11.17	7.0E-01
Cu			0.22	1.0E-01					0.24	2.3E-03	25.76	3.5E+00
Zn			0.29	1.3E-01					10.22	1.2E-01	0.63	2.2E-02
Sr	0.03	1.9E-03	0.10	6.3E-02	0.01	1.5E-03	30.89	2.6E+00	4.07	6.9E-01	0.10	3.6E-02
Rb	6.20	7.2E-01	5.11	1.7E+00	1612	1.8E+01	38.10	1.5E+00	145.9	1.4E+01	12.42	2.4E+00
Y	1.34	1.2E-01	0.39	1.4E-01	0.38	1.4E-02	0.80	6.8E-02	0.31	8.4E-02	0.08	1.8E-03
Zr	0.04	3.5E-03	0.05	9.7E-03	0.03	1.4E-02	8.94	1.1E+00	0.03	5.2E-03	0.98	8.3E-03
Nb	0.04	2.7E-02	5.8E-05	7.3E-06	0.03	2.1E-02	163.9	1.6E+01	0.02	7.7E-03	0.11	5.7E-03

	D^{*Plag}						D^{*Plag}					
	06	SD	48	SD	46	SD	01	SD	20	SD	142	SD
Sc	6.7E-03	7.0E-05	1.3E-02	5.3E-04	2.4E-03	3.5E-04	0.01	2.8E-04	0.04	6.0E-03	0.04	6.5E-03
V	1.5E-03	1.3E-04	1.4E-03	3.0E-04	8.2E-04	2.5E-04	2.1E-04	5.2E-05	8.3E-04	1.3E-04	2.8E-03	5.2E-05
Cr	9.5E-05		3.2E-06						7.2E-04	4.1E-05	1.3E-03	9.1E-05
Co											0.01	
Ni			1.1E-01		4.7E-01	2.7E-02			0.44	2.7E-02	5.89	7.2E-01
Cu			1.93		2.16	5.3E-01			4.91	1.6E-01	5.04	5.0E-01
Zn			3.6E-02		1.7E-01	1.0E-02			13.84	1.1E+00	7.14	3.3E-01
Sr	9.7E-01	5.7E-03	1.1E+00	1.4E-01	5.8E-01	9.0E-03	14232	5.8E+03	96.44	2.8E+00	55.56	2.0E+01
Rb	5.1E-01	3.9E-02	2.5E+01	1.3E+01	2.5E+00	8.8E-01	64.06	6.9E+00	7.13	1.3E+00	0.10	1.6E-02
Y	4.4E-03	2.4E-04	2.3E-02	2.6E-03	2.1E-03	6.5E-04	0.00	6.0E-05	2.4E-03	1.6E-04	0.02	8.8E-03
Zr	2.0E-02	1.5E-02	1.7E-01	1.3E-01	2.0E-04	4.0E-05	0.02	9.2E-03	2.5E-04	9.6E-05	0.17	1.3E-01
Nb	6.7E-03	5.9E-04	2.8E-04	2.1E-04	3.5E-05	2.6E-05	0.02	2.3E-03	7.2E-06	1.6E-06	4.5E-05	1.3E-05

Ca amphibole/Titanite pairs

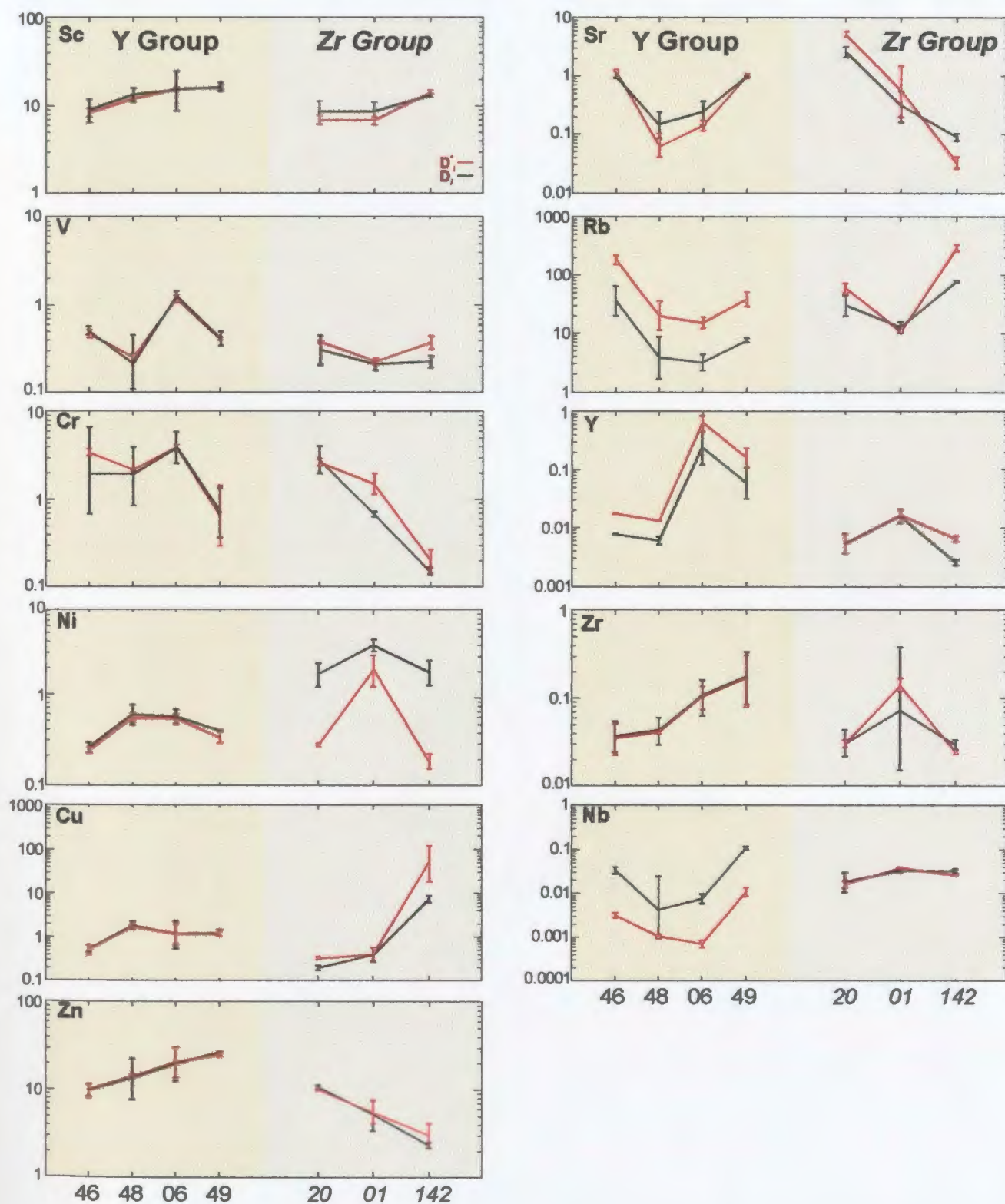


Figure 5.3 Distribution coefficients (D and D*) for mineral pairs for selected trace elements. Y group samples arranged in order of decreasing modal epidote. Zr group samples (*italicized*) comprise the biotite-amphibolite assemblage. Error bars represent 1 standard deviation.

Titanite/Plagioclase pairs

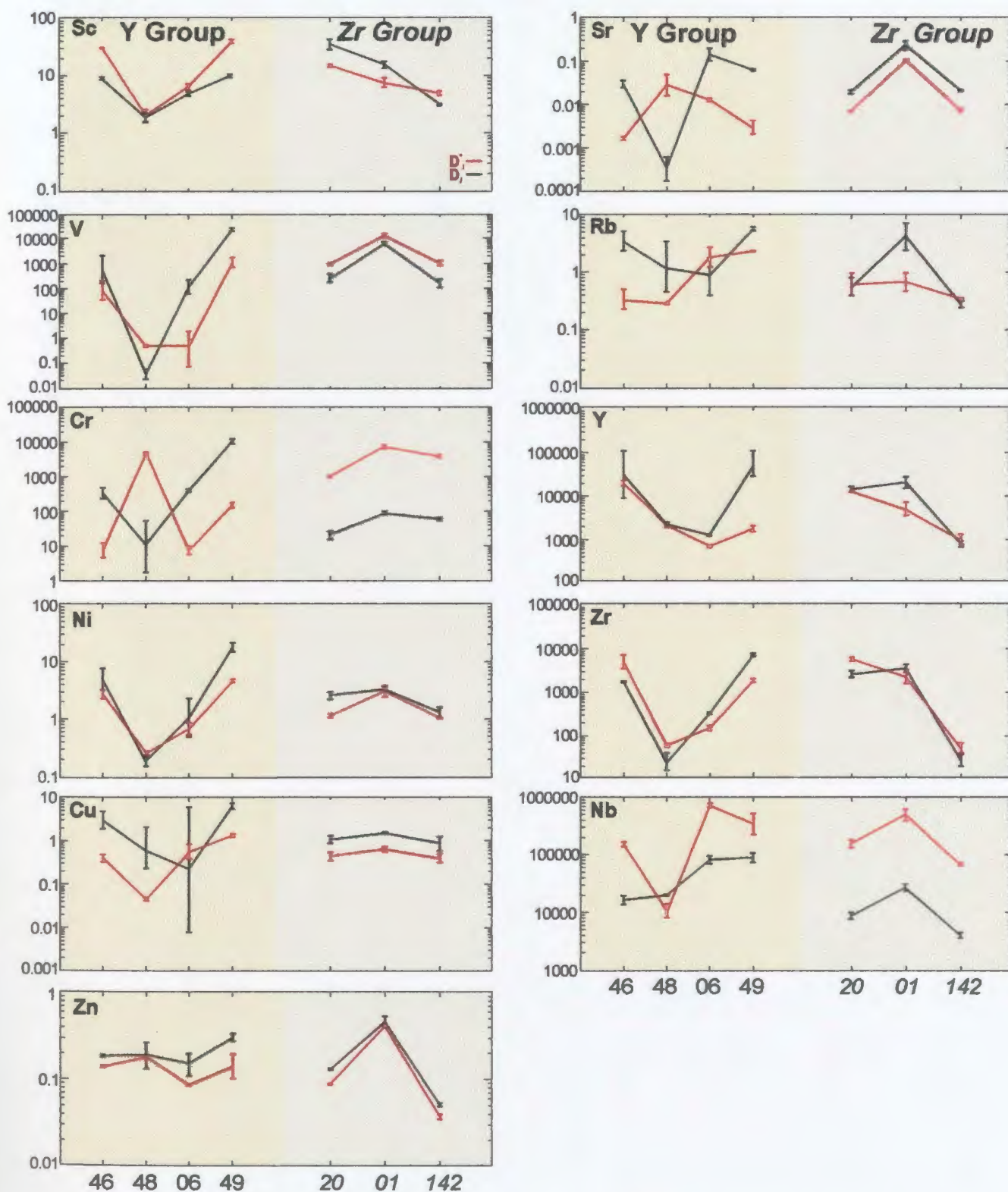


Figure 5.3 (continued). Distribution coefficients (D and D^*) for mineral pairs for selected trace elements. Y group samples arranged in order of decreasing modal epidote. Zr group samples (*italicized*) comprise the biotite-amphibolite assemblage. Error bars represent 1 standard deviation.

Ca amphibole/Plagioclase pairs

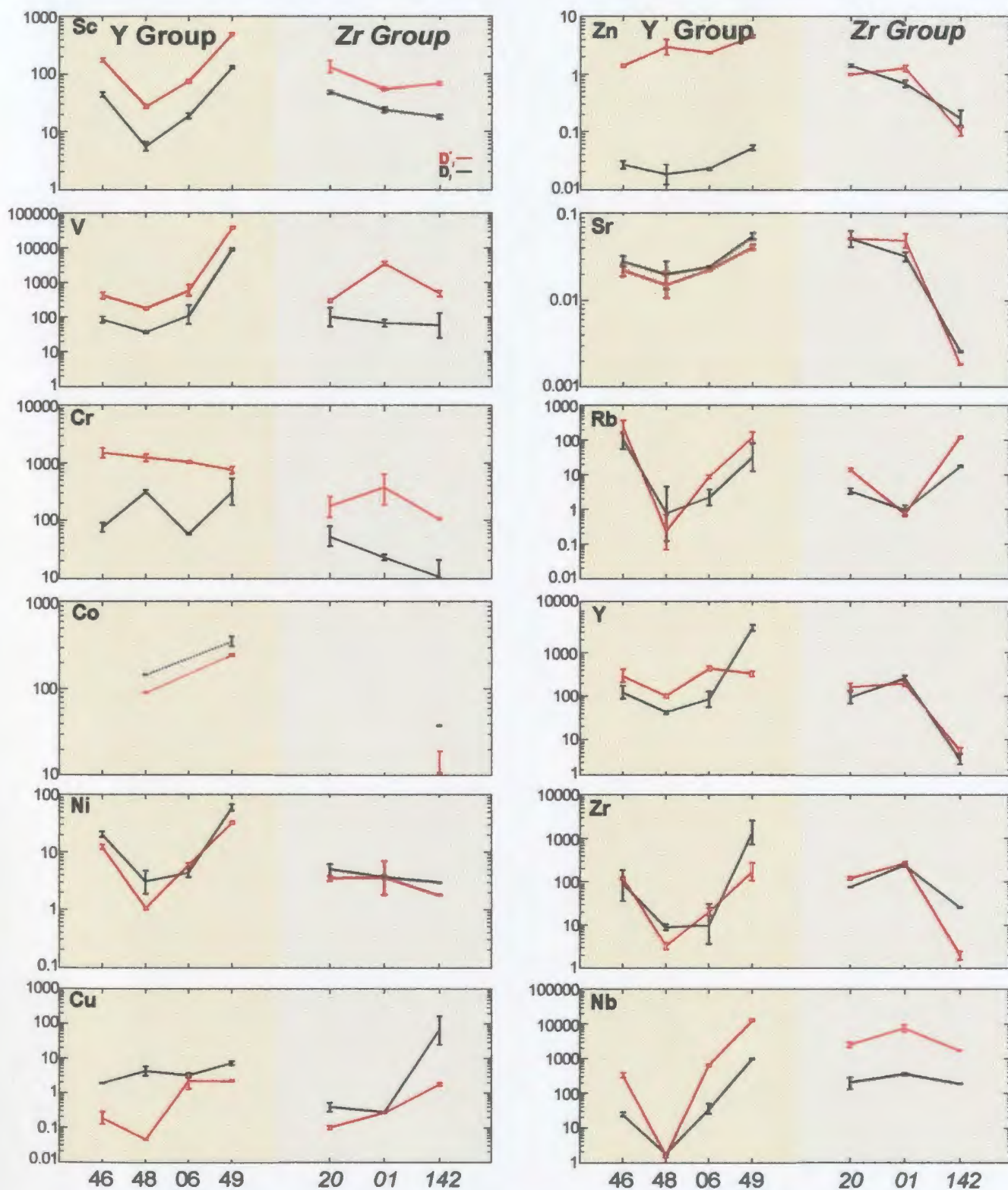


Figure 5.3 (continued). Distribution coefficients (D and D^*) for mineral pairs for selected trace elements. Y group samples arranged in order of decreasing modal epidote. Zr group samples (*italicized*) comprise the biotite-amphibolite assemblage. Error bars represent 1 standard deviation.

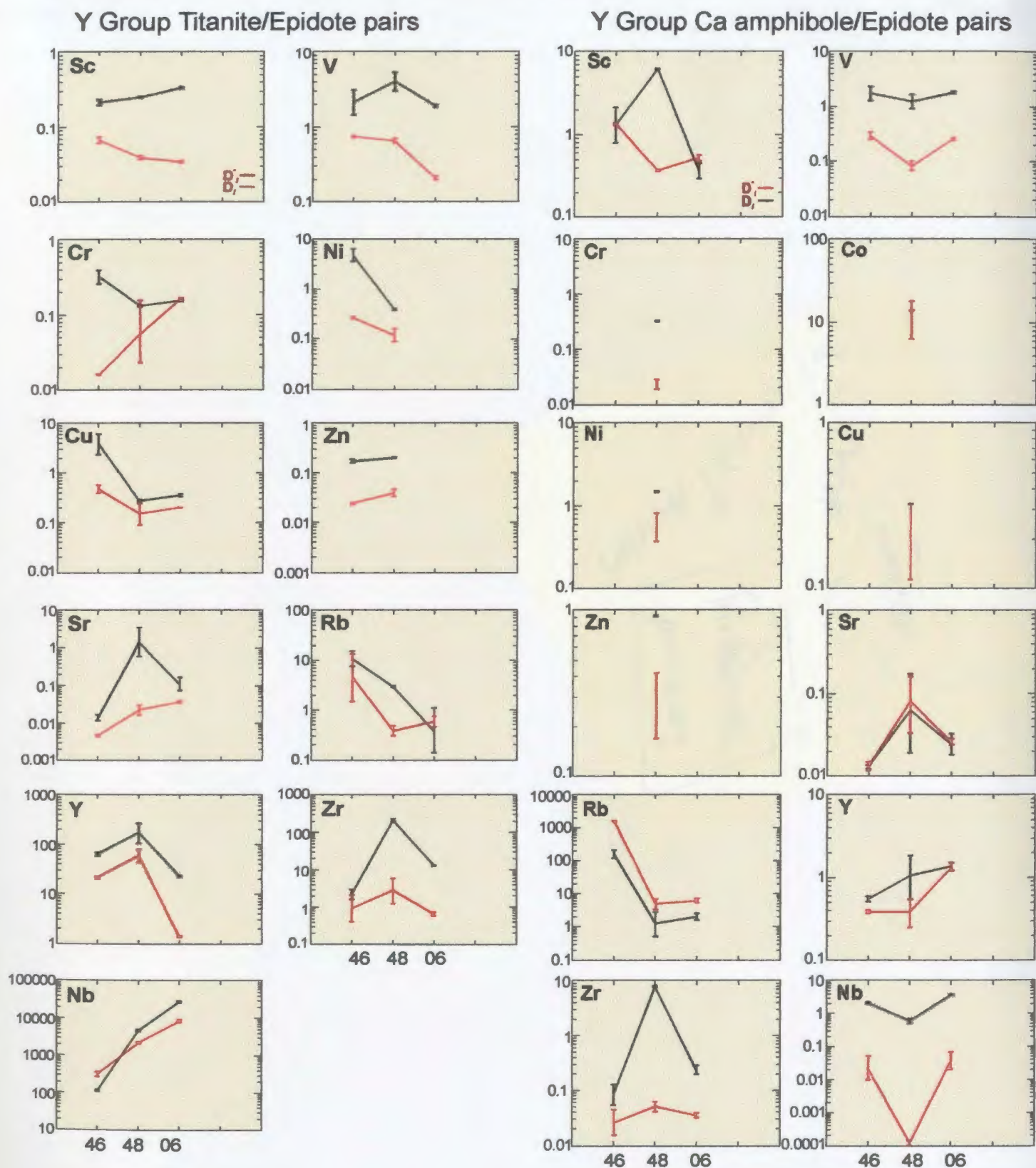


Figure 5.3 (continued). Distribution coefficients (D and D*) for mineral pairs for selected trace elements. Y group samples arranged in order of decreasing modal epidote. Error bars represent 1 standard deviation.

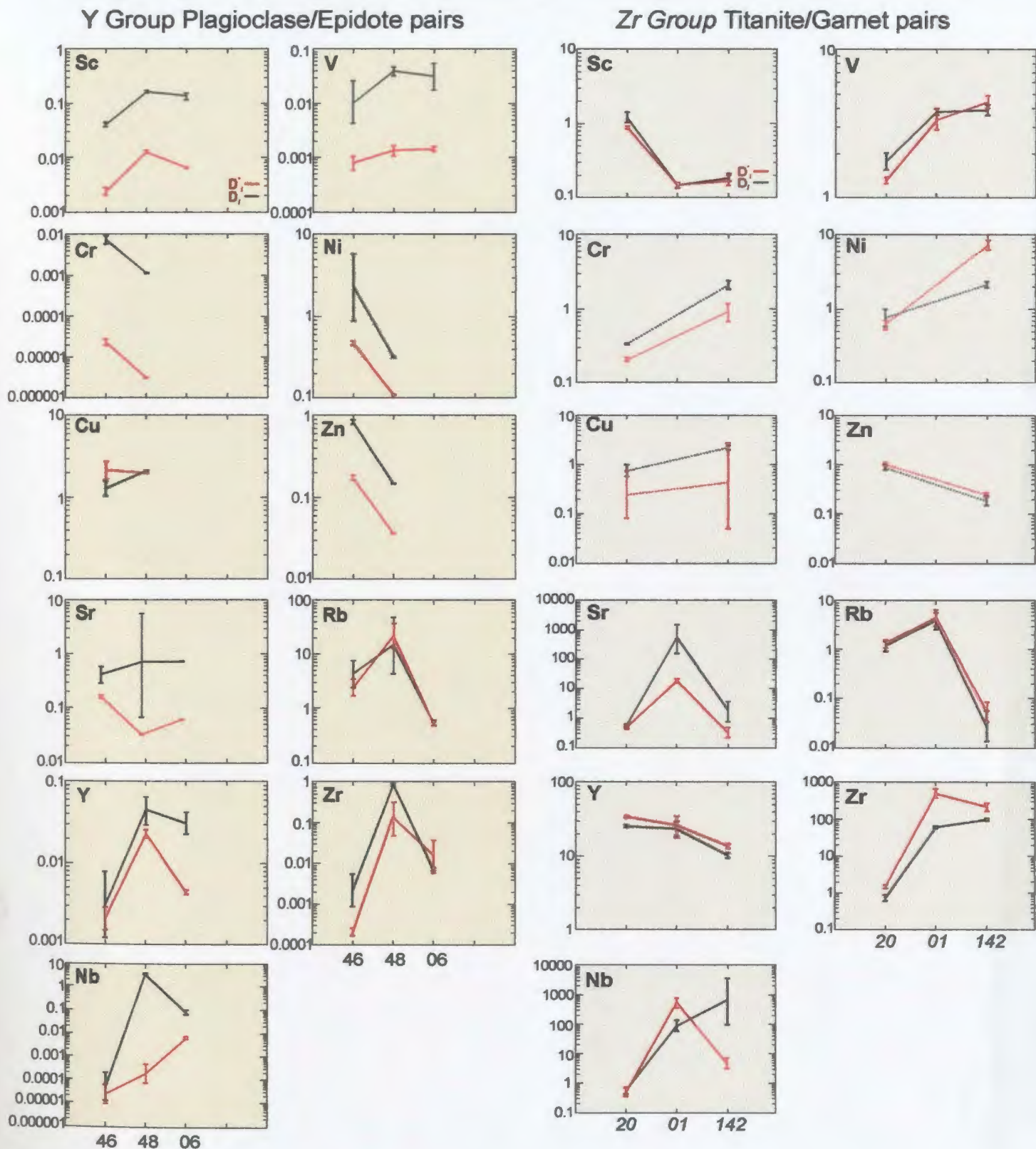


Figure 5.3 (continued). Distribution coefficients (D and D*) for mineral pairs for selected trace elements. Y group samples arranged in order of decreasing modal epidote. Zr group samples (*italicized*) comprise the biotite-amphibolite assemblage. Error bars represent 1 standard deviation.

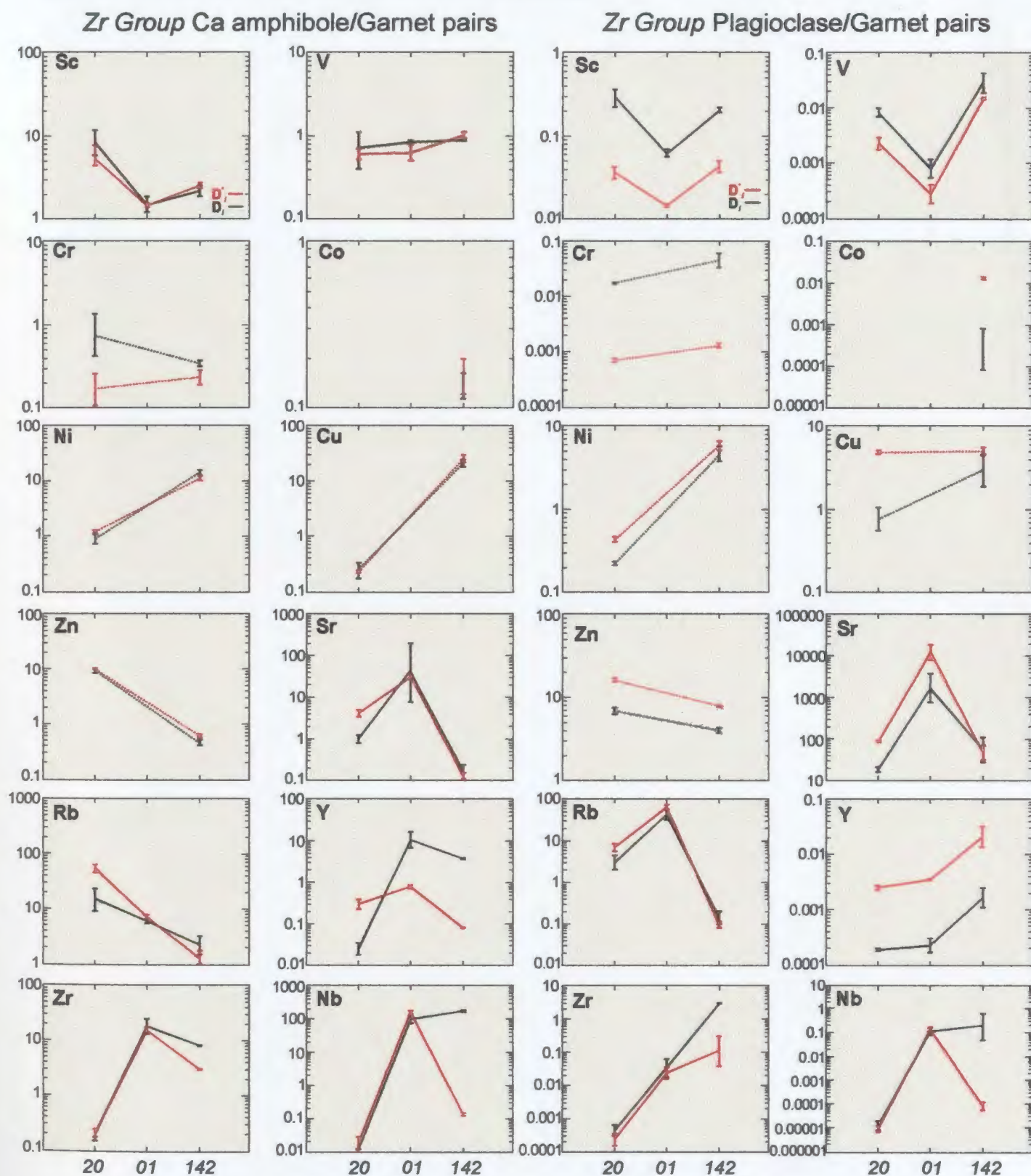


Figure 5.3 (continued). Distribution coefficients (D and D^*) for mineral pairs for selected trace elements. Zr group samples (*italicized*) comprise the biotite-amphibolite assemblage. Error bars represent 1 standard deviation.

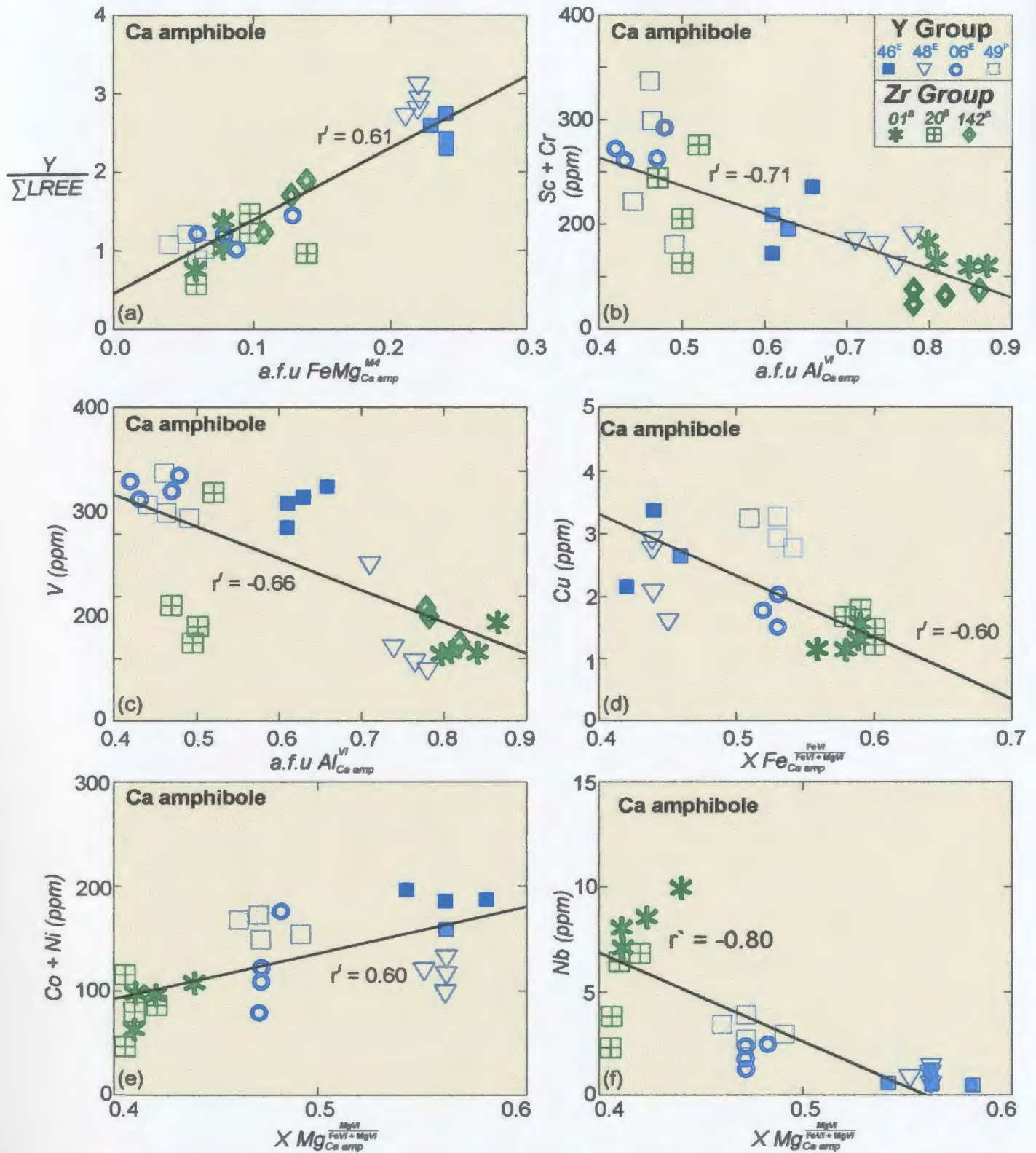


Figure 5.4 (a-f) Bivariate plots showing correlations between major-element composition and selected trace-element concentration in analysed phases. r' denotes Spearman correlation coefficient.

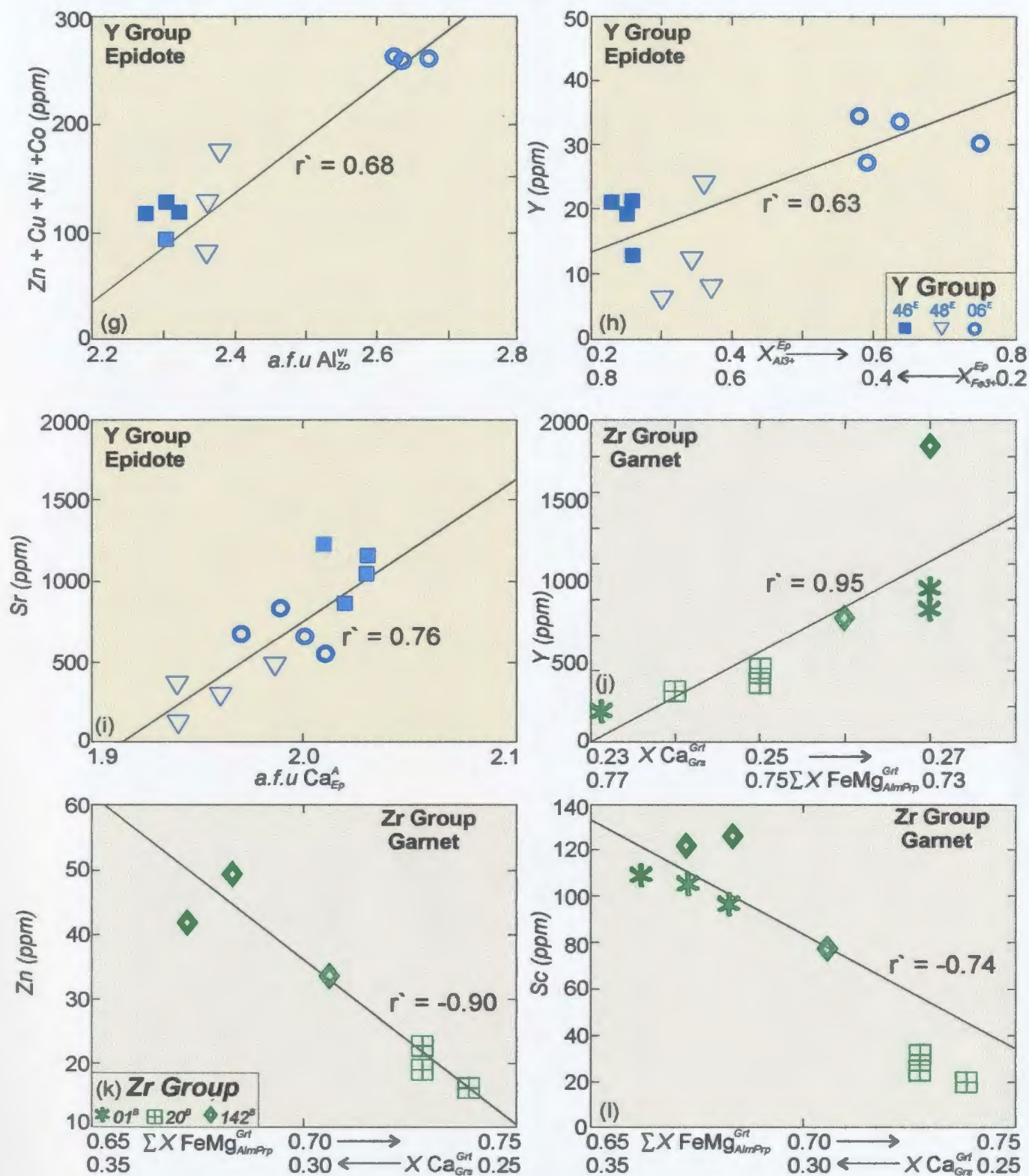


Figure 5.4 (g-l) Bivariate plots showing correlations between major-element composition and selected trace-element concentration in analysed phases. r' denotes Spearman correlation coefficient.

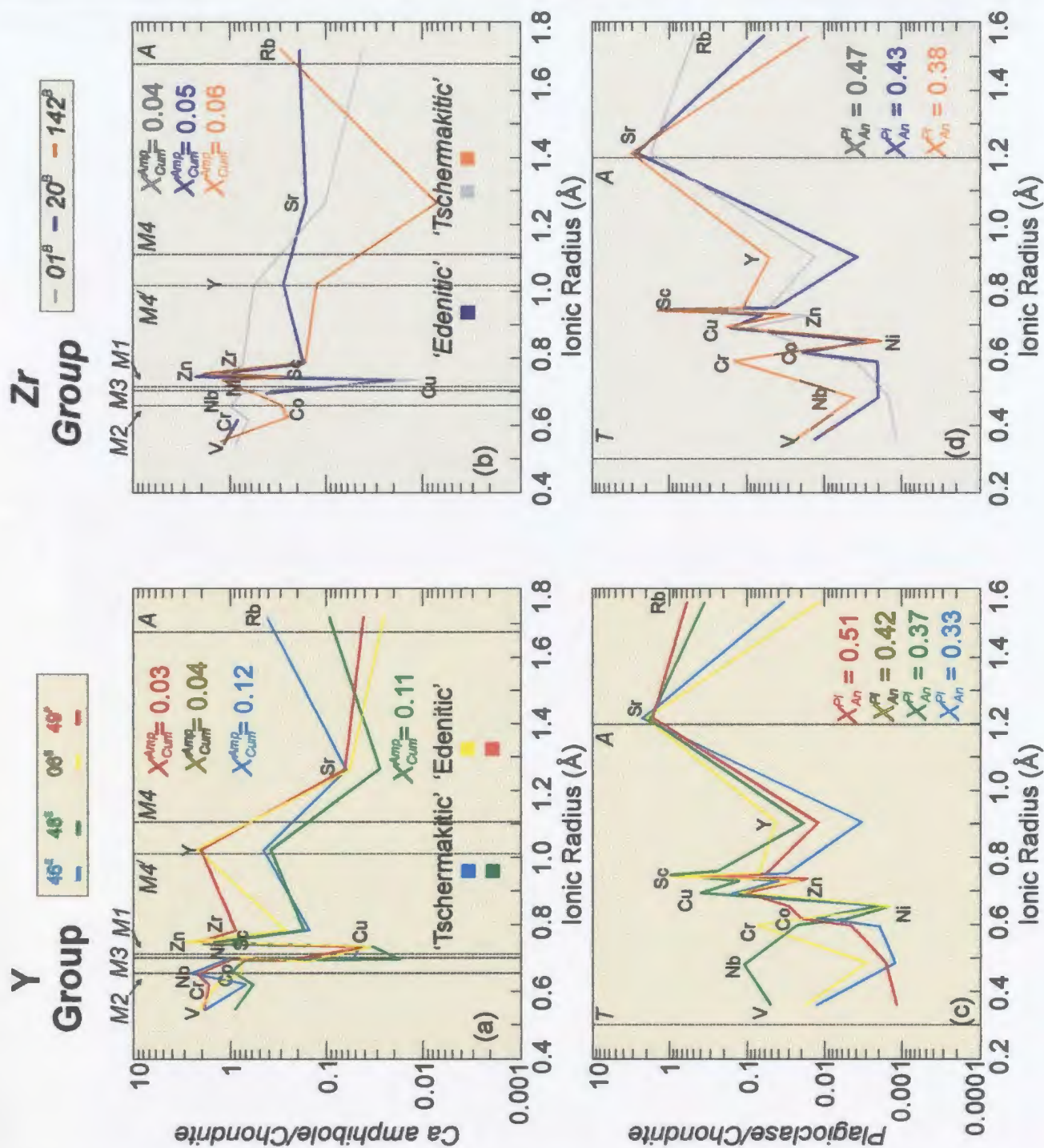


Figure 5.5 Chondrite-normalized trace-element abundance *versus* ionic radius curves for Y and Zr groups in: a-b) Ca amphibole and c-d) plagioclase. Major-element compositions of analysed phases indicated as mole fractions. Dashed lines are optimal site radius (r_o) obtained by subtracting the ionic radius of the O^{2-} anion (1.38\AA) from the observed average cation-oxygen bond length (Smyth & Bish, 1988). Chondrite values from Taylor and McLennan (1985).

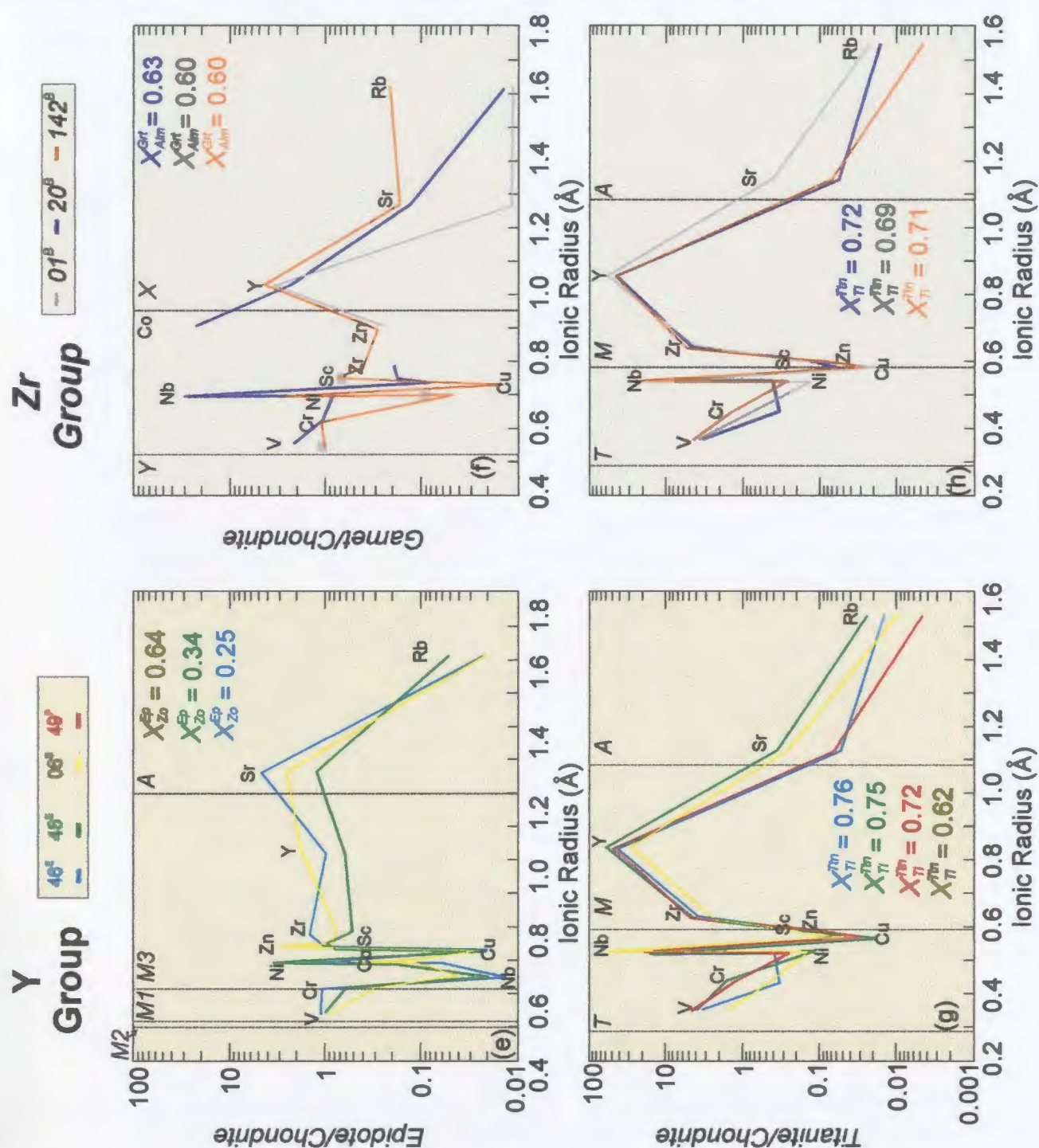


Figure 5.5 (continued). Chondrite-normalized trace-element abundance *versus* ionic radius curves for Y and Zr groups in: e) epidote; f) garnet and g-h) titanite. Major-element compositions of analysed phases indicated as mole fractions. Dashed lines are optimal site radius (r_o) obtained by subtracting the ionic radius of the O^{2-} anion cation (1.38\AA) from the observed average cation-oxygen bond length (Smyth & Bish, 1988). Chondrite values from Taylor and McLennan (1985).

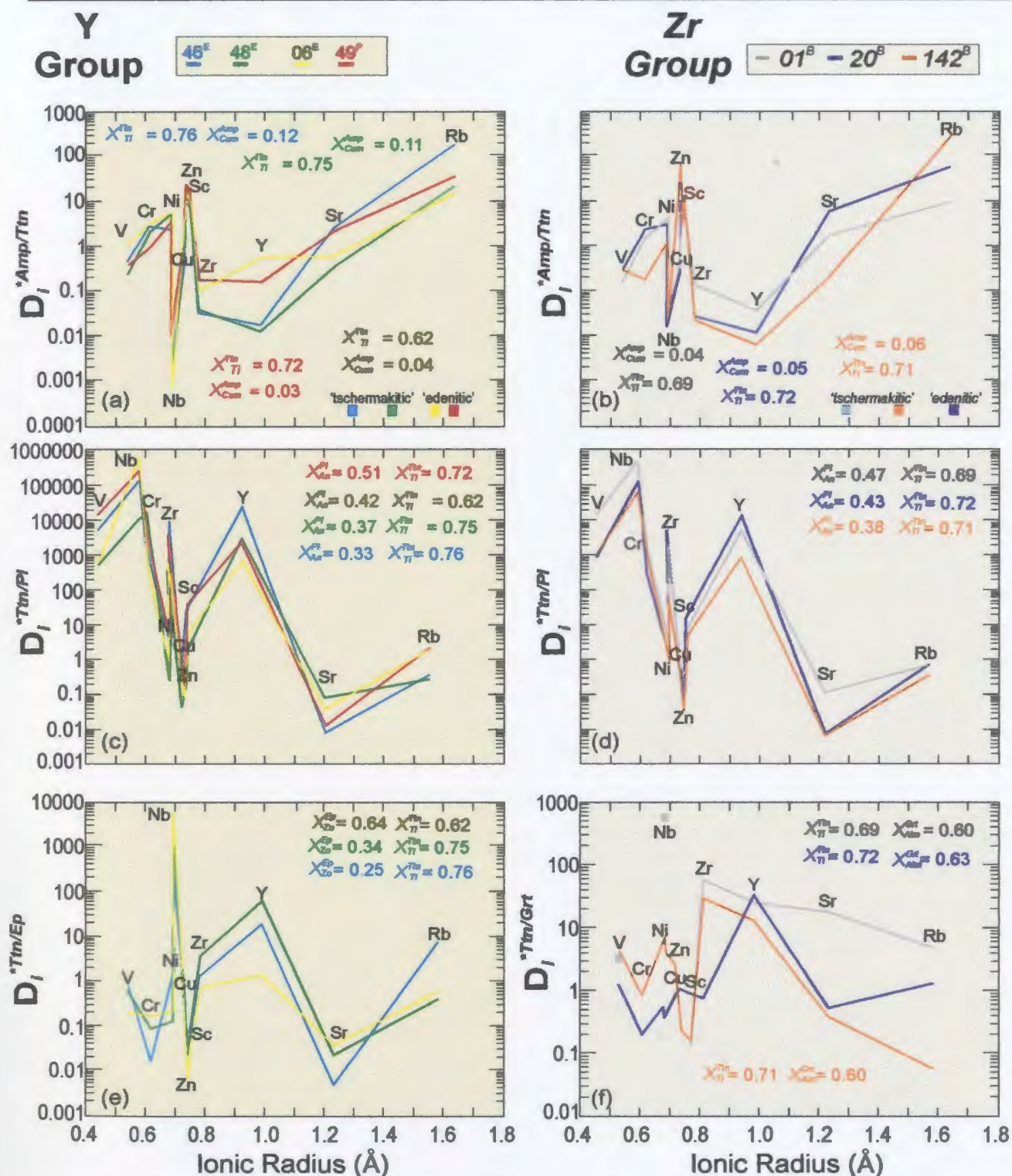


Figure 5.6(a-f) X_i mineral 1/ X_i mineral 2 (D_i^*) versus ionic radius plots (Onuma-type) for mineral pairs analysed by LAM-ICP-MS. Appropriate mole fractions shown for each phase. Superscripts denote rock type: E is epidote amphibolite, P is plagioclase amphibolite and B is biotite amphibolite.

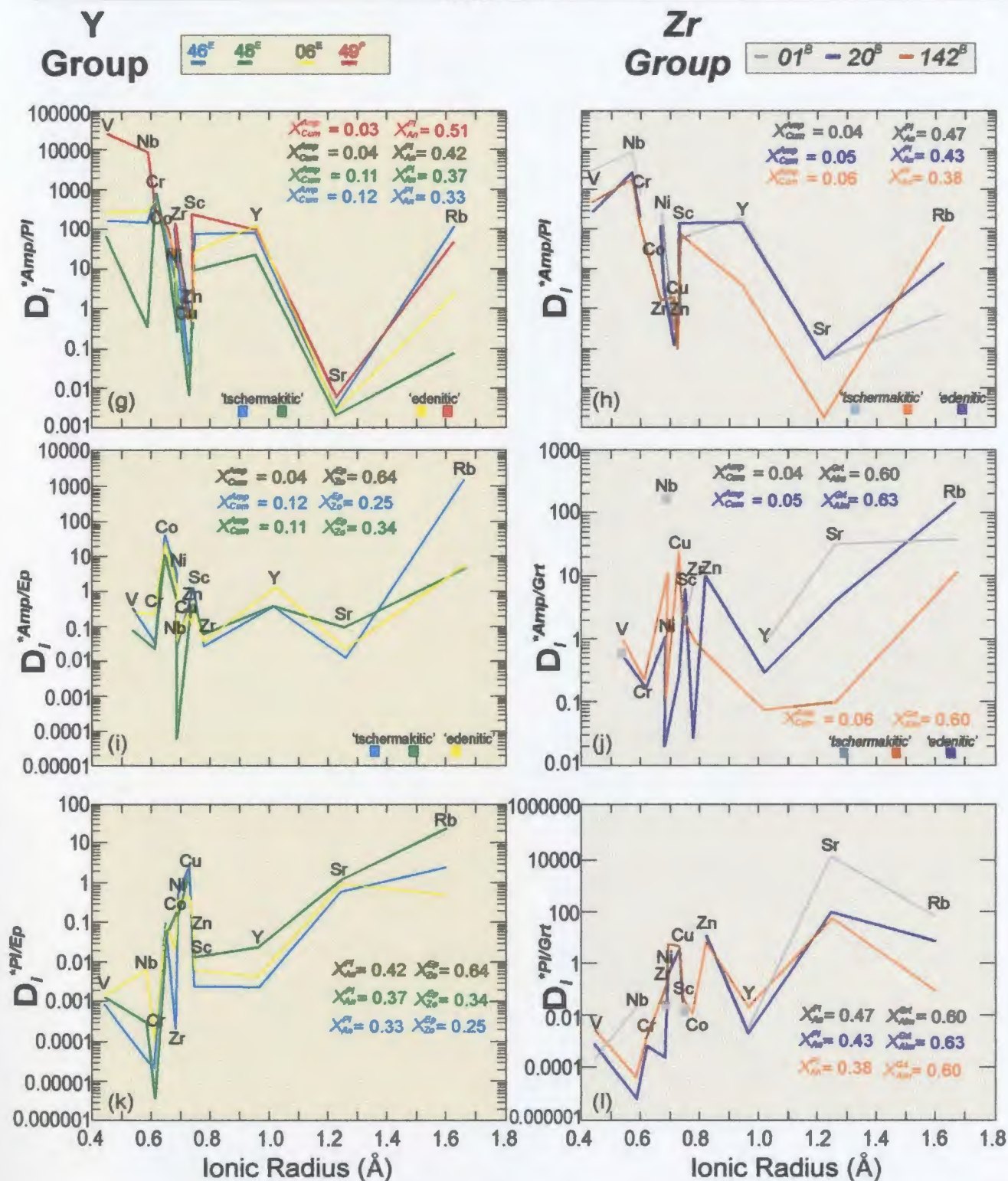


Figure 5.6 (g-l) X_1 mineral 1/ X_1 mineral 2 (D_1^*) versus ionic radius plots (Onuma-type) for mineral pairs analysed by LAM-ICP-MS. Appropriate mole fractions shown for each phase. Superscripts denote rock type: E is epidote amphibolite, P is plagioclase amphibolite and B is biotite amphibolite.

Chapter 6: Mass-Balance and Reaction-Balance Calculations

6.1 Introduction

Mass-balance calculations have been used previously to determine the roles of specific phases as reservoirs or carriers for certain trace elements in metamorphic rocks (e.g., Sorensen and Grossman, 1989; Tribuzio *et al.*, 1996; Eggins *et al.*, 1998; Nagasaki and Enami, 1998; Zack *et al.*, 2002). Such calculations require knowledge of both the concentrations and modal abundances of *all* coexisting phases to calculate a reconstructed whole-rock concentration. The results are then compared with the measured whole-rock major- and trace-element concentrations in the same samples, which serve as an independent quality control. In this study, a variation of the method employed by Zack *et al.* (2002) was followed to perform mass balances for *REEs* and other trace elements (Sc, V, Cr, Ni, Cu, Zn, Sr, Rb, Y, Zr, Nb) on four Y group samples (#s 46, 48, 06, 49) in order to evaluate the relative importance of individual minerals as carriers for the trace elements of interest in epidote-amphibolite and plagioclase-amphibolite assemblages.

In the second part of the chapter, reaction-balance calculations using mineral compositions from epidote-amphibolite and plagioclase-amphibolite assemblages (Y group) from either side of the inferred epidote-out isograd were carried out by algebraic

analysis, utilizing the singular value decomposition technique described by Fisher (1989). This method permits determination of the variance of the system that defines the inferred reaction and enables calculation of stoichiometric coefficients in a multicomponent mineral / composition matrix. Due to the absence of trace-element analyses of apatite and biotite in Zr group samples, no mass balances were performed for this suite.

6.2 Modal Abundance Data

The accurate estimation of the modal abundances of *all* coexisting minerals is as significant as the accurate determination of mineral trace-element concentration data for the calculation of a representative mass balance. Modal abundances of samples for which mass balances were calculated were initially determined using visual estimates and were subsequently refined with the computer software MODAN (Paktunc, 1998) and bulk TiO₂ concentrations (see 2.3.3). Modal estimates for major phases (e.g., Ca amphibole, plagioclase, epidote) are generally straightforward, and can often be approximately visually estimated. However, for minor or trace phases such as titanite, which generally constitutes less than 5 modal percent of a sample, accurate modal estimates can be difficult. Since titanite is known to commonly be enriched in trace elements, it may have major implications for the mass balance of trace elements in many rocks. Hence an accurate estimate of its modal abundance is essential for an accurate mass balance. For example, in a comparable study, Zack *et al.* (2001) showed that rutile,

despite having a modal abundance of only 1.1%, accounted for approximately 90% of the whole-rock budget of selected HFSEs (Nb, Ta, W, Ti, Sb) in eclogites from Trescolmen, Central Alps. The results presented in the following section show that titanite is indeed an important carrier of *REEs* and HFSEs in the analysed samples.

6.3 Bulk Composition

To evaluate the relative importance of each of the phases Ca amphibole, plagioclase, epidote and titanite as a carrier for *REEs* and the other selected trace elements in epidote-amphibolite and plagioclase-amphibolite assemblages, four mass balance calculations were performed on samples from the Y group. Three of these samples equilibrated as epidote-amphibolite (samples 46, 48 and 06 in order of decreasing modal epidote); the remaining sample (49) equilibrated as a plagioclase amphibolite (i.e., it is epidote-free and is referred to herein as plagioclase amphibolite). All samples contain less than 5 % modal quartz, which is assumed to be pure (i.e., contains no *REEs* or other trace elements).

In terms of their major-element bulk compositions, the samples cluster together in the field of typical metabasites in ACF composition space (Figure 6.1a). With respect to trace-element compositions, the four samples have remarkably similar abundances of *REEs* (Figure 6.1b) and comparable concentrations of most analysed trace elements (Figure 6.1c). In detail, Figure 6.1a shows that two of the epidote amphibolites (samples

46 and 48, denoted bulk composition A) are slightly more calcic than the remaining two samples (06, epidote amphibolite and 49, plagioclase amphibolite: denoted bulk composition B). These results are similar to data published by Jamieson (1979) for samples from the same area (shown on Figure 6.1a), which indicate that the presence and the modal abundance of epidote may be to some extent controlled by bulk CaO. The very similar chondrite-normalized bulk-rock *REE* contents of the four samples (Figure 6.1b) indicate that metamorphism was essentially isochemical with respect to the *REE*. With respect to other trace elements, the bulk-rock, chondrite-normalized, trace-element diagram (Figure 6.1c) shows that samples fall into two groups, again corresponding to bulk compositions A and B described above. Samples of bulk composition A, which are slightly more calcic, have higher chondrite-normalized abundances of Sr, V, Cr and Zr and lower abundances of Nb.

In order to explore the possible role of major-element composition in controlling epidote stability across the epidote-out isograd, the small differences in major-element concentrations among the four samples are examined in more detail in Fig. 6.1d-e, particularly with respect to concentrations of the major oxides CaO, Na₂O, Al₂O₃ and Fe₂O₃ (Figure 6.1d), and the ratios of their molecular proportions (Figure 6.1e), which might be expected to exert some control the modal abundance of epidote. Figure 6.1d illustrates that there are slight decreases in bulk-rock concentrations of CaO, Al₂O₃, and Fe₂O₃ with decreasing modal epidote, whereas Na₂O remains almost constant in analysed

samples. However, these variations in major oxides do not match the consistent decline in modal epidote, suggesting that epidote abundance is not exclusively controlled by bulk-rock composition. More significant perhaps to the stability of epidote are the ratios of the molecular proportions of these elements (Figure 6.1d). This figure shows that despite the very limited variations in both $\text{Ca} / \text{Ca} + \text{Na}$ and $\text{Fe}^{3+} / \text{Fe}^{3+} + \text{Al}^{3+}$ ratios, there is a precipitous decline in modal epidote in the vicinity of epidote-out isograd. These data are compatible with the interpretation that the isograd is indeed a result of changing metamorphic grade, as inferred by Jamieson (1979), even though the isogradic reaction is imposed on samples of slightly variable bulk composition. This effect is further evaluated in section 6.6.

It is also appropriate here to consider the relationship between bulk-rock composition and the major-element chemistry of Ca amphibole. As noted, Figure 6.1a shows that samples 46 and 48 (10 and 7 modal % epidote respectively) are slightly more enriched in CaO than samples 06 and 49 (3 and 0% modal epidote respectively). Comparison with Figure 3.14a shows that the Ca amphibole in samples 46 and 48 is 'cummingtonite-rich', whereas that in samples 06 and 49 it is 'cummingtonite-poor', the reverse of what would be expected when the bulk CaO contents of the samples are considered. This paradoxical result is interpreted in terms of a changing effective bulk composition (EBC) available to Ca amphibole during growth, as follows. In relatively calcium-rich bulk compositions (samples 46 and 48, A on Figure 6.1a), it is inferred that

early formed epidote sequestered Ca and Al so as to effectively deplete the remaining bulk composition in these elements, leading to the passive enrichment of the matrix in FeMg and the formation of cummingtonite-rich Ca amphibole (see arrow, Fig. 6.1a). In contrast, in relatively calcium-poor bulk compositions (samples 06 and 49, B on Figure 6.1a), early crystallization of epidote was suppressed, permitting equilibrium partitioning of Ca among epidote, plagioclase and Ca amphibole, leading to the formation of Ca-rich (cummingtonite-poor) Ca amphibole and Ca enrichment of plagioclase. Thus the EBC available to Ca amphibole at bulk composition A was less Ca-rich than the true bulk composition, lessening the apparent compositional contrast among the samples for this phase. This model implies that epidote nucleated before Ca amphibole in the epidote-amphibolite facies assemblage, which is consistent with the observation that epidote coexists with chlorite in the absence of Ca amphibole in some greenschist-facies samples. In summary, there are small differences in the bulk compositions of the four samples, and of the EBCs available to minerals at different stages during metamorphism. Thus, these differences may have affected the distribution and modal abundance of epidote among analysed samples, an effect that is evaluated by retaining reference to bulk compositions A and B in the mass-balance section which follows, and which is subsequently further evaluated using algebraic techniques in the reaction-balancing analysis (section 6.6).

Having qualitatively assessed the scale of major- and trace-element variation in

bulk chemistry of the four samples, the roles of the four minerals as carriers of the *REE* and other trace elements within each sample can now be discussed.

6.4 *REE* Mass-Balance Calculations

For clarity, mass-balance results are presented separately for the *REE* and other trace elements. The data on which the *REE* mass-balance calculations are based are presented in Table 6.1, and the results are illustrated in tripartite figures comprising: (i) a comparison of the reconstructed whole-rock *REE* concentrations (mineral modal abundance multiplied by average *REE* mineral concentration) with the measured whole-rock *REE* concentration (i.e., yielding a measure of the *absolute error* of the mass balance); (ii) a bar graph illustrating the *relative errors* associated with the mass balance, represented as the percent difference between the reconstructed *REE* concentration and the measured whole-rock concentration for each *REE*; and (iii) a stacked bar plot that illustrates the distribution of the calculated whole-rock *REE* concentrations among the phases as the relative proportions of the reconstructed whole-rock abundance.

6.4.1 Epidote Amphibolites: (10-3 modal % epidote)

Results for *sample 46 (10 modal % epidote, bulk composition A)* are presented in Table 6.1 and illustrated in Figure 6.2a. In Figure 6.2a(i), it can be seen that reconstructed *REE* concentrations are comparable to the measured bulk-rock *REE*

abundances, and Figure 6.2a(ii) shows that, although generally slightly underestimated, they are within approximately 20% of the measured bulk-rock *REE* concentrations for all elements except Ho, which is within 31% . Figure 6.2a(iii) shows that despite a modal abundance of only 2%, titanite is the dominant carrier (50-80%) for all *REEs*. Epidote (10 modal %) carries between 10 to 15 % of the *LREE* and approximately 30 % of the Eu budget, and Ca amphibole (65 modal %) sequesters approximately 5 to 30% of the *REE* with a progressive increase from *LREE* to *HREE*. Plagioclase (18 modal %) accounts for minor (< 5%) amounts of La and Eu, but otherwise is an insignificant *REE* carrier. Considering the role of titanite in sequestering most of the *REEs* in this sample (Figure 6.2a(iii)), the slight deficit in the reconstructed whole-rock budgets for most *REEs* may be due to a minor underestimation of the modal abundance of titanite in this sample or the presence of an unrecognized *REE* bearing phase.

Results for *sample 48 (7 modal % epidote, bulk composition A)*, presented in Table 6.1 and illustrated in Figure 6.2b, are similar to those for sample 46, except that the reconstructed bulk-rock *REE* concentrations fit the measured bulk-rock concentrations more closely. Reconstructed concentrations are within 10% of the measured bulk-rock *REE* abundances for all elements except for La, Pr and Eu, which are within 17%. The excess in the reconstructed concentrations of La and Eu may be due to a small overestimate in the modal abundance of epidote. Despite a modal abundance of only 2 %, titanite is again the dominant carrier (50-80%) for all *REEs*. Epidote (7

modal %) carries between 10 to 25% of the *LREE* and Ca amphibole (74 modal %) holds approximately 5 to 25% of the *REE*, again with a progressive increase from *LREE* to *HREE*. Plagioclase (15 modal %) accounts for minor amounts (< 5%) of all *REE* and approximately 15% of the Eu. In contrast to the significant role of epidote as a Eu sink in sample 46, where it accounts for approximately 30% of the reconstructed Eu concentration, epidote from sample 48 accounts for only approximately 5% of the Eu budget. This may imply a different oxidation state between the two samples, thereby resulting in a different valence state of Eu (Eu^{3+} or Eu^{2+}), with Eu^{2+} potentially being the dominant species in sample 48 where plagioclase, as opposed to epidote, is the dominant Eu carrier. The magnitudes of the average Eu anomalies in plagioclase for these samples (≈ 7 in #46 compared to ≈ 22 in #48: Table 4.1) also suggest that Eu^{2+} is the dominant species in sample 48 relative to sample 46. Alternatively, the larger concentration of Eu in epidote in sample 46 may be due to epidote growth at the expense of former plagioclase, inheriting its Eu anomaly. In addition, epidote carries approximately 10-20% of the Gd budget in both samples 46 and 48 and is also a significant carrier (> 20%) of La and Ce.

Results for *sample 06* (3 modal % epidote, bulk composition B: Figure 6.2c) mark a significant redistribution of *REEs* among the coexisting phases. The fit between the reconstructed *REE* concentration and measured bulk-rock abundance is less good than those for the previous samples, but most reconstructed *LREE* concentrations are within

25% of the measured abundances [except La (within 36%) and Pr (within 53%)] and *HREE* are within approximately 10% of the measured bulk-rock abundances. The excesses in the reconstructed *LREE* concentrations suggest either the presence of an unrecognized *LREE*-enriched phase, or more likely, a slight overestimate in the modal abundance of a *LREE*-enriched phase (e.g., epidote). However, in marked contrast to the previous two samples, Ca amphibole (77 modal %) is responsible for 30% to 90% of the *REE* budget, favouring the *M-HREE*. Epidote (3 modal %) carries 10% to 30% of the *LREE*. Titanite (1 modal %) accounts for 5-25% of the *REE* budget, favouring the *LREE* and two of the *HREE* (Tm and Yb). The halving of the titanite modal abundance from 2% in samples 46 and 48 to 1% in sample 06 does not explain all the change in its role as a *REE* carrier; there is a significant shift in *REE* repositories between these samples. Plagioclase (15 modal %) continues its subordinate role accounting for only minor amounts (< 10%) of *LREE* and Eu and insignificant proportions of other elements.

6.4.2 Sample 49 - Plagioclase Amphibolite, 0 modal % epidote, bulk composition B

In contrast to the epidote-amphibolites, the *REE* budget in this sample is distributed among only three phases (Ca amphibole, plagioclase, and titanite). Results for this sample, presented in Table 6.1 and illustrated in Figure 6.2d, demonstrate a tight fit between reconstructed and measured bulk-rock *REE* concentrations for most elements. Reconstructed bulk-rock concentrations are within approximately 20% of the

measured bulk-rock concentrations for all *REE* except La, which is within 32%.

Reconstructed concentrations for *L-MREE* exhibit a deficit, which may indicate the presence of an overlooked *L-MREE*-enriched phase, or a slight underestimate in the modal abundance of an *LREE*-enriched phase (e.g., plagioclase or more likely titanite).

In terms of *REE* reservoirs, this sample exhibits similar behaviour to sample 06 except that epidote is no longer present. Ca amphibole (65 modal %) is the dominant carrier for 70% to 85% of all *REEs*, slightly favouring *MREE* and *HREE*. Plagioclase (29 modal %) carries 5% to 10% of the *LREE* and titanite (1 modal %) accounts for 10% to 20% of the bulk rock *REE* budget.

6.4.3 REE Mass Balance – Summary

There are no significant mass gains/losses of *REEs* among analysed samples (see 3.3.2; Table 3.3 and Figure 6.1b) and their systematic redistribution among coexisting phases is consistent with the equilibrium partitioning of these elements during metamorphism (Table 6.1). In addition, it is clear from the four samples that not only the assemblage and modal abundances of the coexisting phases, but also the phase compositions exhibit significant controls on *REE* partitioning. As the most egregious example, the role of phase composition may be illustrated by comparing the relative *REE* carrier roles of the two types of Ca amphibole, i.e., ‘cummingtonite-rich’ Ca amphibole from epidote amphibolite with abundant epidote (samples 46, 48, bulk composition A)

and 'cummingtonite-poor' Ca amphibole from epidote amphibolite with sparse epidote and from plagioclase amphibolite (sample 06 and 49 respectively, bulk composition B). For the two composition A samples, titanite is the dominant carrier (50-80%) of all *REEs*, with 'cummingtonite-rich' Ca amphibole taking approximately 30% of the *HREE* budget, epidote accounting for up to 20% of the *LREEs* and plagioclase having no significant role as a *REE* carrier. In contrast, in composition B samples, 'cummingtonite-poor' Ca amphibole in both epidote amphibolite and plagioclase amphibolite is the dominant carrier (75 to 85%) of all *REEs*, with titanite accounting for most of the remaining *MREE-HREE* and plagioclase (with epidote where present) carrying minor (< 15%) amounts of *LREE*. When considered in the context of the modal abundances of Ca amphibole in the four samples, which do not show any consistent trend, these results demonstrate the important role of amphibole composition in determining *REE* uptake.

A second, less extreme example of compositional control on *REE* uptake is exhibited by plagioclase. Anorthite-richer plagioclase (06, 49) carries more *LREE* than anorthite-poorer plagioclase (46, 48), which in this case is attributed both to its higher modal abundance, and to the compositional controls imposed by the anorthite molecule on the plagioclase structure, which induce a structural distortion of the *A* site rendering it closer in size to the ionic radius of the *LREE*. The decrease in the *REE* concentration of plagioclase in plagioclase amphibolite (sample 49) relative to sample 06 (Table 4.1) is interpreted as a dilution effect due to the approximate doubling of modal plagioclase

between the two samples.

Titanite has the highest concentrations of *REEs* and despite its low modal abundance, is the dominant carrier for all *REEs* in 'cummingtonite-rich' epidote-amphibolite assemblages, but its role declines in assemblages with 'cummingtonite-poor' Ca amphibole. Epidote has moderate to low modal abundances and moderate to high concentrations of *REEs* (particularly *LREE*). It is an important carrier of *LREE* in epidote amphibolites, becoming progressively enriched in *REE*, especially *LREE*, with decreasing modal abundance.

Figure 6.3 provides another way to assess the mass balance results by providing comparative figures for the measured and reconstructed concentrations of the four phases. In these figures, samples 46 and 48 (bulk composition A), and samples 06 and 49 (bulk composition B), have been averaged to provide snapshots of the carrier roles of each mineral in the two bulk compositions. In addition, changes in the behaviour of each phase with respect to the presence (or lack thereof) of epidote can be assessed. The diagrams on the left-hand side of the figure, which chart the measured absolute abundances of the *REEs* in each phase, show the important changes in the average *REE* contents of Ca amphibole (all *REE*), and plagioclase and epidote (*LREE*) among the two groups of samples of differing bulk composition. Overall abundances of *REEs* in titanite do not show significant change, but there appears to be a subtle increase in the *LREE/HREE* ratio in this mineral between bulk compositions A and B. However, this

may in part be attributed to the anomalous *HREE*-depleted pattern of sample 06 (see section 4.2.5).

The diagrams on the right-hand side of Figure 6.3, which combine the *REE* composition of each phase with its modal abundance, provide an alternative method of assessing the relative roles of the four phases as whole-rock *REE* carriers. The major increase in the role of Ca amphibole as a carrier for all *REEs*, the significant increase in the role of plagioclase as a carrier for the first two *LREE* (La and Ce), and the concomitant decrease in the role of titanite as a carrier for all *REEs*, are all apparent from these figures. In addition, the increased role of epidote as a *LREE* carrier in bulk composition B (sample 06), despite reduced modal abundance, is apparent.

Thus, these figures and the data presented in this section show that the distribution of *REEs* among these samples is linked to a subtle interplay among major- and trace-element whole-rock chemistry, major-element mineral chemistry, mineral assemblage and modal abundance.

6.5 Trace-Element Mass Balance for selected transition metals, LILEs and HFSEs

In order to evaluate the relative importance of the four phases Ca amphibole, plagioclase, epidote and titanite as carriers for the selected first-row transition metals (Sc, V, Cr, Ni, Cu, Zn), LILEs (Sr, Rb), and HFSEs (Y, Zr, Nb) in epidote-amphibolite and plagioclase-amphibolite assemblages, mass-balance calculations were performed on

the same four Y group samples. Brief descriptions of these samples are given in section 6.3 and results are presented and illustrated in Table 6.2 and Figure 6.4a-d respectively. The errors associated with the mass balance for these elements are significantly larger than those for the *REE* mass balance, especially for some first-row transition metals and Zr. Potential reasons for the larger errors are discussed below. Whole-rock analyses of Co were not performed; consequently there are no error estimates for this transition metal. However in all samples, Ca amphibole is the dominant carrier of this element, which is attributed to its high modal abundance and suitable octahedral *M*1-3 sites.

6.5.1 Epidote Amphibolites (10-3 modal % epidote)

Results for *sample 46 (10 modal % epidote)* and *sample 48 (7 modal% epidote)*, both bulk composition *A*, are illustrated in Figure 6.4a-b and are similar. In both samples, the reconstructed concentration patterns for most elements reproduce the measured whole-rock patterns, with the notable exceptions of Zn, which exhibits a large relative excess, and Cu and Zr, both of which exhibit large relative deficits. Ca amphibole is the primary carrier (> 80%) for first-row transition elements (Sc, V, Cr, Ni, Cu, Zn; ^{*v*}*M*1-3 sites) and accounts for lesser proportions (\approx < 25%) of Y, Zr and Nb. Plagioclase and epidote are the primary Sr reservoirs, carrying approximately equal proportions in sample 46 and in an approximate 3:1 carrier ratio in sample 48. Ca amphibole is the dominant (\approx 95%) carrier of Rb in sample 46 but partitions this role

with plagioclase (which carries $\approx 35\%$) in sample 48. Epidote accounts for approximately 15-35% of the Zr and 25% of the Nb in the reconstructed totals and is a minor carrier ($\approx < 5\%$) of other analysed elements. Despite its low modal abundance, titanite is the primary carrier of Y and Nb and the deficits in the reconstructed concentration of Nb may point to slight underestimation of titanite modal abundance.

As with samples 46 and 48, the reconstructed concentration pattern for *sample 06* (3 modal % epidote, bulk composition B) shows significant relative excesses for some elements (Zn, Cr, Ni and Nb) and deficits for others (Cu, Rb and Zr). Ca amphibole is again the primary carrier for first-row transition elements (Sc, V, Cr, Ni, Cu, Zn; $^{VI}M1-3$ sites) and Rb (A site) and accounts for lesser proportions ($\approx < 15\%$) of Sr and Nb. There is a shift in the primary reservoir for Y from titanite to Ca amphibole between samples 46-48 and sample 06, as was the case with the REE, which cannot be entirely attributed to the decrease (by a factor of two) in modal titanite. In addition, the role of titanite as a Nb carrier appears to increase between samples 46-48 and 06, possibly in compensation for the smaller role played by epidote as a Nb carrier in this sample. Plagioclase and epidote carry approximately 60% and 20% respectively of the Sr in this sample, but are subordinate reservoirs for the other analysed elements.

6.5.2 Sample 49 - Plagioclase Amphibolite, 0 modal % epidote, bulk composition B

This sample (bulk composition B) allocates the reconstructed trace-element sum

among three phases (Ca amphibole, plagioclase, and titanite) and results are presented in Table 6.2 and illustrated as Figure 6.4d. The reconstructed totals for most elements are again within approximately 30%, except for Zn (relative excess) and Cu and Zr (relative deficits). In contrast to previous samples, sample 49 exhibits a large relative deficit in the reconstructed concentration of Nb, which may be due to underestimation of the modal abundance of titanite, or to minor (< 0.5% modal), unanalysed ilmenite, a known carrier of this and other HFSEs (Zack *et al.*, 2002). Ca amphibole is again the primary carrier ($\approx 85\%$) of first-row transition elements and also accounts for approximately 65% of the Y and 40% of the Nb in the reconstructed totals. Plagioclase is the main Sr reservoir ($\approx 90\%$) and also accounts for approximately 80% of the reconstructed Rb total, likely reflecting a disequilibrium distribution of this element in the sample. Titanite (and possibly ilmenite, see above) is the primary Nb sink and accounts for approximately 35% of the reconstructed concentration of Y.

6.5.3 Trace-Element Mass Balance – Summary

Given the number of parameters required for a mass balance, including the modal abundances and trace-element concentrations of all coexisting phases, most analysed trace elements are *reasonably* well balanced. Notable exceptions include Zn, Cu, and Zr, and in one sample (49), Nb. The consistent relative excesses in reconstructed Zn concentrations are not well understood and are tentatively attributed to fractionation

during sample ablation and plasma transportation (Longerich *et al.*, 1996). In contrast, the relative deficits in Cu, Zr and Nb, for which there are no analytical explanations, are probably linked to minor (<1%) modal abundances of phases such as chalcopyrite, zircon and ilmenite, which are known to sequester these elements (Rollinson, 1993), but were absent from the mass-balance calculations. Thus, the less good fits of the reconstructed concentrations for these elements are considered to be principally due to the very fine grain sizes of some of the minor phases in which they occur, effectively putting them beyond the resolution of the analysis techniques employed in this study.

As with the *REE*, the averaged relationships between trace-element concentration, modal abundance, and the carrying capacity for each phase in bulk compositions A (46 and 48) and B (06 and 49) are illustrated in Figure 6.5. *Ca amphibole's* role as the dominant carrier of many first-row transition elements is attributed to the large number of octahedral sites (five) per formula unit, the fact that there are three types (*M1-3*) of these sites with slightly different properties, and because of its high modal abundance. The propensity for Rb to be sequestered in *Ca amphibole* (samples 46 and 06) is linked to the presence of the 12-fold *A* site. The very different values of partition coefficients for Rb between *Ca amphibole* and plagioclase in samples 48 and 49 imply disequilibrium partitioning of this element between those phases in one or both of these samples. Figure 6.5 shows that the behaviour of Y is analogous to that of the *REE* in the analysed samples, i.e., for two epidote-amphibolites of composition A

(samples 46 and 48), 'cummingtonite-rich' Ca amphibole plays a subordinate role ($\approx 20\%$) as a Y carrier with titanite being the dominant carrier, whereas in composition B in both epidote-amphibolite (sample 06) and plagioclase-amphibolite (sample 49) assemblages, 'cummingtonite-poor' Ca amphibole is the dominant Y reservoir ($\approx 80\%$) with titanite playing a secondary role. *Plagioclase* is the most important reservoir for Sr and its role increases slightly with decreasing modal epidote (Figure 6.5). In addition, Figure 6.5 shows that *epidote* is a significant carrier of V and Cr and an important Sr reservoir. Most elements sequestered in epidote in epidote amphibolite are held in Ca amphibole in plagioclase amphibolite reflecting the similarities of both the octahedral M1-3 sites in each phase and the Ca amphibole $^{VIII}M4$ site and the epidote ^{VIII}X site. As noted by other authors and shown in Figure 6.5, *titanite* is the principal carrier for Nb and carries significant amounts of other HFSEs (Y, Zr) also. However, due to its decreasing modal abundance and to the compositional changes in Ca amphibole, the role of titanite as an Y reservoir decreases across bulk compositions A and B in the analysed samples. In addition, the data presented here show that titanite undergoes a change in the light/heavy *REE* ratio and significant declines in the concentrations of the highly charged elements V, Cr, Y and Zr, presumably because it is approaching its own stability limit. In the case of Y, the reduction in the partition coefficient between titanite and Ca amphibole ($D_Y^{Ttn/Amp}$), and the decline in modal titanite, combine to make Ca amphibole the dominant carrier of Y in plagioclase amphibolite.

6.6 Reaction Balancing: Algebraic Analysis of the Epidote-out “Reaction Isograd”

A fundamental goal in metamorphic petrology is to understand the basic changes in both phase compositions and phase compatibilities that together result in the metamorphic reactions that can be used as isograds. Since Thompson (1957) pioneered the AFM projection, metamorphic petrologists have used graphical analysis extensively to construct petrogenetic grids by making generalizations about assemblages and mineral compositions (e.g., compilations in Philpotts, 1990; Spear, 1993; Bucher and Frey, 1994). In order to be applicable to a broad range of lithologies and be easy to interpret, such grids ordinarily model natural systems in terms of the smallest number of system components as possible. However, the relationships (i.e., reactions) between coexisting mineral assemblages in natural rocks commonly require too many components for rigorous graphical representation. Recognizing these limitations, Greenwood (1967, 1968) showed that linear algebraic dependencies between multicomponent assemblages are equivalent to graphical intersections (i.e., reactions) on traditional phase diagrams. On this basis, Fisher (1989) introduced and elucidated the use of singular value decomposition (SVD) to petrological problems. Since then, SVD has been used to quantitatively model metamorphic assemblages and reaction isograds (e.g., Gordon *et al.*, 1991; Hartel and Pattison, 1996).

In this section, the computer software Mathematica[®] was employed to perform SVD analysis on the inferred epidote-out reaction (see section 3.5, R 3.2) using major-

element compositions of coexisting phases in epidote-amphibolite and plagioclase-amphibolite assemblages to search for a single, hypothetical, bulk composition that can be expressed as a combination of the mineral compositions in each assemblage. In principle, this is equivalent to the search for a mass balance between the two assemblages. If such a balanced 'reaction' exists, it is permissive that the epidote-out isograd is due to a change in externally imposed conditions, i.e., temperature or pressure, or both (Greenwood, 1967, 1968, Gordon *et al.*, 1991). If so, such a reaction, if present, can then be used to model the redistribution of *REEs* and selected trace elements formerly sequestered in epidote in epidote-amphibolite to coexisting phases in plagioclase-amphibolite facies above the reaction isograd. An explanation of SVD applied to the composite compositional matrix is summarized in Appendix C.

6.6.1 Initial Subjective Assumptions

As a starting point, it is logical to revisit the epidote-out reaction, *R 3.2*:



In this reaction, it is inferred that the major elements sequestered in epidote were largely taken up by slight adjustments in the compositions and modal abundances of Ca amphibole and plagioclase, with plagioclase becoming more abundant and anorthite-rich and Ca-amphibole becoming slightly more abundant and less cummingtonite-rich due to changes in the EBC (see section 6.3). The role of titanite is unclear and it remains an

open question at this stage whether variations in its major- and trace-element chemistry and modal abundance also accompanied this reaction. SiO_2 is indicated on both sides of the reaction as it is not known whether quartz was a reactant or a product in this SiO_2 -saturated system; and the presence of OH-bearing phases on both sides of the reaction, together with the inference of H_2O as a product of the reaction and the absence of carbonates in all the assemblages, can be interpreted to suggest that to a first approximation the system was H_2O -saturated.

The two samples used to test this equilibrium are numbers 46 and 49; in detail, the average major-element compositions of the rims of the phases in these samples analysed by EPMA, expressed as numbers of cations *p.f.u.*, were used (Table 3.4). Thus, the system includes an epidote amphibolite (#46) that contains four phases (Ca amphibole, plagioclase, epidote, titanite) and a plagioclase amphibolite (#49) containing three phases (Ca amphibole, plagioclase, titanite). Sample 46 was selected since it contains the most epidote (10% modal), and sample 49 is the only plagioclase amphibolite for which there are *in situ* mineral analyses. The seven phases in the model reaction account for over approximately 95% of the modes of samples 46 and 49 with the remaining approximate 5% occurring mainly as quartz.

In this analysis, the compositional variability of these seven phases in the two samples is described in terms of the nine cations (Ti^{4+} , Al^{3+} , Fe^{3+} , Fe^{2+} , Mg^{2+} , Mn^{2+} , Ca^{2+} , Na^+ , K^+), that are combined to yield six separate independent components (Ti^{4+} , Al^{3+} ,

Fe^{3+} , $\sum \text{FeMgMn}$, Ca and $\sum \text{NaK}$). Si^{4+} was omitted from the compositional matrix because quartz is in excess in this system, and a similar argument can be extended to the omission of H^+ due to the inferred presence of intergranular H_2O . Fe^{2+} , Mg^{2+} and Mn^{2+} are summed as they occur in significant abundance only in the five M sites in Ca amphibole, i.e., they are not partitioned between two or more phases. K, a very minor component in this system, has been summed with Na, as these two elements substitute for each other in Ca amphibole and plagioclase. Fe^{3+} was calculated on a stoichiometric basis using the procedure of Spear (1993). Despite their similar ionic properties, Al and Fe^{3+} are treated as separate independent components in this analysis since they are partitioned between Ca amphibole, plagioclase, and epidote in different proportions. The possible presence of minor sulphide, ilmenite, or zircon has been noted (sections 3.2, 6.4 and 6.5), but these minerals and the system components required to produce them are ignored in this analysis as they are not considered to be significant participants in the overall isogradic reaction.

Since the interpretation of the results is based on whether or not a mass balance can be found within compositional uncertainty, the slightly larger uncertainties resulting from averaging mineral compositions over the entire thin-section scale make it easier to obtain a mass balance. On the other hand, the scale of equilibrium is larger than if single spot analyses from smaller areas of the thin section were utilized, possibly rendering the results more generally applicable. In any case, for the purposes of the interpretations

presented in this thesis, average compositions are considered more than adequate.

Following Hartel and Pattison (1996), the absolute deviations from perfect cation balance for each constituent are compared with the analytical uncertainty and the reaction is considered adequately balanced if the result is within three times 1σ analytical errors.

Additionally, the compositional matrix used in the SVD determination was unweighted to prevent potential increases in the influence of minor constituents (Gordon *et al.*, 1991).

6.6.2 Phase Rule Variance of Assemblages

The assumption that minerals in abundant and widespread assemblages attained equilibrium under divariant conditions is a common one in metamorphic studies. This assumption can be tested by a determination of the variance of an assemblage. Brinkley (1946a, b; in Gordon *et al.*, 1991) showed that the number of components, c , in a thermodynamic system is equal to the rank of the matrix of vectors that express the compositions of p phases in terms of an initial set of constituents, which in this study are the number of cations $p.fu$ in each of the minerals in each assemblage. The petrologic phase rule,

$$f = c + 2 - p$$

directly follows from this and as shown by Fisher (1989), a variance of less than two means that one or more mass balances can be written for some or all of the phase combinations of the assemblage. For the epidote-amphibolite (#46) and plagioclase-

amphibolite (#49) assemblages studied here, there is a 6 row x 7 column composition matrix formed by columns of the compositions of each phase. SVD analysis is used to determine the rank (c) of this matrix. Therefore, the initial choices of constituents and phases determine the numbers of rows and columns of the composite matrix, and the number of components cannot exceed six, which is the lesser of the number of rows (i.e., 6) or columns (i.e., 7). Accordingly, the SVD of the compositional matrix is required to have a rank of 6 (i.e., $c = 6$) to yield a univariant reaction, or mass balance.

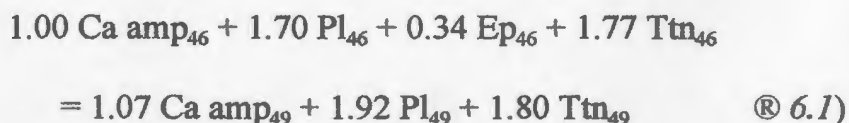
6.6.3 Mass Balance Analysis of Epidote-out Reaction Isograd using SVD

For samples 46 (epidote amphibolite) and 49 (plagioclase amphibolite), the 6 x 7 composite compositional matrix (\mathbf{M}), the resultant stoichiometric reaction coefficients, the reconstructed cation totals derived by multiplying the elements of the composition matrix by the appropriate stoichiometric coefficients, and the error estimates given as the percent deviation from perfect mass balance between reactant and product assemblages, are summarized in Table 6.3. SVD analysis (Appendix C) of \mathbf{M} yields six nonzero singular values, indicating a rank of 6 (i.e., $c = 6$). According to the phase rule, the variance of the system is therefore:

$$f = 6 + 2 - 7 = 1$$

and so it is not necessary to calculate a model matrix (\mathbf{M}') of reduced rank to represent the original composition matrix (Appendix C). In this situation, a mass balance between

samples 46 and 49 is implied. Normalizing the reaction coefficients to one for Ca amp₄₆, the reaction is:



Following the reasoning of Gordon *et al.* (1991), the implied univariant equilibrium relationship between these epidote-amphibolite and plagioclase-amphibolite assemblages is permissive that the epidote-out isograd is due to a change in externally imposed conditions, i.e., temperature or pressure (or both) and not bulk compositional variations (i.e., the difference between compositions A (# 46) and B (# 49) discussed in section 6.3).

Since the calculation of a model matrix of reduced rank was not necessary to satisfy the condition of univariant equilibrium, there are no residuals to compare to 1σ analytical uncertainties. However, by multiplying the columns of the composite compositional matrix by the appropriate stoichiometric coefficients from *R 6.1*, the reconstructed cation totals are obtained (Table 6.3), which when summed for all the phases in samples 46 and 49, represent the numbers of each species of cation on either side of the mass-balanced reaction. The percentage difference between these numbers for each cation species is used to estimate the quality of the reaction balance. In all cases, the errors are within three times the 1σ analytical uncertainty of the EPMA analyses (Table 6.3). The percent absolute deviation of the total number of cations on an arbitrary

side of the model reaction (here 'reactant' side, i.e., # 46) is within 1 % relative difference. When viewed in this manner, the model 'reaction' *R 6.1* between samples 46 and 49 can be interpreted as conveying something close to univariant equilibrium.

From a geological perspective, reaction *6.1* is also a reasonable qualitative representation of the textures and modal variations observed in natural samples throughout the field study area, i.e., it is a reaction isograd following the definition of Carmichael (1970). For example, the breakdown of epidote is linked to increases in the reaction coefficients for Ca amphibole and plagioclase, which are compatible with the previous inference that release of major elements sequestered in epidote (e.g., Ca, Al, Fe³⁺) are related to increases in the abundances of Al and Fe³⁺ (in Ca amphibole) and Ca (in plagioclase) above the epidote-out isograd. On the other hand, reaction *6.1* indicates a slight increase in modal titanite on the product side, which is not supported by modal abundance measurements. This suggests that the reduction in titanite modal abundance in plagioclase amphibolite is an independent reaction, not related to the breakdown of epidote.

Despite the fact that reaction *6.1* provides a reasonable model for observed modal and major-element mineral compositional variations in these rocks, there is no guarantee that this specific reaction occurred. It may represent the 'sum' of a multi-stage reaction history, perhaps involving an approximately discontinuous epidote-consuming reaction followed by more subtle exchange reactions involving major components of Ca

amphibole and plagioclase, and less likely titanite. Nevertheless, reaction 6.1 is a reasonable first-order model of the overall epidote-out reaction isograd and provides a basis for the evaluation of the redistribution of *REEs* and selected trace elements across the reaction isograd.

6.7 Redistribution of *REEs* and Selected Trace Elements Across the Epidote-out Reaction Isograd

The stoichiometric coefficients of the mass-balance reaction 6.1, determined from the major-element mineral compositions of samples 46 and 49, can now be applied to *REEs* and selected trace elements across the model epidote-out isograd. By multiplying the reaction coefficients of *R* 6.1 by measured trace-element abundances (in ppm, analysed by LAM-ICP-MS) it is possible to estimate the *relative changes* in *REE* and trace-element abundances in samples 46 and 49. These calculations do not represent an absolute quantification of the amount of enrichment or depletion of the trace elements, but instead highlight relative changes in the concentrations of the elements on either side of the reaction isograd. For clarity, results are presented separately for *REEs* and selected trace elements.

6.7.1 Redistribution of *REEs* Across the Model Epidote-out Reaction Isograd

R 6.1 describes the overall reaction at the isograd on the basis of SVD analysis

and accounts well for petrographic observations and major-element mineral compositional information. The reconstructed *REE* concentrations of participating phases in *R 6.1*, as well as the relative changes in those reconstructed concentrations, are presented in Table 6.4 and illustrated in Figure 6.6a-b. As with the major cations, the percent absolute deviation of the $\sum REE$ on an arbitrary side of the model mass balance (here 'reactant' side, i.e., # 46) is used to evaluate the overall 'balance' of the reconstructed concentrations.

Figure 6.6a-b provides a convenient way of illustrating the redistribution of *REE* formerly sequestered in epidote to Ca amphibole, plagioclase, and titanite above the isograd. Figure 6.6a is a stacked bar graph that illustrates the relative proportions of *REE* in each phase on both sides of the reaction isograd. On both sides of the reaction isograd, it is clear that titanite overwhelmingly accounts for the majority of the *REE*; for instance, below the isograd titanite accounts for approximately 95% of *LREE* and approximately 98% of the *M-HREE* budgets, a role only slightly diminished above the isograd. The most important change in *REE* carrier roles occurs among the other phases. Below the isograd, epidote and Ca amphibole account for almost all the remaining *LREE* and *M-HREE* respectively, whereas above the isograd, the roles of Ca amphibole as a carrier for all *REE* and plagioclase as a carrier for La and Eu significantly increase. On crossing the isograd, the breakdown of epidote changes the EBC available to Ca amphibole and plagioclase in sample 49 by infusing it with additional *REE*, especially *LREE*. Thus on a

molar basis, the changes in *REE* patterns in Ca amphibole, plagioclase and titanite resulting from the breakdown of epidote can be largely accounted for by net transfer of *REEs* from epidote to the other phases.

However, it is clear from the results displayed in Figure 6.6b that epidote-breakdown cannot be separated from a significant reduction of *LREE* abundance in titanite, the most *REE*-enriched phase, so that the redistributed *REE* across the isograd do not come uniquely from epidote. Ca amphibole (\approx ten times) and plagioclase (\approx five times) both exhibit significant increases in *LREE* abundance above the isograd, which is attributed to both the breakdown of epidote and the approximately one-third reduction in *LREE* abundance in titanite. The increased *LREE* carrying capacities of Ca amphibole and plagioclase are linked to crystal-chemical changes in these phases as the isograd is crossed, i.e., the calcification of the *REE*-hosting *M4* and *A* sites respectively, rendering them more appropriate sites for *REE* substitution. The increased propensity of both of these sites to sequester *LREE* presumably leads to the slight decrease in *LREE* abundance in titanite above the isograd.

Table 6.4 shows that overall there is an approximate 12% deficit in reconstructed molar *REE* abundances above the isograd. Most of this error is attributed to the relatively large deficit (\approx 28%) in reconstructed *LREE* abundance as the errors for *M-HREE* are relatively small (both \approx 7% in excess). The deficit in *LREE* above the isograd may indicate that some *LREE* are lost during progressive metamorphism, but such an

inference is not supported by *LREE* bulk-rock concentrations (Table 3.3, Figure 6.1).

Alternatively, it may indicate that *LREE* formerly sequestered in epidote are partitioned between Ca amphibole, plagioclase, titanite and an additional unrecognized *LREE* bearing phase above the isograd, consistent with the *LREE* deficit for the whole-rock mass balance for sample 49 (Figure 6.2d).

To summarize, the model epidote-out reaction *R 6.1* accounts well for the redistribution of *M-HREE* across the reaction isograd. Titanite is the most *REE*-enriched phase on both sides of the isograd, but its *MREE/LREE* ratio exhibits an increase as the isograd is crossed, presumably an independent effect related to this mineral approaching its own stability limits. Ca amphibole exhibits a significant increase (\approx six times) in $\sum REE$, especially *LREE* (\approx ten times) above the isograd as does plagioclase (\approx six times *LREE*), which are linked to crystal-chemical changes in these phases with increasing metamorphic grade. Errors for *M-HREE* are small ($<10\%$), whereas a larger deficit in *LREE* ($\approx 28\%$) summed over the product side of the epidote-out reaction may be due in part to the presence of an unrecognized phase, which along with Ca amphibole and plagioclase, sequesters some of the *LREE* formerly held in epidote.

6.7.2 Redistribution of Selected Transition Metals, LILEs and HFSEs Across the Model Epidote-out Reaction Isograd

In the same manner as for *REEs*, the model epidote-out reaction *R 6.1* was used to

evaluate the redistribution of selected trace elements across the isograd. Reconstructed trace-element abundances and error estimates are listed in Table 6.5. As for the major cations and *REE*, the percent absolute deviation of the trace-element sum on an arbitrary side of the model mass balance (again 'reactant' side, i.e., # 46) is used to evaluate the overall 'balance' of the reconstructed concentrations. As noted, these trace elements exhibit broader ranges in both ionic charge and radius, and consequently exhibit a broader range of redistribution patterns across the isograd.

Figure 6.7a consists of two bar graphs, one for each sample, that represent the overall distributions of the selected trace elements on either side of the isograd. Below the isograd (left side, Figure 6.7a), epidote plays a significant role in sequestering several transition elements (e.g., Sc, V, Cr, Zn), as well as Sr and to a lesser extent, the HFSEs Zr and Nb. Ca amphibole is the primary host for many of the transition metals and Rb, consistent with propensity of these elements to occupy the ^{VI}M sites and 12-fold A sites respectively. Titanite sequesters significant proportions of V, Ni, and Cu and is by far the dominant carrier of analysed HFSEs. Plagioclase is an important Sr reservoir and carries lesser amounts of Ni, Cu and Rb.

Above the isograd (right side, Figure 6.7a), transition metals formerly held in epidote are mainly redistributed to Ca amphibole (Sc, Ni, Cu, Zn) and titanite (Cr, V). Ca amphibole assumes the previous role of epidote as the secondary HFSE carrier. Plagioclase exhibits a dominant role as the primary reservoir for Sr and Rb. Presumably,

the increased role of plagioclase as a Sr reservoir is linked to epidote breakdown, but the switch in Rb sinks across the isograd from Ca amphibole to plagioclase likely reflects disequilibrium distribution (i.e., due to alteration of plagioclase) of that element.

The bar graphs in Figure 6.7b illustrate the relative differences in the reconstructed concentrations of Ca amphibole, plagioclase, and titanite from below and above the isograd. For most trace elements, concentrations in Ca amphibole and plagioclase are similar on both sides of the isograd; however Cr and the HFSEs (Y, Zr, Nb) exhibit relative increases (≈ 3 -5 times) on the product side, and Figure 6.7a indicates that the source of these elements (Y, Zr, Nb) is epidote. Plagioclase exhibits large relative increases in the reconstructed concentrations for Co and Rb (15 and 20 times respectively) and smaller increases for Y and Zr above the isograd, although it still assumes a negligible carrier role for these elements. As mentioned, the large increase in Rb on the product side probably does not represent an equilibrium distribution. With respect to titanite, all reconstructed trace-element abundances except Cr exhibit small (< 1) relative differences.

The degree of fit for reconstructed trace-element concentrations varies for each element (Table 6.5, Figure 6.7b). Rb and Cr are not adequately 'balanced' and exhibit large excesses above the isograd. Rb, which is known to be a mobile element during alteration and metamorphism (Seewald and Seyfried, 1990), likely reflects disequilibrium distribution. The situation for Cr remains unclear, and is possibly related

to inherited differences in bulk composition between the two samples, or peculiar zoning of this element (e.g., Yang and Rivers, 2001), but Cr composition maps were not collected to verify this. Reconstructed concentrations for Cu, Zn, and Sr exhibit large relative deficits (between ≈ 27 -42%) across the isograd, whereas Nb exhibits a relative excess ($\approx 27\%$) above the isograd. Errors for Cu and Zn may be related to analyses of Ca amphibole and titanite that were in proximity to fine-grained sulphides, resulting in the compositions of these major phases being depleted in these elements. Sr, a low field strength LILE, is known to be mobile during alteration and metamorphism, implying that some Sr may have been lost from the system during metamorphism. Reconstructed concentrations for other analysed elements (Sc, V, Co, Ni, Y, Zr) are within approximately 15% relative difference on either side of the model reaction isograd. The magnitude of the relative increases in the reconstructed concentrations of Y, Zr and Nb in Ca amphibole indicates that the source of these elements was epidote (Figure 6.7). Thus, for most elements, the model epidote-out reaction *R 6.1* is a good first approximation of the observed mineral trace-element variations in the major phases across the isograd.

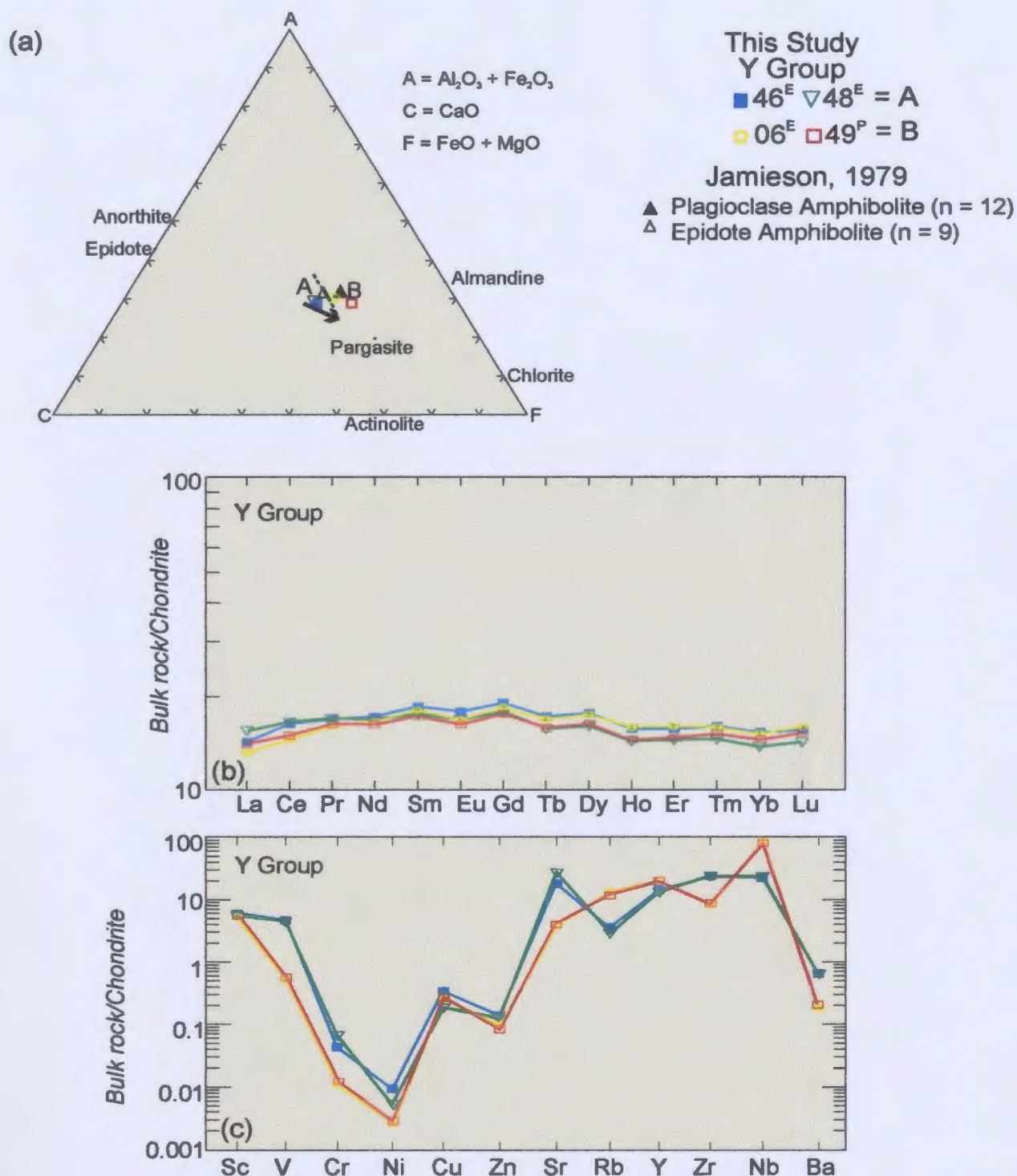
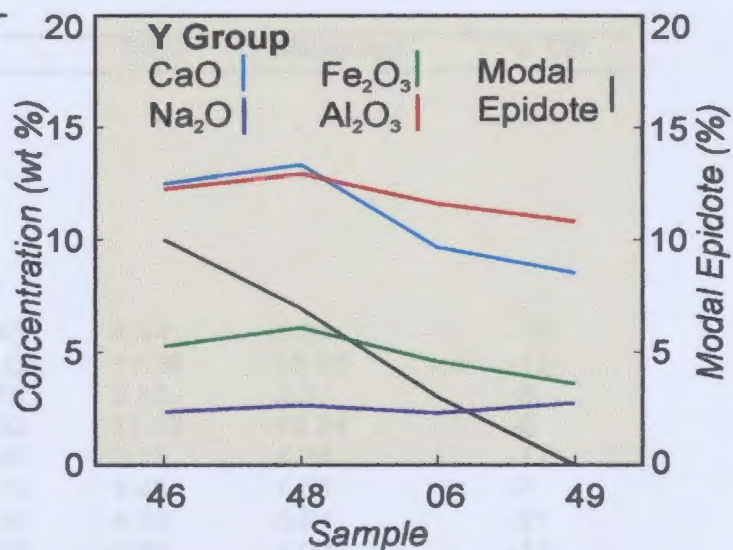


Figure 6.1 Bulk-rock compositions of samples for which mass balances were calculated in terms of: a) ACF compositional space; b) chondrite-normalized REE chemistry, and; c) chondrite-normalized trace-element chemistry. Arrow in (a) denotes the qualitative direction of shift in EBC leading to the formation of cummingtonite-rich amphibole. See text for explanation. Chondrite normalization factors from Taylor and McLennan (1985).

(d)

Sample	46	48	06	49
(wt %)				
CaO	12.49	13.34	9.67	8.57
Na ₂ O	2.39	2.65	2.33	2.74
Fe ₂ O ₃	5.32	6.11	4.61	3.61
Al ₂ O ₃	12.32	13.01	11.63	10.84
Modal Epidote	10	7	3	0



(e)

Sample	46	48	06	49
Molecular proportion				
Ca	0.22	0.24	0.17	0.15
Na	0.04	0.04	0.04	0.04
Fe ³⁺	0.03	0.04	0.03	0.02
Al ³⁺	0.12	0.13	0.11	0.11
$\frac{10 \cdot \text{Ca}}{\text{Ca} + \text{Na}}$	8.52	8.48	8.21	7.76
$\frac{10 \cdot \text{Fe}^{3+}}{\text{Fe}^{3+} + \text{Al}^{3+}}$	2.16	2.31	2.02	1.75
Modal Epidote	10	7	3	0

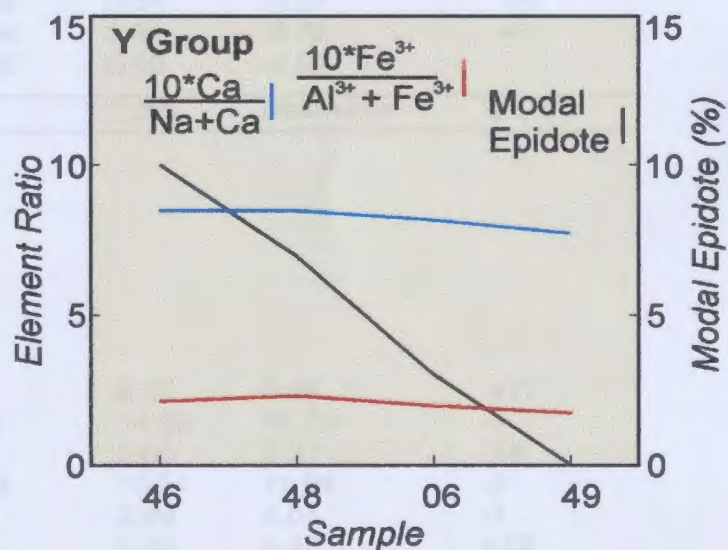


Figure 6.1 Illustration of the changes in modal epidote with changes in bulk-rock compositions in terms of, d) weight percent CaO, Na₂O, Al₂O₃ and Fe₂O₃, and e) the ratios of the molecular proportions of Ca / Ca+Na and Fe³⁺ / Al³⁺ + Fe³⁺.

Chapter 6: Mass-Balance and Reaction-Balance Calculations

Table 6.1 *REE* mass balance. Reconstructed concentrations based on measured abundances (Table 4.1) and mineral modes compared to the measured whole rock total (*italics*) as an independent quality control. See text for full explanation. Results presented here are illustrated in Figure 6.2(a-b).

Sample 46	Amp	Ep	Pl	Ttn	Total	Measured	% Diff.
Y Group: Epidote Amphibolite							
Mode % (+ 5 % Quartz)	65	10	18	2			
Reconstructed <i>REE</i> (ppm)							
La	0.14	0.87	0.02	3.40	4.44	5.26	-16
Ce	0.85	1.71	0.03	11.06	13.66	15.65	-13
Pr	0.15	0.22		1.75	2.13	2.31	-8
Nd	0.92	1.10	0.01	9.20	11.23	12.24	-8
Sm	0.41	0.24		2.90	3.55	4.28	-17
Eu	0.13	0.50	0.02	0.79	1.45	1.55	-7
Gd	0.61	0.93	0.01	3.04	4.59	5.84	-21
Tb	0.15	0.04		0.63	0.81	1.00	-18
Dy	1.29	0.23		4.34	5.86	6.71	-13
Ho	0.23	0.07		0.62	0.92	1.34	-31
Er	0.94	0.14		2.60	3.68	3.91	-6
Tm	0.15	0.02		0.37	0.54	0.57	+5
Yb	1.10	0.16		2.54	3.81	3.79	+1
Lu	0.21	0.03		0.35	0.59	0.59	
Sample 48	Amp	Ep	Pl	Ttn	Total	Measured	% Diff.
Y Group: Epidote Amphibolite							
Mode % (+ 2 % Quartz)	74	7	15	2			
Reconstructed <i>REE</i> (ppm)							
La	0.07	1.71	0.06	4.78	6.62	5.65	+17
Ce	0.45	2.22	0.25	11.77	14.69	15.73	-7
Pr	0.14	0.05	0.02	1.79	2.00	2.31	-14
Nd	0.81	0.28	0.11	10.34	11.54	11.88	-3
Sm	0.36	0.09	0.03	3.52	3.99	4.01	-1
Eu	0.12	0.03	0.25	1.25	1.65	1.45	+13
Gd	0.60	0.49	0.02	4.00	5.12	5.39	-5
Tb	0.16	0.01	0.01	0.69	0.88	0.91	-3
Dy	0.95	0.18	0.04	4.84	6.01	6.05	-1
Ho	0.20	0.01	0.01	0.98	1.19	1.21	-1
Er	0.81	0.05	0.03	2.68	3.57	3.58	
Tm	0.09	0.03		0.40	0.52	0.52	
Yb	0.78	0.02	0.02	2.56	3.38	3.39	-1
Lu	0.12	0.03		0.39	0.54	0.54	

Chapter 6: Mass-Balance and Reaction-Balance Calculations

Table 6.1 *REE* mass balance. Reconstructed concentrations based on measured abundances (Table 4.1) and mineral modes compared to the measured whole rock total (*italics*) as an independent quality control. See text for full explanation. Results presented here are illustrated in Figure 6.2(c-d).

Sample 06	Amp	Ep	Pl	Ttn	Total	Measured	% Diff.
-----------	-----	----	----	-----	-------	----------	---------

Y Group: Epidote Amphibolite

Mode % 77 3 15 1
(+ 4 % Quartz)

Reconstructed *REE* (ppm)

La	2.04	2.49	0.62	1.32	6.47	4.77	+36
Ce	5.72	5.46	1.24	4.72	17.14	13.75	+25
Pr	2.02	0.56	0.05	0.70	3.33	2.18	+53
Nd	9.09	1.93	0.12	3.43	14.57	11.67	+25
Sm	3.72	0.38	0.03	0.79	4.91	4.13	+19
Eu	1.36	0.10	0.02	0.30	1.79	1.46	+22
Gd	4.52	0.34	0.03	0.76	5.64	5.56	
Tb	0.77	0.04	0.01	0.08	0.89	0.98	-9
Dy	5.54	0.23	0.05	0.34	6.15	6.65	-7
Ho	1.12	0.04	0.01	0.04	1.21	1.35	-10
Er	3.40	0.10	0.02	0.07	3.59	3.98	-10
Tm	0.49	0.01		0.12	0.62	0.57	+10
Yb	3.18	0.04	0.01	0.57	3.80	3.75	+1
Lu	0.62	0.01		0.05	0.68	0.60	+12

Sample 49	Amp	Pl	Ttn	Total	Measured	% Diff.
-----------	-----	----	-----	-------	----------	---------

Y Group: Plagioclase Amphibolite

Mode %
(+ 5 % Quartz) 65 29 1

Reconstructed *REE* (ppm)

La	2.59	0.80	0.15	3.53	5.20	-32
Ce	8.97	0.78	2.68	12.43	14.41	-14
Pr	1.53	0.06	0.19	1.78	2.25	-21
Nd	8.26	0.22	2.99	11.47	11.61	-1
Sm	3.02	0.04	0.51	3.57	4.02	-11
Eu	1.08	0.05	0.13	1.26	1.42	-11
Gd	4.46	0.01	0.67	5.14	5.42	-5
Tb	0.77		0.11	0.88	0.92	-5
Dy	5.47	0.01	0.76	6.25	6.00	+4
Ho	1.19		0.15	1.34	1.24	+8
Er	3.58	0.02	0.46	4.06	3.68	+10
Tm	0.51	0.01	0.07	0.58	0.54	+8
Yb	3.59	0.01	0.51	4.11	3.63	+13
Lu	0.52		0.07	0.59	0.59	

Sample 46 Epidote Amphibolite (10% modal epidote)

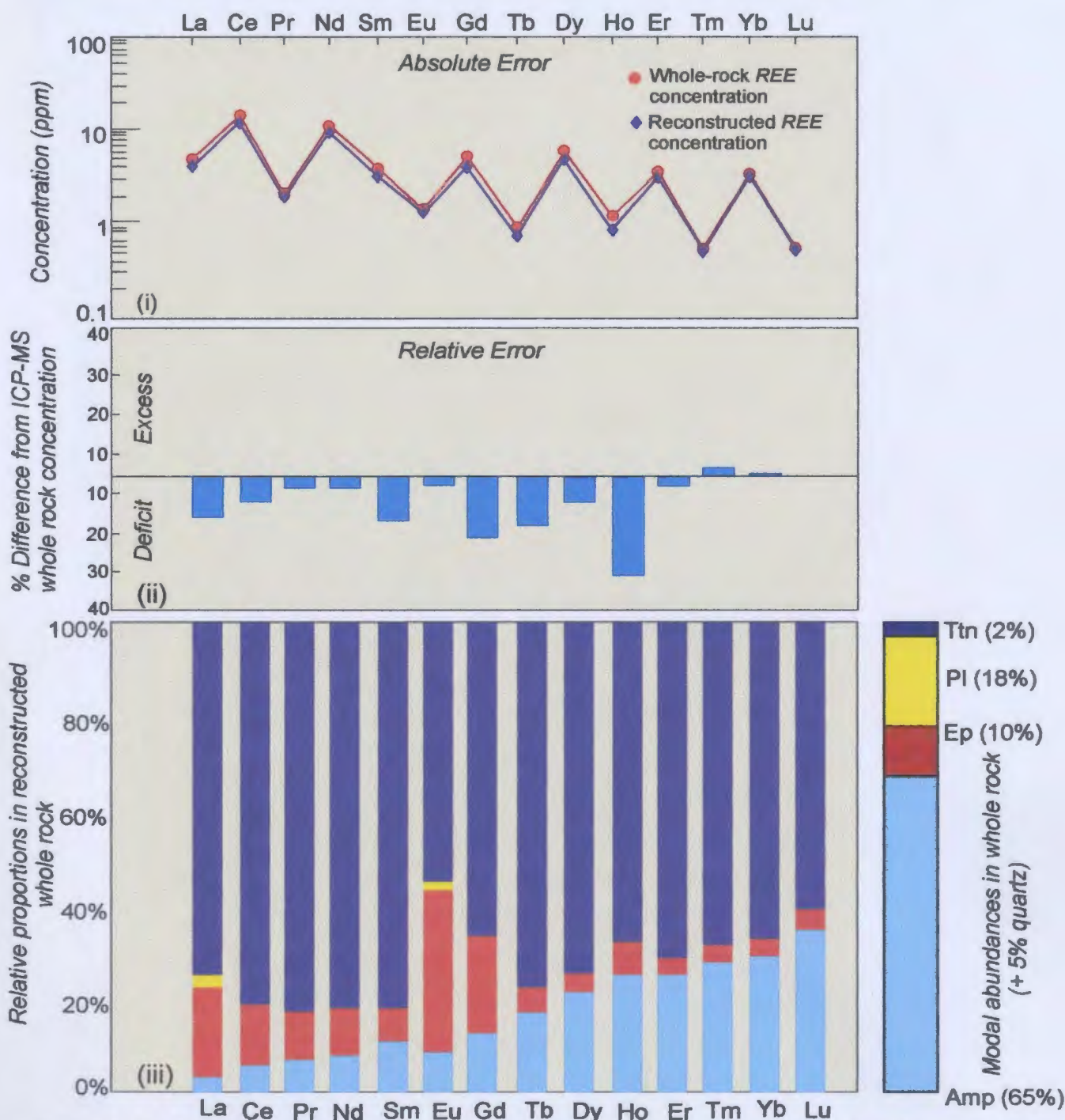


Figure 6.2 (a) Mass balance diagram for sample 46 (Y Group) showing the relative roles of amphibole, plagioclase, epidote, and titanite as REE carriers. Diagram (i) is a comparison of the reconstructed whole-rock concentration (modal abundance \times mineral concentration) compared to bulk-rock REE concentration (measured by solution ICP-MS). Diagram (ii) is the % difference between the reconstructed REE concentration and the measured whole-rock concentration. Diagram (iii) is a bar graph illustrating the relative proportions of REE in each phase.

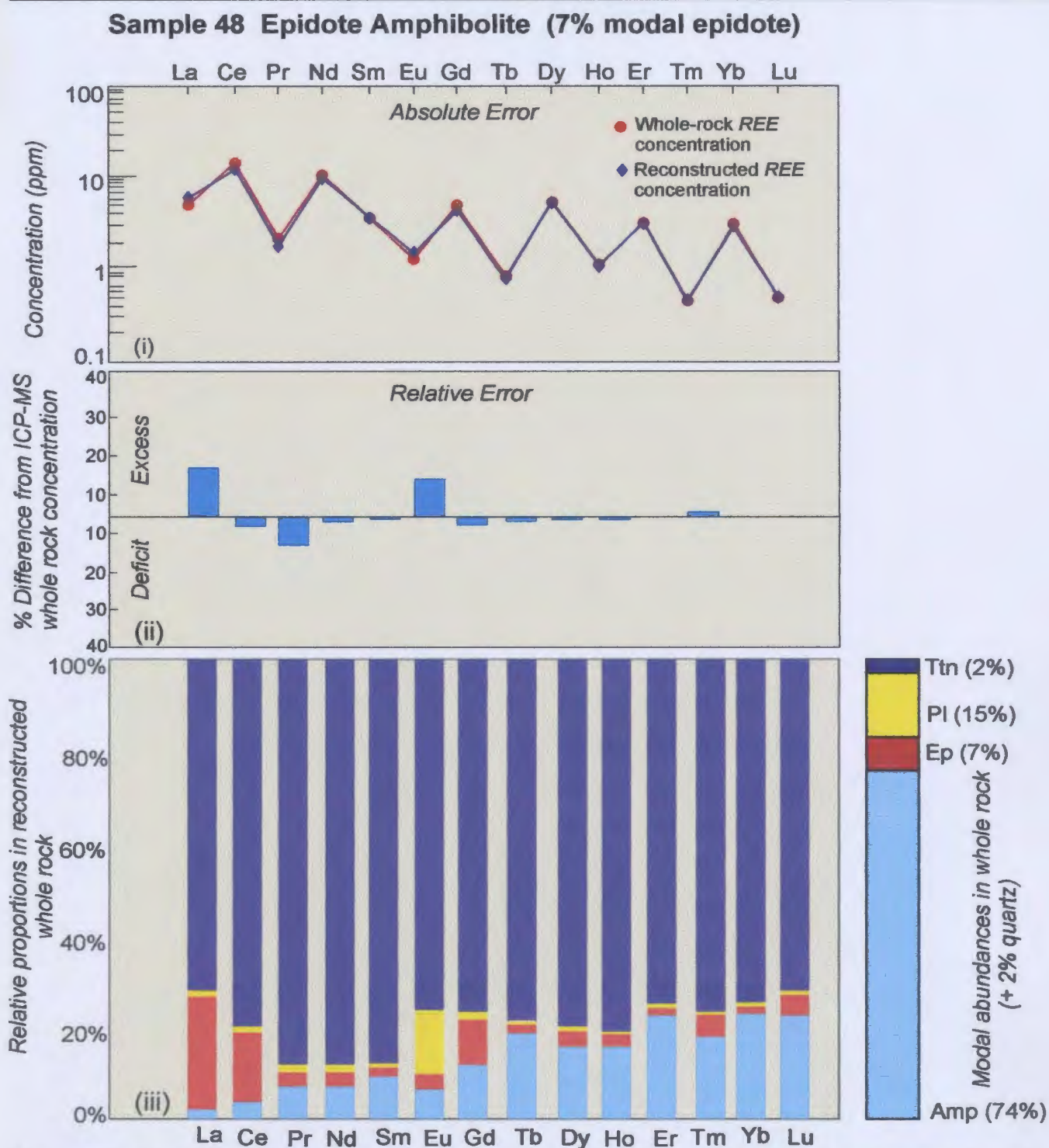


Figure 6.2 (b) Mass balance diagram for sample 48 (Y Group) showing the relative roles of amphibole, plagioclase, epidote, and titanite as *REE* carriers. Diagram (i) is a comparison of the reconstructed whole-rock concentration (modal abundance \times mineral concentration) compared to bulk-rock *REE* concentration (measured by solution ICP-MS). Diagram (ii) is the % difference between the reconstructed *REE* concentration and the measured whole-rock concentration. Diagram (iii) is a bar graph illustrating the relative proportions of *REE* in each phase.

Sample 06 Epidote Amphibolite (3% modal epidote)

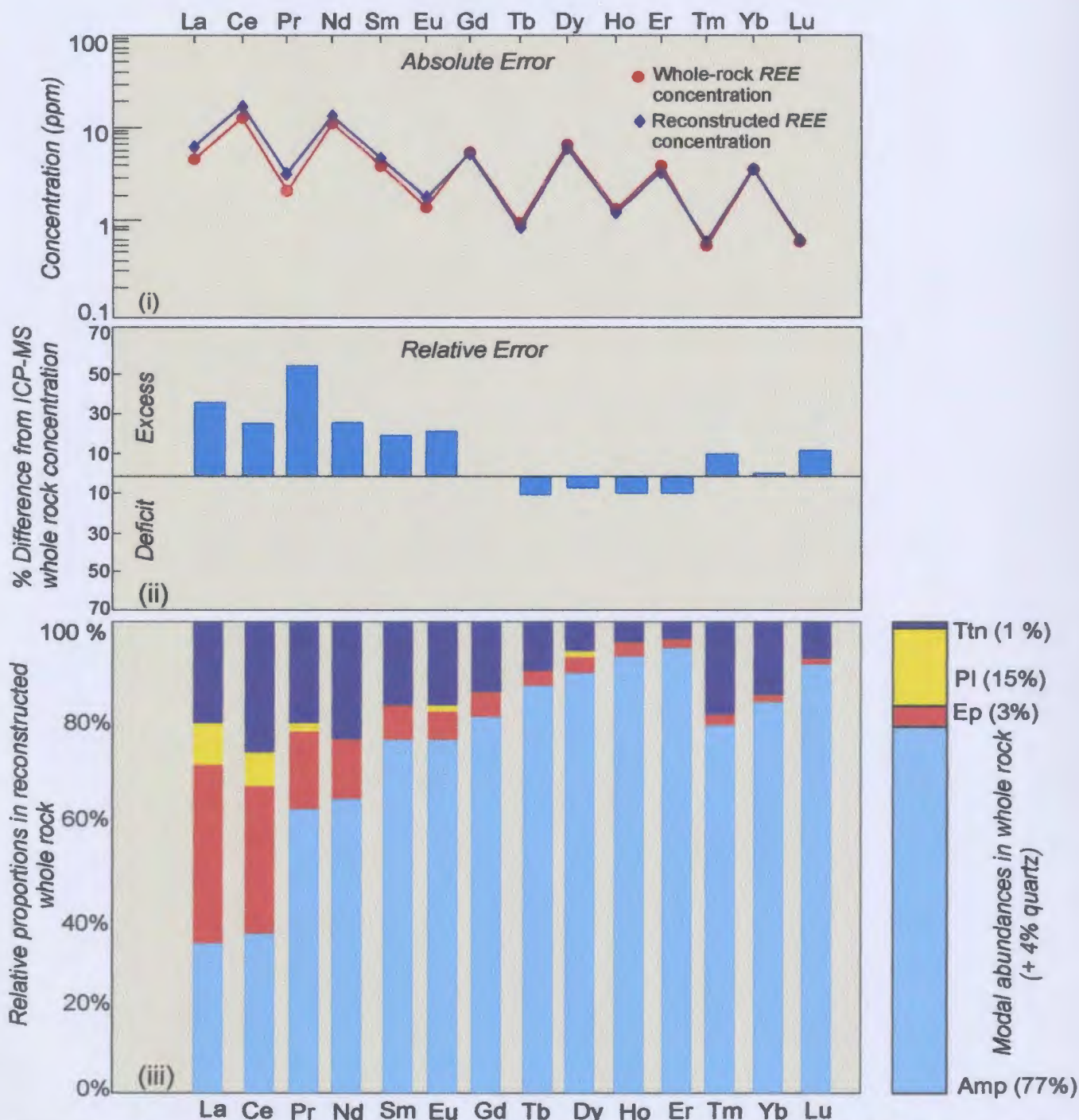


Figure 6.2 (c) Mass balance diagram for sample 06 (Y Group) showing the relative roles of amphibole, plagioclase, epidote, and titanite as *REE* carriers. Diagram (i) is a comparison of the reconstructed whole-rock concentration (modal abundance x mineral concentration) compared to bulk-rock *REE* concentration (measured by solution ICP-MS). Diagram (ii) is the % difference between the reconstructed *REE* concentration and the measured whole-rock concentration. Diagram (iii) is a bar graph illustrating the relative proportions of *REE* in each phase.

Sample 49 Plagioclase amphibolite (0% modal epidote)

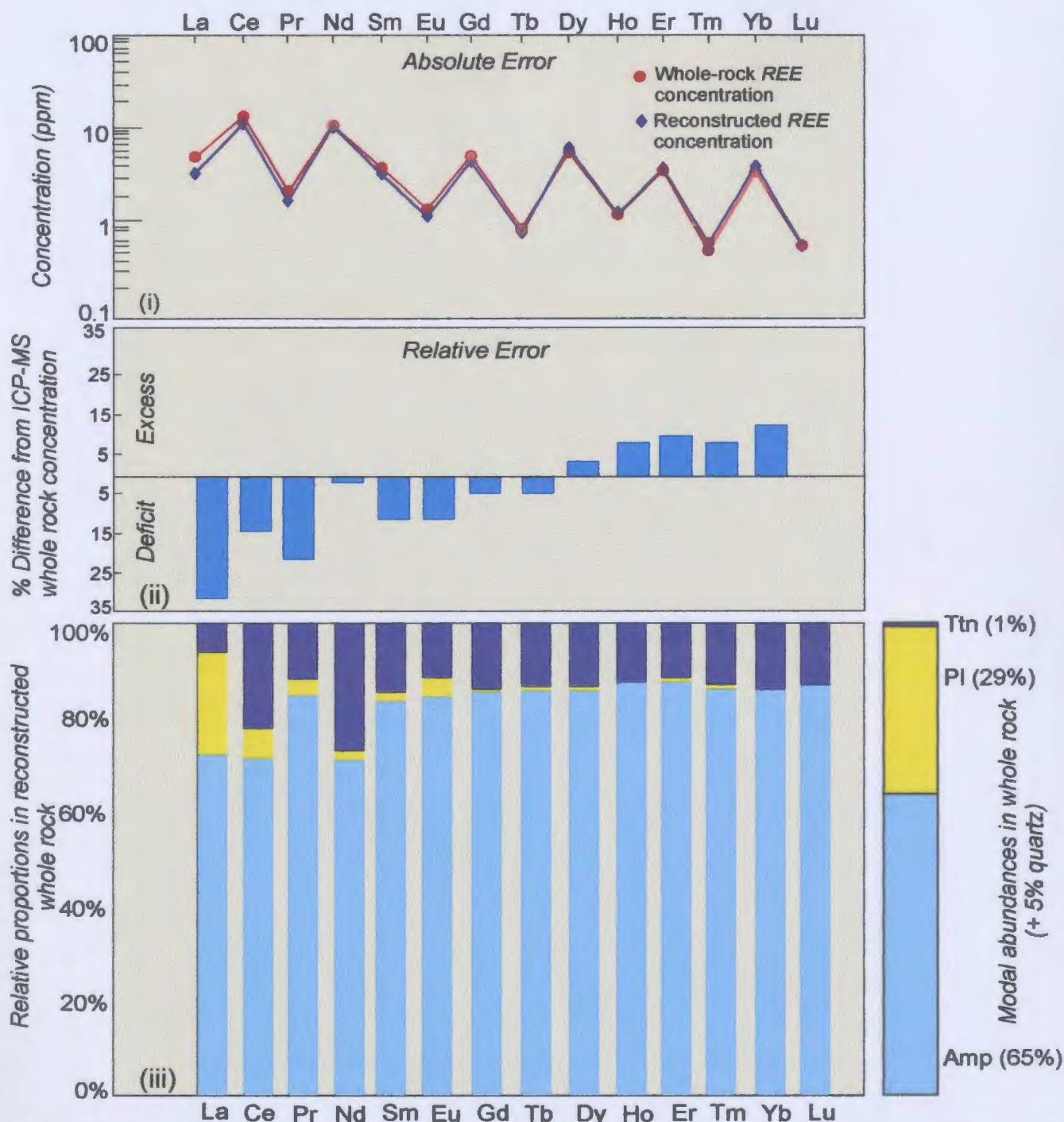


Figure 6.2 (d) Mass balance diagram for sample 49 (Y Group) showing the relative roles of amphibole, plagioclase, and titanite as *REE* carriers. Diagram (i) is a comparison of the reconstructed whole-rock concentration (modal abundance \times mineral concentration) compared to bulk-rock *REE* concentration (measured by solution ICP-MS). Diagram (ii) is the % difference between the reconstructed *REE* concentration and the measured whole-rock concentration. Diagram (iii) is a bar graph illustrating the relative proportions of *REE* in each phase.

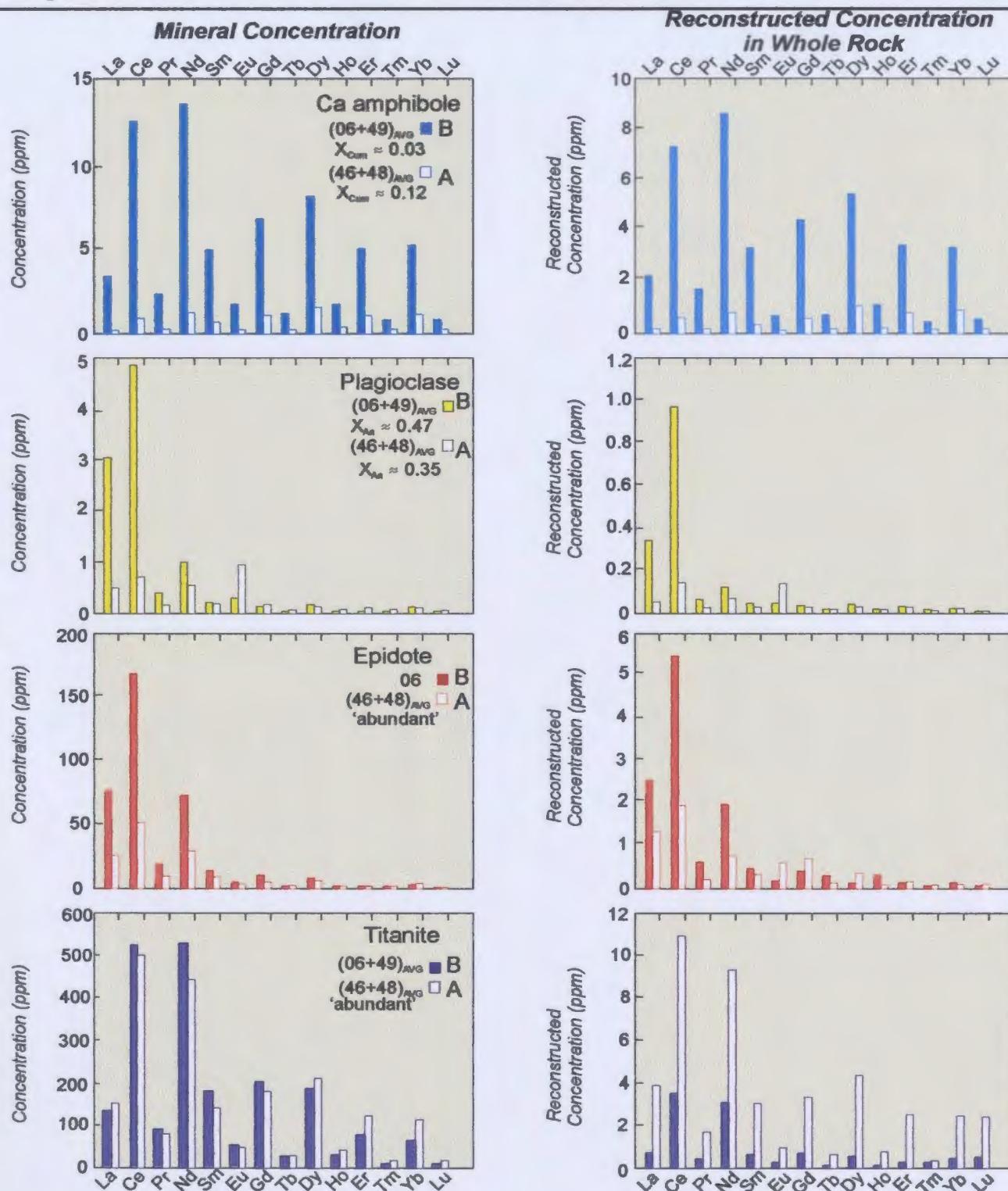


Figure 6.3 Average REE concentrations (LAM-ICP-MS) and average reconstructed REE concentrations (measured x modal abundance) for samples 46+48 (relatively high modal titanite and epidote) relative to samples 06+49 (less modal titanite and epidote).

Chapter 6: Mass-Balance and Reaction-Balance Calculations

Table 6.2 Trace element mass balance. Reconstructed concentrations based on measured abundances (Table 5.1) and mineral modes compared to the measured whole-rock total (*italics*) as an independent quality control. See text for full explanation. Results presented here are illustrated in Figure 6.4(a-b).

Sample 46	Amp	Ep	Pl	Ttn	Total	Measured	% Diff.
Y Group: Epidote Amphibolite							
Mode % (+ 5 % Quartz)	65	10	18	2			
Reconstructed (ppm)							
Sc	41.16	2.38	0.17	0.14	43.85	53	-17
V	297.4	26.00	0.55	18.64	342.6	403	-15
Cr	83.10	20.20	0.45	1.36	105.1	181	-42
Co	51.69	0.04	0.01	n.d.	51.74	n.d.	
Ni	77.56	0.64	2.97	0.90	82.07	80	+3
Cu	2.19	0.16	0.53	0.09	2.97	59	-95
Zn	113.3	8.15	15.57	0.34	137.3	66	+108
Sr	10.19	118.5	99.32	0.30	228.3	219	+4
Rb	8.91	0.07	0.19	0.01	9.18	12	-24
Y	6.15	1.96	0.01	24.33	32.45	32	+1
Zr	10.19	14.46	0.04	10.11	34.79	132	-74
Nb	0.40	1.67		3.86	5.93	8	-26

Sample 48	Amp	Ep	Pl	Ttn	Total	Measured	% Diff.
Y Group: Epidote Amphibolite							
Mode % (+ 2 % Quartz)	74	7	15	2			
Reconstructed (ppm)							
Sc	36.78	2.05	1.16	0.07	40.05	48	-16
V	161.7	15.96	1.73	20.17	199.6	376	-46
Cr	82.31	7.98	0.15	6.64	97.08	260	-62
Co	21.79	0.04	0.01	n.d.	21.84	n.d.	
Ni	60.24	1.36	6.50	0.28	68.38	86	-20
Cu	1.94	0.12	1.48	0.03	3.57	31	-88
Zn	132.8	4.39	13.00	0.37	150.6	57	+164
Sr	5.57	21.45	71.63	2.01	100.7	321	-68
Rb	2.28	0.12	1.74	0.02	4.15	10	-58
Y	5.69	0.86	0.06	24.87	31.48	30	+5
Zr	12.97	3.82	0.36	9.57	26.72	132	-80
Nb	0.15	2.65	0.18	4.85	7.83	9	-13

Chapter 6: Mass-Balance and Reaction-Balance Calculations

Table 6.2 (continued) Trace element mass balance. Reconstructed concentrations based on measured abundances (Table 5.1) and mineral modes compared to the measured whole rock-total (*italics*) as an independent quality control. See text for full explanation. Results presented here are illustrated in Figure 6.4(c-d).

Sample 06	Amp	Ep	Pl	Ttn	Total	Measured	% Diff.
-----------	-----	----	----	-----	-------	----------	---------

Y Group: Epidote Amphibolite

Mode % 77 3 15 1
(+ 4 % Quartz)

Reconstructed (ppm)

Sc	48.59	0.79	0.32	0.06	49.76	46	+8
V	376.7	6.54	0.63	3.99	387.9	428	-9
Cr	217.3	1.75	0.61	0.92	220.6	107	+106
Co	17.48	0.04	0.01	n.d.	17.52	n.d.	
Ni	68.5	0.38	2.05	0.16	71.04	34	+108
Cu	2.05	0.06	0.23	0.02	2.36	33	-93
Zn	196.5	7.26	13.17	0.13	217.1	75	+189
Sr	12.24	20.28	79.69	0.72	112.9	99	+14
Rb	0.63	0.02	0.06		0.71	3	-76
Y	34.38	1.01	0.13	6.23	41.74	33	+26
Zr	20.96	2.45	1.13	2.66	27.20	141	-81
Nb	1.26	0.16		13.50	14.92	9	+66

Sample 49	Amp	Pl	Ttn	Total	Measured	% Diff.
-----------	-----	----	-----	-------	----------	---------

Y Group: Plagioclase Amphibolite

Mode % 65 29 1
(+ 5 % Quartz)

Reconstructed (ppm)

Sc	46.12	0.43	0.05	46.60	46	+1
V	286.9	0.07	11.42	298.5	399	-25
Cr	211.7	0.94	2.54	215.4	159	+35
Co	41.50	0.22	n.d.	41.72	n.d.	
Ni	70.59	2.74	0.29	73.62	51	+44
Cu	2.10	0.32	0.02	2.44	8	-70
Zn	124.8	7.71	0.07	132.6	89	+49
Sr	11.23	114.3	0.19	125.7	99	+26
Rb	0.86	4.84		5.70	5	+14
Y	26.68	0.06	10.84	37.58	31	+21
Zr	58.57	0.11	5.60	64.27	131	-50
Nb	1.82		2.43	4.26	10	-57

Sample 46 Epidote Amphibolite (10% modal epidote)

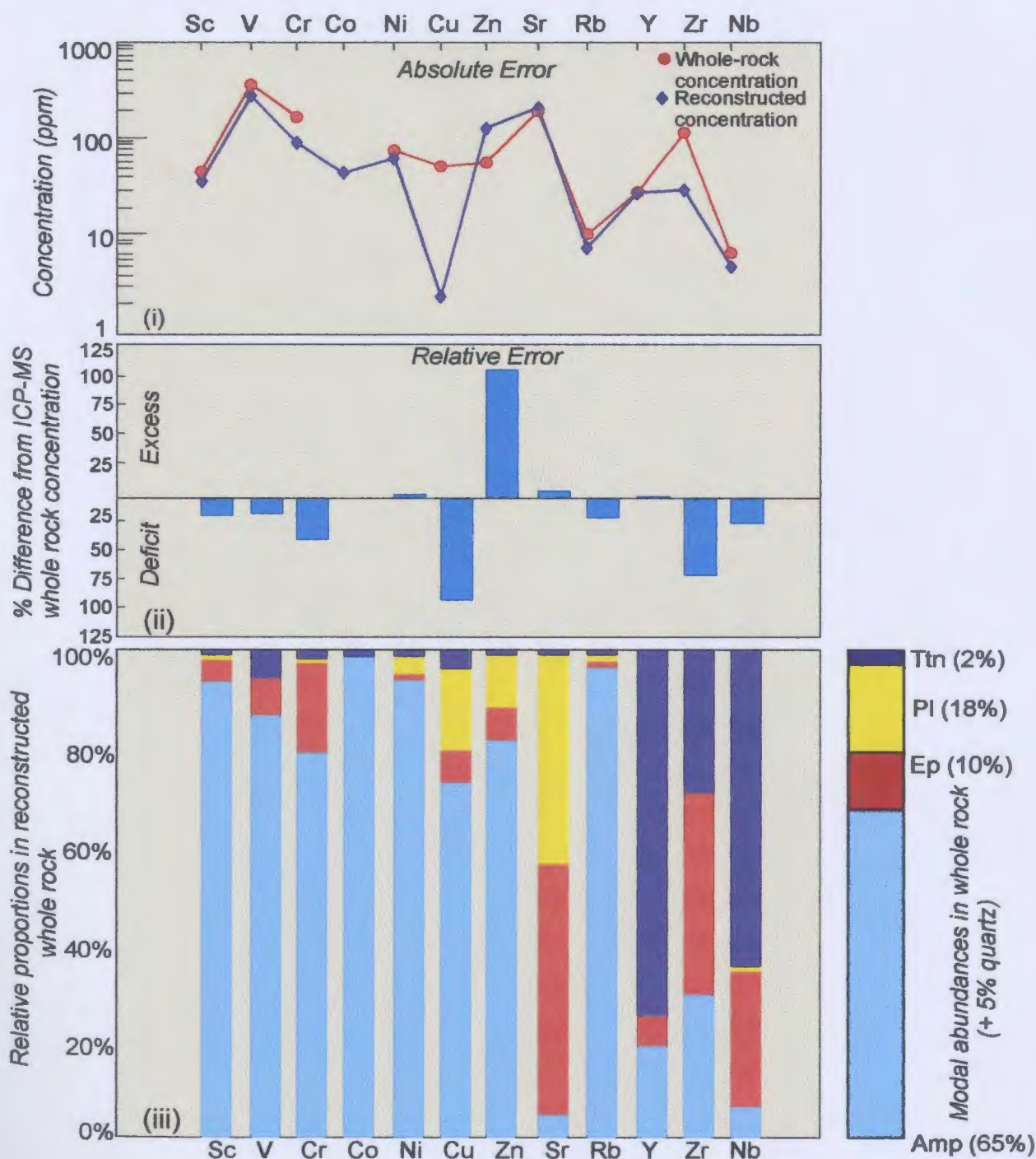


Figure 6.4 (a) Mass balance diagram for sample 46 (Y Group) showing the relative roles of Ca amphibole, plagioclase, epidote, and titanite as trace-element carriers. See Figure 6.1 for explanation of each diagram (i-iii). Selected transition metals include Sc-Zn, LILEs include Sr and Rb, Y, Zr and Nb are HFSEs.

Sample 48 Epidote Amphibolite (7% modal epidote)

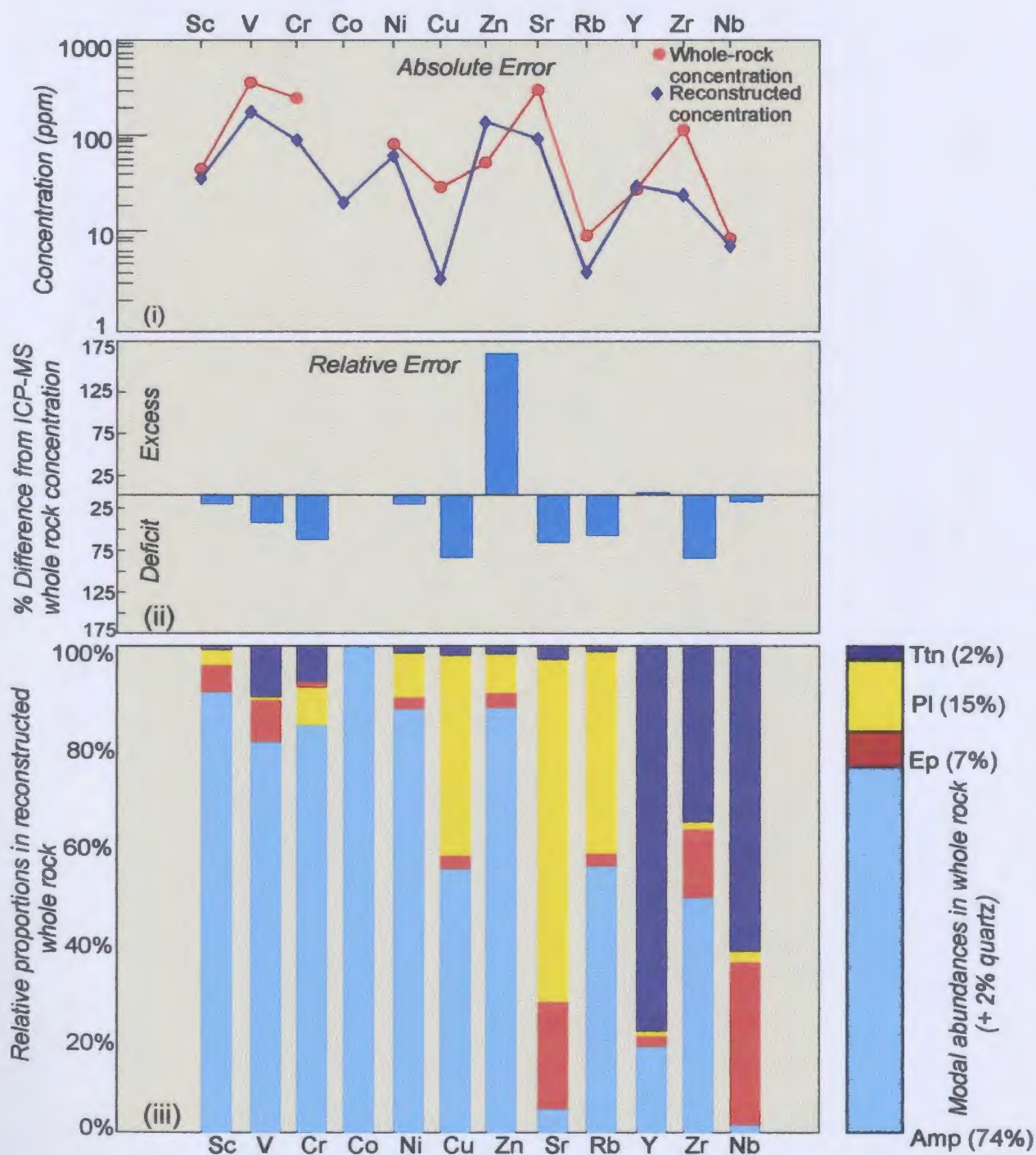


Figure 6.4 (b) Mass balance diagram for sample 48 (Y Group) showing the relative roles of Ca amphibole, plagioclase, epidote, and titanite as trace-element carriers. See Figure 6.1 for explanation of each diagram (i-iii). Selected transition metals include Sc-Zn, LILEs include Sr and Rb, Y, Zr and Nb are HFSEs.

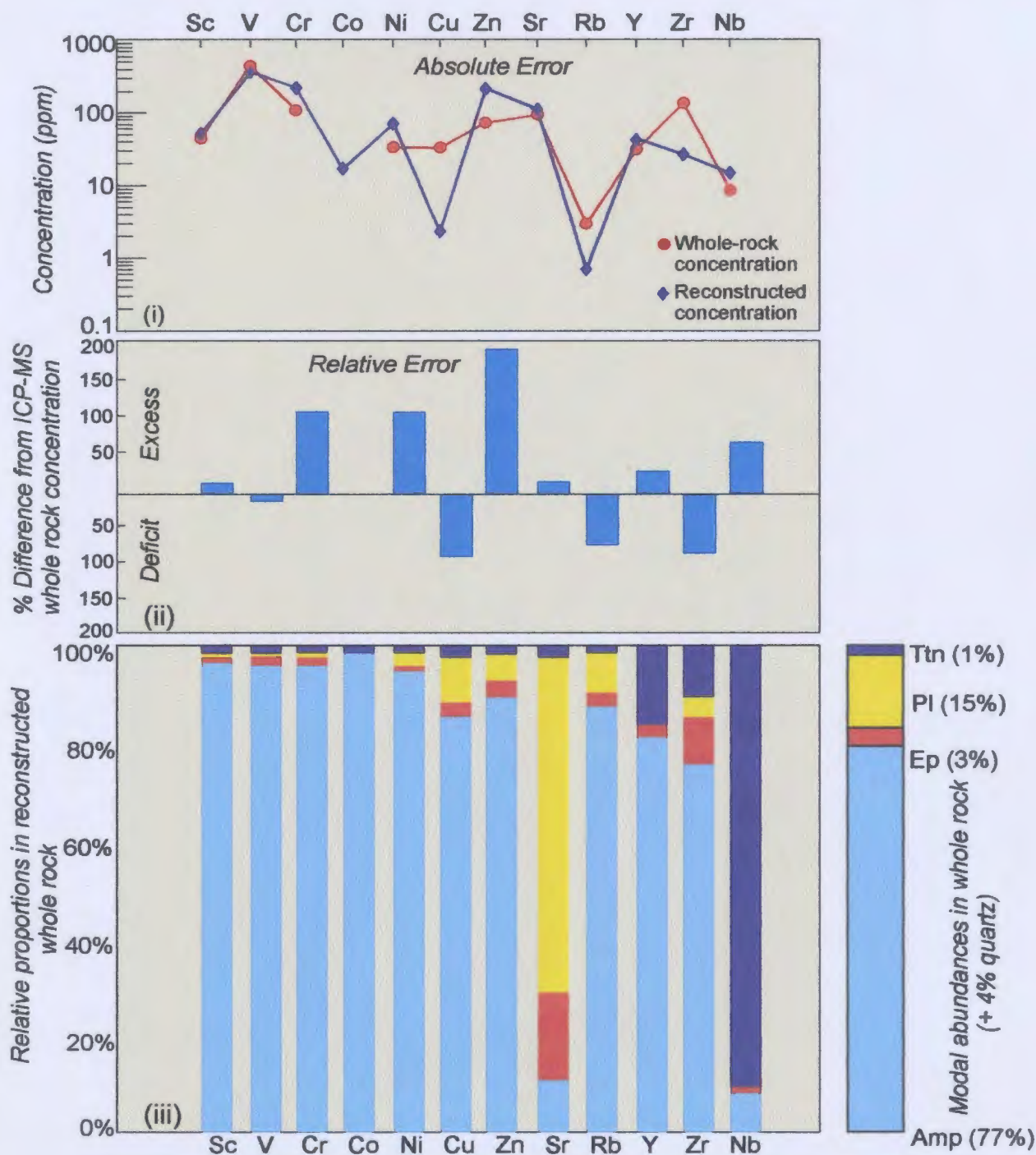
Sample 06 Epidote Amphibolite (3% modal epidote)

Figure 6.4 (c) Mass balance diagram for sample 06 (Y Group) showing the relative roles of Ca amphibole, plagioclase, epidote, and titanite as trace-element carriers. See Figure 6.1 for explanation of each diagram (i-iii). Selected transition metals include Sc-Zn, LILEs include Sr and Rb, Y, Zr and Nb are HFSEs.

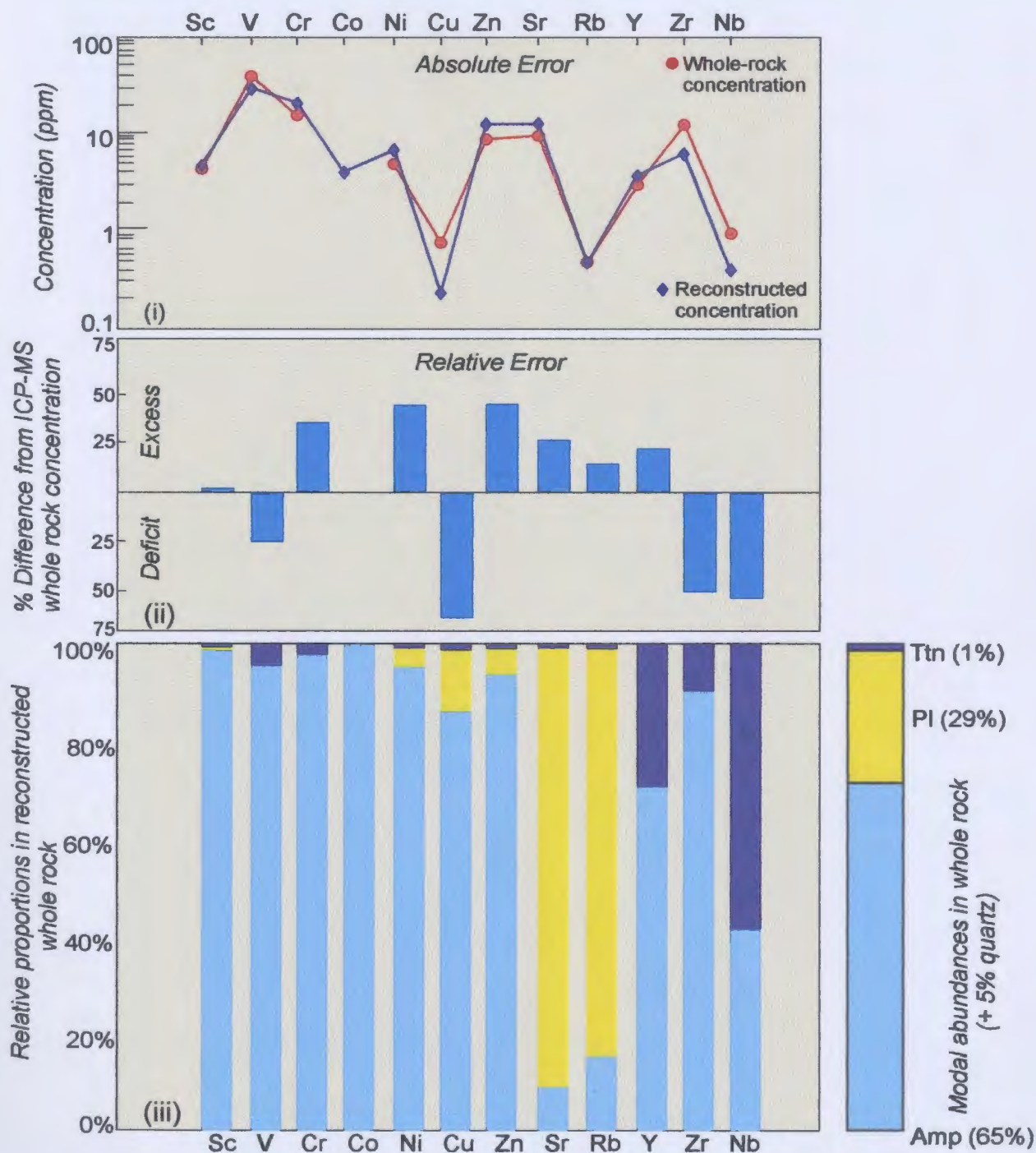
Sample 49 Plagioclase Amphibolite (0% modal epidote)

Figure 6.4 (d) Mass balance diagram for sample 49 (Y Group) showing the relative roles of Ca amphibole, plagioclase and titanite as trace-element carriers. See Figure 6.1 for explanation of each diagram (i-iii). Selected transition metals include Sc-Zn, LILEs include Sr and Rb, Y, Zr and Nb are HFSEs.

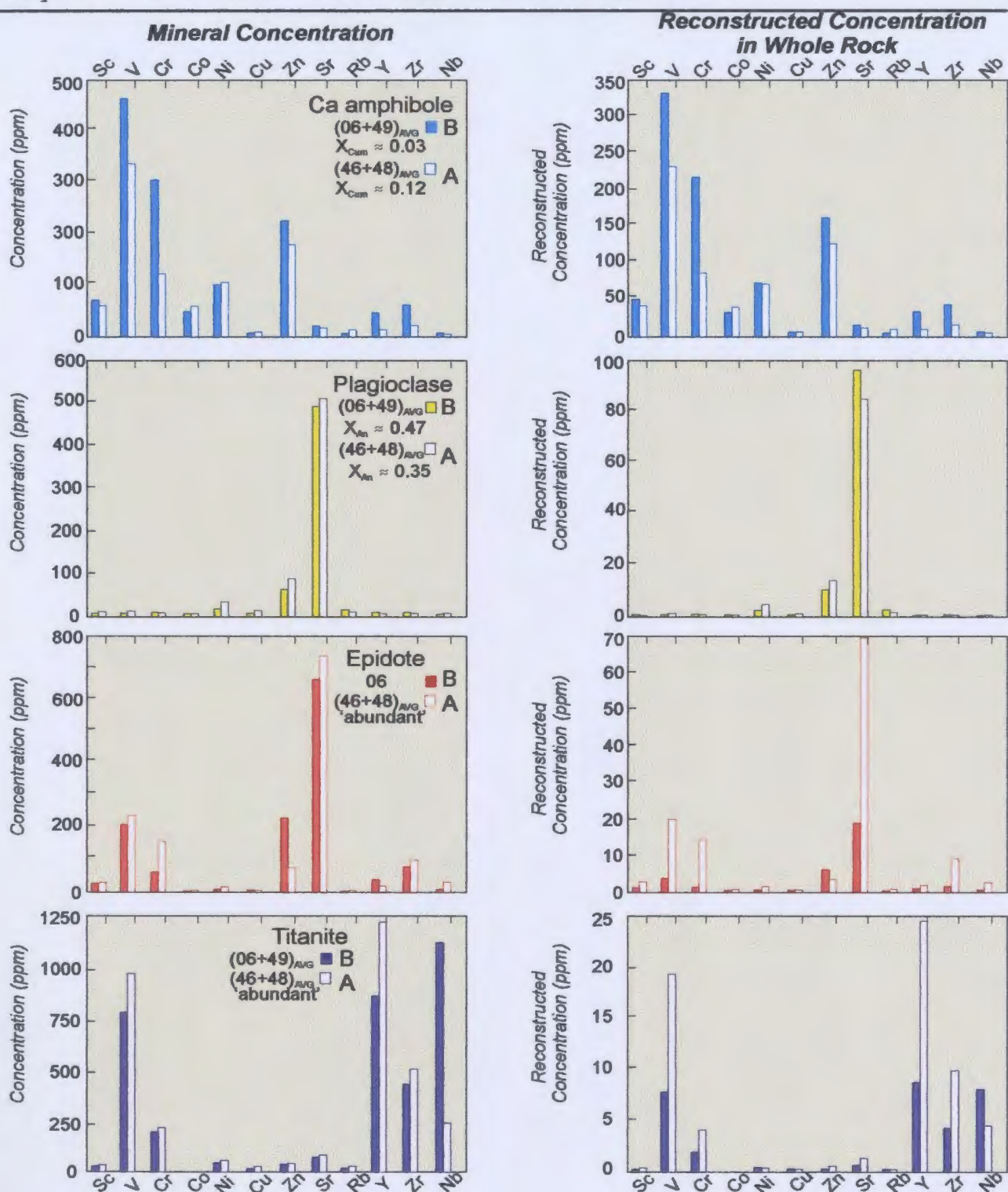


Figure 6.5 Σ Trace-element concentrations (LAM-ICP-MS) and Σ reconstructed trace-element concentrations (measured x modal abundance) for samples 46+48 (relatively high modal titanite and epidote) relative to samples 06+49 (less modal titanite and epidote).

Chapter 6: Mass-Balance and Reaction-Balance Calculations

Table 6.3 Model balanced epidote-out 'reaction' isograd based on SVD analysis of composite compositional matrix (**M**). Percent deviation from perfect mass balance given for percent difference of cations between product and reactant side. See text for explanation. One sigma error estimates based on average mineral cation abundances per formula unit (Appendix A). Reconstructed totals accepted if with three times 1 sigma analytical uncertainty.

Model of Epidote-out Reaction Isograd							
1.00 Ca amp ₄₆ + 1.70 Pl ₄₆ + 0.34 Ep ₄₆ + 1.77 Ttn ₄₆ = 1.07 Ca Amp ₄₉ + 1.92 Pl ₄₉ + 1.80							
Composite Compositional Matrix (M)							
	Ca amp ₄₆	Pl ₄₆	Ep ₄₆	Ttn ₄₆	Ca amp ₄₉	Pl ₄₉	Ttn ₄₉
Ti	0.11	0.00	0.00	0.94	0.12	0.00	0.93
Al	2.11	1.31	2.30	0.05	2.26	1.40	0.07
Fe ³⁺	0.02	0.00	0.81	0.00	0.29	0.00	0.01
FeMgMn	4.48	0.02	0.01	0.01	4.18	0.03	0.00
Ca	1.76	0.34	2.03	1.01	1.94	0.48	0.99
NaK	0.61	0.68	0.00	0.00	0.79	0.47	0.00
Reconstructed Cation Totals							
	Ca amp ₄₆	Pl ₄₆	Ep ₄₆	Ttn ₄₆	Ca amp ₄₉	Pl ₄₉	Ttn ₄₉
Ti	0.11	0.00	0.00	1.66	0.13	0.00	1.67
Al	2.11	2.23	0.78	0.09	2.42	2.69	0.13
Fe ³⁺	0.02	0.00	0.28	0.00	0.31	0.00	0.02
FeMgMn	4.48	0.03	0.00	0.02	4.47	0.06	0.00
Ca	1.76	0.58	0.69	1.79	2.08	0.92	1.78
NaK	0.61	1.16	0.00	0.00	0.85	0.90	0.00
1 σ errors of EPMA							
	Ca amp ₄₆	Pl ₄₆	Ep ₄₆	Ttn ₄₆	Ca amp ₄₉	Pl ₄₉	Ttn ₄₉
Ti	0.01	0.001	0.003	0.01	0.004	0.001	0.04
Al	0.03	0.03	0.03	0.01	0.04	0.03	0.04
Fe ³⁺	0.04	0.001	0.04	0.004	0.05	0.001	0.001
FeMgMn	0.03	0.02	0.001	0.001	0.07	0.01	0.01
Ca	0.03	0.03	0.03	0.01	0.03	0.03	0.05
NaK	0.04	0.03	0.01	0.01	0.03	0.04	0.001
Reconstructed Totals							
	46	49	Diff (%)	Diff*	Diff @ 1 σ	Diff @ 3 σ	
Ti	1.77	1.80	1.61	0.03	0.05	0.15	
Al	5.21	5.23	0.47	0.02	0.01	0.03	
Fe ³⁺	0.30	0.33	11.14	0.03	0.01	0.03	
FeMgMn	4.54	4.53	0.11	0.005	0.02	0.06	
Ca	4.76	4.78	0.30	0.01	0.06	0.18	
NaK	1.77	1.75	1.04	0.02	0.07	0.21	
Total	18.34	18.42	0.68	0.12	0.06	0.18	

* Absolute values of differences between samples 49 ('products') and 46 ('reactants'). All within 3 σ analytical uncertainty.

Chapter 6: Mass-Balance and Reaction-Balance Calculations

Table 6.4 Redistribution of REE among analysed phases using the balanced model epidote-out reaction isograd. Reconstructed concentrations based on measured abundances (Table 4.1) and reaction coefficients (Table 6.3). Percent deviation from perfect mass balance and relative enrichment factors for Ca amphibole, plagioclase and titanite based on the relative differences of reconstructed REEs between product and reactant side of *R* 6.1. See text for explanation.

REE	Ca amp ₄₆	Pl ₄₆	Ep ₄₆	Ttn ₄₆	Ca amp ₄₉	Pl ₄₉	Ttn ₄₉
Recon (ppm)							
La	0.22	0.48	12.18	236.2	4.08	3.50	124.1
Ce	1.18	0.65	23.59	749.3	13.91	3.56	482.8
Pr	0.22	0.06	3.06	113.1	2.42	0.30	86.67
Nd	1.44	0.20	12.38	605.3	13.99	0.95	538.2
Sm	0.66	0.06	2.30	199.9	4.95	0.13	207.9
Eu	0.23	0.15	0.81	70.27	1.65	0.22	62.55
Gd	1.12	0.07	1.72	269.0	7.00	0.06	288.5
Tb	0.19	0.00	0.23	46.20	1.18	0.01	47.25
Dy	1.66	0.03	1.41	324.5	8.29	0.05	352.8
Ho	0.37	0.00	0.26	66.20	1.77	0.01	70.11
Er	1.15	0.03	0.69	195.7	5.16	0.05	204.3
Tm	0.17	0.01	0.09	27.49	0.76	0.01	29.71
Yb	1.24	0.05	0.60	188.2	5.30	0.05	199.9
Lu	0.21	0.00	0.09	25.67	0.84	0.01	26.60
LREE	3.06	1.39	51.20	1704	34.40	8.32	1231
MREE	4.22	0.33	6.73	976.1	24.84	0.48	1029
HREE	2.75	0.09	1.46	437.0	12.06	0.13	461
ΣREE	10.03	1.81	59.40	3117	71.30	8.93	2721
REE	Relative Enrichment Factor (#49 - # 46) / #46			Reconstructed Total (ppm)		Difference (%) {(Σ49 - Σ46) / Σ46}*100	
	Ca amp	Pl	Ttn	46	49		
La	17.92	6.37	-0.47	249.1	131.7	-47.14	
Ce	10.80	4.49	-0.36	774.7	500.2	-35.43	
Pr	9.81	3.70	-0.23	116.5	89.40	-23.23	
Nd	8.73	3.80	-0.11	619.4	553.1	-10.69	
Sm	6.50	1.10	0.04	202.9	213.1	5.00	
Eu	6.25	0.42	-0.11	71.46	64.42	-9.85	
Gd	5.27	-0.20	0.07	271.9	295.5	8.66	
Tb	5.16	1.86	0.02	46.62	48.44	3.89	
Dy	3.99	0.51	0.09	327.6	361.1	10.24	
Ho	3.82		0.06	66.82	71.89	7.58	
Er	3.49	0.65	0.04	197.6	209.5	6.04	
Tm	3.59	1.02	0.08	27.75	30.48	9.83	
Yb	3.29	-0.04	0.06	190.0	205.3	8.05	
Lu	3.08		0.04	25.96	27.45	5.76	
LREE	10.26	5.00	-0.28	1760	1274	-27.57	
MREE	4.88	0.47	0.05	987.3	1054	6.79	
HREE	3.38	0.38	0.05	441.3	472.8	7.13	
ΣREE	6.11	3.94	-0.13	3188	2802	-12.13	

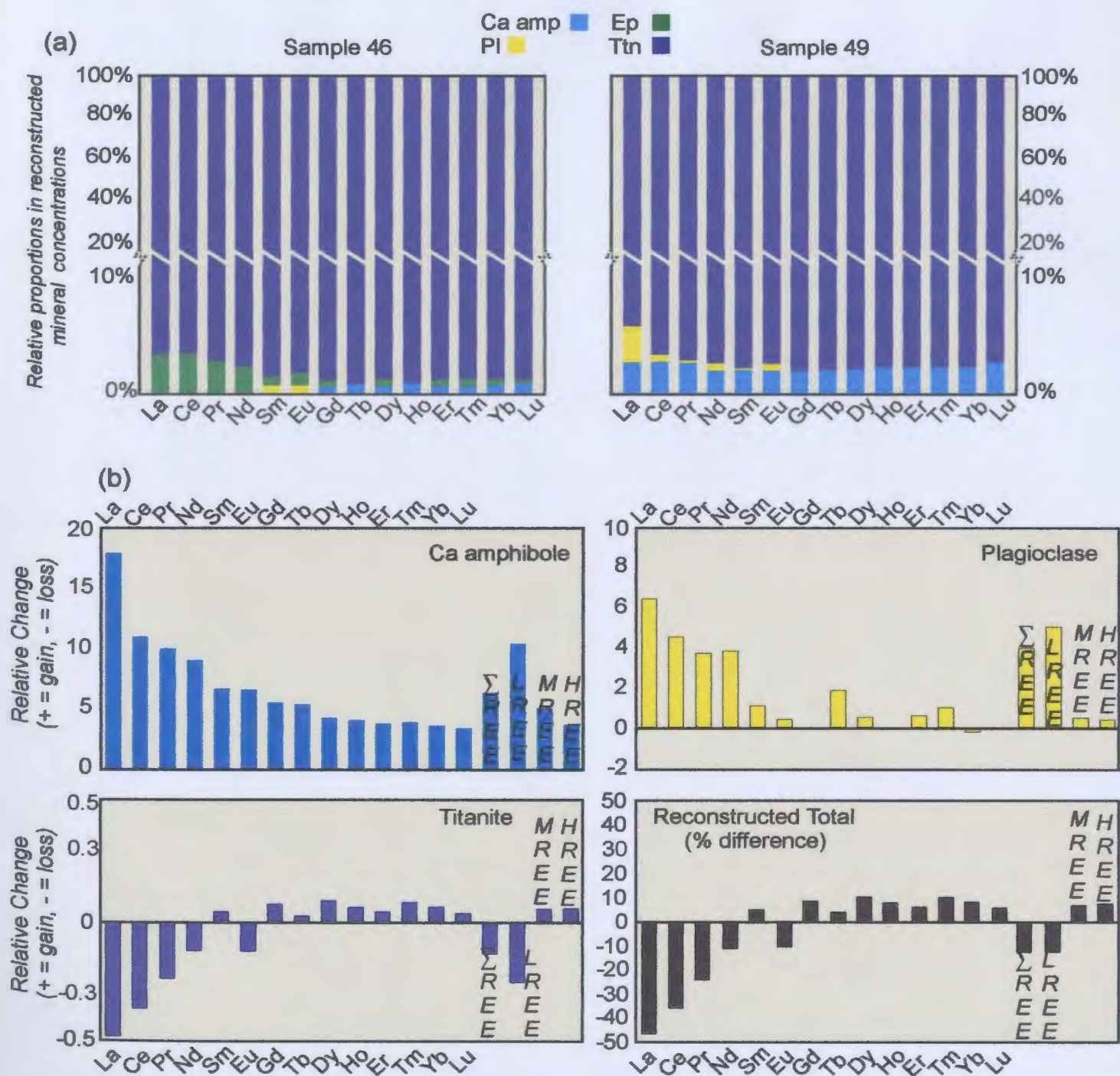


Figure 6.6(a) Bar graphs illustrating the relative proportions of REEs in each phase in samples 46 (below epidote-out isograd) and 49 (above isograd) on the basis of the model epidote-out reaction *R* 6.1. See text for explanation. (b) Bar graphs illustrating the relative differences in reconstructed mineral REE abundances above and below the isograd calculated as $[(49-46)/46]$. The percent difference of the reconstructed totals of all phases (including epidote) summed over the reactant and product side of the model reaction is calculated in the same manner ($\times 100$) as the relative changes in REE mineral abundances.

Chapter 6: Mass-Balance and Reaction-Balance Calculations

Table 6.5 Redistribution of selected trace elements among analysed phases using the balanced model epidote-out reaction isograd. Reconstructed concentrations based on measured abundances (Table 5.1) and reaction coefficients (Table 6.3). Percent deviation from perfect mass balance and relative enrichment factors for Ca amphibole, plagioclase and titanite based on the relative differences of reconstructed abundances between product and reactant side of *R* 6.1. See text for explanation.

Traces Recon (ppm)	Ca amp ₄₆	Pl ₄₆	Ep ₄₆	Ttn ₄₆	Ca amp ₄₉	Pl ₄₉	Ttn ₄₉
Sc	63.33	1.62	8.08	12.01	75.92	3.33	8.39
V	457.5	5.19	88.40	1649	472.4	0.52	2055
Cr	127.9	4.21	68.68	120.12	348.4	7.24	457.2
Co	79.53	0.11	0.13	0.00	68.32	1.68	0.00
Ni	119.3	28.08	2.17	79.53	116.2	21.06	51.39
Cu	3.37	5.02	0.54	8.25	3.45	2.43	4.10
Zn	174.3	147.0	27.71	29.80	205.4	59.18	13.29
Sr	15.68	937.9	402.9	26.67	18.48	877.4	33.57
Rb	13.70	1.80	0.24	0.90	1.42	37.16	0.29
Y	9.46	0.12	6.67	2153.5	43.92	0.48	1950
Zr	15.68	0.34	49.17	894.4	96.41	0.88	1007
Nb	0.62	0.03	5.68	341.61	3.00	0.03	437.4

Traces	Relative Enrichment Factor (#49 - #46) / #46			Reconstructed Total (ppm)		Difference (%) $\{(\sum 49 - \sum 46) / \sum 46\} * 100$
	Ca amp	Pl	Ttn	46	49	
Sc	0.20	1.05	-0.30	85.04	87.63	3.05
V	0.03	-0.90	0.25	2200	2529	14.89
Cr	1.73	0.72	2.81	320.9	812.9	153.34
Co	-0.14	14.81		79.76	70.00	-12.24
Ni	-0.03	-0.25	-0.35	229.1	188.7	-17.66
Cu	0.02	-0.52	-0.50	17.18	9.98	-41.88
Zn	0.18	-0.60	-0.55	378.8	277.9	-26.62
Sr	0.18	-0.06	0.26	1383	929.5	-32.80
Rb	-0.90	19.65	-0.68	16.64	38.87	133.50
Y	3.65	3.08	-0.09	2169	1994	-8.07
Zr	5.15	1.62	0.13	959.6	1104	15.09
Nb	3.86	0.35	0.28	347.9	440.4	26.59

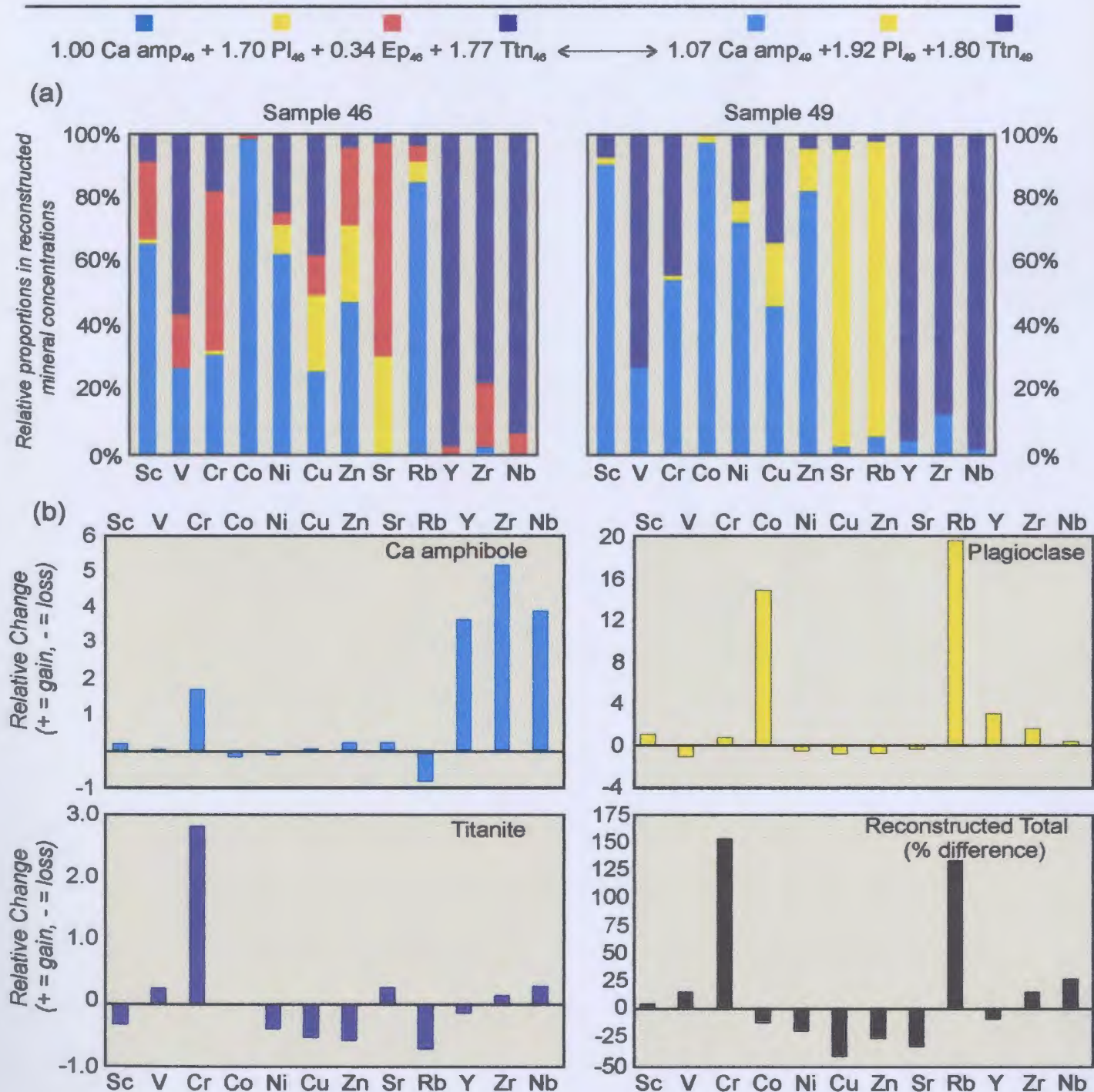


Figure 6.7(a) Bar graphs illustrating the relative proportions of trace elements in each phase in samples 46 (below epidote-out isograd) and 49 (above isograd) on the basis of the model epidote-out reaction *R* 6.1. See text for explanation. (b) Bar graphs illustrating the relative differences in reconstructed trace-element mineral abundances above and below the isograd calculated as $[(49-46)/46]$. The percent difference of the reconstructed totals of all phases (including epidote) summed over the reactant and product side of the model reaction is calculated in the same manner ($\times 100$) as the relative changes in trace-element mineral abundances.

Chapter 7: Conclusions

7.1 Introduction

This study employed an integrated micro-beam approach, namely EPMA and LAM-ICP-MS, to elucidate *in situ* major- and trace-element information contained in epidote-amphibolite, plagioclase-amphibolite, and garnet-amphibolite assemblages in metabasic rocks from the St. Anthony Complex, northern Newfoundland. This approach has provided significant insight into the partitioning behaviour of *REE* and a selected suite of trace elements amongst minerals in these assemblages and, coupled with bulk-rock major- and trace-element data, has enabled the influence of bulk composition on trace-element mineral chemistry and the relative carrying capacities of the analysed minerals in different assemblages to be evaluated.

A logical start to a discussion of the overall conclusions of this thesis is to return to the goals outlined in the first chapter, which included: (i) determination of the approach to equilibrium for a range of trace elements; (ii) determination of quantitative partition coefficient data; (iii) investigation of the compositional influences (e.g., bulk composition, major-element mineral composition, *etc.*) on partitioning between selected trace elements; (iv) calculation of mass balances to determine the major carriers for

specific trace elements in metamorphic minerals over this range of metamorphic grade; and (v) determination of trace element losses/gains across the metamorphic gradient. The results presented in this thesis satisfy all of these goals to some degree, and in addition, provide insight into site distributions within individual phases, as well as pointing the way towards appropriate new directions to answer certain questions raised by this research.

7.2 Discussion of Results

7.2.1 Approach to Equilibrium

The first goal of this thesis was to determine the approach to equilibrium for *REEs* and a range of selected first-row transition metals, high-field-strength-elements, and large-ion lithophile elements (Sc, V, Cr, Co, Ni, Cu, Zn, Sr, Rb, Y, Zr, Nb) in various mineral assemblages in metabasites. The measured systematic distributions of *REEs* among analysed phases in different bulk compositions (i.e., Y and Zr groups) and mineral assemblages (epidote amphibolite, plagioclase amphibolite and biotite amphibolite) indicate equilibrium partitioning was broadly achieved during metamorphism, despite the relatively low grade of the samples. This conclusion is compatible with the results of other recent studies in mid- to upper amphibolite- and eclogite-facies rocks (e.g., Yang, 2002; Zack *et al.*, 2002 respectively), that also

employed a similar *in situ* analytical approach. The results indicate that the low limits of detection afforded by LAM-ICP-MS make it a powerful tool for spatially related mineral trace-element investigations. In addition to the REEs, most of the other analysed trace elements also exhibit consistent behaviour between selected mineral pairs. For example, systematic distributions of Sc, V, Cr, Rb, Y and Nb between Ca amphibole and titanite occur over a range of concentrations and in all the mineral assemblages examined in this study; in epidote amphibolite assemblages, Sc, V, Cr, Ni, Rb and Y are systematically distributed among epidote, titanite and Ca amphibole; and in biotite amphibolite assemblages V and Y are systematically distributed among garnet, Ca amphibole and titanite, all suggesting that equilibration was achieved for these elements. On the other hand, large variations in the partitioning behaviour of a few elements, e.g., Rb between Ca amphibole and plagioclase, suggest that some elements may have had different scales of equilibrium in the analysed samples during amphibolite-facies metamorphism. In addition, the irregular distribution of certain other elements may be due to the presence and/or breakdown of trace-element enriched phases, e.g., irregular Nb distribution between garnet and titanite may be due to micro-inclusions of a Nb-sequestering phase such as ilmenite or rutile in garnet or to the breakdown a Nb-enriched phase resulting in zoning in one or both phases.

7.2.2 Trace-Element Partition Coefficients

Despite major advances in *in situ* analytical techniques over the last two decades, there is a dearth of mineral—mineral trace-element distribution coefficients for coexisting metamorphic phases such as plagioclase, titanite and Ca amphibole. This situation is in marked contrast to that for igneous systems, for which there is a large and rapidly growing database of high quality mineral—liquid partition coefficients. There are several reasons for the more rapid progress of partitioning studies in igneous petrology. Firstly, melt exhibits *relatively* little control on the distribution of a trace element in mineral—melt systems, thus igneous minerals have the potential to reveal compositional and *P-T* information about a source region (Rollinson, 1993). Secondly, igneous systems can be modelled in the laboratory, and many modern partition coefficient data are derived from experimental systems in which synthetic or natural starting materials are doped with elements of interest (e.g., Bottazzi *et al.*, 1999; Oberti *et al.*, 2000; Tiepolo *et al.*, 2000, 2002). Such studies can provide insight into natural systems since variations in *P-T* conditions and bulk composition can be closely monitored. In an attempt to close the gap between the volume of partitioning data in igneous and metamorphic systems by providing new information on partitioning in metamorphic systems, an important goal of *this* study was to calculate trace-element partition coefficients in a *natural* metamorphic system. Thus, Nernst (D_i) and Nielsen (D_i^*) distribution coefficients for REE (see 4.3) and selected trace elements (see 5.3)

were calculated for nine mineral pairs over a range of bulk composition and mineral assemblage.

Despite the limited published information regarding mineral—mineral partition coefficients for common phases in amphibolite-facies metabasites, some comparisons were possible and in general, calculated partition coefficients are comparable to those published by other workers. For example, the magnitudes of *REE* partition coefficients for Ca amphibole—garnet pairs are similar to those reported by Sorensen and Grossman (1989), Kretz *et al.* (1999) and Skublov and Drugova (2003), with *LREE* preferentially partitioning into Ca amphibole, *HREE* preferentially partitioning into garnet and *MREE* approximately equally distributed between each phase. In addition, measured partition coefficients for Gd and Sr for Ca amphibole—plagioclase pairs are in general agreement with those reported by Kretz *et al.* (1999), with Sr exhibiting preference for plagioclase relative to Ca amphibole, and Gd (*MREE*) preferentially partitioning into Ca amphibole. Measured titanite—garnet and Ca-amphibole—titanite partition coefficients for Sc and Lu are similar to those reported by Sorensen and Grossman (1989) for amphibolite-facies metabasites from southern California. These similarities suggest that the data are generally applicable to amphibolite-facies metabasites. Given the absence of epidote—mineral partitioning data in the literature, no direct comparisons between measured epidote—mineral partition coefficients are possible. However, the similarities among partition coefficients measured in this study for Ca amphibole, garnet and titanite

to those in the published literature, and the similarities between the measured *REE* and trace-element concentrations in epidote to epidote trace-element concentrations in other metabasites (e.g., Brunsmann *et al.*, 2000), suggest that measured epidote—mineral partition coefficients are also likely to be representative of epidote-amphibolites in general.

7.2.3 Crystal-Chemical Controls on Trace-element Partitioning

Given the systematic nature of measured trace-element distributions amongst coexisting phases, calculated partition coefficients likely represent equilibrium distributions. Thus, it became instructive in the course of this study to attempt to investigate crystal-chemical controls on the partitioning of *REE* and selected trace elements. In general, changes in major-element mineral chemistry may cause slight adjustments in mineral structure that affect the ability of site polyhedra to host specific trace elements (Smyth and Bish, 1988). Several recent experimental studies combining crystal—liquid partitioning with crystal structure refinements have reported correlations between major and trace elements linked to slight changes in polyhedra for a variety of phases and melt compositions (e.g., Blundy and Wood, 1994; Bottazzi *et al.*, 1999; Oberti *et al.*, 2000; Tiepolo *et al.*, 2000, 2001, 2002, 2003). In addition, Yang *et al.* (1999) showed that trace-element partitioning between coexisting garnet and biotite in amphibolite-facies metapelites was correlated with the major-element compositions of

both phases.

In this study, correlations among *REE*, trace-element abundances, and selected ratios of *L*-, *M*-, and *HREE*s with major-element molar fractions and exchange vectors for Ca amphibole, plagioclase, epidote (Y group) and garnet (Zr group) were discovered, which support the existence of major-element control on incorporation of some trace elements. However, despite being the most *REE*- and trace-element enriched of all the analysed phases, titanite displayed no significant correlations between *REE*, trace elements, or ratios of selected *L-M* or *HREE* with variations in major-element composition. The reason for this is not well understood, but may be due to the limited major-element compositional variability exhibited by this phase.

Analysed Ca amphibole exhibits several correlations among major- and trace-components, primarily linked to the degree of cummingtonite substitution in 8-fold *M4* sites and the (FeMg)^{VI} and Al^{VI} components in octahedral *M1-3* sites. For example, the partitioning of *L*-, *M*-, and *HREE*s exhibits a dependence on the 8-fold coordinated cummingtonite component of Ca amphibole, with ‘cummingtonite-rich’ Ca amphibole preferentially partitioning *M-HREE* relative to *LREE*; and in another example, the partitioning of several transition metals (Sc, Cr, V, Cu, Ni, Co) exhibits dependence on the octahedral Al and \sum FeMg contents of *M1-3* sites. In plagioclase, the ratio of $\sum(L+MREE) / HREE$ is strongly correlated with anorthite content. In analysed epidote, in which major-element substitution on *X* sites is limited, the dominant major-element

control on trace-element distributions is the occupancy of the octahedral $M3$ site, as evident from correlations of Al^{3+} with $\sum REE$, Y and several transition elements (Zn, Cu, Ni, Co). Consistent with results reported by Yang *et al.* (1999), the almandine component in analysed garnet is correlated with *HREE* abundance. These correlations indicate that variations in major-element composition, especially those linked with extensive solid solutions, exert direct control on trace-element substitution by modifying crystallographic site polyhedra to more readily either accept or reject a particular trace element.

Generally, the curves in mineral—mineral partition coefficient *versus* ionic radius diagrams, the so-called Onuma-type diagrams, reflect the combined effects of the ideal site parameters (i.e., radius and elasticity) of both minerals. As a result, they can take on an almost infinite range of shapes, rendering quantitative extraction of the ideal site sizes and elasticities using the strain-compensated *crystal—liquid* partition coefficient equation of Blundy & Wood (1994) impractical.

However, in favourable cases, the structural effects of major-element solid solutions can be qualitatively evaluated utilizing chondrite-normalized concentration *versus* ionic radius plots and Onuma-type diagrams. As an example, the shapes of chondrite-normalized *REE* curves for Ca amphibole correlate with the molar fraction of cummingtonite, with curves for relatively ‘cummingtonite-poor’ Ca amphibole exhibiting slight convexity in the *MREE*, and those for relatively ‘cummingtonite-rich’

Ca amphibole sloping monotonically from *H*- to *LREE*. In case of ‘cummingtonite-poor’ amphibole, the geometric distortion imparted by FeMg in the *M4* site is so small that the bulk properties of the *M4* cavity are defined by Ca, its principal occupant. In contrast, *REE* patterns for ‘cummingtonite-rich’ amphibole are attributed to the occurrence of two cavities of approximately equal importance within the *M4* site (*M4* and *M4'*; Bottazzi *et al.*, 1999) defined by the major-element occupancies of Ca and FeMg respectively.

Summation of the *REE* occupancies for these two cavities yields the measured chondrite-normalized *REE* pattern. In less favourable cases, such as for Ca amphibole—epidote pairs, where each mineral contains analogous sites (e.g., both minerals contain octahedral *M1-3* sites and 8-fold sites dominated by Ca [i.e., epidote *X* site and Ca amphibole *M4* site]), the qualitative extraction of site parameters is more problematic. In addition, elements that exist in variable oxidation states, and hence have variable ionic radii (e.g., first-row transition metals), complicate accurate prediction of site distributions because of their spiky patterns on Onuma-type diagrams.

To summarize, the data produced in this study support the inference that trace cations preferentially partition into polyhedra with the same nominal charge and a similar size to the cation of interest. Differences in charge may be compensated via coupled substitutions or vacancies. In general, the magnitude of the mismatch in ionic charge and radius of a trace element relative to the host polyhedra is directly proportional to the amount of energy required for the substitution to occur (e.g., Blundy and Wood,

1994).

7.2.4 Mass-Balance Considerations

It was shown in this study that the measured trace-element distributions of Ca amphibole, plagioclase, epidote, garnet and titanite were influenced by bulk composition, mineral assemblage (itself a function of P - T and bulk composition), mineral composition and crystal chemistry. Together with modal abundance, these factors contribute to the mass balance for any given element. In terms of bulk composition, investigated samples cluster in AFM compositional space, and carry remarkably similar abundances of *REE*. However, on the basis of their ACF distributions and trace-element abundances, two subgroups were recognized: a relatively calcium-rich subgroup with higher chondrite-normalized abundances of Sr, V, Cr and Zr (composition A); and a relatively calcium-poor subgroup with higher chondrite-normalized abundances of Nb (composition B; see section 3.3 and Figure 6.1). The relative roles of Ca amphibole, plagioclase, epidote, and titanite as carriers for selected trace elements and *REE* in each sample were evaluated in the light of these slight bulk-compositional differences.

Independent of the mineral assemblage, two types of carrier behaviour were exhibited, which corresponded to bulk compositions A and B. In general, where titanite and epidote are relatively abundant (i.e., bulk composition A), these trace-element-enriched phases, especially the former, were the dominant carriers of all Y, Nb and *REE*,

accounting for approximately 90% and 65% of the *LREE* and *HREE* budgets respectively. Ca amphibole was the dominant sink for most transition elements and plagioclase sequestered Sr and minor amounts of *LREE*. However, for samples of bulk composition B, where titanite and epidote are relatively less abundant or in the case of one sample (# 49) where the latter is not present at all, the relative capacities of those phases as trace element or *REE* reservoirs were significantly diminished. Ca amphibole became the dominant carrier of *REE* and Y and remained the dominant carrier of most transition elements. Despite the reduction in its *REE* carrying-capacity, however, titanite remained the dominant Nb sink. With the exception of Sr, and in two samples Rb, plagioclase was a subordinate carrier of all analysed trace elements.

The disappearance of epidote at the epidote-out isograd was shown to be correlated with modal and chemical changes in Ca amphibole and plagioclase. For instance, it was shown that progressive changes in the major-element compositions of both these minerals between bulk compositions A and B directly affect their *REE* and trace-element carrying capacities (e.g., decrease in X_{Cum}^{Amp} , increase in X_{An}^{Pl}), and in addition, plagioclase exhibits a significant increase in modal abundance. As a result, both major-element mineral chemistry (X) and modal abundance (M) affect the partitioning of elements of interest among coexisting metamorphic phases. In turn, both X and M are directly linked to bulk-rock chemistry (see section 3.3) and the intensive variables of metamorphism (P, T). As a result, it is likely that the compositions of the

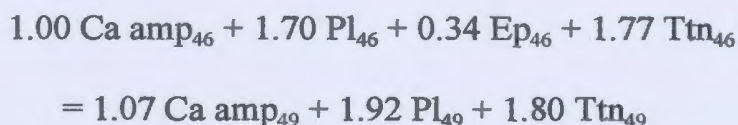
analysed phases also hold cryptic P - T information. However, due to the limited P - T range (≈ 500 - 650°C) of the analysed samples, no attempt was made to calibrate a geothermometer by studying variations in the partition coefficients in mineral pairs in saturated assemblages (e.g., Ti-saturated assemblages coexisting with titanite, Y group). [In the absence of a saturating phase, the effect of bulk composition on element distributions cannot be readily separated from P - T effects on element distributions (Pyle and Spear, 2000)]. However, the data presented in this thesis do provide a series of tests for 'equilibrium' among amphibolite-facies metabasites, and the compositional ranges of elements and partition coefficients between the nine analysed mineral pairs should provide useful reference information for interpreting mineral reactions among other metabasites.

7.2.5 Epidote-out Reaction-Balance Considerations

Noting the different *REE* and trace-element carrier roles of each major phase across bulk compositions A and B, it was logical to investigate the influence of these compositions in controlling epidote stability. As a first approximation, it was shown that despite the limited variations in the ratios of the molecular proportions of both $\text{Ca} / \text{Ca} + \text{Na}$ and $\text{Fe}^{3+} / \text{Fe}^{3+} + \text{Al}^{3+}$, there was a precipitous decline in modal epidote in the vicinity of epidote-out isograd. Thus, it was reasonable to argue that the isograd was a result of changing metamorphic grade, even though this change in grade was imposed on samples

of slightly variable bulk composition.

To determine whether this assumption was valid, the matrix algebraic technique known as singular value decomposition was employed to determine the variance of the reaction and subsequently the stoichiometric reaction coefficients. Input data were the major-element compositions of coexisting phases in representative epidote-amphibolite (composition A) plagioclase-amphibolite (bulk composition B) samples. This technique searches for a single, hypothetical, bulk composition that could be expressed as a combination of the mineral compositions in each assemblage, which is equivalent to the search for a reaction balance between the two assemblages. The following balanced reaction, which is considered to be a good qualitative representation of the textures and modal variations in analysed samples in the field study area, and is within 3 times the 1 σ analytical error of the input data, was achieved:



On the basis of this result, it was concluded that the epidote-out isograd was due primarily to a change in externally imposed conditions, i.e., temperature or pressure, (or both) and not bulk-rock chemical variations (i.e., differences between bulk compositions A and B).

Finally, the mass-balanced reaction was used in combination with *in situ* REE and trace-element analyses to evaluate the redistribution of elements formerly sequestered in

epidote. The model epidote-out reaction accounts well for the redistribution of *M-HREE* across the reaction isograd. Errors, estimated as the relative differences between the sums of reconstructed concentrations each side of the epidote-out reaction are small (<10 %) for $Y + M-HREE$, but larger for the *LREE* ($\approx 28\%$). This may imply the presence of a minor unrecognized phase above the isograd that, along with Ca amphibole and plagioclase, sequesters some of the *LREE* formerly held in epidote and titanite. Titanite is the most *REE*-enriched phase on both sides of the isograd, but its *MREE/LREE* ratio increases as the isograd is crossed, presumably related to the increased capacity of the coexisting phases Ca amphibole and plagioclase to accommodate the *LREE*, which in turn is correlated with major-element compositional changes (Ca enrichment) in these phases. Ca amphibole exhibits a significant increase (\approx six times) in $\sum REE$, especially *LREE* (\approx ten times) above the isograd and plagioclase exhibits an approximate six-fold increase in *LREE*. However, it is clear from the results that epidote-breakdown cannot be separated from a reduction in *LREE* abundance in titanite (\approx one-third reduction) above the isograd. Thus the source of the *LREE* responsible for the increases in Ca amphibole and plagioclase is not uniquely epidote, but involves a contribution from titanite as well.

With respect to other trace elements, epidote plays a significant role in sequestering several transition elements (e.g., Sc, V, Cr, Zn) and Sr ($\approx 10-40\%$) and a lesser role for the HFSEs, Zr and Nb ($\approx <10\%$). Ca amphibole is the primary host for all

transition metals and Rb, whereas titanite sequesters significant proportions of V, Ni, and Cu ($\approx 25-35\%$) and is by far the dominant carrier ($< 80\%$) of analysed HFSEs.

Plagioclase is an important Sr reservoir ($\approx 35\%$) and carries lesser amounts of Ni, Cu and Rb ($\approx 10\%$). Above the isograd, transition metals formerly held in epidote are mainly redistributed to Ca amphibole (Sc, Cr, Ni, Cu, Zn) and titanite (Cr, V). Ca amphibole assumes the previous role of epidote as a secondary HFSE carrier. With the exception of Cr (≈ 3 times increase), titanite's role as a trace-element carrier exhibits little change above the isograd. Plagioclase becomes the primary reservoir for Sr and Rb, and in the case of Sr, the increase in plagioclase is linked to epidote breakdown. However, the switch in Rb sinks across the isograd from Ca amphibole to plagioclase likely reflects disequilibrium distribution of that element.

7.3 Conclusions

The metabasites in the metamorphic sole of the Hare Bay Allochthon, Northern Newfoundland provide an excellent laboratory for the study of the distribution of *REE* and selected other trace elements among various amphibolite-facies assemblages. This study has attempted to add to the relatively small, but growing, set of data pertaining to patterns of, and controls on, the distribution of trace elements among coexisting minerals in metamorphic assemblages. The major conclusions of the study can be summarized as follows:

- 1) The systematic distributions of many analysed trace elements (e.g., *REE*, Sc, V, Cr, Ni, and Y) in epidote amphibolite, plagioclase amphibolite, and biotite amphibolite assemblages are consistent with equilibrium partitioning during amphibolite-facies metamorphism.
- 2) Analysed Ca amphibole, plagioclase, epidote, and garnet all exhibit correlations between trace and major elements, which imply the existence of a major-element control on the incorporation of some trace elements. In some cases, variations in major-element composition affect trace-element substitution at the same site. For example, the ratio of *LREE / HREE* in both plagioclase and Ca amphibole exhibits dependence on the Ca content of the plagioclase *A* site and the extent of cummingtonite substitution in the *M4* site of the Ca amphibole. In other cases, major-element variations in one site can affect trace-element substitution at adjacent sites in the same mineral. For example, Y in epidote *X* sites is correlated with Al^{VI} in adjacent *M3* sites.
- 3) Measured partition coefficients show good agreement with those determined in other studies in amphibolite-facies metabasites. For example, for Ca amphibole—garnet pairs measured D_{REE}^* are similar to those reported for other amphibolites (Sorensen and Grossman, 1989; Kretz *et al.*, 1999; Skublov and Drugova, 2003). In addition, D_{Sr}^* and D_{Gd}^* for Ca amphibole—plagioclase pairs are in general agreement with those reported by Kretz *et al.* (1999) and measured

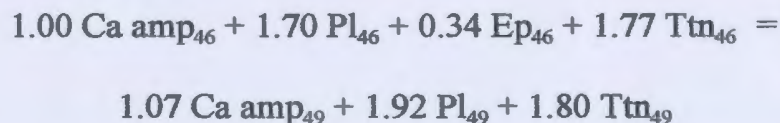
D_{Sc}^* and D_{Lu}^* for titanite—garnet and Ca-amphibole—titanite pairs are similar to those reported by Sorensen and Grossman (1989).

- 4) Calculated mineral—mineral partition coefficients between coexisting phases exhibit a dependence on ionic radius, evident from Onuma-type curves. In favourable cases, in which substitution in the two minerals takes place on non-analogous sites, qualitative information regarding site occupancies and characteristics can be extracted. For example, Onuma-type curves for *REE* partitioning between plagioclase—garnet pairs approach parabolic shapes with maxima and minima that are interpreted to represent the optimal site radii for the *A* and *X* sites in plagioclase and garnet respectively. This confirms that trace-element partitioning occurs by substitution on specific crystallographic sites. In less favourable cases, in which two minerals contain analogous sites (e.g., octahedral *M* sites in Ca amphibole and epidote), Onuma-type curves exhibit spiky patterns and are not as insightful.
- 5) Spiky patterns of transition-element abundances in Onuma-type diagrams cannot be readily related to preference for specific sites in mineral lattices. Possible explanations for these patterns include variable oxidation states and hence ionic radii of several elements (e.g., V, Cr, Ni, Cu), crystal field effects, and variable coordination numbers or bond mechanisms. No attempt has been made to evaluate these data in this study, but they represent an important problem for

future study.

- 6) There is no measurable change in whole-rock $\sum REE$ and $LREE/HREE$ across the epidote-out isograd, implying that metamorphism was essentially isochemical with respect to the *REEs*. This indicates that, in this case, they acted as relatively 'immobile' elements, despite their major redistribution among the coexisting metamorphic phases.
- 7) Results of a mass-balance study show that Y and *REE* carriers are sensitive to small variations in bulk composition, with titanite (2 % modal) and epidote (7-10 % modal) being the main carriers of Y and *REE* in a relatively calcic and Sr-, V-, Cr- and Zr- enriched bulk composition whereas for a relatively calcium-poor and Nb-enriched bulk composition, Ca amphibole (65-75 % modal) is the major Y and *REE* carrier with plagioclase (15-25% modal) assuming a minor role for the *LREE*. The decrease in the modal abundance of titanite and the disappearance of epidote at the epidote-out isograd, in combination with modal and chemical changes in Ca amphibole and plagioclase, directly affect the *REE* and trace-element carrying capacities of these phases. Plagioclase and titanite are the dominant Sr and Nb reservoirs respectively in all assemblages, in both cases increasing their roles across the epidote-out isograd. These results suggest that incremental changes in *P*, *T*, *X*, and *M* all have significant implications for the redistribution of trace elements at and near metamorphic isograds.

- 8) Mass-balance analysis using the algebraic technique of singular value decomposition yielded a model univariant reaction between epidote-amphibolite and plagioclase-amphibolite assemblages, suggesting that the presence/absence of epidote is dominantly controlled by externally imposed conditions (i.e. P and/or T) and not bulk chemical variations in these samples, i.e., the epidote-out reaction is a reaction isograd. Stoichiometric reaction coefficients in the model reaction, which is considered to be a good qualitative representation of the epidote-out reaction isograd on the basis of textures and modal variations observed in natural samples throughout the study area, are (assuming SiO_2 is in excess and H_2O as a product phase):



- 9) The breakdown of epidote across the epidote-out reaction isograd changes the EBC of the model system by infusing *REE*, especially *LREE*. Changes in *REE* patterns in Ca amphibole and plagioclase resulting from the breakdown of epidote can be largely accounted for by net transfer of *REEs* from epidote to those phases. The increased *LREE*-carrying capacities of Ca amphibole and plagioclase above the isograd are correlated to crystal-chemical changes in these phases, i.e., the presence of increased Ca in the *M4* and *A* sites in Ca amphibole and plagioclase respectively renders these cavities more suitable to host the *REE*.

However, a significant reduction in *LREE* abundance in titanite above the isograd suggests that the redistributed *REEs* do not come uniquely from epidote. The increased propensity of Ca amphibole and plagioclase to sequester *LREEs* is inferred to be the cause of the slight decrease in *LREE* abundance in titanite above the isograd.

- 10) Below the isograd, epidote plays a significant role in sequestering several transition elements (e.g., Sc, V, Cr, Zn) and Sr ($\approx 10-40\%$) and also plays a lesser role for the HFSEs, Zr and Nb ($\approx <10\%$). As the isograd is crossed, several transition metals (Sc, Cr, Ni, Cu, Zn) and HFSEs (Y, Zr, Nb) formerly held in epidote are mainly redistributed to Ca amphibole and titanite (Cr, V). Plagioclase acquires significant amounts of Sr and lesser amounts of Y due to the breakdown of epidote. The role of titanite as a trace-element carrier exhibits little change across the isograd for most elements.

7.4 Directions for Further Study

Despite the variety of data that has been presented in this thesis, there is considerable room for future study. From a metamorphic facies point of view, in addition to the amphibolite-facies data present here, studies with a similar scope involving the underlying greenschist- and overlying granulite-facies rocks of the St. Anthony Complex could shed light on the trace-element partitioning behaviour among a

greater number of phases (e.g., chlorite, actinolite, pyroxene, rutile, etc.) over a broader range of P - T conditions. An attempt to analyze the greenschists of the aureole was made in this study, but due to their fine grain size, LAM-ICP-MS analysis was not possible. Perhaps in future, the beam size can be made sufficiently fine to resolve trace-element information contained in fine-grained phases or another microbeam technique with finer sampling resolution (e.g., SIMS or PIXE) could be employed.

From a mineral chemistry point of view, a major caveat of this thesis is the lack of information provided on trace-element mineral zoning. BSE imaging does not reveal any trace-element zoning so future studies should employ CL imaging which is often more sensitive to trace-element zoning than BSE imaging. Zoning information should provide more insight into reaction histories and thereby potentially explain variations in the trace-element abundances not related to bulk composition. However, the scale of trace-element zoning is often very fine, potentially beyond the sampling resolution of LAM-ICP-MS, especially for low-grade metabasites.

Another profitable research direction is towards in-depth evaluation of trace-element site distributions. The role of the $M4'$ cavity in Ca amphibole is highlighted in this study. However, site distributions of transition metals are not well resolved in this study due to their spiky patterns on Onuma-type curves. The roles of oxidation state, coordination number, crystal field effects, and bonding remain to be evaluated. Integrated XRD and LAM-ICP-MS studies pioneered by Botazzi *et al.* (1999) and

Tiepolo *et al.* (2003) in igneous systems point to a possible way forward.

In conclusion, prospective studies of trace-element distributions in metamorphic systems can assess the degree of equilibrium attained by investigating the regularity of patterns of trace-element distributions. Given systematic distributions, it should be possible to calculate mineral—mineral partition coefficients, which are essential for trace-element modelling studies in metamorphic systems. A complex interplay of bulk composition, P and T , and crystal-chemical factors controls the distribution of trace elements in metamorphic systems. Of those, crystal-chemical factors pose the greatest challenge to the calibration of a *widely applicable* trace-element ‘geothermobarometer’. However, the consistency of the analytical results presented in this thesis implies that, to variable degrees, trace elements can and do equilibrate over a range of mineral assemblages and bulk compositions at the thin-section scale in amphibolite-facies metabasites. Furthermore, in this case, most trace elements are redistributed among coexisting solid phases across a metamorphic reaction isograd without significant loss to a metamorphic fluid phase.

REFERENCES

- Albee, A.L. (1965): Phase equilibria in three assemblages of kyanite-zone pelitic schists, Lincoln Mountain quadrangle, central Vermont. *J. Petrol.* **6**, 246-301.
- Apted, M.J. and Liou, J.G. (1983): Phase relations among greenschist, epidote-amphibolite, and amphibolite in a basaltic system. *Am. J. Sci.* **283-A**, 328-354.
- Bea, F., Montero, P., Garut, G., and Zacharini, F. (1997): Pressure dependence of rare earth element distribution in amphibolite and granulite-grade garnets. A LA-ICP-MS study. *Geostandards Newslett.* **21**, 253-270.
- Blundy, J., Robinson, J.A.C. and Wood, B. (1998): Heavy *REE* are compatible in clinopyroxene on the spinel lherzolite solidus. *Earth Planet. Sci. Lett.* **160**, 493-504.
- Blundy, J. and Wood, B. (1994): Prediction of crystal-melt partition coefficients from elastic moduli. *Nature* **372**, 452-454.
- Bottazzi, P., Tiepolo, M., Vannucci, R., Zanetti, A., Brumm, R., Foley, S.F. and Oberti, R. (1999): Distinct site preferences for heavy and light *REE* in amphibole and the prediction of $^{Amph/L}D_{REE}$. *Contrib Mineral Petrol.* **137**, 36-45.
- Brenan, J.M., Shaw, F.J., Ryerson, F.J., and Phinney, D.L. (1995): Experimental determination of trace-element partitioning between pargasite and a synthetic hydrous andesitic melt. *Earth Planet. Sci. Lett.* **135**, 1-11.
- Brice, J.C. (1975): Some thermodynamic aspects of the growth of strained crystals. *J. Crystal Growth* **28**, 249-253.
- Brinkley, S.R., Jr.
(1946a): Note on the conditions of equilibrium for systems of many constituents. *J. chem. Phys.*, **14**, 563-564.
(1946b): "Note on the conditions of equilibrium for systems of many constituents". *J. chem. Phys.*, **14**, 563-564.

References

- Brunsmann, A., Franz, G., Erzinger, J. and Landwehr, D. (2000): Zoisite- and clinozoisite -segregations in metabasites (Tauren Window, Austria) as evidence for high-pressure fluid-rock interaction. *J. Metamorphic Geol.* **18**, 1-21.
- Bucher, K. and Frey, M. (1994): *Petrogenesis of Metamorphic Rocks* 6th Edition. Springer-Verlag, New York.
- Cabanis, B. and Lecolle, M. (1989): Le diagramme La/10-Y/15-Nb/8: un outil pour la discrimination des series volcaniques et la mise en evidence des processus de mélange et/ou de contamination crustale. *C.R. Acad. Sci. Ser. II*, **309**, 2023-2029.
- Calon, T. J. (1980): Mylonites at the base of the ophiolite at White Hills Peridotite, northern Newfoundland. *Geol. Soc. Of Am. Abstracts with programmes*. **12**, 27.
- Carmichael, D.M. (1970): Intersecting isograds in the Whetstone Lake area, Ontario. *J. Petrol.* **11**, 147-181.
- Chernoff, C.B. and Carlson, W.D. (1997): Trace element zoning as a record of chemical disequilibrium during garnet growth. *Geol.* **27**, 555-558.
- Cooper, J.R. (1937): Geology and mineral deposits of the Hare Bay area. Nfld. Dept. Nat. Res., Geol. Sec. Bull., 9, 36p.
- Curtis, C.D. and Brown, P.E. (1971): Trace element behaviour in zoned metasomatic bodies of Unst, Scotland. *Contrib. Mineral Petrol.* **31**, 87-93.
- Dahl, P.S., When, D.C. and Feldmann, S.G. (1993): The systematics of trace-element partitioning between coexisting muscovite and biotite in metamorphic rocks from the Black Hills, South Dakota, USA. *Geochim. Cosmochim. Acta* **57**, 2487-2505.
- Deer, W.A., Howie, R.A. and Zussman, J. (1966; 1992 2nd Edition): *An Introduction to the Rock-Forming Minerals*. Longman House, Burnt Mill, Harlow, Essex, England.
- Devore, G.W.
(1955a): The role of adsorption in the fractionation and distribution of elements. *J. Geol.* **63**, 159-190.

References

- (1955b): Crystal growth and the distribution of elements. *J. Geol.* **63**, 471-494.
- (1957): The association of strongly polarizing cations with weakly polarizing cations as a major influence in element distribution, mineral composition, and crystal growth. *J. Geol.* **65**, 178-195.
- Dewey, J.F. and Bird, J.M. (1971): Origin and emplacement of the ophiolite suite: Appalachian ophiolites in Newfoundland. *J. Geophys. Res.* **76**, 3179-3206.
- Dostal, J., Strong, D.F. and Jamieson, R.A. (1980): Trace element mobility in the mylonite zone within the ophiolite aureole, St. Anthony Complex, Newfoundland. *Earth Plant. Sci. Lett.* **49**, 188-192.
- Eggins, S.M., Woodhead, J.D., Kinsley, L.P.J., Mortimer, G.E., Sylvester, P., McCulloch, M.T., Hergt, J.M., Handler, M.R. (1997): A simple method for precise determinations of ≥ 40 trace elements in geological samples by ICPMS using enriched isotope internal standardisation. *Chem. Geol.* **134**, 311-326.
- Engel, A.E.J. and Engel, C.G. (1960): Progressive metamorphism and granitization of major paragneiss, northwest Adirondack Mountains, New York. II. Mineralogy. *Geol. Soc. Am., Bull.* **71**, 1-58.
- Ercit, T.S. (2002): The mess that is "Allanite" *Can. Mineral.* **40**, 1411-1419.
- Fedorowich, J.S., Jain, J.C., Kerrich, R. and Sopuck, V. (1995): Trace element analysis of garnet by laser-ablation microprobe ICP-MS. *Can. Mineral.* **33**, 469-480.
- Fisher, G.W. (1989): Matrix analysis of metamorphic mineral assemblages and reactions. *Contrib. Mineral. Petrol.* **102**, 69-77.
- Gasparik, T. (1984): Two-pyroxene thermobarometry: new experimental data in the system CaO-MgO-Al₂O₃-SiO₂. *Contrib. Mineral. Petrol.* **87**, 87-97.
- Goldschmidt, V.M. (1937): The principles of distribution of chemical elements in minerals and rocks. *J. Chem. Soc. Lond.* **140**, 655-637.
- Gordon, T.M., Ghent, E.D., and Stout, M.Z. (1991): Algebraic analysis of the biotite-

References

- sillimanite isograd in the File Lake area, Manitoba. *Can. Mineral.* **29**, 673-686.
- Govindaraju, K. (1994): Compilation of working values and sample descriptions for 338 geostandards. *Geostand. Newslett.* **18**, 16.
- Grauch, R. (1989): Rare earth elements in metamorphic rocks. In: Geochemistry and mineralogy of rare earth elements (Lipin, B.R. and McKay, G. A. eds). Mineralogical Society of America. Washington, DC, United States. *Reviews in Mineralogy*, 21; 147-167.
- Greenwood, H.J.
(1967): The *N*-dimensional tie-line problem. *Geochim. Cosmochim. Acta* **31**, 465-490.
(1968): Matrix methods and the phase rule in petrology. *XXIII International Geol. Congress* **6**, 267-279.
- Griffin, W.L., Smith, D., Ryan, C.G., O'Reilly, S.Y. and Win, T.T (1996): Trace element zoning in mantle minerals: metasomatism and thermal events in the upper mantle. *Can. Mineral.* **34**, 1179-1193.
- Hartel, T.H.D. and Pattison, D.R.M. (1996): Genesis of the Kapuskasing (Ontario) migmatitic mafic granulites by dehydration melting of amphibolite: the importance of quartz to reaction progress. *J. Metamorphic Geol.* **14**, 591-611.
- Hickmott, D.D. and Shimizu, N. (1990): Trace element zoning in garnet from the Kwoiek Area, British Columbia: disequilibrium partitioning during garnet growth? *Contrib. Mineral. Petrol.* **104**, 619-630.
- Hickmott, D.D., Shimizu, N., Spear, F.S. and Selverstone, J. (1987): Trace element zoning in a metamorphic garnet. *Geol.* **15**, 573-576.
- Hickmott, D.D., and Spear, F.S. (1992): Major and trace element zoning in garnets from calcareous pelites in the NW Shelburne Falls quadrangle, Massachusetts: garnet growth histories in retrograded rocks. *J. Petrol.* **33**, 965-1005.
- Jackson, S.E. (2001): LAMTRACE ver. 2.10: LAM-ICP-MS Data Reduction Spreadsheet

References

for Lotus 123 ver. 5 or "MILLENNIUM" for Windows 95 or NT4 Onwards.
sijackso@laurel.ocs.mq.edu.au

Jaffe, H.W. (1951): The role of yttrium and other minor elements in the garnet group.
Am. Mineral. **36**, 133-155.

Jamieson, R.A.

(1979): *The St. Anthony Complex, Northwestern Newfoundland: A petrological Study of the Relationship Between a Peridotite Sheet and its Dynamothermal Aureole*. Ph.D. thesis, Memorial Univ. of Newfoundland, St. John's, Newfoundland.

(1981): Metamorphism during ophiolite emplacement – the petrology of the St. Anthony Complex. *J. Petrol.* **22**, 397-443.

(1986): *P-T* paths from high temperature shear zones beneath ophiolites. *J. Metamorphic Geol.* **4**, 3-22.

Jamieson, R.A. and Strong, D.F.

(1978): Dynamic and chemical implications of a late syntectonic shear zone within the ophiolite aureole, St. Anthony Complex, northwestern Newfoundland. *GAC/MAC G.S.A. Abst. W. Prog.* **3**, 1978 Ann. Mtg., Toronto pp.428-429.

(1981): A metasomatic mylonite zone within the ophiolite aureole, St. Anthony Complex, north-western Newfoundland. *Am. J. Sci.* **281**, pp.264-281.

Jenner, G.A., Longerich, H.P., Jackson, S.E., Fryer, B.J. (1990): ICP-MS- A powerful tool for high-precision trace-element analysis in Earth Sciences: Evidence from analysis of selected U.S.G.S. reference samples. *Chem. Geol.*, **83**: 133-148.

Jensen, B.B. (1973): Patterns of trace element partitioning. *Geochim. Cosmochim. Acta.* **37**, 2227-42.

Jensen, L.S. (1976): A new cation plot for classifying subalkalic volcanic rocks. Ontario Div. Mines. Misc. Pap. 66.

Johnson, K.T.M. (1998): Experimental determination of partition coefficients for rare-

References

- earth and high-field-strength elements between clinopyroxene, garnet, and basaltic melt at high pressures. *Contrib. Mineral. Petrol.* **133**, 60-68.
- Krauskopf, K.B. and Bird, D.K. (1995): *Introduction to Geochemistry*. 3rd edition McGraw-Hill Incorporated.
- Kretz, R.
(1959): Chemical study of garnet, biotite, and hornblende from gneisses of southwestern Québec, with emphasis on distribution of elements coexisting minerals. *J. Geol.* **67**, 371-402.

(1961): Some applications of thermodynamics to coexisting minerals of variable composition. Examples: orthopyroxene-clinopyroxene and orthopyroxene-garnet. *J. Geol.* **69**, 361-387.
- Kretz, R., Campbell, J.L., Hoffman, E.L., Hartree, R. and Teesdale, W.J. (1999): Approaches to equilibrium in the distribution of trace elements among the principal minerals in a high-grade metamorphic terrane. *J. Metamorphic Geol.* **17**, 41-59.
- Lanzirotti, A. (1995): Yttrium zoning in metamorphic garnets. *Geochim. Cosmochim. Acta* **59**, 4105-4110.
- Leake, B.E., Wolley, A.R., Arps, C.E.S., Birch, W.D., Gilbert, M.C., Grice, J.D., Hawthorne, F.C., Kato, A., Kisch, H.J., Krivovichev, V.G., Linthout, K., Laird, J., Mandarino, J.A., Maresch, W.V., Nickel, E.H., Nicholas, M.S.R., Schumacher, J.C., Smith, D.C., Stephenson, N. C. N., Umgarretti, L., Whittaker, E.J.W. and Youzhi, G. (1997): Nomenclature of amphiboles: report of the subcommittee on amphiboles of the international mineralogical association, commission on new minerals and mineral names. *Can. Mineral.*, **35**, 219-246.
- Leake, B.E., Wolley, A.R., Birch, W.D., Burke, E.A.J., Ferraris, G., Grice, J.D., Hawthorne, F.C., Kisch, H.J., Krivovichev, V.G., Schumacher, J.C., Stephenson, J.C. and Whittaker, E.J.W. (2003): Nomenclature of amphiboles: additions and revisions to the international mineralogical association's 1997 recommendations. *Can. Mineral.*, **41**, 1355-1362.

References

- Lindsley, D.H. (1983): Pyroxene thermometry. *Am. Mineral.* **68**, pp. 477-493.
- Longerich, H.P. (1995): Analysis of pressed pellets of geological samples using wavelength-dispersive X-ray fluorescence spectrometry. *X-ray Spectrom.* **24**, 123-136.
- Longerich, H.P., Günther, D. and Jackson, S.E. (1996): Elemental fractionation in laser-ablation inductively-coupled mass-spectrometry. *Fresenius J. Anal. Chem.* **355**, 538-542.
- Longerich, H.P., Jenner, G.A., Fryer, B.J. and Jackson, S.E. (1990): Inductively coupled plasma-mass spectrometric analysis of geological samples: A critical evaluation based on case studies. *Chem. Geol.* **83**, 105.
- Maxwell, J.A. (1968): *Rock and Mineral Analysis*. © Interscience Publishers
- Mazzucchelli, M., Rivalenti, G., Vannucci, R., Bottazzi, P., Ottolini, L. Hofmann, A.W., Sinigoi, S. & Demarchi, G. (1992): Trace element distribution between clinopyroxene and garnet in gabbroic rocks of the deep crust: an ion microprobe study. *Geochim. Cosmochim. Acta* **56**, 2371-2385.
- Meschede, M. (1986): A method of discriminating between different types of mid-ocean ridge basalts and continental tholeiites with the Nb-Zr-Y diagram. *Chem. Geol.*, **56**, 207-218.
- Nagaski, A. and Enami, M. (1998): Sr-bearing zoisite and epidote in ultra-high pressure (UHP) metamorphic rocks from the Su-Lu province, eastern China: an important Sr reservoir under UHP conditions. *Am. Mineral.* **83**, 240-247.
- Nesse, W.D. (2000): *Introduction to Mineralogy*. © Oxford University Press.
- Nielsen, R.L. (1985): A method for the elimination of the compositional dependence of trace element distribution coefficients. *Geochim. Cosmochim. Acta* **49**, 1775-1779.
- Novak, G.A. and Gibbs, G. V. (1971): The crystal chemistry of silicate garnets. *Amer. Min.*, **56**, 791-825.

References

- Oberti, R., Vannucci, R., Zanetti, A., Tiepolo, M. & Brumm, R.C. (2000): A crystal chemical re-evaluation of amphibole/melt and amphibole/clinopyroxene D_{Ti} values in petrogenetic studies. *Am. Mineral.*, **85**, 407-419.
- Onuma, N., Higuchi, H., Wakita, H. & Nagasawa, H. (1968): Trace element partitioning between two pyroxenes and the host lava. *Earth Plant. Sci. Lett.* **5**, 47-51.
- Paktunc, A. Dogan (1998): MODAN: An interactive computer program for estimating mineral quantities based on bulk composition. *Com. Geosci.* **24**, 425-431.
- Pan, Y. and Fleet, M.E. (1996): Intrinsic and external controls on the incorporation of rare earth elements in calc-silicate minerals. *Can. Mineral.*, **34**, 147-159.
- Pearce, J.A. (1982): Trace element characteristics of lavas from destructive plate boundaries. *In Andesites*, Thorpe, R.S. (ed.). Wiley, Chichester, pp. 525-548.
- Pearce, J.A. and Cann, J.R. (1973): Tectonic setting of basic volcanic rocks determined using trace element analyses. *Earth Plant. Sci. Lett.*, **19**, 290-300.
- Pearce, J.A. and Norry, M.J. (1979): Petrogenetic implications of Ti, Zr, Y and Nb variations in volcanic rocks. *Contrib. Mineral. Petrol.*, **69**, 33-47.
- Pearce, N.J.G., Perkins, W.T., Westgate, J.A., Gorton, M.P., Jackson, S.E., Neal C.R. & Chenery, S.P. (1997): A compilation of new and published major and trace element data for NIST SRM 610 and NIST SRM 612 glass reference materials. *Geostandards Newsletter*, **21**, 115-144.
- Philpotts, A.R. (1990): *Principles of Igneous and Metamorphic petrology*. Prentice Hall, Englewood Cliffs, New Jersey.
- Povarennykh, A.S. (1972): *Crystal Chemical Classification of Minerals*. Plenum: New York.
- Pyle, J.M. and Spear, F.S. (2000): An empirical garnet (YAG) xenotime thermometer. *Contrib. Mineral. Petrol.* **138**, 51-58.

References

- Rollinson, H (1993): *Using Geochemical Data: evaluation, presentation, interpretation*. Longman Group UK Limited.
- Schwandt, C.S., Papike, J.J. and Shearer, C.K. (1996): Trace element zoning in pelitic garnet of the Black Hills, South Dakota. *Am. Mineral.* **81**, 1195-1207.
- Schwartz, H.P. (1967): The effect of crystal field stabilization on the distribution of transition metals between metamorphic minerals. *Geochim. Cosmochim. Acta* **31**, 503-517.
- Scotford, D.M. (1973): Strontium partitioning between coexisting K-feldspar and plagioclase as an indicator of metamorphic grade in southwestern New Hampshire. *Geol. Soc. Am., Bull.* **84**, 3985-3995.
- Seewald, J.S. and Seyfried, W.E. (1990): The effect of temperature on element mobility in subseafloor hydrothermal systems: constraints from basalt alteration experiments. *Earth Planet. Sci. Lett.*, **101**, 388-403.
- Shannon, R.D. (1976): Revised effective ionic radii and systematic studies of interatomic distances in halides and chalcogenides. *Acta crystallogr.* **A32**, 751-767.
- Skublov, S and Drugova, G. (2003): Patterns of trace-element distribution in calcic amphiboles as a function of metamorphic grade. *Can. Mineral.* **41**, 383-392.
- Smyth, J.R. and Bish, D.L. (1988): *Crystal Structures and Cation Sites of the Rock Forming Minerals*. Allen & Unwin Inc, Winchester, Mass. USA.
- Sorensen, S.S. and Grossman, J.N.
(1989): Enrichment of trace elements in garnet amphibolites from a paleo-subduction zone: Catalina Schist, southern California. *Geochim. Cosmochim. Acta* **53**, 3155-3177.

(1993): Accessory minerals and subduction zone metasomatism: a geochemical comparison of two mélanges (Washington and California, U.S.A.) *Chem. Geol.* **110**, 269-297.

References

Spear, F.S.

(1981): An experimental study of hornblende stability and compositional variability in amphibolite. *Am. J. Sci.* **281**, 697-734.

(1993): *Metamorphic Phase Equilibria and Pressure-Temperature-Time Paths*. Mineralogical Society of America Monograph, Washington, D.C.

Sylvester, P. (Ed.) (2001): *Laser-Ablation-ICP-MS in the Earth Sciences: Principles and Applications*. Mineralogical Association of Canada. Short course series 29, 243 pp.(series editor: Robert Raeside).

Sylvester, P., Tubrett, M., King, P and Poujol, M. (2003): Analytical Geochemistry group. MUN Activities and Financial Report. April 2002 - September 2003.

Taylor, M. and Brown G.E. (1976): High-temperature structural study of the $P_{2/a} < > A_2/a$ phase transition in synthetic titanite, CaTiSiO_6 , *Amer. Min.* **61**, 435-47.

Taylor, R.P., Jackson, S.E., Longerich, H.P. & Webster, J.D. (1997): In-situ trace element analysis of individual silicate melt inclusions by laser ablation microprobe-inductively coupled plasma-mass spectrometry (LAM-ICP-MS). *Geochim. Cosmochim. Acta* **61**, 2559-2567.

Taylor, S.R. and McLennan, S.M. (1985): *The Continental Crust: its Composition and Evolution*. Blackwell Scientific, Boston, Massachusetts.

Thompson, J.B. (1957): The graphical analysis of mineral assemblages in pelitic schists *Am. Mineral.* **42**, 842-858.

Thompson, J.B. Jr. (1981): An introduction to the mineralogy and petrology of the biopyriboles. *Mineral. Soc. America Rev. Mineral.* **9A**, 141-188.

Tiepolo, M., Botazzi, P., Foley, S.F., Oberti, R., Vannucci, R. and Zanetti, A. (2001): Fractionation of Nb and Ta from Zr and Hf at mantle depths: The role of titanian pargasite and kaersutite. *Journal of Petrology*, **42**, 221-232.

Tiepolo, M., Oberti, R. and Vannucci (2002): Trace-element incorporation in titanite:

References

- constraints from experimentally determined solid/liquid partition coefficients. *Chem. Geol.* **191**, 105-119.
- Tiepolo, M., Vannucci, R., Bottazzi, P., Oberti, R., Zanetti, A., Foley, S. (2000): Partitioning of rare earth elements, Y, Th, U, and Pb between pargasite, kaersutite, and basanite to trachyte melts: Implications for percolated and veined mantle. *Geochem. Geophys. Geosyst* (*G³*) **1**, paper number 2000GC000064
- Tiepolo, M., Vannucci, R., Oberti, R., Foley, S.F., Bottazzi, P. and Zanetti, A. (2000): Nb and Ta incorporation and fractionation in titanian pargasite and kaersutite: crystal-chemical constraints and implications for natural systems. *Earth Planet. Sci. Lett.* **176**, 185-201.
- Tiepolo, M., Zanetti, A., Oberti, R., Brumm, R., Foley, S. and Vannucci, R. (2003): Trace -element partitioning between synthetic potassic-riches and silicate melts, and contrasts with the partitioning behaviour of pargasites and kaersutites. *Eur J. Mineral.* **15**, 329-340.
- Tribuzio, R., Messiga, B., Vannucci, R., and Bottazzi, P (1996): Rare earth element redistribution during high-pressure low-temperature metamorphism in ophiolitic Fe-gabbros (Liguria, north western Italy): implications for light *REE* mobility in subduction zones. *Geology* **24**, 711-714.
- Tuke, M.J. (1968): Autochthonous and allochthonous rocks in the Pistolet Bay area in northernmost Newfoundland. *Can. J. Earth Sci.* **5** pp. 501-513.
- Turekian, K.K. and Phinney, W.C. (1962): The distribution of Ni, Co, Cr, Cu, Ba, and Sr between biotite-garnet pairs in a metamorphic sequence. *Am. Mineral.* **47**, 1434-1441.
- Van Westrenen, W., Blundy, J.D. and Wood
(1999) Crystal-chemical controls on trace element partitioning between garnet and anhydrous silicate melt. *Am. Mineral.* **84**, 838-847.

References

- (2000): Effect of Fe^{2+} on garnet-melt trace element partitioning: Experiments in FCMAS and quantification of crystal-chemical controls in natural systems. *Lithos* **53**, 191-203.
- (2001): High field strength element/rare earth element fractionation during partial melting in the presence of garnet: Implications for identification of mantle heterogeneities. *Geochem. Geophys. Geosyst* (G^3) **2**, paper number 2000GC000133
- Virgo, D. (1968): Partition of strontium between coexisting K-feldspar and plagioclase in some metamorphic rocks. *J. Geol.* **76**, 331-346.
- Williams, H.
- (1975): Structural succession, nomenclature, and interpretation of transported rocks in western Newfoundland. *Can. J. Earth Sci.* **12**, 1874-1894.
- (1995): Taconic allochthons in Newfoundland (Humber Zone); in *Geology of the Appalachian-Caledonian orogen in Canada and Greenland*, (ed) H. Williams; Geological Survey of Canada, *Geology of Canada*, no. 6, 843-890 (also Geological Society of America, *The Geology of North America*, v. F-1).
- Williams, H. and Smyth, W.R. (1983): Geology of the Hare Bay Allochthon; In *Geology of the Strait of Belle Isle area, northwestern insular Newfoundland, southern Labrador and adjacent Quebec*; Geological Survey of Canada, *Memoir* 400, 109-141.
- Williams, H. and Stevens, R.K. (1974): The ancient continental margin of North America. In *The Geology of Continental Margins*, (eds) C.A. Burk and C.L. Drake; 781-796.
- Wilson, J.T. (1966): Did the Atlantic close and then re-open? *Nature* **211**, 676-681.
- Witt-Eickschen, G. and Harte, B. (1994): Distribution of trace elements between

References

- amphibole and clinopyroxene from mantle peridotites of the Eifel (western Germany): an ion microprobe study. *Chem. Geol.* **117**, 235- 250.
- Wood, D.A. (1980): The application of a Th-Hf-Ta diagram to problems of tectonomagmatic classification and to establishing the nature of crustal contamination of basaltic lavas of the British Tertiary volcanic province. *Earth Planet. Sci. Lett.*, **50**, 11-30.
- Wood, B.J. and Fraser, D.G. (1976): Elementary thermodynamics for Geologists. Oxford University Press
- Yang, P. (2002): *Trace Element partitioning between coexisting metamorphic minerals and trace element zoning in metamorphic minerals from Gagnon Terrane, western Labrador*. Ph.D. thesis, Memorial Univ. of Newfoundland, St. John's, Newfoundland.
- Yang, P., Rivers, T., and Jackson, S. (1999): Crystal-chemical and thermal controls on trace element partitioning between coexisting garnet and biotite in metamorphic rocks from western Labrador. *Can. Mineral.* **37**, 443-468.
- Yang, P., and Rivers, T.
(2000): Trace element partitioning between coexisting biotite and muscovite from metamorphic rocks, western Labrador: structural, compositional and thermal controls. *Geochim. Cosmochim. Acta* **64**, 1451-1472.

(2001): Chromium and manganese zoning in pelitic garnet and kyanite: Spiral, overprint, and oscillatory(?) zoning patterns and the role of growth rate. *J. Metamorphic Geol.* **19**, 455-474.

(2002): The origin of Mn and Y annuli in garnet and the thermal dependence of P in garnet and Y in apatite in calc-pelite and pelite, Gagnon terrane, western Labrador. *Geological Material. Resch.* **4**, 1-35.

References

- Zack, T., Kronz, A., Foley, S.F. and Rivers, T. (2002): Trace element abundances in rutiles from eclogites and associated garnet mica schists. *Chem. Geology*. **184**, 97-122.

Appendix A: Electron Microprobe and LAM-ICP-MS Data

Ten major elements and twenty-six trace elements were analyzed in the minerals Ca amphibole, plagioclase, epidote, garnet and titanite in eight samples by energy-dispersive EPMA and LAM-ICP-MS. The same grains, and where possible the same locations within the grains, were analysed by the two methods, with the EPMA being carried out before the more destructive LAM-ICP-MS analyses. In most samples, four different grains of each mineral species in each thin section were analysed, which together with the average values are presented in this appendix. One sigma standard deviations for major elements, *REEs*, and analysed trace elements are listed in Tables 3.4, 4.1 and 5.1 respectively. Grain selection was based on several criteria, including size, inferred equilibrium texture, proximity to other analysed phases, and inferred equilibrium relationships with other analysed phases. Numbers of ions in the mineral formulae were calculated on the basis of 23 oxygens in Ca amphibole, 8 oxygens in plagioclase, 12.5 oxygens in epidote, 12 oxygens in garnet and 20 oxygens in titanite. Fe^{3+} in Ca amphibole, garnet and titanite was calculated by charge balance following the method of Spear (1993); all Fe in epidote was assumed to be Fe^{3+} . Major-element concentrations, (EPMA), were used as internal standards for the trace-element analyses (Ca for Ca amphibole, epidote, titanite, garnet and Si for plagioclase) to adjust for differences in ablation yield between samples and the calibration standard. Data acquisition was performed in peak jumping mode (time resolved analyses: TRA).

Appendix A: Electron Microprobe and LAM-ICP-MS Data

Table A1. Major-element composition and structural formulae of Ca amphibole analysed by EPMA in this study. *Italics* indicate Zr group. Number of cations calculated on the basis of 23 O per formula unit.

Amphibole	46-1	46-2	46-3	46-4	48-1	48-2	48-3	48-4
SiO ₂	43.78	43.37	42.59	43.75	45.29	43.76	44.75	44.13
TiO ₂	0.96	0.89	1.10	1.07	0.71	0.75	0.88	1.11
Al ₂ O ₃	11.61	11.97	12.54	11.39	12.24	13.43	12.81	13.07
FeO	15.55	15.53	16.11	15.28	15.71	15.35	15.98	15.25
MnO	0.32	0.32	0.29	0.23	0.39	0.53	0.48	0.35
MgO	11.26	11.33	10.72	11.38	11.38	10.91	11.02	10.96
CaO	10.94	10.96	10.73	10.95	11.35	11.23	11.33	11.09
Na ₂ O	2.03	1.86	2.20	1.88	1.77	2.03	2.03	1.96
K ₂ O	0.06	0.24	0.14	0.06	0.20	0.15	0.11	0.14
Total	96.46	96.47	96.42	95.92	99.05	98.14	99.40	98.04
Si	6.57	6.50	6.43	6.59	6.60	6.45	6.52	6.49
Ti	0.11	0.10	0.12	0.12	0.08	0.08	0.10	0.12
Al	2.05	2.12	2.23	2.02	2.10	2.33	2.20	2.27
Fe ³⁺		0.09						
Fe ²⁺	1.95	1.86	2.03	1.92	1.92	1.89	1.95	1.88
Mn	0.04	0.04	0.04	0.03	0.05	0.07	0.06	0.04
Mg	2.52	2.53	2.41	2.55	2.47	2.40	2.39	2.40
Ca	1.76	1.76	1.73	1.77	1.77	1.77	1.77	1.75
Na	0.59	0.54	0.64	0.55	0.50	0.58	0.57	0.56
K	0.01	0.05	0.03	0.01	0.04	0.03	0.02	0.03
Total	15.60	15.59	15.66	15.56	15.53	15.60	15.58	15.54
<i>T-site</i>								
Si	6.57	6.50	6.43	6.59	6.61	6.45	6.52	6.49
Al ^{IV}	1.43	1.50	1.57	1.41	1.40	1.55	1.48	1.51
Fe ³⁺								
Ti								
Total	8	8	8	8	8	8	8	8
<i>M1-3 sites</i>								
Al ^{VI}	0.62	0.61	0.66	0.61	0.71	0.78	0.72	0.76
Fe ³⁺		0.09						
Ti	0.11	0.10	0.13	0.12	0.08	0.08	0.10	0.12
FeMg	4.27	4.20	4.21	4.27	4.21	4.13	4.18	4.12
Total	5	5	5	5	5	5	5	5
<i>M4-site</i>								
FeMg	0.24	0.24	0.26	0.23	0.22	0.22	0.22	0.21
Ca	1.76	1.76	1.74	1.77	1.77	1.77	1.77	1.75
Na		0.00					0.01	0.04
Total	2	2	2	2	2	2	2	2
<i>A-site</i>								
Na	0.59	0.54	0.64	0.55	0.50	0.58	0.56	0.52
K	0.01	0.05	0.03	0.01	0.04	0.03	0.02	0.03
Total	0.60	0.59	0.67	0.56	0.53	0.60	0.58	0.54
X Mg	0.56	0.58	0.54	0.57	0.56	0.56	0.55	0.56
X Fe	0.44	0.42	0.46	0.43	0.44	0.44	0.45	0.44
X _{Cum}	0.12	0.12	0.13	0.12	0.11	0.11	0.11	0.11

Appendix A: Electron Microprobe and LAM-ICP-MS Data

Table A1. Major-element composition and structural formulae of Ca amphibole analysed by EPMA in this study. *Italics* indicate Zr group. Number of cations calculated on the basis of 23 O per formula unit.

Amphibole	49-1	49-2	49-3	49-4	06-1	06-2	06-3	06-4
SiO ₂	41.41	41.11	41.61	41.46	41.30	42.95	41.05	41.77
TiO ₂	1.16	1.05	1.10	1.08	1.14	0.86	1.10	1.08
Al ₂ O ₃	12.98	12.94	12.41	12.81	12.53	11.84	12.46	12.48
FeO	19.75	19.83	19.10	19.84	18.99	19.91	20.06	20.04
MnO	0.35	0.49	0.49	0.30	0.45	0.30	0.48	0.42
MgO	8.72	8.57	9.03	8.67	9.02	9.13	8.47	8.81
CaO	11.95	12.13	12.21	11.99	11.79	11.73	12.09	12.13
Na ₂ O	1.90	1.69	1.77	1.79	1.89	1.82	1.86	1.87
K ₂ O	1.44	1.47	1.33	1.36	1.40	1.26	1.25	1.21
Total	99.65	99.28	99.05	99.30	98.50	99.80	98.83	99.81
Si	6.20	6.17	6.24	6.22	6.24	6.40	6.20	6.23
Ti	0.13	0.12	0.12	0.12	0.13	0.10	0.12	0.12
Al	2.29	2.29	2.19	2.26	2.23	2.08	2.22	2.19
Fe ³⁺	0.22	0.36	0.30	0.27	0.20	0.16	0.35	0.33
Fe ²⁺	2.25	2.13	2.09	2.22	2.20	2.32	2.19	2.17
Mn	0.04	0.06	0.06	0.04	0.06	0.04	0.06	0.05
Mg	1.95	1.92	2.02	1.94	2.03	2.03	1.91	1.96
Ca	1.92	1.95	1.96	1.93	1.91	1.87	1.96	1.94
Na	0.55	0.49	0.51	0.52	0.55	0.53	0.54	0.54
K	0.28	0.28	0.25	0.26	0.27	0.24	0.24	0.23
Total	15.83	15.77	15.74	15.78	15.82	15.77	15.79	15.76
<i>T-site</i>								
Si	6.20	6.17	6.24	6.22	6.24	6.40	6.20	6.23
Al ^{IV}	1.80	1.83	1.76	1.78	1.16	1.60	1.80	1.77
Fe ³⁺								
Ti								
Total	8	8	8	8	8	8	8	8
<i>M1-3 sites</i>								
Al ^{VI}	0.49	0.46	0.44	0.49	0.47	0.48	0.42	0.43
Fe ³⁺	0.22	0.36	0.30	0.27	0.20	0.16	0.35	0.33
Ti	0.13	0.12	0.12	0.12	0.13	0.10	0.13	0.12
FeMg	4.16	4.06	4.14	4.12	4.20	4.26	4.10	4.12
Total	5	5	5	5	5	5	5	5
<i>M4-site</i>								
FeMg	0.08	0.05	0.04	0.07	0.09	0.13	0.04	0.06
Ca	1.92	1.95	1.96	1.93	1.91	1.87	1.96	1.94
Na								
Total	2	2	2	2	2	2	2	2
<i>A-site</i>								
Na	0.55	0.49	0.52	0.52	0.55	0.53	0.55	0.54
K	0.28	0.28	0.26	0.26	0.27	0.24	0.24	0.23
Total	0.83	0.77	0.77	0.78	0.82	0.77	0.79	0.77
X Mg	0.46	0.47	0.49	0.47	0.48	0.47	0.47	0.47
X Fe	0.54	0.53	0.51	0.53	0.52	0.53	0.53	0.53
X _{Cum}	0.04	0.03	0.02	0.03	0.04	0.06	0.02	0.03

Appendix A: Electron Microprobe and LAM-ICP-MS Data

Table A1. Major-element composition and structural formulae of Ca amphibole analysed by EPMA in this study. *Italics* indicate Zr group. Number of cations calculated on the basis of 23 O per formula unit.

Amphibole	20-1	20-2	20-3	20-4	01-1	01-2	01-3	01-4
SiO ₂	40.65	39.82	40.61	40.53	41.53	41.65	41.66	43.43
TiO ₂	0.93	1.03	1.24	1.28	1.30	0.94	1.05	0.88
Al ₂ O ₃	12.71	12.52	12.24	12.64	14.04	14.13	13.75	12.16
FeO	21.07	21.38	20.90	20.32	18.54	18.90	19.14	19.15
MnO	0.58	0.43	0.38	0.32	0.28	0.21	0.28	0.22
MgO	7.49	7.13	7.43	7.71	7.34	7.38	7.40	8.42
CaO	11.49	11.65	11.50	11.53	11.65	11.78	11.73	11.75
Na ₂ O	1.64	1.59	1.55	1.54	1.33	1.42	1.22	1.49
K ₂ O	1.57	1.58	1.54	1.63	1.16	1.09	1.16	0.82
Total	98.15	97.13	97.39	97.50	97.18	97.50	97.39	98.33
Si	6.23	6.18	6.27	6.24	6.32	6.33	6.35	6.53
Ti	0.11	0.12	0.14	0.15	0.15	0.11	0.12	0.10
Al	2.29	2.29	2.23	2.29	2.52	2.53	2.47	2.15
Fe ³⁺	0.24	0.33	0.18	0.16				
Fe ²⁺	2.46	2.45	2.52	2.45	2.36	2.40	2.42	2.41
Mn	0.08	0.06	0.05	0.04	0.04	0.03	0.04	0.03
Mg	1.71	1.65	1.71	1.77	1.67	1.67	1.68	1.89
Ca	1.89	1.94	1.90	1.90	1.90	1.92	1.91	1.89
Na	0.49	0.48	0.46	0.46	0.39	0.36	0.36	0.43
K	0.31	0.31	0.30	0.32	0.23	0.23	0.23	0.16
Total	15.81	15.81	15.76	15.78	15.58	15.58	15.58	15.59
<i>T-site</i>								
Si	6.23	6.18	6.27	6.24	6.33	6.34	6.35	6.53
Al ^{IV}	1.77	1.82	1.73	1.76	1.68	1.67	1.66	1.47
Fe ³⁺								
Ti								
Total	8	8	8	8	8	8	8	8
<i>M1-3 sites</i>								
Al ^{VI}	0.52	0.47	0.50	0.53	0.85	0.87	0.81	0.68
Fe ³⁺	0.24	0.33	0.18	0.16			0.02	
Ti	0.11	0.12	0.14	0.15	0.15	0.11	0.12	0.10
FeMg	4.13	4.09	4.18	4.16	4.01	4.03	4.05	4.22
Total	5.00	5.00	5.00	5.00	5.00	5.00	5.00	5.00
<i>M4-site</i>								
FeMg	0.14	0.06	0.10	0.10	0.06	0.08	0.08	0.11
Ca	1.86	1.94	1.90	1.90	1.90	1.92	1.92	1.89
Na					0.04	0.00		0.00
Total	2.00	2.00	2.00	2.00	2.00	2.00	2.00	2.00
<i>A-site</i>								
Na	0.49	0.48	0.46	0.46	0.35	0.36	0.36	0.43
K	0.31	0.31	0.30	0.32	0.23	0.23	0.26	0.16
Total	0.79	0.79	0.77	0.78	0.58	0.58	0.62	0.59
X Mg	0.41	0.40	0.40	0.42	0.41	0.41	0.41	0.44
X Fe	0.59	0.60	0.60	0.58	0.59	0.59	0.59	0.56
X _{Cum}	0.07	0.03	0.05	0.05	0.03	0.04	0.04	0.05

Appendix A: Electron Microprobe and LAM-ICP-MS Data

Table A1. Major-element composition and structural formulae of Ca amphibole analysed by EPMA in this study. *Italics* indicate Zr group. Number of cations calculated on the basis of 23 O per formula unit.

Amphibole	142-1	142-2	142-3	142-4	46 Avg	48 Avg	49 Avg	06 Avg
SiO ₂	41.37	41.61	41.72	42.86	43.37	44.48	41.40	41.77
TiO ₂	1.34	1.12	1.33	1.02	1.01	0.86	1.10	1.05
Al ₂ O ₃	14.30	14.34	15.07	12.91	11.88	12.89	12.78	12.33
FeO	20.24	20.30	20.07	19.22	15.62	15.57	19.63	19.75
MnO	0.31	0.22	0.24	0.26	0.29	0.44	0.41	0.41
MgO	7.10	7.13	7.26	7.68	11.17	11.07	8.75	8.86
CaO	11.62	11.56	11.57	11.62	10.89	11.25	12.07	11.93
Na ₂ O	1.66	1.51	1.52	1.27	1.99	1.95	1.79	1.86
K ₂ O	1.18	1.09	1.15	1.00	0.12	0.15	1.40	1.28
Total	99.12	98.87	99.92	97.83	96.32	98.66	99.32	99.24
Si	6.23	6.27	6.21	6.48	6.52	6.52	6.21	6.27
Ti	0.15	0.13	0.15	0.12	0.11	0.10	0.12	0.12
Al	2.54	2.55	2.64	2.30	2.11	2.23	2.26	2.18
Fe ³⁺		0.01			0.02	0.00	0.29	0.26
Fe ²⁺	2.55	2.55	2.50	2.43	1.94	1.91	2.17	2.22
Mn	0.04	0.03	0.03	0.03	0.04	0.06	0.05	0.05
Mg	1.59	1.60	1.61	1.73	2.50	2.42	1.96	1.98
Ca	1.88	1.87	1.85	1.88	1.76	1.77	1.94	1.92
Na	0.49	0.44	0.44	0.37	0.58	0.55	0.52	0.54
K	0.23	0.21	0.22	0.19	0.03	0.03	0.27	0.25
Total	15.70	15.66	15.65	15.53	15.60	15.56	15.78	15.79
<i>T-site</i>								
Si	6.24	6.27	6.22	6.48	6.52	6.52	6.21	6.27
Al ^{IV}	1.77	1.73	1.78	1.52	1.48	1.48	1.79	1.58
Fe ³⁺								
Ti								
Total	8	8	8	8	8	8	8	8
<i>M1-3 sites</i>								
Al ^{VI}	0.78	0.82	0.86	0.78	0.63	0.74	0.47	0.45
Fe ³⁺		0.01			0.02		0.29	0.26
Ti	0.15	0.13	0.15	0.12	0.12	0.10	0.12	0.12
FeMg	4.07	4.05	4.00	4.10	4.24	4.16	4.12	4.17
Total	5	5	5	5	5	5	5	5
<i>M4-site</i>								
FeMg	0.11	0.13	0.14	0.09	0.24	0.22	0.06	0.08
Ca	1.88	1.87	1.85	1.88	1.76	1.77	1.94	1.92
Na	0.01		0.01	0.03		0.01		0.00
Total	2	2	2	2	2	2	2	2
<i>A-site</i>								
Na	0.47	0.44	0.43	0.34	0.58	0.54	0.52	0.54
K	0.23	0.21	0.22	0.19	0.03	0.03	0.27	0.25
Total	0.70	0.65	0.65	0.54	0.61	0.56	0.79	0.79
X Mg	0.39	0.39	0.39	0.42	0.56	0.56	0.47	0.47
X Fe	0.62	0.61	0.61	0.58	0.44	0.44	0.53	0.53
X _{Cum}	0.05	0.06	0.07	0.04	0.12	0.11	0.03	0.04

Appendix A: Electron Microprobe and LAM-ICP-MS Data

Table A1. Major-element composition and structural formulae of Ca amphibole and plagioclase analysed by EPMA in this study. *Italics* indicate Zr group. Number of cations calculated on the basis of 23 O per formula unit (amphibole) and 8 O per formula unit (plagioclase).

Amphibole	20 Avg	01 Avg	142 Avg	Plagioclase	46-1	46-2	46-3	46-4
SiO ₂	40.40	42.07	41.89	SiO ₂	58.77	57.88	62.30	60.76
TiO ₂	1.12	1.04	1.20	TiO ₂	0.03		0.11	0.04
Al ₂ O ₃	12.53	13.52	14.15	Al ₂ O ₃	22.99	27.10	25.07	25.25
FeO	20.92	18.93	19.96	FeO	1.63	0.30	0.27	0.11
MnO	0.43	0.25	0.26	MnO	0.09			0.01
MgO	7.44	7.64	7.29	MgO	0.02	0.13	0.07	0.03
CaO	11.54	11.73	11.59	CaO	7.68	7.93	6.28	6.52
Na ₂ O	1.58	1.36	1.49	Na ₂ O	8.17	6.72	8.51	7.96
K ₂ O	1.58	1.06	1.10	K ₂ O	0.02	0.60	0.09	0.15
Total	97.54	97.60	98.94	Total	99.23	100.54	102.52	100.63
Si	6.23	6.38	6.30	<i>T-Site</i>				
Ti	0.13	0.12	0.14	Si	2.67	2.58	2.70	2.68
Al	2.28	2.42	2.51	Ti				
Fe ³⁺	0.23	0.00	0.00	Al	1.23	1.42	1.28	1.31
Fe ²⁺	2.47	2.40	2.51	Fe	0.06	0.01	0.01	
Mn	0.06	0.04	0.03	Mn				
Mg	1.71	1.73	1.63	Mg		0.01		
Ca	1.91	1.91	1.87	Total	3.96	4.02	3.99	3.99
Na	0.47	0.39	0.43					
K	0.31	0.21	0.21	<i>A-site</i>				
Total	15.79	15.58	15.63	Ca	0.37	0.38	0.29	0.31
<i>T-site</i>				Na	0.72	0.58	0.72	0.69
Si	6.23	6.38	6.30	K		0.03	0.01	
Al ^{IV}	1.77	1.62	1.70	Total	1.09	0.99	1.00	1.00
Fe ³⁺								
Ti								
Total	8	8	8	X Ca	0.34	0.38	0.29	0.31
<i>M1-3 sites</i>				X Na	0.66	0.58	0.71	0.69
Al ^{VI}	0.50	0.80	0.81	X K		0.03		
Fe ³⁺	0.23	0.00	0.00					
Ti	0.13	0.12	0.14					
FeMg	4.14	4.08	4.06					
Total	5	5	5					
<i>M4 site</i>								
FeMg	0.10	0.08	0.12					
Ca	1.90	1.91	1.87					
Na	0.00	0.01	0.01					
Total	2	2	2					
<i>A-site</i>								
Na	0.47	0.38	0.42					
K	0.31	0.22	0.21					
Total	0.78	0.59	0.63					
X Mg	0.41	0.42	0.39					
X Fe	0.59	0.58	0.61					
X _{Cum}	0.05	0.04	0.06					

Appendix A: Electron Microprobe and LAM-ICP-MS Data

Table A1. Major-element composition and structural formulae of plagioclase analysed by EPMA in this study. *Italics* indicate Zr group. Number of cations calculated on the basis of 8 O per formula unit.

Plagioclase	48-1	48-2	48-3	48-4	49-1	49-2	49-3	49-4
SiO ₂	58.40	61.64	59.52	58.79	57.66	56.88	54.69	54.78
TiO ₂	0.16	< DL	0.09	< DL	< DL	< DL	0.14	< DL
Al ₂ O ₃	26.35	26.04	26.65	26.10	24.77	24.93	26.91	27.12
FeO	0.38	0.20	0.19	0.32	0.75	1.06	0.38	0.31
MnO	< DL	< D.L	< DL	< DL	0.14	< DL	< DL	< DL
MgO		0.14	0.06	< DL	0.27	< DL	0.06	< DL
CaO	8.06	6.71	7.54	7.63	9.78	10.46	9.55	9.67
Na ₂ O	7.40	7.06	6.84	7.39	5.22	4.62	5.78	5.54
K ₂ O	< DL	0.44	0.64	0.12	< DL	< DL	0.16	0.10
Total	100.59	101.88	101.20	100.35	98.45	97.95	97.48	97.51
<i>T-site</i>								
Si	2.60	2.68	2.62	2.62	2.62	2.61	2.52	2.52
Ti	0.01							
Al	1.38	1.33	1.38	1.37	1.33	1.35	1.46	1.47
Fe	0.01	0.01	0.01	0.01	0.03	0.04	0.01	0.01
Mn					0.01			
Mg		0.01			0.02			
Total	4.00	4.03	4.01	4.00	4.00	4.00	4.00	4.01
<i>A-site</i>								
Ca	0.38	0.31	0.36	0.36	0.48	0.51	0.47	0.48
Na	0.64	0.59	0.58	0.64	0.46	0.41	0.52	0.49
K		0.02	0.04				0.01	
Total	1.02	0.93	0.98	1.00	0.94	0.92	1.00	0.97
X Ca	0.37	0.37	0.36	0.36	0.51	0.56	0.48	0.49
X Na	0.62	0.64	0.60	0.64	0.49	0.44	0.52	0.51
X K			0.04					

Appendix A: Electron Microprobe and LAM-ICP-MS Data

Table A1. Major-element composition and structural formulae of plagioclase analysed by EPMA in this study. *Italics* indicate Zr group. Number of cations calculated on the basis of 8 O per formula unit.

Plagioclase	06-1	06-2	06-3	06-4	20-1	20-2	20-3	01-1
SiO ₂	57.98	58.18	57.33	58.11	59.63	56.81	55.07	55.76
TiO ₂	< DL	0.08	< DL	0.19	0.20	< DL	< DL	0.16
Al ₂ O ₃	26.22	26.43	26.94	26.38	25.90	26.23	26.26	26.87
FeO	0.23	0.13	0.36	< DL	0.27	0.21	0.34	0.27
MnO	< DL	< DL	< DL	< DL	0.07	0.12	< DL	< DL
MgO	< DL	< DL	< DL	0.08	< DL	< DL	0.06	0.12
CaO	8.40	8.43	9.56	8.45	7.36	8.55	8.96	9.27
Na ₂ O	6.51	6.84	6.57	6.49	5.54	6.06	5.83	6.15
K ₂ O	0.10	< DL	0.10	< DL	1.37	0.09	< DL	0.06
Total	99.44	99.88	100.87	99.62	100.26	97.87	96.45	98.48
<i>T-site</i>								
Si	2.61	2.60	2.56	2.61	2.65	2.59	2.56	2.54
Ti					0.01			
Al	1.39	1.39	1.42	1.40	1.36	1.41	1.44	1.44
Fe			0.01		0.01	0.01	0.01	0.01
Mn								
Mg								0.01
Total	4.00	3.99	3.99	4.00	4.03	4.01	4.01	4.01
<i>A-site</i>								
Ca	0.41	0.40	0.46	0.41	0.35	0.42	0.45	0.45
Na	0.57	0.59	0.57	0.56	0.48	0.54	0.53	0.54
K			0.01		0.08			
Total	0.98	0.99	1.03	0.97	0.91	0.96	0.98	0.99
X Ca	0.42	0.40	0.45	0.42	0.35	0.42	0.45	0.45
X Na	0.58	0.59	0.55	0.58	0.48	0.54	0.53	0.54
X K					0.08			

Appendix A: Electron Microprobe and LAM-ICP-MS Data

Table A1. Major-element composition and structural formulae of plagioclase analysed by EPMA in this study. *Italics* indicate Zr group. Number of cations calculated on the basis of 8 O per formula unit.

Plagioclase	01-2	01-3	142-1	142-2	142-3	46 AVG	48 AVG	49 AVG
SiO ₂	54.66	55.55	58.88	58.75	59.29	59.93	59.59	56.00
TiO ₂	< DL	0.06	< DL	< DL	0.07	< DL	0.08	< DL
Al ₂ O ₃	27.11	26.86	26.82	26.16	26.72	25.10	26.28	25.93
FeO	0.33	0.33	0.17	0.36	0.34	0.58	0.27	0.62
MnO	0.15	< DL	< DL	< DL	< DL	< DL	< DL	< DL
MgO	0.07	0.09	0.14	0.09	< DL	0.06	< DL	0.09
CaO	9.63	9.42	8.55	7.98	7.91	7.10	7.49	9.87
Na ₂ O	5.55	5.79	6.87	7.25	7.45	7.84	7.17	5.29
K ₂ O	< DL	< DL	< DL	0.08	0.08	0.22	0.31	0.07
Total	97.28	97.96	101.12	100.50	101.72	100.73	101.01	97.85
<i>T-site</i>								
Si	2.52	2.54	2.60	2.61	2.61	2.66	2.63	2.57
Ti								
Al	1.47	1.45	1.39	1.37	1.38	1.31	1.37	1.40
Fe	0.01	0.01	0.01	0.01	0.01	0.02	0.01	0.02
Mn	0.01							0.001
Mg		0.01	0.01	0.01		0.002		0.005
Total	4.01	4.01	4.01	4.00	4.00	4.00	4.01	4.00
<i>A-site</i>								
Ca	0.48	0.46	0.40	0.38	0.37	0.34	0.35	0.48
Na	0.50	0.51	0.59	0.62	0.64	0.68	0.61	0.47
K						0.01	0.02	0.00
Total	0.97	0.98	0.99	1.01	1.01	1.02	0.98	0.95
X Ca	0.49	0.47	0.41	0.38	0.37	0.33	0.37	0.51
X Na	0.51	0.53	0.59	0.62	0.63	0.66	0.62	0.49
X K						0.01	0.01	

Appendix A: Electron Microprobe and LAM-ICP-MS Data

Table A1. Major-element composition and structural formulae of plagioclase and epidote analysed by EPMA in this study. *Italics* indicate Zr group. Number of cations calculated on the basis of 8 O per formula unit (plagioclase) and 12.5 O per formula unit (epidote).

Plagioclase	06 AVG	20 AVG	01 AVG	142 AVG	Epidote	06-1	06-2	06-3
SiO ₂	57.90	57.17	55.33	58.98	SiO ₂	39.55	40.00	40.62
TiO ₂	0.07	0.07	0.09	< DL	TiO ₂	< DL	0.12	< DL
Al ₂ O ₃	26.49	26.13	26.95	26.57	Al ₂ O ₃	28.82	28.87	31.31
FeO	0.19	0.27	0.31	0.29	Fe ₂ O _{3T}	6.67	6.60	3.70
MnO	< DL	0.07	< DL	< DL	Mn ₂ O ₃	0.04	0.13	0.31
MgO	< DL	< DL	0.09	0.09	MgO	0.03	0.20	0.13
CaO	8.71	8.29	9.44	8.15	CaO	24.64	24.52	24.49
Na ₂ O	6.60	5.81	5.83	7.19	Na ₂ O	< DL	0.29	0.07
K ₂ O	0.06	0.50	< DL	0.06	K ₂ O	< DL	< DL	< DL
Total	99.95	98.19	97.91	101.11	Total	99.68	100.49	100.42
<i>T-site</i>					<i>T-Site</i>			
Si	2.59	2.60	2.53	2.61	Si	3.05	3.05	3.05
Ti		0.002			Total	3.05	3.05	3.05
Al	1.40	1.40	1.45	1.38				
Fe	0.003	0.01	0.01	0.01				
Mn			0.002		<i>M1-3 Sites</i>			
Mg			0.005	0.01	Ti		0.03	
Total	4.00	4.01	4.01	4.00	Al	2.62	2.60	2.77
					Fe	0.43	0.42	0.23
<i>A-site</i>					Mn		0.01	0.02
Ca	0.42	0.40	0.46	0.39	Mg		0.02	0.02
Na	0.57	0.51	0.52	0.62	Total	3.05	3.07	3.04
K	0.001	0.03						
Total	0.99	0.94	0.98	1.00	<i>X-Site</i>			
					Ca	2.04	2.01	1.97
X Ca	0.42	0.43	0.47	0.38	Na		0.04	0.01
X Na	0.58	0.54	0.53	0.61	K			
X K		0.03			Total	2.04	2.05	1.98
					X Zo	0.59	0.58	0.75
					X Ps	0.41	0.41	0.23
					X Pm		0.01	0.02

Appendix A: Electron Microprobe and LAM-ICP-MS Data

Table A1. Major-element composition and structural formulae of epidote analysed by EPMA in this study. Number of cations calculated on the basis of 12.5 O per formula unit.

Epidote	06-4	46-1	46-2	46-3	46-4	48-1	48-2	48-3
SiO ₂	40.15	37.20	38.01	38.40	38.46	40.40	39.90	40.52
TiO ₂	< DL	< DL	0.27	0.21	0.15	0.09	0.12	0.09
Al ₂ O ₃	30.20	23.95	23.68	24.53	24.22	25.03	25.97	25.93
Fe ₂ O _{3T}	5.75	12.56	12.28	11.24	11.62	11.41	10.07	9.71
Mn ₂ O ₃	< DL	0.12	0.11	0.12	< DL	0.20	0.10	0.19
MgO	< DL	0.14	0.23	0.12	0.19	< DL	< DL	0.08
CaO	24.45	23.85	23.03	23.55	23.33	23.26	23.87	23.29
Na ₂ O	< DL	0.25	0.08	0.07	< DL	0.33	0.46	0.17
K ₂ O	< DL	< DL	0.06	< DL	< DL	< DL	< DL	0.07
Total	100.56	97.81	97.51	98.24	97.82	100.42	100.27	99.44
<i>T-Site</i>								
Si	3.05	3.03	3.09	3.09	3.10	3.15	3.11	3.15
Total	3.05	3.03	3.09	3.09	3.10	3.15	3.11	3.15
<i>M1-3 Sites</i>								
Ti			0.02	0.01	0.01	0.02	0.03	0.02
Al	2.70	2.30	2.27	2.32	2.30	2.30	2.38	2.38
Fe	0.36	0.86	0.83	0.76	0.78	0.74	0.66	0.63
Mn		0.01	0.01	0.01		0.01	0.01	0.01
Mg		0.02	0.03	0.01	0.02			0.01
Total	3.06	3.20	3.16	3.11	3.11	3.07	3.08	3.05
<i>X-Site</i>								
Ca	1.99	2.08	2.01	2.03	2.02	1.94	1.99	1.94
Na		0.04	0.01	0.01		0.05	0.07	0.03
K			0.01					0.01
Total	1.99	2.12	2.04	2.04	2.02	1.99	2.06	1.98
X Zo	0.66	0.26	0.23	0.25	0.27	0.30	0.36	0.37
X Ps	0.34	0.73	0.75	0.70	0.71	0.74	0.63	0.62
X Pm		0.01	0.02	0.05	0.02	0.01	0.01	0.01

Appendix A: Electron Microprobe and LAM-ICP-MS Data

Table A1. Major-element composition and structural formulae of epidote and garnet analysed by EPMA in this study. *Italics* indicate Zr group. Number of cations calculated on the basis of 12.5 O per formula unit (epidote) and 12 O per formula unit (garnet).

Epidote	06 Avg	46 Avg	48 Avg	Garnet	01-1	01-2	01-3	01-4
SiO ₂	40.08	38.02	40.27	SiO ₂	37.85	38.11	38.18	38.36
TiO ₂	< DL	0.16	0.10	TiO ₂	0.15	0.39	< DL	< DL
Al ₂ O ₃	29.80	24.09	25.64	Al ₂ O ₃	21.25	21.39	21.28	21.33
Fe ₂ O _{3T}	5.68	11.93	10.40	FeO	27.58	30.42	26.77	28.26
Mn ₂ O ₃	0.12	0.09	0.16	MnO	2.35	0.92	2.55	2.19
MgO	0.09	0.17	< DL	MgO	2.49	2.86	2.27	2.47
CaO	24.53	23.44	23.47	CaO	9.99	8.52	11.08	10.01
Na ₂ O	0.09	0.10	0.32	Na ₂ O	< DL	< DL	< DL	< DL
K ₂ O	< DL	< DL	< DL	K ₂ O	< DL	< DL	< DL	< DL
Total	100.29	97.84	100.04	Total	101.51	102.61	102.13	102.62
<i>T-Site</i>				<i>T-Site</i>				
Si	3.05	3.08	3.14	Si	2.97	2.97	2.98	2.98
Total	3.05	3.08	3.14	Total	2.97	2.97	2.98	2.98
<i>M1-3 Sites</i>				<i>Y-Site</i>				
Ti	0.01	0.01	0.02	Ti	0.01	0.02		
Al	2.67	2.30	2.36	Al	1.97	1.96	1.96	1.95
Fe	0.36	0.81	0.68	Fe ³⁺	0.02	0.02	0.04	0.05
Mn	0.01	0.01	0.01	Total	2.00	2.00	2.00	2.00
Mg	0.01	0.02	0.003					
Total	3.06	3.15	3.07	<i>X-Site</i>				
<i>X-Site</i>				Fe	1.79	1.96	1.71	1.79
Ca	2.00	2.03	1.96	Mn	0.16	0.06	0.17	0.14
Na	0.01	0.02	0.05	Mg	0.29	0.33	0.26	0.29
K		0.001	0.002	Ca	0.84	0.71	0.93	0.83
Total	2.01	2.05	2.01	Na				
				K				
				Total	3.08	3.06	3.07	3.05
X Zo	0.64	0.28	0.34	X Alm	0.58	0.64	0.56	0.59
X Ps	0.35	0.72	0.64	X Prp	0.09	0.11	0.09	0.09
X Pm	0.01		0.02	X Grs	0.27	0.23	0.30	0.27
				X Sps	0.05	0.02	0.05	0.05

Appendix A: Electron Microprobe and LAM-ICP-MS Data

Table A1. Major-element composition and structural formulae of garnet analysed by EPMA in this study. *Italics* indicate Zr group. Number of cations calculated on the basis of 12 O per formula unit.

Garnet	20-1	20-2	142-1	142-2	01 Avg	20 Avg	142 Avg
SiO ₂	39.24	38.23	38.30	38.43	38.13	38.74	38.37
TiO ₂	0.22	0.44	0.35	0.24	0.15	0.33	0.29
Al ₂ O ₃	21.43	21.28	21.09	21.33	21.31	21.35	21.21
FeO	29.39	30.00	27.55	28.98	28.26	29.70	28.26
MnO	0.80	0.96	2.35	1.44	2.00	0.88	1.90
MgO	2.59	2.91	2.25	2.64	2.52	2.75	2.44
CaO	8.97	9.09	10.03	9.46	9.90	9.03	9.75
Na ₂ O	0.23	0.23	0.12	0.12	< DL	0.23	0.12
K ₂ O	0.60	< DL	< DL	0.15	< DL	0.30	0.08
Total	103.23	102.92	101.92	102.65	102.22	103.08	102.28
<i>T-Site</i>							
Si	3.02	2.96	2.99	2.98	2.97	2.99	2.99
Total	3.02	2.96	2.99	2.98	2.97	2.99	2.99
<i>Y-Site</i>							
Ti	0.01	0.03	0.02	0.01	0.01	0.02	0.02
Al	1.94	1.94	1.94	1.95	1.96	1.94	1.95
Fe ³⁺	0.05	0.03	0.04	0.04	0.03	0.04	0.03
Total	2.00	2.00	2.00	2.00	2.00	2.00	2.00
<i>X-Site</i>							
Fe	1.84	1.91	1.76	1.84	1.81	1.88	1.81
Mn	0.05	0.06	0.16	0.10	0.13	0.06	0.13
Mg	0.30	0.34	0.26	0.30	0.29	0.32	0.28
Ca	0.74	0.75	0.84	0.79	0.83	0.75	0.81
Na	0.03	0.03	0.01	0.02		0.03	0.01
K	0.06			0.01		0.03	0.01
Total	3.02	3.09	3.04	3.06	3.06	3.07	3.05
X Alm	0.63	0.63	0.59	0.61	0.60	0.63	0.60
X Prp	0.10	0.11	0.09	0.10	0.09	0.10	0.09
X Grs	0.25	0.24	0.27	0.26	0.27	0.25	0.27
X Sps	0.02	0.02	0.05	0.03	0.04	0.02	0.04

Appendix A: Electron Microprobe and LAM-ICP-MS Data

Table A1. Major-element composition and structural formulae of titanite analysed by EPMA in this study. *Italics* indicate Zr group. Number of cations calculated on the basis of 20 O per formula unit.

Titanite	46-1	46-2	46-3	48-1	48-2	48-3	49-1	49-2
SiO ₂	30.21	30.11	30.08	31.06	31.10	30.90	30.17	30.45
TiO ₂	37.72	37.76	37.89	38.72	37.84	38.83	36.83	37.97
Al ₂ O ₃	1.49	1.26	1.35	1.29	1.49	0.97	2.03	1.76
Fe ₂ O ₃	0.92	1.05	1.01	0.95	1.03	0.86	0.96	0.54
Mn ₂ O ₃	0.18	< DL	0.17	0.06	< DL	< DL	< DL	0.14
MgO	0.03	0.10	< DL	0.14	< DL	< DL	< DL	< DL
CaO	28.59	28.31	28.72	29.12	28.98	28.89	28.49	27.84
Na ₂ O	< DL	0.11	< DL	< DL	< DL	< DL	< DL	< DL
K ₂ O	< DL	< DL	< DL	< DL	< DL	< DL	< DL	< DL
Total	98.94	98.49	99.05	101.14	100.44	100.44	98.47	98.57
<i>T-Site</i>								
Si	3.99	3.99	3.98	4.01	4.05	4.02	4.00	4.02
Total	3.99	3.99	3.98	4.01	4.05	4.02	4.00	4.02
<i>M-Site</i>								
Ti	3.75	3.77	3.77	3.76	3.70	3.80	3.68	3.77
Al	0.23	0.20	0.21	0.20	0.23	0.15	0.32	0.23
Fe ³⁺	0.02	0.03	0.02	0.04	0.06	0.05		
Total	4.00	4.00	4.00	4.00	4.00	4.00	4.00	4.00
<i>A-Site</i>								
Mn								
Fe ²⁺	0.07	0.04	0.04	0.03	0.03	0.03	0.07	0.04
Mg				0.03				
Ca	4.05	4.02	4.07	4.03	4.04	4.03	4.05	3.94
Na		0.03						
K								
Total	4.11	4.09	4.11	4.09	4.07	4.06	4.12	3.98
X Ti	0.75	0.77	0.77	0.76	0.70	0.80	0.68	0.77
X Al	0.23	0.20	0.21	0.20	0.23	0.15	0.32	0.23
X Fe ³⁺	0.02	0.03	0.02	0.04	0.06	0.05		

Appendix A: Electron Microprobe and LAM-ICP-MS Data

Table A1. Major-element composition and structural formulae of titanite analysed by EPMA in this study. *Italics* indicate Zr group. Number of cations calculated on the basis of 20 O per formula unit.

Titanite	06-1	06-2	06-3	20-1	20-2	20-3	142-1	142-2
SiO ₂	30.89	30.23	30.20	29.94	30.19	29.67	30.17	30.27
TiO ₂	35.67	35.77	36.83	36.94	36.87	36.67	37.70	36.33
Al ₂ O ₃	1.97	1.78	1.27	1.56	1.47	1.41	1.47	1.97
Fe ₂ O ₃	1.53	2.00	1.22	1.07	0.88	1.09	0.85	1.19
Mn ₂ O ₃	0.14	0.12	0.19	0.17	0.08	0.12	0.22	0.16
MgO	< DL	< DL	0.06	< DL	< DL	0.06	0.08	0.17
CaO	27.73	28.54	27.98	28.14	27.88	27.85	28.08	27.59
Na ₂ O	0.34	0.08	< DL	< DL	0.11	0.06	0.11	< DL
K ₂ O	< DL	< DL	< DL	< DL	0.07	< DL	< DL	< DL
Total	98.10	98.32	97.51	97.65	97.30	96.67	98.48	97.48
<i>T-site</i>								
Si	4.10	4.03	4.05	4.01	4.05	4.01	4.00	4.05
Total	4.10	4.03	4.05	4.01	4.05	4.01	4.00	4.05
<i>M-Site</i>								
Ti	3.57	3.59	3.70	3.72	3.72	3.73	3.76	3.65
Al	0.31	0.28	0.20	0.25	0.23	0.22	0.24	0.30
Fe ³⁺	0.12	0.12	0.10	0.03	0.02	0.05		0.05
Total	4.00	4.00	4.00	4.00	4.00	4.00	4.00	4.00
<i>A-Site</i>								
Mn								
Fe ²⁺		0.01	0.04	0.04	0.04	0.04	0.06	0.07
Mg								
Ca	3.95	4.08	4.02	4.04	4.00	4.03	3.99	3.95
Na	0.08				0.03		0.03	
K					0.04			
Total	4.03	4.08	4.02	4.07	4.10	4.07	4.08	4.02
X Ti	0.57	0.59	0.70	0.72	0.72	0.73	0.76	0.65
X Al	0.31	0.28	0.20	0.25	0.23	0.22	0.24	0.30
X Fe ³⁺	0.12	0.12	0.10	0.03	0.02	0.05		0.05

Appendix A: Electron Microprobe and LAM-ICP-MS Data

Table A1. Major-element composition and structural formulae of titanite analysed by EPMA in this study. *Italics* indicate Zr group. Number of cations calculated on the basis of 20 O per formula unit.

Titanite	01-1	01-2	01-3	46 Avg	48 Avg	49 Avg	06 Avg	01 Avg
SiO ₂	29.30	30.38	29.40	30.13	31.02	30.31	30.44	29.69
TiO ₂	35.40	37.46	35.36	37.79	38.46	37.40	36.09	36.08
Al ₂ O ₃	2.15	1.70	2.06	1.37	1.25	1.89	1.67	1.97
Fe ₂ O ₃	0.71	0.65	0.85	0.99	0.95	0.75	1.58	0.74
Mn ₂ O ₃	< DL	0.19	0.06	0.13	< DL	0.07	0.15	0.08
MgO	0.05	< DL	< DL	< DL	< DL	< DL	< DL	< DL
CaO	27.14	27.67	26.87	28.54	29.00	28.16	28.08	27.23
Na ₂ O	< DL	< DL	< DL	0.06	< DL	< DL	0.14	< DL
K ₂ O	< DL	0.12	< DL	< DL	< DL	< DL	< DL	< DL
Total	94.69	97.94	94.49	98.77	100.56	98.52	97.92	95.65
<i>T-Site</i>								
Si	4.03	4.03	4.05	3.99	4.03	4.01	4.06	4.04
Total	4.03	4.03	4.05	3.99	4.03	4.01	4.06	4.04
<i>M-Site</i>								
Ti	3.66	3.74	3.66	3.76	3.75	3.72	3.62	3.69
Al	0.34	0.26	0.34	0.21	0.20	0.28	0.26	0.31
Fe ³⁺				0.02	0.05		0.11	
Total	4.00	4.00	4.00	4.00	4.00	4.00	4.00	4.00
<i>A-site</i>								
Mn								
Fe ²⁺	0.07	0.03	0.07	0.05	0.03	0.05	0.01	0.06
Mg					0.01			
Ca	4.00	3.94	3.96	4.05	4.03	3.99	4.02	3.97
Na				0.01			0.03	
K								
Total	4.07	3.97	4.03	4.10	4.07	4.05	4.04	4.02
X Ti	0.66	0.74	0.66	0.76	0.75	0.72	0.62	0.69
X Al	0.34	0.26	0.34	0.21	0.19	0.28	0.26	0.31
X Fe ³⁺				0.02	0.05		0.11	

Appendix A: Electron Microprobe and LAM-ICP-MS Data

Table A1. Major-element composition and structural formulae of titanite analysed by EPMA in this study. *Italics* indicate Zr group. Number of cations calculated on the basis of 20 O per formula unit.

Titanite	20 Avg	142 Avg
SiO ₂	29.94	30.22
TiO ₂	36.82	37.01
Al ₂ O ₃	1.48	1.72
Fe ₂ O ₃	1.02	1.02
Mn ₂ O ₃	0.12	0.19
MgO	< DL	0.12
CaO	27.96	27.83
Na ₂ O	0.06	0.07
K ₂ O	< DL	< DL
Total	97.16	98.00
<i>T-Site</i>		
Si	4.02	4.02
Total	4.02	4.02
<i>M-Site</i>		
Ti	3.72	3.71
Al	0.23	0.27
Fe ³⁺	0.03	0.03
Total	4.00	4.00
<i>A-Site</i>		
Mn		
Fe ²⁺	0.04	0.06
Mg		
Ca	4.02	3.97
Na	0.01	0.01
K	0.01	
Total	4.08	4.05
X Ti	0.72	0.71
X Al	0.23	0.27
X Fe ³⁺	0.03	0.03

Appendix 1: Electron Microprobe and LAM-ICP-MS Data

Table A2 Trace-element compositions of the five major minerals analysed by LAM ICP-MS. *Italics* indicate Zr group. Blank indicates below detection limit, n.d. indicates element not determined.

Amphibole	46-1	46-2	46-3	46-4	48-1	48-2	48-3	48-4
ppm								
Sc	36.50	72.20	70.40	74.20	37.40	50.90	51.40	59.10
V	446.0	492.0	479.0	413.0	170.0	163.0	355.0	186.0
Cr	75.10	145.0	220.0	71.30	131.0	135.0	114.0	64.90
Co	67.50	79.90	88.90	81.80	24.60	31.30	31.60	30.30
Ni	91.30	118.0	167.0	101.0	73.50	87.00	87.00	78.10
Cu	4.05	1.32	2.65	5.46	3.93	2.89	1.61	2.06
Zn	117.0	198.0	184.0	198.0	165.0	193.0	174.0	186.0
Sr	14.50	16.50	18.00	13.70	5.67	5.41	12.40	6.64
Rb	11.00	17.00	15.50	11.30	0.21	0.46	11.60	0.08
Y	11.10	9.30	8.09	9.33	6.93	6.22	9.97	7.65
Zr	13.10	17.40	18.40	13.80	18.50	23.40	13.50	14.70
Nb	0.87	0.57	0.52	0.51	0.04	0.03	0.70	0.02
La	0.22	0.20	0.25	0.20	0.10	0.09	0.14	0.09
Ce	1.31	1.23	1.33	0.85	0.53	0.46	0.68	0.61
Pr	0.24	0.24	0.25	0.18	0.12	0.12	0.19	0.14
Nd	1.41	1.45	1.43	1.46	0.83	0.76	1.09	1.17
Sm	0.63	0.68	0.66	0.67	0.48	0.41	0.69	0.65
Eu	0.19	0.26	0.25	0.21	0.16	0.12	0.14	0.17
Gd	1.21	1.21	1.10	0.95	0.85	0.82	1.20	1.04
Tb	0.23	0.20	0.17	0.17	0.17	0.15	0.22	0.17
Dy	1.98	1.74	1.53	1.40	1.16	1.08	1.71	1.29
Ho	0.48	0.31	0.36	0.31	0.27	0.30	0.37	0.30
Er	1.45	1.12	1.08	0.94	0.82	0.85	1.09	0.84
Tm	0.24	0.14	0.15	0.14	0.12	0.12	0.17	0.13
Yb	1.69	1.12	1.10	1.03	1.05	0.80	0.90	1.05
Lu	0.32	0.16	0.20	0.15	0.17	0.16	0.15	0.21
Hf					0.03	2.37		
Ta					0.02	0.02		

Appendix 1: Electron Microprobe and LAM-ICP-MS Data

Table A2 (continued) Trace-element compositions of the five major minerals analysed by LAM ICP-MS. *Italics* indicate Zr group. Blank indicates below detection limit, n.d. indicates element not determined.

Amphibole	49-1	49-2	49-3	49-4	06-1	06-2	06-3	06-4
ppm								
Sc	74.10	77.20	67.00	65.50	57.70	71.80	63.10	59.80
V	432.0	491.0	411.0	432.0	535.0	476.0	488.0	458.0
Cr	54.50	427.0	144.0	677.0	266.0	315.0	284.0	264.0
Co	61.40	71.70	62.30	60.00	90.80	n.d.	n.d.	n.d.
Ni	104.0	136.0	91.40	103.0	97.40	117.0	77.10	64.10
Cu	2.71	2.75	4.56	2.88	1.75	1.46	5.41	2.02
Zn	192.0	203.0	181.0	192.0	184.0	190.0	347.0	300.0
Sr	17.60	19.0	14.20	18.30	20.00	14.40	13.40	15.80
Rb	1.56	0.93	2.49	0.34	0.91	0.65	1.26	0.46
Y	42.30	45.30	40.10	36.50	48.70	44.20	46.40	39.30
Zr	31.50	198.0	32.20	98.70	25.90	51.50	12.60	18.90
Nb	3.14	2.10	2.80	3.19	2.48	0.97	1.24	1.85
La	3.94	3.98	3.82	3.50	4.44	2.65	1.37	2.68
Ce	13.80	13.80	12.90	11.50	17.00	11.80	7.43	10.80
Pr	2.34	2.36	2.30	2.06	2.75	2.62	1.69	1.95
Nd	13.30	12.70	13.50	12.80	17.70	13.60	11.80	11.70
Sm	4.82	4.65	4.51	4.53	6.10	5.02	4.83	4.34
Eu	1.59	1.66	1.41	1.51	2.24	1.67	1.76	1.49
Gd	6.48	6.86	6.23	6.61	7.38	6.44	7.34	5.87
Tb	1.11	1.18	1.05	1.06	1.38	1.24	1.21	1.00
Dy	7.94	8.42	7.39	7.25	9.82	7.02	8.80	7.19
Ho	1.76	1.83	1.56	1.45	1.91	1.59	1.81	1.46
Er	4.96	5.51	4.52	4.29	5.78	4.63	5.39	4.42
Tm	0.76	0.78	0.69	0.60	0.94	0.64	0.75	0.62
Yb	5.26	5.52	4.88	4.16	6.89	4.13	5.61	4.42
Lu	0.89	0.80	0.81	0.64	0.90	0.81	0.77	0.66
Hf								
Ta								

Appendix 1: Electron Microprobe and LAM-ICP-MS Data

Table A2 (continued) Trace-element compositions of the five major minerals analysed by LAM ICP-MS. *Italics* indicate Zr group. Blank indicates below detection limit, n.d. indicates element not determined.

Amphibole	20-1	20-2	20-3	20-4	01-1	01-2	01-3	01-4
ppm								
Sc	93.70	35.80	57.50	23.60	47.50	35.30	16.50	24.30
V	224.0	201.0	471.0	253.0	206.0	266.0	166.0	204.0
Cr	266.0	259.0	68.30	23.80	67.20	83.60	118.0	239.0
Co	n.d.	n.d.	n.d.	n.d.	24.60	31.30	31.60	30.30
Ni	97.40	117.0	46.70	68.90	33.20	63.70	89.70	61.70
Cu	1.75	1.46	1.23	1.69	1.47	0.49	0.90	0.43
Zn	184.0	190.0	162.0	204.0	81.80	82.30	96.40	81.50
Sr	43.80	51.50	25.90	53.10	16.70	33.00	27.60	33.90
Rb	2.96	4.03	9.26	9.23	0.88	1.87	1.20	1.56
Y	6.68	3.69	10.60	2.98	27.00	22.70	12.60	18.60
Zr	17.00	14.30	14.30	25.10	189.0	9.00	16.20	69.50
Nb	6.52	3.76	1.34	6.88	8.10	8.32	7.04	10.80
La	0.75	0.46	0.71	0.15	0.75	0.72	0.58	0.73
Ce	3.17	1.93	2.92	0.70	3.99	3.89	3.14	4.15
Pr	0.63	0.37	0.53	0.13	0.97	0.95	0.68	1.03
Nd	3.39	2.42	2.99	0.79	6.70	6.56	4.82	7.37
Sm	1.17	0.67	0.96	0.25	3.38	3.13	2.12	3.51
Eu	0.52	0.26	0.48	0.13	0.98	0.92	0.54	1.14
Gd	1.29	0.77	1.50	0.45	4.98	4.08	2.61	4.34
Tb	0.17	0.12	0.27	0.07	0.86	0.69	0.39	0.70
Dy	1.18	0.71	1.89	0.47	5.45	4.76	2.71	4.19
Ho	0.25	0.14	0.42	0.12	0.96	0.90	0.50	0.73
Er	0.63	0.42	1.15	0.31	2.55	2.36	1.25	1.76
Tm	0.09	0.06	0.19	0.05	0.32	0.30	0.18	0.22
Yb	0.67	0.40	1.32	0.39	2.11	1.92	1.01	1.32
Lu	0.12	0.06	0.20	0.06	0.28	0.25	0.14	0.14
Hf								
Ta								

Appendix 1: Electron Microprobe and LAM-ICP-MS Data

Table A2 (continued) Trace-element compositions of the five major minerals analysed by LAM ICP-MS. *Italics* indicate Zr group. Blank indicates below detection limit, n.d. indicates element not determined.

Amphibole	142-1	142-2	142-3	142-4	46 Avg	48 Avg	49 Avg	06 Avg
ppm								
Sc	70.24	58.94	65.78	46.56	63.33	49.70	70.95	63.10
V	390.1	275.7	300.2	281.0	457.5	218.5	441.5	489.3
Cr	55.56	60.78	44.98	38.20	127.9	111.2	325.6	282.3
Co	10.12	6.34	11.45	5.49	79.53	29.45	63.85	22.70
Ni	70.05	80.44	45.29	27.44	119.3	81.40	108.6	88.90
Cu	101.5	79.89	88.45	90.46	3.37	2.62	3.23	2.66
Zn	18.05	26.78	24.78	19.99	174.3	179.5	192.0	255.3
Sr	2.30	1.80	2.01	1.49	15.68	7.53	17.28	15.90
Rb	10.00	12.44	8.21	9.51	13.70	3.09	1.33	0.82
Y	1.99	2.12	2.89	3.16	9.46	7.69	41.05	44.65
Zr	20.11	24.76	15.90	6.55	15.68	17.53	90.10	27.23
Nb	8.90	10.78	6.90	4.26	0.62	0.20	2.81	1.63
La	2.00	2.00	2.17	1.44	0.22	0.10	3.81	2.79
Ce	10.80	9.94	11.00	8.40	1.18	0.57	13.00	11.76
Pr	2.89	2.52	2.52	2.24	0.22	0.14	2.27	2.25
Nd	19.40	19.20	15.00	13.70	1.44	0.96	13.08	13.70
Sm	8.88	8.98	6.66	6.33	0.66	0.56	4.63	5.07
Eu	2.60	3.81	2.74	2.31	0.23	0.15	1.54	1.79
Gd	11.10	13.80	8.78	7.12	1.12	0.98	6.55	6.76
Tb	1.69	2.36	1.48	1.13	0.19	0.18	1.10	1.21
Dy	11.20	14.90	9.46	7.50	1.66	1.31	7.75	8.21
Ho	2.03	2.88	1.95	1.49	0.37	0.31	1.65	1.69
Er	5.01	7.92	4.99	3.96	1.15	0.90	4.82	5.06
Tm	0.65	1.09	0.81	0.56	0.17	0.14	0.71	0.74
Yb	4.10	6.49	4.78	3.99	1.24	0.95	4.96	5.26
Lu	0.57	0.89	0.68	0.52	0.21	0.17	0.78	0.78
Hf	0.15	0.08	0.09	1.12		0.60		
Ta	0.04	0.01		0.79		0.01		

Appendix 1: Electron Microprobe and LAM-ICP-MS Data

Table A2 (continued) Trace-element compositions of the five major minerals analysed by LAM ICP-MS. *Italics* indicate Zr group. Blank indicates below detection limit, n.d. indicates element not determined.

Amphibole	20 Avg	01 Avg	Avg 142	Plagioclase	46-1	46-2	46-3	46-4
ppm								
Sc	52.65	30.90	60.38		0.76	0.62	1.64	0.81
V	287.3	210.5	311.8		0.33	6.87	4.58	0.44
Cr	154.3	127.0	49.88		1.77	2.17	2.35	3.61
Co	29.45	8.35	8.35		0.25			
Ni	82.50	62.08	55.83		4.07	43.60	9.13	9.28
Cu	1.53	0.82	90.08		1.01	3.21	1.54	6.04
Zn	185.0	85.50	22.40		79.70	98.10	88.50	79.60
Sr	43.58	27.80	1.90		349.0	686.0	557.0	615.0
Rb	6.37	1.38	10.04		0.41	0.10	0.27	3.45
Y	5.99	20.23	2.54		0.01	0.16	0.07	0.04
Zr	17.68	70.93	16.83		0.09	0.50	0.10	0.10
Nb	4.63	8.57	7.71		0.01	0.01	0.02	0.02
La	0.52	0.69	1.90		0.16	0.22	0.66	0.08
Ce	2.18	3.79	10.04		0.23	0.35	0.78	0.17
Pr	0.42	0.91	2.54		0.02	0.04	0.07	0.02
Nd	2.40	6.36	16.83		0.09	0.19	0.12	0.06
Sm	0.76	3.04	7.71		0.03	0.03	0.04	0.05
Eu	0.34	0.89	2.87		0.04	0.13	0.08	0.11
Gd	1.00	4.00	10.20		0.03	0.04	0.06	0.04
Tb	0.16	0.66	1.67				0.01	
Dy	1.06	4.28	10.77		0.01	0.04	0.02	0.01
Ho	0.23	0.77	2.09					
Er	0.63	1.98	5.47		0.01	0.01	0.04	0.01
Tm	0.10	0.26	0.78				0.01	0.01
Yb	0.69	1.59	4.84		0.02	0.02	0.02	0.06
Lu	0.11	0.20	0.66					
Hf			0.36					
Ta			0.21					

Appendix I: Electron Microprobe and LAM-ICP-MS Data

Table A2 (continued) Trace-element compositions of the five major minerals analysed by LAM ICP-MS. *Italics* indicate Zr group. Blank indicates below detection limit, n.d. indicates element not determined.

Plagioclase	48-1	48-2	48-3	48-4	49-1	49-2	49-3	49-4
ppm								
Sc	7.43	6.98	7.50	8.94	0.48	5.46	0.52	0.48
V	4.60	6.58	9.11	25.90	0.25	0.74	0.05	0.05
Cr	0.39	2.38	0.37	0.85	1.17	11.90	0.75	1.27
Co	0.17				0.16	2.99	0.20	0.15
Ni	38.90	51.50	18.40	64.60	1.84	38.80	1.74	1.50
Cu	0.92	19.80	10.80	7.94	0.38	3.97	0.36	0.35
Zn	49.00	189.0	27.70	81.10	25.30	49.70	20.60	27.70
Sr	432.5	417.5	442.5	617.5	300.0	937.0	285.0	306.0
Rb	1.72	40.10	2.43	2.03	0.05	77.30	0.03	0.03
Y	0.28	0.44	0.34	0.54	0.39	0.58	0.01	0.02
Zr	1.30	2.04	3.35	2.84	0.12	1.63	0.05	0.04
Nb	0.32	0.26	0.20	4.05	0.01	0.06	0.00	0.00
La	0.41	0.43	0.81	0.70	2.49	3.18	0.75	0.88
Ce	0.59	0.58	0.75	1.69	2.79	3.12	0.67	0.84
Pr	0.33	0.05	0.14	0.30	0.29	0.24	0.04	0.06
Nd	0.43	0.36	0.73	1.75	0.87	0.88	0.09	0.15
Sm	0.18	0.21	0.28	0.26	0.11	0.14	0.01	0.02
Eu	1.65	0.90	1.74	2.25	0.10	0.21	0.07	0.08
Gd	0.32	0.16	0.13	0.34	0.06	0.05	0.01	0.01
Tb	0.03	0.03	0.04	0.07	0.01	0.02		0.00
Dy	0.13	0.16	0.15	0.24	0.03	0.06	0.01	0.01
Ho	0.05	0.03	0.03	0.06	0.01	0.01		
Er	0.07	0.09	0.21	0.03	0.05	0.06		
Tm	0.03	0.03	0.02	0.03	0.01	0.02		
Yb	0.14	0.07	0.12	0.08	0.07	0.04		0.01
Lu	0.03	0.03	0.01	0.03	0.01	0.01		
Hf	7.58	1.10	0.70	2.63				
Ta	1.65	0.80	0.70	0.02				

Appendix 1: Electron Microprobe and LAM-ICP-MS Data

Table A2 (continued) Trace-element compositions of the five major minerals analysed by LAM ICP-MS. *Italics* indicate Zr group. Blank indicates below detection limit, n.d. indicates element not determined.

Plagioclase	06-1	06-2	06-3	06-4	20-1	20-2	20-3	01-1
ppm								
Sc	1.01	1.28	2.94	3.39	1.07	2.04	1.28	3.21
V	2.11	2.38	10.50	1.80	3.76	4.80	1.96	0.62
Cr	1.88	5.31	4.58	4.41	2.86	4.16	4.85	7.12
Co	0.16				0.25	0.00	0.03	1.65
Ni	13.40	7.32	22.20	11.70	25.87	13.77	17.54	21.24
Cu	1.01	0.45	3.94	0.76	2.62	4.56	7.52	2.36
Zn	64.80	98.90	82.60	105.0	128.8	128.3	122.8	50.15
Sr	413.0	482.0	552.0	678.0	692.0	864.5	890.9	456.2
Rb	0.49	0.26	0.30	0.42	0.46	2.00	3.98	38.70
Y	0.32	1.09	1.52	0.44	0.09	0.09	0.07	0.68
Zr	0.11	0.34	0.37	29.20	0.34	0.15	0.20	0.94
Nb	0.02	0.02	0.05	0.03	0.01	0.03	0.03	0.04
La	4.16	1.43	4.12	5.25	0.27	0.70	0.22	4.08
Ce	7.34	3.44	8.27	9.26	0.41	0.86	0.36	4.35
Pr	0.43	0.36	0.62	0.62	0.04	0.08	0.04	0.42
Nd	1.26	0.83	1.29	1.85	0.19	0.15	0.12	1.31
Sm	0.22	0.18	0.22	0.30	0.04	0.06	0.07	0.18
Eu	0.20	0.16	0.27	0.23	0.10	0.14	0.16	0.20
Gd	0.13	0.17	0.19	0.12	0.05	0.08	0.06	0.08
Tb	0.01	0.03	0.03	0.02		0.01		0.02
Dy	0.11	0.21	0.34	0.23	0.03	0.03	0.02	0.06
Ho	0.01	0.03	0.04	0.03				0.02
Er	0.04	0.06	0.10	0.04	0.02	0.05	0.02	0.08
Tm	0.02	0.03	0.02	0.01		0.01	0.01	0.02
Yb	0.05	0.08	0.16	0.24	0.03	0.05	0.08	0.08
Lu	0.01	0.02	0.02	0.01				0.01
Hf								
Ta								

Appendix 1: Electron Microprobe and LAM-ICP-MS Data

Table A2 (continued) Trace-element compositions of the five major minerals analysed by LAM ICP-MS. *Italics* indicate Zr group. Blank indicates below detection limit, n.d. indicates element not determined.

Plagioclase	01-2	01-3	142-1	142-2	142-3	46 AVG	48 AVG	49 AVG
ppm								
Sc	0.76	1.34	1.65	4.64	4.47	0.96	7.71	1.73
V	0.07	0.18	3.30	11.40	3.90	3.05	11.55	0.27
Cr	1.38	3.16	4.54	6.79	6.43	2.48	1.00	3.77
Co	0.28	0.59	0.16		0.02	0.06	0.04	0.88
Ni	2.49	6.99	17.06	28.05	18.53	16.52	43.35	10.97
Cu	0.54	0.99	1.23	4.32	1.53	2.95	9.87	1.27
Zn	34.45	43.11	114.3	135.1	148.9	86.48	86.70	30.83
Sr	438.0	534.5	654.0	891.0	943.6	551.8	477.5	457.0
Rb	0.04	9.70	0.62	0.51	0.61	1.06	11.57	19.35
Y	0.02	0.14	0.86	1.74	0.86	0.07	0.40	0.25
Zr	0.06	0.27	0.28	14.97	32.95	0.20	2.38	0.46
Nb		0.01	0.03	0.07	0.05	0.01	1.21	0.02
La	1.19	1.79	4.88	6.75	7.12	0.28	0.59	1.82
Ce	1.09	1.77	9.06	12.90	12.80	0.38	0.90	1.85
Pr	0.07	0.13	0.60	0.93	0.87	0.04	0.21	0.16
Nd	0.16	0.39	1.68	2.22	2.50	0.12	0.82	0.50
Sm	0.02	0.05	0.31	0.36	0.41	0.04	0.23	0.07
Eu	0.10	0.13	0.28	0.39	0.34	0.09	1.64	0.11
Gd	0.01	0.02	0.22	0.25	0.19	0.04	0.24	0.03
Tb			0.02	0.04	0.03		0.04	0.01
Dy	0.01	0.02	0.21	0.45	0.34	0.02	0.17	0.03
Ho			0.03	0.06	0.04		0.04	0.01
Er		0.01	0.07	0.12	0.07	0.02	0.10	0.03
Tm			0.03	0.03	0.02		0.02	0.01
Yb		0.02	0.09	0.28	0.31	0.03	0.10	0.03
Lu			0.02	0.02	0.02		0.03	
Hf							3.00	
Ta							0.79	

Appendix 1: Electron Microprobe and LAM-ICP-MS Data

Table A2 (continued) Trace-element compositions of the five major minerals analysed by LAM ICP-MS. *Italics* indicate Zr group. Blank indicates below detection limit, n.d. indicates element not determined.

Plagioclase	06 AVG	20 AVG	01 AVG	142 AVG	Epidote	06-1	06-2	06-3
ppm								
Sc	2.16	1.46	1.77	3.58		3.50	26.60	35.80
V	4.20	3.51	0.29	6.20		39.90	325.0	252.0
Cr	4.05	3.95	3.89	5.92		58.40	n.d.	n.d.
Co	0.04	0.09	0.84	0.06		1.20	n.d.	n.d.
Ni	13.66	19.06	10.24	21.21		12.60	n.d.	n.d.
Cu	1.54	4.90	1.30	2.36		2.11	n.d.	n.d.
Zn	87.83	126.6	42.57	132.8		242.0	n.d.	n.d.
Sr	531.3	815.8	476.2	829.5		650.0	563.3	663.3
Rb	0.37	2.15	16.15	0.58		1.56	0.47	0.44
Y	0.84	0.08	0.28	1.15		26.90	34.70	30.00
Zr	7.50	0.23	0.42	16.07		7.75	115.0	93.30
Nb	0.03	0.02	0.02	0.05		0.04	16.90	0.09
La	3.74	0.40	2.35	6.25		123.0	47.00	82.90
Ce	7.08	0.54	2.40	11.59		269.0	103.0	182.0
Pr	0.50	0.05	0.21	0.80		31.70	11.30	18.60
Nd	1.31	0.15	0.62	2.13		127.0	43.30	64.30
Sm	0.23	0.06	0.08	0.36		21.90	8.53	12.60
Eu	0.22	0.13	0.15	0.34		5.59	3.48	4.17
Gd	0.15	0.06	0.04	0.22		15.00	7.01	8.41
Tb	0.02		0.01	0.03		1.69	1.10	1.27
Dy	0.22	0.02	0.03	0.33		7.89	6.45	7.63
Ho	0.03	n.d.	0.01	0.04		1.17	1.39	1.34
Er	0.06	0.03	0.03	0.09		2.38	3.69	3.21
Tm	0.02	0.01	0.01	0.03		0.25	0.52	0.45
Yb	0.13	0.05	0.03	0.23		1.49	3.34	3.04
Lu	0.01			0.02		0.19	0.46	0.42
Hf							4.13	2.29
Ta							1.00	0.03

Appendix 1: Electron Microprobe and LAM-ICP-MS Data

Table A2 (continued) Trace-element compositions of the five major minerals analysed by LAM ICP-MS. *Italics* indicate Zr group. Blank indicates below detection limit, n.d. indicates element not determined.

Epidote	06-4	46-1	46-2	46-3	46-4	48-1	48-2	48-3
ppm								
Sc	40.00	32.60	16.30	16.00	30.20	1.75	43.10	42.90
V	255.0	417.0	180.0	256.0	187.0	79.20	329.0	276.0
Cr	n.d.	n.d.	333.0	231.0	244.0	n.d.	n.d.	342.0
Co	n.d.	1.56	n.d.	n.d.	n.d.	1.76	n.d.	n.d.
Ni	n.d.	n.d.	12.70	6.75	6.04	n.d.	n.d.	58.40
Cu	n.d.	n.d.	1.00	1.93	3.45	n.d.	n.d.	5.00
Zn	n.d.	n.d.	102.0	109.0	115.0	n.d.	n.d.	188.0
Sr	826.7	1550	1270	1050	870.0	373.3	483.3	62.60
Rb	0.45	2.73	0.05	0.06	0.03	0.14	0.76	4.07
Y	42.60	12.30	20.80	20.00	25.40	4.01	26.20	6.59
Zr	110.0	171.0	278.0	89.30	40.20	0.56	135.0	28.10
Nb	4.11	0.09	1.71	64.40	0.57	0.02	109.0	4.44
La	52.40	8.72	37.00	24.70	72.90	6.62	24.40	0.98
Ce	113.0	17.10	81.00	49.40	130.0	11.80	79.50	3.77
Pr	14.60	2.24	9.84	6.21	17.70	1.22	10.50	0.72
Nd	56.00	11.00	38.90	24.40	71.30	5.62	43.60	4.04
Sm	12.60	2.35	7.47	4.49	12.80	1.22	10.10	1.27
Eu	6.22	0.56	2.32	1.61	5.03	0.47	3.44	0.38
Gd	11.20	1.95	5.54	3.47	9.29	0.84	7.01	1.41
Tb	1.67	0.36	0.73	0.54	1.11	0.12	1.02	0.20
Dy	10.50	2.32	4.83	3.44	6.02	0.81	5.65	1.33
Ho	1.68	0.52	0.86	0.70	0.92	0.16	1.05	0.26
Er	4.03	1.35	2.29	2.26	2.18	0.39	2.83	0.73
Tm	0.45	0.18	0.27	0.34	0.24	0.04	0.36	0.11
Yb	3.00	1.64	1.95	2.16	1.25	0.32	2.78	0.65
Lu	0.38	0.28	0.30	0.29	0.16	0.07	0.37	0.11
Hf	3.97	4.78	n.d.	n.d.	n.d.	n.d.	4.67	n.d.
Ta	0.03	0.03	n.d.	n.d.	n.d.	n.d.	7.86	n.d.

Appendix 1: Electron Microprobe and LAM-ICP-MS Data

Table A2 (continued) Trace-element compositions of the five major minerals analysed by LAM ICP-MS. *Italics* indicate Zr group. Blank indicates below detection limit, n.d. indicates element not determined.

Epidote	06-Avg	46 Avg	48 Avg	Garnet	01-1	01-2	01-3	01-4
ppm								
Sc	26.48	23.78	29.25		23.50	19.60	18.10	22.90
V	217.9	260.0	228.1		342.0	252.0	213.0	184.0
Cr	58.40	202.0	114.00		n.d.	n.d.	n.d.	n.d.
Co	1.20	0.39	0.59		n.d.	n.d.	n.d.	n.d.
Ni	12.60	6.37	19.47		n.d.	n.d.	n.d.	n.d.
Cu	2.11	1.59	1.67		n.d.	n.d.	n.d.	n.d.
Zn	242.0	81.50	62.67		n.d.	n.d.	n.d.	n.d.
Sr	675.8	1185	306.42		1.46	10.20	0.10	0.26
Rb	0.73	0.72	1.66		0.13	0.40	0.17	0.21
Y	33.55	19.63	12.27		72.40	38.70	52.80	110.0
Zr	81.51	144.6	54.55		6.03	9.02	8.48	5.09
Nb	5.28	16.69	37.82		3.73	0.17	0.03	0.06
La	76.33	35.83	10.67		0.12	1.80	0.01	0.06
Ce	166.8	69.38	31.69		0.36	3.02	0.06	0.22
Pr	19.05	9.00	4.15		0.08	0.38	0.05	0.05
Nd	72.65	36.40	17.75		0.97	2.10	0.77	0.96
Sm	13.91	6.78	4.20		1.84	1.52	1.54	1.99
Eu	4.87	2.38	1.43		1.82	1.74	2.02	1.71
Gd	10.41	5.06	3.09		5.43	3.74	5.26	8.41
Tb	1.43	0.68	0.45		1.31	0.72	1.06	1.86
Dy	8.12	4.15	2.60		11.20	5.88	8.20	17.40
Ho	1.40	0.75	0.49		2.72	1.33	1.77	4.06
Er	3.33	2.02	1.32		8.65	4.26	5.78	12.70
Tm	0.42	0.26	0.17		1.37	0.62	0.81	1.91
Yb	2.72	1.75	1.25		9.57	4.87	6.43	14.40
Lu	0.36	0.26	0.18		1.44	0.68	0.83	2.18
Hf	2.60	1.20	1.56					
Ta	0.27	0.01	2.62					

Appendix 1: Electron Microprobe and LAM-ICP-MS Data

Table A2 (continued) Trace-element compositions of the five major minerals analysed by LAM ICP-MS. *Italics* indicate Zr group. Blank indicates below detection limit, n.d. indicates element not determined.

Gamet	20-1	20-2	142-1	142-2	142-3	142-4	01 Avg	20 Avg
ppm								
Sc	6.86	4.66	26.60	16.90	28.50	20.90	21.03	5.76
V	656.0	409.0	191.0	178.0	328.0	243.0	247.8	532.5
Cr	176.0	226.0	396.0	189.0	140.0	110.0	n.d.	201.0
Co	n.d.	n.d.	23.80	20.70	25.10	18.80	n.d.	n.d.
Ni	105.0	67.10	6.28	4.41	4.75	4.67	n.d.	86.05
Cu	9.14	3.46	1.03	0.90	1.18	0.87	n.d.	6.30
Zn	22.70	16.30	41.80	33.40	55.20	31.90	n.d.	19.50
Sr	42.20	33.50	4.66	105.0	58.40	6.49	3.00	37.85
Rb	0.54	0.35	2.10	3.89	18.90	2.30	0.23	0.45
Y	49.90	44.00	110.0	64.90	116.0	66.10	68.48	46.95
Zr	398.0	944.0	15.30	19.40	5.26	5.63	7.16	671.0
Nb	508.0	187.0	55.70	63.90	0.05	0.06	1.00	347.5
La	0.40	0.56	0.94	2.82	0.21	0.71	0.50	0.48
Ce	1.45	5.45	3.94	11.90	0.38	1.18	0.91	3.45
Pr	0.26	0.67	0.81	2.47	0.07	0.18	0.14	0.46
Nd	2.76	3.08	5.28	14.20	0.71	1.01	1.20	2.92
Sm	1.24	1.64	3.82	5.45	1.63	1.25	1.72	1.44
Eu	0.58	0.55	2.49	3.64	1.82	1.33	1.82	0.56
Gd	1.86	4.03	10.70	7.51	7.84	4.51	5.71	2.95
Tb	0.62	0.65	2.28	1.34	1.89	1.02	1.24	0.63
Dy	5.95	6.91	18.40	9.96	17.80	9.42	10.67	6.43
Ho	1.93	1.52	3.90	2.20	4.27	2.41	2.47	1.73
Er	6.52	5.93	10.80	6.74	13.10	7.20	7.85	6.23
Tm	1.36	0.96	1.65	1.06	1.96	1.16	1.18	1.16
Yb	11.50	7.23	11.10	8.06	13.70	8.32	8.82	9.37
Lu	1.34	1.09	1.64	1.27	1.94	1.20	1.28	1.22
Hf								
Ta								

Appendix 1: Electron Microprobe and LAM-ICP-MS Data

Table A2 (continued) Trace-element compositions of the five major minerals analysed by LAM ICP-MS. *Italics* indicate Zr group. Blank indicates below detection limit, n.d. indicates element not determined.

Garnet	142-Avg	Titanite	46-1	46-2	46-3	48-1	48-2	48-3
ppm								
Sc	23.23		6.01	9.02	5.33	2.98	4.74	3.01
V	235.0		1040	916.0	840.0	1010	1380	636.0
Cr	208.8		83.50	94.80	25.30	28.70	922.00	45.70
Co	22.10		n.d.	n.d.	n.d.	n.d.	n.d.	n.d.
Ni	5.03		40.20	44.00	50.60	8.30	12.00	22.10
Cu	0.99		6.35	3.57	4.07	1.67	1.47	1.25
Zn	40.58		15.70	18.50	16.30	11.50	7.35	35.90
Sr	43.64		14.50	17.40	13.30	31.60	19.70	250.0
Rb	6.80		0.36	0.96	0.21	1.28	0.08	1.13
Y	89.25		1420	1180	1050	1260	1130	1340
Zr	11.40		401.0	277.0	838.0	331.0	409.0	696.0
Nb	29.93		211.0	163.0	205.0	276.0	233.0	219.0
La	1.17		170.0	184.0	46.40	185.0	239.0	106.0
Ce	4.35		553.0	503.0	214.0	608.0	685.0	472.0
Pr	0.88		87.50	74.20	30.00	104.0	108.0	89.30
Nd	5.30		460.0	382.0	184.0	564.0	562.0	517.0
Sm	3.04		145.0	125.0	68.80	176.0	166.0	175.0
Eu	2.32		51.30	44.60	23.20	62.50	61.50	60.50
Gd	7.64		185.0	162.0	109.0	222.0	200.0	217.0
Tb	1.63		31.60	27.30	19.40	35.60	31.80	34.70
Dy	3.90		217.0	187.0	146.0	254.0	228.0	244.0
Ho	3.20		43.70	37.50	31.00	48.90	45.60	46.70
Er	9.46		130.0	108.0	93.70	138.0	136.0	134.0
Tm	1.46		18.50	15.20	12.90	18.90	19.90	18.30
Yb	10.30		127.0	102.0	89.90	128.0	143.0	117.0
Lu	1.51		17.70	14.30	11.50	16.30	19.50	14.30
Hf			n.d.	n.d.	n.d.	n.d.	n.d.	n.d.
Ta			n.d.	n.d.	n.d.	n.d.	n.d.	n.d.

Appendix 1: Electron Microprobe and LAM-ICP-MS Data

Table A2 (continued) Trace-element compositions of the five major minerals analysed by LAM ICP-MS. *Italics* indicate Zr group. Blank indicates below detection limit, n.d. indicates element not determined.

Titanite	49-1	49-2	06-1	06-2	06-3	20-01	20-2	20-3
ppm								
Sc	5.20	4.12	10.80	2.61	3.65	7.52	7.18	6.06
V	1320	964.0	413.0	458.0	327.0	978.0	878.0	886.0
Cr	214.0	294.0	164.0	50.70	60.00	89.15	60.05	46.58
Co	n.d.	n.d.	n.d.	n.d.	n.d.	n.d.	n.d.	n.d.
Ni	24.30	32.80	12.30	18.60	16.80	42.10	47.30	47.77
Cu	2.74	1.82	1.95	2.82	1.91	4.96	3.82	4.37
Zn	7.19	7.58	9.17	20.70	10.10	17.10	17.40	16.57
Sr	18.00	19.30	44.40	106.0	66.90	15.95	15.35	14.18
Rb	0.19	0.13	0.18	0.20	0.64	0.66	0.58	0.36
Y	1770	397.0	1640	121.0	108.0	1300	1115	1133
Zr	572.0	547.0	250.0	276.0	273.0	339.0	557.5	671.7
Nb	277.0	209.0	2340	1350	2310	187.0	184.0	199.0
La	123.0	14.90	168.0	132.0	320.0	177.0	115.2	89.93
Ce	457.0	79.40	890.0	472.0	992.0	528.0	358.5	318.7
Pr	77.50	18.80	199.0	69.80	142.0	80.85	52.10	46.95
Nd	474.0	124.0	1290	343.0	646.0	421.0	283.0	263.0
Sm	180.0	51.10	549.0	78.60	125.0	135.0	96.90	90.87
Eu	56.30	13.20	137.0	30.30	54.10	47.95	33.90	31.45
Gd	254.0	66.50	610.0	55.50	75.80	173.5	135.5	130.5
Tb	41.60	10.90	88.30	6.79	7.81	29.45	23.35	22.75
Dy	316.0	76.00	477.0	35.90	33.60	202.0	166.5	164.7
Ho	62.70	15.20	62.00	4.44	3.87	40.60	34.25	34.20
Er	181.0	46.00	120.0	8.72	7.44	119.0	100.9	102.1
Tm	26.20	6.81	11.80	1.14	0.78	16.85	14.05	14.22
Yb	171.0	51.20	57.20	4.31	3.67	114.5	95.95	98.10
Lu	22.50	7.06	4.92	0.49	0.42	16.00	12.90	13.00
Hf	n.d.	n.d.	n.d.	n.d.	n.d.	n.d.	n.d.	n.d.
Ta	n.d.	n.d.	n.d.	n.d.	n.d.	n.d.	n.d.	n.d.

Appendix 1: Electron Microprobe and LAM-ICP-MS Data

Table A2 (continued) Trace-element compositions of the five major minerals analysed by LAM ICP-MS. *Italics* indicate Zr group. Blank indicates below detection limit, n.d. indicates element not determined.

Titanite	142-1	142-2	01-1	01-2	01-3	46 Avg	48 Avg	49 Avg
ppm								
Sc	4.66	4.39	3.86	3.88	3.29	6.79	3.58	4.66
V	1142	1053	1195	1008	822.3	932.0	1009	1142
Cr	254.0	274.0	106.6	115.1	188.9	67.87	332.1	254.0
Co	n.d.	n.d.	n.d.	n.d.	n.d.	n.d.	n.d.	n.d.
Ni	28.55	30.68	10.15	17.05	18.12	44.93	14.13	28.55
Cu	2.28	2.05	1.57	1.36	1.36	4.66	1.46	2.28
Zn	7.39	7.48	9.43	21.63	27.08	16.83	18.25	7.39
Sr	18.65	18.98	25.65	134.9	175.2	15.07	100.4	18.65
Rb	0.16	0.15	0.68	0.61	0.98	0.51	0.83	0.16
Y	1083	740.3	1195	1235	1291	1216	1243	1083
Zr	559.5	553.3	370.0	552.5	587.3	505.3	478.7	559.5
Nb	243.0	226.0	254.5	226.0	230.8	193.0	242.7	243.0
La	68.95	41.93	212.0	172.5	141.3	133.5	176.7	68.95
Ce	268.2	173.8	646.5	578.5	530.7	423.3	588.3	268.2
Pr	48.15	33.48	106.0	98.65	94.87	63.90	100.4	48.15
Nd	299.0	211.5	563.0	539.5	532.3	342.0	547.7	299.0
Sm	115.6	83.33	171.0	170.5	173.7	112.9	172.3	115.6
Eu	34.75	23.98	62.00	61.00	61.00	39.70	61.50	34.75
Gd	160.3	113.4	211.0	208.5	215.0	152.0	213.0	160.3
Tb	26.25	18.58	33.70	33.25	34.37	26.10	34.03	26.25
Dy	196.0	136.0	241.0	236.0	243.0	183.3	242.0	196.0
Ho	38.95	27.08	47.25	46.15	46.88	37.40	47.07	39.0
Er	113.5	79.75	137.0	135.0	135.0	110.6	136.0	113.5
Tm	16.51	11.66	19.40	19.10	18.67	15.53	19.03	16.51
Yb	111.1	81.15	135.5	130.0	123.2	106.3	129.3	111.1
Lu	14.78	10.92	17.90	16.90	15.50	14.50	16.70	14.78
Hf	n.d.	n.d.	n.d.	n.d.	n.d.	n.d.	n.d.	n.d.
Ta	n.d.	n.d.	n.d.	n.d.	n.d.	n.d.	n.d.	n.d.

Appendix 1: Electron Microprobe and LAM-ICP-MS Data

Table A2 (continued) Trace-element compositions of the five major minerals analysed by LAM ICP-MS. *Italics* indicate Zr group. Blank indicates below detection limit, n.d. indicates element not determined.

Titanite	06 Avg	01 Avg	20 Avg	142 Avg
ppm				
Sc	5.69	3.68	6.92	4.53
V	399.3	1008	914.0	1098
Cr	91.57	136.8	65.26	264.0
Co	n.d.	n.d.	n.d.	n.d.
Ni	15.90	15.11	45.72	29.61
Cu	2.23	1.43	4.38	2.17
Zn	13.32	19.38	17.02	7.43
Sr	72.43	111.9	15.16	18.81
Rb	0.34	0.76	0.53	0.15
Y	623.0	1241	1183	911.9
Zr	266.3	503.3	522.7	556.4
Nb	2000	237.1	190.0	234.5
La	206.7	175.3	127.4	55.44
Ce	784.7	585.1	401.7	221.0
Pr	136.9	99.84	59.97	40.81
Nd	759.7	544.9	322.3	255.3
Sm	250.9	171.7	107.6	99.44
Eu	73.80	61.33	37.77	29.36
Gd	247.1	211.5	146.5	136.8
Tb	34.30	33.77	25.18	22.41
Dy	182.2	240.0	177.7	166.0
Ho	23.44	46.76	36.35	33.01
Er	45.39	135.7	107.3	96.63
Tm	4.57	19.06	15.04	14.08
Yb	21.73	129.6	102.9	96.13
Lu	1.94	16.77	13.97	12.85
Hf	n.d.	n.d.	n.d.	n.d.
Ta	n.d.	n.d.	n.d.	n.d.

Appendix B: Assessment of Precision and Accuracy of Data

Accurate analyses are paramount in understanding the geology and geochemistry of any geologic region. In addition, it is important to assess the quality of the data set so that the conclusions are supported by the data set. For this thesis, four main analytical techniques (see 2.3) were utilized to produce a data set including major- and trace-element chemistry of metabasites and their constituent minerals in greenschist- to amphibolite-facies assemblages. The following sections provide an overview of the detection limits, precision, and accuracy of the various analytical techniques employed.

X-Ray Fluorescence

Details for the preparation of pressed pellets for bulk-rock major- and trace-element determination are provided by Longerich (1995) and summarized in 2.3.1. Limits of detection vary depending on the elemental group analysed. For analyses utilizing pressed pellets, Longerich (1995) quoted detection limits in the 0.1-0.7 ppm range for Rb, Y, and Nb up to approximately 100 ppm for major oxides like Na₂O and MgO. Detection limits for other routinely analysed elements are provided in Longerich (1995).

Four replicate analyses were performed on three different standards (BHVO-1, SY-2, and DTS-1 depending on the major or trace element) and results are presented and illustrated in Table A3 and Figure A1 respectively. Precision is generally excellent (0-3

Appendix B: Assessment of Precision and Accuracy of Data

% R.S.D.: based on Jenner *et al.*, 1990) for all analysed major oxides and trace elements except for Sc which has an R.S.D of 18.8%. The high R.S.D of Sc is due in part to high detection limits reported for this element (Sylvester *et al.*, 2003).

Accuracy of the four replicate analyses is quoted as the percent relative difference from known values (Govindaraju, 1994) for three selected standards (BHVO-1, SY-2 and DTS-1: see Table A3 and Figure A1). Excellent accuracy (0-3% relative difference based on Jenner *et al.*, 1990) was returned for the major oxides SiO_2 , TiO_2 , $\text{Fe}_2\text{O}_{3\text{T}}$, MgO , CaO , Na_2O , K_2O , and P_2O_5 and the trace elements Sc, V, Cr, Ni, Cu, Zn, Sr, Rb, and Ba. Good accuracy (3-7%: based on Jenner *et al.*, 1990) was returned for Al_2O_3 and Zr with a calculated value of 7.81% relative difference for Y. Nb was the only element above 10% relative difference.

Inductively Coupled Plasma Mass Spectrometry (ICP-MS)

Selected trace elements (Y, Zr, Nb, Ba, Hf, and Ta) and *REE* were determined by the sodium peroxide (Na_2O_2) sinter method of Longerich *et al.* (1990). This is the preferred method since it breaks down many silicate minerals that are difficult to digest using the acid digest method.

For this method, 0.2 g of rock powder are added to 0.8 g of Na_2O_2 in a Ni crucible where it is sintered in a muffle furnace at 480°C for 1.5 hours. The crucible is removed from the furnace, covered and allowed to cool for 20 minutes while 10 ml of distilled

Appendix B: Assessment of Precision and Accuracy of Data

water is added, a few drops at a time. The cover is then rinsed into the crucible and the mixture is transferred to a centrifuge tube where distilled water is added to make the volume 30 ml and the subsequent mixture is centrifuged for 15 minutes.

The residue remaining in the crucible is dissolved in 2.5 ml of 8 N HNO₃ and 1 ml of 2% oxalic acid. Again, the crucible is rinsed with 0.2 N HNO₃ and this is added to the centrifuge tube, which in turn is transferred to a clean centrifuge tube and diluted with distilled water to a final volume of 50 g. The solutions are further diluted prior to analysis, and 2 g of sample and 8 g of 0.2 N HNO₃ are weighted into 12 ml test tube producing a solution with a sample concentration of approximately 0.7g/kg. This solution is mixed with an on-line standard addition 'spike' at the ratio 1 part 'spike' to 2 parts sample yielding a solution that has a concentration of 0.5 g rock sample/kg solution.

Detection limits for the Na₂O₂ sinter method are provided by Longerich *et al.* (1990), where they are described in two forms: (i) the calibration limit of detection (CLD), and (ii) the mean limit of detection (MLD) of the reagent blanks. Of these, the MLD is a more representative measure of the detection limit since it accounts for possible contamination by reagents and sample preparation equipment whereas the CLD does not. Longerich *et al.* (1990) reported detection limits in the 0.009 ppm (CLD) to 0.006 ppm (MLD) range for Lu (*HREE*) and 0.07 ppm (CLD) to 0.14 ppm (MLD) for Nd.

Four replicate analyses of standard BR-688 were performed by sinter method and analysed by ICP-MS (see 2.3.1) and are reported in Table A3 and illustrated in Figure

A1. Precision for all *REE* and analysed trace elements except Ta (13.78% R.S.D.) are in the good (3-7% R.S.D.) to excellent (0-3% R.S.D.) range following the criteria of Jenner *et al.* (1990). Accuracy for all *REE* is in the good to excellent range except for two *MREE* (Tb, Dy: both \approx 8% R.S.D.) With the exception of Y and Th (good to excellent range), the relative differences for analysed trace elements range from reasonable (\approx 10% R.S.D.) to poor (e.g., Ta). Possible reasons for poor Ta precision and accuracy are linked to dissolution problems (Sylvester *et al.*, 2003).

Electron Probe Microanalyser (EPMA)

Details of the EPMA setup at Memorial University are given in section 2.3.2. In general, the instrument was used in two ways: (i) back-scattered electron (BSE) mode to aid in the choice of locations for the analysis spots since BSE imaging enables assessment of potential major-element mineral zoning and the presence of inclusions or alteration; and (ii) to carry out quantitative major-element mineral analyses of selected grains in 100 μm thick polished thin sections by energy dispersive (ED) analysis.

The precision of the instrument is a function of count rate and the reproducibility of the count rate. However, since the ED system is extremely stable, precision is generally calculated as a function of count rate and an empirically determined precision factor (F), for each element. In general, the square root of a measured concentration multiplied by F yields the approximate precision. Precision factors are listed in Table

A4. A qualitative assessment of accuracy under standard operating conditions employed in this thesis is approximately $\pm 2\%$ relative, with accuracy degrading as detection limits (DL ≈ 0.05 wt%) are approached.

Laser Ablation Microprobe ICP-MS (LAM-ICP-MS)

The LAM-ICP-MS setup at Memorial University has been described by numerous authors (e.g., Taylor *et al.*, 1997; Sylvester, 2001 among many others) and a brief overview of the instrument and operating conditions are discussed in section 2.3.2. In this thesis, the instrument was used to determine trace-element concentrations in coexisting minerals *in situ*, using the same 100 μm thick polished thin sections that had been previously analysed by EPMA.

Taylor *et al.* (1997) quoted detection limits in the range of 20-60 ppb for mono-isotopic *REE*. Yang (2002) reports detection limits, defined by 3σ counting errors on analyses of BCR 2, in the range of 3-35 ppb for high mass elements (Rb to Ta) and 68-6000 ppb for low mass elements (Li to Zn).

Since LAM-ICP-MS is a destructive *in situ* technique, it is impossible to perform repeated measurements on the same spot, thereby rendering it difficult to measure precision. To alleviate this problem, repeated analyses of a U.S. Geological Survey glass reference BCR-2G were performed under similar operating parameters to routine analyses, and in turn, were used to estimate precision (Table A4, Figure A1). The precision for all *REE* is within approximately 10% R.S.D., except Tb, which is

Appendix B: Assessment of Precision and Accuracy of Data

approximately 32% R.S.D. However, the long-term MUN average, which is probably a more representative measure of precision, is 13 % R.S.D. for this element. Most of the other analysed trace elements are within approximately 10% R.S.D., except for Ni, which has a R.S.D. of approximately 25% (Table A4). However, it should be noted that Longerich *et al.* (1996) stated that chalcophile elements such as Cu and Ni often exhibit poor precision due to fractionation during sample ablation and transportation. Accuracy is reported as the percent difference between repeated measurements of SRM BCR 2 and the long-term Memorial University average for this glass (Table A4 and Figure A1). All *REE* analyses except Ho ($R.D._{Ho} = 11.49\%$) are within approximately 10% relative difference as are most trace elements with the notable exceptions of the chalcophile elements Ni ($R.D._{Ni} = 21.81\%$) and Zn ($R.D._{Zn} = 15.05\%$).

Representative ablation patterns for analysed phases are illustrated in counts per second *versus* time plots in Figure A2. Typical acquisition parameters were 60 to 80 seconds measurement of the argon carrier gas blank followed by approximately 20 to 50 seconds of measurement with the laser switched on and material being ablated. Pit sizes varied from 30-60 μm depending on the target material, pulse energy, and duration of ablation. The raw counts were processed off-line with CONVERT software and data reduction was performed using LAMTRACE software (Jackson, 2001). Examination of LAMTRACE graphical output (Figure A2) allows the selection of appropriate background and signal time intervals for integration.

Appendix B: Assessment of Precision and Accuracy of Data

Procedure for the estimation of FeO and Fe₂O₃ in whole rocks (modified Pratt method)

REAGENTS

Ammonium metavanadate solution: Dissolve 10 g of reagent grade NH₄VO₃ in 110 ml H₂SO₄ (1:1), dilute to 1 litre and store in a glass bottle or in the reservoir of an automatic pipet.

Acid mixture (H₃PO₄ : H₂SO₄ : H₂O = 1:2:2): Add 400 ml of H₂SO₄ to 400 ml of H₂O in a 1500 ml beaker, cool in a water bath, then add 200 ml of concentrated H₃PO₄.

Boric acid solution

Ferrous ammonium sulfate solution (0.05 N): Dissolve 9.8 g Fe(NH₄SO₄) in freshly boiled and cooled H₂O

Barium Diphenylamine Sulfonate solution (0.2%): Dissolve 0.2 g in 100 ml H₂O.

PROCEDURE

1. Weigh 0.200 g (if FeO is likely to be greater than 10 % use 0.100 g of rock powder) of rock powder into a 60 ml plastic vial.
2. To each vial (and 4 additional vials to serve as blanks) add 5 ml of ammonium vanadate solution.
3. Swirl gently forming a uniform slurry and add 10 ml of hydrofluoric acid.
4. Loosely cover the vials and let stand in a fume-hood until the sample is

Appendix B: Assessment of Precision and Accuracy of Data

completely decomposed (absence of gritty particles).

5. To each vial add 10 ml of the sulfuric-phosphoric acid mixture.
6. Pour the contents of the vial into 100 ml of boric acid solution in a 400 ml beaker; rinse out the vial with an additional 100 ml of boric acid solution and add the rinsings to the 400 ml beaker.
7. Stir the contents of the beaker to effect complete dissolution of the contents of the vial and add, from an automatic pipet, 10 ml of ferrous ammonium sulfate solution.
8. Add 1 ml of barium diphenylamine sulfonate indicator and titrate to a grey endpoint with a standard potassium dichromate solution using a 10 ml semi-micro buret.

CALCULATION

$$\text{Wt. \% FeO} = \frac{\text{ml sample} - \text{ml blank}^*}{1000} \times N_{\text{K}_2\text{Cr}_2\text{O}_7} \times 71.85 \times \frac{100}{\text{sample wt (g)}}$$

$$N_{\text{K}_2\text{Cr}_2\text{O}_7} = 0.05$$

* Average of 4 blank values.

No standards were run during this procedure so there is no assessment of either precision or accuracy.

Appendix B: Assessment of Precision and Accuracy of Data

Table A3 Precision and accuracy for standards used in this study for XRF and solution ICP-MS analyses. R.S.D. is the standard deviation divided by the mean. Percent difference is calculated as: $[(\text{average-known}/\text{known}) \times 100]$. Known values from Govindaraju, 1994. BR-688 MUN average from ICP-MS runs 161-191 (2001-2002).

XRF

n = 4	Standard	Study	R.S.D. (%)	Known	% Diff
(wt %)					
SiO ₂	BHVO-1	49.15	0.1	49.94	-1.58
Al ₂ O ₃	SY-2	12.57	0.3	11.75	+6.98
TiO ₂	BHVO-1	2.79	0.1	2.71	+2.95
Fe ₂ O _{3T}	SY-2	6.31	0.2	6.31	0.00
MgO	BHVO-1	49.58	0.1	49.58	0.00
MnO	SY-2	0.3	0.8	0.32	-6.25
CaO	SY-2	8.09	0.1	8.026	+0.80
Na ₂ O	SY-2	4.22	0.3	4.31	-2.09
K ₂ O	SY-2	4.17	0.6	4.23	-1.42
P ₂ O ₅	SY-2	0.52	1.0	0.54	-3.70

(ppm)

Sc	BHVO-1	33	18.8	32	+3.13
V	BHVO-1	317	0.9	317	0.00
Cr	DTS-1	3990	0.1	3990	0.00
Ni	DTS-1	2360	0.5	2360	0.00
Cu	BHVO-1	137	0.8	136	+0.74
Zn	BHVO-1	101	1.1	105	-3.81
Sr	SY-2	271	0.6	271	0.00
Rb	SY-2	220	0.3	217	+1.38
Ba	SY-2	450	1.4	460	-2.17
Y	SY-2	118	0.2	128	-7.81
Nb	SY-2	34.4	0.4	29	+18.62
Zr	SY-2	296	0.7	280	+5.71

ICP-MS BR-688

n = 4	Study	R.S.D. %	MUN avg	% Diff	Study	R.S.D. %	MUN avg	% Diff	
REE (ppm)					Traces (ppm)				
La	4.91	4.41	4.98	-1.49	Y	16.77	3.07	17.81	-5.81
Ce	11.23	3.76	11.55	-2.80	Zr	65.03	4.93	59.15	+9.94
Pr	1.60	3.41	1.65	-2.91	Nb	5.55	5.68	4.87	+14.00
Nd	7.90	2.31	8.03	-1.58	Ba	203.63	2.99	163.33	+24.67
Sm	2.34	1.57	2.30	+1.57	Hf	1.75	5.51	1.54	+13.93
Eu	0.99	1.40	0.94	+5.11	Ta	0.28	13.78	0.18	+56.39
Gd	3.06	0.27	2.88	+6.39	Th	0.33	5.26	0.33	+1.06
Tb	0.52	2.91	0.48	+8.02					
Dy	3.49	3.15	3.21	+8.74					
Ho	0.70	0.23	0.70	-0.71					
Er	2.07	0.30	2.10	-1.31					
Tm	0.30	0.68	0.30	+0.50					
Yb	2.04	1.86	2.00	+1.88					
Lu	0.32	1.02	0.30	+7.00	MUN average of BR-688 runs 161-191 (2001-2002)				

MUN average of BR-688 runs 161-191 (2001-2002)

Appendix B: Assessment of Precision and Accuracy of Data

Table A4 Precision and accuracy for standard BCR 2G analyses by LAM-ICP-MS. R.S.D. is the standard deviation divided by the mean. Percent difference is calculated as: [(average-known/known)*100]. Known values from Govindaraju, 1994. BCR 2 MUN average from LAM-ICP-MS analyses from 1996-2002 (n = 235).

LAM-ICP-MS BCR 2

n = 35	Study	% R.S.D.	MUN avg	% Diff
--------	-------	----------	---------	--------

REE

(ppm)

La	22.16	5	24.48	+3.24
Ce	48.90	4	52.19	+2.62
Pr	5.93	4	6.43	+5.89
Nd	25.25	3	27.25	+4.83
Sm	5.54	9	6.09	+8.72
Eu	1.73	5	1.86	+6.93
Gd	5.37	7	6.28	+7.71
Tb	0.80	32	1.10	-5.65
Dy	5.33	6	5.84	+8.54
Ho	1.02	10	1.14	+11.49
Er	2.92	11	3.38	+7.74
Tm	0.42	12	0.49	+8.63
Yb	2.94	8	3.32	+0.62
Lu	0.41	9	0.49	+3.88

Traces

(ppm)

Sc	32.14	5	31.88	+2.21
V	413.6	4	411.1	-1.02
Cr	15.51	9	16.00	0.00
Co	38.05	4	37.27	-0.72
Ni	10.61	25	10.17	+21.81
Cu	15.59	8	17.54	+7.68
Zn	154.0	9	149.0	-15.06
Sr	315.3	4	323.1	+4.11
Y	27.53	6	30.60	+5.88
Rb	42.95	12	44.50	+5.82
Zr	145.8	9	168.8	+8.46
Nb	11.47	9	12.71	+3.30

EPMA

	Na	Mg	Al	Si	K	Ca	Ti	Mn	Fe
Precision	.040	.018	.015	.015	.020	.021	.025	.035	.040
Factor (F)									

Where $1\sigma = F^*/\text{concentration}$

Appendix B: Assessment of Precision and Accuracy of Data

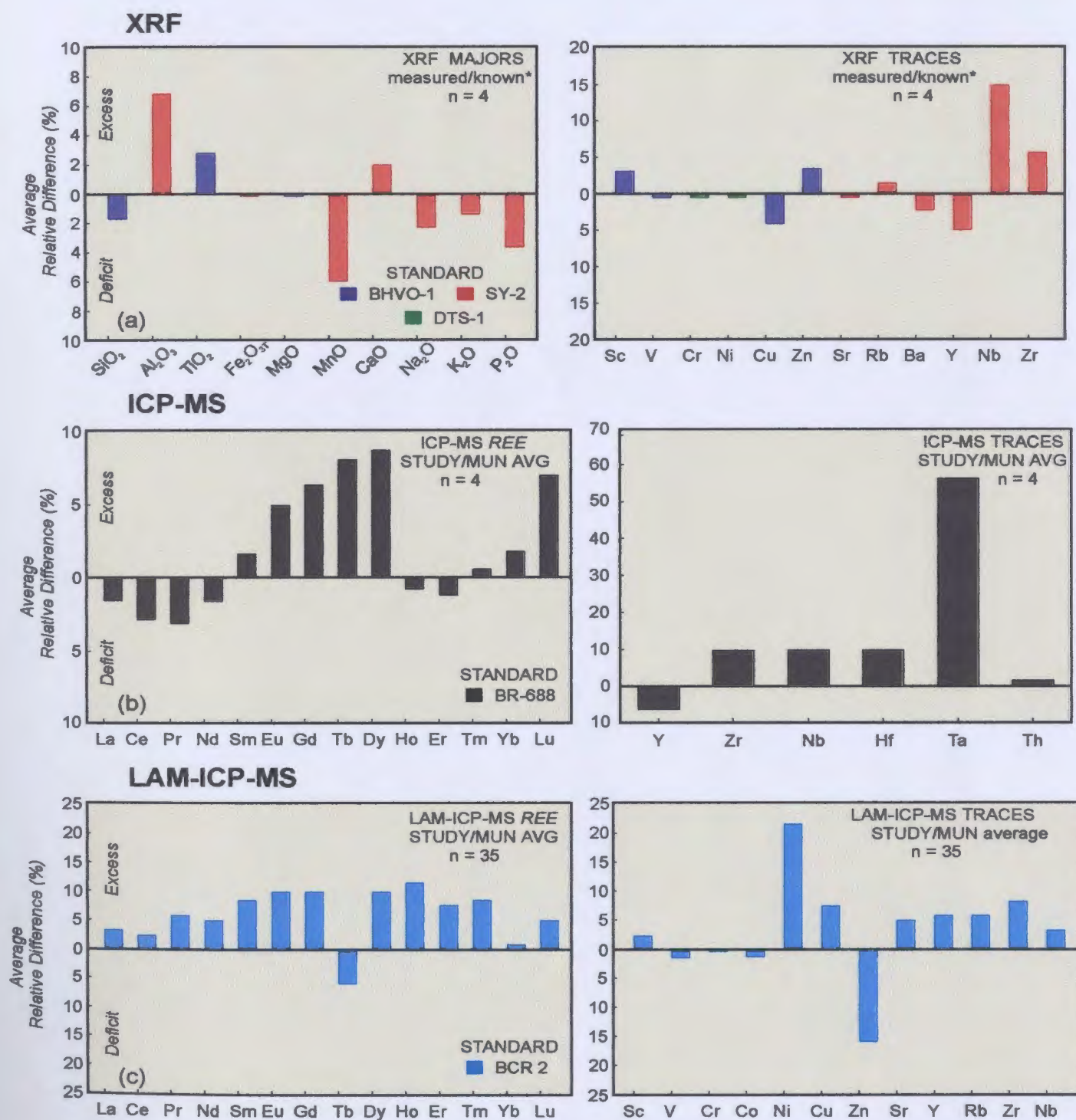


Figure A1 Estimation of accuracy for: a) XRF; b) solution ICP-MS; and c) LAM-ICP-MS. Results presented as percent relative difference $[(\text{mean determination} - \text{known}) / (\text{known}) * 100\%]$. Known values from: a) Govindaraju (1994), b) MUN average from run 161-191 and c) MUN average BCR-2 values from 1996-2002 (n = 235).

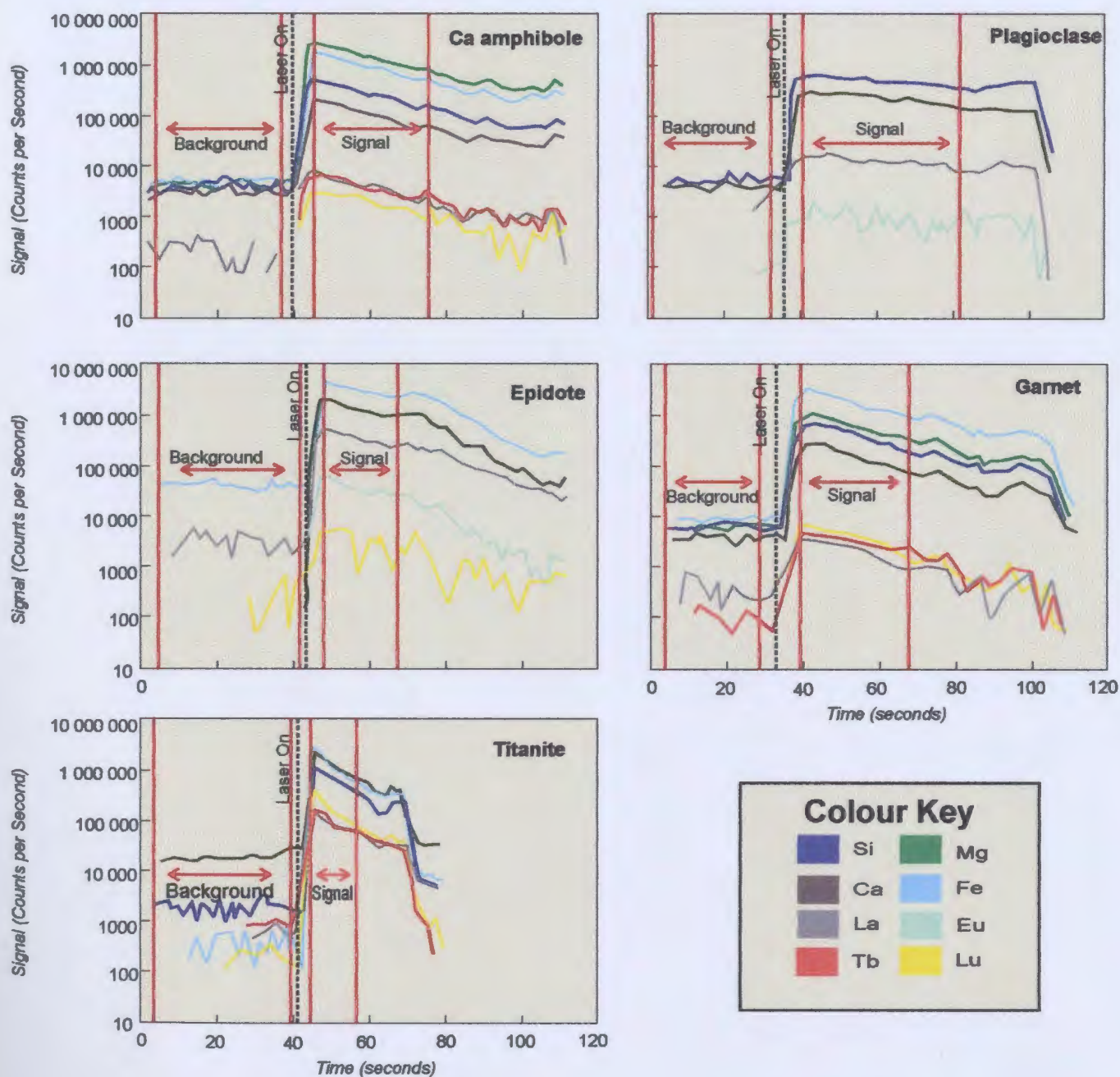


Figure A2 Representative LAMTRACE signal intensity (counts per second) vs time (seconds) plots for the five minerals analysed in this study. Final data were calculated by subtracting the integral of the signal from the integral of the background (indicated by red arrows between red vertical lines). Black dashed line denotes time at which laser was switched on.

Appendix C: Singular Value Decomposition Analysis

Calculation of the mass balance of the inferred epidote-out reaction isograd in this thesis was carried on by the method of singular value decomposition (SVD), which was introduced to geology with worked petrologic examples by Fisher (1989). SVD is based on a theorem of matrix analysis which says that any m by n matrix \mathbf{M} can be expressed as the product of a column orthogonal matrix \mathbf{U} , a diagonal n by n matrix \mathbf{W} , and the transpose of an orthogonal n by n matrix \mathbf{V} :

$$\mathbf{M} = \mathbf{U}\mathbf{W}\mathbf{V}^T \quad C\ 1$$

The number of non-zero diagonal terms in \mathbf{W} (i.e., singular values) gives the rank of \mathbf{M} , which is equivalent to the number of components (c) in the system. The columns of \mathbf{U} correspond to the non-zero terms in \mathbf{W} on an orthonormal basis for the composition space of \mathbf{M} . The columns of \mathbf{V} correspond to the zero diagonal elements of \mathbf{W} on an orthonormal basis for the null space (i.e., reaction space) of \mathbf{M} . Thus the reaction coefficients are given by the last column of \mathbf{V} , or the last row of \mathbf{V}^T .

The SVD of a matrix can be computed using various commercial software packages such as Mathematica®, which was used for the calculations in this thesis. The initial assumptions and starting compositions of the phases used in the SVD analysis are given in section 6.6.1. They result in the composite composition matrix \mathbf{M} shown in Table C.1.

Appendix C: Singular Value Decomposition Analysis

	Ca amp ₄₆	Pl ₄₆	Ep ₄₆	Ttn ₄₆	Ca amp ₄₉	Pl ₄₉	Ttn ₄₉
Ti	0.11	0.00	0.00	0.94	0.12	0.00	0.93
Al	2.11	1.31	2.30	0.05	2.26	1.40	0.07
Fe ³⁺	0.02	0.00	0.81	0.00	0.29	0.00	0.01
FeMgMn	4.48	0.02	0.01	0.01	4.18	0.03	0.00
Ca	1.76	0.34	2.03	1.01	1.94	0.48	0.99
NaK	0.61	0.68	0.00	0.00	0.79	0.47	0.00

Table C.1. Composition matrix formed by the phases in the inferred reaction isograd (columns) and the independent major-element components used to describe them (rows). Subscripts 46 and 49 refer to sample numbers of epidote amphibolite and plagioclase amphibolite respectively used in the reaction mass balance. Choice of independent components is discussed in the text.

The results of SVD analysis of this 7 phase by 6 component matrix are listed in Table A5. The number of singular values given by **W** is 6, indicating a rank of 6, which suggests that a univariant relationship exists between assemblages 46 and 49, therefore implying a mass balance. Since a univariant relationship exists for this 6 component, 7 phase system, there is no need to create a model matrix of lower rank to satisfy the mass balance condition of univariance as required by the phase rule.

As a side note, *if* this had been necessary, as is sometimes the case (see Gordon *et al.*, 1991; Hartel and Pattison, 1996), a model matrix **M'** could have been calculated by

setting the smallest singular value of \mathbf{W} to zero and then multiplying through by \mathbf{U} and \mathbf{V}^T following equation C 1. A measure of the adequacy of the model matrix \mathbf{M}' could have been evaluated by computing residuals resulting from the subtraction of \mathbf{M} from \mathbf{M}' . In turn, the residuals would then have been evaluated against a matrix σ consisting of analytical uncertainties by computing the ratio of the residuals to the analytical uncertainties of each element in each phase, giving a matrix σ' . In general, if the values of σ' are within three times the 1σ analytical uncertainties, the model matrix \mathbf{M}' is considered an adequate representation of \mathbf{M} . If this is the case, \mathbf{M}' can be then evaluated using SVD analysis.

These steps were avoided in the SVD analysis used in this thesis by simplifying the components in \mathbf{M} at the outset, as follows. The major-element compositions of phases in samples 46 and 49 were chosen to represent assemblages below and above the epidote-out isograd. Both samples contain quartz, i.e., SiO_2 -saturated, so Si was omitted from the composition matrix \mathbf{M} . Similarly, the assumption was made that both assemblages coexisted with an H_2O -rich fluid phase at the time of their crystallization, rendering the activity of H_2O unity in both assemblages. Both these assumptions underpin the widely used ACF diagram for metabasites and its proven utility over many decades indicates that they are not unrealistic in many metabasites. In addition, since Ca amphibole is the only phase that contains appreciable FeMg, the components were added. Finally, Mn and K, both present in negligible amounts, were included with FeMg and Na

respectively.

Since \mathbf{M}' was not computed in this analysis, there are no residuals to compare to \mathbf{M} . Thus, the adequacy of the model univariant mass-balance reaction was evaluated by summing the absolute values of the deviations from perfect mass balance for all elements, and comparing those values with the summed values arising from analytical uncertainties (see Table 6.3). All deviations were within three times 1σ analytical uncertainty so the mass balance was accepted.

The stoichiometrically-balanced model reaction was then used to evaluate the redistribution of *REE* and other trace elements across the epidote-out isograd. This was done by multiplying reaction coefficients by *REE* and trace-element concentrations for each phase on both sides of the reaction. The relative differences in the sum of *REEs* and trace elements between the reactant and product sides of the reaction were used to measure the adequacy of the mass balance (Tables 6.4 and 6.5).

Appendix C: Singular Value Decomposition Analysis

Table A5 Results of SVD analysis of compositional matrix **M** (see text) in the form of $\mathbf{M} = \mathbf{U}\mathbf{W}\mathbf{V}^T$ using the computer software Mathematica. Singular values italicized. Reaction coefficients underlined.

M	Ca amp ₄₆	Pl ₄₆	Ep ₄₆	Ttn ₄₆	Ca amp ₄₉	Pl ₄₉	Ttn ₄₉
Ti	0.11	0.00	0.00	0.94	0.12	0.00	0.93
Al	2.11	1.31	2.30	0.05	2.26	1.40	0.07
Fe ³⁺	0.02	0.00	0.81	0.00	0.29	0.00	0.01
FeMgMn	4.48	0.02	0.01	0.01	4.18	0.03	0.00
Ca	1.76	0.34	2.03	1.01	1.94	0.48	0.99
NaK	0.61	0.68	0.00	0.00	0.79	0.47	0.00

U

-0.0347114	0.1043650	0.6636270	-0.5028610	-0.0629775	-0.5391350
-0.4968610	0.5561890	-0.4937540	-0.1606760	-0.3073350	0.2823440
-0.0540091	0.1935990	-0.0201961	0.4762660	0.6883050	0.5085290
-0.7464170	-0.6515780	0.0470096	0.0822008	-0.0021870	0.0966249
-0.4156550	0.4663720	0.5209680	0.2423390	0.0709380	-0.5239840
-0.1382020	0.0149880	-0.2044050	-0.6549800	0.6502140	-0.2951550

W

7.770800	0.000000	0.000000	0.000000	0.000000	0.000000
0.000000	3.026390	0.000000	0.000000	0.000000	0.000000
0.000000	0.000000	1.771940	0.000000	0.000000	0.000000
0.000000	0.000000	0.000000	0.931580	0.000000	0.000000
0.000000	0.000000	0.000000	0.000000	0.220667	0.000000
0.000000	0.000000	0.000000	0.000000	0.000000	0.016199

V^T

-0.6708550	-0.1159620	-0.2622350	-0.0623807	-0.6663800	-0.1264310	-0.0616540
-0.2974500	0.2922070	0.7851810	0.1950940	-0.1590470	0.3271280	0.1981360
0.0189584	-0.3429820	-0.5302570	0.6353300	0.0020271	-0.3024090	0.6197520
0.0111877	-0.6138320	0.5463730	-0.2524090	0.0117523	-0.4444050	-0.2514330
-0.5888870	0.2882600	-0.0242917	-0.0133230	0.6326960	-0.4109320	-0.0134624
-0.2565330	-0.4356050	-0.0877330	-0.4539280	0.2751790	0.4904760	0.4630350

$$0.256533 \text{ Ca amp}_{46} + 0.435605 \text{ Pl}_{46} + 0.087733 \text{ Ep}_{46} + 0.453928 \text{ Ttn}_{46} \\ = 0.275179 \text{ Ca amp}_{49} + 0.490476 \text{ Pl}_{49} + 0.463035 \text{ Ttn}_{49}$$

Normalizing reaction coefficients to coefficient for Ca amp₄₆, the model reaction is:

$$1.00 \text{ Ca amp}_{46} + 1.70 \text{ Pl}_{46} + 0.34 \text{ Ep}_{46} + 1.77 \text{ Ttn}_{46} = 1.07 \text{ Ca amp}_{49} + 1.92 \text{ Pl}_{49} + 1.80 \text{ Ttn}_{49}$$

